Dynamical study of the exoplanets and debris disks revealed by SPHERE

Laetitia Rodet

▶ **To cite this version:**

Laetitia Rodet. Dynamical study of the exoplanets and debris disks revealed by SPHERE. Cosmology and Extra-Galactic Astrophysics [astro-ph.CO]. Université Grenoble Alpes, 2019. English. NNT : 2019GREAY033 . tel-02481239

HAL Id: tel-02481239

https://theses.hal.science/tel-02481239

Submitted on 17 Feb 2020

HAL is a multi-disciplinary open access archive for the deposit and dissemination of scientific research documents, whether they are published or not. The documents may come from teaching and research institutions in France or abroad, or from public or private research centers.

L'archive ouverte pluridisciplinaire **HAL**, est destinée au dépôt et à la diffusion de documents scientifiques de niveau recherche, publiés ou non, émanant des établissements d'enseignement et de recherche français ou étrangers, des laboratoires publics ou privés.

Communauté
UNIVERSITÉ Grenoble Alpes

THÈSE

Pour obtenir le grade de

DOCTEUR DE LA COMMUNAUTE UNIVERSITE GRENOBLE ALPES

Spécialité : **Astrophysique**

Arrêté ministériel : 25 mai 2016

Présentée par

Laetitia Rodet

Thèse dirigée par **Hervé Beust, Astronome, OSUG**, et
codirigée par **Mickaël Bonnefoy, Chargé de recherche, CNRS**

préparée au sein du **Laboratoire Institut de Planétologie et d'Astrophysique de Grenoble**
dans **l'École Doctorale de Physique - Grenoble**

Étude dynamique des exoplanètes et des disques de débris révélés par SPHERE

Thèse soutenue publiquement le **3 septembre 2019**,
devant le jury composé de :

Mme, Carine, BABUSIAUX
Astronome à l'IPAG - Grenoble, Présidente
M., Aurélien, CRIDA
Maître de conférence à l'UNS - Nice, Rapporteur
M., Matthew, KENWORTHY
Professeur à l'Observatoire de Leiden - Pays-Bas, Rapporteur
M., Jean-Charles, AUGEREAU
Astronome à l'IPAG, Examinateur
Mme, Beth, BILLER
Professeure à l'Université d'Édimbourg - Royaume-Unis, Examinatrice
M., Markus, JANSON
Professeur à l'Université de Stockholm - Suède, Examinateur
Mme, Anne-Marie, LAGRANGE
Directrice de recherche à l'IPAG - Grenoble, Examinatrice
M., Dong, LAI
Professeur à l'Université Cornell - USA, Examinateur

Acknowledgments

This thesis was extremely enriching for me in many regards, thanks to the contribution of numerous people.

First of all, I would like to thank the members of the jury, especially the referees Aurélien Crida and Matthew Kenworthy and the president Carine Babusiaux, for accepting to spend time and energy evaluating my work. I would also like to thank Dong Lai for offering me a post-doc offer at Cornell University, allowing me to experience research and life in the United States in a prestigious environment.

Of course, I would like to thank my two advisors, Hervé Beust and Mickaël Bonnefoy. They accepted to hire me as a Ph.D. student even if I knew barely anything of astrophysics or numerical methods at that time. I learned a lot from their complementary teaching, and their support opened many doors for my future career. I am also thankful that they encouraged me to keep a balanced life by having decent working hours, avoiding work on week-ends and taking vacations; in a world that has become so competitive, what should be considered normal has too often become a luxury that we dare not afford.

My Ph.D. went well also because of the nice working environment: a friendly team, a dedicated follow-up by the members of my CSI, Alain Lecavelier des Étangs, Geoffroy Lesur and Estelle Moraux, and by the GAD, that looks after the well-being of Ph.D. students, a very helpful and understanding technical and administrative group, and the people of all the lab with which we shared lunch and festive events.

I would like to mention more particularly my fellow Ph.D., post-docs and interns comrades, for the great friendly atmosphere and intense chats. Special thanks to my co-bureau Nico for fruitful discussions on a very wide range of subjects, from a colander full of screws to the meaning of life. For everyone, I hope that pragmatism will not crush our idealism.

Finally, I would like to thank my family, that always encouraged my scientific interests while giving me freedom and trust, my friends, with deep and long-lasting complicities that large distances could not attack. Last but not least, I am grateful to the everyday presence of Étienne by my side, whose brightness, passion and convictions make my life meaningful.

Abstract

Several decades after the discovery of the first debris disks and exoplanets, lots of questions remain regarding the mechanisms of formation and evolution of planetary systems. The recent progress of high-resolution high-contrast direct imaging, illustrated by the instruments VLT/SPHERE and Gemini/GPI, enables the astrophysicists to unveil the outer architecture (> 5 au) of young (< 200 Myr) extrasolar systems when the dynamical interactions are frequent. This work sheds light on the origin and dynamical evolution mechanisms of planetary systems through the detailed study of key systems resolved with SPHERE and through the developing of dedicated tools.

The first part of this manuscript tackles the subject of N-body simulations. Numerous algorithms have been proposed and implemented, with different compromises on their speed, accuracy, and versatility. Among these algorithms, SWIFT HJS allows us to model for secular times architectures that are very different from our Solar System. It is thus an essential tool to the study of planetary to stellar companions with non-negligible mass ratio, which are often encountered with direct imaging. Within my Ph.D., the functionalities of the algorithm were extended to handle hierarchy changes and close encounters, which can play an important part in the dynamical history of planetary systems. The code was used to study in detail the puzzling system HD 106906, in particular, the interactions between its main components (binary star, planet, debris disk).

In the second part of the manuscript, I introduce the subject of orbital fitting. The observation of a system at different epochs allows theoretically the retrieval of the orbital characteristics. However, the problem is often complex and degenerate, in particular when the observations span a small fraction of the orbital period. The widely used MCMC statistical approach gives robust estimates in most of the cases. These estimates are then used to study the history and stability of the system, and the interactions between orbits and with the environment, notably the disks. This role of orbital fitting is here illustrated by the study of several benchmark systems imaged with SPHERE.

Résumé

Plusieurs décennies après l'identification des premiers disques de débris et des exoplanètes, les mécanismes de formation et d'évolution des systèmes planétaires sont encore loin d'être élucidés. Les récents progrès de l'imagerie directe à haute résolution et haut contraste, illustrés par les instruments VLT/SPHERE et Gemini/GPI, nous permettent désormais de révéler et d'étudier en détail l'architecture externe ($>$ 5 ua) des systèmes extrasolaires jeunes ($<$ 200 Myr), à un âge où les interactions dynamiques sont encore fréquentes. Mon travail de thèse apporte un éclairage sur l'origine et les mécanismes d'évolution dynamique des systèmes planétaires à travers l'étude détaillée de systèmes clefs résolus par SPHERE et le développement d'outils de modélisations dédiés.

La première partie de ce manuscrit aborde l'étude dynamique via les simulations N-corps. De nombreux algorithmes ont été proposés et implémentés, avec des choix de compromis différents sur leur vitesse, leur précision et leur polyvalence. Parmi ces algorithmes, SWIFT HJS permet de modéliser des architectures très différentes de notre Système Solaire sur des temps séculaires. C'est donc un outil essentiel pour étudier l'influence des planètes massives, naines brunes et compagnons stellaires souvent rencontrés en imagerie directe. Durant ma thèse, les fonctionnalités de l'algorithme ont été étendues pour pouvoir modéliser les changements de hiérarchie et les rencontres proches, des aspects de la mécanique orbitale qui ont souvent un rôle crucial dans l'histoire dynamique des systèmes planétaires. Ce code a notamment été utilisé pour étudier en profondeur l'énigmatique système HD 106906 et les différentes interactions entre ses principaux composants (binaire, planète, disque de débris).

Dans la deuxième partie du manuscrit, j'introduis la problématique de l'ajustement orbital. Si l'observation d'un système à différentes époques permet théoriquement de retrouver les caractéristiques de son orbite, le problème peut se révéler complexe et dégénéré, en particulier quand le temps d'observation est insuffisant pour correctement échantillonner l'orbite. L'approche statistique la plus couramment adoptée, le MCMC, permet d'obtenir des estimations fiables dans la plupart des cas. Ces estimations sont ensuite exploitées pour étudier l'histoire et la stabilité du système et les interactions entre orbites et avec l'environnement, notamment les disques. Ce rôle de l'ajustement orbital est ici illustré dans les études de plusieurs systèmes de référence, imagés par SPHERE.

Contents

Introduction **9**
1 Extrasolar systems . . . 10
1.1 Stars in Moving Groups . . . 10
1.2 Multiple systems . . . 11
1.3 Planets and Brown Dwarfs . . . 12
1.4 Disks . . . 14
2 Formation and Evolution . . . 15
2.1 Stars . . . 15
2.2 Planets . . . 17
3 Direct imaging . . . 20
3.1 State of the art . . . 21
3.2 SPHERE . . . 22
3.3 Science: Planets and disks . . . 23
4 Dynamics . . . 24
4.1 2-body problem: notations and resolution . . . 24
4.2 Hamiltonian representation . . . 27
4.3 Jacobi coordinates . . . 29
4.4 Perturbed 2-body problem, Lagrange equations . . . 29
4.5 Secular approximation and Hamiltonian maps . . . 30
4.6 Mean-Motion Resonances (MMR) . . . 32
4.7 Perturbation in a debris disk . . . 34
4.8 Stellar fly-by . . . 35
4.9 Close encounters . . . 37
5 Summarized Context . . . 37

1 N-body simulations of extrasolar systems **39**
1 State of the art . . . 40
1.1 Available codes . . . 40
1.2 Classical integrators . . . 42
1.3 Symplectic integration . . . 45
1.4 SWIFT HJS . . . 54
1.5 Non-Keplerian forces . . . 57
2 Code development . . . 58
2.1 Development of surrogate tools for `Swift HJS` . . . 58
2.2 Handling hierarchy change . . . 61
2.3 Handling close encounters . . . 68

3 Understanding the peculiar architecture of the system HD 106906 . . 79
3.1 Investigating the dynamical evolution 81
3.2 Refining the scenario 97

2 Orbital fitting of imaged companions 112
1 Levenberg-Marquardt algorithm (LM) 115
2 Markov Chain Monte Carlo (MCMC) 117
2.1 Overview 117
2.2 The Metropolis-Hastings algorithm for transition probability . 117
2.3 Guiding the walk in multiple dimensions: the Gibbs sampler . 119
2.4 Evaluation of the convergence 120
2.5 Beginning the walk 121
2.6 Building a consistent sample 121
3 Application to orbital fitting 122
3.1 Likelihood 122
3.2 Prior distributions 123
3.3 Choice of the MCMC parameters 125
3.4 Analysis 126
3.5 Comparison with alternative approaches for orbital fitting . . 129
4 Improvements 132
4.1 Modular organization 132
4.2 Convergence 133
4.3 Analysis of the chains 133
4.4 Handling systematic offsets between data sets 136
5 Application to the characterization of companions observed with SPHERE137
5.1 HR 2562: A brown dwarf carving a debris disk 137
5.2 51 Eri: An eccentric giant planet in a hierarchical system . . . 153
5.3 HD 206893: An intriguing brown dwarf 169
5.4 HD 100453: A stellar companion shaping a protoplanetary disk?173
5.5 GJ 504: two different ages and a possible obliquity 177
6 Application to the astrometric binaries 181
6.1 TWA 22: good accordance with evolutionary model predictions182
6.2 GJ 2060: underluminous and eccentric binary in the AB Dor moving group 182
6.3 AB Dor B: toward empirical isochrones for the AB Dor moving group 208
7 Combining absolute and relative astrometry 211

Conclusion and Perspectives 219

Bibliographie 222

Appendix 232
1 Definition of the orbital elements 232
2 Solving the Kepler equation 234
3 Perturbation by an inner companion 235

Introduction

Contents

1 Extrasolar systems 10
1.1 Stars in Moving Groups 10
1.2 Multiple systems 11
1.3 Planets and Brown Dwarfs 12
1.4 Disks 14
2 Formation and Evolution 15
2.1 Stars 15
2.2 Planets 17
3 Direct imaging 20
3.1 State of the art 21
3.2 SPHERE 22
3.3 Science: Planets and disks 23
4 Dynamics 24
4.1 2-body problem: notations and resolution 24
4.2 Hamiltonian representation 27
4.3 Jacobi coordinates 29
4.4 Perturbed 2-body problem, Lagrange equations 29
4.5 Secular approximation and Hamiltonian maps 30
4.6 Mean-Motion Resonances (MMR) 32
4.7 Perturbation in a debris disk 34
4.8 Stellar fly-by 35
4.9 Close encounters 37
5 Summarized Context 37

Before entering into the details of my work on the dynamical study of extrasolar systems, this chapter aims to review the present understanding of extrasolar systems, the open questions regarding their formation and evolution, and the role taken by the direct imaging approach. It also introduces the mathematical tools that are needed to study orbital mechanics, along with the different mechanisms that are known to significantly excite the orbits.

1 Extrasolar systems

Our knowledge about extrasolar systems has dramatically increased for the last two decades. The huge samples of stars that were characterized by the latest large surveys (Hipparcos, 2-MASS, Gaia) enable the computation of robust statistics. On the other hand, though new planets are discovered on a daily basis, our knowledge about the architecture of planetary systems is still sparse because a large part of the planetary population remains undetected by the large-scale surveys. I will here present an overlook of the present understanding of stellar and sub-stellar objects, and in particular of the characteristics that are relevant for their dynamical study (masses, multiplicity, separations, eccentricities...). Because of the observational constraints induced by direct imaging (angular separation, contrast), most of the studies that I performed targeted systems in nearby young moving groups. I will thus begin the introduction with this topic.

1.1 Stars in Moving Groups

Most of the stars form in clusters, as these are the leftovers of the huge molecular clouds in which star formation takes place (Porras et al. 2003). If the old age of the Solar System does not provide robust certainties about its conditions of birth, several features (abundances, architecture) hint for past interactions with neighboring stars, suggesting a dense native region (Pfalzner et al. 2015). Depending on the density and structure of these clusters, their evolution and interest significantly differ.

Stellar associations or moving groups are collections of stars that, by their clustering and their similarities (chemical composition, similar velocities), are thought to originate from a common birth. Contrarily to the globular and open clusters, the members of moving groups are not bound. The life expectancy of the structure is thus reduced (often less than 100 Myr). Their density is thought to be only slightly superior to the density of the field (e.g., Fernández et al. 2008; Rodet et al. 2017). A variety of comoving stellar groups near the Sun have been identified in the last decades, such as the ~ 25 Myr old β Pictoris moving group or the $50-150$ Myr old AB Doradus moving group (Zuckerman & Song 2004). New members are regularly added, as more stars have their kinematics unveiled by the various observational surveys (such as Gaia, Gagné & Faherty 2018)

Very young associations that contain a significant number of the short-lived (10-100 Myr) O and B-type stars are known as OB associations. The closest one is the Scorpius-Centaurus (Sco-Cen) association (100 pc, De Zeeuw et al. 1999), which is actively studied and comprises directly imaged planets, brown dwarfs and debris disks (e.g.; Bailey et al. 2014; Chauvin et al. 2017; Bonnefoy et al. 2017).

Because the cluster members are of similar age and chemical composition, their property (such as distance, age, metallicity, velocity...) are more easily determined than they are for isolated stars. Moreover, the known moving groups are young and nearby, which makes them ideal targets for direct imaging, because the angular separation of the companions is then larger and their contrast is enhanced by the thermal heat gained at formation. Observing the systems at young age allows putting constraints on the formation and evolution pathways. The members of young moving groups are thus a natural target for deep characterization, model calibration and eventually for the search of exoplanets. Most of the systems studied in this thesis are members of young moving groups (Sco-Cen, AB Doradus, β Pictoris).

1.2 Multiple systems

Planetary formation is not inhibited by stellar companions, as multiple systems have been found to host planets. Several of them have been discovered in the last decade, whether orbiting one star with a distant companion (S-type, e.g., Doyle et al. 2011) or orbiting the center of mass of a binary (P-type, e.g., Bonavita et al. 2016). Dynamical interactions with the companion might induce eccentricity and inclination variations. Due to the high proportion of multiple stars and the rich dynamics within, the study of planets in non-single systems is a growing field (e.g., Martin 2018; Asensio-Torres et al. 2018) and takes up a significant part of my work, from the design of specific numerical tools to the study of the system HD 106906 (Chapter 1).

The multiplicity frequency of the different types of stars is now well constrained (see Fig. 1), thanks to dedicated surveys using both spectroscopic and visual observations. A bit less than half of Solar-type stars (Raghavan et al. 2010) and more than half of higher mass stars are multiple (Duchêne & Kraus 2013). On the other hand, low-mass stars (< 0.5 $M_\odot$) are very common, but they appear to have the lowest fractions of multiple systems, less than a third (Delfosse et al. 2004; Dieterich et al. 2012). Triple and higher-order systems represent about 25% of all solar-type multiple systems (Duchêne & Kraus 2013). To maintain their stability, there are organized within a strictly hierarchical scheme, with high period ratios.

Characterizing the orbital features of multiple stars are important, as eccentric or inclined stellar companions induce dynamical perturbations in planetary systems if the semi-major axes ratio is neither too small nor too large. The orbital features of binary stars are not strongly constrained, but their eccentricity distribution suggest a flat distribution (see Fig. 1) and their separation seems to follow the simple Opik's law (logarithmically-flat distribution, $f(a) \sim 1/a$, Kouwenhoven 2006).

Most of the time, the multiplicity of directly imaged systems is not well constrained, because tight binaries are not resolved. Some observational programs are now dedicated to the radial velocity monitoring of the stars targeted by direct imaging, in search of planetary or stellar companions at close separations (Lagrange et al. 2013). HD 106906 is a perfect example of such case, where the planet was discovered before the binary status of the host star (Bailey et al. 2014; Lagrange et al. 2019).

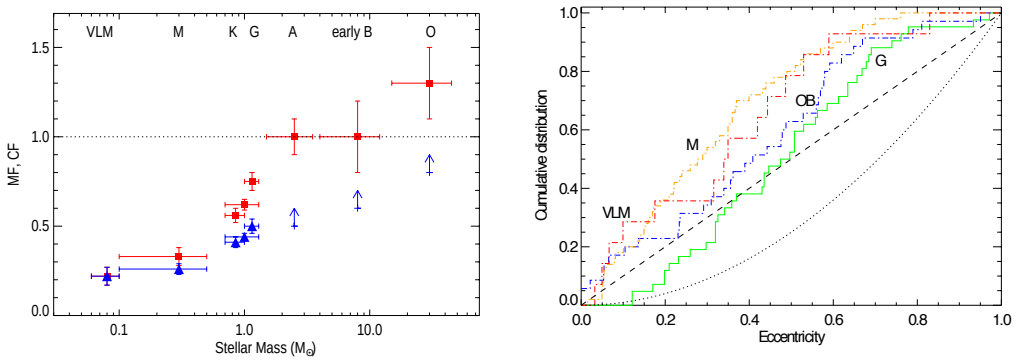

Figure 1 – Multiplicity (blue) and companion (red) frequency with respect to stellar mass (left) and cumulative eccentricity distribution for various types of stars (Very Low Mass, M-type, G-type and OB-type), by comparison with a flat (dashes) or thermal (dots) distribution (right). The figures are from Duchêne & Kraus (2013).

1.3 Planets and Brown Dwarfs

Until 1995 and the discovery of 51 Peg b, the first exoplanet around a main-sequence star, the Solar System was our only laboratory to comprehend our origins, and in particular the planets' formation and dynamical evolution. With almost 4,000 exoplanets confirmed in more than 2,000 systems to date[1], we are now able to apprehend the planetary population beyond the Solar System framework, and henceforth we acquired the certainty that planets are ubiquitous, that the Solar System is far from being the norm among planetary systems, and that planetary systems exhibit an unexpected diversity (Winn & Fabrycky 2015).

Exoplanets are now mainly revealed by their primary transit detected by space-based telescopes (Corot, Kepler/K2, TESS). This method enables the retrieval of robust statistics on the population of (edge-on) short periods planets, from Earths to giant planets. It also revealed several Earth-sized planets within the habitable zone of M-dwarf stars (Gillon et al. 2016; Bonfils et al. 2018). The second most fruitful technique is Doppler spectroscopy, an indirect approach that makes use of the variation of the host star's radial velocity to probe the short periods planets at any inclination (except face-on). Additionally, planets may be detected by the small gravitational lens effect that they create when transiting a background star (microlensing), or by the monitoring of the host star's wobble on the skyplane (astrometry). Complementary to these indirect methods, direct imaging uniquely allows the probing of the population of giant planets at large orbital radii where the indirect techniques are inefficient (> 5 au) and to conduct in-depth spectro-photometric characterization of their physical and atmospheric properties (see Sec. 3).

Different types of planets have been identified so far: the more numerous small-mass planets (Earth, Super-Earth and Neptune-mass, with $M \lesssim 30\ M_\oplus$ and $R \lesssim 4\ R_\oplus$) and the giant planets (Jupiter to Super-Jupiter). Among these, the distribution of mass is not uniform and is not entirely understood, as for the radius

[1] according to the extrasolar planets encyclopedia `http://exoplanet.eu`

gap evidenced around 2 $R_\oplus$ in Kepler data (Fulton et al. 2017).

The latest results of these surveys indicate that the occurrence of planets around main-sequence stars is high: at least 75 % within 10 yr of orbital period (Mayor et al. 2011), and about 30 % for Super-Earths ($R \gtrsim 2\ R_\oplus$) within 400 days (Zhu et al. 2018), which do not exist in our Solar System. Low mass planets are mostly distributed between 10 and 100 days (Mayor et al. 2011). Giant planets are significantly less abundant than the smaller planets, with a probability of around 10% within orbital periods of a few years. Though the first detected exoplanet, 51 Peg b, was a so-called hot Jupiter (with a period shorter than 10 days), this population appears to be quite rare ($\lesssim 1\%$, Mayor et al. 2011).

Correlations between the presence of planets and the property of the host stars are also being investigated. The studies suggest that giant planets are associated with higher heavy-element abundance (Fischer & Valenti 2005) and more massive stellar hosts (Johnson et al. 2010; Nielsen et al. 2019). Such constraints are important to discriminate different formation pathways (see Sec. 2).

As the orbital characteristics are often not well constrained, the distribution of the eccentricity and its correlation to the mass and separation is not entirely understood yet. From the radial velocity surveys, it appears that the low eccentricities in the Solar System are not standard. Exoplanets can orbit on very eccentric orbits (up to ~ 0.9!), especially the giant planets that have periods longer than 100 days. On the other hand, the closest planets have been circularized by tidal effects with the host stars and exhibit very low eccentricities (Mayor et al. 2011; Winn & Fabrycky 2015).

Similarly, the planetary orbital momentum can be significantly misaligned (even retrograde) with the stellar axis of rotation (high obliquity, Winn & Fabrycky 2015). High obliquities are correlated with high temperature of the star and low tidal parameters, suggesting a complex entanglement of the different physical processes at stakes (e.g., Lai 2012).

The findings of significantly eccentric planets or planets with high obliquity contradict the expectations from the planetary formation theories, that predict formation within the stellar rotation plan and circularization of the orbits through interactions with the protoplanetary disk. Therefore, planetary synthesis models are now taking into account the further dynamical evolution of the system to retrieve the observed population (see Sec. 2).

Brown dwarfs are substellar objects that fuse deuterium, but cannot sustain the fusion of ordinary hydrogen. Their masses range from the upper limit of the planet realm ($\sim 13\ M_J$) to the very-low-mass stars ($80\ M_J$), although the significance of the mass frontiers is often debated (see Sec. 2). Theoretically predicted by Kumar (1962), the first companion brown dwarf, GL 229 B, has been discovered in the same year than 51 Peg b. Since then, the infrared catalogs (2-MASS,...) exhibited numerous isolated brown dwarfs. The frontier between giant planets and brown dwarfs is blurred (Chabrier et al. 2014), in particular since the discovery of planetary mass companions at very wide orbits, companion brown dwarfs with a planetary-like mass ratio (see Fig. 2) or isolated planetary-mass objects (e.g., Gagné et al. 2018). The difference between planets and brown dwarfs is also found in the occurrence rate: brown dwarfs companions are much rarer than their planetary counterpart at

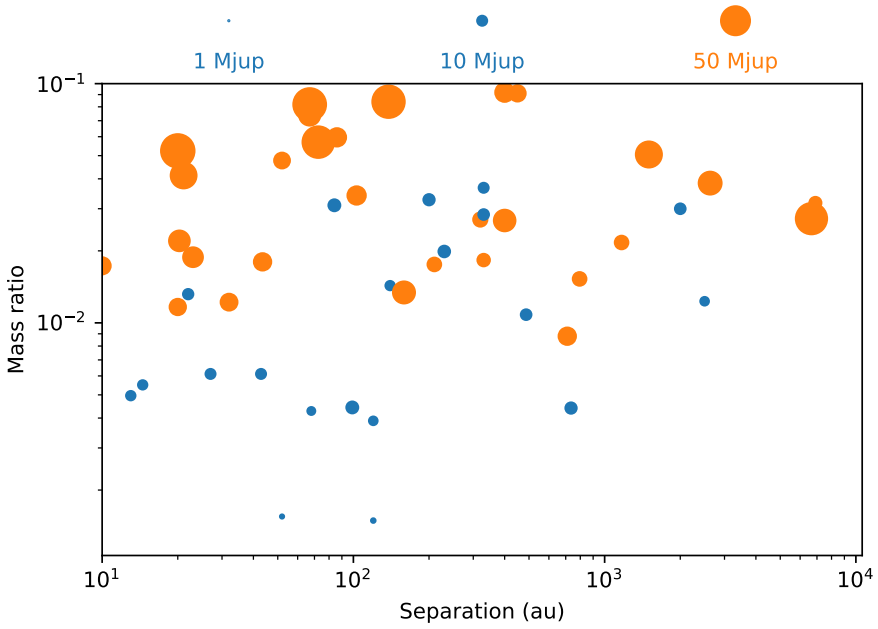

Figure 2 – Mass ratios with respect to separation for the known companions with separations greater than 10 au and mass ratios below 0.01. Data taken from exoplanet.eu. Objects below 13 M_J are depicted in blue (planets), those above are depicted in orange (brown dwarfs).

short separations ($< 1\%$ around Solar-type stars). This lack is referred to as the brown dwarf desert and has been observed in multiple observational surveys. They suggest separate formation mechanisms between planetary and stellar companions (Sahlmann et al. 2011; Chabrier et al. 2014).

In my PhD, I was involved in the study of directly imaged companions. I describe in more details the population observed with this technique in Sec. 3.

1.4 Disks

Protoplanetary disks are circumstellar disks of dense gas and dust that surround the young stars in the first million years of their life (Haisch et al. 2001). Strong uncertainties remain regarding their structure, notably their density profile and their viscous properties (Morbidelli & Raymond 2016). Their study is essential to the understanding of the formation and early evolution of planetary systems, notably the accretion process (see Sec. 2) and the interaction between the gas and dust and the orbits (e.g., migration). Different steps of planetary formation have been imaged by ALMA (gap carving in HL Tau, Brogan et al. 2015) and SPHERE (accretion in PDS 70, Keppler et al. 2018)

After a few million years, the gas is progressively accreted by the star or the planets, or photo-dissociated and dismissed into the interstellar medium. Transition disks are thought to trace this key step in the disk lifetime. They are characterized by a gap in the spectral energy distribution, hinting for a large cavity opened within the disk, that for some systems has been resolved (van der Marel et al. 2018). This is notably the case of the system 10-Myr system HD 100453, that is characterized in van

der Plas et al. (2019) (Chapter 2 Sec. 5.4), or of the 5-Myr-old system PDS 70, for which two planets has been resolved in the cavity (Keppler et al. 2018; Haffert et al. 2019). In the general case, the processes and time necessary for a protoplanetary disk to loose all its gas and become a debris disk is not well understood yet, as cavities are not necessarily populated by planets (van der Marel et al. 2018) and as the collisions of planetesimals are creating gas in parallel (Kral et al. 2017; Hughes et al. 2018).

Debris disks are the remnants of planet formation processes. They mainly consist of small dust particles resulting from ongoing collisional cascades from kilometer-sized parent bodies. Therefore, the presence of these disks indicates that the formation process led to large bodies, and potentially planets. At least 20 % of Sun-like exoplanet host stars harbor debris disks (Marshall et al. 2014), including the Solar System (asteroid and Kuiper belts).

The dust particles composing the disk emit according to their temperature, and scatter the light of the host star in wavelengths comparable to their size. The temperatures of the dust ranges from 1500 K (close-in, also called exozodies) to 50 K in the outer parts of the disk. In the visible or near-infrared bands (SPHERE, ...) the stellar flux dominates the thermal emission of the dust, so that the main contribution of the dust comes from the scattered light of micron-size dust particles. Infrared excess in the Spectral Energy Distribution (SED) of a system is thus a good indicator of the presence of debris disks.

Dusty systems are thought to be better candidates to harbor giant planets, so that some direct imaging surveys are targeting them in priority to improve the yield (Meshkat et al. 2017), given the low occurrence of giant planets at long separation. To further increase the occurrence, some surveys aim for debris disks with unusual features, which are often caused by dynamical interactions with a companion. Eleven planets or brown dwarfs in eight different systems have been imaged so far around young stars with debris disks (see Fig. 6), among which the system HD 106906 that I have been extensively studying (Chapter 1).

The study of debris disks has developed along with the study of exoplanets, as it allows the probing of the neighborhood of a planet, hints for additional companions, or give constraints on the mass or orbital elements (Wyatt 2018). Contrary to the protoplanetary disk case, the interaction between planets and dust can be efficiently modeled by non-viscous N-body dynamics, and several features can be computed with analytic or semi-analytic configurations (see Sec. 4.7).

2 Formation and Evolution

2.1 Stars

Stars are thought to form inside giant molecular clouds. Over millions of years, they gradually collapse and fragment to form small, dense protostars and their accretion disk. Different collapsing mechanisms take place depending on the density of the cloud, and the link between the cloud geometry, the core mass function and the initial mass function is still to be clarified (Motte et al. 2018).

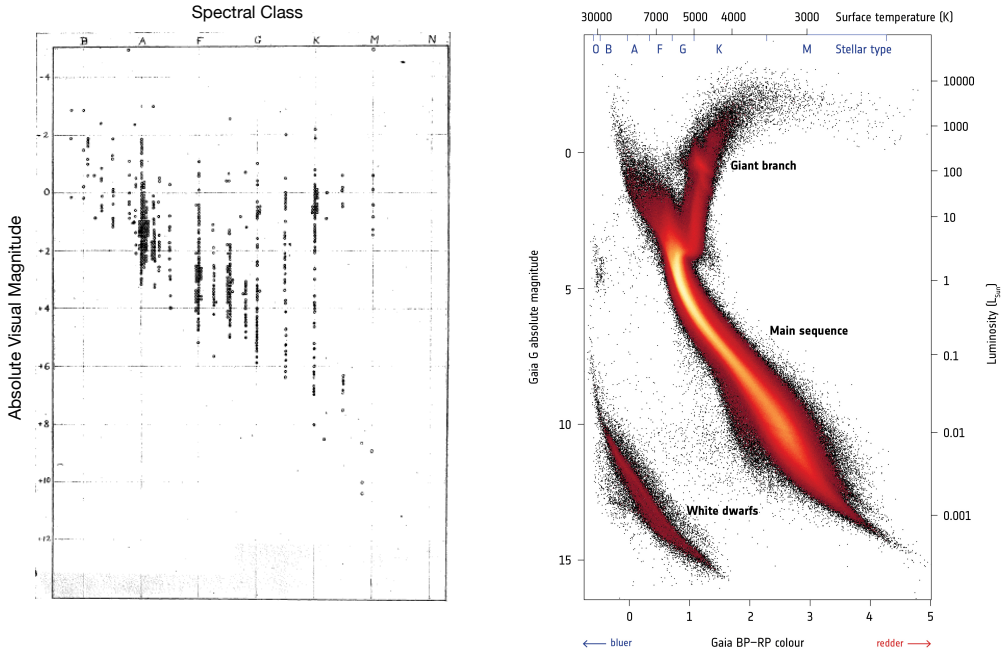

Figure 3 – Hertzsprung-Russel Diagram: (left) original from Russell (1914) and (right) derived from Gaia DR2. Picture published by the Gaia Data Processing and Analysis Consortium.

At the beginning of the 20$^{\text{th}}$ century, Ejnar Hertzsprung and Henry Norris Russell represented the stars on a luminosity-temperature diagram, now called the Hertzsprung-Russell diagram (HRD), and evidenced a pattern in the distribution: the main-sequence. Our statistics and understanding of stellar evolution have made a lot of progress since then (see Fig. 3). The beginning of a star's life, before it reaches the zero-age main sequence, has been in particular deeply investigated through the development of evolutionary models. The latter rely on equations of state describing the stellar interior structure and can make use of atmospheric models to define boundary conditions and predict emergent spectra. Different families of models exist (e.g., Siess et al. 2000; Feiden et al. 2015; Baraffe et al. 2015), ranging from very low mass (0.01 $M_{\odot}$) to massive (7 $M_{\odot}$) stars. Some account for the pre-main sequence phase, but most describe the main-sequence evolution extending to Gyr time-scales. Their physical and chemical ingredients (e.g., nuclear rates, opacity, atmospheric parameters) are frequently updated to account for the newest observations (e.g., Baraffe et al. 2015). The models relate the age and mass of stellar and substellar objects to the measured broadband photometry, surface gravity, radius, luminosity, and effective temperature. They are therefore a key tool for estimating the mass from the measured luminosity of any imaged objet.

The models predictions still need to be calibrated in various mass and age regimes (e.g., Hillenbrand & White 2004; Mathieu et al. 2007). Uncertainties related to the object formation process (early accretion history, etc.) exist in the pre-main sequence (PMS) regime (Baraffe et al. 2002). Further uncertainties may be added for low-mass

stars, which have strong convection, rotation and magnetic activity (Mathieu et al. 2007; Somers & Pinsonneault 2015). The calibration of models for young low-mass stars is treated in more details within Rodet et al. (2018) in Chapter 2 Sec. 6. Such understanding is essential to properly constrain the age and mass of young stars. Moreover, the evolutionary models of giant planets directly derive from the models of low-mass stars, so that calibrating the latter can help to constrain the former.

2.2 Planets

The extremely diverse physical and orbital characteristics of exoplanets led to frequently revise the scenarios for planet formation, as most features of their observed distributions are not yet accounted for.

2.2.1 Formation

Contrary to the stellar formation, which takes place at the center of a collapsing gas cloud, the planetary formation occurs within the circumstellar disks forming around the protostar as a consequence of angular momentum conservation. Several formation paradigms are currently proposed.

The most conventional is the core accretion scenario (Pollack et al. 1996), which is the privileged choice for the planets of our Solar System. In this model, planets begin their formation with the settling and growth of dust grains in the disk mid-plane, that will slowly accrete each other to form planetesimals. When they reach approximately 1,000 km in diameter, the accretion slows down (oligarchic and chaotic growth) until the dispersion of the disk gas, and the final formation of rocky planets or planetary cores (Baruteau et al. 2016). This formation mechanism is consistent with the observed correlations between planets and stellar host metallicity (Santos et al. 2004; Mulders 2018). If the protoplanets reach sufficiently high mass ($10 - 15$ $M_\odot$) within the lifetime of the protoplanetary disk ($\lesssim$ 10 Myr), they can further accrete gas and become the cores of giant planets. The growth of the core depends on the separation and disk density, and traditional core accretion fails to produce planets at large separations, for the formation timescale would then exceed the lifetime of the protoplanetary disk (Baruteau et al. 2016). Taking into account migration processes in the core-accretion model has the potential to speed up core growth (Mordasini et al. 2009). However, this strongly depends on the migration rate, that is currently poorly constrained (Baruteau et al. 2016). On the other hand, a new model for the accretion of solids has been recently proposed, called pebble accretion, which can form planetary cores in a more efficient way (formation of an earth-mass core in some thousands of orbits, which is less than 1 Myr even at tens of astronomical units). Still, the processes driving the growth of macroscopic particles remain poorly understood (boucing barrier, meter-size barrier), which prevents us to predict effectively when, where and how many protoplanets form in a disk (Morbidelli & Raymond 2016). Nevertheless, the core accretion scenario predicts low eccentricities and low inclinations, due to planet-disk interactions. Plus, the runaway accretion needed to accrete gas on giant planets are though to be possible only beyond the "snow line", at a few astronomical units, where water exists as a solid (Winn & Fabrycky 2015).

On the other hand, the gravitational instability scenario is a faster process ($\sim$ 1,000 yr) that is able to form giant planets at large separation from an instability in the protoplanetary disk (Boss 1997). The relatively recent discoveries of massive planets at large separations relived this theory, which was otherwise not favored for the planets of the Solar system. In this model, the protoplanetary disk fragments into dense clumps in its outer parts (typically 50 to 100 au). This pathway could lead to the formation of planets in some tens of orbital periods, which is significantly faster than the core accretion scenario. The so-formed giant planets could have no solid core. This is a good candidate formation mechanism to account for the discovery of giant planets and brown dwarfs at tens or hundreds of astronomical units, although it remains controversial and consistent models are still developing to include the effects of the magnetic fields (Chabrier et al. 2014). Like the core-accretion scenario, gravitational instability cannot account for high eccentricities and inclinations (Winn & Fabrycky 2015). Tidal downsizing scenario has been recently proposed to form the planets at short separations and to account for the lack of giant planets at large separations ($>$ 50 au). This theory includes gravitational instability, strong migration and tidal disruption of the gaseous clumps, and can produce giant planets as well as stellar companions and rocky planets (Nayakshin 2017).

Finally, collapse within the protostellar core phase, like multiple stars, is a plausible option to account for the observations of very wide or even isolated brown dwarf companions and planetary-mass objects, that could have not formed a priori within the disk of a star (Sumi et al. 2011; Gagné et al. 2014, 2018). The distribution of masses of such companions would likely resemble the low-mass end of the stellar initial mass function (Chabrier et al. 2014).

A better description of the mass and separation distribution of planets will help to discriminate the formation scenarios, although the observed distributions will reflect both the formation and dynamical evolution of the systems. The system HD 106906 Bailey et al. (2014) is a perfect example of this complexity: the very wide separation of the planet suggests a star-like formation pathway, but a planet-like formation might be possible if the planet underwent a dynamical scattering (see Chapter 1 Sec. 3).

2.2.2 Physical evolution

Much effort has been devoted to the modeling of sub-stellar objects during the past decades, improving our knowledge of their evolutionary properties and their atmospheres. Theoretical models can now predict the characteristic properties of the exoplanets mass, radius and atmospheric signature. Evolutionary tracks have been computed, adapted to various mass ranges, dust proportions (so-called DUSTY or COND models), and atmosphere compositions (Chabrier et al. 2000; Baraffe et al. 2003; Mordasini 2013). Many points remain badly understood, as spread and discrepancies from the theoretical predictions are regularly observed, such as inflated radii or spectral reddening (see the study of HD 206893, Chapter 2 Sec. 3) (Baraffe et al. 2010). For the moment, substellar evolutionary models focus on the description of giant planets and brown dwarfs, and derive in part from the physics of stellar models.

After the accretion, a new-born planet cools down, significantly in the beginning of its life, in times ranging from 10 Myr for small planets to a few 100 Myr for the more massive. In principle, we can then derive the mass and the radius from the spectroscopy and photometry, through comparisons with theoretical spectra. However, the theoretical models strongly depend on the physics of the gas accretion phase (e.g., Cumming et al. 2018).

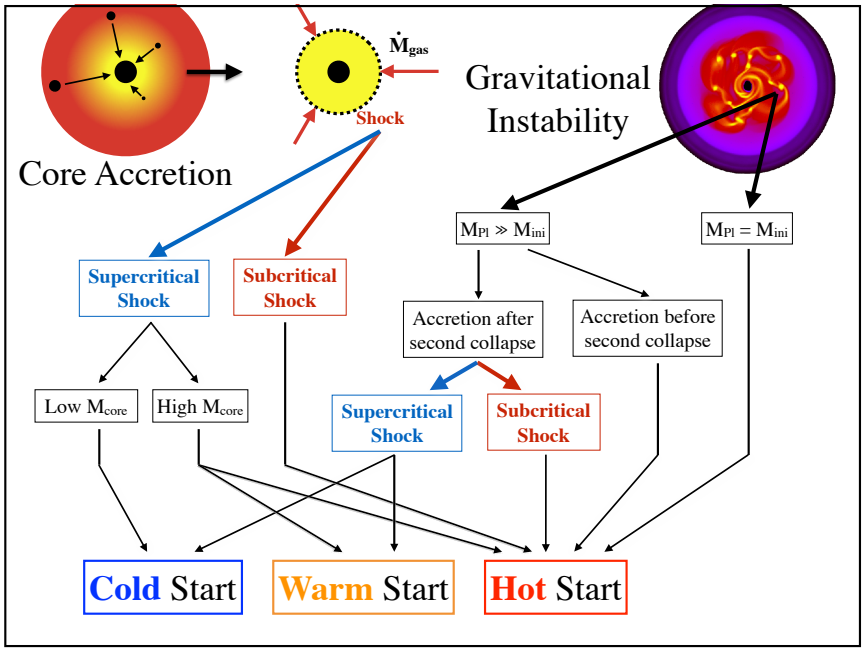

Figure 4 – Summary of the various pathways to giant planet formation leading to different post-formation entropies, from Baruteau et al. (2016). M_{ini} denotes the initial mass of the clump formed by gravitational instability.

The initial (post-accretion) luminosity of young giant planets remains an open question of giant planet formation. The uncertainty primarily lies in how much energy is radiated away from the in-falling material during the accretion. The limiting conditions obtained by adjusting the efficiency of the shocks lead to the so-called "hot" and "cold" start models (see Fig. 4). At 1 Myr, the luminosity difference between the two starts for a giant planet can represent a factor of 10 to 1,000 (Fig. 3, Mordasini 2013). This is particularly problematic for the characterization of directly imaged planets (generally young), as it leads to high uncertainties in their mass estimate that prevents a robust dynamical analysis of the system. At later ages ($\sim$ 100 Myr), the importance of the initial conditions decreases and so does the distinction between the two start models (Spiegel & Burrows 2012).

2.2.3 Orbital evolution

Over the last decades, planet migration has become an unavoidable ingredient to explain the configuration of some planetary systems, in particular the mean-motion resonance chains and giant planets at close separation. The phenomenon occurs at the beginning of a planet's life, when it is still embedded in the protoplanetary

disk. Its orbital motion creates a spiral density wave in the gas distribution, which in return exerts a torque on the planet. As a result, the angular momentum of the planet's orbit changes, and the orbit expands or contracts depending on the sign of the torque. This leads to radial migration towards or away from the central star.

For low-mass planets, the migration time scale decreases linearly with the planet's mass (Lin & Papaloizou 1986), and becomes significant (less than the disk lifetime) only for planets of a few Earth masses. Until the disk structure is not significantly perturbed by the planet, we refer to the migration as type I. When the influence of the planet becomes sufficient to open an annular gap within the disk (mass > 10 $M_{\oplus}$) , the planet is locked in its gap and follows the accretion of the disk gas onto the star. This is called type II migration (Baruteau et al. 2014).

However, migration depends on a variety of poorly constrained physical characteristics of the protoplanetary disk, such as the viscosity, surface density, or height profiles (Crida & Morbidelli 2007). The current understanding of the migration theories struggles to reproduce the known planetary population (Mordasini et al. 2009), essentially because the theory predicts a very efficient migration that pushes most planets towards the inner zones of the system (Morbidelli & Raymond 2016). As well as shrinking the separation distribution, this process would give rise to dynamical interactions between the different objects of a system. This could have possibility been the case in the binary system HD 106906, where the migration could have pushed the planet towards the central binary star and lead to an ejection to the outer parts of the system (see Chapter 1 Sec. 3).

Giant planet migration is thought to be a key mechanism that structured the architecture of our Solar System. Specificity such as the mass depletion between the Earth and Jupiter orbits (in particular the low-mass of Mars) can be accounted for with an early inward migration of Jupiter, which would have reversed when Saturn formed (Grand Tack, Walsh et al. 2011).

Combined with the physical evolution of their structure and the interaction with the gaseous disk, planets experience critical orbital evolution after their formation, through interactions between themselves. The reality of post-gas dynamical evolution is supported by observational evidence,such as the relatively low number of resonant chains and the common non-zero eccentricities (Morbidelli 2018). In the Solar System, this led to the so-called Nice model, that accounts for the small body population in the Solar System by modeling the coupled orbital evolution of Jupiter and Saturn (Morbidelli et al. 2007; Nesvorný 2018). Hot Jupiters may also originate from interactions with planetary or stellar companions, through a combination of processes referred to as high-eccentricity migration (Hamers et al. 2017; Teyssandier et al. 2019).

3 Direct imaging

Direct imaging is presently the only viable method to complete our view of planetary systems architectures and to set constraints onto the giant planet formation scenarios at large (> 5 au) separations. It occupies an important niche with a potential for growth in the near future, in particular in the coming era of the extremely large

telescopes (TMT, GMT, E-ELT). The detection of photons from the atmosphere of planetary companions gives precious information about their composition and physical properties (effective temperature, surface gravity, atmospheric properties). Furthermore, direct imaging can detect planets in formation in the primordial gas disk (such as PDS 70; Keppler et al. 2018; Haffert et al. 2019). On top of constraining the physics of accretion, this gives valuable inputs on the very young architecture of planetary systems, which can be then compared to more evolved systems to investigate the dynamical evolution.

3.1 State of the art

Two main difficulties arise when trying to resolve a planet: its faintness compared to the stellar luminosity, and its small angular separation from the star. For example, Jupiter seen from 50 pc away would appear at an angular separation of 100 mas (3.10^{-5} degrees), and with a contrast in luminosity of 10^{-8} (4.5 Gyr). For younger ages (10 Myr), the intrinsic luminosity increases the contrast to $10^{-5} - 10^{-6}$ (respectively for hot-start and cold start, Mordasini 2013). These observational specifications require high-angular resolution high-contrast instruments, and only the highest performing ones (2nd generation, namely VLT/SPHERE and Gemini South/GPI) can currently hope to detect young Jupiters at 5 au. To detect a Gyr-old Earth in the habitable zone of a Solar-type star, a contrast of 10^{-10} and an angular separation of 20 mas (at 50 pc) have to be reached. The generation of imaging instruments on the ELTs will be able to reach that separation, but the limits in contrast will probably be the main technical hurdle.

The high performance on the 8-10 meter-class telescopes (VLT, Gemini, Subaru, Keck, LBT) rests upon a set-up that enables for high angular resolution (giant telescope and adaptative optics), the use of a coronagraph to attenuate the light from the star, and differential imaging techniques.

The recent refinements of adaptive optics (Extreme-Adaptative Optics) is one of the key ingredient that accounts for the gain in angular resolution (Chauvin 2016). Indeed, observations from the ground are strongly hindered by the turbulence in Earth's atmosphere, which affects the light propagation, blurring the Point-spread function (PSF, spread of order 1"). Adaptive optics compensate for this turbulence through a wavefront sensor, a deformable mirror whose surface shape is controlled by actuators, and a real-time controller. Extreme-Adaptive Optics are characterized by a higher frequency of adaptation (> 1 kHz), finer corrections (more than a thousand actuators) and an enhanced stability of the set-up. SPHERE's PSF has a typical size of 0.04", a gain of more than 10 compared to the seeing-limited case.

Coronagraphs reduce the impact of the quasi-static speckle noise when searching for faint companions. They achieve this by decreasing the diffracted light of the star where planets are looked for, and decreasing the intensity of the star to prevent saturating the detector. It pushes back contrast limits, in particular in the inner zone of the system, by decreasing by more than 100 the intensity of the stellar light.

Finally, a variety of techniques exists to minimize the residual flux structures (Speckles), from correction algorithms fine-tuning the deformable mirror (Give'on et al. 2007) to differential procedures (reference, angular, spectral, polarimetric, e.g.

Marois et al. 2006).

The implementation of the differential imaging techniques on the planet imager instruments has been critical to reveal the scattered light emission of planets and faint disks. Consequently, the morphology of the disks (asymmetries, spirals, carving...) can be revealed and studied in great details.

3.2 SPHERE

SPHERE[2] (Spectro-Polarimetric High-contrast Exoplanet REsearch) is a second generation high-angular resolution high-contrast instrument installed on the UT3/VLT in Chile (Beuzit et al. 2008). It has been developed by a consortium of 11 institutes in 5 European countries, led by IPAG in Grenoble. Since its first-light in 2014, it has shared its observing time between open-time programs and 260 nights of Guaranteed Time Observations (GTO), mainly devoted to the search and characterization of exoplanets (Chauvin et al. 2017). SPHERE is designed to give optimal performance for stellar targets up to 9 mag, which is enough to build a sample of 400 to 600 young stars of the Solar neighborhood (Beuzit et al. 2008).

SPHERE is composed of three modules. The main one, IRDIS, is a near-infrared dual-beam imaging module that has a wide field of view (11"), and works in a broad range of near-infrared wavelengths (0.95 to 2.32 μm). The two beams, corresponding to two neighboring spectral channels, have been carefully chosen so that one of the two corresponds to a absorption line of companions atmospheres (e.g., methane), to strengthen the detection. The very high astrometric precision (a few mas) combined to the large field of view makes IRDIS unique for the characterization of companions from 10 au to wide orbits (several 100 au). Most of the data used in this thesis were thus observed with IRDIS.

A second module, the integral field spectrograph (IFS), allows the sampling of the frequency space at low resolution over a field of view of 1.73". This module is used to characterize the spectrum of the companions in the 0.95-1.65 μm range (R $\sim$ 30) and in the 0.95-1.35 μm range (R $\sim$ 50). On top of giving precious information about the composition of the companions, it allows the estimation of their physical properties (Teff, log g, radius, mass).

Finally, ZIMPOL is a polarimeter working in the visual range (0.6-0.9 μm). The use of polarimetry singles out the reflected stellar light, which is otherwise extremely faint. This module is used to resolve debris disks and to detect the reflected emission of evolved planets (so far unsuccessfully).

All three instruments benefit from a robust image and pupil stability, ensured through the common path facility, that measure and adjust in real time the differential image movements. Thanks to its extremely adaptive optics and to the large diameter of the VLT, the PSF of SPHERE has a a typical size of 40 mas (around 4 pixels square). A good modeling of the PSF then allows the constraints of the positions of the objects with a precision of 1 to 5 mas (compared to $\sim$ 10 mas for the older generation of NaCo or HAO). A good precision on the position is essential to the orbital monitoring of the detected companions, because it allows the detection of an orbital motion in a reasonable time ($\sim$ 1 yr) despite their long periods ($\gtrsim$ 100

[2]Website: `https://sphere.osug.fr/spip.php?rubrique6&lang=en`

yr). The coronagraph is limited to an inner working angle of $\lesssim$ 100 mas, preventing to probe the inner regions around the central star (see Fig. 5).

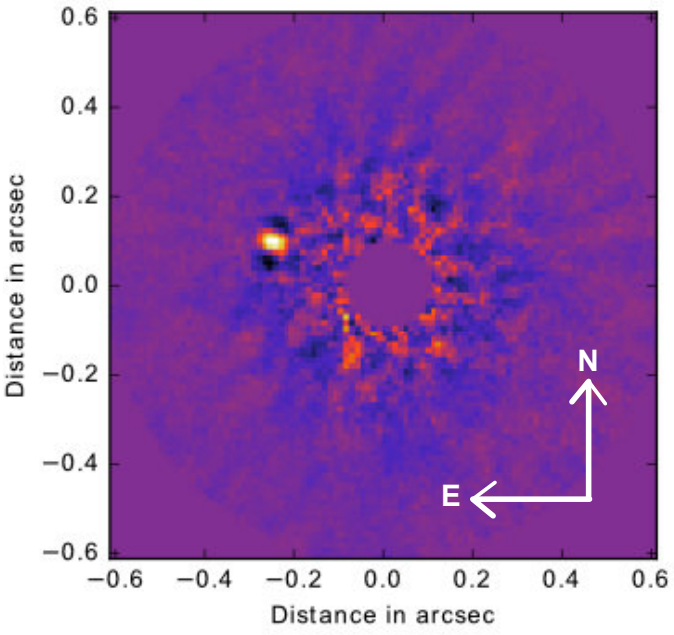

Figure 5 – SPHERE/IRDIS image of the brown-dwarf companion HD 206893 in the H-band filter (1.6255 μm). The cut of the inner zone is due to the coronagraph. The companion is detected at a separation of 270 mas ($\sim$ 10 au) and has a contrast of $3.6.10^{-5}$.

Two quantities are necessary to ensure the consistency of the astrometry along different epochs : the pixel scale, to derive the separation in arcseconds, and the instrument orientation on sky (true North), to allow comparisons between the position angles. Their calibration is performed based on carefully-chosen astrometric fields (binaries, clusters) with accurate positions and a good on-sky coverage throughout the year. The pixel scale exhibits only negligible variations over time for a given setup (of order 0.01 mas for SPHERE/IRDIS, a hundred times less than the typical error), so that its calibration is reliable (Maire et al. 2016). On the other hand, the precise derivation of true North is subject to systematic changes between epochs. The typical variation for a given setup in SPHERE is of order 0.15 °, which is similar than the typical error (Maire et al. 2016).

3.3 Science: Planets and disks

Several past and ongoing surveys have revealed a scarce but interesting population of young gas giants on wide orbits, making use of different instruments: VLT/-NACO (e.g., Rameau et al. 2013; Vigan et al. 2017), VLT/SPHERE (e.g., Chauvin et al. 2017), Gemini South/GPI (e.g., Nielsen et al. 2019), SUBARU (e.g., Uyama et al. 2017), Keck II/NICRC2, Gemini North/NIRI and Gemini South/NICI (e.g., Galicher et al. 2016), MagAO/Clio2+FIRE (Janson et al. 2013) and other instruments probing the near infrared domain (e.g., Baron et al. 2018). Their results point

toward a low occurrence ($\leq$ 10 %) of giant planets ($>$ 5 M_J) at separations larger than 10 au (Nielsen et al. 2019), very low ($<$ 3 %) for very wide separations (1000 to 5000 au, Baron et al. 2018).

The SHINE survey with SPHERE targets 500 young, nearby stars with a 200 nights budget (Chauvin et al. 2017). Each target has to be observed twice within at least a 1-yr interval in order to distinguish bound companions from background stars, using their relative proper motion. For now, SHINE has discovered two planets (HIP 65426 b and PDS 70 b; Chauvin et al. 2017; Keppler et al. 2018) and 2 brown dwarfs (HD 206893 B and HIP 64892 B; Milli et al. 2017; Cheetham et al. 2018), although the final statistics are not yet available (the end of the survey is expected in 2020). SHINE also has contributed significantly to the characterization of most known imaged companions and, occasionally, debris disks. I have been working on five of these systems (HD 106906, HR 2562, HIP 206893 and 51 Eri), plus four stellar systems also imaged by SPHERE (GJ 2060, TWA 22, AB Dor B and HD 100453). The detailed study of these systems are described in specific sections of this thesis in Chapter 2.

The SPHERE consortium also performs the DISKS survey to look for disks (of gas and/or debris). Around 40 gas disks and 30 debris disks have been detected for the first time in scattered light since the beginning of the survey. The observations already enabled a taxonomical study of protoplanetary disks brightness, extension and morphology (Garufi et al. 2018).

Fig. 6 sums up the directly imaged companions at the time of the writing of this thesis, according to exoplanet.eu (I corrected the catalog to account for numerous unrecorded updates). HR 8799 and PDS 70 are the only imaged systems with multiple companions. The detection of brown dwarfs at thousands of au (or even isolated) suggests that they can form from their own cloud collapse. The very wide orbit of giant planets such as HD 106906 is not well accounted for. This is a reason why we chose to investigate dynamical scenarios for this system, and we propose a more complicated formation pathways (see Chapter 1 Sec. 3).

4 Dynamics

This section intends to set the basics of the celestial mechanics used in the thesis. I will introduce the Hamiltonian framework that is the ground of the symplectic integrators of Chapter 1. I will then present different aspects of the perturbed 2-body problem, that will be used in both Chapters 1 and 2. This section makes use of the online course of Duriez (2002).

4.1 2-body problem: notations and resolution

In a Galilean referential, the equation of motion of the 2-body problem is

$$\ddot{\boldsymbol{r}} = -\frac{\mu}{r^3}\boldsymbol{r} \tag{1}$$

where $\boldsymbol{r}$ is the position vector between the two bodies and μ the product of the gravitational constant G and the total mass of the system. Three constant quantities

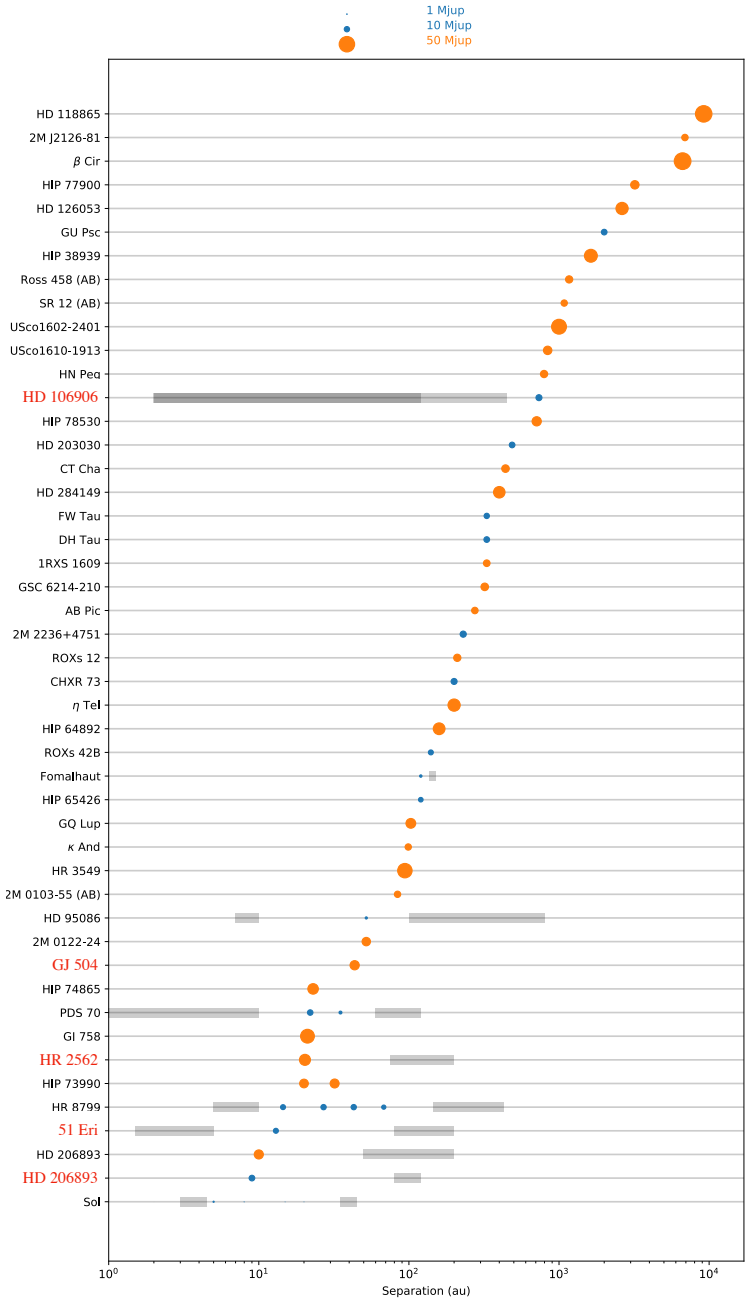

Figure 6 – Architecture of the directly imaged main-sequence systems with a planet or brown dwarf companion. The binary-type mass ratios (> 0.05) and the post-main sequence systems are not represented. The blue color indicates objects below the 13 M_J mass limit, and the grey rectangles indicates disks (of debris, except from PDS 70). The red names indicate the systems whose studies are depicted in this thesis.

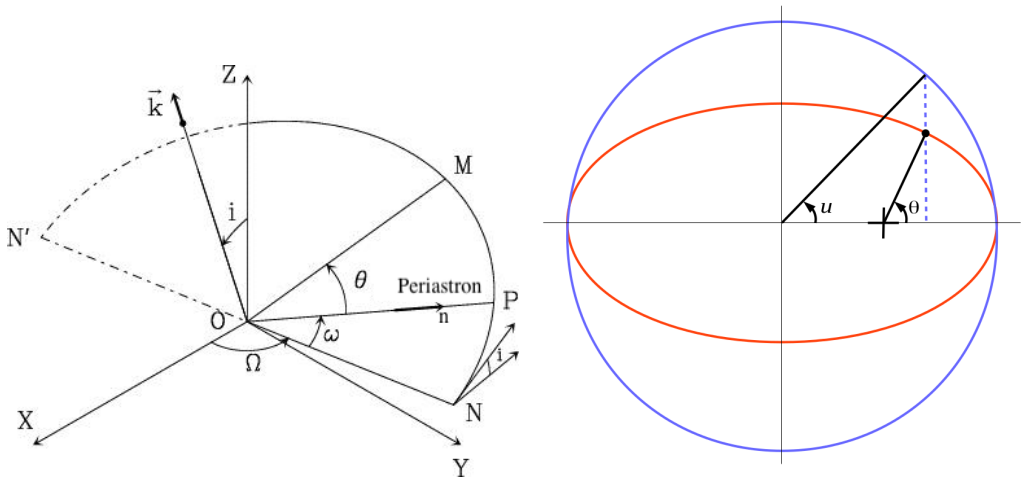

Figure 7 – (left) Representation of the five angular orbital elements. (right) Schematic of the true and eccentric anomaly in the orbital plane.

are used to describe the problem:

- The energy $E = \frac{1}{2}|\dot{\boldsymbol{r}}|^2 - \frac{\mu}{r}$;
- The angular momentum $\boldsymbol{C} = \boldsymbol{r} \wedge \dot{\boldsymbol{r}}$;
- The eccentricity vector $\boldsymbol{e} = \frac{\dot{\boldsymbol{r}} \wedge \boldsymbol{C}}{\mu} - \frac{\boldsymbol{r}}{r}$.

The energy controls the size of the orbit described by $\boldsymbol{r}$. The angular momentum is normal to the orbital plane (along $\boldsymbol{k}$ in Fig. 7). Finally, the eccentricity vector points towards the direction of smallest value of $\boldsymbol{r}$ (periastron).

An alternative representation of the trajectory is given by the six orbital elements:

- The semi-major axis $a = |\frac{\mu}{2E}|$;
- The eccentricity e which is the norm of the eccentricity vector;
- The inclination $i = \arccos\left(\frac{C_z}{C}\right)$;
- The longitude of the ascending node $\Omega = \arctan\left(-\frac{C_x}{C_y}\right)$;
- The argument of periastron $\omega = \arctan\left(-\frac{e_z}{(\boldsymbol{C} \wedge \boldsymbol{e})_z}\right)$;
- The true anomaly θ, polar angle of $\boldsymbol{r}$ in the plane normal to $\boldsymbol{C}$, measured from $\boldsymbol{e}$.

The two angles i and Ω define the plane of the trajectory, ω its orientation, a and e its shape and θ the current position on the trajectory (see Fig. 7). It can be shown (see Appendix) that $\boldsymbol{r}$ follows a conic section of equation:

$$r = \frac{C^2}{1 + e\cos(\theta)} \tag{2}$$

$$\text{with } \dot{\theta} = \frac{C}{r^2} \quad (2^{nd}\ \textit{Kepler law}) \tag{3}$$

When the trajectory is elliptic ($e < 1$), the period of the orbit is given by:

$$P^2 = \frac{4\pi^2 a^3}{\mu} \quad (3^{rd}\ \textit{Kepler law}) \tag{4}$$

and the orbital elements correspond to the elliptic elements:

$$a = \frac{r_a + r_p}{2}$$

$$e = \frac{r_a - r_p}{2a}$$

where $r_p = r(\theta = 0)$ is the periastron (shortest separation) and $r_a = r(\theta = \pi)$ is the apoastron (largest separation). We may equivalently use the time of periastron passage t_p instead of the true anomaly θ.

To link the time evolution to the geometrical evolution, we define the eccentric anomaly u, whose geometric representation is presented on Fig. 7. It can be linked both to the true anomaly θ and to the time, through the mean anomaly $M \equiv 2\pi t/P$. The equations are:

$$r(\theta) = a(1 - e\cos(u)) \tag{5}$$

$$M = u - e\sin(u) \quad \textit{(Kepler equation)} \tag{6}$$

Similar relations can be derived in the hyperbolic case, with hyperbolic functions and opposite signs. The solution of the Kepler equation is known as series, but most of the time, iterative approaches are used (Danby & Burkardt 1983, see Appendix).

4.2 Hamiltonian representation

The orbital elements just described can be introduced with the Hamiltonian mechanics framework. It is particularly useful for the perturbed case (see Sec. 4.4), as it allows the derivation of the evolution equations of each of the orbital elements, which are much more workable than the equations of evolution of the classical coordinates.

The Lagrangian (per unit mass) is defined as the difference between the kinetic energy and the potential energy. In the 2-body problem, with the previously defined notations, it is

$$\mathcal{L} = \frac{1}{2}\dot{\boldsymbol{r}}^2 + \frac{\mu}{r} \quad , \tag{7}$$

The conjugate moment $\boldsymbol{p}$, defined as the derivative of $\mathcal{L}$ with respect to $\dot{\boldsymbol{r}}$, is:

$$\boldsymbol{p} \equiv \frac{\mathrm{d}\mathcal{L}}{\mathrm{d}\dot{\boldsymbol{r}}} = \dot{\boldsymbol{r}} \quad . \tag{8}$$

The Hamiltonian is then defined as

$$H \equiv \boldsymbol{p}\dot{\boldsymbol{r}} - \mathcal{L} \tag{9}$$

$$= \frac{1}{2}\boldsymbol{p}^2 - \frac{\mu}{r} \quad , \tag{10}$$

and the following equations (Hamilton equations) hold

$$\dot{\boldsymbol{r}} = \frac{\partial H}{\partial \boldsymbol{p}} = \boldsymbol{p} \quad , \quad \dot{\boldsymbol{p}} = -\frac{\partial H}{\partial \boldsymbol{r}} = -\frac{\mu}{r^3}\boldsymbol{r} \tag{11}$$

which transform the three-dimension second-order differential equations (Eq. 1) into two equivalent three-dimension first-order differential equations. When the system is conservative, as it is here, the Hamiltonian represents the energy and is conserved.

To adopt new coordinates (orbital elements) for the description of the system, we must check that they are canonic, that is that their evolution follows the structure of Hamilton equations. This is the case for the Delaunay variables, that we use to describe the elliptic (bound) case (the quantities on the same line are conjugated) :

$$M \qquad L = \sqrt{\mu a} \tag{12}$$

$$\omega \qquad C = \sqrt{\mu a(1-e^2)} \tag{13}$$

$$\Omega \qquad \Theta = \sqrt{\mu a(1-e^2)}\cos(i) \tag{14}$$

In these new variables, the Hamiltonian writes

$$H = -\frac{\mu^2}{2L^2} \tag{15}$$

and the evolution equations

$$\frac{\mathrm{d}M}{\mathrm{d}t} = \frac{\partial H}{\partial L} = \frac{\mu^2}{L^3} = \sqrt{\frac{\mu}{a^3}} \qquad \frac{\mathrm{d}L}{\mathrm{d}t} = -\frac{\partial H}{\partial M} = 0 \tag{16}$$

$$\frac{\mathrm{d}\omega}{\mathrm{d}t} = \frac{\partial H}{\partial C} = 0 \qquad \frac{\mathrm{d}C}{\mathrm{d}t} = -\frac{\partial H}{\partial \omega} = 0 \tag{17}$$

$$\frac{\mathrm{d}\Omega}{\mathrm{d}t} = \frac{\partial H}{\partial \Theta} = 0 \qquad \frac{\mathrm{d}\Theta}{\mathrm{d}t} = -\frac{\partial H}{\partial \Omega} = 0 \tag{18}$$

We retrieve the conservation of the orbital elements and the third Kepler law.

In the case of a coplanar problem, the mean longitude λ and the plane longitude of periastron ϖ are used:

$$\lambda = M + \omega + \Omega \qquad L = \sqrt{\mu a} \tag{19}$$

$$\varpi = \omega + \Omega \qquad P = L(\sqrt{1-e^2} - 1) \tag{20}$$

4.3 Jacobi coordinates

Let there be N bodies of masses $(m_j)_{j=1..N}$, described by their position $(\boldsymbol{r_j})_{j=1..N}$ in the barycentric coordinates. Alternative coordinates description are used to reduce the problem to $N-1$ two-body problems.

The first alternative is to particularize one of the body, for example the Sun in the Solar System, and compute the relative position of the other bodies from it. If the other bodies' masses are small enough with respect to the Sun's mass, each body is following its orbit around the Sun as a 2-body problem.

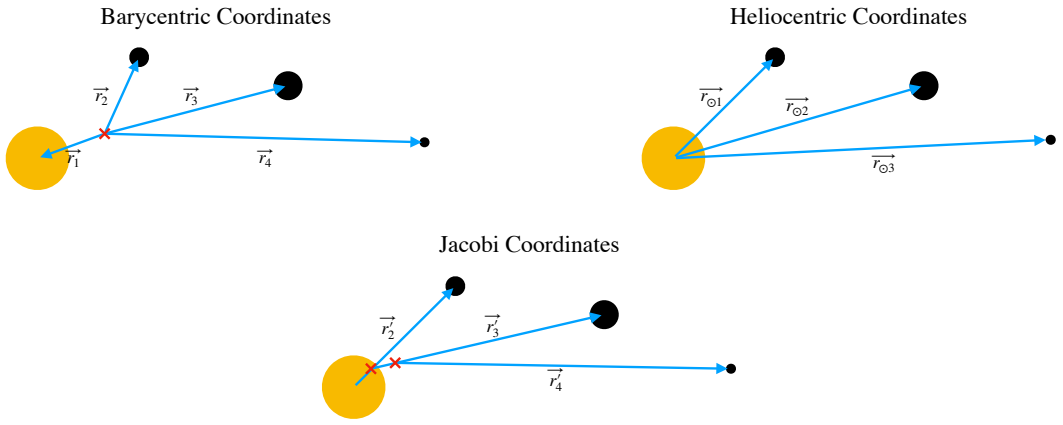

Figure 8 – Representation of three different descriptions of the N-body problem.

However, in practice, the masses of the bodies are not entirely negligible (and sometimes not at all). In that case, the referential centered on the Sun is not Galilean. A more rigorous description is given by the Jacobi coordinates, where the bodies are first ordered along their distance to a rotation center (Sun, center of mass) and their relative positions are computed with respect to the successive centers of mass (see Fig. 8). The new positions $(\boldsymbol{r'_j})_{j=1..N}$ are given by:

$$\boldsymbol{r'_1} = \frac{1}{m_{\text{tot}}} \sum_{j=1}^{N} m_j \boldsymbol{r_j} \tag{21}$$

$$\boldsymbol{r'_j} = \boldsymbol{r_j} - \sum_{k=1}^{j-1} \frac{m_k}{m_{\text{tot,j-1}}} \boldsymbol{r_k} \text{ for } j \geq 2 \tag{22}$$

where $m_{\text{tot,j}}$ designates the total mass of bodies up to j. The position $\boldsymbol{r'_0}$ is the constant position of the total center of mass, so that the problem can be reduced to $N-1$ two-body problems. The Jacobi coordinates can be generalized for several centers of rotation by the Hierarchical Jacobi coordinates. This is the basis of my team's N-body integrator `Swift HJS`, which I describe extensively in Chapter 1.

4.4 Perturbed 2-body problem, Lagrange equations

In the ideal 2-body problem, the previously defined orbital elements a, e, i, Ω, ω and t_p remain constant. Most of the time however, additional forces (tidal, viscous

interactions with the disk) or additional bodies perturb the scheme and the orbital elements evolve.

The orbital elements are defined from the vectors position and velocity, so that their definition stands even if the situation does not correspond to an ideal 2-body problem. In such case, they are not conserved and, at for any given time, they correspond to the orbital elements of the traced orbit if the problem would suddenly become Keplerian.

If a perturbative potential U was added to the problem, the Hamiltonian would become:

$$H = -\frac{\mu^2}{2L^2} + U \tag{23}$$

and the new equations of motion would write:

$$\frac{\mathrm{d}M}{\mathrm{d}t} = \frac{\partial H}{\partial L} = \frac{\mu^2}{L^3} + \frac{\partial U}{\partial L} \qquad \frac{\mathrm{d}L}{\mathrm{d}t} = -\frac{\partial H}{\partial M} = -\frac{\partial U}{\partial M} \tag{24}$$

$$\frac{\mathrm{d}\omega}{\mathrm{d}t} = \frac{\partial H}{\partial C} = \frac{\partial U}{\partial C} \qquad \frac{\mathrm{d}C}{\mathrm{d}t} = -\frac{\partial H}{\partial \omega} = -\frac{\partial U}{\partial \omega} \tag{25}$$

$$\frac{\mathrm{d}\Omega}{\mathrm{d}t} = \frac{\partial H}{\partial \Theta} = \frac{\partial U}{\partial \Theta} \qquad \frac{\mathrm{d}\Theta}{\mathrm{d}t} = -\frac{\partial H}{\partial \Omega} = -\frac{\partial U}{\partial \Omega} \tag{26}$$

Rewritten with the classical orbital elements, we obtain the Lagrange equations:

$$\sqrt{\mu a}\frac{\mathrm{d}a}{\mathrm{d}t} = -2a\frac{\partial U}{\partial M} \tag{27}$$

$$\sqrt{\mu a}e\frac{\mathrm{d}e}{\mathrm{d}t} = -(1-e^2)\frac{\partial U}{\partial M} + \sqrt{1-e^2}\frac{\partial U}{\partial \omega} \tag{28}$$

$$C\sin(i)\frac{\mathrm{d}i}{\mathrm{d}t} = -\cos(i)\frac{\partial U}{\partial \omega} + \frac{\partial U}{\partial \Omega} \tag{29}$$

$$C\sin(i)\frac{\mathrm{d}\Omega}{\mathrm{d}t} = -\frac{\partial U}{\partial i} \tag{30}$$

$$Ce\sin(i)\frac{\mathrm{d}\omega}{\mathrm{d}t} = -(1-e^2)\sin(i)\frac{\partial U}{\partial e} + e\cos(i)\frac{\partial U}{\partial i} \tag{31}$$

$$\frac{\mathrm{d}M}{\mathrm{d}t} = n + \frac{1}{\sqrt{\mu a}}\left(2a\frac{\partial U}{\partial a} - C(\frac{\mathrm{d}\omega}{\mathrm{d}t} + \cos(i)\frac{\mathrm{d}\Omega}{\mathrm{d}t})\right) \tag{32}$$

Even with the simplest form of perturbative potential U, these equations can often not be solved. To simplify their resolution, we often develop them in perturbative series (of the semi-major axes, masses or eccentricities ratios typically), and/or we average the Hamiltonian over the fast rotating variables. The latter approach is called secular approximation, and is used when the studied perturbations happen on a time scale significantly larger than the orbital periods.

4.5 Secular approximation and Hamiltonian maps

In practice, the Lagrange equations are too complex to solve exactly, even for the simplest perturbative potential (remote third body for example). The secular approximation is a method valid for lightly perturbed Keplerian motion. It consists

in dividing the problem into two time-scales: the small time-scales (comparable to the orbital period), and the longer (secular) time-scales. The potential U is then expressed as a function of both rapidly oscillating variables (θ) and slowly-varying variables (the other orbital elements). We then average over θ and replace the orbital elements by their averaged value. We can then study the evolution of these averages. Rigorous mathematical derivations of the correctness of this approach are given in Morbidelli (2002), using series of Fourier coefficients. If several orbits are considered, the integration is performed independently on each rapidly oscillating terms, if the periods are not commensurable. Otherwise, we are in a situation of mean-motion resonance (see Sec. 4.6).

In the secular approximation, the semi-major axis a is always constant, as it is the conjugate of the mean anomaly (which is rapidly oscillating). The stability of the semi major axis is thus a condition sine qua none for the use of the secular approach. This is true as soon as the energy perturbation from the Keplerian case is small with respect to the Keplerian energy.

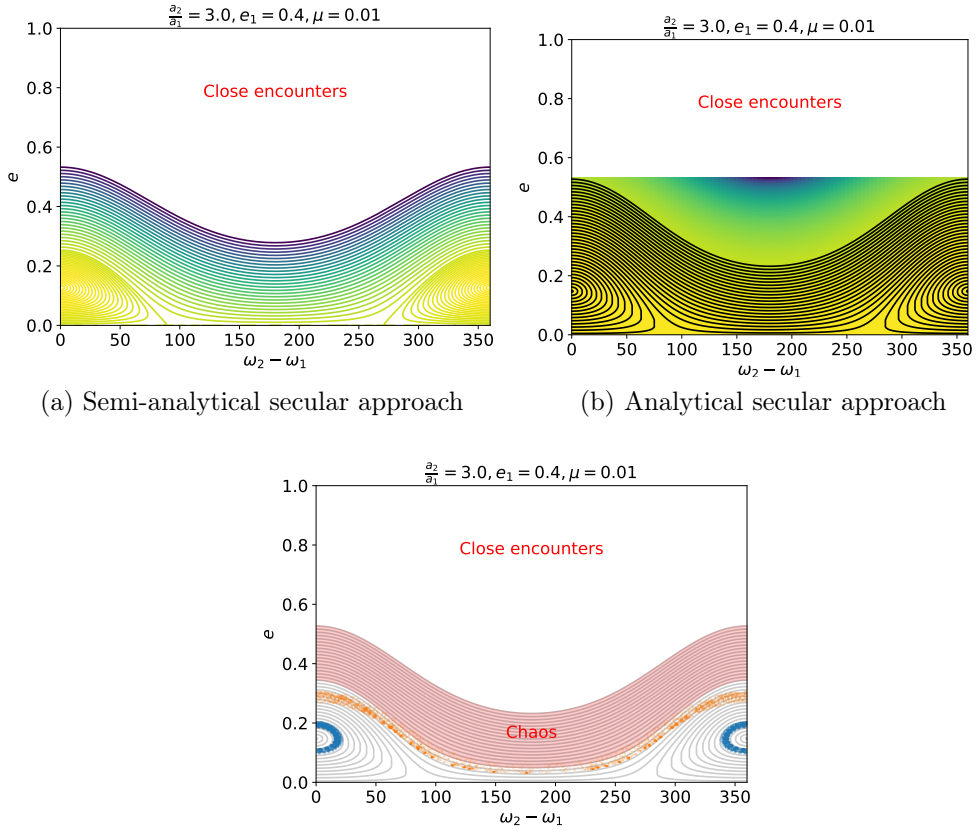

(a) Semi-analytical secular approach

(b) Analytical secular approach

(c) Numerical approach

Figure 9 – Hamiltonian maps for the evolution of an outer body (2) perturbed by an inner companion (1).

When the problem is coplanar, the secular Hamiltonian has only two degrees of freedom: the average eccentricity e and argument of periastron ω. The problem can then be represented by a contour map (see Fig. 9). As the Hamiltonian is

conserved, the evolution of the system must follow the iso-energy lines. On Fig. 9, I used three different approaches to compute the Hamiltonian map for an orbit perturbed by an inner planetary companion. Such a perturbation will induce precession (in around 500 orbital periods for a semi-major axes ratio of 3), as well as secular eccentricity variations. Map (a) is obtained through a semi-analytical approach: the secular Hamiltonian is computed numerically for every couple (e, ω), without any approximation, to obtain an exact secular energy map. On map (b), I superposed to the semi-analytical map the complete analytical resolution $e(\omega)$ for small e and high semi-major axis ratio with the companion (the resolution is detailed in the Appendix). This resolution follows very faithfully the map (a), even for moderate eccentricities. Finally, I superposed to the analytical lines the outcome of two different simulations with the N-body code Swift HJS (see Chapter 1), with two different initial eccentricities and running for 10 precession periods. Both simulations follow the theoretical predictions. The red zone labeled chaos corresponds to the numerical estimate of the chaotic zone from Petrovich (2015), for which the secular approximation does not hold.

In the secular theory, the displacement on the equi-energy lines on the Hamiltonian maps is performed at the rate of the precession. The low eccentricity approximation predicts a homogeneous precession, which gives a good estimate. In some cases, where the two orbits are initially nearly aligned and the outer orbit has low eccentricity, the longitude of the periastron is confined to and oscillates within a part of the parameter space. This situation is called libration.

4.6 Mean-Motion Resonances (MMR)

Two orbits are said to be in a mean-motion resonance configuration when their periods are commensurable. In that case, we cannot average the Hamiltonian over the two orbital motions independently in the secular approach. Instead, the average is made over the least common multiple of the two periods, and the relative positions of each bodies is computed directly from the time. MMRs are usually noted $p+q : p$, meaning that the body we study undergoes $p + q$ revolutions while the perturber does p, where p and q are integers. $|q|$ is the order of the resonance, positive when the perturber is an outer body and negative otherwise. The lower the order, the greater the effect of the resonance. The commensurability of the periods leads to fixed conjunctions localization, and the order $|q|$ also represents the number of conjunctions (see Fig. 10).

The secular Hamiltonian can no longer be computed analytically for any eccentricity, because of the resolution of the Kepler equation to derive the positions of each bodies with time. Thus, we analyze the problem using the semi-analytical Hamiltonian map, as in Fig. 9 (a). In the MMR case, the Hamiltonian depends of one more parameter: the initial relative position of the bodies, or equivalently the longitude of the conjunctions σ. This longitude is often computed with respect to the longitude of periastron of the body of interest. It can be written as a function of the mean longitudes:

$$\sigma = \frac{p+q}{q}\lambda_1 - \frac{p}{q}\lambda_2 - \varpi_2 \tag{33}$$

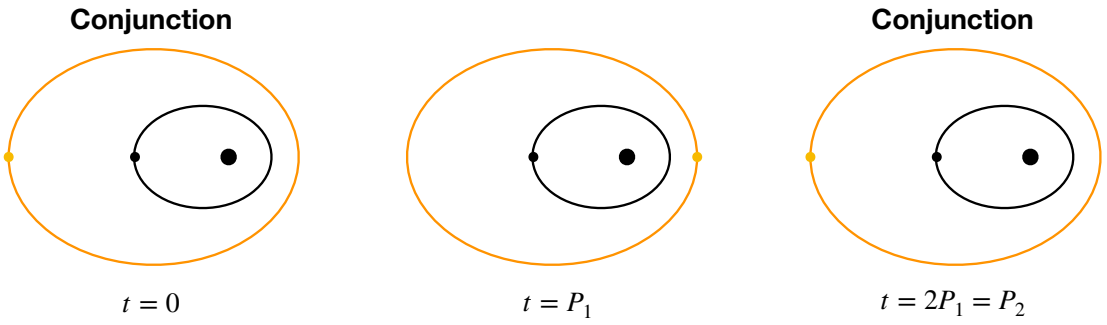

Figure 10 – Example of a stable 1:2 MMR. The conjunctions occur only when the bodies are at apoastron, which guaranties the stability of the system.

Given that $(p+q)P_2 = pP_1$, σ is constant on the short time scales. On secular time scale, the mean-motion resonance is characterized by the libration of σ around an equilibrium value (Morbidelli & Moons 1993).

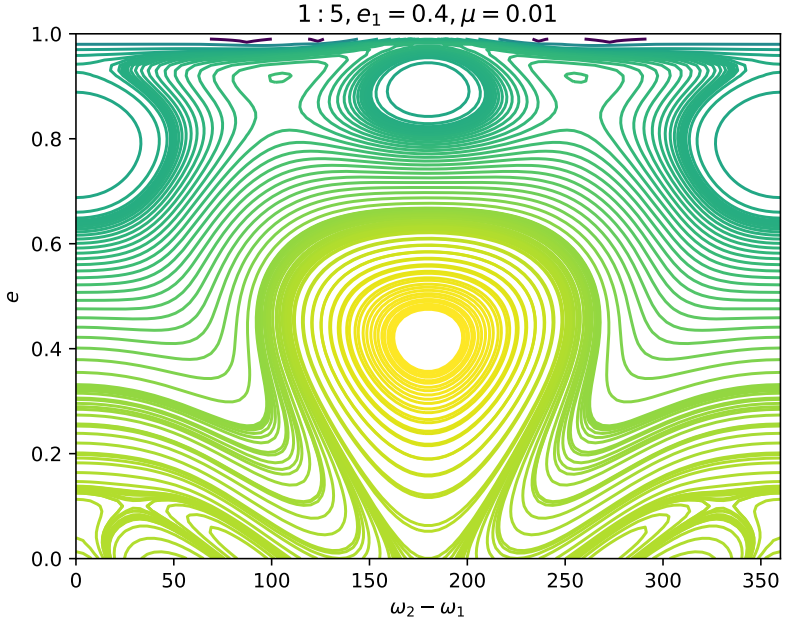

Figure 11 – Hamiltonian maps for the evolution of an outer body (2) perturbed by an inner companion (1), in a 1:5 MMR.

One can note that σ represents the longitude of the conjunctions of the mean longitude, which may be different from the true geometrical longitude. The more stable case is when the conjunction occurs at apoastron, that is when $\sigma = \pi$. As σ is defined modulo $2\pi/|q|$ (there are $|q|$ conjunctions), it is equivalent to $\sigma = 0$ for even $|q|$, $\sigma = \pi/|q|$ for odd $|q|$.

Let us consider our previous example of an inner eccentric giant planet perturbing a lighter body, which is studied in Fig. 9. If instead the semi-major axis ratio is 2.924

instead of 3, it is in a configuration of 1:5 MMR. The corresponding Hamiltonian map is drawn on Fig. 11 for $\sigma = \pi/4$ (neglecting its libration). We see that the resonance induces strong eccentricity variation, except in some localized zones of low eccentricities.

Because it induced such raises of eccentricity in otherwise stable configurations, mean motion resonances are thought to be a factor of destabilization in planetary systems (Beust & Morbidelli 1996). Various studies showed that disk-induced migration is creating naturally resonant chains, as resonant configurations are relatively robust and can stop the planetary migration (resonance capture, e.g. Snellgrove et al. 2001). In Rodet et al. (2017), we used MMR to suggest an early ejection of the planet in system HD 106906 by a $1:6$ resonance with its host binary (Chapter 1 Sec. 3). However, resonance capture depends on a variety of parameters (migration rate, eccentricity damping time scale, mass ratios...), which could account for the lack of observed MMR in Kepler data (Xu & Lai 2017).

On the other hand, MMR can be a stabilizing factor if the eccentricity of the larger body is small. Such configurations can be observed in the Solar System, where the non-stable MMR configurations have long been ejected. The more illustrative case is the $3:2$ resonance between Neptune and Pluto, that ensures that the bodies never encounter when their orbits are close.

4.7 Perturbation in a debris disk

The general theories described above give the tools to study the relative influence of companions on each other, but also the effect of a companion on a debris disk. The Hamiltonian maps portraying the effect of an inner companion on outer orbits can be used to model the structures induced in outer belts of debris. A similar analysis allows the computation of the effect of an outer companion on an inner belt, or to compute the perturbation induced by an inclined companion. For sufficient relative inclination between two orbits ($\sim 40\ °$), the eccentricity can reach extremely high values, the inclination varies significantly, and there may be libration of anti-aligned orbits. This configuration is called Lidov-Kozai resonance (Kozai 1962).

The coupling between eccentricity and precession in debris disk creates large scale structures that can change significantly their shape and brightness distribution. In the transient state from a circular shape and a homogeneous density distribution, the different precession rates of each zones of the disk (depending on their separation) naturally creates spiral features. After several precession periods, the longitudes of periastron are randomized and the disk appears eccentric, with periastron grouped around the periastron of the perturber. This phenomenon is called pericenter glow by Wyatt et al. (1999).

In a less subtle fashion, perturbers can deplete significantly parts of debris disks. First, they create a cavity at the location of their orbit, of a width depending strongly on the semi-major axis and eccentricity, and moderately on the mass ratio. The size and features of this so-called chaotic zone have been thoroughly studied during the last decades, both analytically and numerically. The overlapping of first-orders MMRs gives a theoretical estimate in the circular case (around 2 Hill radii, Wisdom 1980, see Fig. 13), that can be then extended to the eccentric case (Mustill &

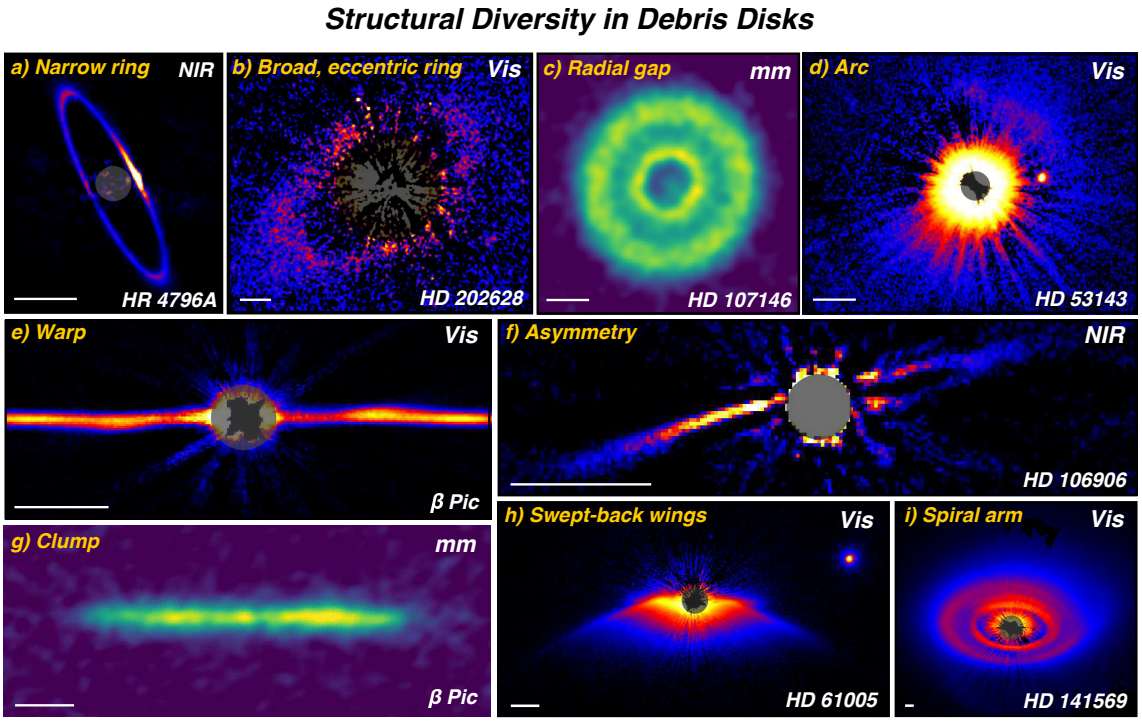

Figure 12 – Mosaic of debris disks observations, taken from Hughes et al. (2018) (references therein). The scale bars represent 50 au. The images were taken with SPHERE (a), HST/STIS (b, d, e, h, i), ALMA (c, g) and GPI (f).

Wyatt 2012). Numerical tables and fits are computed for different mass ratios and eccentricities (Holman & Wiegert 1999; Lazzoni et al. 2018; Regály et al. 2018).

Similarly to the transition disks case, planetary perturbers may not be the only possible causes of the asymmetries and perturbations observed in debris disks (e.g., Moór et al. 2014). Among the possible sources are the stellar fly-bys (see next subsection) and the self-stirring mechanism (Kenyon & Bromley 2004). In the latter, the emergent largest planetesimals (Pluto-size objects) perturb the orbits of neighboring smaller bodies, increasing their inclination and eccentricities. This results in destructive collisions and initiates a collisional cascade through the disk. The relative contributions of self-stirring and planetary stirring in observed debris systems is an issue that is still being investigated (Kennedy & Wyatt 2010).

Direct imaging is the only technique that can resolve the features of the disk and use them to probe their environment. The sample of observed debris disk indicates that large cavities and asymmetries are common. Examples of such cases are shown on Fig. 12. Some of the few cases where a companion was also resolved (HD 106906, HR 2562) are presented in the next chapters.

4.8 Stellar fly-by

In the course of their long life, stars are bound to encounter occasionally other stars. Most of the time, such encounters (or fly-bys) do not significantly impact the architecture of the systems. However, in some cases, they lead to dramatic changes: carving of the debris belts, excitation of the planetary eccentricities and inclina-

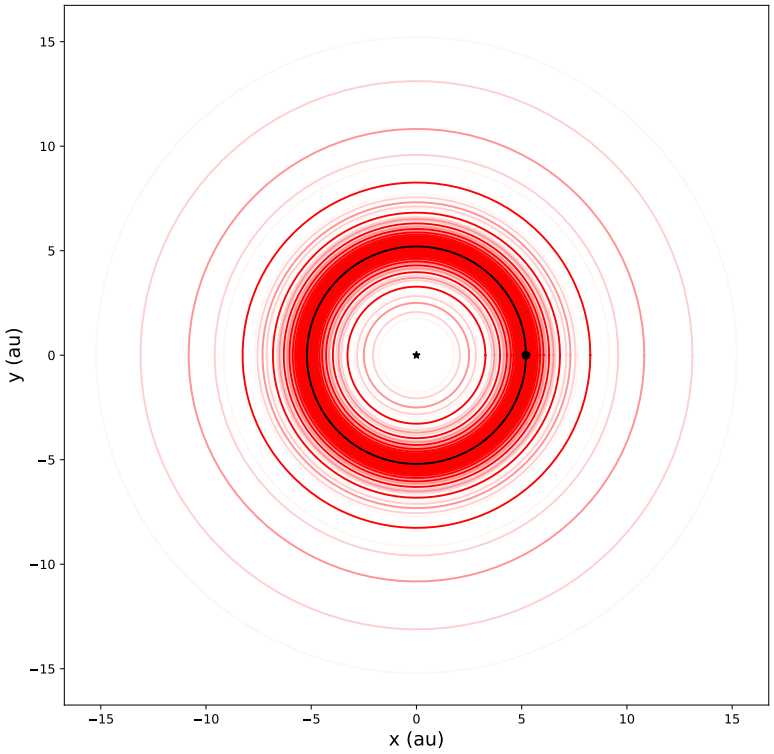

Figure 13 – Representation of the MMRs of orders $q \leq 4$ around Jupiter (in black). The strength of the lines represents the order of the resonance (1 is strong, 4 is weak). It creates a chaotic zone around Jupiter, that shapes the asteroid belt.

tions, or even planetary captures in some rare cases. The study of the consequences of stellar fly-bys is important, as it could account for some puzzling observed architectures, such as wide separations or retrograde orbits. This is particularly relevant for planetary systems in stellar clusters, as the high stellar density increases the chances of consequential encounters.

The secular theory can be extended to hyperbolic Keplerian trajectories. The average is then performed over all the infinite trajectory and not only over one orbit. Such approach was adopted first in Heggie & Rasio (1996), and was used in Rodet et al. (2019), when studying the effect of the fly-bys on the planet in system HD 106906 (Chapter 1 Sec. 3).

On the other hand, the analytic computation shows that the consequences of the encounters depend strongly on its geometric characteristics, through multiple factors. To account for this diversity, most of the studies choose a numerical approach, where they compute the dynamical evolution of numerous systems and study the statistics of the final population. They could compute survival rates, eccentricity raises, and reproduce captures and retrograde orbits (Malmberg et al. 2011; Li et al. 2019). The consequences of the stellar fly-bys may be cumulative, or even indirect, as

the excitation of the eccentricities in planetary systems can lead to close encounters and scattering (Cai et al. 2017).

If the fly-by hypothesis is sometimes considered to explain the specificity of a system (Pfalzner et al. 2018), no planetary systems are known to have undergone a fly-by. HD 106906 is currently the most serious contender, since the discovery of two fly-bys candidates. The system HD 141569 may be currently experiencing a close fly-by that is shaping a massive debris disk (Reche et al. 2009). This is also possibly the case for several protostellar disks in star-forming regions (e.g., RW Aur, Rodriguez et al. 2018).

4.9 Close encounters

Finally, when the eccentricities in a multiplanetary system becomes critical, or if the migration changes the semi-major axis ratios to unsafe values, a body can be caught in a close encounter with another body, where the trajectories of at least one of the bodies is suddenly strongly disturbed from its Keplerian orbit. Close encounters will almost always lead to a definitive ejection from the system. Indeed, if both bodies remain bound, the periodicity of the orbits implies that they will meet again in the treacherous terrain. Thus, if the first close encounter does not immediately provoke an ejection, the subsequent encounters will do so.

As the close encounters are sudden (compared to the orbital period), the probability of observing a system experiencing one is very low. Even the complete ejection to the outer limit of the system takes around 1,000 yr, a very short time interval compared to the million to billion years-old systems that we observe. However, the observation of wide companions with high relative velocities could still reveal themselves to be ejected bodies (Beust et al. 2016). In our Solar system, we regularly observe close encounters between the massive planets and the asteroids or comets. This is why the handling of close encounters was one of the first features implemented in the N-body integrators designed to model the Solar System (see Chapter 1). The implementation of close encounters in my team's code `Swift HJS` is one of the issue tackled in this thesis (Chapter 1 Sec. 2.3).

5 Summarized Context

In summary, my thesis takes place in the context of a massive flow of observational inputs yielded by SPHERE. We are on the verge of unveiling the key characteristics of the architectures of extrasolar systems, and with it, to understand the formation and evolution processes. The dynamical analysis is an essential part to achieve this understanding from the observations.

The relative positions are fitted by a Keplerian orbit to determine the orbital elements of the system. This requires powerful statistical procedure, because of the relatively high number of parameters (> 6) and the sometimes poor constraints. The procedure, as well as its applications to eight different systems, is described in Chapter 2. The statistics of the orbital elements are essential to characterize the architectures. The sample of directly imaged planet is still too small to draw statistical conclusions on the orbital elements distribution. However, the presence of

wide giant planets and the eccentricity of some fitted orbits are already meaningful inputs concerning the formation and evolution pathways. Moreover, the dynamical mass can be computed from the orbital elements, and is valuable to the calibration of evolutionary models, especially for young low-mass stars. The analysis of two such astrometric binaries led to a first-author paper, reproduced in Chapter 2.

N-body simulations can then be used to refine the orbital constraints or investigate unexpected features. As seen above, the stability of N-body systems with $N \geq 3$ is not ensured, and the influence of companions on each other and on their environment are often not negligible. In Chapter 1, I present the current N-body integrators available in the literature, and the new version I designed of the team code `Swift HJS` to take into account hierarchy changes and close encounters. This part of my thesis rests principally upon the study of system HD 106906, a rare system with a potentially rich dynamical history. Its analysis led to two first-author papers (one just submitted), reproduced in Chapter 1.

Chapter 1

N-body simulations of extrasolar systems

Contents

1 State of the art 40

1.1 Available codes 40

1.2 Classical integrators 42

1.3 Symplectic integration 45

1.4 Swift HJS 54

1.5 Non-Keplerian forces 57

2 Code development 58

2.1 Development of surrogate tools for `Swift HJS` 58

2.2 Handling hierarchy change 61

2.3 Handling close encounters 68

3 Understanding the peculiar architecture of the system HD 106906 79

3.1 Investigating the dynamical evolution 81

3.2 Refining the scenario 97

In the Introduction, we reviewed the formalism of the N-body problem and saw that the analytical approach is limited as soon as 3 bodies are involved. Average evolutions (secular) or strong instabilities can be determined from a detailed study of the equations, but N-body dynamics is strongly chaotic for $N > 2$ and thus do not allow for precise conclusions most of the time.

Numerical simulations are a natural approach when studying N-body dynamics, because of the simplicity of the equations of motion and the complexity of their analytical resolution. They allow for the study of evolutions on multiple time-scales (from fractions of an orbital period to secular times) and are not limited by the number of bodies. In the study of extrasolar systems, they are used to predict the stability of the companions, their past and future evolution or some observational features that will help to constrain the rest of the system (disk carving, transit timing variation...).

However, numerical simulations imply approximation errors, if only the computer round-off errors (15 significant decimal digits precision in double precision), that accumulates at each operation. When the implementation is unbiased, this evolves at minimum with the square root of the number of steps (Brouwer 1937). On the other hand, when the resolution of the problem is approximated, the error piles up along the integration. For example, the Runge-Kutta framework in N-body dynamics induces an energy error that evolves linearly with the number of steps (Rein & Spiegel 2014).

In orbital mechanics, we are often interested in long-term evolution of orbits, that corresponds to several thousands to million time-steps. To model the Solar System 4.5 billion years evolution for example, one needs a time step an order of magnitude lower than Mercury's orbit, so that 400 billion time steps are needed. At each time steps, multiple calculations are performed, so that the total energy error becomes quickly so important that the accuracy of the integration becomes questionable and the planets orbital stability is not ensured.

Thus, the design and coding of an optimal scheme to integrate the motion in N-body problems is a complex and active branch in astrophysics. The optimization criteria generally chosen is the energy error, as the stability of an orbit is determined by its energy. Different schemes might be optimal depending on the problem, and I will first review the existing integrators before introducing the code at the center of my PhD, `Swift HJS`, the new versions I developed, and the corresponding astrophysical applications.

1 State of the art

1.1 Available codes

N-body simulations were developed during the 20^{th} century, along with the progress of computer science. The first approach was naturally to use truncated series of the position, using the derivatives, to integrate the evolution of the bodies. Varying the order, the numbers of iterations, the time step or the structure of the equations, the possibilities are large and the codes highly adaptable. I regroup this approach under the category "Classical integrators" in Sec. 1.2, and give an overview of the most

widely-used set-ups in celestial dynamics. The most famous ones are the Runge-Kutta methods (Sec. 1.2.1), which combine the derivatives at different fractions of the time-step to reduce the error. They have been upgraded and refined over the years, but a significant improvement of the precision can be reached by opting for the Bulirsch-Stoer approach, which adds an extrapolation step (Sec. 1.2.2). The implementation of these approaches is described in Press et al. (1989), and can be found in most computational languages. But if a Bulirsch-Stoer algorithm is quicker than the equivalent (in accuracy) Runge-Kutta method, it is still computationaly costly, and the time step must be small enough to capture precisely the features of the trajectory.

In the 1990s, the necessity to integrate systems for a gigantic number of time steps with a constraint of stable energy gave birth to the symplectic integrators. They allow the integration of a problem with larger time steps without endangering the conservation of the energy, as long as the problem is similar to an exactly solvable problem. Luckily, that is the case in orbital dynamics, for the computation of a Keplerian motion is analytically known. Symplectic integrators are thus highly specific to the problem they model, but increase the speed of several orders of magnitude with no concession on the energy stability. Different mappings (depending on the choice for the reference Keplerian orbits) are used in the literature, and I describe them quickly in Sec.1.3. Three implementations have been developed before 2000, that are still available and used today: `SWIFT RMVS` (Sec. 1.3.4), `SymBa` and `Mercury` (Sec. 1.3.3). All can integrate Solar-System-like architectures and resist to close encounters, so that preferring one or another is more of a personal choice (although `Mercury` is probably the most widely-used). Facing with the dynamical study of extrasolar systems with possible non-Solar-System types architectures, Beust (2003) introduced `SWIFT HJS` (Sec. 1.3.5). I used this integrator for most of my work, and it is the basis of the new code `ODEA` that I will present below (Sec. 2).

Recently, the development of super computers and the complexity of the processes studied, that often include additional forces (collisions, tidal forces, interactions with the gaseous environment...), led Rein & Spiegel (2014) to advocate for the return to classical integrators with variable time-steps. Indeed, if the implementation is of sufficiently high-order, then classical integrators might be stable enough to ensure the conservation of the energy for billions of time-scale. To support their claim, Rein & Spiegel (2014) introduced the `IAS15` integrator, a 15^{th} order Gauss-Radau algorithm, that inspires from the classical integrator `RADAU` (Sec. 1.2.3). This code is embedded into a multi-purpose Python package, `REBOUND` (Rein & Liu 2012), designed specifically for N-body dynamics. However, although `IAS15` might be the natural choice for high-precision N-body simulations with strongly pertubed Keplerian motions, the symplectic integrators remain the most efficient choice for very long-term integrations when the Keplerian motion is dominant.

1.2 Classical integrators

In the barycentric referential frame, N-body dynamics is controlled by the following Hamiltonian (see Introduction Sec. 4.2):

$$H = \sum_{i=1}^{N} \frac{\boldsymbol{p_i}^2}{2m_i} - \sum_{1 \leq i < j \leq N} \frac{G m_i m_j}{r_{ij}} \quad , \tag{1.1}$$

where (m_i) are the masses of the bodies, $(\boldsymbol{r_i})$ their positions, $(\boldsymbol{p_i})$ their momenta, and $\boldsymbol{r_{ij}} = \boldsymbol{r_j} - \boldsymbol{r_i}$ the relative positions.

In this framework, the equations of motion (Hamilton equations) of body i writes

$$\dot{\boldsymbol{r}}_{\boldsymbol{i}} = \frac{\partial H}{\partial \boldsymbol{p_i}} = \frac{\boldsymbol{p_i}}{m_i} \quad ; \tag{1.2}$$

$$\dot{\boldsymbol{p}}_{\boldsymbol{i}} = -\frac{\partial H}{\partial \boldsymbol{r_i}} = \sum_{j \neq i} \frac{G m_i m_j}{r_{ij}^3} \boldsymbol{r_{ij}} \quad , \tag{1.3}$$

or simply

$$\ddot{\boldsymbol{r}}_{\boldsymbol{i}} = \sum_{j \neq i} \frac{G m_j}{r_{ij}^3} \boldsymbol{r_{ij}} \quad . \tag{1.4}$$

These differential equations are not solvable for $N > 2$, but they can be solved by computation within classical numerical integration schemes of arbitrary order. For the following introductions to the algorithms, the handbook of Press et al. (1989) has been used.

1.2.1 Runge-Kutta

The Runge-Kutta scheme of integration is a family of simple and well-known iterative methods to give approximate solutions of ordinary differential equations of the form $\dot{y} = f(t, y)$. In our case, $y = (\boldsymbol{r_1}, \boldsymbol{v_1}, ..., \boldsymbol{r_N}, \boldsymbol{v_N})$ is a $6N$ dimension vector. Given a time-step h, the Runge-Kutta method evaluates f at fractions of h and sums the results with coefficients chosen to optimize the error on y.

If the most simple Runge-Kutta schemes are the first order Euler method (one sub-step) and the second order leap-frog method (three sub-steps), the most widely used is generally referred to as RK4, as it is a fourth order method (error on the order h^5). These simple schemes are often not sufficient for orbital dynamics, as the errors pile up and induce drifts in the constants of the problem (see Fig. 1.1).

In order to improve the precision of classical algorithms, the first option is to increase their orders, for example by adding more steps in the Runge-Kutta frameworks. This generally guarantees a better precision, although it is not ensured (high coefficients can make the high-order terms not negligible). However, the computation time becomes increasingly long when the order of the algorithm increases. Another option is to consider adaptive time-steps. Adaptive time-steps indubitably add some complexity to the algorithm, but it gives a much better control on the

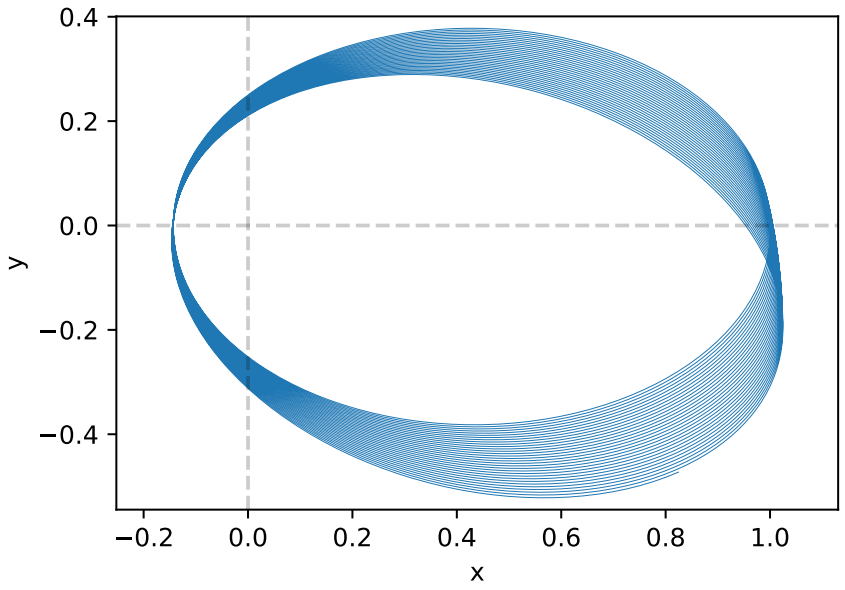

Figure 1.1 – Second order Runge-Kutta model of an orbit (2-body problem) after 100 periods P, with a time step of $P/100$. The semi-major axis is not conserved, and the orbit artifically precesses.

accuracy and speed of the scheme, by decreasing or increasing the time-step according to the behavior of the function to probe. In orbital mechanics, it would ensure the robustness of the algorithm at periastron passage or in case of close encounters between two bodies on different orbits.

Adaptive time-steps can be implemented from the Runge-Kutta approach. The simplest possibility is to compare the outputs of the Runge-Kutta algorithm with time steps h and $h/2$, and then adjusting h so that the difference between the two outputs is below our accuracy goal. Other schemes compare the outputs of two different Runge-Kutta-like formula.

1.2.2 Bulirsch-Stoer

The Bulirsch-Stoer algorithm is a robust integrator that pushes to its limit the idea of adaptive time-steps (Bulirsch & Stoer 1966). This algorithm is both precise and flexible, and is often used in so-called hybrid symplectic integrators to handle strongly perturbed Keplerian motions, as will be developed in Sec. 1.3. I chose this algorithm to implement new features in Swift HJS, detailed in Sec. 2.3.

The idea of the Bulirsch-Stoer approach is to compute the next value of y with decreasing values of the time-step h. Decreasing h produces more and more precise estimates of y. When enough values have been computed (minimum 3), we fit a rational function to probe the evolution of the prediction with respect to the time step. We then evaluate the limit when h tends to 0 (see Fig. 1.2), with an arbitrary precision (estimated from the goodness of the fit) with a much smaller number of steps that would be theoretically required.

Let is be H the initial time step and y_n the current value of y. The successive

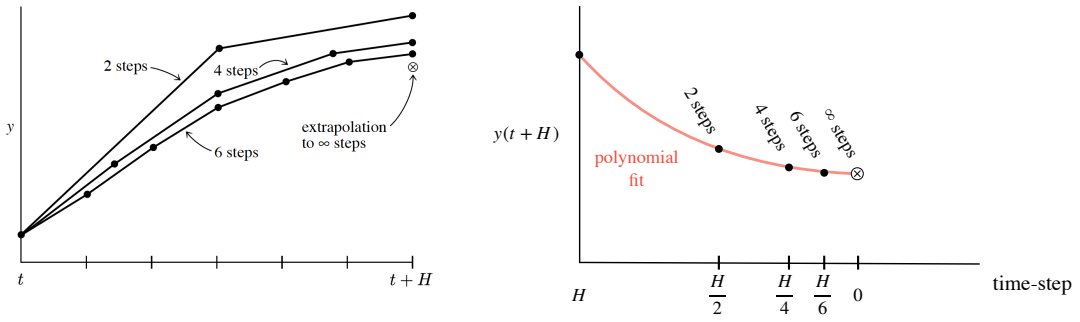

Figure 1.2 – Bulirsch-Stoer method to solve the differential equation of y. The left image is taken from Press et al. (1989). A large interval H is spanned by different sequences of finer and finer substeps. A rational extrapolation then gives an answer that is supposed to correspond to infinitely fine substeps.

time steps from which the limit will be retrieved have the form $h = H/j$, where j is an increasing even number. To compute the value of y after a time H (y_{n+1}), the Bulirsch-Stoer algorithm then calls j times a simple routine with time step h. We use a second order scheme designed to call the function f only once at each substep (to limit the computational cost).

Given y_n and H, a sequence of outputs $(y^j_{n+1})_j$ is then computed. Each time a new j is computed, a rational fitting is performed to estimate the limit when j tends to infinity and its uncertainty. Until this uncertainty does not match our precision goal (defined beforehand) we go higher in j. Thus, we do not know in advance how many time steps will be necessary.

To interpolate the sequence with a rational function and extrapolate its value at 0, Neville's algorithm is used, where the extrapolation is recursively updated each time a new point is added, and that naturally provides an estimate of its error. The next H will be scaled according to the previous number of substeps j.

1.2.3 Gauss-Radau and IAS15

Another approach is to fix the timesteps, but iterate on the results with a predictor-corrector scheme. We define an ensemble of substeps (h_j) spanning a step H, and compute the respective values $y_j = y(h_j)$. At first, the derivative of y is supposed constant throughout H and a simple integration gives the (y_j). Then, the (y_j) are used to compute better estimates of themselves. With a proper truncation of the serial expansion of $\dot{y}$, it is possible to express each y_j as a function of (y_k) where $k \leq j$ only. Then, the updates can be made progressively

The role of the h_j is essential here. To optimize the method, Everhart (1985) thought of using the Gaussian spacings traditionally used to compute integrals, which are not equally spaced. The peculiar scheme where the computation makes use of the lower bound of the interval (i.e. the initial conditions) is called Gauss-Radau integration.

In Everhart (1985), the quadrature uses 4 substeps (9^{th} order) and the predictor-corrector scheme uses a fixed number of iterations to optimize the (y_j). The overall

algorithm is called the `RADAU` code.

More recently, Rein & Spiegel (2014) presented the `IAS15` algorithm, that takes over the `RADAU` code, but uses 8 substeps (15^{th} order integrator) and a dynamic predictor-corrector scheme to adapt the number of iterations to the desired precision. Moreover, they added a module to automatically set and adapt the large time-step H. It is chosen smaller than the typical time-scale of the problem, and is obtained by a rescaling of the last term of the expansion of $\dot{y}$. Finally, they optimize their algorithm to limit the computer round-off errors to there minimal increment. It is accessible within the `Rebound` Python package.

1.2.4 Hermite scheme

Finally, time-symmetric schemes can be used to minimize the error on the energy. An algorithm is time-symmetric if an integration for Δt then $-\Delta t$ returns exactly to the initial situation. This property theoretically guaranties energy conservation. An algorithm based on Hermite interpolation of the acceleration has been proposed by Kokubo et al. (1998) (P(EC)^n Hermite scheme). The algorithm is fourth order, but uses an iterative process to improve the accuracy. The formula depends symmetrically on the times before and after the steps. The time step is updated after each step, and is different for each body.

In any case, classical integrators rely on the time-step or on the number of iterations to gain in precision. Such an approach is computationally costly, especially since the algorithms must resolve at each time the curvature of the Keplerian motion. Symplectic integrators adopted a more specific approach to integrate the problem, based on the analytic resolution of a surrogate problem.

1.3 Symplectic integration

To solve the equations of motion in orbital mechanics and keep the error low on the energy, a different line of integrators appeared in the 1980s, symplectic integrators. Instead of lowering fiercely the order of magnitude of the positions uncertainty, these integrators adopt a different approach, that is to solve analytically/to machine-precision a surrogate problem similar to the real problem. For this method to be useful, this surrogate problem must be simple to solve (not computationally costly) and have an energy close to the real Hamiltonian. Due to the nature of the time evolution of Hamilton's equation, not only symplectic integrators do not accumulate errors on H, but they also conserve the differential volume $d\boldsymbol{r} \wedge d\boldsymbol{p}$.

Symplectic integrators can be substantially faster than classical integrators in celestial dynamics, because the time step does not need to be as small to conserve the energy. On the other hand, symplectic integrators lack flexibility, in particular for the adaptation of the time step. Indeed, the time step is part of the scheme, and changing it will break the symplecticity if no special care is given. This problem and some strategies to handle it will be introduced within the following presentation of the mappings.

1.3.1 General theory

Let us call the surrogate Hamiltonian $\tilde{H}$. If it is exactly solvable, the algorithm is symplectic: it exactly preserves the areas in phase space and exhibit no long-term drift of the energy.

In order to design a proper $\tilde{H}$ in orbital mechanics, the key idea is to split the Hamiltonian into two integrable parts:

$$H = H_{\mathrm{A}} + H_{\mathrm{B}} \quad . \tag{1.5}$$

Several splittings are possible, depending on the problem at hand. Both parts should be integrable within computer round-off errors. $\tilde{H}$ corresponds to the successive integration of these parts separately.

To understand the error that we introduce by integrating the surrogate Hamiltonian, a bit of theory on the evolution of Hamiltonian systems is needed. In that framework, the evolution of any variable $y(t, (\boldsymbol{r_i}), (\boldsymbol{p_i}))$ is given by:

$$\frac{\mathrm{d}y}{\mathrm{d}t} = \{y, H\} + \frac{\partial y}{\partial t} \quad , \tag{1.6}$$

where the Poisson brackets are defined as follows: $\{f, g\} = \sum_i \frac{\partial f}{\partial \boldsymbol{r_i}} \frac{\partial g}{\partial \boldsymbol{p_i}} - \frac{\partial f}{\partial \boldsymbol{p_i}} \frac{\partial g}{\partial \boldsymbol{r_i}}$.

Let us define the operators $A = \{., H_{\mathrm{A}}\}$ and $B = \{., H_{\mathrm{B}}\}$. Let us suppose that y does not depend directly on time (for example $y = \boldsymbol{r_i}$ or $\boldsymbol{p_i}$). Then its evolution writes:

$$\dot{y} = (A + B)y \quad . \tag{1.7}$$

This differential equation is formally solvable:

$$y(t + \Delta t) = e^{\Delta t(A+B)} y(t) \tag{1.8}$$

However, in most cases, the effect of the operator $\exp(\Delta t(A + B))$ is not exactly or easily calculable to computer round-off limits. By choosing H_{A} and H_{B} that are exactly solvable, we ensure that we are able to compute the evolution under $\exp(\Delta t A)$ and $\exp(\Delta t B)$ alone, and thus the evolution of their composition $\exp(\Delta t B) \exp(\Delta t A)$.

Let us define S as the operator corresponding to the evolution of the surrogate Hamiltonian $S = \{., \tilde{H}\}$, where $\tilde{H}$ consists in an evolution along H_{A} followed by an evolution along H_{B}. The product of the exponential of two operators can be computed as a series of commutators, with the Baker-Campbell-Hausdorff formula. Thus, we can express the first orders of S as a function of Δt, A and B:

$$S = A + B - \frac{\Delta t}{2}[A, B] + O(\Delta t^2) \quad . \tag{1.9}$$

Finally, it can be shown that $[A, B] = -\{., \{H_{\mathrm{A}}, H_{\mathrm{B}}\}\}$. The surrogate Hamiltonian is therefore:

$$\tilde{H} = H + \frac{\Delta t}{2}\{H_{\mathrm{A}}, H_{\mathrm{B}}\} + O(\Delta t^2) \quad . \tag{1.10}$$

Eq. 1.8 tells us that if $H_{\rm B}$ is not explicitly time-dependent, $\{H_{\rm A}, H_{\rm B}\}$ corresponds to the time derivative of $H_{\rm B}$ if the Hamiltonian was only $H_{\rm A}$. Therefore, the leading term of the energy error scales as the variation of $H_{\rm B}$ and not directly as $H_{\rm B}$. This is important to evaluate the relevance of the splitting (see Sec. 2.2).

For a second order symplectic integrator, three steps are used instead of two. The method consists in integrating $H_{\rm B}$ for $\Delta t/2$ then $H_{\rm A}$ for Δt, then again $H_{\rm B}$ for $\Delta t/2$, where Δt is the time step. A similar analysis than above shows that the surrogate Hamiltonian then writes:

$$\tilde{H} = H - \frac{\Delta t^2}{12}\{\{H_{\rm A}, H_{\rm B}\}, H_{\rm A} + \frac{1}{2}H_{\rm B}\} + O(\Delta t^4) \quad . \tag{1.11}$$

Exchanging $H_{\rm A}$ and $H_{\rm B}$ gives a non equivalent second-order scheme. Second order integrators are often enough when $\tilde{H}$ is designed to be close to H. A good way to ensure that is to make $H_{\rm B}$ small (perturbative part). Higher order integrators are nevertheless possible (Yoshida 1990).

1.3.2 Leap-frog mapping

The Leap-frog mapping is the most natural splitting, and can be used for a wide range of physical problems. It consists in separating the kinetic energy from the potential energy ("T+V" scheme). In our problem, it gives:

$$H_{\rm A} = \sum_{i=1}^{N} \frac{\boldsymbol{p_i}^2}{2m_i} \quad ; \tag{1.12}$$

$$H_{\rm B} = -\sum_{1\leq i<j\leq N} \frac{Gm_i m_j}{r_{ij}} \quad . \tag{1.13}$$

An evolution controlled by $H_{\rm A}$ writes (Hamilton equations):

$$\dot{\boldsymbol{r_i}} = \frac{\partial H_{\rm A}}{\partial \boldsymbol{p_i}} = \frac{\boldsymbol{p_i}}{m_i} \quad ; \tag{1.14}$$

$$\dot{\boldsymbol{p_i}} = -\frac{\partial H_{\rm A}}{\partial \boldsymbol{r_i}} = 0 \quad , \tag{1.15}$$

the momenta are constant and the positions evolve linearly. On the other hand, an evolution controlled by $H_{\rm B}$ writes:

$$\dot{\boldsymbol{r_i}} = \frac{\partial H_{\rm B}}{\partial \boldsymbol{p_i}} = 0 \quad ; \tag{1.16}$$

$$\dot{\boldsymbol{p_i}} = -\frac{\partial H_{\rm B}}{\partial \boldsymbol{r_i}} = \sum_{j\neq i} \frac{Gm_i m_j}{r_{ij}^3}\boldsymbol{r_{ij}} \quad , \tag{1.17}$$

the positions are constant and the momenta evolve linearly.

An evolution controlled by the surrogate Hamiltonian thus corresponds to the succession of inertial drifts (H_A) and velocity kicks (H_B). The latter does not correspond to any physical process, but is formally well defined.

We usually call leap-frog the second-order scheme of this splitting, which is a kick for $\Delta t/2$, a drift for Δt, and again a kick for $\Delta t/2$. However, this splitting does not usually have $H_\mathrm{A} \gg H_\mathrm{B}$, so that the second order scheme is not sufficient to ensure that the relative steady energy error is small ($O(t^2)$). Higher order leap-frog is used in N-body dynamics by the integrator `Janus` in the Python package `Rebound` (Rein & Tamayo 2017).

1.3.3 Mixed variable symplectic (MVS)

The leap-frog method is not specific to orbital mechanics, and does not take advantage of the known features of the problem. The main idea of the mixed variable symplectic mapping is that all the bodies trajectories are lightly perturbed Keplerian orbits, and that we know how to compute the exact resolution of the Keplerian motion to machine precision.

This scheme was first designed when no exoplanet was yet found, so it was meant exclusively for application to the Solar System. The motion is thus divided into two parts: Keplerian orbits around the Sun and perturbations by the other planets.

$$H_\mathrm{A} = \sum_{i=1}^{N} \left(\frac{\boldsymbol{p_i'}^2}{2m_i'} - \frac{G m_i m_\odot}{r_i'} \right) \quad ; \tag{1.18}$$

$$H_\mathrm{B} = \sum_{i=1}^{N} \left(\frac{G m_i m_\odot}{r_i'} - \frac{G m_i m_\odot}{r_{i\odot}} \right) - \sum_{1 \leq i < j \leq N} \frac{G m_i m_j}{r_{ij}} \quad . \tag{1.19}$$

where $\boldsymbol{r_i'}$ is the location of body i with respect to the center of mass of the bodies interior to its orbit (Jacobi coordinates, see Introduction Sec. 4.3), and $\boldsymbol{p_i'}$ is the relative conjugate momentum. An evolution controlled by H_A writes:

$$\dot{\boldsymbol{r_i'}} = \frac{\partial H_\mathrm{A}}{\partial \boldsymbol{p_i'}} = \frac{\boldsymbol{p_i'}}{m_i} \quad ; \tag{1.20}$$

$$\dot{\boldsymbol{p_i'}} = -\frac{\partial H_\mathrm{A}}{\partial \boldsymbol{r_i'}} = -\frac{G m_i m_\odot}{r_i'^3} \boldsymbol{r_i'} \quad , \tag{1.21}$$

which corresponds to a purely Keplerian evolution. On the other hand, an evolution controlled by H_B writes:

$$\dot{\boldsymbol{r_i'}} = \frac{\partial H_\mathrm{B}}{\partial \boldsymbol{p_i'}} = 0 \quad ; \tag{1.22}$$

$$\dot{\boldsymbol{p_i'}} = -\frac{\partial H_\mathrm{B}}{\partial \boldsymbol{r_i'}} \equiv m_i \boldsymbol{a_i^B} \left((\boldsymbol{r_j'}) \right) \quad , \tag{1.23}$$

the positions are constant and the momenta evolve linearly with an acceleration $\boldsymbol{a^B}$.

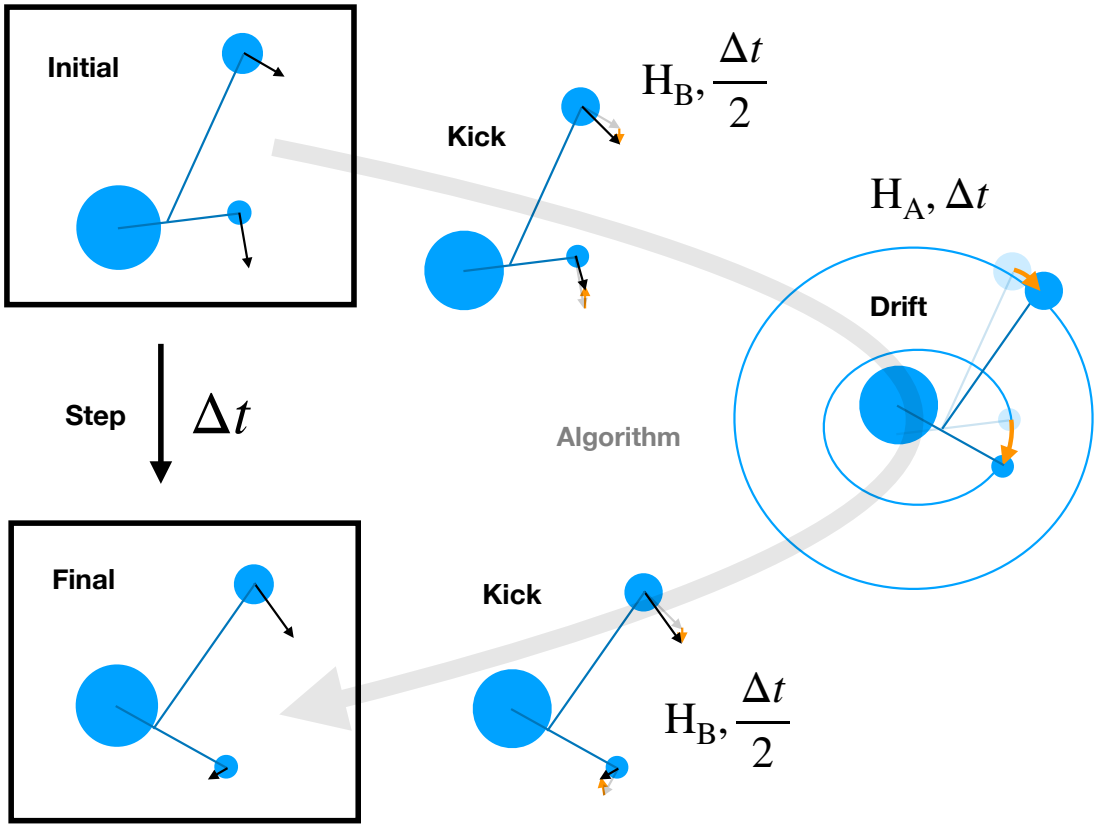

Figure 1.3 – Schematic of the kick-drift-kick procedure in the MVS framework.

Assuming that the Sun is the dominant mass ($m_\odot \gg m_i$) and that there is no close encounters between the planets, then H_B remains significantly smaller than H_A and the second order scheme is accurate enough. Moreover, as each term is exactly solvable, the time step does not need to be dramatically small. It is generally assigned to 1/20 of the smaller orbit in the modeled system to ensure 10^{-6} relative energy conservation in nominal cases.

This MVS mapping was suggested in Wisdom & Holman (1991), and was implemented three years later in `SWIFT RMVS` by Levison & Duncan (1994) (the appellation Mixed Variable Symplectic refers to the frequent switches of the code between Cartesian coordinates and Keplerian elements, and the R stands for Regularized). For the first time, it was computationally possible to integrate the Solar System for the entirety of its lifetime.

The scheme is very efficient for lightly perturbed Keplerian motions, but gives poor results when H_B becomes large, such as in the case of close encounters (typically comets entering the 3 Hill Radius zone). In `SWIFT RMVS`, Levison & Duncan (1994) handled the problem by switching scheme (heliocentric to planetocentric) and time steps whenever a body encounters another. At each of these interventions, however, energy errors are introduced, so that the algorithm is not truly symplectic anymore.

The scheme was then complexified by Saha & Tremaine (1994) to allow for individual time steps. It enabled a fastest and more precise integration, for the evolution of planet Pluto could be computed with a longer time-step than Mercury,

while Mercury's orbital evolution could keep its accuracy. However, the time steps could still not be changed.

1.3.4 Democratic heliocentric: `SyMBA` and `Mercury`

In the 1990s, the problem of adapting time steps in symplectic algorithms was a great issue among dynamicists. In that quest, a new Hamiltonian splitting was introduced, democratic heliocentric, that kept the idea of Wisdom & Holman (1991)'s mixed variables.

Duncan et al. (1998) introduced this mapping in their `SyMBA` integrator (where `SyMBA` stands for Symplectic Massive Body Algorithm), designed to adapt individually the time-steps without losing the symplecticity. Their approach is to define successive shells around each body, with an associated time step that decreases with the proximity of the shell. However, these variable individual time-steps does not behave well in the Jacobi coordinates, because each body revolves around a different center. Thus, Duncan et al. (1998) introduced the democratic heliocentric method. In this framework, the Hamiltonian is split in three parts:

$$H_{\mathrm{A}} = \sum_{i=1}^{N} \left(\frac{\boldsymbol{p_i}^2}{2m_i} - \frac{G m_i m_\odot}{r_{i\odot}} \right) \quad ; \tag{1.24}$$

$$H_{\mathrm{B}} = - \sum_{1 \leq i < j \leq N} \frac{G m_i m_j}{r_{ij}} \quad ; \tag{1.25}$$

$$H_{\mathrm{C}} = \frac{1}{2m_\odot} \left(\sum_{i=1}^{N} \boldsymbol{p_i} \right)^2 \quad . \tag{1.26}$$

It consists in a heliocentric coordinates ($\boldsymbol{r_{i\odot}}$) and barycentric velocities (momentum $\boldsymbol{p_i}$) description. To include the shell description and adaptative time steps, the potential part of H_{A} is decomposed into a sum of potentials different for each shell. The resulting integrator is truly symplectic, but, according to Chambers (1999), it is rather cumbersome to implement in practice, and it does not retain the great speed advantage of the basic symplectic method.

Inspired by the Duncan et al. (1998) approach and using the democratic heliocentric description, Chambers (1999) created `Mercury` one year later. Introduced as a hybrid symplectic integrator, `Mercury` handles close encounters with a Bulirsch-Stoer integrator (Sec. 1.2.2). To keep as much as possible the symplecticity of the integrator, the parts of H_{B} that grow large in case of close encounters is transferred into H_{A} when it cannot be neglected anymore. It is done so with a smoothing function, scaled with the Hill radii.

In the original paper and the version that is currently found online, there is a small mistake in Mercury's implementation (Wisdom 2016). The derivative of the smoothing function should have been included in the evolution equations, but it is not. This error has been corrected in the Mercury implementation in the Rebound package (`Mercurius`, Rein et al. 2019).

1.3.5 Hierarchical Jacobi Symplectic (HJS)

The previously presented mappings have been designed to properly integrate the Solar System components. All of them have their advantages and disadvantages depending on the exact nature of the problem to be solved. Though the dedicated papers are contemporaries with the first exoplanet discoveries, the Solar System echoes each of the discussions around symplectic codes. The central mass in even referred to as $m_\odot$ in the papers, and the solar mass is hard-coded in some of the implementations.

Today, the use of the N-body codes is not restricted to the Solar System anymore. With the rapid increase of exoplanet discoveries, including multi-planetary systems, the need for efficient N-body simulations has become strong to model the interaction between planets or planets and debris disk. However, the architecture of the Solar System is not universal. From giant planets to multiple stars, the single dominant mass paradigm is not always the most appropriate description.

In Chambers et al. (2002), the authors develop two new versions of `Mercury`, designed for s-type planets in wide binary stars and for p-type planets in tight binary stars (circumbinary planets). In these versions, the democratic heliocentric method was modified to take into account the large motions of the stars, but the philosophy stayed the same.

Yet, as long as there is lightly perturbed Keplerian motion involved, symplectic integrators can theoretically model efficiently the evolution in any orbital configurations, assuming that the proper description is adopted. In Beust (2003), the Hierarchical Jacobi coordinates are introduced that generalized the Mixed variable symplectic approach to account for any architecture. They are implemented in the `Swift HJS` code.

The Hierarchical Jacobi coordinates description is based on orbits instead of on bodies. An orbit consists in a collection of two non-empty sets of bodies, the set of centers and the set of satellites, that have empty intersection. We can chose by convention to name centers the heaviest set and satellite the lightest. As an example, the Sun-Earth-Moon problem can be represented by two orbits: the Earth-Moon orbit, with the Earth as a center and a Moon as a satellite, and the Sun-Earth-Moon orbit, with the Sun as a center and the Earth and Moon as satellites. Orbits can be schematized as lines, linking the center of mass of the satellite to the center of mass of the centers. An example of such representation is shown on Fig. 1.4.

In all problems in orbital mechanics, a hierarchy can then be defined as a collection of orbits comprising all bodies and satisfying the following rule: for all couples of orbit k and $l \neq k$, one of the three subsequent propositions applies

- orbits k and l have no common bodies (orbits k and l are *foreign*);
- orbit k is comprised in the centers or satellites of orbit l (orbit k is *inner* to orbit l);
- orbit l is comprised in the centers or satellites of orbit k (orbit k is *outer* to orbit l).

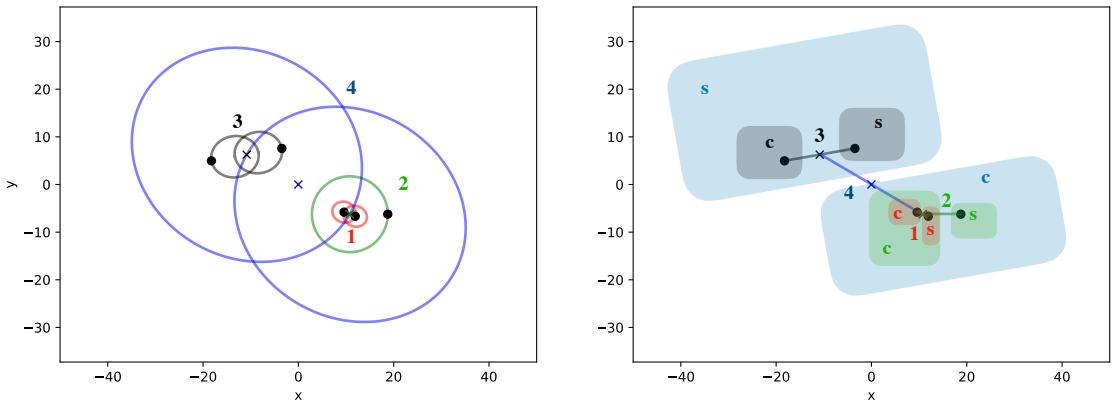

Figure 1.4 – Schematic of a non-Solar type hierarchy, with 5 bodies and 4 nested orbits. On the left, the orbits are represented by the trajectory of the centers and satellites around their center of mass. On the right, they are represented by simple lines linking the centers of mass of satellites and centers. The letters c and s designate respectively the centers and satellites of each orbit.

For a given problem numerous hierarchies are possible, but most of the time a natural hierarchy arises, that decreases to a minimum the perturbations between each orbit, so the problem is approximately a set of independent Keplerian motions. As an example, Fig. 1.4 shows a valid hierarchy defined in a 5-body problem. Orbits 1 is inner to orbit 2, as the bodies of orbit 1 are entirely within the set of centers of orbit 2. Orbit 2 and 3 are foreign, as they have no bodies in common. Finally, orbit 4 is outer to orbits 1, 2 and 3 are inner to orbit, because they are each embedded in one of the sets of orbit 4.

During my PhD, I worked extensively on this orbital representation, to work on the new versions of `Swift HJS`. Several results come directly from the rules defined above.

First, a hierarchy of N bodies is made of exactly $N-1$ orbits. This can be proved by mathematical induction. The reasoning is represented on Fig. 1.5. From two bodies, only one orbit can be defined. Supposing that the proposition is true for $n-1$ bodies, then let us consider n bodies and define an arbitrary orbit with c centers and s satellites. As c, s and $n-s-c$ are both inferior or equal to n, then the total number of orbits is the sum of $s-1$, $c-1$, $n-s-c$ (counting the first orbit as a body) and 1 (the first orbit). It gives a total of $n-1$ orbits.

From this proposition, we derive that there is at least one orbit composed of two bodies, and one composed of $N-1$ bodies. This can be showed by contradiction, because the contrary would leave room for another orbit, which is not possible given the fixed number of orbits.

In `SWIFT HJS`, the orbits are numbered from 2 to N. Finally, we define μ_k and η_k as the total mass of the satellites and centers respectively of orbit k. The total dynamical mass in orbit k is then $M_k = \mu_k + \eta_k$ and the reduced mass $m'_k = \mu_k \eta_k / M_k$.

In this formalism, a new set of N coordinates $(\boldsymbol{r}'_k, \boldsymbol{p}'_k)_{i=1,..,N}$ are designed with a Jacobi-like approach: $\boldsymbol{r}'_k$ is the relative position of the center of mass of orbit k's satellites with respect to that of its centers (the centers of mass are represented by

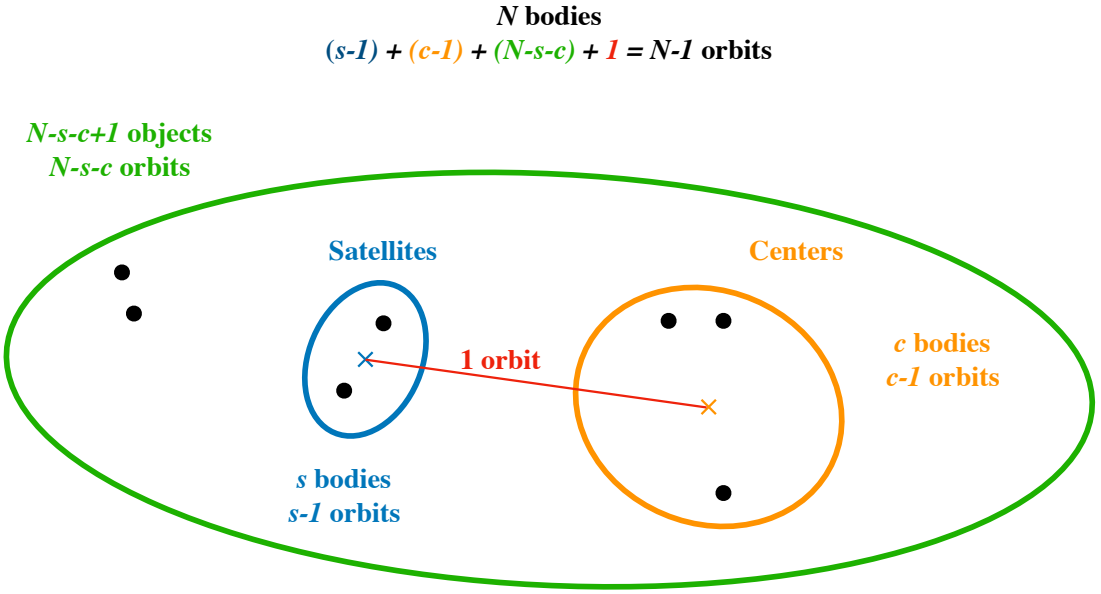

Figure 1.5 – Illustration of the mathematical induction to show that a N-body problem admits hierarchies with exactly $N-1$ orbits.

crosses in Fig. 1.4, and $\boldsymbol{p}'_k$ is the relative conjugate momentum. The first coordinates $\boldsymbol{r}'_1$ and $\boldsymbol{p}'_1$ are the position and impulsion of the center of mass. These positions and conjugate momenta derive from a canonical transformation that let the Hamiltonian invariant. They can be expressed with the bodies coordinates as

$$\boldsymbol{r}'_k = \sum_{i,\text{ satellites of k}} \frac{m_i \boldsymbol{r}_i}{\mu_k} - \sum_{i,\text{ centers of k}} \frac{m_i \boldsymbol{r}_i}{\eta_k} \quad ; \tag{1.27}$$

$$\boldsymbol{p}'_k = m'_k \left(\sum_{i,\text{ satellites of k}} \frac{\boldsymbol{p}_i}{\mu_k} - \sum_{i,\text{ centers of k}} \frac{\boldsymbol{p}_i}{\eta_k} \right) \quad . \tag{1.28}$$

The Hamiltonian can then be split as follows

$$H_\text{A} = \sum_{k=2}^{N} \frac{{p'_k}^2}{2m'_k} - \frac{G\mu_k\eta_k}{r'_k} \quad ; \tag{1.29}$$

$$H_\text{B} = \sum_{k=2}^{N} \frac{G\mu_k\eta_k}{r'_k} - \sum_{1\leq i<j<\leq N} \frac{Gm_im_j}{r_{ij}} \quad . \tag{1.30}$$

The key idea is that H_B does not depend on the momenta $\boldsymbol{p}'_k$, and that H_A naturally splits into a sum of independent Keplerian problems. This is a direct consequence of the fact that the kinetic energy writes as a weighted sum of the $\boldsymbol{p}'^{\,2}_k$ terms (no crossed terms $\boldsymbol{p}'_k\boldsymbol{p}'_l$). An evolution controlled by H_A writes:

$$\dot{\boldsymbol{r}'_i} = \frac{\partial H_{\rm A}}{\partial \boldsymbol{p}'_i} = \frac{\boldsymbol{p}'_i}{m'_i} \quad ; \tag{1.31}$$

$$\dot{\boldsymbol{p}'_i} = -\frac{\partial H_{\rm A}}{\partial \boldsymbol{r}'_i} = -\frac{G\mu_k\eta_k}{r_i'^3}\boldsymbol{r}'_i \quad , \tag{1.32}$$

which corresponds to a purely Keplerian evolution. On the other hand, an evolution controlled by $H_{\rm B}$ writes:

$$\dot{\boldsymbol{r}'_i} = \frac{\partial H_{\rm B}}{\partial \boldsymbol{p}'_i} = 0 \quad ; \tag{1.33}$$

$$\dot{\boldsymbol{p}'_i} = -\frac{\partial H_{\rm B}}{\partial \boldsymbol{r}'_i} \equiv m'_i \boldsymbol{a}_i^{\boldsymbol{B}}\left((\boldsymbol{r}'_j)\right) \quad , \tag{1.34}$$

the positions are constant and the momenta evolve linearly with an acceleration denoted $\boldsymbol{a}^{\boldsymbol{B}}$, that derives from $H_{\rm B}$.

This description is fully symplectic, and a second-order scheme can be adopted as $H_{\rm A} \gg H_{\rm B}$ when the hierarchy is marked, without any condition on dominant mass ratios. `Swift HJS` is thus fitted to integrate planetary systems as well as stellar systems (Beust 2003). An example of non-Solar type hierarchy that can be integrated with the code is represented on Fig. 1.4.

However, by its very nature, any change of hierarchy (including close encounters) is not easy to handle in `Swift HJS`. In its original version, the code does not handle close encounters. This issue is discussed in 2.2 and 2.3, where new versions of the algorithm are presented.

1.4 Swift HJS

Swift HJS is an implementation of the Hierarchical Jacobi Symplectic description, designed by Beust (2003) to model hierarchical systems. It is coded in Fortran, and keeps the same organization than its ancestor `Swift RMVS`. The core code, organized around the module *swift_hjs.f,* makes use of around 60 sub-modules, that ranges from the computation of a sine to the performing of a symplectic step. The solving of the Keplerian part alone requires many of these modules, to properly and efficiently model elliptic, hyperbolic and parabolic orbits.

1.4.1 Core algorithm

The core of the algorithm is a kick-drift-kick procedure illustrated on Fig. 1.3 and whose implementation is represented on Fig. 1.6. In this framework, an evolution for Δt is made of an evolution controlled by $H_{\rm B}$ for $\Delta t/2$, $H_{\rm A}$ for Δt, and $H_{\rm B}$ for $\Delta t/2$. Only the velocities evolve during the first and last phase, while both the position and velocity evolved along a Keplerian orbit in the middle phase. Two modules require non-trivial computation: the derivation of the acceleration induced by $H_{\rm B}$ (perturbative acceleration $\boldsymbol{a}^{\boldsymbol{B}}$), and the computation of the Keplerian drift.

The acceleration of the Jacobian coordinates of orbit k is given by:

$$\boldsymbol{a}_{\boldsymbol{k}}^{\prime \boldsymbol{B}} = \sum_{\substack{i \in \mathrm{Sat}_k \\ j \notin k}} \frac{G m_i m_j}{\mu_k r_{ij}^3} \boldsymbol{r_{ij}} - \sum_{\substack{i \in \mathrm{Cen}_k \\ j \notin k}} \frac{G m_i m_j}{\eta_k r_{ij}^3} \boldsymbol{r_{ij}} + \sum_{\substack{i \in \mathrm{Cen}_k \\ j \in \mathrm{Sat}_k}} \frac{G m_i m_j}{m_k'} \left(\frac{1}{r_k'^3} - \frac{1}{r_{ij}^3} \right) \boldsymbol{r_{ij}} \quad (1.35)$$

For each orbit, it compiles the interactions between the satellites, between the centers, and with the outer bodies. This operation scales as N^3.

To go from the Jacobi coordinates to the barycentric coordinates (and *vice-versa*), a transformation matrix is computed from the hierarchy at the beginning of the simulation. This matrix gives the relative weight of bodies in each orbit, and is described in Beust (2003).

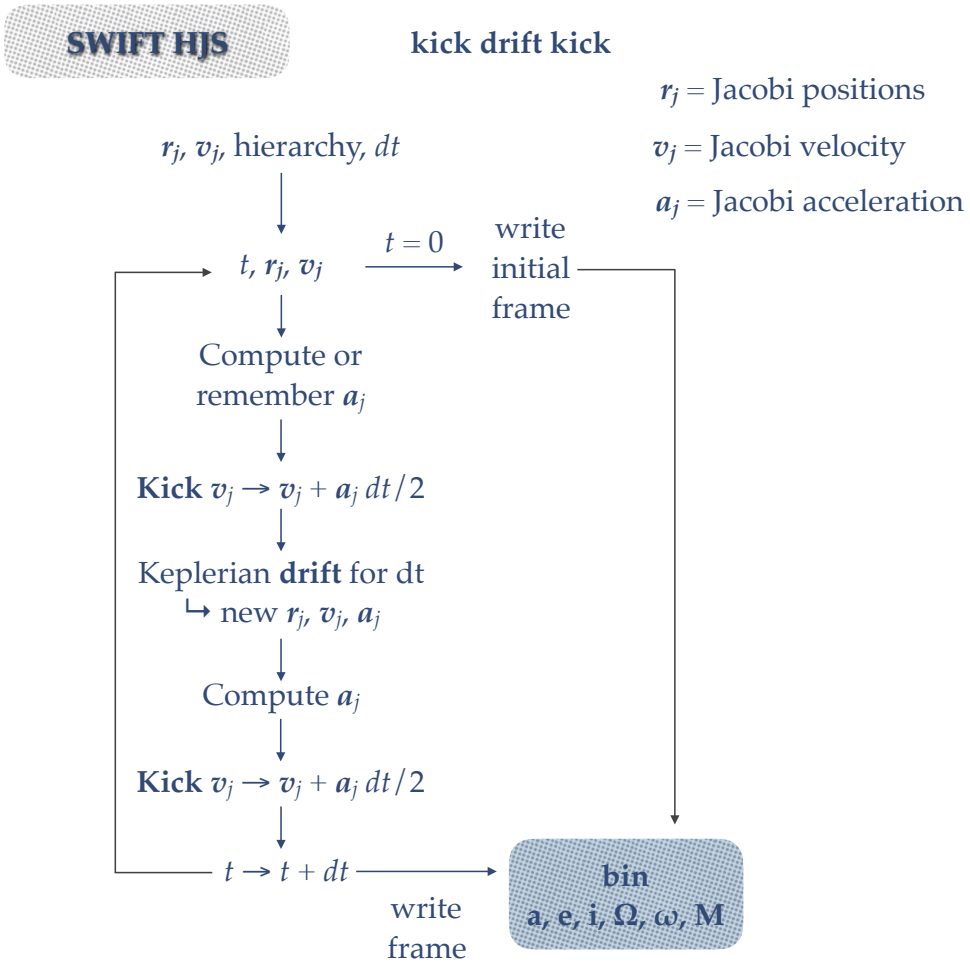

Figure 1.6 – Schematic of the core algorithm of Swift HJS.

On the other hand, each orbital evolution is computed independently. First, the orbital elements are derived from the Jacobi coordinates. Then, the Kepler equation is solved to derive the new eccentric anomaly using the Danby iterative

method (see Appendix). The Danby method is optimized so that the computer accuracy is reached with a small number of iterations (below three for elliptic orbits, below ten for hyperbolic orbit).

1.4.2 Modules

The core algorithm takes the initial coordinates of the bodies and test particles, their hierarchy, and returns a binary file comprising the orbital elements with respect to time. An efficient use of the code involves the design of additional modules, for easy initialization and analysis of the data. They are summarized in Fig. 1.7.

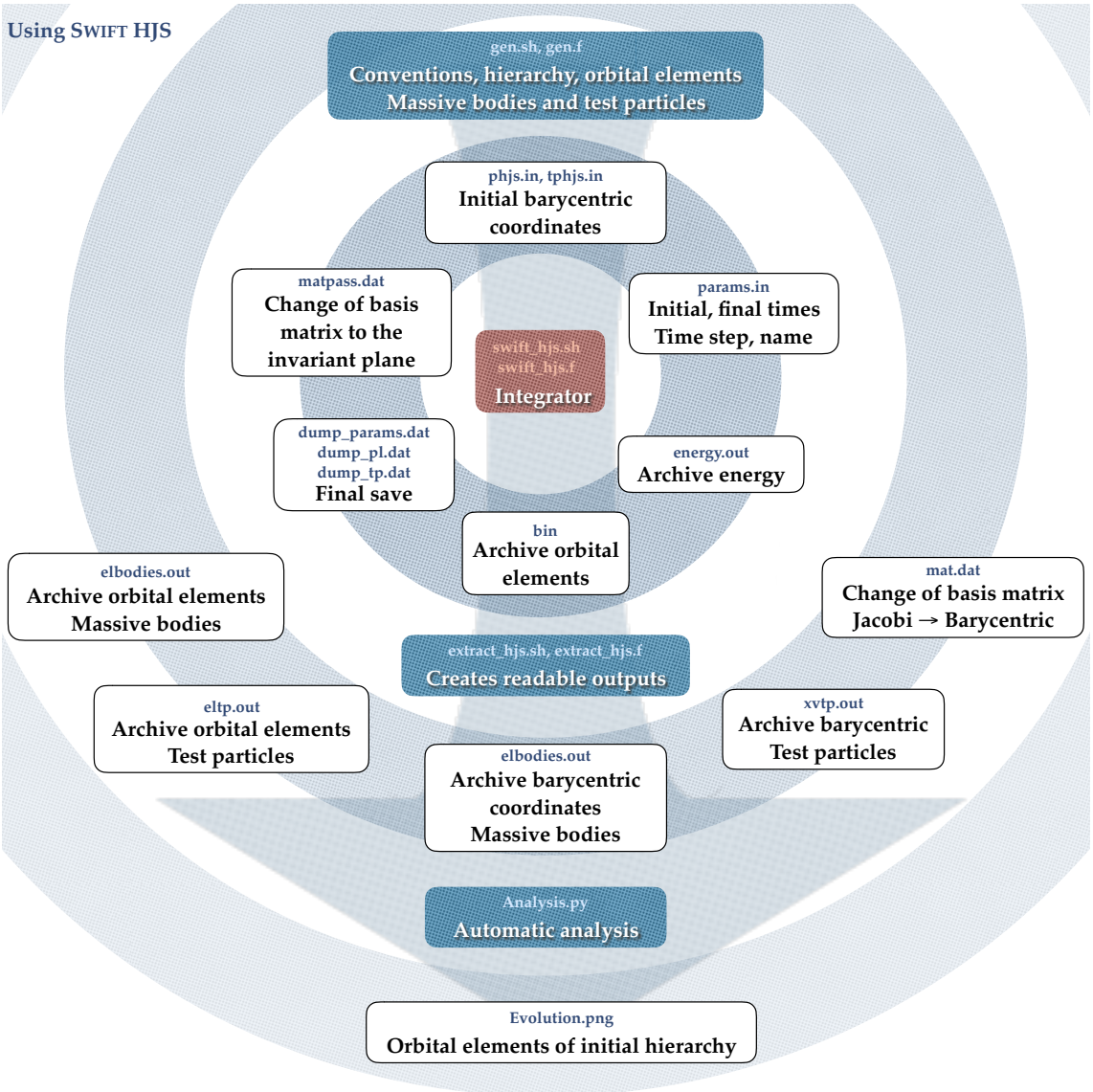

Figure 1.7 – Schematic of the inputs and outputs of SWIFT HJS. The user inputs are filled in *gen.sh* and *params.in*.

It is often useful to have an intermediate module to translate our constraints into acceptable inputs. This is the role of the routine *gen*, which takes the orbital elements of the orbits and the hierarchy of the massive bodies and test particles. The

routine is straightforward for the massive bodies, but involves some computation to generate a disk of test particles (see below).

Post-processing routines are also needed to makes use of the simulation. First, a module extracts the desired information from the raw binary output (which contains the history of the orbital elements of each massive bodies and test particles). Then, we make use of a more practical langage (Greg or Python for example) to plot the evolution of the different quantities, or represent the graphical evolution of the disk.

1.4.3 Treatment of test particles

The study of planetary systems often involves the study of debris belts. In N-body simulations, the dust is modeled at first order by massless bodies (or test particles) that interact with the massive bodies but not with each other. Test particles are specifically considered in `Swift HJS` as the handling of their hierarchy is slightly different. Indeed, they are the only satellites of their orbit and their orbit is invisible to the bodies and other test particles evolution.

Their evolution follows the same pattern as the massive bodies, a kick-drift-kick procedure presented above. However, their perturbative acceleration writes, in the barycentric coordinates:

$$\boldsymbol{a^B} = \frac{G\eta}{r'^3}\boldsymbol{r'} + \sum_{k \text{ with tp}\in\text{Sat}_k} \frac{G\eta_k}{r_k'^3}\boldsymbol{r'_k} - \sum_{k \text{ with tp}\in\text{Cen}_k} \frac{G\mu_k}{r_k'^3}\boldsymbol{r'_k} - \sum_{j\in\text{Cen}_{\text{tp}}} \frac{Gm_j}{(\boldsymbol{r}-\boldsymbol{r_j})^3}(\boldsymbol{r}-\boldsymbol{r_j}) \tag{1.36}$$

and in the Jacobi coordinates:

$$\boldsymbol{a'^B} = \boldsymbol{a^B} - \sum_{j\in\text{Cen}_{\text{tp}}} \frac{m_j}{\eta}\boldsymbol{a_j^B} \quad . \tag{1.37}$$

1.5 Non-Keplerian forces

The study of planetary systems often involve tidal forces or interactions with the primordial gas (such as migration), so that the possibility of taking into account these phenomena are essential to a good algorithm. All the integrators presented above can handle additional non-Keplerian forces.

Let us name $\boldsymbol{F}\left((\boldsymbol{q_i}),(\boldsymbol{p_i})\right)$ the sum of non-Keplerian force acting on the system. If $\boldsymbol{F}$ is not conservative, the Hamiltonian is not conserved anymore. The equations of motion now read:

$$\dot{\boldsymbol{r_i}} = \frac{\partial H}{\partial \boldsymbol{p_i}} = \frac{\boldsymbol{p_i}}{m_i} \quad ; \tag{1.38}$$

$$\dot{\boldsymbol{p_i}} = -\frac{\partial H}{\partial \boldsymbol{p_i}} = \sum_{j\neq i} \frac{Gm_im_j}{r_{ij}^3}\boldsymbol{r_{ij}} + \boldsymbol{F} \quad , \tag{1.39}$$

Whatever the dependence of the force, these equations fit into all the frameworks described previously. The use of the symplectic mappings remains possible, but

is relevant only if $\boldsymbol{F}$ has a small effect compared to the gravitational forces, and can thus be integrated as a perturbative effect, similar to the treatment of H_{B}. Depending on the form of $\boldsymbol{F}$, the integration may be exact (if it only depends on the position for example) or approximate.

2 Code development

2.1 Development of surrogate tools for `Swift HJS`

2.1.1 Analysis and representation of the outputs

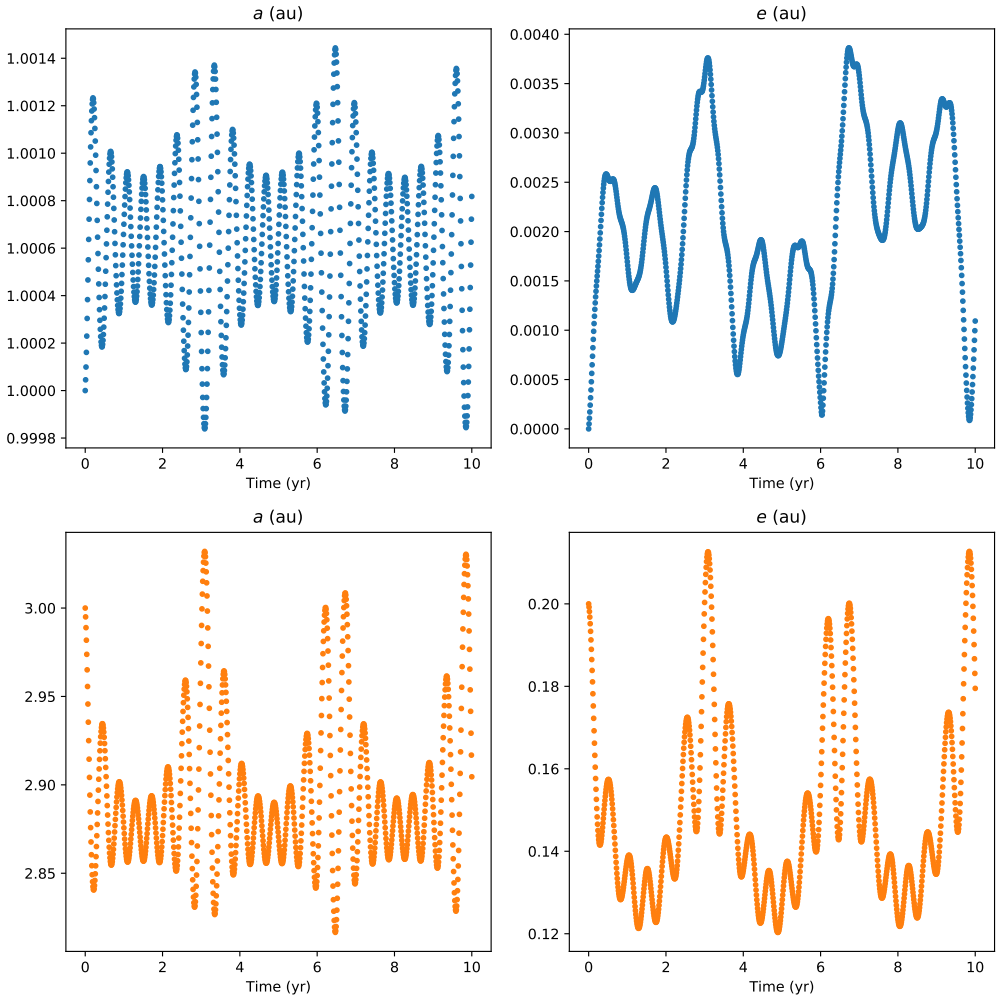

Figure 1.8 – Example of automatic analysis by the module *Analysis.py* of a simulation with `Swift HJS`. The evolutions of each orbit orbital elements (columns) of each orbits (lines) are computed, but only the semi-major axes and eccentricities are represented here.

Before my PhD, the analysis of the simulation was coded in the `GreG` language, that is part of the `GILDAS` working group software developed by IPAG and IRAM in

Grenoble. As part of this PhD, I have developed new routines in Python. First, an extract routine is used to compute the position and orbital elements of the massive bodies and test particles, inspiring from the output files of the `Mercury` code. Then, a first analysis routine is used to plot the overall evolution of the massive bodies orbital elements, as an overview of the entire integration (see Fig. 1.8).

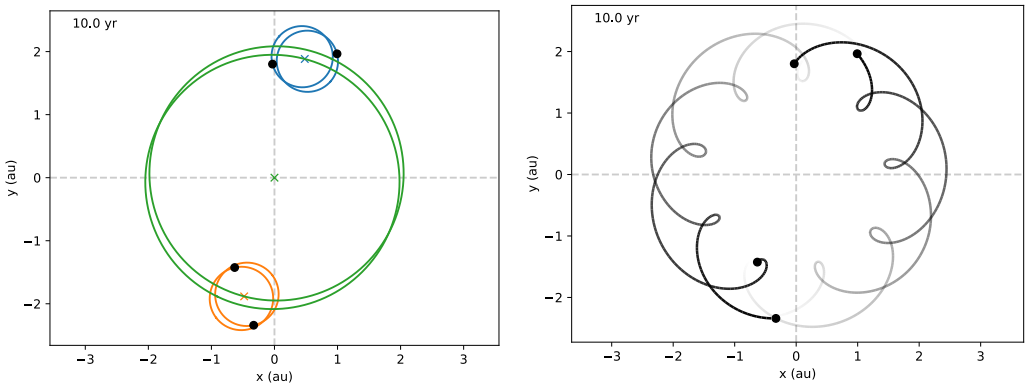

Figure 1.9 – Snapshots of a simulation of a quadruple system with `Swift HJS`.

Furthermore, I wrote more complex routines to visualize the evolution of the bodies and orbits. Examples of visualizations can be seen on Fig. 1.9, whether with orbits or trajectories. The relevant representation depends on the problem.

2.1.2 The special case of test particle

The analysis of the test particle evolution in the simulations involves different modules, mostly because test particles are often defined as a group with numerous objects (1,000 - 10,000). It is practical to set the characteristics of the belt rather than the individual characteristics of each particles. Such initialization is provided for in the *gen* routine. Semi-major axis, eccentricity and inclination ranges must be provided, along with the plane of reference and the center(s) of rotation. In the course of my PhD, I worked multiple times with debris disks, the corresponding work being described in the next sections (HD 106906, HD 206893 and HR 2562). Depending on the situation, the base plane of the disk was not always the reference plane of the planets (ecliptic), so that I improved the existing routine to compute a transformation matrix from the ecliptic to the wanted plane. Then, the characteristics of the disk (in terms of orbital elements) could be given and retrieved in the desired plane.

Once the simulation is done, the test particles may be simply plotted along with the massive bodies to have a first overview of the disk geometry (Fig 1.10 left). However, such representation does not allow grasping the structures that might appear. The representation can therefore be completed with a density map (2D histograms, Fig 1.10 right). When we are interested in the secular evolution, the number of particles can be artificially increased (to get a more precise map) by filling the orbits of the existing particles.

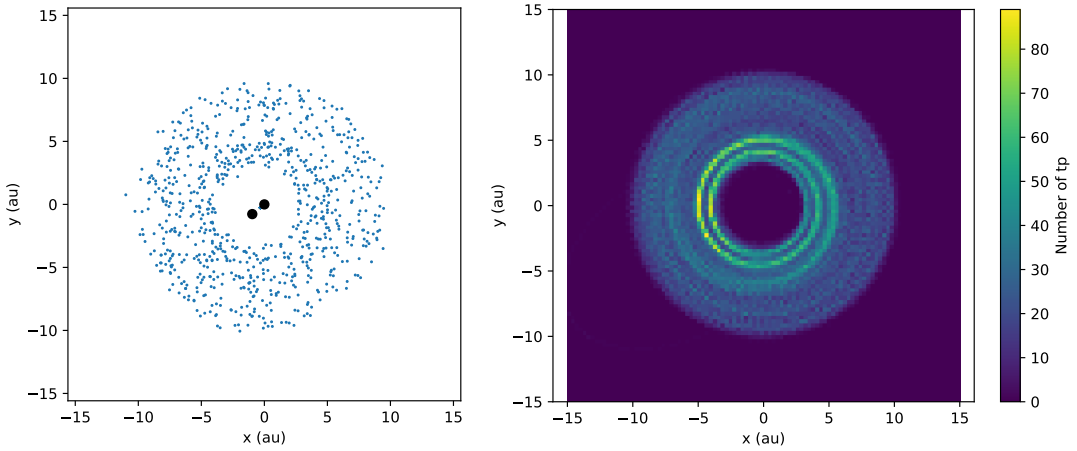

Figure 1.10 – Representations of the ouput of the simulation of a circumbinary debris disk with `Swift HJS`. The two figures correspond to the same data comprising the characteristics of 1,000 test particles. In the right figure, the orbits of each test particles have been artificially filled with 1,000 additional particles, so that a 2D histogram of the density can be computed.

2.1.3 Treatment of migration

In the study of the extrasolar system HD 106906 (see Sec. 3), we needed to take into account the effect of migration in the coplanar case. Due to the interaction between the protoplanetary disk and planets, planetary migration is currently not very well constrained though it is a crucial ingredient of the early formation and evolution of systems architecture (see Introduction). The most accurate way to include migration into a study is to include the gas dynamics, but even then the constraints are always loose regarding the gas aspect ratio, density and viscosity. Thus, we used an effective migration force with a constant migration rate $v_{\rm mig} = da/dt$ in case of no additional perturbation. This assumption is not exactly realistic, but we were interested in the dynamics of the planet in a specific narrow zone, so that the variation of the migration rate may be negligible at first order. Assuming a simple form and no eccentricity change or precession, we then derived theoretically the expression of the migration force per mass $\boldsymbol{F}_{\rm mig}$ for each orbit i (the derivation is explained in Rodet et al. 2017 below):

$$\boldsymbol{F}_{\rm mig} = \frac{m'_i v_{\rm mig} \pi}{P_i \sqrt{1-e_i^2}} \left(1 + \frac{1}{2}(1 - \frac{r'_i}{a_i})\right) \boldsymbol{e_\theta} \quad , \tag{1.40}$$

where P_i is the period, a_i the semi-major axis and e_i the eccentricity of orbit i, and $\boldsymbol{e_\theta}$ is the unit vector of the polar base associated with the true anomaly θ. It can be computed from the Jacobi vector position and velocity at a given time:

$$\boldsymbol{e_\theta} = \frac{\boldsymbol{r'_i} \wedge \dot{\boldsymbol{r}}'_i}{\|\boldsymbol{r'_i} \wedge \dot{\boldsymbol{r}}'_i\|} \wedge \frac{\boldsymbol{r'_i}}{r'_i} \quad . \tag{1.41}$$

Though we use the velocity to compute $\boldsymbol{e_\theta}$, the vector depends in fact on the true anomaly and the orbital plane (fixed in the problem) alone. Thus, $\boldsymbol{F}$ depends only

on the position, so that its integration within `Swift HJS`'s scheme is immediate. Its effect is accounted for in the kick part, where the position is fixed and the velocity is linearly increased. The new perturbative evolution of orbit i is then

$$\dot{\boldsymbol{r}}'_{\boldsymbol{i}} = \frac{\partial H_{\mathrm{B}}}{\partial \boldsymbol{p}'_{\boldsymbol{i}}} = 0 \quad ; \tag{1.42}$$

$$\dot{\boldsymbol{p}}'_{\boldsymbol{i}} = -\frac{\partial H_{\mathrm{B}}}{\partial \boldsymbol{r}'_{\boldsymbol{i}}} = m' i \boldsymbol{a}_{\boldsymbol{i}}^{\boldsymbol{B}} \left((\boldsymbol{r}'_{\boldsymbol{j}}) \right) \quad , \tag{1.43}$$

where $\boldsymbol{a}_{\boldsymbol{i}}^{\boldsymbol{B}} \left((\boldsymbol{r}'_{\boldsymbol{j}}) \right)$ corresponds to the previously introduced (Eqs. (1.34) and (1.35)) perturbative evolution of orbit i without migration.

This derivation of $\boldsymbol{F}_{\mathrm{mig}}$ is somewhat arbitrary (assumption of a simple form), and neglects possibly important effects (eccentricity damping, variation of the migration direction and strength...). However, in the following study, it was used to evaluate qualitatively the possiblity of a scenario, and a simple approach was adopted to reduce computational costs. More complicated effective models were used for example within `Mercury` in Xu & Lai (2017).

2.2 Handling hierarchy change

The architecture of planetary systems are subject to constant variations. In an old system such as the Solar System, the variations of the orbital elements of the planets are small, so that the global hierarchy of the major planets remains the same, but the smaller bodies (comets, asteroids) can still be subjected to major changes in case of close encounter with a planet. In young systems, observations suggest that strong interactions between planetary bodies are common (Morbidelli 2013). In this thesis, we refer as close encounter a phenomenon that deviates significantly and over a short timescale an orbital trajectory from its current Keplerian motion. This definition is partly arbitrary, as it depends on our accuracy goal to evaluate the significance of the deviation.

The symplectic mappings that take advantage of the analytic resolution of the Kepler motion do not handle well close encounters, and even less hierarchy changes. They are designed for problems where the non-Keplerian parts of the motions (H_{B}) are small with respect to the Keplerian parts (H_{A}), so that the error becomes out of control in case of close encounters. This error does not decreases if the hierarchy has changed after the close encounter, because the splitting of the Hamiltonian is entirely based on the initial hierarchy.

Handling hierarchy change is not a priority for most of the symplectic integrators, as they are based on the Solar System architecture and are not fitted to change the hierarchy whatsoever. However, `Swift HJS` is designed to work efficiently with any hierarchy, and it is thus natural to implement the possibility of a hierarchy change within the algorithm. Strictly speaking, when changing the hierarchy, the symplectic nature of the algorithm does not hold anymore, as the splitting of the Hamiltonian changes. This is also true for any change of the time step. A new approximate Hamitonian is integrated from an already approximated scheme, which means that the error budget raises potentially at each hierarchy change. However,

the algorithm is designed for orbital dynamics, where systems are not subject to frequent reorganization of their architecture.

The new version of SWIFT HJS that handles hierarchy changes is called `ODEA`. It was presented in Rodet et al. (2019) (above), with an application to system HD 106906. In this section, I will introduce the new version with more details.

2.2.1 Criterion to evaluate a hierarchy

Similarly to the handling of close encounters, the computation of a good criterion to evaluate the relevance of the Hamiltonian splitting is the central point of the algorithm. Traditionally in a planetary system, the Hill radius around a given planet is used to scale the bodies relative distances. The Hill radius corresponds to the position of the first Lagrange point, that is the point between the center and the satellite where the sum of the gravitational forces and the centripetal force cancel. At this point, a massless particle is theoretically motionless in the co-rotating frame. The Hill radius r_H from the center (mass η) verifies:

$$-\frac{G\eta}{(r-r_H)^2}+\frac{G\mu}{r_H^2}+\frac{G(\mu+\eta)}{r^3}(\frac{\eta}{\eta+\mu}r-r_H)=0 \quad , \tag{1.44}$$

where r is the distance between the center and the satellite (mass μ). Solving this equation is equivalent to finding the root of a 5-degree polynomial. An approximated result can be derived if the satellite's mass is negligible before the center's mass: $r_H/a=\sqrt[3]{\mu/3\eta}$. However, there is no dominant mass a priori in `ODEA`, contrary to `Mercury`. Moreover, the little eccentricities of the massive bodies in `Mercury` allow neglecting the variation of the radius r and replace it by the semi-major axis a. Again, this is not the case in `ODEA`, that is fitted to study any orbit, whatever its eccentricity, including hyperbolic trajectory. Thus, the Hill radius, heavy to compute and unreliable in the general case, will not be considered here.

We demand the criterion to satisfy two points: being correlated with the error induced by the symplectic splitting (Eq. 1.11), and being fast to compute. As it must be computed at each time step, its computation must be fast compared to the most expensive step, which is the computation of the perturbative acceleration $\boldsymbol{a^B}$. From Eq. (1.35), each acceleration $\boldsymbol{a_i^B}$ scales as N^2, because all the residual accelerations between the bodies within the orbit have to be taken into account. So the total cost of the step (computation of the $\boldsymbol{a_i^B}$ for each orbit) scales as $O(N^3)$.

The quantity that is best correlated with the error is the error itself. The energy error can be computed from Eqs. 1.10 and 1.11 in the framework of `Swift HJS`. It gives:

$$H_{\rm err} = \frac{\Delta t}{2}\{H_{\rm A}, H_{\rm B}\} = \frac{\Delta t}{2}\{\sum_{k=2}^{N} \frac{p_k^2}{2m_k}, H_{\rm B}\} \tag{1.45}$$

$$= -\frac{\Delta t}{2}\sum_{k=2}^{N} \frac{\boldsymbol{p_k}}{m_k}\frac{\partial}{\partial \boldsymbol{r_k}} H_{\rm B}) \tag{1.46}$$

$$= \frac{\Delta t}{2}\sum_{k=2}^{N} \boldsymbol{p_k a_k^B} \tag{1.47}$$

in the first-order case, and, with some more steps,

$$H_{\rm err} = -\frac{\Delta t^2}{12}\{\{H_{\rm A}, H_{\rm B}\}, H_{\rm A} + \frac{1}{2}H_{\rm B}\} \tag{1.48}$$

$$\approx -\frac{\Delta t^2}{12}\{\{H_{\rm A}, H_{\rm B}\}, H_{\rm A}\} \tag{1.49}$$

$$\begin{aligned}\approx -\frac{\Delta t^2}{12}\Bigg(&\sum_{k=2}^{N}\frac{GM_k}{r_k^3}\frac{p_k^2}{m_k}\left(1 - 3\frac{(\boldsymbol{p_k}.\boldsymbol{r_k})^2}{p_k^2 r_k^2}\right)\\ &-\sum_{k=2}^{N}\sum_{l=2}^{N}\sum_{1\le i<j\le N}\frac{Gm_i m_j(M_{jl}^{-1} - M_{il}^{-1})(M_{jk}^{-1} - M_{ik}^{-1})}{m_k m_l r_{ij}^3}\boldsymbol{p_k}.\boldsymbol{p_l}\left(1 - 3\frac{(\boldsymbol{p_l}.\boldsymbol{r_{ij}})(\boldsymbol{p_k}.\boldsymbol{r_{ij}})}{(\boldsymbol{p_k}.\boldsymbol{p_l})r_{ij}^2}\right)\\ &-\sum_{k=2}^{N}\frac{1}{m_k}\left(\frac{G\mu_k\eta_k}{r_k^3}\boldsymbol{r_k} - \sum_{1\le i<j\le N}\frac{Gm_i m_j(M_{jk}^{-1} - M_{ik}^{-1})}{r_{ij}^3}\boldsymbol{r_{ij}}\right).\frac{G\mu_k\eta_k}{r_k^3}\boldsymbol{r_k}\Bigg)\end{aligned} \tag{1.50}$$

in the second-order case, where M is the transformation matrix from the barycentric to the Jacobi coordinates, such that $\boldsymbol{r'_k} = M_{kj}\boldsymbol{r_j}$ and $\boldsymbol{r_j} = M_{jk}^{-1}\boldsymbol{r_k}$.

Clearly, the expression of the error given by Eq. 1.50 for the second-order case is too complicated to be a good criterion. The error of the first-order scheme given by Eq. 1.47 is a good basis however, as it is proportional to $\boldsymbol{a^B}$, which is already computed in the integration. We are searching for a criterion to measure the relevance of the hierarchy, whatever the time step or the velocities. Moreover, each orbit does not weight the same in the energy error, but the hierarchy should fit at best every orbit nevertheless. All in all, we define the individual criteria of orbit k as

$$c_k = \frac{a_k^B}{a_k^{\rm Kep}} \tag{1.51}$$

where $a_k^{\rm Kep}$ is the Keplerian acceleration, induced by $H_{\rm A}$. We set the threshold, below which every c_k should remain, at 0.2. Assuming a well-chosen timescale ($< P/20$), it would correspond to an energy ratio $H_{\rm err}/H_{\rm A}$ of 0.01. Above, a new hierarchy is searched for. It is important to note that the criterion only indicates when to search for a new hierarchy, but does not guaranty that a better hierarchy will be found. Conversely, a non-optimal hierarchy can have low criterion or energy error. But as the search for a new hierarchy is computationally costly, we limit it to the cases

when the integration error becomes high. The value of the criterion threshold can be adjusted in the code, but in most cases that I tested, no better hierarchy existed for configurations below this threshold.

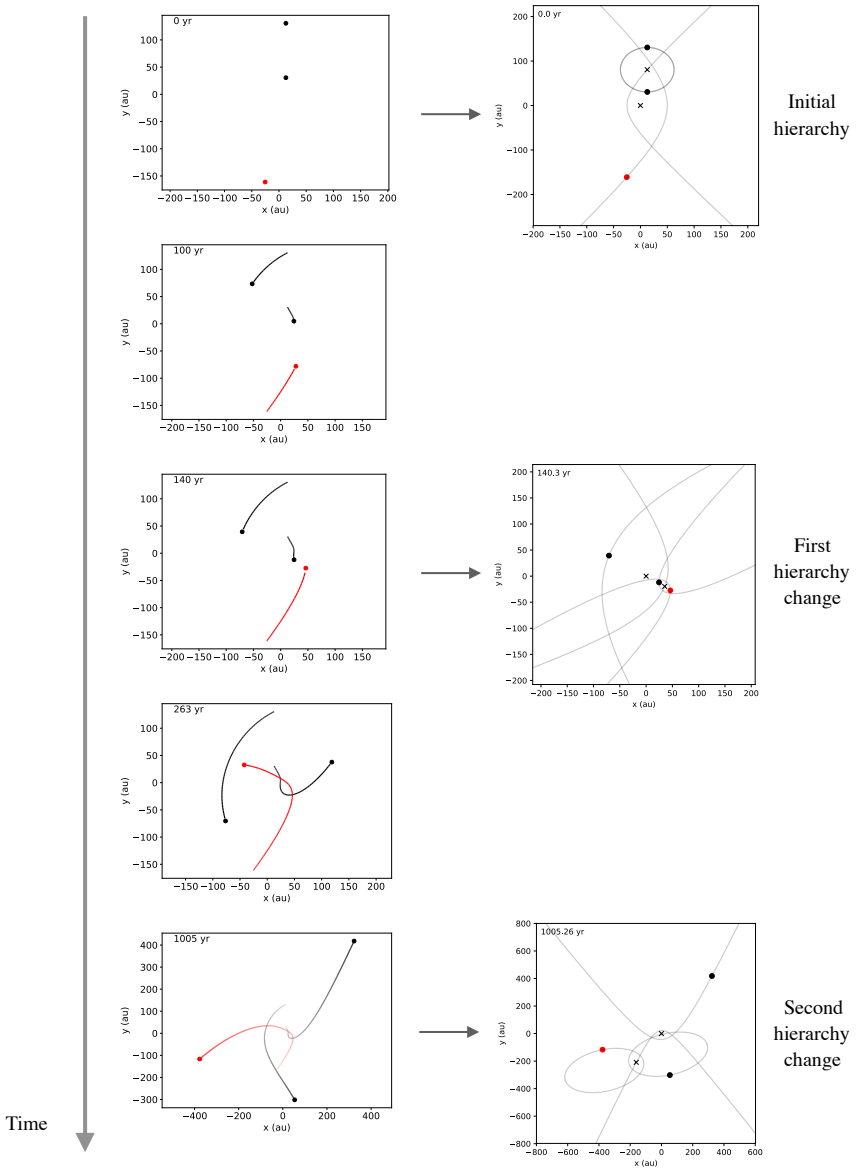

Figure 1.11 – Test case for the new algorithm, where a red body disrupt a black binary and is captured by one of the companion.

The criterion makes sense only if the time scale is adapted to the current hierarchy. Changing the time step in a symplectic integrator breaks the symplecticity, but so does a hierarchy change, so that the time step can be changed at the same time. Empirical considerations give a time step of 1/20 of the smallest period to ensure an energy error below 10^{-6} in the nominal cases (Levison & Duncan 1994), and we chose 1/20 of the periastron to account for eccentricities.

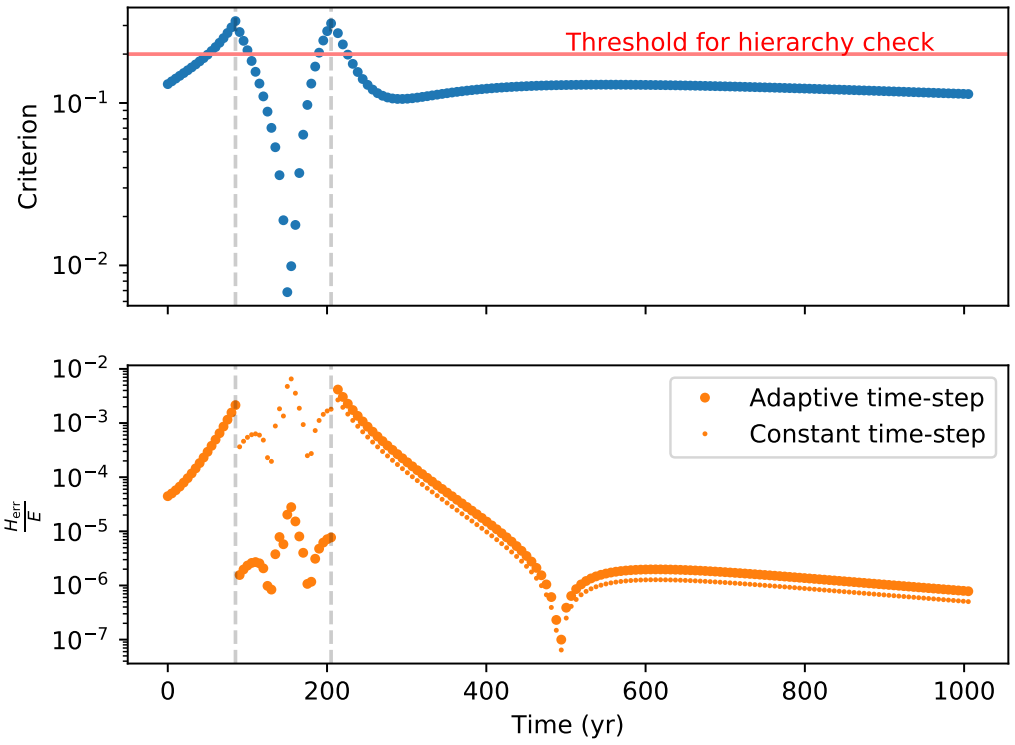

Figure 1.12 – Comparison between the criterion for hierarchical change (maximum of all the c_k) and the error term in the Hamiltonian, depending on whether the time scale is fixed (small points) or evolves (big points). The grey lines correspond to hierarchy changes. The drop of the error around 500 yr is not significant (see text).

We represented in Fig. 1.12 the simultaneous evolution of the criteria along with the evolution of H_{err} in a particular test case. This test case corresponds to a close encounter between three stars of same mass, which leads to two hierarchy changes (see Fig. 1.11). The energy error is very high in that case, because each body has similar mass, and it is not representative of most of the situation that the algorithm will encounter, but corresponds to an extreme case. We see that the criterion evolves smoothly, is correlated to the error and prevents the energy error to go over 0.01. Without the change of the hierarchy, the error ratio would have reached 100%.

We see that the criterion is not completely following the evolution of the error of the second-order scheme. This error, given by the convoluted expression of Eq. 1.50, exhibit some drops and peaks along the system evolution, which do not reflect either a peculiar physical configuration or on the acceleration ratio. However, the criterion succeeds to identify the critical zones for which the error raises and which correspond to an inadequate hierarchy. It is important to realize here that the criterion is only used to avoid the costly process of building a new hierarchy at every step. In the phase around a hierarchy change, the energy error will inevitably raise, whatever the hierarchy. In Fig. 1.12, a better hierarchy is found when the criterion raises around 0.3. Thus, changing the value of the threshold will have no effect on the

energy error if it stays under 0.3, but it will change the computation time, because each step above the criterion involves a search for the best hierarchy. On the other hand, increasing the criterion above 0.3 will delay the hierarchy change and increase the energy error.

2.2.2 Designing a new hierarchy

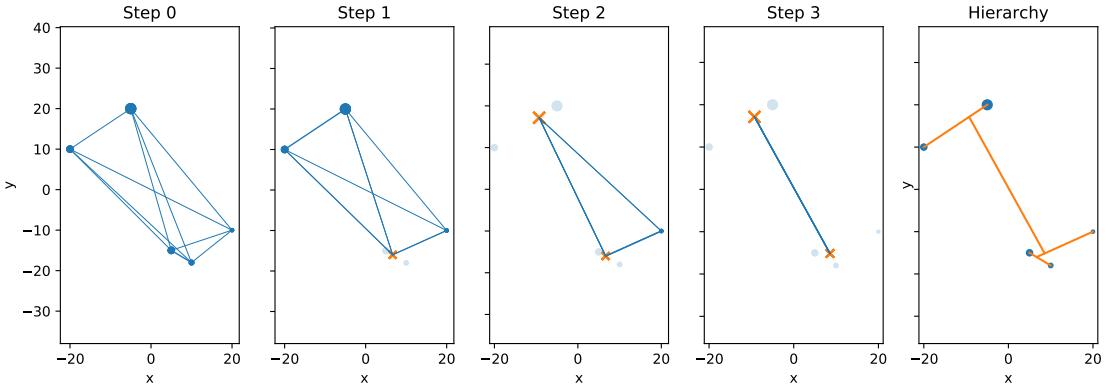

Figure 1.13 – Iterative procedure to build a hierarchy. The blue points represent the bodies, the width of the blue lines represent the strength of the acceleration between two bodies/orbits. The orange crosses represent the centers of masses of the outermost orbits. The orange lines represent the orbits.

Once the criterion points out that the scheme is inappropriate, we choose an iterative procedure that is designed to optimize the acceleration ratio from the current positions of the bodies.

An example of the algorithm is described in Fig. 1.13. At first (step 0), we compute a two-dimensional symmetric array that compiles the Keplerian acceleration between two bodies $a_{ij}^{\mathrm{Kep}} = G(m_i + m_j)/r_{ij}^2$. The strongest acceleration gives the first orbit, then the two bodies are replaced by their center of mass and the array is updated: the accelerations a_{ij}^{Kep} where i and j belongs to the new orbit are discarded (set to -1), and those where i belongs to the new orbit and not j (and vice versa) are replaced by the accelerations between the particle i and the center of mass of the new orbit $G(m_i + M_1)/|\boldsymbol{r_i} - \boldsymbol{r_1}|^2$ (step 1). The procedure continues with remaining bodies until N-1 orbits are defined (at step N-1, only one center of mass remains, comprising every body, and this is ensured by the demonstration of Sec. 1.3.5).

Then, if the computed hierarchy is different than the current one, the hierarchy is replaced. A new transformation matrix from/to the Jacobi coordinates is then computed. However, the algorithm keeps in mind the initial hierarchy and uses it to write the outputs, so that the user gets the orbital elements for the orbits they initially define.

The procedure is similar for test particles, whether their orbit should be redefined because of a change of hierarchy of the massive bodies, or because their orbit is too strongly perturbed. There are $2N - 1$ possibilities for the orbit of a test particle: around a massive body (N) or around an orbit ($N-1$). For each of these possibility, the Keplerian acceleration is computed, an the larger is chosen (see Fig. 1.14).

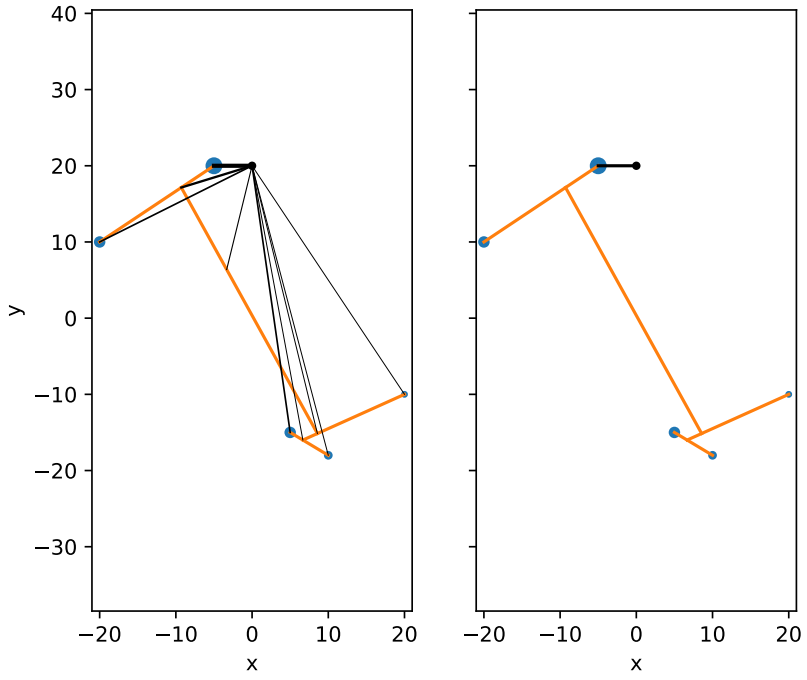

Figure 1.14 – Procedure to compute the hierarchy of a test particle. The blue points represent the massive bodies, the orange lines the orbits, the black point the test particle, and the width of the black line the strength of the acceleration between the test particle and the bodies/orbits.

2.2.3 Specific modules

Some additional modules have been introduced with the new version.

First, a new output file is produced by the algorithm to monitor the evolution of the hierarchy. This new output is then used in the automatic analysis routine to compute a schematic of the different hierarchies (see Fig. 1.15), and the evolution of the orbital elements taking into account hierarchy changes.

To store the hierarchy, I used the formalism that is implemented in Swift HJS, with an $N-1 \times N$ array representing the status of the N bodies (center, satellite or outer) in the $N-1$ orbits. The details of the hierarchy and barycentric coordinates evolution enable the compilation of the orbital elements in the different hierarchies. The design of the schematic to represent visually the hierarchies is more challenging, as the order of the bodies must be rearranged according to the hierarchy and the orbits ranked according to their number of bodies.

Moreover, two options have been added for a better monitoring, that should be specified in the parameters file. The first one defines if an initial check of the hierarchy is required, and the second one if the time step should be changed in case of hierarchy changes.

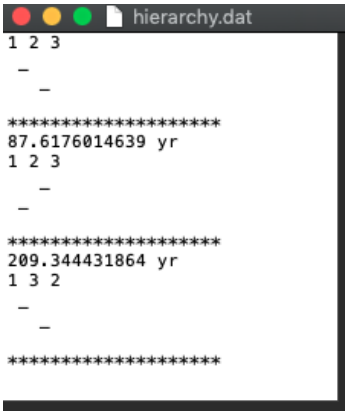

Figure 1.15 – Output of the automatic analysis routine that sums up the different hierarchy changes, with the times of change. The integer represent the bodies, and the underscores the orbits.

2.2.4 Strengths and limitations

Taking into account possible hierarchy changes allows the code to adapt to an evolving architecture within a symplectic frame (symplectic everywhere but during the changes), and consequently avoid to lose control on the accuracy. However, this accuracy remains not optimal, as a change of hierarchy takes place in a situation of strong perturbations of the Keplerian scheme. To correctly resolve this critical phase, one of the classical integrator described above must be used, or the time step must be sufficiently small, which often decreases the interest of using a symplectic integrator.

Moreover, the symplecticity of the integrator is broken sharply at each hierarchy change, creating an incompressible offset of energy, equal to the value of the energy error at the moment of the change. In case of several hierarchy changes (or, even worse, recurring), these offsets pile up and the integrator greatly loses its interest. The sharpness of the change cannot be avoided, as the alternative (smoothing function to go from on hierarchy to another) leads to an extremely complex Hamiltonian, for it should comprise every possible hierarchies, not integrable and heavy to compute.

Nevertheless, this first version of `ODEA` is in working order. It is the only symplectic integrators that can handle hierarchical changes, and is very efficient in some specific cases, such as the study of HD 106906 (see Sec. 3). Both the functioning of the algorithm and the study of the system are detailed in a submitted paper (reproduced below). But to extend the resilience of the algorithm, a hybrid approach is required to resolve more precisely the close encounters.

2.3 Handling close encounters

In the last subsection, I described how we could handle evolving architectures by adapting the hierarchy. This lowers the error associated with the integration scheme. However, in some transitional states, the problem cannot be reduced to slightly perturbed Keplerian orbits, so that changing the hierarchy is not enough to limit the

error to a satisfying threshold. At these parts of the integration, a mixed approach should be adopted, where the integration makes use of a classical integrator. In the last year of my thesis, I worked on the implementation of such an approach into `ODEA`, and a dedicated paper is in preparation. Inspiring by `Mercury`, the classical integrator used is a Bulirsch Stoer algorithm (Sec. 1.2.2), which is very precise (the desired precision can be chosen) and does not depend on the structure of the problem.

2.3.1 Implementation into the scheme

Implementing the mixed approach is rather straightforward in the heliocentric coordinates used in `Mercury` and `SyMBA`, because the terms associated with a close encounter can be isolated without difficulty. In the Jacobi and the Hierarchical Jacobi coordinates, each body is located with respect to the center of mass of the inner bodies, so that a close encounter affects multiple terms of the Hamiltonian. Two approaches are then possible. The first is rather brutal: whenever an orbit is perturbed, the sympectic scheme is set aside and all the problem is integrated with a classical algorithm. On the other hand, a softer approach adopted by all the integrators presented in Sec. 1.2 is to keep the original symplectic approach for the non-perturbed orbits, and to integrate only the perturbed orbits with the classical algorithm. The latter approach is the one we chose, although its implementation is more challenging in the HJS framework than in the MVS framework, because of the non-restricted form of the hierarchy.

An essential point for the implementation of this mixed approach is the following results, flowing from the definitions of the orbits: For any couple of bodies i and j, a unique orbit k_0 exists for which i is a satellite and j a center, or *vice versa*. From this, the perturbation Hamiltonian H_{B} can be rewritten in the following way:

$$H_{\mathrm{B}} = \sum_{\text{orbits } k=2}^{N} \left(\frac{G\mu_k\eta_k}{r'_k} - \sum_{\substack{i \text{ cen } k \\ j \text{ sat } k}} \frac{Gm_im_j}{r_{ij}} \right) \tag{1.52}$$

Moreover, for each couple of bodies i and j, the terms $\boldsymbol{r_{ij}}$ can be written as a linear combination of $\boldsymbol{r'_l}$, with no contributions of the orbits l that are outer or foreign to their orbit k_0. It follows that, from Eq. 1.35, the residual acceleration $\boldsymbol{a_k^B}$ can be written only with $\boldsymbol{r'_l}$ with l inner than k. We thus see that strictly separating the problem between perturbed and non-perturbed orbits is not possible because of the entanglement terms. If an orbit k is perturbed, it is however possible to divide the Hamiltonian between orbits inner or equal to k, and orbits outer or foreign to k. We shall describe in more details this separation in what follows.

As before, we choose a criterion to probe the problem and the relevance of the symplectic splitting. The criterion should not depend on the velocities, to preserve the possibility of directly integrating H_{B} without approximation. For any criterion c_k, the Hamiltonian can be separated into:

$$H_{\rm A} = \sum_{\text{orbits } k=2}^{N} \left(\frac{p_k'^2}{2m_k'} - \frac{G\mu_k\eta_k}{r_k'} + \left(\frac{G\mu_k\eta_k}{r_k'} - \sum_{\substack{i \text{ cen } k \\ j \text{ sat } k}} \frac{Gm_im_j}{r_{ij}} \right) c_k \right) \tag{1.53}$$

$$H_{\rm B} = \sum_{\text{orbits } k=2}^{N} \left(\left(\frac{G\mu_k\eta_k}{r_k'} - \sum_{\substack{i \text{ cen } k \\ j \text{ sat } k}} \frac{Gm_im_j}{r_{ij}} \right) (1 - c_k) \right) \tag{1.54}$$

Let us consider the case of a Heaviside-like criterion, which is 1 if the orbit is perturbed and 0 otherwise (null derivative with respect to positions or velocities). In the (r_k', p_k') variables, the Hamilton equations with respect to $H_{\rm A}$ give:

$$\dot{\boldsymbol{r_k}} = \frac{\boldsymbol{p_k'}}{m_k} \tag{1.55}$$

$$\dot{\boldsymbol{p_k}} = -\frac{G\mu_k\eta_k}{r_k^3}\boldsymbol{r_k}(1 - c_k) - \sum_{1 \leq i < j < \leq N} \frac{Gm_im_j}{r_{ij}^3}(M_{jk}^{-1} - M_{ik}^{-1})\boldsymbol{r_{ij}}c_{k_0} \tag{1.56}$$

where $k_0(i, j)$ is the index of the unique orbit such as i is center and j is satellite. Using a Keplerian drift for integrating $H_{\rm A}$ is only possible for orbits that have $c_k = 0$ and $c_l = 0$ for all l such as $k \subset l$. The $H_{\rm A}$-induced drift of the other orbits (those that are either perturbed or inner to a perturbed orbit) is integrated with the Bulirsch-Stoer algorithm (Sec. 1.2.2). Indeed, the term $M_{jk}^{-1} - M_{ik}^{-1}$ vanishes if neither i nor j belong to orbit k, or if they belong to the same sets (centers or satellites) of orbit k. In particular, it vanishes when k_0 is inner or foreign to k, so that inner or foreign perturbed orbits can be ignored while integrating k.

As an example, let us suppose that orbit 2 is perturbed ($c_2 > 0$) in the configuration depicted by Fig. 1.16, because the satellite C is perturbed by the binarity of the center AB. In the sum of Eq. 1.56, only two pairs of body (i, j) will have a non-zero c_{k_0}: A-C and B-C, for which $k_0 = 2$ (one body is center and the other satellite of orbit 2). Moreover, in the evolution of orbit 3 and 4, the terms $M_{jk}^{-1} - M_{ik}^{-1}$ will vanish because orbit 2 is foreign to orbit 3 and inner to orbit 4. Thus, the evolution with respect to $H_{\rm A}$ of orbits 1 and 2 will be integrated with the Bulirsch-Stoer algorithm, while for the orbits 3 and 4 the evolution remains Keplerian.

Let us consider an orbit k which is neither perturbed, nor is inner to a perturbed orbit. Its evolution driven by $H_{\rm A}$ writes:

$$\dot{\boldsymbol{r_k}} = \frac{\boldsymbol{p_k'}}{m_k} \tag{1.57}$$

$$\dot{\boldsymbol{p_k}} = -\frac{G\mu_k\eta_k}{r_k^3}\boldsymbol{r_k} \tag{1.58}$$

which is the classical Keplerian drift, implemented exactly in the original algorithm. On the other hand, the evolution of a perturbed orbit, for which it exists by definition an orbit k_0 outer or equal to k which has a non-zero c_{k0}, is given by Eqs. 1.55 and

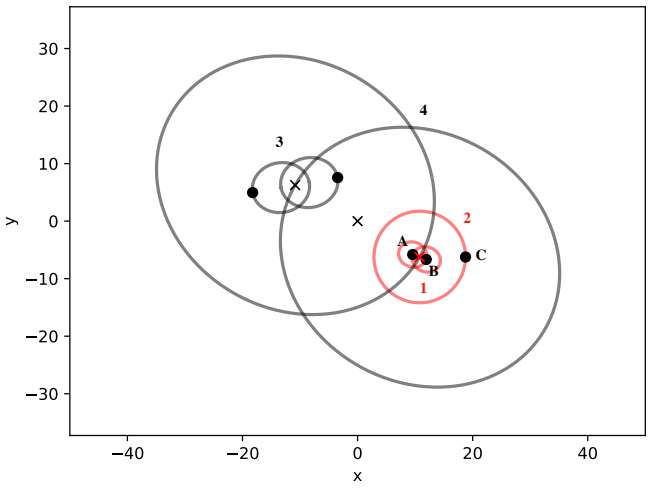

Figure 1.16 – Example of a hierarchic configuration where orbit 2 is perturbed. Both orbits 1 (because it is inner to 2) and 2 will be integrated with the Bulirsch-Stoer algorithm.

(1.56). Neither terms in Eq. 1.56 do vanish, so that the evolution is then not exactly solvable. The corresponding r_{ij} term depends on inner orbits r'_l, which are also perturbed by definition. The Bulirsch-Stoer algorithm must solve the coupled evolution of all the perturbed orbits.

Moreover, the evolution controlled by $H_{\rm B}$ is always integrable as it still not depend on the velocities. The acceleration corresponds to the acceleration $\boldsymbol{a_k^B}$ of Eq. 1.35, with each term being weighted by a factor $(1 - c_{k_0})$. This weighted acceleration will be denoted $\boldsymbol{\alpha_k^B}$.

The new structure of the core is summarized on Fig. 1.17. Each time the acceleration is computed, both $\boldsymbol{a_k^B}$ and $\boldsymbol{\alpha_k^B}$ are computed (the two may be different if at least one orbit is perturbed). Indeed, the non-weighted accelerations are still needed to compute the criteria.

2.3.2 Criterion to evaluate perturbations

Inspiring from the handling of hierarchy changes, we choose the following criterion :

$$c_k = \mathrm{He}\left(\frac{\Delta t}{\tau_k^{\rm Kep}}\frac{a_k^B}{a_k^{\rm Kep}} - c_{\rm crit}\right) \tag{1.59}$$

where He is the Heaviside function, $c_{\rm crit}$ represents an arbitrary threshold and a_k^B is given by Eq. 1.35. The previously used accelerations ratio $a_k^B/a_k^{\rm Kep}$ is here weighted by the ratio between the time step and the Keplerian time, which I define as $\tau_k^{\rm Kep} = \sqrt{r_k^3/GM_K}$. The addition of this weight illustrates the difference with the previous version: we are no longer looking for the better hierarchy in a problem, independently from the time step, but we are now trying to control the energy error.

The term $\frac{\Delta t}{\tau_k^{\rm Kep}}\frac{a_k^B}{a_k^{\rm Kep}}$ in the criterion corresponds roughly to the energy error in

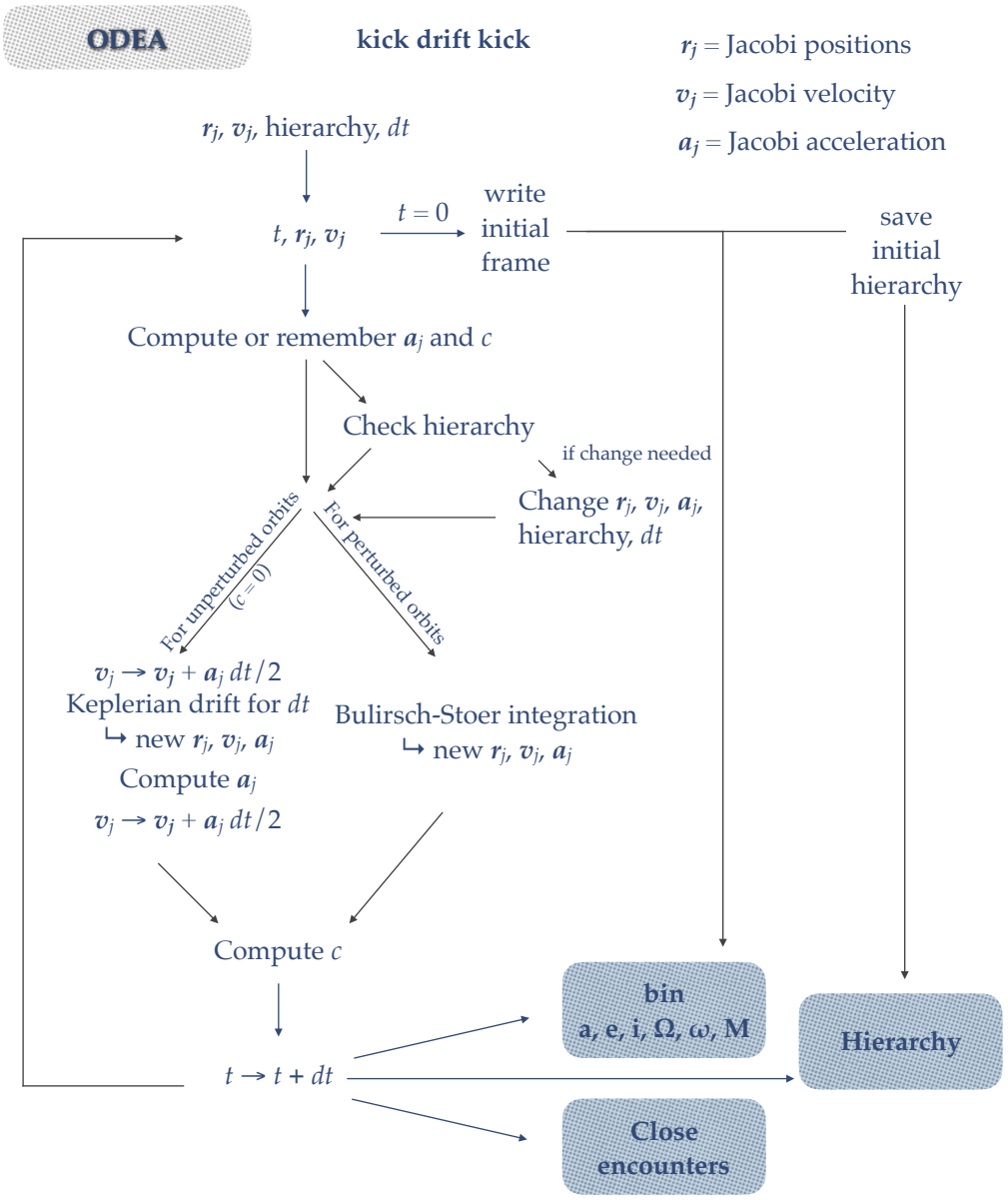

Figure 1.17 – Schematic of the core algorithm of `ODEA`.

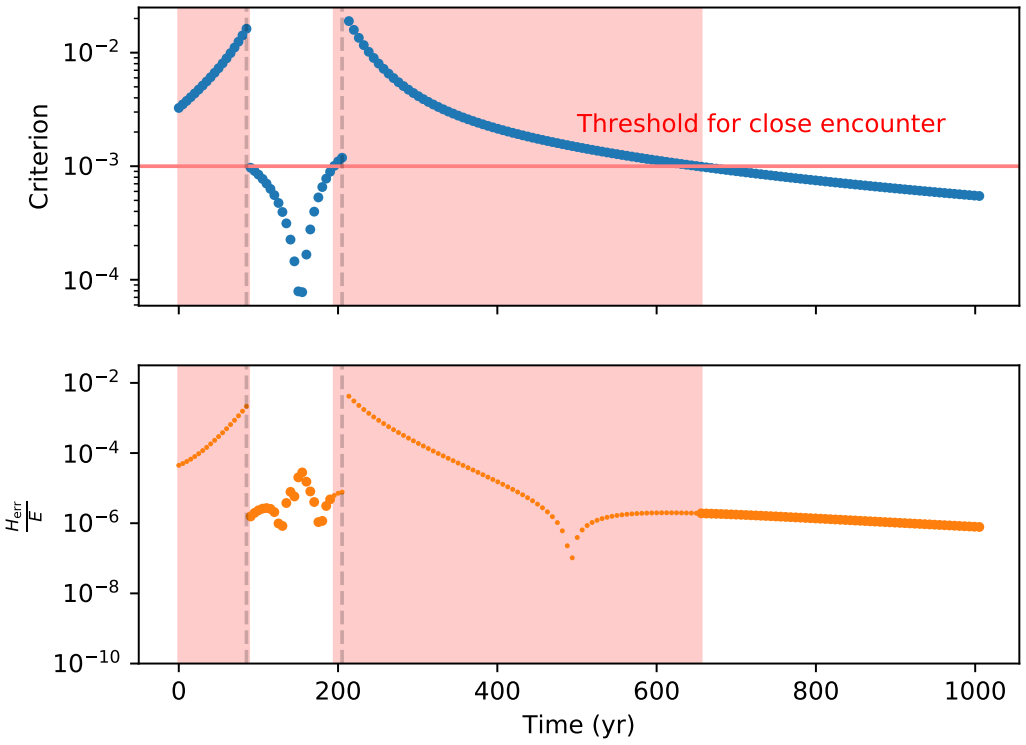

Figure 1.18 – Comparison between the criterion for close encounters (maximum of all the c_k) and the error term in the Hamiltonian. The grey lines correspond to hierarchy changes, the red zones to periods where at least one orbit is perturbed (criterion above threshold). The energy error in the red zone (small dots) is indicative of what it would be without the new implementation.

the first-order scheme. Its relation with the error in the second-order case is not straightforward, but its value gives an upper bound, as the first-order scheme is less accurate a priori than the second-order scheme. This can be seen on Fig. 1.18. Consequently, we fix the critical threshold to $c_{\text{crit}} = 10^{-3}$, but its value can be changed in the core code according to the precision goal.

I tested the different versions of the code on the previously introduced extreme examples of a close encounter between 3 equal-mass massive bodies. The output in terms of energy error and trajectories is represented in Fig. 1.19. Hierarchy changes avoid reaching high energy error. However it does not ensure that the final total energy will be more precise than the classical SWIFT HJS case, because the hierarchy change break the symplectic nature, so that the return of an unperturbed situation might not compensate the energy offset. However, preventing the energy error to explode even temporarily allows a reliable computation of the trajectory. On the other hand, the close encounter version greatly limits the energy error, on top of keeping track of the trajectory. In the example, only the 100-200 yr part, between the two hierarchy changes (visible on Fig. 1.12), and the end of the simulation is integrated without Bulirsch-Stoer.

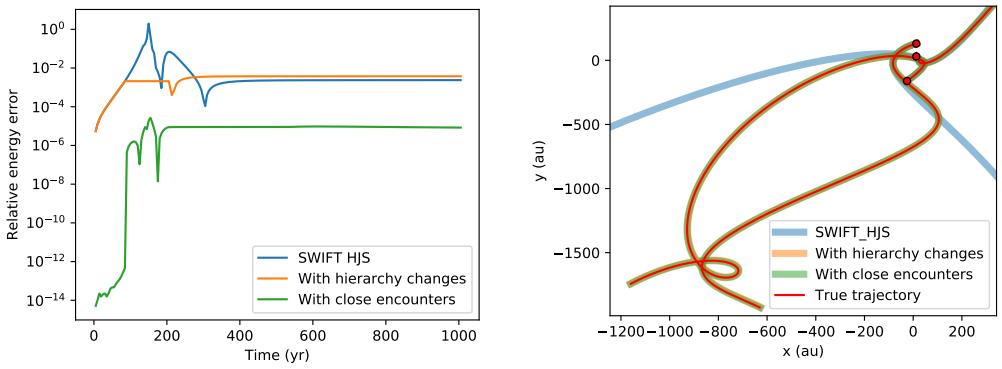

Figure 1.19 – Comparison of the different versions of the code, on the same test case (highly perturbed three-body system). The interpretation can be found in the text.

This computation of the criterions for each orbit grows with N^3, which is not negligible a priori. The algorithm remains efficient because the computation of the criterion makes use of quantities (the accelerations) that are already computed in the code at the beginning and the end of each time step. However, the necessary accelerations should also be computed at each step of the Bulirsch-Stoer algorithm, so that the computation could potentially grow heavy. To avoid that, the criterion keeps its value throughout a step. It modifies in theory the nature of the criterion function, but does not impact the equations in practice.

In `Mercury`, to avoid integrating with a Keplerian drift an orbit that becomes perturbed during the time step, a quick polynomial integration module is implemented to predict the future close encounters (Chambers 1999). This is possible/computationaly interesting because of the simplicity of the criterion. In our case, such approach would be far too heavy to encode. Instead, a time step is redone if a criterion becomes non-zero during it.

2.3.3 The case of test particles

All the new features of `ODEA` are relevant for both massive bodies and test particles. Indeed, the latter are used to model the structures of debris disk, and each individual particles can be either captured or ejected by the interaction with the massive bodies of the system. Similarly than for the orbits of massive bodies, we compute a criterion c for each test particle, also based on the ratio between the $H_{\rm B}$-induced acceleration a^B (Eq. 1.36) and the Keplerian acceleration.

The massless nature of test particles implies that no other bodies depends on their evolution, although each one of them depend on the evolution of massive bodies. The orbit of a test particle is embedded within the hierarchy of massive bodies, so that the same results than for massive bodies hold. Thus, only when $c = 0$ and if the particle's orbit is not inner to the perturbed orbit of massive bodies, then its evolution is simply computed with the usual analytical kick-drift-kick approach. Otherwise, its $H_{\rm A}$-induced acceleration is computed with the Bulirsch Stoer algorithm.

In the classical version of `Swift HJS`, the evolution of the test particles only

requires the positions of the massive bodies at the beginning and end of the time step, plus their velocities after the first kick. However, a perturbed test particle's evolution along $H_{\rm A}$ is coupled to the evolution of the massive bodies around which it revolves, so that their motion has to be integrated alongside the motion of the perturbed test particles.

2.3.4 Smooth transitions

In `Mercury`, the criterion is a smooth function that takes value between 0 and 1. We can inspire from that to smooth our criterion. However, the criterion's derivatives should then be taken into account in the evolution.

The Hamilton equations for $H_{\rm A}$ now are

$$\dot{\boldsymbol{r}_k} = \frac{\boldsymbol{p'_k}}{m_k} \tag{1.60}$$

$$\begin{aligned}\dot{\boldsymbol{p}_k} = & -\frac{G\mu_k\eta_k}{r_k'^3}\boldsymbol{r'_k}(1-c_k) - \sum_{1\leq i<j<\leq N}\frac{Gm_im_j}{r_{ij}^3}(M_{jk}^{-1}-M_{ik}^{-1})\boldsymbol{r_{ij}}c_{k_0} \\ & + \sum_{l=2}^{N}\left(\frac{G\mu_l\eta_l}{r'_l} - \sum_{\substack{i \text{ cen } l \\ j \text{ sat } l}}\frac{Gm_im_j}{r_{ij}}\right)\frac{\mathrm{d}c_l}{\mathrm{d}\boldsymbol{r'_k}}\end{aligned} \tag{1.61}$$

so that the precedent description is still valid as long as the new term vanishes when k is not perturbed. This is the case when the criterion is a function of the accelerations ratio described above, because then it depends only on the inner orbits. Thus, if orbit k is not perturbed, then the criterion c_l of any perturbed orbit l will not depend on $\boldsymbol{r'_k}$ because k is either foreign or outer to l by definition.

On the other hand, the evolution along $H_{\rm B}$ also includes derivative terms. The subsequent accelerations are still analytically integrable however, as they still not depend on the velocities.

A smooth criterion would be

$$c_k = f\left(\frac{\Delta t}{\tau_k^{\rm Kep}}\frac{a_k^B}{a_k^{\rm Kep}} - c_{\rm crit}\right) \tag{1.62}$$

where

$$f(y) = \frac{y^2}{2y^2-2y+1} \tag{1.63}$$

This is one of the simplest form that can be thought of to smooth the acceleration ratio, with $f(0)=0$, $f(1)=1$, $f'(0)=0$ and $f'(1)=0$. The resulting Hamiltonian is thus $\mathcal{C}^1$, even in case of perturbation. However, the derivative is nevertheless tedious to compute. It writes:

$$\frac{\mathrm{d}c_l}{\mathrm{d}\boldsymbol{r'_k}} = \Delta t f' \left(\frac{\Delta t}{\tau_k^{\mathrm{Kep}}} \frac{a_k^B}{a_k^{\mathrm{Kep}}} - c_{\mathrm{crit}} \right) \left(\frac{1}{a_k^B \tau_l^{\mathrm{Kep}} a_l^{\mathrm{Kep}}} \left(-2\delta_{kl} \frac{G^2 M_k^2}{r_k^6} \boldsymbol{r_k} - \right. \right.$$
$$\delta_{kl} \frac{GM_k}{r_k^3} \sum_{1 \leq i < j \leq N} \frac{G m_i m_j (M_{jk}^{-1} - M_{ik}^{-1})}{m_k r_{ij}^3} \boldsymbol{r_{ij}} (1 - 3 \frac{\boldsymbol{r_{ij}} . \boldsymbol{r_k}}{r_k^2})$$
$$- \frac{GM_l}{r_l^3} \sum_{1 \leq i < j \leq N} \frac{G m_i m_j (M_{jl}^{-1} - M_{il}^{-1})(M_{jk}^{-1} - M_{ik}^{-1})}{m_l r_{ij}^3} (\boldsymbol{r_k} - 3 \frac{(\boldsymbol{r_{ij}} . \boldsymbol{r_l})}{r_{ij}^2} \boldsymbol{r_{ij}})$$
$$+ \sum_{1 \leq i < j \leq N} \sum_{1 \leq a < b \leq N} \frac{G^2 m_i m_j m_a m_b (M_{jl}^{-1} - M_{il}^{-1})(M_{jk}^{-1} - M_{ik}^{-1})(M_{bl}^{-1} - M_{al}^{-1})}{m_l^2 r_{ij}^3 r_{ab}^3}$$
$$\left. \left. (\boldsymbol{r_{ab}} - 3 \frac{(\boldsymbol{r_{ij}} . \boldsymbol{r_{ab}})}{r_{ij}^2} \boldsymbol{r_{ij}}) \right) + \frac{a_k^B}{(\tau_l^{\mathrm{Kep}} a_l^{\mathrm{Kep}})^2} \delta_{kl} \frac{\boldsymbol{r_k}}{2\tau_k^{\mathrm{Kep}} r_k} \right) \tag{1.64}$$

$$\text{with } f'(y) = \frac{2y(1-y)}{(2y^2 - 2y + 1)^2} \tag{1.65}$$

This derivative is very complicated and the computation of the related terms in the accelerations grow as N^6 (although it is still linear in the number of test particles). As a part of the evolution in both H_{A} and H_{B}, it has to be computed many times per time step, in particular for the perturbed orbits in the Bulirsch-Steor algorithm. The advantages of using a smooth criterion have thus to be discussed and weighted. In `Mercury`, the term has simply been ignored, introducing an error in the integrator (Wisdom 2016). The new implementation available in the Rebound package solves this issue (Rein et al. 2019), and the authors additionally tested several smoothing functions, including a Heaviside threshold. They concluded on the negligible impact of this choice on the integration. However, a recent study by Hernandez (2019) shows that a smooth Hamiltonian improves significantly the long-term precision for chaotic problems. A smooth version of the Hamiltonian is under development in ODEA, so that dedicated tests will enable the comparison of its efficiency and precision with the non-smoothed version.

2.3.5 Specific modules

The structure of `ODEA` being essentially similar to that of `Swift HJS`, the general architecture of the code and its articulation with its modules do not drastically evolve. Figure 1.21 details the new organization. The initialization routine in particular remains identical to the previous version. The post-processing, however, has become more complex.

On top of the archival file that compiles the hierarchy, introduced in the previous version, a new output is produced by the core code that monitors the close encounters (*ce.out*). Whenever an orbit is perturbed, the time and number of the orbit is saved. When the orbit stabilizes, a new line is included into the file with the number of the orbit, the beginning time of the close encounter, and its ending time. If the

simulation ends before the end of the perturbation, a line is added at the end of the integration with only the beginning time.

This new output allows the upgrade of the Analysis routine to represent the close encounters on the orbital elements evolution plots, along with the hierarchy evolution. The values of the orbital elements in the new hierarchies are not a direct output of the code, since the data files elbodies and eltp are archives of the orbital elements in the initial hierarchy, for consistency. Thus, the Analysis module reads the archives of the positions and the hierarchy and recompute from them the orbital elements in the new hierarchy.

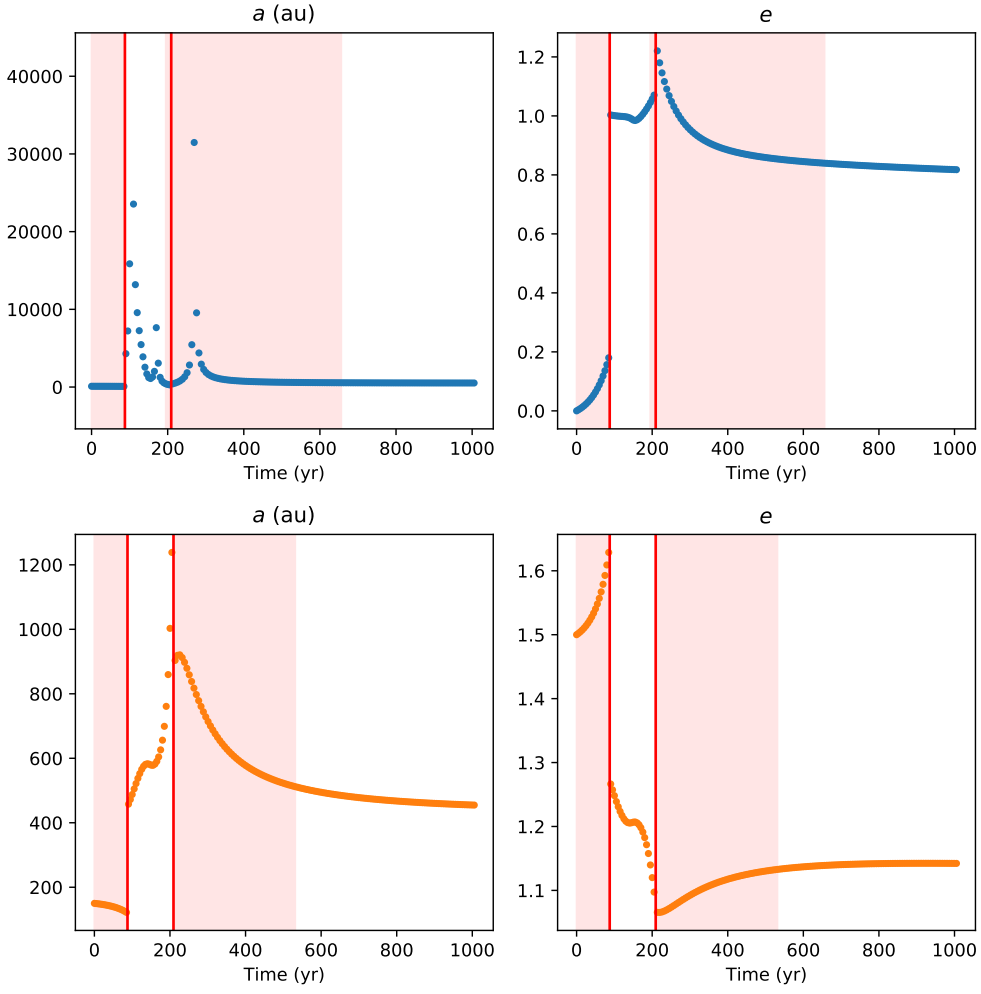

Figure 1.20 – Example of automatic analysis by the module Analysis.py of a simulation with `ODEA`. The evolution of each orbit orbital elements (columns) of each orbits (lines) is computed, but only the semi-major axes and eccentricities are represented here. The red zones indicates that the orbit is considered perturbed. The red vertical lines indicates hierarchy changes.

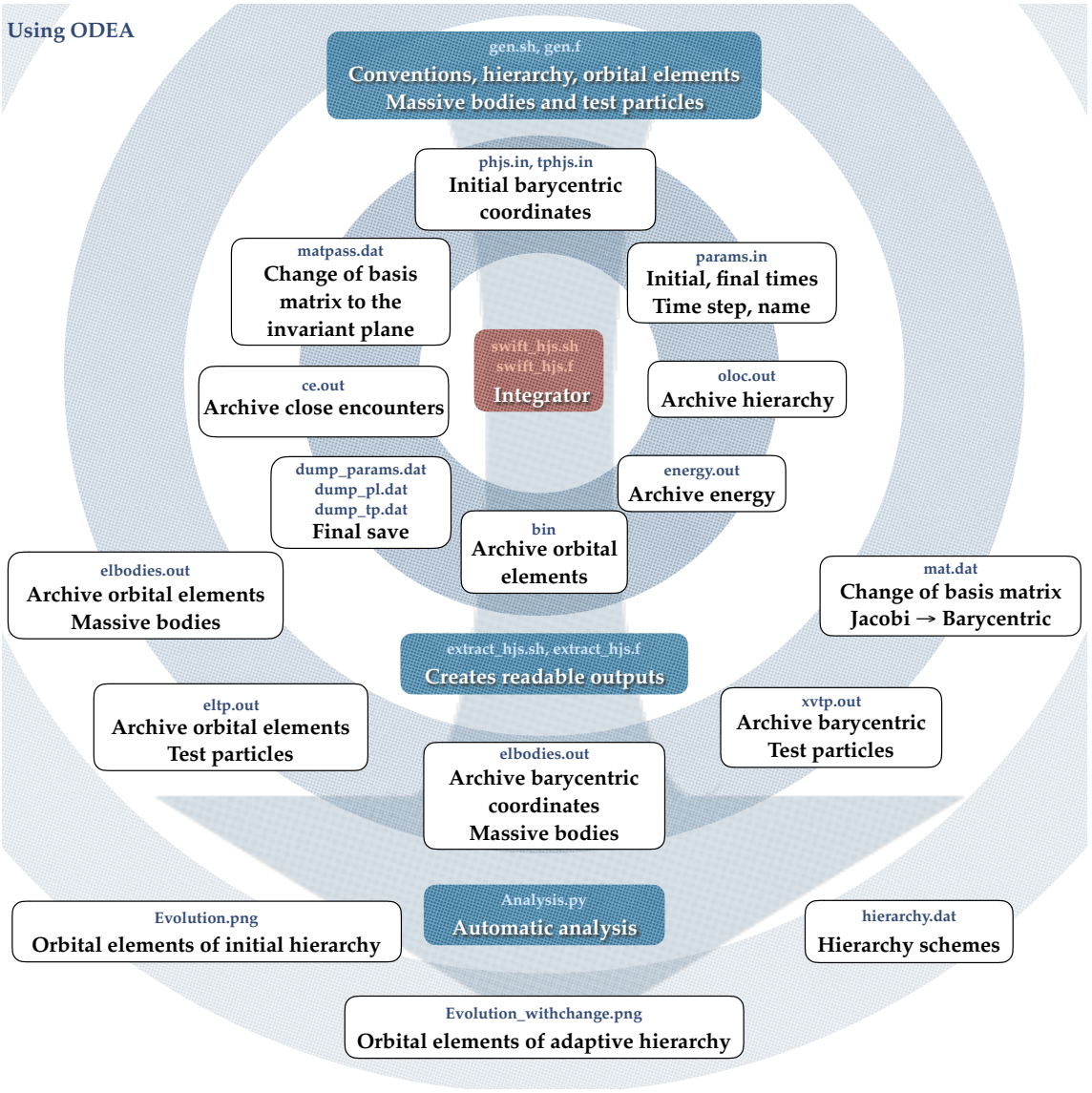

Figure 1.21 – Schematic of the inputs and outputs of `ODEA`. The user inputs are filled in *gen.sh* and *params.in*.

2.3.6 Conclusion on `Odea`

A first conclusion of my work is that expanding the scope of `Swift HJS` to include hierarchy changes and close encounters is definitely challenging. `Swift HJS` has been designed as a generalization of the previous symplectic schemes that only handle Solar-System-like architecture. Each features that may be applied in other codes in a straightforward way have to be generalized for any hierarchy before being transferred to `Swift HJS`. Thus, if the mixed approach implementation is rather painless in `Mercury`, thanks to the stable hierarchy and the fact that encounters only affect two bodies at a time, it becomes an ordeal in `Swift HJS`, where perturbed orbits may potentially include all the bodies.

As I finish this thesis, the final version of `ODEA` is not yet produced. However, most of the theoretical design and numerical implementations have been made, and

	Symplectic	Handles any architectures	Handles hierarchy changes	Handles close encounters	Smooth
`ODEA`	✓	✓	✓	✓	×
`Swift HJS`	✓	✓	×	×	✓
`Mercury`	✓	×	×	✓	∼
`IAS15`	×	∼	∼	✓	✓

Table 1.1 – Summary of the characteristics of different N-body codes. The Hamiltonian in `Mercury` is $\mathcal{C}^1$, so that it has some smoothness properties. `IAS15` does not make use of the hierarchy for the integration, but the post-processing routines in the Python Package are designed in the Jacobi coordinates and do not handle evolving hierarchies with multiple rotation centers.

the evolution of massive bodies can already be integrated with hierarchical changes and close encounters. Moreover, a version including hierarchical changes for both massive bodies and test particles is in working order, and has already been used in a submitted paper (see Sec. 3). These versions already have their designated analysis tools for post-processing. The modules added to the original code `Swift HJS` are either quick to compute or rarely appealed to. The extension of close encounters to test particles is theoretically equivalent, and will follow naturally once the numerical aspects are efficiently taken care of.

`ODEA` will be presented in an upcoming dedicated paper. It is a versatile tool, able to adapt to either architecture and to handle any evolution, however catastrophic. A summary and comparison of `ODEA`'s properties is displayed in Table 1.1. Such tools will be necessary to study the diversity of planetary systems that we are beginning to unveil. The possibility to take into account non-Keplerian forces has not been implemented yet, but it is a natural upgrading perspective, notably to take into account migration or tidal forces. Treated as additional perturbing terms in H_{B}, they can be simply included into the described close encounter procedure.

3 Understanding the peculiar architecture of the system HD 106906

HD 106906 is a rare and intriguing system. Located in the Lower-Centaurus-Crux association which is part of the Sco-Cen OB association, it comprises a tight binary, a wide and asymmetric debris disk and a giant planet at very large separation, possibly misaligned with the disk plane (see Fig.1.22). This wide planet challenges the models of planetary formation, and the presence of a debris disk makes this system a benchmark for the planet/disk interactions. Indeed, it is one of the rare systems around which both a companion and a disk have been imaged, and the very low mass ratio between the host star and the planetary companion is unique as such separation (see Introduction Fig. 2).

The young (5-15 Myr) Sco-Cen association is known for several decades to be the nearest OB association (around 100 pc away), and the kinematics and properties

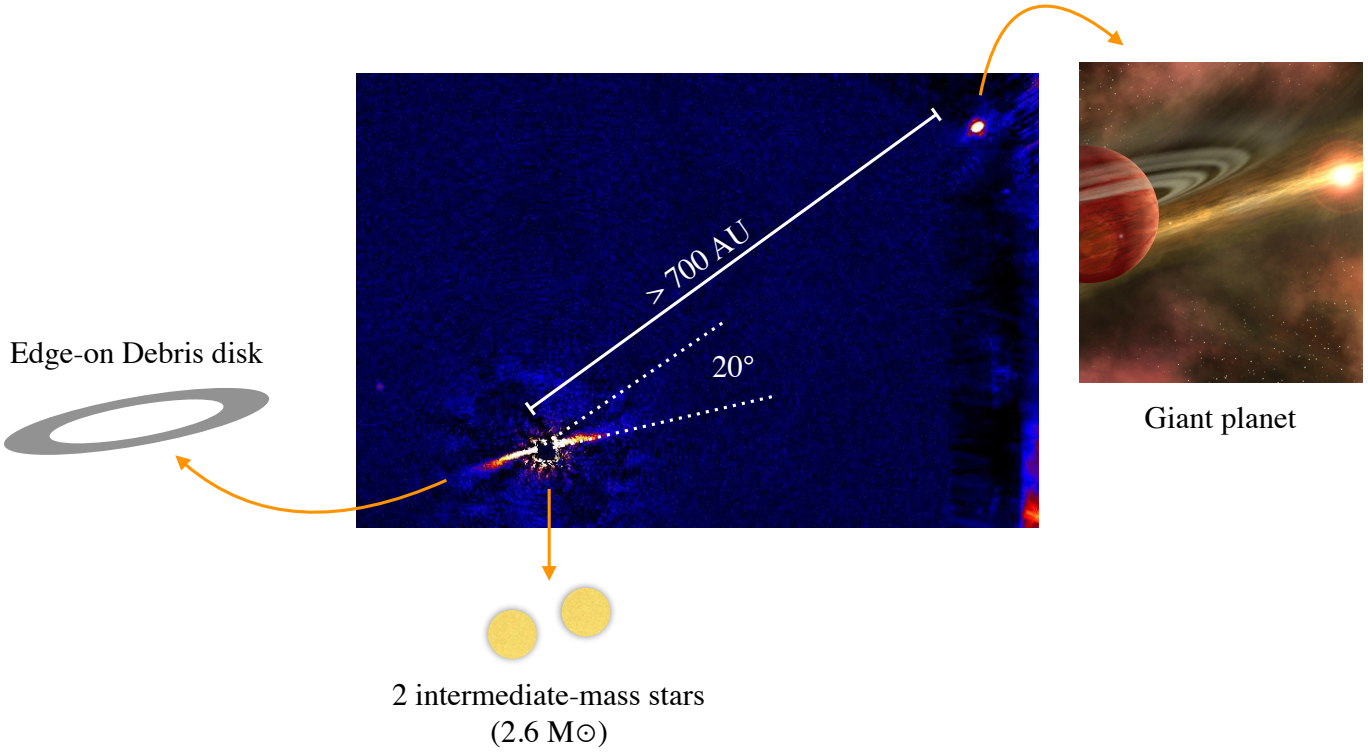

Figure 1.22 – Presentation of system HD 106096. SPHERE image from Lagrange et al. (2016).

of its young stars have thus been thoroughly characterized (De Zeeuw et al. 1999). In a survey using the space telescope Spitzer, targetting specifically the association, Chen et al. (2005) discovered a large infrared excess in the spectral energy distribution of HD 106906, indicating a massive debris disk. Further characterization with Magellan/MIKE confirmed this excess and led to an estimate of its properties (disk mass, luminosity, temperature; Chen et al. 2011). The shape of the spectral energy distribution suggests that the disk is devoid of both hot and warm material, which led Bailey et al. (2014) to look for a companion with the Magellan Adaptative Optics (MagAO). The planetary mass companion HD 106906 b was then discovered at 7" from the host star, putting the spotlight on the system. High signal-to-noise spectral characterization concluded on a spectral type L1.5 ±1 and confirmed a mass at the upper limit of the planet realm (Daemgen et al. 2017). New observations with SPHERE (Lagrange et al. 2016), HST, GPI (Kalas et al. 2015) and MagAO (Wu et al. 2016) resolved the debris disk and revealed its strong asymmetries. SPHERE is the only instrument capable of imaging both the debris disk and the planet in its large field of view (Fig. 1.22). Since then, numerous studies explored the interactions between the planet and the disk (Jílková & Zwart 2015; Nesvold et al. 2017; Lazzoni et al. 2018), suggesting an eccentric orbit with a periastron just outside the disk outer radius, and a possible inner companion to carve the inner edge. The masses and separations of the different components of the system are summarized in Table 1 of Rodet et al. (2017) below.

At the beginning of my thesis work, the binary nature of the host star was

revealed by HARPS and PIONIER radial velocity and interferometric measurements Lagrange et al. (2019). This hypothesis of a past scattering of the companion to its current position had thus to be investigated. This was done in two designated papers, Rodet et al. (2017) and Rodet et al. (2019), that are introduced below and that are making use of `Swift HJS` and `ODEA`.

3.1 Investigating the dynamical evolution

In Rodet et al. (2017), we explored possible scenarios to account for the peculiarities of the system. To this goal, we performed numerous N-body simulations and made use of Swift HJS to model the non-Solar type architecture. We suggest that the planet formed within the disk, closer to the central binary star, and migrated towards it until it got caught in a mean-motion resonance. The resonance would have then enhanced the planet eccentricity until its periastron would be decreased to a critical value, where interactions with the binary could have ejected it on a wide orbit. Such orbit would remain strongly unstable, except if some exterior force would further circularize it. This stabilizing factor could be a passing star (fly-by). However, the probability of such fly-by to happen is not high given our knowledge of the neighborhood density. The entire study is detailed below.

A&A 602, A12 (2017)
DOI: 10.1051/0004-6361/201630269
© ESO 2017

Astronomy & Astrophysics

Origin of the wide-orbit circumbinary giant planet HD 106906

A dynamical scenario and its impact on the disk

L. Rodet[1], H. Beust[1], M. Bonnefoy[1], A.-M. Lagrange[1], P. A. B. Galli[1,2], C. Ducourant[3], and R. Teixeira[2]

[1] Univ. Grenoble Alpes, CNRS, IPAG, 38000 Grenoble, France
e-mail: laetitia.rodet@univ-grenoble-alpes.fr
[2] Instituto de Astronomia, Geofísica e Ciências Atmosféricas, Universidade de São Paulo, Rua do Matão, 1226, Cidade Universitária, 05508-900, São Paulo – SP, Brazil
[3] Laboratoire d'Astrophysique de Bordeaux, Univ. Bordeaux, CNRS, B18N, Allée Geoffroy Saint-Hilaire, 33615 Pessac, France

Received 16 December 2016 / Accepted 4 March 2017

ABSTRACT

Context. A giant planet has been recently resolved at a projected distance of 730 au from the tight pair of young (~13 Myr) intermediate-mass stars HD 106906AB in the Lower Centaurus Crux (LCC) group. The stars are surrounded by a debris disk which displays a ring-like morphology and strong asymmetries at multiple scales.
Aims. We aim to study the likelihood of a scenario where the planet formed closer to the stars in the disk, underwent inward disk-induced migration, and got scattered away by the binary star before being stabilized by a close encounter (fly-by).
Methods. We performed semi-analytical calculations and numerical simulations (Swift_HJS package) to model the interactions between the planet and the two stars. We accounted for the migration as a simple force. We studied the LCC kinematics to set constraints on the local density of stars, and therefore on the fly-by likelihood. We performed N-body simulations to determine the effects of the planet trajectories (ejection and secular effects) onto the disk morphology.
Results. The combination of the migration and mean-motion resonances with the binary star (often 1:6) can eject the planet. Nonetheless, we estimate that the fly-by hypothesis decreases the scenario probability to less than 10^{-7} for a derived local density of stars of 0.11 stars/pc^3. We show that the concomitant effect of the planet and stars trajectories induce spiral-features in the disk which may correspond to the observed asymmetries. Moreover, the present disk shape suggests that the planet is on an eccentric orbit.
Conclusions. The scenario we explored is a natural hypothesis if the planet formed within a disk. Conversely, its low probability of occurrence and the fact that HD 106906 b shares some characteristics with other systems in Sco-Cen (e.g., HIP 78530, in terms of mass ratio and separation) may indicate an alternative formation pathway for those objects.

Key words. methods: numerical – celestial mechanics – planetary systems – planets and satellites: dynamical evolution and stability – planet-disk interactions

1. Introduction

More than 3500 exoplanets have been found in the last three decades[1], but few among them have been detected to be hundreds of astronomical units (au) from their star. As the development of direct imaging reveals more of those wide planetary-mass companions, classical theories of planet formation fail at explaining their origin. In the two scenarios, core accretion (Pollack et al. 1996) and gravitational instability (Boss 1997), the planets form within the primordial gas disk. However, the limited extent of the disk (see e.g. Fig. 5 in Lieman-Sifry et al. 2016) does not enable the formation of a giant planet far away from its star. Thus, when the star around which orbits the very wide and massive HD 106906AB b turned out to be a binary star (Lagrange et al. 2016b), it has been suggested that dynamical interactions could account for the current position of the planet (Lagrange et al. 2016b; Wu et al. 2016).

The planet HD 106906 (or also HIP 59960) is located at a distance of 103 ± 4 pc (Van Leeuwen 2007) and belongs to the Lower Centaurus Crux (LCC) group, which is a subgroup of the Scorpius-Centaurus (Sco-Cen) OB association (De Zeeuw et al. 1999). The LCC group has a mean age of 17 Myr, with an age-spread of about 10 Myr (Pecaut et al. 2012). In recent years, high contrast imaging has revealed the circumstellar environment of HD 106906AB: an 11 ± 2 M_J planet located at 732 ± 30 au in projected separation (Bailey et al. 2013) and an asymmetric debris disk nearly viewed edge-on, imaged by SPHERE (Lagrange et al. 2016a), GPI and HST (Kalas et al. 2015) and MagAO (Wu et al. 2016). More recently, the binary nature of HD 106906 was inferred thanks to observations with the instruments HARPS and PIONIER (Lagrange et al. 2016b). It turns out to be a 13 ± 2 Myr old SB2 binary consisting of two F5 V-type stars with very similar masses. Table 1 summarizes the key characteristics of the system components. No further information is known about the orbit of the planet, which must have an orbital period of at least 3000 years. The binary orbit is also not much constrained yet, but given its short orbital period (<100 days), it will presumably be better known in the near future.

The edge-on debris disk has an unusual shape: its luminous intensity has a very asymmetric profile. The longest peak, pointing westward, extends up to 550 au, while the east edge reaches 120 au only (see Figs. 1 and 3 of Kalas et al. 2015). Conversely, below 120 au, the disk is more luminous on its east side than on its west side. This reversed asymmetry might suggest the presence of a spiral density wave extending over the whole disk, and

[1] http://exoplanet.eu

Table 1. Key characteristics of the HD 106906 system.

System component	Mass	Projected separation
HD 106906 AB	~1.34 and ~1.37 $M_\odot$[a]	0.36–0.58 au[a]
HD 106906 b	11 ± 2 M_J[b]	732 ± 30 au[b]
Disk	0.067 M_{Moon}[c]	from 65 ± 3 to ~550 au[d,e]

References. [(a)] Lagrange et al. (2016b); [(b)] Bailey et al. (2013); [(c)] Chen et al. (2011); [(d)] Kalas et al. (2015); [(e)] Lagrange et al. (2016a).

viewed edge-on from the Earth. Finally, a large cavity splits the disk into two debris belts. Chen et al. (2014) modeled the stars' excess emission and suggested 13.7 and 46 au for the radii of the belts. The latter likely corresponds to the one imaged by Lagrange et al. (2016a) and Kalas et al. (2015) at ~50 au.

Despite the richness of the observations, the geometry and kinematics of the whole system are strongly underconstrained. If the actual planet-binary distance is less than 1000 au, then the orbit inclination with respect to the plane of the disk must be significant (20 degrees). However, a coplanar configuration cannot be excluded, but the separation should then be around 3000 au. In any case, the large separation between the planet and the central binary, as well as the possible misalignment between the planet orbit and the debris disk, challenges classical mechanisms of planet formation.

According to current theories, planet formation takes place in the primordial gaseous disk. However, as we mentioned above, forming a giant planet via core accretion or gravitational instability at 700 au or more from any central star appears very unlikely, first due to the lack of circumstellar gas at that distance, and second because the corresponding formation timescale would exceed the lifetime of the gaseous disk. The disk asymmetries (in particular the suspected spiral structure) indicate strong ongoing dynamical interaction with the dust. This may suggest that the planet did not form where it resides today, but may have formed inside and be scattered afterwards. The recently discovered binary nature of HD 106906AB is indeed a source of potentially strong dynamical perturbations that could trigger planet scattering.

The purpose of this paper is to investigate both analytically and numerically the scenario that could have lead to the present-day characteristics of the HD 106906 system starting from a planet formation within the circumbinary disk. As viscosity-induced migration tends to make the planet move inwards, in Sect. 2 we will study the likelihood of an ejection via interactions with the binary, and we will then discuss in Sect. 3 how the planet could have stabilized on such a wide orbit. Finally, in Sect. 4 we briefly analyze the effect of this scattering scenario on the disk and the processes that could have shaped it as it currently appears. Numerical simulations in our analysis have been performed using the Swift_HJS symplectic integration package (Beust 2003), a variant of the Swift package developed by Levison & Duncan (1994), but dedicated to multiple stellar systems.

2. Ejection

2.1. Basic scenario

We investigated how HD 106906 b, supposed initially orbiting the binary on a nearly coplanar orbit, could have been ejected from the disk via dynamical interactions. When it is located far away enough from its host stars, a circumbinary planet may have a very stable orbit. On the other hand, if it migrates too close to the binary, it undergoes a close encounter with the stars and can be ejected.

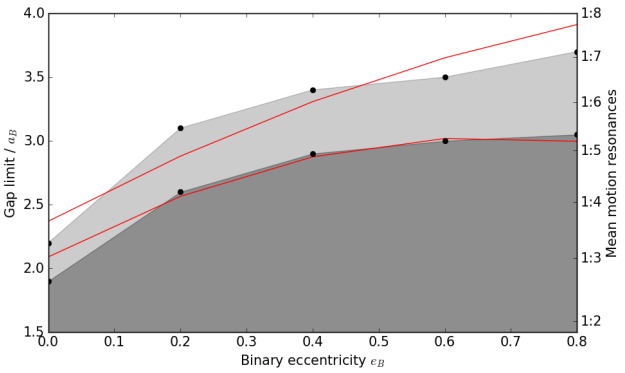

Fig. 1. Chaotic zone (in dark gray) as a function of the binary eccentricity, for binary components of same masses. The lighter part designates a critical zone, where some test particles can survive. The red lines represent the lower and upper critical orbit parabolic fits found by Dvorak (1986) in its study of circumbinary planet stability. The 1:6 commensurability is the strongest outside the chaotic zone (see Sect. 2.2) for $e_B \geq 0.4$.

The binary is surrounded by a chaotic zone where no stable circumbinary orbit is possible. Dvorak (1986) uses a semi-analytical approach to compute the upper critical orbit (lower radius of the stable zone) and lower critical orbit (upper radius of the chaotic zone) around two stars of same masses for different binary eccentricities, and found that this gap size typically ranges between two and three times the semi-major axis of the binary orbit. Numerical results for this mass ratio are missing, so that we computed the limits of the gap with our Swift_ HJS package and compared them to the semi-analytical approach in Fig. 1. In each simulation, the evolutions of 10 000 test particles have been studied during 10^5 orbital periods of the binary. The particles have been randomly chosen with semi-major axes between 1.5 and four times the binary semi-major axis a_B, eccentricities between 0 and 0.1, and inclinations with respect to the binary orbital plan between 0 and 3°. The time step has been chosen to be 1/20 of the binary orbital period.

Artymowicz & Lubow (1994) showed that this chaotic zone also affects the gas of the disk, with gap sizes similar to the values given by our algorithm (Beust 2003). Consequently, as the migration necessarily stops at the inner edge of the disk, the planet should never reach the chaotic zone this way. It will remain confined close to the lower critical orbit, where it may never be ejected. Mean-motion resonances (hereafter MMR) may help overcoming this difficulty. During its inward migration, the planet is likely to cross MMRs with the binary. It may then be captured by the resonance and furthermore undergo an eccentricity increase that could drive its periastron well inside the chaotic zone.

2.2. Mean-motion resonances

Nested orbits are in a configuration of MMR when their orbital periods are commensurable. For fixed masses and neglecting the precession, this is fully controlled by the semi-major axis ratio a_B/a (subscript B refers to the binary): the orbits are said to be in a $p+q$: p resonance when

$$\frac{T_B}{T} = \left(\frac{a_B}{a}\right)^{3/2} \sqrt{\frac{m_B}{m_B + m}} = \frac{p+q}{p}, \quad (1)$$

where p, q are integers, and T and m designate respectively Keplerian periods and masses. Resonances are described using the characteristic angle

$$\sigma = \frac{p+q}{q}\lambda_{\rm B} - \frac{p}{q}\lambda - \omega, \tag{2}$$

where λ designates the mean longitude and ω the periastron longitude. σ represents the longitude of a conjunction between the binary and the planet, where all three bodies are aligned, measured from the line of apsides of the planet. If σ stops circulating and begins to oscillate around an equilibrium position (libration), it means that the conjunctions repeatedly occur roughly at the same places on the planet orbit: the system is locked in the resonant configuration. If the resonant conjunction occurs in the location where the interacting bodies are sufficiently far away from each other (like in the Neptune-Pluto case), then the resonance acts as a stabilizing mechanism that prevents close encounters. MMRs are nevertheless known to enhance eccentricities. If the eccentricities are too highly excited, then the conjunctions may no longer occur at safe locations, often causing instability. For a review on MMRs, see Morbidelli (2002).

The way a MMR can enhance the eccentricity of the planet can be studied in a semi-analytical way. Details about this procedure are given in Beust (2016), Beust & Morbidelli (2000) and Yoshikawa (1989). Basically, if we restrict the study to orbits with negligible σ-libration, the interaction Hamiltonian can be averaged over the motion of the binary for constant σ. This gives a one degree of freedom autonomous Hamiltonian. Phase-space diagrams with level curves of this Hamiltonian can then be drawn in $(\nu \equiv \omega - \omega_{\rm B}, e)$ space to explore the overall dynamics. To adapt the method to this unusual case where the inner bodies have similar masses, we calculated the resonant Hamiltonian of a planet orbiting the center of mass of a binary with binary mass parameter $\mu \equiv m_2/m_{\rm B}$ (where m_2 is the mass of the second star):

$$H = -\frac{Gm_{\rm B}}{2a} - Gm_{\rm B}\left(\frac{1-\mu}{|\boldsymbol{r}+\mu\boldsymbol{r}_{\rm B}|} + \frac{\mu}{|\boldsymbol{r}-(1-\mu)\boldsymbol{r}_{\rm B}|} - \frac{1}{|\boldsymbol{r}|}\right) - \frac{p+q}{p}\frac{2\pi}{T_{\rm B}}\sqrt{Gm_{\rm B}a}, \tag{3}$$

where G is the gravitational constant, $\boldsymbol{r}_{\rm B} \equiv \boldsymbol{R_2} - \boldsymbol{R_1}$ and $\boldsymbol{r} \equiv \boldsymbol{R} - (\mu\boldsymbol{R_1} + (1-\mu)\boldsymbol{R_2})$ if $\boldsymbol{R}$, $\boldsymbol{R_1}$ and $\boldsymbol{R_2}$ are respectively the position vectors of the planet, the first and the second component of the binary. We could then perform the integration over the orbital motions and derive the phase space diagram for the interesting commensurabilities. The result is displayed in Fig. 2 in the 1:6 MMR case, for a binary eccentricity of $e_{\rm B} = 0.4$. Most of the level curves of the Hamiltonian exhibit important change in the planet eccentricity; therefore, starting at low eccentricity, the resonant interaction can drive the planet to higher eccentricity regime and cause it to cross the chaotic zone (indicated in red on the figure) at periastron, leading to ejection.

Our choice of focusing on the 1:6 mean-motion resonance should not be surprising. Indeed, according to Fig. 1, it is the lowest order resonance that lies outside the chaotic zone for $e_{\rm B} \geq 0.4$: it occurs at $a/a_{\rm B} \simeq 3.3$. Any lower order (thus potentially stronger) resonance such as 1:2, 1:3, etc. falls inside the chaotic zone, and could not be reached by the planet according to our scenario. Moreover, the topology of the diagram depends on the binary eccentricity: the higher it is, the higher is the change of eccentricities depicted by the level curves. And those curves are flat for a circular binary orbit.

However, the semi-analytical study is not sufficient here to study the dynamical route that leads to ejection. Indeed, libration

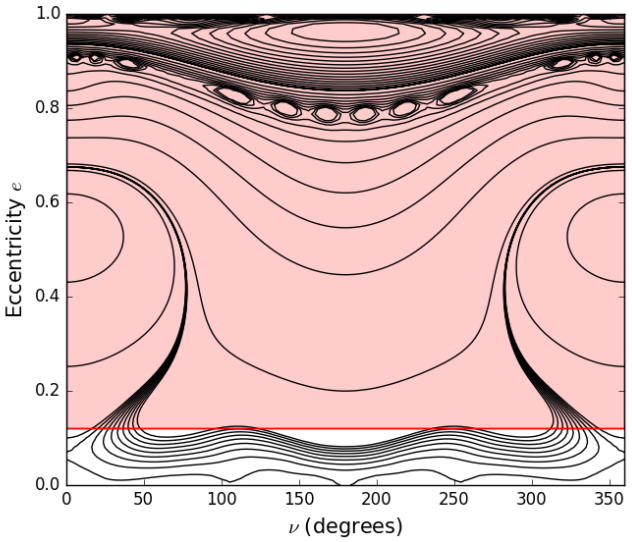

Fig. 2. Isocontour in the $(\nu = \omega - \omega_{\rm B}, e)$ phase space of the average interaction Hamiltonian of a test particle trapped in 1:6 mean-motion resonance with a binary eccentricity of $e_{\rm B} = 0.4$, assuming a binary mass parameter of $\mu = 1/2$. Each curve represents a trajectory in the (ν, e) space. Above the red line, the planet has part of its orbit in the chaotic zone.

Table 2. Effect of the 1:6 mean-motion resonance and ejection duration for different eccentricities of the binary, starting with a planet eccentricity of $e = 0.05$.

Binary eccentricity	Effect of the 1:6 MMR
$e_{\rm B} = 0.0$	no ejection
$e_{\rm B} = 0.2$	no ejection
$e_{\rm B} = 0.4$	ejection in 100–1000 yr
$e_{\rm B} = 0.6$	ejection in 100–1000 yr
$e_{\rm B} = 0.8$	ejection in 100 yr

Notes. For $a_{\rm B} = 0.4$ au, the 1:6 resonance corresponds to a planet semi-major axis around $a = 1.3$ au.

of the resonant angle σ and chaos on short timescale, not taken into account in the computation of the phase-space diagram, are not negligible for a binary with mass parameter close to 1/2. We thus performed numerical simulations of 10^5 binary orbital periods of dynamical evolution for different binary eccentricities and different initial angular conditions, to study the stability of different ratio of MMR. All runs were performed starting with a semi-major axis close to the resonant value, with a time step set to 1/20 of the binary orbital period.

Only a few resonances located outside the chaotic zone are finally able to trigger ejection: the 1:6 and the 1:7 one. The simulations allowed to check not only the ability of the resonances to generate instability, but also the time needed to eject the planet, as well as the typical width of the starting resonant zone that leads to ejection, which is typically 0.01 au. Table 2 summarizes the results obtained with various $e_{\rm B}$ values and $\mu = 1/2$ with the 1:6 resonance.

The simulations confirm that resonance stability depends on binary eccentricity $e_{\rm B}$, and that the resonance gets weaker when the order of the resonance $|q|$ increases. An important result is that whenever ejection occurs, it happens within a very short timescale, always much shorter than the typical time needed ($\lesssim$1 Myr) to form the planet from the gaseous disk. Our first conclusion is thus that the planet cannot have formed within

the resonance. This validates the idea outlined above that it first formed at larger distances in a more stable position, and furthermore migrated inwards and was possibly trapped in a mean-motion resonance before being ejected. In the following, we investigate this scenario.

2.3. Migration

In recent decades, planet migration has become an unavoidable ingredient to explain the configuration of some planetary systems. Due to tidal interactions with the primordial gas disk, giant planets (mass > 10 $M_\oplus$) undergo first a type I, and furthermore a type II migration once they have created a gap in the disk (Baruteau et al. 2014). It consists of a drift that can be directed toward the star, whose characteristic timescale depends on the position, and characteristics of the planet and on the viscous properties of the disk.

We have assumed that the planet has approximately reached its final mass when it arrives at the location of unstable MMRs, that is between 1 and 2 au from the stars. The characteristic time of migration varies in inverse proportion to the quantity $\alpha_\nu h^2 \Sigma$, where α_ν is the viscosity parameter, h the aspect ratio and Σ the surface density (Lin & Papaloizou 1986). However, not only the values of those quantities are unknown in HD 106906 primordial disk, but also this simple dependency does not seem to match nor the known planetary population (Mordasini et al. 2009) neither the results inferred by hydrodynamical simulations (Dürmann & Kley 2015). Taking this fact into account, estimating the mass of the primordial disk to be around 0.6% of the stellar mass (Andrews et al. 2013) and varying the viscosity parameter and the aspect ratio around the observed values (e.g., Pinte et al. 2015), we obtained a large range of migration timescales. To obtain the largest overview without trying every single velocity, we choose to run our tests with four different migration velocities at 2 au: 10^{-3}, 10^{-4}, 10^{-5} and 10^{-6} au/yr.

Simulating the whole process of disk-induced migration in the circumbinary environment is beyond the scope of the present paper. Using a hydrodynamic code, Nelson (2003) computed the migration of a planet in a circumbinary disk and show that it was likely to get locked into a mean-motion resonance. As their stars had very different masses, their results can not be applied here, so we choose to add to the SWIFT_HJS code an additional extra-force that mimics the migration mechanisms they observed. This force is designed in such a way that its secular effect averaged over the orbital motion of the planet just induces the desired steady-state semi-major axis drift $\mathrm{d}a/\mathrm{d}t = v_{\rm mig}$, $v_{\rm mig}$ being a fixed arbitrary migration velocity, and has no effect on the eccentricity nor on the longitude of periastron. Further details about the choice of the force are provided in Appendix A. We derive:

$$\boldsymbol{F}_{\rm mig} = \frac{v_{\rm mig} n}{2\sqrt{1-e^2}} \left(1 + \frac{1}{2}\left(1 - \frac{r}{a}\right)\right) \boldsymbol{e}_{\boldsymbol{\theta}}, \tag{4}$$

where $(\boldsymbol{e}_{\boldsymbol{r}}, \boldsymbol{e}_{\boldsymbol{\theta}})$ are the 2-D cylindrical radial and orthoradial unit vectors in the local referential frame attached to the planet's motion. Thus, $\boldsymbol{F}_{\rm mig}$ depends on the planet position via the radius r, the vector $\boldsymbol{e}_{\boldsymbol{\theta}}$ and the planet mean angular motion $n = 2\pi/T$. The parameter $v_{\rm mig}$ is set at the beginning of the simulation, according to the timescale we want for the migration. We note that with the above convention, inward migration corresponds to $v_{\rm mig} < 0$. Of course, the migration is implicitly assumed to hold as long as the planet moves inside the disk.

Whether migration would inhibit or enhance the effects of MMR is not a straightforward issue. Resonance trapping induced by type II migration was found to exist for some commensurabilities between two protoplanets orbiting a star (Snellgrove et al. 2001; Nelson & Papaloizou 2002). But MMRs with a binary are more difficult to predict, especially those located near the chaotic zone, like those we are focusing on here. Moreover, the expected lifetime of the gas disk is roughly three million years around massive stars (Haisch Jr et al. 2001; Ribas et al. 2015), so that the formation, migration and hypothetical ejection must all occur by this time.

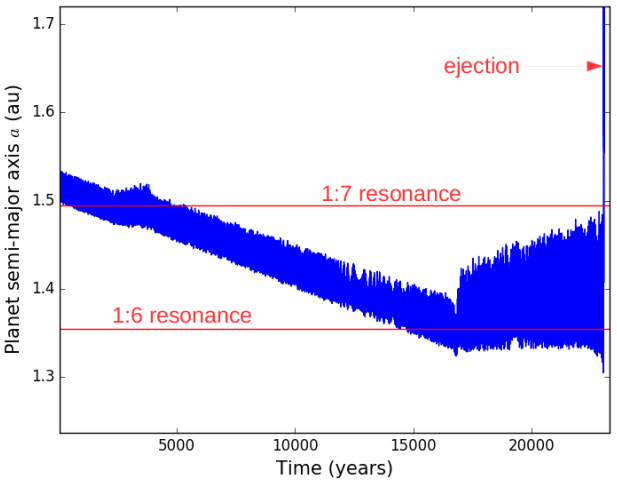

Fig. 3. Evolution of the planet semi-major axis with respect to time for a binary eccentricity of $e_{\rm B} = 0.2$ and a 10^{-5} au/yr migration velocity. The semi-major axis of the binary has been set to $a_{\rm B} = 0.4$ au. The plot illustrates the migration, then ejection, of the planet after it has been trapped into a 1:6 resonance. The effect of the 1:7 resonance, weaker, is also visible on the plot. As the planet has a perturbed Keplerian motion around the binary, the exact locations of MMRs are not straightforward to derive (see Appendix B).

We thus performed numerical simulations, where the planet was initially put outside (~2 au) the zone of interest. Whether the planet formed just outside the critical zone or whether it migrated toward there is irrelevant, only the values of the orbital elements and migration velocity at the entrance of the zone of interest matter to conclude on the possibility of ejection. Migration was added using the additional force depicted in Eq. (4), with the diverse migration velocity prescriptions described above. The simulations were pursued until the planet gets captured in a mean-motion resonance and furthermore ejected, or until it reaches the inner edge of the disk, that is, the chaotic zone, in the case of no resonant capture. Again, the time step has been taken to be $\lesssim T_{\rm B}/20$. The main result is that migration, regardless of its velocity or of the binary eccentricity, always leads to a resonant trapping followed by an ejection after a reasonable amount of time spent in the resonance.

In Fig. 3, an example of the effect of both migration and resonances is visible via the evolution of the semi-major axis of the planet. The figure illustrates the full dynamical evolution corresponding to $v_{\rm mig} = 10^{-5}$ au/yr and $e_{\rm B} = 0.2$. In addition to high frequency oscillations that illustrate the chaotic nature of the dynamics, we see a gradual semi-major decrease at a speed corresponding to the initial prescription, followed by a capture in the 1:6 MMR resonance that finally leads to ejection. Interestingly, we note a temporary trapping in the 1:7 resonance than occurs before the final capture in the 1:6. The 1:7 resonance appears not to be strong enough to fully inhibit the migration, while the 1:6 does.

Table 3. First unstable resonance and corresponding ejection time for different eccentricities of the binary and different migration velocities, starting with $e = 0.05$ and $a = 2$ au.

Migration	10^{-3} au/yr	10^{-4} au/yr	10^{-5} au/yr	10^{-6} au/yr
$e_B = 0$	1:4, 50 yr	1:4, 10^3 yr	1:5, 10^4 yr	1:5, 10^5 yr
$e_B = 0.2$	1:5, 50 yr	1:6, 10^3 yr	1:6, 10^4 yr	1:7, 5×10^4 yr
$e_B = 0.4$	1:6, 100 yr	1:6, 500 yr	1:6, 2×10^3 yr	1:7, 2×10^4 yr
$e_B = 0.6$	1:6, 100 yr	1:6, 100 yr	1:6, 2×10^3 yr	1:6, 10^4 yr
$e_B = 0.8$	1:6, 100 yr	1:7, 500 yr	1:8, 10^4 yr	1:7, 2×10^4 yr

Notes. The ejection time corresponds to the time needed to eject the planet starting from the beginning of the MMR trapping.

Table 3 summarizes the ejection times obtained in the various cases tested. Comparing Tables 3 and 2, we note that migration, despite causing important small-scale variability of the semi-major axis, enhances resonant instabilities. However, this efficiency is probably overestimated because of the simplicity of our migration model. Deeper analysis of the disk-planet interaction close to the resonance would be needed. Moreover, close to its inner edge, the disk is strongly shaped by the binary and some eccentric ring-like features may affect the protoplanet migration (Mutter et al. 2016).

We may now summarize the analysis that has been conducted in this section by reviewing the time evolution of this tentative ejection process. The formation of a giant planet takes a variable amount of time depending on the process and the location: from several periods if formed via gravitational instabilities to a million periods if formed via core accretion (Chabrier et al. 2014). Consequently, in order for HD 106906 b to acquire its mass, it must have formed in a relatively stable location over the timescale involved, at least at a distance of 2 au. However, as giant planets are believed to form beyond the snow line, whose location is estimated to ∼10 au around ∼3 $M_\odot$ star (Kennedy & Kenyon 2008), the stability of the planet formation position is a priori ensured. After a substantial growth of the planet, migration occurs, whose strength depends on the primordial disk characteristics, and pushes the planet into a less stable zone. For the planet to be ejected, it has to enter the zone of destabilizing resonances (1:6, 1:7), which lies around 1.5 au (Fig. 3). All in all, if $a_{\rm formation}/v_{\rm mig}$ is inferior to the disk life-expectancy, the scattering of the planet is a natural outcome in a system with binary mass ratio close to unity.

3. Stabilization

3.1. The idea of a close encounter

In the previous subsection, we demonstrate that a giant planet which formed reasonably close to the binary is likely to undergo an ejection. However, ejection does not imply stabilization on a distant orbit around the binary, as it is most likely the case for HD 106906 b. Eventually, the planet follows an hyperbolic trajectory and does not need more than 10 000 years to completely fly away from its host star. Indeed, suppose that the planet gets ejected on a still-bound orbit via a close encounter with the binary: the orbit may have a very distant apoastron, but its periastron will necessarily lies in the region where it originates, that is the immediate vicinity of the binary. Therefore, after one orbital period, the planet is back at periastron and undergoes a new violent encounter with the binary that is likely to cause ejection. Such episodes have been actually recorded in our simulations.

Thus, in order to stop the ejection process and stabilize the planet orbit, an additional dynamical process is needed to lower its eccentricity and increase its periastron. In the absence of other wide companion of similar mass orbiting the binary (Lagrange et al. 2016a), a close encounter with a passing star is a natural candidate. Recalling that the Sco-Cen association must have had a more important stellar density several million years ago, this event might have occurred with non negligible probability.

The impact of dynamical interactions on planetary systems in open clusters has been studied intensively since the discovery of the first exoplanets. An effective cross section has been computed by Laughlin & Adams (1998), that characterizes the minimal encounter distance needed to raise the eccentricity of a Jovian planet at 5 au from 0 to over 0.5. They found $\langle\sigma\rangle = (230\ \text{au})^2$, which gives a stellar encounter rate of about 0.01 disruptive encounter in our system lifetime. More precisely, Parker & Quanz (2012) conducted N-body simulation to observe the planet orbital elements after a fly-by, and found a probability between 20 and 25% that a 30 au planet undergoes at least a 10% eccentricity change in a ten million year period. In our case, the situation seems even easier, because we want to modify the orbit of an unstable planet already far from its star, thus with a trajectory that can easily be swayed. However, the encounter needs to happen at the right time of the planet life, during the ∼1000 years that would last the ejection. Moreover, the encounter should be weak enough not to definitely eject the planet, but strong enough to circularize the orbit to a reasonable eccentricity. We note that weak encounters are more likely to occur than strong ones.

3.2. Probability of a stabilizing fly-by

Of course, not all fly-by geometries will generate the desired effect. The fly-by is entirely defined by the mass of the passing star M_*, the closest approach (or periastron) to the binary p_*, the velocity of the passing star at closest approach v_*, the inclination i_* of the passing star orbit with respect to the planet orbit, its longitude of ascending node Ω_* measured from the line of apsides of the planet orbit, and the argument of periastron ω_* with respect to the line of nodes. A scheme of the effect of a stellar fly-by is sketched in Fig. 4 in the coplanar case, in a configuration voluntarily favorable to a restabilization: when the planet is at the apoastron of a wide unstable orbit. In fact, the apoastron is also the most likely position of the planet, as it spend there most of its time.

Figure 5 shows the results of a parametric study limited to coplanar fly-bys (we studied the inclined cases as well) for a given angle ω_* (45 degrees), in (p_*, v_*) 2D parameter space, for three different M_* values (0.1, 1 and 5 $M_\odot$) and assuming the planet was at the apoastron of a very wide unstable orbit before the encounter (such as in Fig. 4). The planet is 1000 au away from the binary when the fly-by occurs, this is why a cut-of can

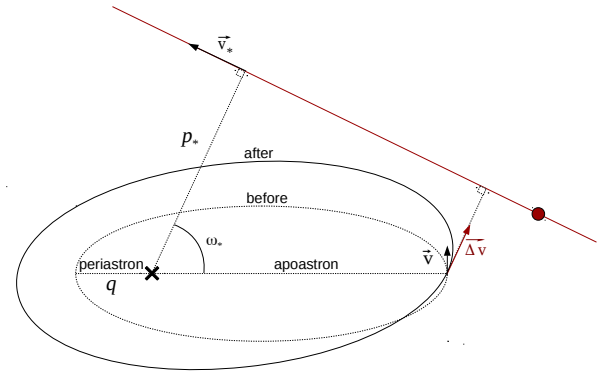

Fig. 4. Example of a coplanar configuration where a passing star (in red) stabilizes a wide unstable planet orbit. Before the fly-by, the planet orbit still has a very low periastron, and after it gets much wider, thanks to the interaction with the passing star. We recall that according to Kepler's laws, the planet spends most of its time near apoastron, so that any fly-by is likely to occur when the planet is at or near this point.

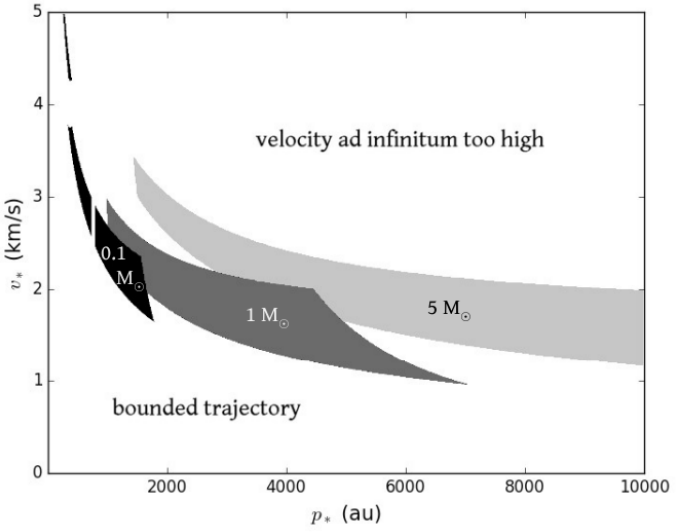

Fig. 5. Area in the disruptive star phase space which succeed to raise the periastron from 1 au to over 2 au in the case of a coplanar encounter of periastron argument $\omega_* - \omega = 45$ degrees. v_* designates the maximum relative velocity of the disruptive star, p_* designates its smaller distance from the binary.

be seen around $p_* = 1000\cos(\frac{\pi}{4})$ au. In each case, the gray area represents the zone in parameter space that is reachable (plausible v_*) and actually causes a significant periastron increase of the planet. In this peculiar configuration, taking into account the distribution of p_* and v_* (see below), a stabilization is very likely.

As a more general approach, the probability of a convenient encounter can be estimated by an integration over the relevant fly-by parameters. Taking a homogeneous distribution of stars in the cluster with characteristic distance d, and a Gaussian distribution of relative velocities with dispersion σ, the number of fly-bys that would raise the planet periastron above $q_{\rm stable}$ is

$$N_{q_{\rm f}>q_{\rm stable}} = \frac{\tau_{\rm ejection}}{\tau_{\rm cluster}} \int_0^{+\infty} \frac{{\rm d}p_*}{4\pi {\rm d}^2} \int_0^{2\pi} p_* {\rm d}\omega_* \int_{\sqrt{\frac{2GM}{p_*}}}^{+\infty} {\rm d}v_*\, n_v(v_*, p_*) \times \int_0^{\pi} {\rm d}i_* \sin i_* \int_0^{2\pi} {\rm d}\Omega_*\, \mathcal{H}e(q_{\rm f} - q_{\rm stable}), \quad (5)$$

where $q_{\rm f}$ is the final periastron reached by the planet after the fly-by perturbation, $\tau_{\rm ejection}$ is the characteristic time of ejection, $\tau_{\rm cluster} \equiv d/\sigma$ is the characteristic time in the cluster (timescale needed to have a convenient fly-by), $\mathcal{H}e$ is the Heaviside function and n_v the velocity distribution of unbound stars

$$n_v(v_*, p_*) = 4\pi v_* \sqrt{v_*^2 - \frac{2GM}{p_*}} \left(\frac{3}{2\pi\sigma^2}\right)^{3/2} \exp\left(-\frac{3\left(v_*^2 - \frac{2GM}{p_*}\right)}{2\sigma^2}\right). \quad (6)$$

This gives the probability of having a stabilizing fly-by, for a given mass M_* of the passing star. Apart from the role of M_* (see Fig. 5), this probability is strongly though indirectly dependent on the orbital parameters of the planet before the fly-by, that is on the state of advancement of the planet ejection. It is higher when the planet lies initially on a wide, unstable but still bound orbit (as in Fig. 4). On the other hand, it is nearly zero as long as the planet is still close to the binary (i.e., before ejection) and if it is already on a hyperbolic trajectory. In order to compute analytically the value of $\mathcal{H}e(q_{\rm f} - q_{\rm stable})$ for every set of parameters $(p_*, v_*, i_*, \Omega_*, \omega_*)$ given any initial planet position and velocity, we assume a linear trajectory for the perturber. The direction of the velocity change caused by this approximated encounter can then be analytically derived, as well as the new planet orbit. In the computation, we assumed a velocity dispersion of $\sigma = 0.2$ au/yr (1 km s^{-1}) (Madsen et al. 2002), and the order of magnitude of the characteristic time of ejection $\tau_{\rm ejection}$ has been set to 10^3 yr.

The most critical dependence of our formula (5) is on the local distance between stars d. The present and past density of the LCC is not known. Therefore, we attempted to determine it through a kinematic study in Appendix D. From 141 stars for which complete data could be retrieved, we could trace back the density of LCC through time. The results show that the early density was roughly 1.7 times the present density, evaluated around 0.05 star/pc^3 in the close neighborhood of HD 106906. Moreover, the contribution of field stars (not related to LCC) has been estimated to be similar to the contribution of LCC. From this piece of information, we derived that the present local density is lower than ≈0.11 star/pc^3. This density, consistent with the density of the solar neighborhood (Reid et al. 2002), corresponds to $d \sim 2$ pc. If our scenario happened in such an environment, the probability of a close encounter ($p_* < 5000$ au) just following the planet ejection is below 1×10^{-7}.

Nevertheless, our estimate of the LCC density is based on a small number of luminous (and mostly early-type) stars for which the kinematics can be inferred. In our case, the fly-by of any object more massive than the planet can stabilize the orbit and impact our probabilities. Therefore, we considered the extreme case where neighboring bodies in the cluster are separated by $d = 0.1$ pc, a density similar to the one taken in Laughlin & Adams (1998) and Parker & Quanz (2012). We report the probabilities for that high density and for the case of a 1 $M_\odot$ perturber in Table 4, for different initial conditions. We note that the number of encounters for any $d > 5000$ au roughly scale with d^{-3}, so that lower-density results can be easily retrieved from the table.

Table 4. Number of close encounters with a 1 $M_\odot$ star raising the planet periastron above a given value (2, 50 or 150 au) depending on the trajectory of the planet before the fly-by.

Periastron superior to	2 au	50 au	150 au
Unstable elliptic trajectory	8×10^{-4}	5×10^{-5}	2×10^{-5}
Slow hyperbolic trajectory	1×10^{-4}	2×10^{-5}	6×10^{-6}
Fast hyperbolic trajectory	$<1 \times 10^{-6}$	$<1 \times 10^{-6}$	$<1 \times 10^{-6}$

Notes. These values have been obtained from Eq. (5).

3.3. Conclusions

Table 4 shows that the probability of a stabilizing fly-by remains low. As outlined above, the most favorable case corresponds to initially wide elliptical orbits before encounter. However, most of the time, the planet is directly ejected on an hyperbolic orbit instead of a wide elliptical orbit. And even if this occurs, the subsequent periastron passages in the vicinity of the binary quickly lead to a definitive ejection.

The probabilities have been computed for a 1 $M_\odot$ perturber only, less than half of our system 2.7 $M_\odot$ star. Though the perturber to host star mass ratio do matter to evaluate the fly-by impact (e.g., Jílková et al. 2016), the 1 $M_\odot$ results give an upper bound that accounts for the encounter with lighter stars, and a rough estimate for encounters with heavier stars (see Fig. 5), which are less abundant.

We therefore conclude that while our scenario uses generic ingredients (migration, MMR, fly-by), it is not very likely to happen because of the low probability of a fly-by-assisted stabilization. An indirect proof could be provided if we could see traces of planet ejection on the disk. Moreover, constraints on the present-day orbit of HD 106906 b would certainly help refining this scenario: a very high planet eccentricity could raise its likelihood, but the secular effect of such a planet passage in the disk every thousands of years would have big consequences on the disk morphology.

4. Debris disk

In this section, we investigate the consequences of our scattering scenario on the disk particles repartition, to check whether it matches the observations (short-distance asymmetry, long-distance asymmetry and extended inner cavity).

4.1. Ejection through the disk

An essential part of the scenario we outline in this paper is the violent scattering of the planet by the binary. Most of the time, the planet switches directly from a close orbit around the binary to a fast hyperbolic trajectory toward the edge of the system. As of yet we did not mention the effect of such an ejection on the debris disk surrounding HD 106906AB. The passage of a $\sim$10 $M_{\rm Jup}$ planet across the disk should presumably induce drastic perturbations on it. In order to investigate this issue, we ran a N-body simulation with 10 000 test particles, neglecting the interactions between them to access the first order of perturbation. The particles have been randomly chosen with semi-major axes between 5 and 100 au, eccentricities between 0 and 0.05, and inclinations with respect to the binary orbital plan between 0 and 2°. As the main effect of the ejection is due to close encounters between the planet and the disk particles, we use the package Swift_RMVS (Levison & Duncan 1994) that is designed to handle such trajectories. However, this package is not devised to work in multiple stellar system, so that the binary will be here approximated by a single star. The binary effect on the dust being negligible above 5 au for the duration of the perturbation (approximately ten times the planet ejection time, that is 10 000 years), this approximation has almost no consequences on the final dust distribution. Time steps have been set to at most 1/20 of the particles orbital periods, but Swift_RMVS automatically adjusts them to manage close encounters.

The result is displayed in Fig. 6. After the initial spiral-like propagation of the eccentricity disturbance created by the planet, the disk homogenizes on an oblong asymmetric shape that could possible match the needle we observe up to $\sim$500 au. In the case where the planet is first scattered on a wide eccentric orbit before being ejected, the process gives eccentricity to some test particles, but the effect is negligible compared to the effect of the ejection that comes next. However, in any case, the asymmetry might not last forever. Orbital precession induced by the inner binary (not taken into account in our simulation) should finally randomize the longitudes of periastron of the particles on a much longer timescale and restore the initial axisymmetric disk shape. For a particle orbiting the binary at 100 au, the precession period (see Appendix C) due to the binary is $\sim 4 \times 10^7$ yr. Of course it is shorter closer to the star, but this remains comparable or larger than the age of the system except in the innermost parts of the disk. Hence still observing the asymmetry today at 500 au should not be surprising even if was created a long time ago. However, our mechanism cannot explain the reversed asymmetry at shorter distance. This inversion presumably corresponds to a spiral density wave extending across the disk that needs a steady-state perturbation to be sustained over a long enough timescale.

4.2. The effect of a stellar encounter

In Sect. 3, we discussed the possibility that a stellar fly-by could have stabilized the planet mid-ejection. The effect of such encounters on a disk has been studied intensively (for example in Breslau et al. 2014; Jílková et al. 2016). This effect is of course very dependent on the mass ratio of the stars and on the encounter periastron and eccentricity.

In fact, most encounters that would stabilize an unstable planet are compatible with the current shape of the disk. We can, for example, consider the case of a 1 $M_\odot$ star perturber. The majority of the suitable encounters have periastrons superior to 1000 au (see Fig. 5). According to the computations of Jílková et al. (2016), this and the high mass of our star implies that all the disk particles will remain bound. Indeed, the transfer radius, that is the minimum radius where capture is possible, is well superior to the observed limit of the debris disk. For our disk to be depleted, the transfer radius should be inferior to $\approx$100 au, which corresponds to an encounter periastron around 250 au. Thus, though the problem is strongly underconstrained, our scenario is likely to be compatible with the existence of the disk.

4.3. Secular carving

The secular action of the planet orbiting the binary on its present day large stabilized orbit is an obvious long-term source of perturbation on the disk. We note that we make here a clear distinction between the initial, short term perturbation triggered by the planet on the disk during its ejection process, which effect has been described in the previous subsection, and the long-term

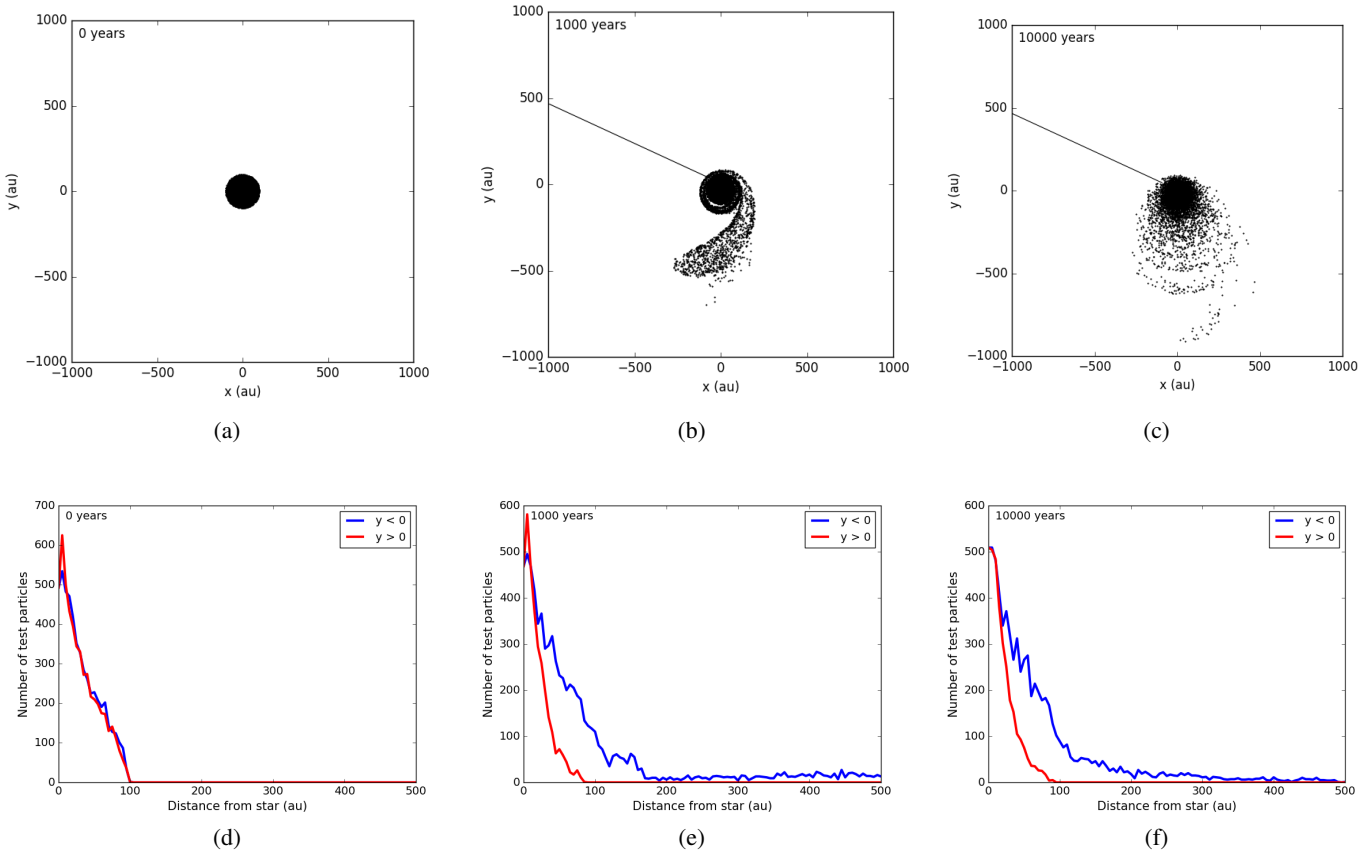

Fig. 6. *N*-body simulation showing the consequence of the ejection of a 11 M_J planet through a disk. *From left to right*, the snapshots have been taken 0, 1000 and 10 000 years after the ejection. The planet starts on an hyperbolic orbit similar to what we observe in the simulations we performed: $a = 10$ au and $e = 1.1$ (corresponding to periastron $q = 1$ au). Above is a spatial representation of the top view of the disk (the planet trajectory is depicted in black), below is the density along the y axis, integrated over the x and z axis.

secular action of the planet as it moves on its distant bound orbit. It is known that eccentric companions (planets or substellar) orbiting at large distance a star surrounded by a disk create spiral density waves within the disk (Augereau & Papaloizou 2004). To a lesser extent, binaries do the same on circumbinary disks (Mutter et al. 2016). The following study nevertheless shows that the asymmetry currently observed in the HD 106906 disk cannot be due to the sole action of the binary, but rather requires an outer source of perturbation like the planet, that enhances the density waves induced by the binary.

We investigate here the secular action of the planet on the disk, combined with that of the binary, using simulations with our Swift_HJS package. Of course with only a projected position, our knowledge of the current orbit of the planet is sparse. Some orbital configurations may nevertheless be ruled out as they would lead to a destruction of the disk. Jilkova & Zwart (2015) studied intensively the impact of each orbital configuration on the disk via the percentage of particles that remain bound $n_{\rm bound}$ and the fraction of bound particles that suit the observation constraints $f_{\rm d/b}$. Although nor the disk neither the binary was resolved at that time, their conclusion still can be used, at least on a qualitative level. They showed that a planet periastron larger than 50 au or an inclination larger than five to ten degrees is enough to keep a relatively good agreement with the observations ($f_{\rm d/b} > 0.5$) without completely depleting the disk. However, to better match the observations ($f_{\rm d/b} > 2/3$), the periastron must lie outside the outer radius of the disk. The maximal inclination is constrained by the observation, that is about twenty degrees. No further constraints can be provided by the simulation of Jilkova and Zwart to rule out any inclination between zero and 20 degrees if the planet orbit does not go across the disk. They point out that Kozai-like mechanisms can lead to some wobbles in inclination, but small enough for the disk to remain in a nearly coplanar state.

Assuming that the planet fulfills these requirements, we compute the asymmetries induced on the disk and compare the result to the observation. The disk was initially made of 10 000 test particles with same initial conditions than in the previous subsection. The result of a typical run is displayed in Fig. 7. Basically, if the periastron of the planet is close enough to the outer edge of the disk, it generates an important asymmetry in the disk within a timescale of between five and ten million years ($\sim 10^8$ binary periods, $\sim 10^3$ planetary orbit). In Fig. 8, the density profile has been computed along the x axis. The resulting plot displays an asymmetry similar to the observations: the east side (in blue) is brighter than the west side on short scale, but its density drops well above the west side density. The shape of the perturbation resembles a circular arc, but it actually consists of two overlapping spiral arcs, one driven by the planet and the other one created by the binary.

This issue can be studied analytically. The approach is analogous to the study without binary, as conducted in Wyatt (2005). Consider a test particle orbiting the binary. Suppose that the planet has a Keplerian orbit around the center of mass of the binary, so that the system is hierarchical. The instantaneous

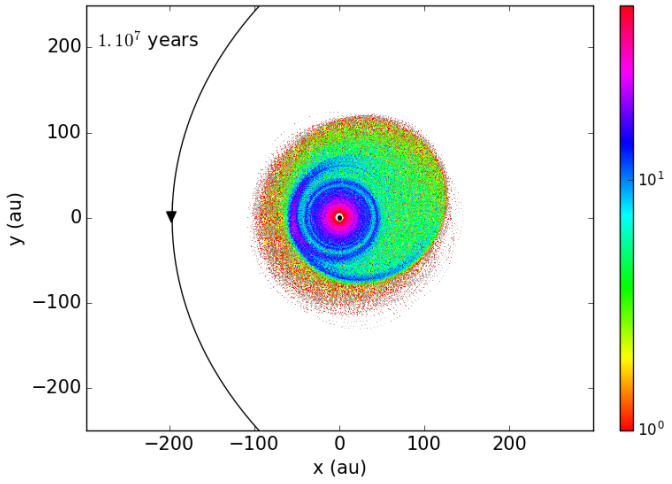

Fig. 7. Top view of the evolution of the debris disk after ten million years of perturbation by a planet on a coplanar orbit whose coplanar orbit has a periastron of 200 au and an apoastron of 1000 au. The color scale represents the relative density. Strong asymmetries can be seen.

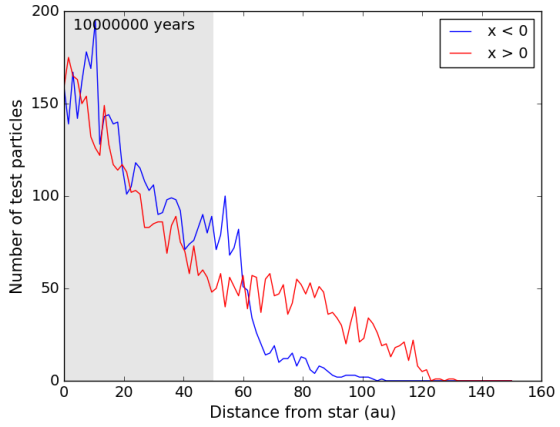

Fig. 8. Density along the x axis, integrated over the y and z axis, obtained from Fig. 7. The gray zone marks approximately the cavity that we observe today. The asymmetry seems to reverse when we get farther to the stars.

Hamiltonian controlling its motion can be written as

$$H = H_{\rm Kep} + H_{\rm bin} + H_{\rm pla}, \tag{7}$$

where $H_{\rm Kep} = -Gm_{\rm B}/2a$ is the pure Keplerian Hamiltonian, and where the two remaining terms constitute the disturbing function, one part arising from the binary, and the other part from the planet. For a binary of mass parameter μ, these independent perturbations are written

$$H_{\rm bin} = -\frac{Gm_{\rm B}(1-\mu)}{|\boldsymbol{r}-\mu\boldsymbol{r}_{\rm B}|} - \frac{Gm_{\rm B}\mu}{|\boldsymbol{r}-(1-\mu)\boldsymbol{r}_{\rm B}|} - H_{\rm Kep}; \tag{8}$$

$$H_{\rm pla} = -Gm_{\rm p}\left(\frac{1}{|\boldsymbol{r}-\boldsymbol{r}_{\rm p}|} - \frac{\boldsymbol{r}\cdot\boldsymbol{r}_{\rm p}}{r_{\rm p}^3}\right), \tag{9}$$

where, in a frame whose origin is at the center of mass of the binary, $\boldsymbol{r}$ is the position vector of the particle, $\boldsymbol{r}_{\rm B}$ is the radius vector between the two individual stars, $m_{\rm p}$ is the mass of the planet, and $\boldsymbol{r}_{\rm p}$ is its position vector. More generally, B subscribed quantities will refer to parameters of the binary, p subscribed quantities to the planet, while unsubscribed parameters will correspond to the orbiting particle.

Both terms of the disturbing function are then expanded in ascending powers of the semi-major axis ratios $a_{\rm B}/a$ and $a/a_{\rm p}$, truncated to some finite order (three here) and averaged independently over all orbital motions, assuming implicitly that the particle is not locked in any mean-motion resonance with the planet or with the binary. Higher orders terms of the disturbing function will be neglected on initial examination, but their influence will be studied in a forthcoming paper. The secular evolution of the particle's orbital elements is then derived via Lagrange equations. Details on this procedure are given in Appendix C.

Starting from a disk made of particles on circular orbits, we use this theory to compute their instantaneous polar coordinates $(r(t), \theta(t))$ in the disk and compute theoretical synthetic images. The result is shown in Fig. 9, which must be compared with Fig. 7. We note the presence of a circular arc very similar to the one obtained in the numerical simulation. This peculiar shape is due to the combination of two spiral waves winded in opposite senses, induced by the planet and the binary via differential precession and eccentricity excitation on the disk particles.

The test particles precession velocities and periastrons are represented in Fig. 10 as a function of their semi-major axis. In the inner part of the disk, the precession is dominated by the binary, so that the speed of the orbital precession decreases with increasing semi-major axis. The results is a trailing spiral wave that can be seen in Fig. 9. Conversely, in the outer part of the disk, the precession is mostly due to the planet, so that its is now an increasing function of the semi-major axis. This creates a leading spiral density wave. The superposition of both spirals in the intermediate region generates the observed circular arc. The exact location of this arc corresponds to the periastron of the particles whose semi-major axis minimizes the precession velocity, that is, around 55 au. Moreover, we see in Fig. 10 that all particles from $a \sim 60$ au to ~100 au have the same periastron. The combination of the two effects enhances the density of the arc, as can be observed in Figs. 7 and 9.

The two spirals are, however, not fully independent. Orbital precession of the particles actually has no visible effect on their global distribution in the disk as long as their orbits are circular. In Appendix C, we show that due to the small size of its orbit and its mass ratio close to one, the binary has very little influence on the eccentricity of the particles compared to the planet, even in the inner part of the disk. In fact, while the outer spiral is fully due to the planet, in the inner spiral, the eccentricity oscillations are also driven by the planet, while the precession is controlled by the binary. Moreover, the contrast of the density wave highly depends on the planet orbital shape (the amplitude of the eccentricity oscillations is roughly proportional to $e_{\rm p}$ within our approximation). For example, if the planet apoastron is 1000 au, its periastron should be less than 500 au ($e > 0.3$) in order to create a significant asymmetry as the one we observe, in a reasonable timescale.

5. Discussion

5.1. Disk cavity

In the previous sections, we did not study the origin of the large cavity observed within the disk by Lagrange et al. (2016a) and Kalas et al. (2015). It is possible that one or more unseen planets could have carved and sustained this cavity. In that case, one of those unseen planet may be responsible for the ejection of the known one, instead of one of the binary star. Those planet(s), if

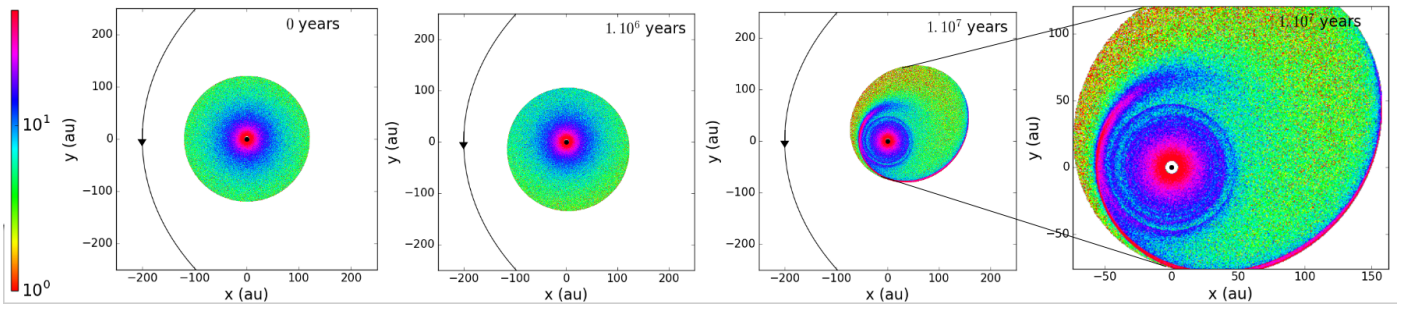

Fig. 9. 2D representation of a debris disk after 0, 10^6 and 10^7 years under the third-order approximation of the influence of the binary and a planet whose periastron is 200 au and apoastron is 1000 au. The color scale represents the local number of particles. At first, only the edge of the disk is affected, but after 10^7 years, two spirals components appear within the disk.

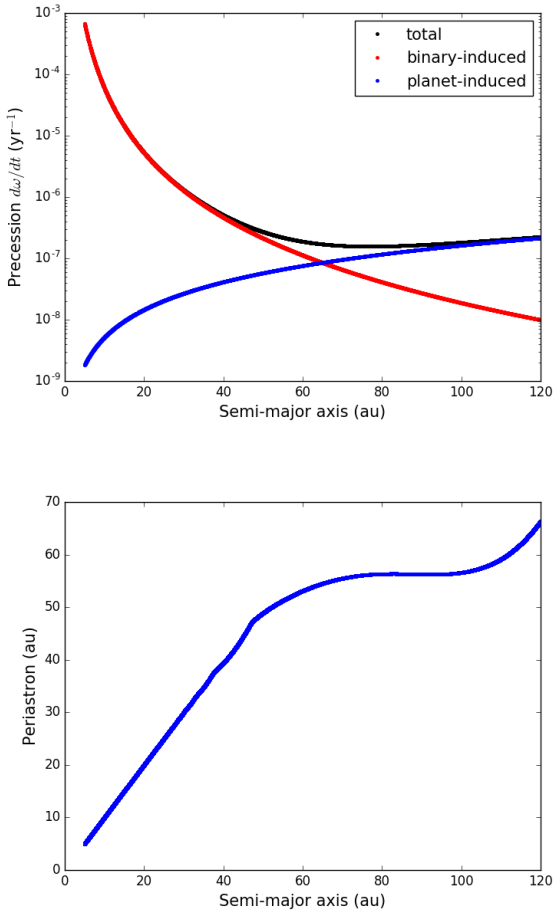

Fig. 10. Precession velocities (above) and periastrons (below) of Fig. 9 test particles with respect to their semi-major axis (that does not change with time) after ten million years evolution. Above, the red curve displays the precession induced by the binary, the blue curve by the planet and the black curve depicts both contributions.

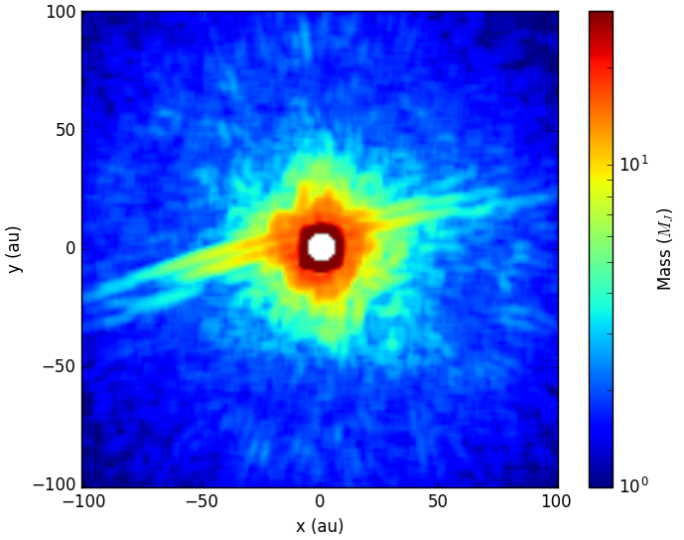

Fig. 11. Minimum mass of planets (in Jupiter masses) that can be detected into the H2 data published in Lagrange et al. (2016a) around HD 106906. The contrasts has been translated into masses using Baraffe et al. (2003) model adapted to the SPHERE filters.

on eccentric orbits, could also influence the shape of the disk (Lee & Chiang 2016). Therefore, we ran N-body simulations with the Swift_RMVS package (the same setting as in the Debris Disk section) to quantify at first order the minimum mass of a single planet, checking if it can carve the observed cavity between the two belts of debris surrounding the pair of stars. This assumes that if one planet alone is responsible for gap, its mass will be higher than in the case where multiple planets are considered. The end result must reproduce the inner edge of the cavity at 13 Myr located between 10 and 15 au (inferred from the IR excess modeling, Chen et al. 2014). We assume that the outer edge of the cavity around corresponds to the separation of the ring (65 au) measured on the SPHERE images (Lagrange et al. 2016a). The simulations give a minimum mass of 30 M_J for a single non-eccentric planet located at 30 au, which is well above the detection limits in Fig. 6 of Lagrange et al. (2016a). However, the disk is viewed edge-on, so that the coronagraph used during the observation (radius of 93 mas or 9.5 au) hides part of the orbital plan. In Fig. 11 we computed a 2D detection-limits map from the data published in Lagrange et al. (2016a). The map confirms that a small zone around the coronagraph has detection sensitivity above 30 M_J. An additional giant planet on a 30 au circular orbit will spend 20% of its time (ten years) in this blind zone and therefore could have been missed. For the case of an eccentric orbit, the mass of the perturber could be only 1 M_J. This is too low compared to the known planet mass to produce an ejection, but high enough to have a noticeable effect on the disk morphology.

5.2. Alternative scenarios

Our scenario makes use of standard ingredients (resonances, migration, scattering, fly-by) envisioned or observed in young

planetary systems (Baruteau et al. 2014) and account for all known components of the system. Nevertheless, the low probability of occurrence we estimate in Sect. 3 because of the need for a nearby star fly-by at the right time makes the scenario implausible. If we suppose that the planet was in fact on a stable orbit before the fly-by, then this fly-by event could have happened at any time, and not necessarily during the early age of the system. However, the probability for a fly-by to have a significant effect on the planet without ejecting it decreases dramatically when the planet gets closer to its host star. Taking the data from Parker & Quanz (2012), we can expect a probability of around 0.1 for a disruption superior to 10% on eccentricity without ejection for a 30 au Jovian planet in the system lifetime. Among the disruptive encounters, it is then hard to tell how many would put the planet on a suitable orbit (apoastron greater than 700 au, that is $e > 0.75$). Plus, such a change of orbit would lead to a very small planet periastron, which will strongly deplete the disk (see Sect. 4.2).

Alternatively, the planet could have been stolen from another system. Indeed, captured planets tend to have eccentric orbit (Malmberg et al. 2011). However, for the final orbit to be so wide, the initial orbit must also have been wide (Jílková et al. 2016). All in all, such a scenario would only turn over the problem, as we would have to account for the wide initial orbit on the first place.

Conversely, the disk could replace the fly-by in our scenario. Indeed, to follow the idea of Kikuchi et al. (2014), the planet could have been accelerated by the gas at its apoastron after a first scattering, and its orbit could have been rendered stable this way. It is interesting to note that some of the circumstellar disks of ~2.5 $M_\odot$ stars recently resolved with ALMA at high angular resolution shows gas extending up beyond the separation of HD 106906 b (e.g., Walsh et al. 2016, and references therein). The total mass of HD 106906 A and B is around 2.7 $M_\odot$ and it is therefore possible that the binary bore such an extended primordial disk that would have circularized the orbit of the ejected HD 106906 b.

Before the discovery of HD 106906AB binary status that indicates strong gravitational interactions, Bailey et al. (2013) suggested that it may have formed in situ. On the one hand, the existence of extended protoplanetary disks implies that our planet may have formed in HD 106906AB primordial disk. On the other hand, HD 106906 b is not the only planetary-mass companion detected at very large projected separation, and such bodies have usually no known scatterers in their environment (see Bryan et al. 2016, even though their study was conducted over a small number of systems less wide than HD 106906 and with lighter stars). Among the systems harboring a planetary-mass companion of similar separation and mass ratio, we can name HIP 77900[2] (Aller et al. 2013), HIP 78530 (Lafrenière et al. 2011), or the triple system Ross 458 (Goldman et al. 2010). In Fig. 12, we represented the wide young planetary-mass companions discovered by direct imaging. We note that HD 106906 b has the lowest planet/star mass ratio above 100 au. The proximity of HIP 78530A b and HIP 77900A b (two brown dwarfs that are also part of Sco-Cen) in that diagram, could indicate that HD 106906AB b formed in situ (within the disk, or like a stellar companion).

[2] Contrary to HD 106906 b, HIP 77900 b has not been confirmed by the common proper motion test. Nonetheless, Aller et al. (2013) argue that low-gravity features in HIP 77900 b spectrum is compatible with the object being a member of Sco-Cen, and therefore a plausible companion to HIP 77900 A.

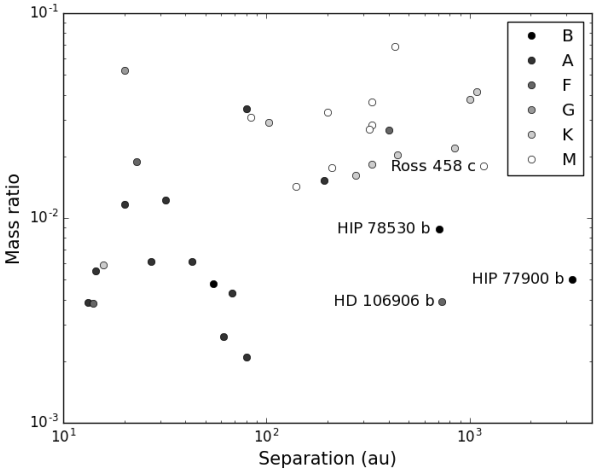

Fig. 12. Planet mass ratios with respect to projected separation. Only planets that belong to young systems (<0.1 Gyr) are displayed, with the exception of the circumbinary planet Ross 458 c. HD 106906 b has the lowest mass ratio beyond 100 au. HIP 78530 b and HIP 77900 b are its two closest neighbors in the diagram. Being identified as brown dwarfs, they may have formed in situ by cloud collapse. Data retrieved from the exoplanets.eu database.

6. Conclusion

We have shown that HD 106906AB b could have formed within the primordial disk and be scattered away on a wide orbit during the first ten million years of the system life. This scenario involves the combination of disk-induced migration and mean-motion resonances with the binary. However, if the scattering is likely to occur, the stabilization of the planet on its current wide orbit is delicate, and requires more than gravitational interactions with the binary. A fly-by scenario has been suggested, but the stabilization only occurs for a restricted part of the overall encounters trajectories. The low density (<0.11 stars/pc^3) that we estimated for the LCC makes a close encounter even more unlikely.

The disk has multiple features, that each could be explained within the frame of our scenario, but also outside of this frame. Two spiral density waves are created if the planet have for the last ten million years had an eccentric orbit with periastron around 200 au. A needle extending to 500 au could have been created by the ejection of the planet, but a smaller needle could be provoked by an eccentric and inclined outer orbit (see Fig. 7) or by an eccentric inner orbit (Lee & Chiang 2016). Nesvold et al. (2017) also studied the secular effect of an eccentric, inclined outer orbit for HD 106906 b in a recent paper, and could produce asymmetries whose brightness repartition is consistent with the observations.

The scenario we explored builds on the observed components of the system (disk, binary star) and on the hypothesis that the planet could not have formed via core accretion or gravitational instability at several hundreds of au. Nevertheless, the low probability of occurrence of our scenario demands that we reconsider those assumptions. Alternative hypothesis like the circularization of the planet orbit via the interaction with the disk gas or in situ formation could explain the present architecture of the system. But this requires that the disk extends up to the separation of the planet and contains enough gas at that separation. Recent high quality images of circumstellar disks extending beyond 700 au around massive stars and the close properties of

other systems in Sco-Cen (HIP 78530A b and HIP 77900A b) argue for this alternative formation pathway.

Finally, we note that many of the methods depicted here are easily generalizable to other circumbinary environment. *N*-body simulations with a simple migration force can be applied on any circumbinary planet to have a quick overlook of the stability of its early trajectory. Fly-by may not be the most efficient process to stabilize a planet, because of the rarity of suitable close encounters. Destabilization by a fly-by is much more probable. Finally, ejection, outer and inner orbits can create huge asymmetries in the disk during the first ten million years of a system. In particular, an inner orbit enhances the dynamical perturbations created by an outer orbit by speeding up the precession, while the outer orbit if eccentric can enhance the perturbations created by the inner orbit by providing eccentricity to the disk.

Acknowledgements. We thank the anonymous referee for reviewing our work and for insightful comments which improved the manuscript. The project is supported by CNRS, by the Agence Nationale de la Recherche (ANR-14-CE33-0018, GIPSE), the OSUG@2020 labex and the Programme National de Planétologie (PNP, INSU) and Programme National de Physique Stellaire (PNPS, INSU). Most of the computations presented in this paper were performed using the Froggy platform of the CIMENT infrastructure (https://ciment.ujf-grenoble.fr), which is supported by the Rhône-Alpes region (GRANT CPER07_13 CIRA), the OSUG@2020 labex (reference ANR10 LABX56) and the Equip@Meso project (reference ANR-10-EQPX-29-01) of the programme Investissements d'Avenir, supervised by the Agence Nationale pour la Recherche. This work has made use of data from the European Space Agency (ESA) mission *Gaia* (http://www.cosmos.esa.int/gaia), processed by the *Gaia* Data Processing and Analysis Consortium (DPAC, http://www.cosmos.esa.int/web/gaia/dpac/consortium). Funding for the DPAC has been provided by national institutions, in particular the institutions participating in the *Gaia* Multilateral Agreement. This research has made use of the SIMBAD database operated at the CDS (Strasbourg, France). P.A.B.G. acknowledges financial support from the São Paulo State Science Foundation (FAPESP). We thank Cecilia Lazzoni and François Ménard for fruitful discussions.

References

Aller, K. M., Kraus, A. L., Liu, M. C., et al. 2013, ApJ, 773, 63
Andrews, S. M., Rosenfeld, K. A., Kraus, A. L., & Wilner, D. J. 2013, ApJ, 771, 129
Artymowicz, P., & Lubow, S. H. 1994, ApJ, 421, 651
Augereau, J.-C., & Papaloizou, J. 2004, A&A, 414, 1153
Bailer-Jones, C. A. L. 2015, PASP, 127, 994
Bailey, V., Meshkat, T., Reiter, M., et al. 2013, ApJ, 780, L4
Baraffe, I., Chabrier, G., Barman, T. S., Allard, F., & Hauschildt, P. 2003, A&A, 402, 701
Barbier-Brossat, M., & Figon, P. 2000, A&AS, 142, 217
Baruteau, C., Crida, A., Paardekooper, S.-J., et al. 2014, Protostars and Planets VI, 667
Beust, H. 2003, A&A, 400, 1129
Beust, H. 2016, A&A, 590, L2
Beust, H., & Morbidelli, A. 2000, Icarus, 143, 170
Boss, A. P. 1997, Science, 276, 1836
Breslau, A., Steinhausen, M., Vincke, K., & Pfalzner, S. 2014, A&A, 565, A130
Bryan, M. L., Bowler, B. P., Knutson, H. A., et al. 2016, ApJ, 827, 100
Chabrier, G., Johansen, A., Janson, M., & Rafikov, R. 2014, Protostars and Planets VI, 619
Chen, C. H., Mamajek, E. E., Bitner, M. A., et al. 2011, ApJ, 738, 122
Chen, C., Mittal, T., Kuchner, M., et al. 2014, VizieR Online Data Catalog: J/ApJS/211/25
de Bruijne, J. H. J. 1999, MNRAS, 310, 585
Desidera, S., Covino, E., Messina, S., et al. 2015, A&A, 573, A126
De Zeeuw, P., Hoogerwerf, R. V., de Bruijne, J. H., Brown, A., & Blaauw, A. 1999, ApJ, 117, 354
Duflot, M., Figon, P., & Meyssonnier, N. 1995, A&AS, 114, 269
Duriez, L. 1992, Mod. Meth. Cel. Mech., 13, 9
Dürmann, C., & Kley, W. 2015, A&A, 574, A52
Dvorak, R. 1986, A&A, 167, 379
Galli, P. A. B., Teixeira, R., Ducourant, C., Bertout, C., & Benevides-Soares, P. 2012, A&A, 538, A23
Galli, P. A. B., Moraux, E., Bouy, H., et al. 2017, A&A, 598, A48
Girard, T. M., van Altena, W. F., Zacharias, N., et al. 2011, AJ, 142, 15
Goldman, B., Marsat, S., Henning, T., Clemens, C., & Greiner, J. 2010, MNRAS, 405, 1140
Gontcharov, G. A. 2006, Astron. Lett., 32, 759
Haisch Jr, K. E., Lada, E. A., & Lada, C. J. 2001, ApJ, 553, L153
Holmberg, J., Nordström, B., & Andersen, J. 2007, A&A, 475, 519
Jílková, L., & Zwart, S. P. 2015, MNRAS, 451, 804
Jílková, L., Hamers, A. S., Hammer, M., & Zwart, S. P. 2016, MNRAS, 457, 4218
Johnson, D. R. H., & Soderblom, D. R. 1987, AJ, 93, 864
Kalas, P. G., Rajan, A., Wang, J. J., et al. 2015, ApJ, 814, 32
Kennedy, G. M., & Kenyon, S. J. 2008, ApJ, 673, 502
Kikuchi, A., Higuchi, A., & Ida, S. 2014, ApJ, 797, 1
Kordopatis, G., Gilmore, G., Steinmetz, M., et al. 2013, AJ, 146, 134
Lafrenière, D., Jayawardhana, R., Janson, M., et al. 2011, ApJ, 730, 42
Lagrange, A.-M., Langlois, M., Gratton, R., et al. 2016a, A&A, 586, L8
Lagrange, A.-M., Mathias, P., Absil, O., et al. 2016b, A&A, submitted
Laskar, J., & Boué, G. 2010, A&A, 522, A60
Laughlin, G., & Adams, F. C. 1998, ApJ, 508, L171
Lee, E. J., & Chiang, E. 2016, ApJ, 827, 125
Levison, H. F., & Duncan, M. J. 1994, Icarus, 108, 18
Lieman-Sifry, J., Hughes, A. M., Carpenter, J. M., et al. 2016, ApJ, 828, 25
Lin, D., & Papaloizou, J. 1986, ApJ, 309, 846
Lindegren, L., Lammers, U., Bastian, U., et al. 2016, A&A, 595, A4
Madsen, S., Dravins, D., & Lindegren, L. 2002, A&A, 381, 446
Malmberg, D., Davies, M. B., & Heggie, D. C. 2011, MNRAS, 411, 859
Mermilliod, J.-C., Mayor, M., & Udry, S. 2009, A&A, 498, 949
Morbidelli, A. 2002, Modern Celestial Mechanics, Advances in Astronomy and Astrophysics (CRC)
Mordasini, C., Alibert, Y., Benz, W., & Naef, D. 2009, A&A, 501, 1161
Mutter, M. M., Pierens, A., & Nelson, R. P. 2016, MNRAS, in press
Nelson, R. P. 2003, MNRAS, 345, 233
Nelson, R. P., & Papaloizou, J. C. 2002, MNRAS, 333, L26
Nesvold, E. R., Naoz, S., & Fitzgerald, M. P. 2017, ApJ, 837, L6
Parker, R. J., & Quanz, S. P. 2012, MNRAS, 419, 2448
Pecaut, M. J., & Mamajek, E. E. 2016, MNRAS, 461, 794
Pecaut, M. J., Mamajek, E. E., & Bubar, E. J. 2012, ApJ, 746, 154
Pinte, C., Dent, W. R., Menard, F., et al. 2015, ApJ, 816, 25
Pollack, J. B., Hubickyj, O., Bodenheimer, P., et al. 1996, Icarus, 124, 62
Preibisch, T., & Mamajek, E. 2008, in Handbook of Star Forming Regions, Vol. II, ed. B. Reipurth, 235
Reid, I. N., Gizis, J. E., & Hawley, S. L. 2002, AJ, 124, 2721
Ribas, Á., Bouy, H., & Merín, B. 2015, A&A, 576, A52
Robin, A. C., Reylé, C., Derrière, S., & Picaud, S. 2003, A&A, 409, 523
Roeser, S., Demleitner, M., & Schilbach, E. 2010, AJ, 139, 2440
Snellgrove, M., Papaloizou, J., & Nelson, R. 2001, A&A, 374, 1092
Song, I., Zuckerman, B., & Bessell, M. S. 2012, AJ, 144, 8
Torres, C. A. O., Quast, G. R., da Silva, L., et al. 2006, A&A, 460, 695
Van Leeuwen, F. 2007, A&A, 474, 653
Walsh, C., Juhász, A., Meeus, G., et al. 2016, ApJ, 831, 200
Wenger, M., Ochsenbein, F., Egret, D., et al. 2000, A&AS, 143, 9
Wilson, R. E. 1953, General catalogue of stellar radial velocities (Carnegie Institute Washington D.C. Publication)
Wu, Y.-L., Close, L. M., Bailey, V. P., et al. 2016, ApJ, 823, 24
Wyatt, M. C. 2005, A&A, 440, 937
Yoshikawa, M. 1989, A&A, 213, 436
Zacharias, N., Finch, C. T., Girard, T. M., et al. 2012, VizieR Online Data Catalog: I/322

Appendix A: Ad hoc force to account for type II migration

We searched for a coplanar migration force $\boldsymbol{F}_{\rm mig}$ that induces a constant variation of the planet average semi-major axis, but no change in the planet average eccentricity, nor in the periastron longitude. Let $\boldsymbol{F}_{\rm mig} = F_r \boldsymbol{e_r} + F_\theta \boldsymbol{e_\theta}$ be the description of the force in the local referential attached to the planet movement. Gauss equations are (Duriez 1992):

$$C\frac{\mathrm{d}a}{\mathrm{d}t} = 2a^2(F_\theta + e\boldsymbol{F}_{\rm mig}\cdot\boldsymbol{e_y}); \tag{A.1}$$

$$C\frac{\mathrm{d}e}{\mathrm{d}t} = r(e+\cos\theta)F_\theta + a(1-e^2)\boldsymbol{F}_{\rm mig}\cdot\boldsymbol{e_y}; \tag{A.2}$$

$$Ce\frac{\mathrm{d}\omega}{\mathrm{d}t} = r\sin\theta F_\theta - a(1-e^2)\boldsymbol{F}_{\rm mig}\cdot\boldsymbol{e_x}, \tag{A.3}$$

where $\boldsymbol{e_x}$ and $\boldsymbol{e_y}$ are the vectors in the fixed frame and $C = \sqrt{GMa(1-e^2)}$. We want to assume a simple form for F_r and F_θ that could then be easily averaged over time. The simplest position-dependent force would be $F_r = A(1 + c\cos u)$ et $F_\theta = B(1 + d\cos u)$, where A, B, c and d are unknown functions of (a, e), constant at first order over a one-period integration. Our conditions are then summarized to:

$$\frac{\mathrm{d}\bar{a}}{\mathrm{d}t} = v_{\rm mig} \iff \frac{2B\sqrt{1-e^2}}{n} = v_{\rm mig}; \tag{A.4}$$

$$\frac{\mathrm{d}\bar{e}}{\mathrm{d}t} = 0 \iff B(2e^2d - 3e^3 + 3e - 2d) = 0; \tag{A.5}$$

$$\frac{\mathrm{d}\bar{\omega}}{\mathrm{d}t} = 0 \iff A\sqrt{1-e^2}(c-2e) = 0, \tag{A.6}$$

where $n = \sqrt{GM/a^3}$ is the mean motion. Taking $A = 0$, $B = nv_{\rm mig}/(2\sqrt{1-e^2})$, any c and $d = 3e/2$, we finally obtain Eq. (4).

Appendix B: Location of mean-motion resonances

Equation (1) gives the semi-major axis of a resonant circumbinary planet when its orbit is purely Keplerian. When we take into account the perturbation caused by the binary on the planet orbit, the commensurability of periods that characterizes MMRs can not be easily associated with a semi-major axis, mainly due to orbital precession.

The movement of a circumbinary planet (binary of mass parameter μ) is controlled by the Hamiltonian

$$H = -\frac{Gm_{\rm B}}{2a} - Gm_{\rm B}\left(\frac{1-\mu}{|\boldsymbol{r}+\mu\boldsymbol{r}_{\rm B}|} + \frac{\mu}{|\boldsymbol{r}-(1-\mu)\boldsymbol{r}_{\rm B}|} - \frac{1}{|\boldsymbol{r}|}\right) \tag{B.1}$$

$$= H_{\rm Kep} + H_{\rm bin}, \tag{B.2}$$

where $H_{\rm Kep} = -Gm_{\rm B}/(2a)$ is the Keplerian Hamiltonian, and where $H_{\rm bin}$ is given by Eq. (8). If the planet orbits at sufficiently large distance from the binary, $H_{\rm bin}$ is a perturbative term that triggers orbital evolution of the planet. This can be investigated analytically via a truncated expansion of $H_{\rm bin}$ in ascending powers of $a_{\rm B}/a$, and an averaging over both orbital motions. To lowest order, this yields

$$H_{\rm bin} \simeq -\frac{\mu(1-\mu)}{4}\frac{Gm_{\rm B}a_{\rm B}^2}{a^3}\frac{3e_{\rm B}^2+2}{(1-e^2)^{3/2}}. \tag{B.3}$$

Strictly speaking, this approximation is not valid at the exact location of MMRs, as the motions of both orbits are not independent anymore, but it gives a good insight of the perturbation of the planet orbit when it is near the MMRs. Moreover, numerical verifications show that this order two approximation is still relevant for $a \geq 3a_{\rm B}$, and could thus be made to study the 1:6 resonance. Lagrange equations (Duriez 1992) then give

$$\frac{\mathrm{d}\omega}{\mathrm{d}t} = \frac{3\mu(1-\mu)}{4}n\left(\frac{a_{\rm B}}{a}\right)^2\frac{\frac{3}{2}e_{\rm B}^2+1}{(1-e^2)^2}; \tag{B.4}$$

$$\frac{\mathrm{d}\lambda}{\mathrm{d}t} = n + \frac{3\mu(1-\mu)}{2}n\left(\frac{a_{\rm B}}{a}\right)^2\frac{\frac{3}{2}e_{\rm B}^2+1}{(1-e^2)^{\frac{3}{2}}} + \left(1-\sqrt{1-e^2}\right)\frac{\mathrm{d}\omega}{\mathrm{d}t}, \tag{B.5}$$

where n is the Keplerian mean-motion. Thus, if $T_0(a)$ is the Keplerian period $2\pi/n$, then the period of the mean longitude T_λ is

$$T_\lambda = \frac{T_0(a)}{1 + \frac{3\mu(1-\mu)}{4}\left(\frac{a_{\rm B}}{a}\right)^2\frac{\frac{3}{2}e_{\rm B}^2+1}{(1-e^2)^{\frac{3}{2}}}\left(1+\frac{1}{\sqrt{1-e^2}}\right)}. \tag{B.6}$$

The MMR configuration is characterized by the steadiness of $\sigma = (p+q)/q\lambda_{\rm B} - p/q\lambda - \omega$. However, in our study, the planet orbit remains almost circular until ejection, so that the planet line of apsides is not a good reference. Taking the binary line of apsides (constant in time) as the new reference, the resonance characterization writes $T_\lambda = p/(p+q)T_{\rm B}$. All in all, the resonant location $a_{\rm res}$ satisfies

$$T_\lambda(a_{\rm res}) = \frac{p}{p+q}T_{\rm B}. \tag{B.7}$$

Appendix C: Spiral density wave

As mentioned in the text, the motion of a particle moving in a circumbinary disk is controlled by the Hamiltonian $H_{\rm Kep} + H_{\rm bin} + H_{\rm pla}$, where $H_{\rm bin}$ and $H_{\rm pla}$ are perturbative terms given by Eqs. (8) and (9). Following the approach of Wyatt (2005), these terms are then expanded in ascending powers of $a_{\rm B}/a$ and $a/a_{\rm p}$, truncated to some finite order and averaged over the orbital motion of both orbits (see Laskar & Boué 2010). To second order and third order, the result is

$$U_2 = -\frac{\mu(1-\mu)}{4}\frac{Gm_{\rm B}a_{\rm B}^2}{a^3}\frac{\frac{3}{2}e_{\rm B}^2+1}{(1-e^2)^{\frac{3}{2}}} - \frac{1}{4}\frac{Gm_{\rm p}a^2}{a_{\rm p}^3}\frac{\frac{3}{2}e^2+1}{(1-e_{\rm p}^2)^{\frac{3}{2}}}; \tag{C.1}$$

$$U_3 = \frac{15\mu(1-\mu)(1-2\mu)}{16}\frac{Gm_{\rm B}a_{\rm B}^3}{a^4}\frac{e\cos(\omega-\omega_{\rm B})e_{\rm B}(\frac{3}{4}e_{\rm B}^2+1)}{(1-e^2)^{\frac{5}{2}}} + \frac{15}{16}\frac{Gm_{\rm p}a^3}{a_{\rm p}^4}\frac{e_{\rm p}\cos(\omega-\omega_{\rm p})e(\frac{3}{4}e^2+1)}{(1-e_{\rm p}^2)^{\frac{5}{2}}}. \tag{C.2}$$

In HD 106906 configuration, the binary mass parameter is very close to 1/2, and the semi-major axis of the binary is very small compared to the distance between the binary and the relevant part of the disk, between 50 and 100 au. Thus, the binary part of U_3 can be neglected. Using Lagrange equations, we derive the

equations of evolution:

$$\frac{\mathrm{d}\omega}{\mathrm{d}t} = \frac{3}{16}n\left(\frac{a_\mathrm{B}}{a}\right)^2 \frac{\frac{3}{2}e_\mathrm{B}^2+1}{(1-e^2)^2} + \frac{3}{4}\frac{m_\mathrm{p}}{m_\mathrm{B}}n\left(\frac{a}{a_\mathrm{p}}\right)^3 \frac{\sqrt{1-e^2}}{(1-e_\mathrm{p}^2)^{\frac{3}{2}}} - \frac{15}{16}\frac{m_\mathrm{p}}{m_\mathrm{B}}ne_\mathrm{p}\left(\frac{a}{a_\mathrm{p}}\right)^4 \frac{\sqrt{1-e^2}\cos(\omega-\omega_\mathrm{p})(1+\frac{9}{4}e^2)}{e(1-e_\mathrm{p}^2)^{\frac{5}{2}}}; \quad \text{(C.3)}$$

$$\frac{\mathrm{d}e}{\mathrm{d}t} = -\frac{15}{16}\frac{m_\mathrm{p}}{m_\mathrm{B}}ne_\mathrm{p}\left(\frac{a}{a_\mathrm{p}}\right)^4 \frac{\sin(\omega-\omega_\mathrm{p})}{(1-e_\mathrm{p}^2)^{\frac{5}{2}}}; \quad \text{(C.4)}$$

$$\frac{\mathrm{d}M}{\mathrm{d}t} = \frac{3}{16}n\left(\frac{a_\mathrm{B}}{a}\right)^2 \frac{\frac{3}{2}e_\mathrm{B}^2+1}{(1-e^2)^2} - \frac{7}{4}\frac{m_\mathrm{p}}{m_\mathrm{B}}n\left(\frac{a}{a_\mathrm{p}}\right)^3 \frac{\left(1+\frac{3}{7}e^2\right)}{(1-e_\mathrm{p}^2)^{\frac{3}{2}}} + \frac{15}{16}\frac{m_\mathrm{p}}{m_\mathrm{B}}ne_\mathrm{p}\left(\frac{a}{a_\mathrm{p}}\right)^4 \frac{\cos(\omega-\omega_\mathrm{p})(1+\frac{29}{4}e^2+\frac{9}{4}e^4)}{e(1-e_\mathrm{p}^2)^{\frac{5}{2}}}, \quad \text{(C.5)}$$

where M is the mean anomaly, $n = \sqrt{Gm_\mathrm{B}/a^3}$ is the mean motion and a is a constant of motion in the secular regime. As we want to study the evolution of an initially almost circular particle orbit, we note that we cannot neglect the planetary part of U_3, because of the $1/e$ factor in $\mathrm{d}\omega/\mathrm{d}t$. The two first equation are coupled, Eq. (C.5) will be solved in a second phase after injection of their solution. These equations are nonetheless irregular for small eccentricity regime. Thus, we will use the complex variable $z = e\exp(\mathrm{i}\omega)$ to render them regular (Wyatt 2005). Moreover, from Eq. (C.4), we can deduce that the eccentricity is maximum when $\omega = \omega_\mathrm{p}$. This information, combined with the initial value of the Hamiltonian, allows us to compute the maximal eccentricity as a function of a. These maximums prove themselves to be less than 0.5 in any case, so that we can linearize the system in z for an easier solving. It yields

$$\frac{\mathrm{d}z}{\mathrm{d}t} = i\left((A_{\mathrm{B},1}+A_{\mathrm{p},1})z - A_{\mathrm{p},2}\right),\ z = e\exp(\mathrm{i}\omega), \quad \text{(C.6)}$$

where

$$A_{\mathrm{B},1} = \frac{3}{16}n\left(\frac{a_\mathrm{B}}{a}\right)^2\left(\frac{3}{2}e_\mathrm{B}^2+1\right); \quad \text{(C.7)}$$

$$A_{\mathrm{p},1} = \frac{3}{4}\frac{m_\mathrm{p}}{m_\mathrm{B}}n\left(\frac{a}{a_\mathrm{p}}\right)^3\left(1-e_\mathrm{p}^2\right)^{-\frac{3}{2}}; \quad \text{(C.8)}$$

$$A_{\mathrm{p},2} = \frac{15}{16}\frac{m_\mathrm{p}}{m_\mathrm{B}}ne_\mathrm{p}\left(\frac{a}{a_\mathrm{p}}\right)^4\left(1-e_\mathrm{p}^2\right)^{-\frac{5}{2}}. \quad \text{(C.9)}$$

We now solve the system and get the eccentricity, precession and mean anomaly as a function of time. For null initial eccentricity, it is written

$$e(t) = \frac{2A_{\mathrm{p},2}}{A_{\mathrm{B},1}+A_{\mathrm{p},1}}\left|\sin\left(\frac{(A_{\mathrm{B},1}+A_{\mathrm{p},1})t}{2}\right)\right|; \quad \text{(C.10)}$$

$$\omega(t) = \frac{A_{\mathrm{B},1}+A_{\mathrm{p},1}}{2}t \pmod{\pi} - \frac{\pi}{2} + \omega_\mathrm{p}; \quad \text{(C.11)}$$

$$M(t) = (n + A_{\mathrm{B},1} - \frac{7}{3}A_{\mathrm{p},1} + \frac{1}{8}A_{\mathrm{p},2})t + M(0). \quad \text{(C.12)}$$

If we represent the motion of z on the complex plane, we get exactly the circle depicted in Fig. 2 of Wyatt (2005). These formula were used to generate Fig. 9.

Appendix D: Density of stars around HD 106906

The first step to investigate the density of stars around the HD 106906 system is to build a complete list of known members in the LCC subgroup of the Sco-Cen association. Our list of LCC members is based on previous surveys of this region (De Zeeuw et al. 1999; Preibisch & Mamajek 2008; Song et al. 2012; Pecaut & Mamajek 2016) and consists of 369 stars. In the following, we estimate the current density of stars around the planetary system and its evolution in time. Thus, our methodology requires prior knowledge of the distances, proper motions and radial velocities for the individual stars in our sample.

The *Tycho-Gaia* Astrometric Solution (TGAS, Lindegren et al. 2016) from the *Gaia* data release 1 provides trigonometric parallaxes and proper motions for 203 stars in our sample. To access more proper motion data, we also searched for this information in the PPMXL (Roeser et al. 2010), UCAC4 (Zacharias et al. 2012) and SPM4 (Girard et al. 2011) catalogs. Doing so, we find proper motions for 368 stars of the sample. We use the TGAS proper motions for the 203 stars and take the weighted mean of the multiple measurements given by the other catalogs (PPMXL, UCAC4 and SPM4) for the remaining 165 stars. Then, we searched the SIMBAD/CDS databases (Wenger et al. 2000) for radial velocity information using the data mining tools available on the site. The radial velocities that we use in this work come from Wilson (1953), Duflot et al. (1995), Barbier-Brossat & Figon (2000), Torres et al. (2006), Gontcharov (2006), Holmberg et al. (2007), Mermilliod et al. (2009), Chen et al. (2011), Song et al. (2012), Kordopatis et al. (2013) and Desidera et al. (2015). We found radial velocity for 184 stars of our sample.

We apply the methodology developed by Bailer-Jones (2015) to convert parallaxes into distances (see Sect. 7 of his paper). The systematic errors of about 0.3 mas in the TGAS parallaxes reported by Lindegren et al. (2016) were added quadratically to the parallax uncertainties. The three-dimensional position of the stars are calculated from the individual distances in a XYZ grid where X points to the Galactic center, Y points in the direction of Galactic rotation, and Z points to the Galactic north pole. The reference system has its origin at the Sun. Then, we use the procedure described in Johnson & Soderblom (1987) to compute the UVW components of the spatial velocity for each star that are given in the same reference system. We perform a 3σ clipping in the distribution of proper motions, parallaxes, radial velocities and spatial velocities to remove obvious outliers. This procedure reduces the dataset to a total of 312 stars, but only 141 stars in this sample exhibit published radial velocities and 102 stars have complete data (proper motions, radial velocities and parallaxes). Based on this subset of 102 stars we calculate a revised mean spatial velocity of the LCC association of $(U, V, W) = (-8.5, -21.1, -6.3) \pm (0.2, 0.2, 0.2)$ km s^{-1} (not corrected for the solar motion).

We note that 39 stars in the sample of 141 stars with known radial velocities do not have published parallaxes in the TGAS catalog. Individual parallaxes (and distances) can be inferred for these stars from the moving-cluster method under the assumption that they are co-moving. This method uses proper motions, radial velocities and the convergent point position of the moving group to derive individual parallaxes for group members (Galli et al. 2012). We emphasize that the so-derived kinematic parallaxes are meaningful and provide valuable information in this work to increase the number of stars with measured parallax in our sample. We adopt the space motion listed above and the formalism described in Sect. 2 of Galli et al. (2017) to

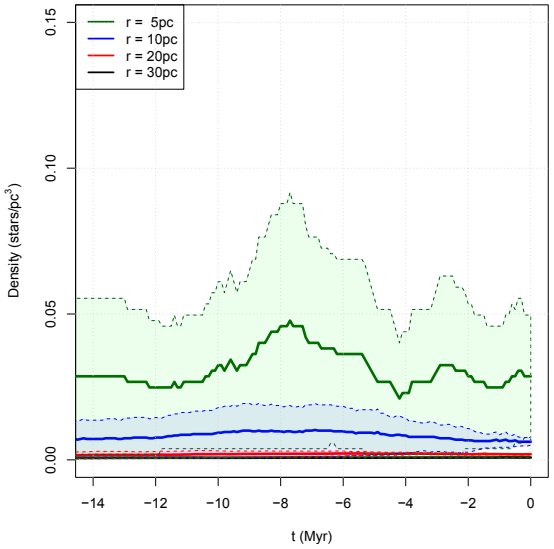

Fig. D.1. Evolution of the density of stars for different radii around the HD 106906 planetary system. The colored regions indicate the upper and lower limits (at the 1σ level) for the density of stars at a given radius.

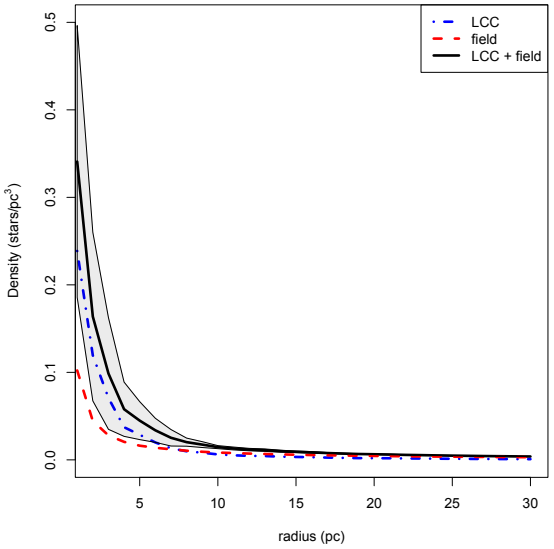

Fig. D.2. Current density of stars in the vicinity of the HD 106906 system inferred from LCC cluster members and field stars. The colored region indicates the upper/lower limits (at the 1σ level) for the final density of stars (cluster + field) at different radii around the target.

estimate the convergent point position and the kinematic parallaxes for each group member. Using a velocity dispersion of $\sigma_v = 1.5$ km s^{-1} and distance estimate of 120 pc for the LCC association (see e.g., de Bruijne 1999) we find a convergent point solution located at $(\alpha_{\rm cp}, \delta_{\rm cp}) = (104.8°, -37.2°) \pm (1.0°, 0.8°)$ with chi-squared statistics $\chi^2_{\rm red} = 0.92$ and correlation coefficient of $\rho = -0.98$. To gain confidence in the so-derived kinematic parallaxes we compare our results with the trigonometric parallaxes from the TGAS catalog for the stars in common. We find a mean difference of 0.1 mas and rms of 0.6 mas, that are significantly smaller than the typical error on the kinematic parallaxes (~0.8 mas) derived from the moving-cluster method in this analysis. This confirms the good agreement between the two datasets. Thus, the final sample with complete information (proper motion, radial velocity and parallax) that we use in this work to estimate the early density of stars around HD 106906 consists of 141 stars.

In a subsequent analysis, we consider the present day location of the 141 stars and use the UVW spatial velocity for each star to calculate their XYZ positions backward in time. We compute the stellar positions as a function of time in steps of 0.1 Myr from $t = 0$ (current position) to $t = -14.0$ Myr. The latter value is chosen to be consistent with an upper limit for the age estimate of the HD 106906 system as derived by Pecaut et al. (2012) from different evolutionary models. Then, we count the number of stars in the vicinity of HD 106906 for different radii ($r = 5, 10, 15, ..., 30$ pc) and determine the density of stars around the target. Figure D.1 illustrates the results of this investigation. Our analysis indicates that the early density of stars around HD 106906 (at $t = -7.7$ Myr) was higher than the current value by a factor of about 1.7 for $r = 5$ pc. At this stage it is important to mention that our result for density of stars is restricted to known members of the LCC association with complete data in our sample for which we can calculate spatial velocities and compute their positions back in time. As soon as new data (parallaxes and radial velocities) from the upcoming surveys (e.g., *Gaia*) become available and other group members are identified, a more refined analysis of this scenario will be made possible.

One alternative approach to better constrain the density of stars around HD 106906 consists of investigating the contribution of field stars (not related to the LCC association) in our solution. In this context, we use the model of stellar population synthesis from Robin et al. (2003) to simulate a catalog of pseudo-stars and their intrinsic properties (e.g., distances, spectral types, ages, magnitudes, etc.) in the direction of the HD 106906 system. We run the model with a distance range from 0 to 300 pc and a solid angle of 20 deg^2 centered around the target. These values are chosen to include known members of the LCC association that is clearly spread in angular extent and exhibits significant depth effects along the line of sight. We do not constrain our simulations in magnitudes and spectral types to get a more complete picture of the stellar population in this region. We use a distance step of 0.5 pc in our simulations that is the minimum value that can be used in the model. The synthetic stars are all supposed to be at the same coordinates. So, we run a number of 1000 simulations to generate random coordinates for the simulated stars and use them (together with the distances provided by the model) to calculate the stellar three-dimensional positions in the XYZ grid. Figure D.2 shows the density of stars around HD 106906 for different radii obtained from our sample of LCC stars, the pseudo-stars from our simulations and a combined result that includes both (cluster + field). Although this analysis cannot be extrapolated backward in time (as in Fig. D.1), it yields a more refined value for the current ($t = 0$) density of stars. However, we emphasize that the results obtained for small radii around the target (i.e., $r \leq 5$ pc) are calculated with a small number of stars (typically, less than ten stars) and they should be regarded with caution. Thus, we conclude that the present-day density of stars in the vicinity of the HD 106906 system for $r > 5$ pc is $\leq$0.07 stars/pc^3 (within the 1σ error bars). We infer from the results presented in Fig. D.1 an upper limit of ~0.11 stars/pc^3 for the density of stars around HD 106906, a result that will need further confirmation as soon as more data becomes available.

3.2 Refining the scenario

Two years after the Rodet et al. (2017) study, the release of Gaia data allowed for a deeper study of the system's neighborhood. Taking into account Gaia proper motions and additional radial velocity measurements, De Rosa & Kalas (2019) evidenced two stellar candidates, HIP 59716 and HIP 59721, possibly bound, that might have had a close fly-by with HD 106906 some million years ago. This fly-by could have been the crucial ingredient to prevent the planet from being permanently ejected from the system after a scattering by the binary host star, in the scenario described in Rodet et al. (2017) above.

We then collaborated to write another paper studying the impact of the fly-by, given the information on the perturbers (Rodet et al. 2019). In this paper, I first present the code Odea, that handled hierarchy changes but not yet close encounters. I ran a set of 10,000 4-body simulations, computed their effect on the planet, and compared it to theoretical predictions. The paper sets an upper limit to the distance at closest approach, in order to have a dynamically significant fly-by (significant decrease of the planet eccentricity, raise of the planet elevation above the disk plane, disk warp): 0.01-0.05 pc depending on the planet initial apoastron. It confirms that such a close fly-by is possible from both perturbers, though the precision on the relative parallax and radial velocity does not conclude the study. The entire study, submitted to A&A, is detailed below.

Astronomy & Astrophysics manuscript no. Article
April 18, 2019
©ESO 2019

ODEA: Orbital Dynamics in a complex Evolving Architecture

Application to the planetary system HD 106906

L. Rodet[1], H. Beust[1], M. Bonnefoy[1], R. J. De Rosa[2], P. Kalas[3], A.-M. Lagrange[1]

[1] Univ. Grenoble Alpes, CNRS, IPAG, F-38000 Grenoble, France
e-mail: laetitia.rodet@univ-grenoble-alpes.fr
[2] Kavli Institute for Particle Astrophysics and Cosmology, Stanford University, Stanford, CA 94305
[3] Department of Astronomy, University of California, Berkeley, CA 94720

Received –; accepted –

ABSTRACT

Context. Symplectic integrators are widely used in orbital dynamics. However, they have been developed for Solar system-type architectures, and can not handle evolving hierarchy, in particular in systems with two or more stellar components. Such configuration may have occurred in the history of HD 106906, a tight pair of F-type stars surrounded by a debris disk and a planetary-mass companion on a wide orbit.
Aims. We present the new algorithm Odea, based on the symplectic algorithm Swift Hjs, that can model any system (binary,...) with unstable architecture. We study the peculiar system HD 106906 as a testcase for the code.
Methods. We define and compute a criterion based on acceleration ratios to indicate when the initial hierarchy is not relevant anymore. A new hierarchy is then computed. The code is applied to study the two fly-bys that occurred on system HD 106906, recently evidenced by De Rosa & Kalas (2019), to determine if they could account for the wide orbit of the planet. Thousands of simulations have been performed to account for the uncertainty on the perturbers coordinates and velocities.
Results. The algorithm is able to handle any change of hierarchy, temporary or not. We used it to fully model HD 106906 encounters. The simulations confirm that the fly-bys could have stabilized the planet orbit, and show that it can account for the planet probable misalignment with respect to the disk plane as well as the disk morphology. However, that requires a small distance at closest approach ($\lesssim 0.05$ pc), and this configuration is not guaranteed.
Conclusions. Odea is the natural choice for the study of non-Solar type architecture. It can now adapt to an evolving hierarchy, and is thus suitable to study capture of planets and dust. Further observations of the perturbers, in particular their radial velocity, are required to conclude on the effects of the fly-by on system HD 106906.

Key words. methods: numerical – celestial mechanics – planets and satellites: dynamical evolution and stability – planets and satellites: individual: HD 106906 – planet-star interactions - stars: kinematics and dynamics

1. Introduction

1.1. Symplectic algorithms

In the context of the rapid increase of exoplanet discoveries, the need for efficient N-body simulations has become strong to model the evolution of complex systems and the interaction between planets, planets and debris disk, or within debris disks. Symplectic integrators are widely used for dynamical simulations of planetary systems, as they present two major advantages with respect to other N-body integrators: First, they exhibit no long-term accumulation of energy error, which is essential to ensure orbital stability through the integration. On the other hand, they provide a gain of at least one order of magnitude in computation speed, for equivalent accuracy, because they allow one to adopt a much larger time-step than other integrators for the same result. In 1991, Wisdom and Holman devise the first symplectic map specifically designed for N-body problems with a central dominant mass (Wisdom & Holman 1991). Since then, numerous codes implemented this structure that are still widely used today (e.g., Swift, Levison & Duncan 1994, Mercury Chambers 1999).

Yet, sympleptic integrators can model the interactions between multiple stars, moon, or simply planets whose mass are non negligible with respect to the central mass as well. They are versatile tools well suited to characterize the great diversity of extrasolar system architectures, well beyond the framework of our Solar System. Efforts were made to extend the scheme to binary stars in two modified versions of Mercury (Chambers et al. 2002), but it could not be generalized to multiple systems with other hierarchies. In this context, Beust (2003) designed a symplectic scheme valid for any type of hierarchical architecture, and implemented it with Swift Hjs. This generalized the theoretical frame of Wisdom and Holman to any hierarchical system.

However, in Swift Hjs, the hierarchical structure of the system is given at the beginning of the run and must be preserved along the integration. This is a severe limitation as it prevents the efficient modeling of non stable hierarchies with e.g. orbital captures (planets, dust), whereas such situations may be numerous among young systems. With Swift Hjs, handling accurately such configurations is only possible adopting a very small time-step, which is

of course not optimal. This motivated us to build a new version of SWIFT HJS, ODEA, that tackles this issue.

In the following, we describe the new code in detail, and present a full application to the complex system of HD 106906. Before that, we present this system and our motivations for modeling it and using it as a benchmark for our new code.

1.2. HD 106906

The system HD 106906 (HIP 59960) is located at a distance of 103.3 ± 0.5 pc (Brown et al. 2018) and belongs to the Lower Centaurux Crux (LCC) group, which is a subgroup of the Scorpius-Centaurus (Sco-Cen) OB association (De Zeeuw et al. 1999). The LCC group has a mean age of 15 ± 3 Myr, with an age spread of 6 Myr (Pecaut & Mamajek 2016). HD 106906 is a 2.58 ± 0.04 $M_\odot$ spectroscopic binary star, on an eccentric (0.66) and tight (0.6 au) orbit (Lagrange et al. 2019). Moreover, high contrast imaging has revealed an asymmetric debris disk (Kalas et al. 2015; Lagrange et al. 2016) and a giant planet on a wide orbit (projected separation from the binary: 735 ± 5 au, Bailey et al. 2013). At such a separation, the planet relative motion can not be detected with present imaging instruments on a reasonable time basis. The orbital inclination with respect to the plane of the disk is probably significant (20°), but a coplanar configuration cannot be excluded. The planet mass has been estimated at 11 ± 9 M_J mass from hot-start models by Daemgen et al. (2017).

Two major scenarios compete for the formation of giant planets (e.g., Baruteau et al. 2016). In the core accretion scenario, planets begin their formation with the growth of dust grains and the formation of planetesimals, that will slowly accrete each other to form terrestrial planets or planetary cores. On the other hand, the gravitational instability scenario is a faster process that is able to form giant planets at large separation from an instability in the protoplanetary disk. In both cases, planet formation takes place in the primordial gaseous disk. Forming a giant planet at 700 au or more from any central star appears very unlikely in any of those scenarios, first due to the lack of circumstellar gas at that distance, and second because the corresponding formation timescale would exceed the lifetime of the gaseous disk. This led Rodet et al. (2017) to propose a dynamical scenario to account for the planet's current separation. The scenario involves a traditional planetary formation within the gaseous disk, an inward migration and a subsequent scattering by the binary. However, for the planet to remain bound, an external perturbation such as a fly-by is necessary in order to reduce its eccentricity and stabilize its orbit in a bound configuration.

Recently, De Rosa & Kalas (2019) investigated the stellar neighborhood of system HD 106906 in Gaia DR2 (Brown et al. 2018), and discovered two stars that have recently come within 1 pc of the central binary HD 106906 AB. Given the uncertainty on the perturbers distances and radial velocities, De Rosa & Kalas concluded that there was a possibility that the fly-by was dynamically significant for the planet evolution history. This motivates us to reinvestigate the Rodet et al. (2017) scenario, using ODEA, to check this possibility.

2. Algorithm

2.1. Structure of the code: SWIFT HJS

Let us consider the gravitational N-body problem, with masses $(m_i)_{i=1,..,N}$, positions $(\boldsymbol{r}_i)_{i=1,..,N}$ and impulsions $(\boldsymbol{p}_i)_{i=1,..,N}$. The Hamiltonian is

$$H = \sum_{i=1}^{N} \frac{{\boldsymbol{p_i}}^2}{2m_i} - \sum_{1 \leq i < j \leq N} \frac{G m_i m_j}{r_{ij}} \quad , \tag{1}$$

where G is the constant of gravitation and $r_{ij} = ||\boldsymbol{r}_j - \boldsymbol{r}_i||$ is the distance between bodies i and j.

In the current version of SWIFT HJS, as in the other similar codes, the integrator do not solve H exactly, but a surrogate Hamiltonian $\tilde{H}$. The latter is chosen to be close to the real one, and exactly solvable. In that case, the algorithm is symplectic: it exactly preserves the areas in phase space and exhibit no long-term drift of the energy.

In order to design a proper $\tilde{H}$ in orbital mechanics, the key idea is to split the Hamiltonian into two integrable parts:

$$H = H_\mathrm{A} + H_\mathrm{B} \quad . \tag{2}$$

Several splitting have been suggested (e.g., Wisdom & Holman 1991; Saha & Tremaine 1994; Chambers 1999), most of them consisting on a Keplerian part and a perturbation part. Both parts are then integrable within computer round-off errors. $\tilde{H}$ corresponds to the successive integration of these parts separately. For a second order symplectic integrator, a so-called leap-frog method can be used. It consists in integrating H_B for $\Delta t/2$ (kick), then H_A for Δt (drift), then again H_B for $\Delta t/2$ (kick), where Δt is the time step.

SWIFT HJS is based on the Hierarchical Jacobi Symplectic method introduced by Beust (2003), where the description is based on orbits instead of on bodies. An orbit consists in a collection of two non-empty sets of bodies, the set of centers and the set of satellites, that have empty intersection. In all problems in orbital mechanics, a hierarchy can then be defined as a collection of orbits comprising all bodies satisfying the following rule: for all couples of orbit k and $l \neq k$, one of the three subsequent propositions apply

- orbits k and l have no common bodies (orbits k and l are *foreign*);
- orbit k is comprised in the centers or satellites of orbit l (orbit k is *inner* to orbit l);
- orbit l is comprised in the centers or satellites of orbit k (orbit k is *outer* to orbit l).

A so-defined hierarchy is made of exactly $N-1$ orbits. In SWIFT HJS, the orbits are numbered from 2 to N. Finally, we define μ_k and η_k as the total mass of the satellites and centers respectively in orbit k. The total dynamical mass in orbit k is then $M_k = \mu_k + \eta_k$ and the reduced mass $m'_k = \mu_k \eta_k / M_k$.

In this formalism, a new set of N coordinates $(\boldsymbol{r'}_k, \boldsymbol{p'}_k)_{i=1,..,N}$ are designed with a Jacobi-like approach: $\boldsymbol{r'}_k$ is the relative position of the center of mass of orbit k's satellites with respect to that of its centers, and $\boldsymbol{p'}_k$ is the relative conjugate momentum. The first coordinates

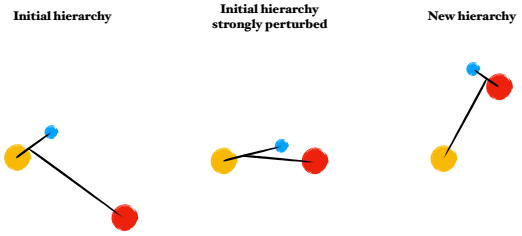

Fig. 1. Example of hierarchy change in the case of a capture. At first the red body orbits the yellow–blue pair. After a strong interaction, it captures the small blue body.

$\boldsymbol{r'}_1$ and $\boldsymbol{p'}_1$ are the position and impulsion of the center of mass. These positions and conjugate momenta derive from a canonical transformation that let the Hamiltonian invariant. They can be expressed with the bodies coordinates as

$$\boldsymbol{r'}_k = \sum_{i,\text{ satellites of k}} \frac{m_i \boldsymbol{r}_i}{\mu_k} - \sum_{i,\text{ centers of k}} \frac{m_i \boldsymbol{r}_i}{\eta_k} \tag{3}$$

$$\boldsymbol{p'}_k = m'_k \left(\sum_{i,\text{ satellites of k}} \frac{\boldsymbol{p}_i}{\mu_k} - \sum_{i,\text{ centers of k}} \frac{\boldsymbol{p}_i}{\eta_k} \right) \tag{4}$$

The Hamiltonian can then be split as follows

$$H_{\mathrm{A}} = \sum_{k=2}^{N} \frac{{p'_k}^2}{2m'_k} - \frac{G\mu_k\eta_k}{r'_k} \quad ; \tag{5}$$

$$H_{\mathrm{B}} = \sum_{k=2}^{N} \frac{G\mu_k\eta_k}{r'_k} - \sum_{1\leq i<j<\leq N} \frac{Gm_im_j}{r_{ij}} \quad . \tag{6}$$

When the hierarchy is sufficiently clear (that is if the orbits are almost Keplerian), $H_{\mathrm{B}} \ll H_{\mathrm{A}}$. As H_{A} is a Keplerian Hamiltonian describing $N-1$ independent orbits, the drift consists of evolving each Keplerian orbits. On the other hand, as H_{B} depends exclusively on the positions, the kick consists of a linear raise of the velocity, with an acceleration $\boldsymbol{a}^{\boldsymbol{B}}$.

2.2. Building a new hierarchy

The above scheme is well adapted to lightly perturbed Keplerian orbits in a fixed hierarchy, but becomes strongly unsuitable if the initial hierarchy evolves, whether temporarily or definitively (see example Fig. 1).

Thus, when the hierarchy is not relevant anymore (that is the splitting in the initial H_{A} and H_{B} does not optimize the error), a module of the algorithm will design a new hierarchy from the current positions of the bodies. For this, the algorithm computes a two-dimensional symmetric array that compiles the Keplerian acceleration between two bodies $a_k^{\mathrm{Kep}} = GM_k/r_{ij}^2$, where M_k is the sum of the masses. The strongest acceleration gives the first orbit, then the two bodies are replaced by their center of mass and the array is updated, and again until the last orbit comprises all bodies. We first checked that this algorithm always returns the existing hierarchy when no change is expected. Then, if the computed hierarchy is different than the current one, the hierarchy must be changed.

If the hierarchy needs to be changed, so is the time-step Δt. We choose a Keplerian-like time $\min_k T_k/20$, where

$$T_k = \sqrt{\frac{4\pi^2 a_k^3 \mid 1 - e_k \mid^3}{GM_k}} \tag{7}$$

if orbit k is bound or if its smallest approach has not yet occurred, or

$$T_k = \sqrt{\frac{4\pi^2 {r'_k}^3}{GM_k}} \tag{8}$$

otherwise. The choice to adapt or not the time step is given to the user.

Strictly speaking, when changing the hierarchy, the symplectic nature of the algorithm does not hold anymore, as the splitting of the Hamiltonian is entirely based on the hierarchy. This is also true for any change of the time step. A new approximate Hamitonian is integrated from an already approximated scheme, which means that the error budget raises potentially at each hierarchy change. However, the algorithm is designed for orbital dynamics, where systems are not subject to frequent reorganization of their architecture. Designing a new Hamiltonian when the initial hierarchy is not suited anymore allows to limitate the error on each orbit, which will otherwise become out of control. This is basically the same problem as the one raised by close encouters in planetary dynamics. When handling close encounters, Levison & Duncan (1994) (in SWIFT RMVS) and Chambers (1999) (in Mercury) temporarily change the way of splitting the Hamiltonian when transferring to H_A the part of H_B that concerns the close encounter, even sometimes changing the hierarchy to planetocentric. Conceptually, a close encounter within a planetary system can be viewed as a temporary change of hierarchy that eventually returns to the initial hierarchy. Here we are concerned by changes that can be permanent.

2.3. Checking the relevance of the hierarchy

Performing a hierarchy change is quite costly, as all the acceleration couples have to be computed at each step (multiple operations that scale as $O(N^3)$). Checking for a possible change at each time-step, with the result that most of the time the current hierarchy would be left unchanged, would thus amount to a considerable loss of efficiency. Prior to launching the entire hierarchy re-building process, an efficient algorithm with a simpler criterion must be applied to check whether it is appropriate or not. The most exact criterion would be the theoretical energy error associated to the symplectic mapping, but its computation is tedious (grows as N^4). The criterion must be fast to compute (maximum as N^3, like the accelerations) and correlated to the error.

In Mercury (Chambers 1999), the criterion to spot close encounters is the ratio between the relative distances and the Hill radii, assuming the latter roughly constant. This is a legit criterion for the study of the Solar system, but it is not relevant to our case. Indeed, the Hill radius is not easy to compute for eccentric orbit, it depends strongly on the orbital parameters (which is subject to variation in the general case) and it is not satisfyingly correlated to the errors in a complex architecture.

We choose to compute at each step the ratio $a_k^B/a_k^{\rm Kep}$ for each orbit k, and declare the hierarchy questionable if it is higher than 0.2 for at least one orbit. The computation of that criterion also scales as $O(N^3)$ in theory, but it uses the acceleration a^B that is already computed in any step of the integration, so that the extra cost remains limited. In a Solar-System like configuration, the derivation of the Hill radius is based on a simpler consideration.

2.4. The case of test particles

The study of planetary systems often involved the study of debris belts. In N-body simulations, the dust is modeled at first order by massless bodies (or test particless) that interact with the massive bodies but not with each other. Test particles must be specifically considered in Odea as the handling of their hierarchy is slightly different. Indeed, they are the only satellites of their orbit and their orbit is invisible to the bodies and other test particles evolution. When looking for a new hierarchy, Odea will not consider the test particles, for it searches foremost to optimize the energy error budget related to the massive bodies.

When the hierarchy of the massive bodies changes, each test particle must find its natural orbit given its relative position. A similar procedure to the hierarchy building of massive bodies is then performed. For a consistent hierarchy, the test particles have $2N-1$ possibilities for their orbit: around one massive bodies (N) or around one orbit ($N-1$). Thus, for each test particle, a $2N-1$ array is computed, compiling the Keplerian accelerations. The maximal element will correspond to the new particle configuration.

Finally, a test particle may also be subject to a hierarchy change, independently of the massive bodies architecture evolution. Thus, the acceleration ratio criterion is computed at each time step to check the suitability of the particle orbit, and a new orbital configuration is investigated if necessary following the previous procedure.

2.5. Comparison with other codes

Several symplectic algorithms have been introduced since the formalization of the first symplectic map for orbital mechanics, including the widely used Mercury (Chambers 1999). Most of them are designed to work in Solar-System-like hierarchy. Chambers et al. (2002) introduced two algorithms, derived from Mercury, to model planetary motions in binary systems. However, to our knowledge, no symplectic integrator are able to integrate indifferently any types of hierarchy, or a more complex hierarchy, except from Swift Hjs.

Moreover, no symplectic integrator that we know of are designed to handle long or definitive hierarchy change. Such situations can be encountered in case of a stellar fly-by, or of a capture of debris disk dust by a stellar or planetary companion. The subsequent study of system HD 106906 is a perfect example of situations that can not be tackled by ordinary symplectic algorithms: binary fly-by and dust capture.

On an other hand, Rein & Spiegel (2014) argue that a high-order classical integrator is quicker and more accurate than symplectic integrators. This may be true for some complex cases, or if we aim for a very high precision. However, symplectic integrators have encoded the exact resolution of the Keplerian motion, while a classical integrator makes no hypothesis for the form of the motion, and has to solve from scratch the differential equations of motion. Thus, for lightly perturbed Keplerian motion, symplectic algorithms are certainly more practical than classical integrators. The time steps can be large without endangering the stability of the orbits.

For example, in the case of HD 106906, the simulations involved very different scales, from the planet periastron to the wide hyperbolic orbit of the perturbers. A classical integrator would have to adapt its time step to the smallest distance, while a symplectic integrator can adopt a larger timescale without compromising the stability of the planet orbit.

We also point out that Swift Hjs never makes the assumption that the orbits we are considering are actually bound. The only requirement is that the sum of the Keplerian interactions associated with the hierarchy (i.e. H_A) must represent most of the full Hamiltonian. Some of the *orbits* we are considering can thus be hyperbolic, and this will be the case in a fly-by configuration. The Kepler solver used to integrate H_A handles bound or unbound orbits as well.

3. Application to system HD 106906

3.1. Characterizing the perturbers

Searching for potential stellar perturbers in Sco-Cen during the previous 15 Myr, De Rosa & Kalas (2019) identified two perturbers in LCC (Pecaut et al. 2012): HIP 59716 and HIP 59721. Located around 11 pc (projected 0.5°) from HD 106906 and 0.5 pc (projected 30") from each other, their relative velocities suggest an encounter with HD 106906 a few million years ago. The coordinates and velocities of the three systems are summarized in Table 1 of De Rosa & Kalas (2019). As can be seen on Fig. 2, the relative separation and velocity between HD 106906 and its perturbers lie essentially on the direction to Earth. Unfortunately, the quantities projected in this direction (distance and radial velocity) have the larger observational uncertainties, which creates a high dispersion on the closest encounters, in particular for the most promising candidate HIP 59716 (Fig. 3).

We note that the relative velocities between each systems ($\sim$ 4 km/s) are four times higher than the velocity dispersion reported for LCC (1.13 ± 0.07 km/s; Madsen et al. 2002), that was used in Rodet et al. (2017). We will see in subsection 3.3 that the effect of a fly-by is inversely proportional to the velocity of the passing star.

The masses of HIP 59716 and HIP 59721 have been estimated respectively 1.37 $M_\odot$ for HIP 59716 and 1.22 $M_\odot$ for HIP 59721 from the spectral types. HD 106906 binary mass has been estimated to 2.58 ± 0.04 $M_\odot$ from radial ve-

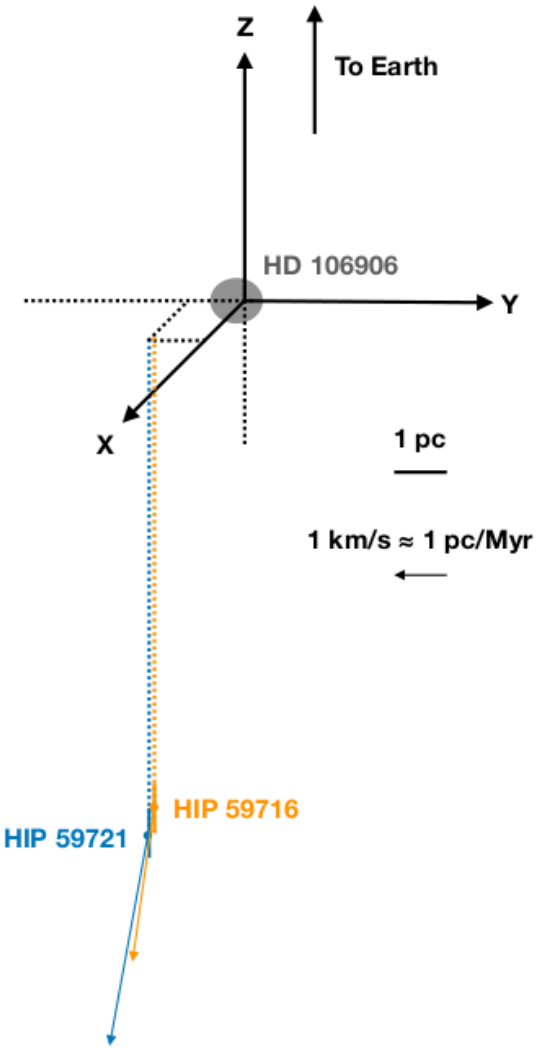

Fig. 2. Representation of HD 106906, HIP 59716 and HIP 59721 current positions and velocities in HD 106906 rest frame (disk lies in the YZ plane, observed extension in the -Y direction).

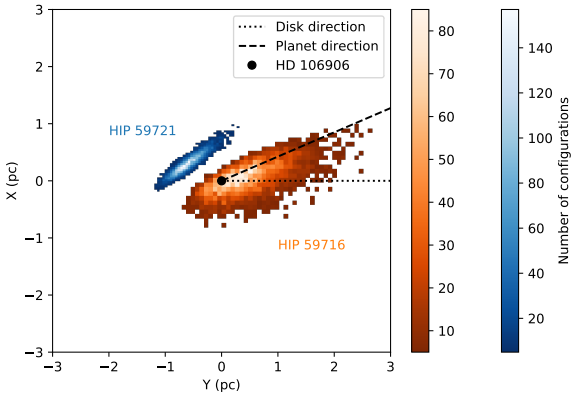

Fig. 3. Two dimension histograms of the coordinates of the intersection points between the perturbers trajectories and the XY plane, assuming linear trajectories.

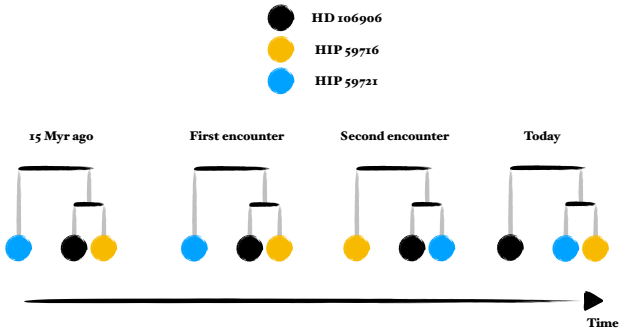

Fig. 4. Representation of a typical evolution of the hierarchy in the three-body simulations of HD 106906 fly-bys with Odea. All orbits here are hyperbolic.

locity and interferometric measurements by Lagrange et al. (2019).

3.2. Simulating the encounters

N-body simulations performed by De Rosa & Kalas (2019) indicate that the galactic gravitational potential has a negligible influence on the characteristics of the encounters. Moreover, the binarity of HD 106906 does not affect the encounters, because of the very high ratio between the closest approaches and the binary separation (> 1000). In order to efficiently determine the parameters of the encounters, we first performed 10,000 simulations with Odea, including three bodies: HD 106906 ABb ($2.58 + 0.01$ $M_\odot$), HIP 59716 and HIP 59721. The mass of HD 106906 and the algorithm that we present here are the only differences with De Rosa & Kalas study at that point.

The initialization of the simulations is designed with a Monte-Carlo approach, following De Rosa & Kalas. The 3×6 parameters and their respective precision are the right ascension α (0.05 mas), the declination δ (0.002 mas), the parallax π (0.05 mas), the proper motion of the right ascension $\mu_\alpha \cos\delta$ (0.05 mas/yr), the proper motion of the declination μ_δ (0.05 mas/yr) and the radial velocity γ (up to 1.7 km/s). The parameters are drawn from a normal distribution centered on their measured values, with a dispersion equal to the observations uncertainties, taking into account the correlations given by Gaia catalog. Then, we trace back the stars trajectory to observe the encounters.

Most of the simulations follow the same hierarchy evolution, represented on Fig. 4: the first fly-by involves HIP 59716 and the second HIP 59721, before the two perturbers get very close at each other as can be seen today. The hierarchy will thus naturally evolves to take into account the successive encounters. Computing the eccentricity of several sets of configurations, we evaluated that the two perturbers have currently a 2.1 ± 0.1 % chance of being gravitationally bound to each other. However, De Rosa & Kalas point out that the probability of them having such similar angular positions and proper motions without being bound are extremely low.

We launched 10,000 simulations for 15 Myr, corresponding to a backward evolution from our days to the formations of the stars. At first sight, 10,000 simulations may not seem enough to correctly sample the 18 parameters confidence intervals. However, most of the parameters are strongly constrained, the only strong uncertainties being the perturbers

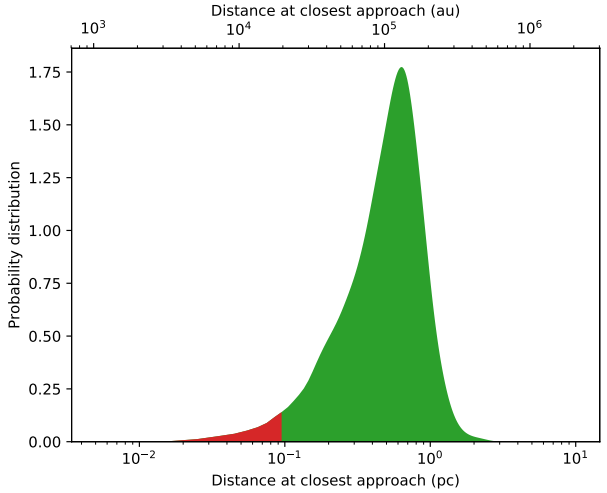

Fig. 5. Distribution of the distances at closest approach. The following study will focus on the red part, that corresponds to fly-by closer than 0.1 pc (3.6 % of the configurations).

relative radial velocities and distances, that is 4 parameters. Thus, these are the critical parameters that must be correctly sampled, and 10,000 is then a sufficient number. The initial time-step was set to 1,000 yr, with outputs every 1,000 yr. To account for the possibility of the two perturbers being bound, we performed an additional 10,000 simulations with only bound configurations. It comes down essentially to selecting only the configurations where the perturbers have similar radial velocities.

The distances at closest approach were computed for each simulation (Fig. 5). Most of the encounters occur with a closest approach between 0.3 and 2 pc, with a maximal probability around 0.6 pc, consistent with the results of De Rosa & Kalas. We then reviewed the simulations for which a close (< 0.1 pc) fly-by occurred, from any one or both of the two perturbers. 359 configurations were selected, that is around 4% of the total number of studied configurations. In most cases ($\gtrsim 90\%$), HIP 59716 encounters HIP 106906 at the shortest distance. For the bound configurations, the peak is around 0.4 pc but the number of close fly-bys is roughly the same. HIP 59716 coordinates distributions are presented on Fig. 7. Most of the parameters of the configurations with close fly-bys are drawn randomly within the configurations, except for the radial velocity, where we see that the configurations leading to a close fly-by correspond to the higher radial velocities (closer to the radial velocity of HIP 59721). The distributions for the two other bodies are presented on Fig. 13 and 14 in the appendix.

The distributions of the time and velocities of the perturber at closest approach are represented on Fig. 6 (only the cases where the distance was less than 0.1 pc). Most of the encounters occur between 4 and 2 Myr ago, with a velocity between 2 and 6 km/s.

3.3. Effect on the planet

3.3.1. Setup

Once the configurations for which a close fly-by occur within the 15 Myr of the system life have been identified, we launch a new set of simulations, this time including the

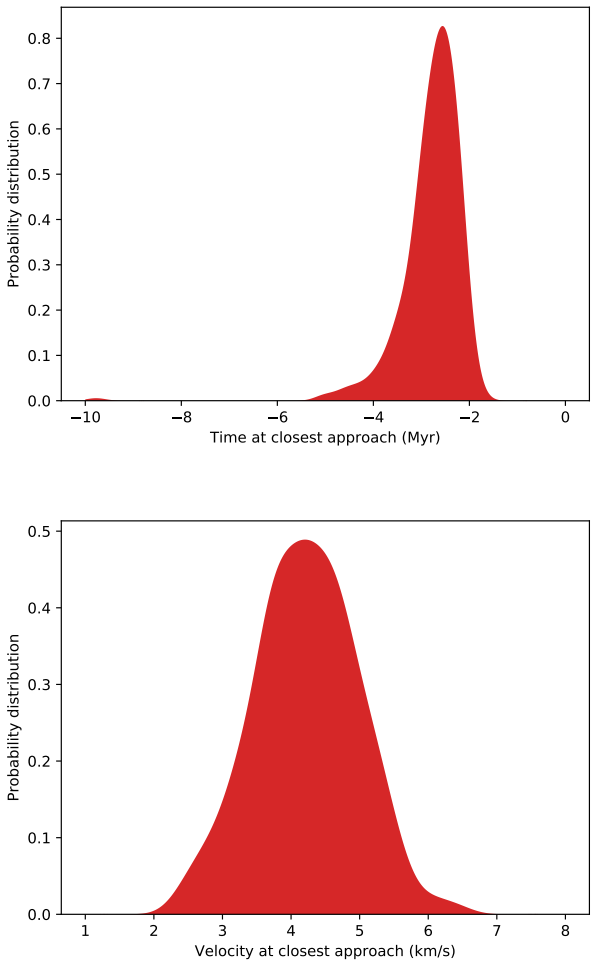

Fig. 6. Distribution of the times and velocities at closest approach, for the cases where the distance at closest approach is less than 0.1 pc.

planet. The bodies are initialized at their position at the end of the first simulation, that is at their position 15 Myr ago. HD 106906 is separated into two bodies, namely the binary HD 106906 AB (2.58 $M_\odot$), and the planet HD 106906 ABb (0.01 $M_\odot$). The simulations are launched from 15 Myr ago to the present epoch, so that the final outcome represents the current positions of the bodies. The time-step was set to 100 yr, with outputs every 1,000 yr.

In the study of Rodet et al. (2017), the destabilization of the planet takes place after a violent encounter with the central binary, in the beginning of the system's life. The outcome was either a definitive ejection on a hyperbolic trajectory, or a transitional state where the eccentricity raised dramatically without passing 1. The probability of the different outcomes depends on the characteristics of the encounter, which is highly underconstrained. In the case of a hyperbolic trajectory, a subsequent stabilization by a fly-by must be precisely synchronized, and is thus difficult to achieve. Thus, we study here the case of a highly eccentric transitional bound orbit. The periastron should roughly correspond to the separation of the planet when the perturbation occurred, around 1 au. On the other hand, the apoastron will remained mostly unchanged after a fly-by. The current projected separation implies a minimal value

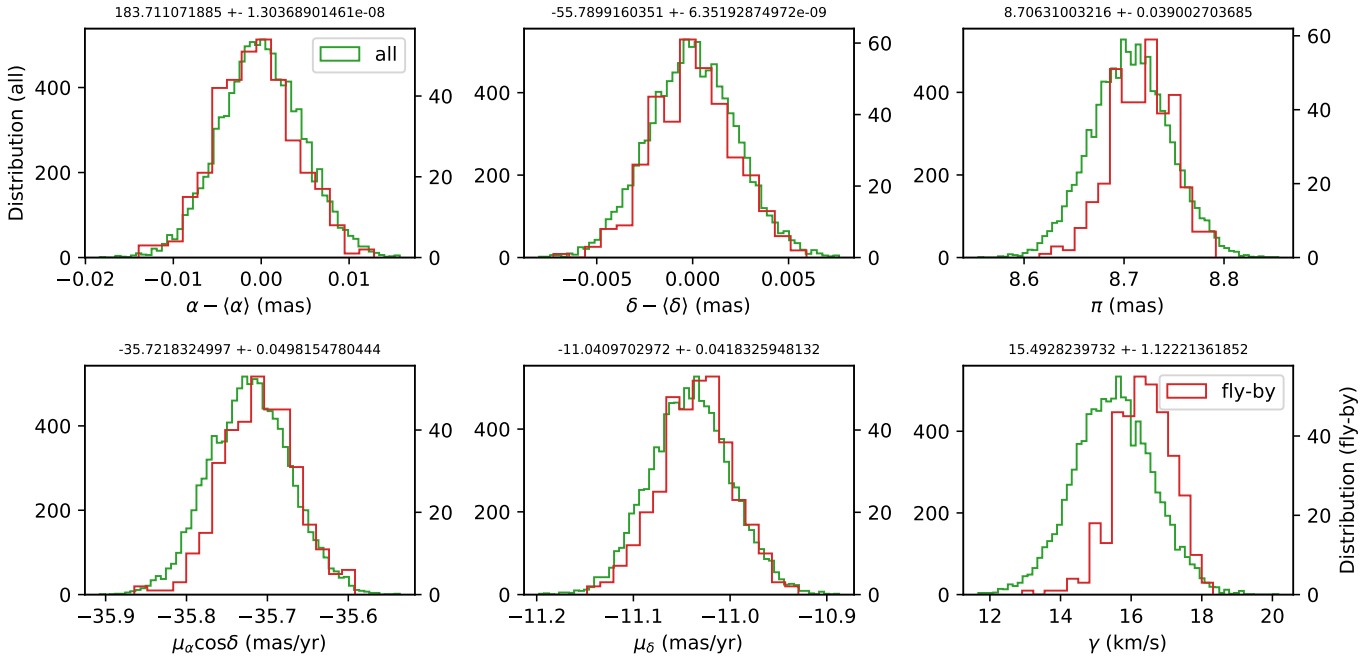

Fig. 7. Initial distribution (today) of HIP 59716 coordinates and velocities for the 10,000 simulated cases (green), and for the 359 cases where a fly-by closer than 0.1 pc occurred (red).

of 730 au. Moreover, the probability is higher to observe the planet near apoastron: it spends 2/3 of its time at a separation greater than 700 au for an apoastron of 1,000 au, and 95 % for an apoastron of 3,000 au. All in all, two sets of simulations are performed, where the planet is initialized with a periastron of 1 au and an apoastron of 1,000 (a = 500.5 au, e = 0.998) or 3,000 au (a = 1500.5 au, e = 0.9993).

The necessary energy to completely eject the planet is $\frac{1}{2}GM_{\rm HD106906}/a_p$, where a_p is the initial semi-major axis of the planet and $M_{\rm HD106906}$ the mass of the host binary. From its current position close to the central binary, a definitive ejection requires around 1 $M_\odot au^2/yr^2$. A proportion of 2.10^{-3} less corresponds to an elliptic trajectory with apoastron 1,000 au, and 2.10^{-4} $M_\odot au^2/yr^2$ less corresponds to 10,000 au. Thus, from an energetic point of view, reaching a high apoastron on a still bound orbit in the ejection process is nearly as costly as being definitely ejected.

For a fly-by to have a meaningful role in the dynamical history of the planet, it has to decrease the planet eccentricity by increasing the periastron to a safer value (an increase of the order of the astronomical unit at least). The timescale of the fly-by is much larger than the orbital period of the planet, so that the initial position of the planet on its orbit is not a relevant parameter in the simulations. Moreover, in our scenario, the planet formed within the disk, so that its orbit was initially coplanar with the disk mid-plane. We assume that the planet apoastron is aligned with the observed extension of the disk. A close encounter with the central binary will retain this coplanarity if the inclination of the binary orbit is similar to that of the disk plane, which seems likely from the first estimates of its orbital parameters (Lagrange et al. 2019). As the fly-by is likely to keep the apoastron roughly unchanged and the eccentricity high (consistent with the observed patterns of the disk according to Jílková & Zwart 2015; Nesvold et al. 2017; Rodet et al. 2017), this is consistent with the current position of the planet.

3.3.2. Results

The conclusion of the study depends essentially on the possibility for the fly-by to increase significantly the periastron. This effect is stongly correlated to the distance at closest approach. We thus represented the periastron change with respect to the distance at closest approach for the outputs of the two sets of simulations on Figs. 8 and 9.

Whether for a 1,000 or 3,000 au apoastron, a 0.1 pc encounter is not enough to significantly raise the periastron: a closer fly-by is required. For the 1,000 au apoastron case, the distance at closest approach must be less than 0.01 pc, that is 2, 000 au. For the 3,000 au apoastron case, the destabilization is certainly easier, but the distance at closest approach must still be less than 0.05 pc, that is 10, 000 au. For such distances, the results are essentially identical for the bound cases, as the separation between the two perturbers is greater of similar than the distance at closest approach with HD 106906. On our initial 10,000 draws, respectively 2 and 20 resulted in a periastron increase superior to 1 au for the 1,000 and 3,000 au apoastron cases, and 1 and 2 lead to the ejection of the planet (for distance at closest approach similar or less than the planet semi-major axis).

Moreover, coplanarity of the planet orbit with the disk plan is expected if the planet formed within the disk. The current projected planet misalignment with the disk plane is currently estimated at 23 degrees, although a lower angle (and even coplanarity) would be possible if the planet true separation is greater than its projected separation ($\gtrsim$ 3000 au for coplanarity). A 23° misalignment corresponds to a minimal altitude of $\sim$ 280 au above the disk plane, and such gain of altitude is rarely seen in the simulations, even in the most favorable case of a high initial apoastron. This would

suggest that the misalignment (or part of it at least) is an illusion due to projection effects.

3.3.3. Theory

We first study the periastron increase as a function of the distance at closest approach, and compare it to the theoretical predictions. The computation of the following theoretical formula is explained in the appendix. The simplest approach is the impulse approximation, where the fly-by is assumed to be instantaneous and trigger a sudden velocity change on the planet. Although this cannot be considered as representative for the reality if we compare the fly-by time-scale with the orbital period of the planet, this approximation often provides a good estimate. In this framework, Brunini & Fernandez (1996) show that the fly-by increases the planet velocity by:

$$|\Delta v_p| \lesssim \frac{2GM_*}{VD^2} a_p \tag{9}$$

where v_p is the planet velocity, M_* is the perturber's mass, V its velocity at closest approach, D its distance at closest approach, and a_p the planet semi-major axis. This formula nevertheless applies to circular orbits only (Brunini & Fernandez 1996). By supposing that the new orbit intersects the old one at apoastron, the planet eccentricity e_p takes part, and we have a change of semi-major axis $\Delta a_p = -a_p \Delta e_p$, which gives a change of periastron $\Delta\text{peri} = -2a_p\Delta e_p$. Finally, one gets (see appendix):

$$|\Delta\text{peri}| \lesssim 8\frac{GM_*}{\sqrt{GM_{\text{HD106906}}}} \frac{a_p^{\frac{5}{2}}}{VD^2} \tag{10}$$

It can be adapted to an eccentric orbit, as was done in Rodet et al. (2017), by supposing that the perturbations occur only at apoastron. Then, stating that the apoastron is preserved, one gets $\Delta a_p = -a_p\Delta e_p/(1+e_p)$ and $\Delta\text{peri} = -2a_p\Delta e_p/(1+e_p)$. Finally, using Eq. 9 to quantify the velocity increase at apoastron, one gets (see appendix):

$$|\Delta\text{peri}| \lesssim 8\frac{GM_*}{\sqrt{GM_{\text{HD106906}}}} \frac{a_p^{\frac{5}{2}}}{VD^2} \frac{\sqrt{(1-ep)(1+e_p)}}{3-e_p} \tag{11}$$

On the other hand, a more rigorous approach is to compute the secular evolution of the orbital elements of the planet during the passage of the perturber. Heggie & Rasio (1996) used that method to determine the eccentricity increase of a companion, and found a complex formula depending on all 6 orbital elements of the perturber's orbit. In this framework, the semi-major axis is invariant throughout the fly-by. Considering a coplanar orbit and a perturber's eccentricity significantly higher than 1 (strongly unbound orbit), the maximum is:

$$|\Delta\text{peri}| \lesssim \frac{5}{2}\frac{GM_*}{\sqrt{GM_{\text{HD106906}}}} \frac{a_p^{\frac{5}{2}}}{VD^2} e_p\sqrt{1-ep^2} \tag{12}$$

The three theoretical predictions are represented on Figs. 8 and 9: circular impulse, apoastron impulse and secular approximation. They all correspond to maximum values, as the true periastron evolution depends on the angular

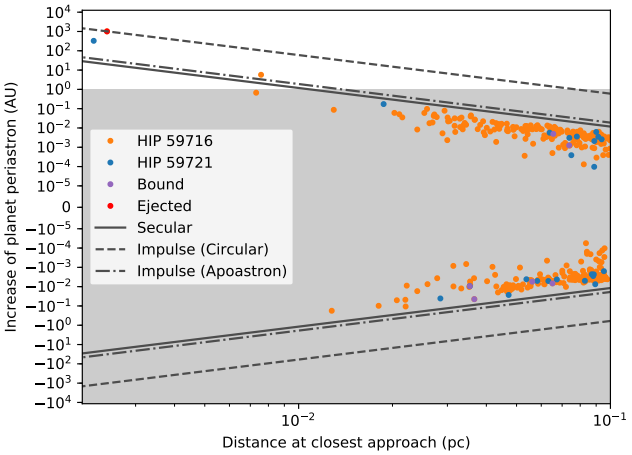

Fig. 8. Periastron increase with respect to the distance at closest approach, from N-body simulations (dots) and theoretical approaches (lines), for the closer fly-bys, and for an initial planetary apoastron of 1,000 au. The grey part corresponds to a periastron change inferior to +1 au, which will not secure the planet stability.

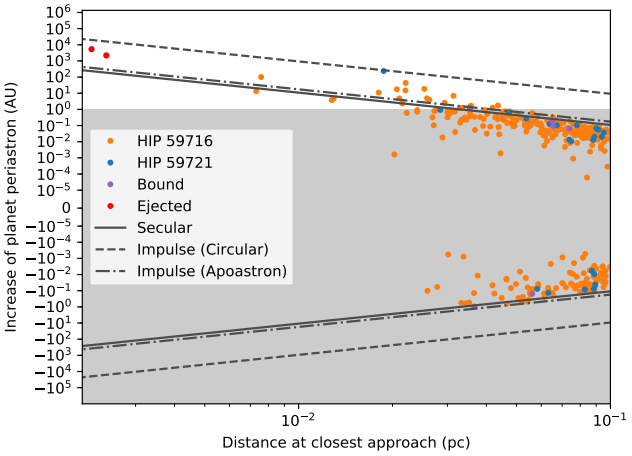

Fig. 9. Periastron increase with respect to the distance at closest approach, from N-body simulations (dots) and theoretical approaches (lines), for the closer fly-bys, and for an initial planetary apoastron of 3,000 au. The grey part corresponds to a periastron change inferior to +1 au, which will not secure the planet stability.

characteristics of the encounter. The velocity V is set to its mean value over all closest approaches, around 4 km/s. M_* was set to 1.3 $M_\odot$, but the increase depends weakly on the perturber's exact mass. The eccentricity e_p is set to its initial value, an approximation that becomes less relevant when $\Delta e_p \gtrsim 1 - e_p = 2.10^{-3}$ (for closest approach less or around 0.01 pc).

We see on Fig. 8 that the periastron change is best modeled by the secular approximation, but is also correctly approached by the impulse approximation at apoastron. It suggests that the effect of both perturbers on the planet can be estimated by the effect of the perturber that had the closest approach. This is also true for the cases where the two perturbers are bound (see Appendix).

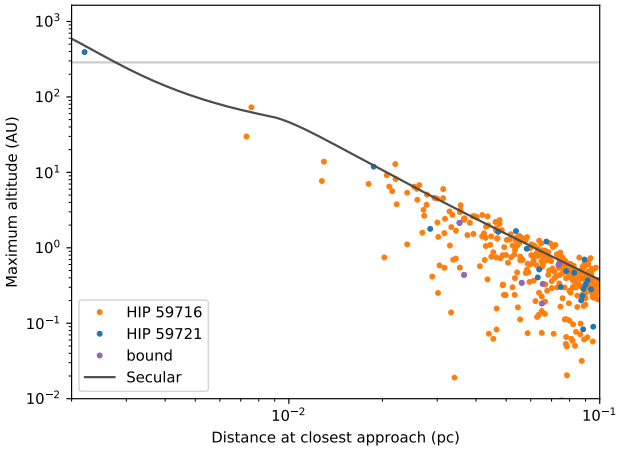

Fig. 10. Maximal altitude with respect to the distance at closest approach, from N-body simulations (dots) and secular theoretical approach (line), for the closer fly-bys, and for an initial planetary apoastron of 1,000 au. The grey line indicates the projected elevation of the planet.

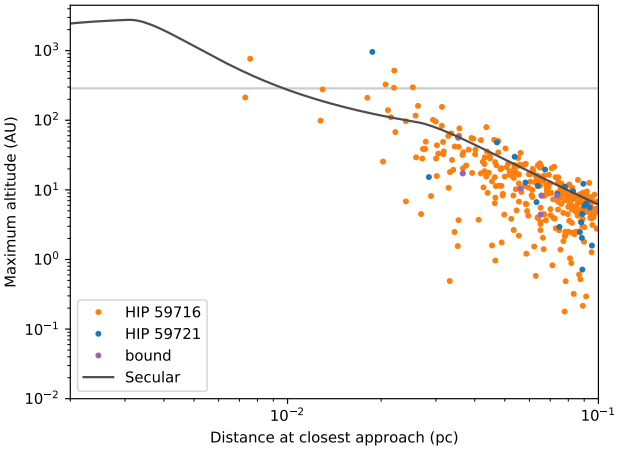

Fig. 11. Maximal altitude with respect to the distance at closest approach, from N-body simulations (dots) and secular theoretical approach (line), for the closer fly-bys, and for an initial planetary apoastron of 3,000 au. The grey line indicates the projected elevation of the planet.

Furthermore, we seek to estimate if the fly-by could account for the possible misalignment of the planet with the debris disk plane. Depending on the exact value of the argument of periastron ω_p, a very eccentric orbit does not necessarily have a large elevation above the disk plane, even if it is highly inclined. To have a meaningful plan misalignment, the planet should have an inclination change combined with a shift of the argument of its periastron that results in a significant elevation above the disk plane. For any Keplerian orbit, the maximum elevation $z_{\max}$ above the reference plane is given by:

$$z_{\max} = a_p \sin(i_p) \left(\sqrt{1 - e_p^2 \cos^2(\omega_p)} + e_p |\sin(\omega_p)| \right) \quad . \tag{13}$$

Obviously, with $e_p \sim 1$ and $\omega_p \sim 0$ or π, $z_{\max}$ remains small irrespective of the value of i_p.

We thus computed the change in $z_{\max}$, inspiring from Heggie & Rasio (1996). The details are explained in the appendix. The resulting maximal altitude is represented on Fig.10 and 11.

3.3.4. Discussion

From both approaches, theoretical and numerical, in the most favorable case, it appears that a fly-by has a significant impact on the planet (periastron increase above 1 au) only if its closest approach is less than 0.05 pc, that is 10,000 au. This corresponds to a small subset among the initial draws, not because of an incompatibility with the observations, but because of the high dispersion of closest approaches, underconstrained by the observations.

We checked that the distance at closest approach is not correlated to the time at closest approach, nor to the velocity at closest approach. Considering the compatibility between our results and the dynamical scenario proposed in Rodet et al. (2017), the time of the fly-by must be considered. Given our simulations, the closest approach occurred likely 2 to 4 Myr ago (3 ± 1 Myr). However, our scenario account for the ejection of the planet only in the beginning of the system life, when protoplanetary disk is still present and can effectively trigger planetary migration. Given the disk lifetime for massive stars (~ 3 Myr, Ribas et al. 2015) and the system assumed age (15 Myr), 2 to 4 Myr ago is significantly too late for the fly-by to have a decisive role. However, a younger age for the system (10 Myr, compatible with LCC age spread of 6 Myr) could still account for this discrepancy.

3.4. Effect on the disk

The effects of a fly-by on a disk may be significant, depending on the parameters of the encounter. The case of a dynamically efficient fly-by can be observed in system HD 141569, where the ongoing encounter has been deeply studied in Reche et al. (2009). In this system, the fly-by could be responsible for truncation, spiral formation, collisional evolution, eccentricity and inclination raise. In our study, the effect of the fly-by on test-particles will be essentially similar to that on the planet. Since the test particles in a debris disk have a nearly circular orbit, the fly-by will increase the eccentricity, significantly or not depending on the distance of closest approach. Moreover, all fly-by characteristics being equal, particles inclination will be excited differently depending on their distance to the host star. The disk might then be warped. The sensitivity of the scattered-light images of the disk are not sufficient to reveal a weak warp, but the warp can induce further instabilities and asymmetries in the disk that could account for its non-standard shape.

We chose among the previous cases a situation with a very short distance at closest approach (1,000 au), with a medium relative inclination (~ 45 °) and ran a simulation with the three massive bodies (HD 106906 ABb and the perturbers) and 1,000 test particles. The particles have initially semi-major axes evenly shared between 10 and 600 au, eccentricity below 0.05, and an inclination spread of 2 degrees. The simulation was launched for 100 000 years

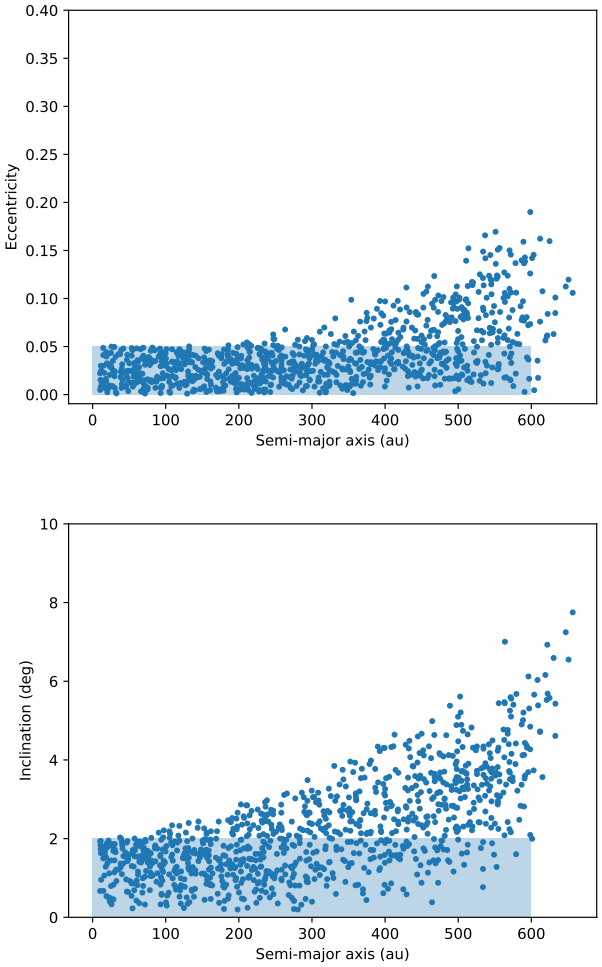

Fig. 12. Orbital elements of the test particles after a close fly-by. The lightly blue zones represent the initial configuration.

around the fly-by epoch, with a time step of 1 yr. The resulting disk is represented on Fig. 12.

On the other hand, the repeating passing of the planet within the disk would have stronger consequences. If a very small percentage is ejected over one period ($\lesssim 0.01$ %), the mean eccentricity of the particles raise from 0.02 at each passage. For the disk to remain long-lived in its current shape, Jílková & Zwart (2015) (non collisional simulations) and Nesvold et al. (2017) (collisional simulations) estimated that the planet orbit should not cross the disk. Thus, the planet periastron should be outer to the observed $\sim$ 100 au outer disk radius. Within our scenario, it means that this enlargement of the periastron occurred rather quickly, whether or not it was caused entirely by the fly-by. In any case, the planet interactions would have cover the track of the fly-by-induced perturbations

The new structure of the code allows to estimate the percentage of dust capture by the planet. It turns out that temporary (less than 10 yr) capture is experienced by about 5% of the dust at each passage, but no permanent captures were produced.

4. Conclusion

In this paper, we present the N-body symplectic code Odea, that is able to study multiple systems in evolving architectures. We use it to study the rare planetary system HD 106906. We confirm that the two stars identified by De Rosa & Kalas (2019) could have helped stabilizing the planet after a destabilization by its host binary star. This scenario could account for the wide separation of the planet, its possible elevation with respect to the disk plane, as well as the structures evidenced within the disk.

However, the significance of the encounter strongly depends on the distances at closest approach. With the current precision on the three systems configuration (especially the relative radial velocities and distances), it is not possible to establish the role of the flybys. To circularize the planet orbit if it was previously ejected on a wide trajectory, a fly-by closer than 0.05 pc is needed (assuming apoastron $\leq$ 3,000 au), which is one order of magnitude below the uncertainty on the closest approach. The simulations show that the angular configuration is favorable when this condition is met.

Any indication of HD 106906 b relative motion would be helpful to constrain its orbit, and thus its dynamical history. More precise parallaxes and radial velocities for HIP 59716 and HIP 59721 are necessary to constrain the distances at closest approach, and conclude on the effect of the fly-bys on the system dynamical evolution.

Odea handles hierarchy changes in systems with non-Solar-system-type architectures. It can model efficiently captures and fly-bys. Through a criterion based on accelerations ratios, a new hierarchy is defined when the current is perturbed. Odea's natural upgrade is the implementation of a Mercury-like approach to handle close encounters, that is transitional states of non-Keplerian movements.

Acknowledgements. The project is supported by CNRS, by the Agence Nationale de la Recherche (ANR-14-CE33-0018, GIPSE), the OSUG@2020 labex and the Programme National de Planétologie (PNP, INSU) and Programme National de Physique Stellaire (PNPS, INSU). Most of the computations presented in this paper were performed using the Froggy platform of the CIMENT infrastructure (https://ciment.ujf-grenoble.fr), which is supported by the Rhône-Alpes region (GRANT CPER07_13 CIRA), the OSUG@2020 labex (reference ANR10 LABX56) and the Equip@Meso project (reference ANR-10-EQPX-29-01) of the programme Investissements d'Avenir, supervised by the Agence Nationale pour la Recherche. P.K. and R.J.D.R. thank support from NSF AST-1518332, NASA NNX15AC89G and NNX15AD95G/NEXSS. This work benefited from NASA's Nexus for Exoplanet System Science (NExSS) research coordination network sponsored by NASA's Science Mission Directorate.

References

Bailey, V., Meshkat, T., Reiter, M., et al. 2013, ApJ, 780, L4
Baruteau, C., Bai, X., Mordasini, C., & Mollière, P. 2016, Space Sci. Rev., 205, 77
Beust, H. 2003, A&A, 400, 1129
Brown, A., Vallenari, A., Prusti, T., et al. 2018, arXiv preprint arXiv:1804.09365
Brunini, A. & Fernandez, J. A. 1996, Astronomy and Astrophysics, 308, 988
Chambers, J. E. 1999, Monthly Notices of the Royal Astronomical Society, 304, 793
Chambers, J. E., Quintana, E. V., et al. 2002, AJ, 123, 2884
Daemgen, S., Todorov, K., Quanz, S. P., et al. 2017, Astronomy & Astrophysics, 608, A71
De Rosa, R. J. & Kalas, P. 2019, The Astronomical Journal, 157, 125
De Zeeuw, P., Hoogerwerf, R. v., de Bruijne, J. H., Brown, A., & Blaauw, A. 1999, ApJ, 117, 354

Heggie, D. C. & Rasio, F. A. 1996, Monthly Notices of the Royal Astronomical Society, 282, 1064
Jílková, L. & Zwart, S. P. 2015, MNRAS, 451, 804
Kalas, P. G., Rajan, A., Wang, J. J., et al. 2015, ApJ, 814, 32
Lagrange, A.-M., Langlois, M., Gratton, R., et al. 2016, A&A, 586, L8
Lagrange, A.-M., Mathias, P., Absil, O., et al. 2019, A&A, in press
Levison, H. F. & Duncan, M. J. 1994, Icarus, 108, 18
Madsen, S., Dravins, D., & Lindegren, L. 2002, Astronomy & Astrophysics, 381, 446
Nesvold, E. R., Naoz, S., & Fitzgerald, M. P. 2017, ApJ, 837, L6
Pecaut, M. J. & Mamajek, E. E. 2016, Monthly Notices of the Royal Astronomical Society, 461, 794
Pecaut, M. J., Mamajek, E. E., & Bubar, E. J. 2012, The Astrophysical Journal, 746, 154
Reche, R., Beust, H., & Augereau, J.-C. 2009, Astronomy & Astrophysics, 493, 661
Rein, H. & Spiegel, D. S. 2014, Monthly Notices of the Royal Astronomical Society, 446, 1424
Ribas, Á., Bouy, H., & Merín, B. 2015, Astronomy & Astrophysics, 576, A52
Rodet, L., Beust, H., Bonnefoy, M., et al. 2017, Astronomy & Astrophysics, 602, A12
Saha, P. & Tremaine, S. 1994, arXiv preprint astro-ph/9403057
Wisdom, J. & Holman, M. 1991, AJ, 102, 1528

Appendix

Derivation of the changes of planet periastron due to the fly-by in the impulse approximation

Circular impulse

The expression of the change of the planet velocity is given in Eq. 9. Supposing that the new orbit intersects the old one at apoastron or periastron, we have $\Delta a_p = a_p \Delta e_p$. Moreover, the velocity of the planet if on a circular orbit is $v_p = \sqrt{GM_{\rm HD106906}/a_p}$. Thus, the eccentricity is

$$|\Delta e_p| = \frac{|\Delta a_p|}{a_p} = 2\frac{|\Delta v_p|}{v_p} \lesssim 4\frac{GM_*}{\sqrt{GM_{\rm HD106906}}}\frac{a_p^{\frac{3}{2}}}{VD^2}$$

and the periastron is then given by $\Delta\text{peri} = \Delta a_p - a\Delta e_p = -2a_p\Delta e_p$.

Apoastron impulse

Stating instead that the apoastron is preserved, one gets $\Delta a_p = -a_p\Delta e_p/(1+e_p)$. Within the impulse framework, the change of velocity involves the velocity at apoastron, so that the velocity writes $v_p = \sqrt{GM_{\rm tot}/a_p}\sqrt{(1-e)/(1+e)}$. Thus,

$$\frac{\Delta v_p}{v_p} = -\frac{\Delta a_p}{2a_p} - \frac{\Delta e_p}{1-ep^2} = -\frac{\Delta e_p}{2(1+e_p)} - \frac{\Delta e_p}{1-ep^2}$$

which gives

$$\begin{aligned}|\Delta e_p| &= -2\frac{|\Delta v_p|}{v_p}\frac{1-e_p^2}{3-e_p} \\ &\lesssim 4\frac{GM_*}{\sqrt{GM_{\rm HD106906}}}\frac{a_p^{\frac{3}{2}}}{VD^2}\frac{(1+ep)^{\frac{3}{2}}\sqrt{1-e_p}}{3-e_p}\end{aligned}$$

and the periastron is then given by $\Delta\text{peri} = \Delta a_p(1-e_p) - a\Delta e_p = -2a_p\Delta e_p/(1+e_p)$.

Derivation of the changes of planet orbital characteristics due to the fly-by in the secular approximation

Perturbative potential

We inspire from Heggie & Rasio (1996) to derive the first-order perturbation of the planet orbital elements in the secular approximation.

Following Heggie & Rasi, we number respectively 1, 2 and 3 HD 106906 central star, HD 106906 b and one of the stellar perturber. The position of the planet relative to its host star is denoted by $\boldsymbol{r}$, and the position of the third body relative to HD 106906 center of mass is denoted by $\boldsymbol{R}$. In this framework, the evolution of the planet orbit verifies:

$$\begin{aligned}\ddot{\boldsymbol{r}} &= -\frac{GM_{12}}{r^3}\boldsymbol{r} + \boldsymbol{\nabla} U \\ U &= \frac{Gm_3M_{12}}{m_1m_2}\left(\frac{m_2}{|\boldsymbol{R} - \frac{m_1}{M_{12}}\boldsymbol{r}|} - \frac{m_1}{|\boldsymbol{R} + \frac{m_2}{M_{12}}\boldsymbol{r}|}\right) \\ &= \frac{G_m 3r^2}{2R^3}\left(3(\frac{\boldsymbol{r}.\boldsymbol{R}}{rR})^2 - 1\right) + O((\frac{r}{R})^3)\end{aligned}$$

where U is the perturbative potential.

In the secular approximation, U is averaged over the orbit of HD 106906 planetary orbit. The implicit assumptions is that all orbital elements but the anomaly have a longer evolution timescale than the orbital period. As we are interested in the first order evolution, we only integrate the dominant part in a_p/a (quadripole order). Then, we use Lagrange equations to retrieve the evolution of the eccentricity, the inclination and the longitude of periastron.

Eccentricity and periastron change

After we first averaged over the planet orbital motion, the secular evolution of the eccentricity obtained at the quadrupole level writes:

$$\frac{de_p}{dt} = \frac{15Gm_3R_xR_ya_p^{\frac{3}{2}}e_p\sqrt{1-ep^2}}{2R^5\sqrt{GM_{12}}}$$

where the x-y plane is the initial plane of the planet (plane of the disk), and the x direction is given by the planet initial periastron. To compute the first order of the change of e after the fly-by, we integrate de/dt along time from $-\infty$ to $+\infty$ by fixing all variables to their initial values but the angular evolution of the stellar perturber.

Heggie & Rasio computed in their Eq. (7) the change in eccentricity as a function of the angular parameters of the encounter, and we exactly retrieve their expression. The maximum efficiency is obtained for a coplanar encounter, where all the transferred angular momentum apply only on the eccentricity. Stating that the eccentricity of the perturber's orbit is significantly more than 1 ($V = 3$ km/s and $D = 1$ pc gives $e \sim 500$, $D = 0.1$ pc gives $e \sim 50$), we obtain

$$\Delta e_p = -\frac{5}{2}\frac{M_*}{\sqrt{M_{\rm HD106906}M_{\rm tot}}}\frac{a_p^{\frac{3}{2}}}{D^{\frac{3}{2}}}\frac{e_p\sqrt{1-e_p^2}}{\sqrt{e}}\sin(2\Omega + 2\omega)$$

where Ω is the longitude of the ascending node and ω the argument of the periastron of the perturber hyperbolic orbit. The maximum is obtained for $\Omega + \omega = \pi/4$. Moreover, the eccentricity e depends on D, V and $GM_{\rm tot}$ as $V = \sqrt{GM_{\rm tot}(1+e)/D}$ so that $\sqrt{e} \simeq V\sqrt{D/GM_{\rm tot}}$. Thus, the eccentricity change satisfies:

$$|\Delta e_p| \lesssim \frac{5}{2}\frac{GM_*}{\sqrt{GM_{\rm HD106906}}}\frac{a_p^{\frac{3}{2}}}{VD^2}e_p\sqrt{1-ep^2} \tag{14}$$

On the other hand, the semi-major axis is constant in the secular approximation. The periastron is then given by $\Delta\text{peri} = -a\Delta e_p$.

Inclination change

The secular evolution of the inclination obtained at the quadrupole level writes:

$$\frac{di_p}{dt} = -\frac{3Gm_3a_p^{\frac{3}{2}}\left(4e_p^2+1\right)R_xR_z}{2R^5\sqrt{\left(1-e_p^2\right)GM_{12}}}$$

We then integrate as before to compute the change of inclination Δi_p.

$$\begin{aligned}\Delta i_p =& \frac{3}{2}\frac{GM_*}{\sqrt{GM_{\rm HD106906}}}\frac{a_p^{\frac{3}{2}}}{VD^2}\frac{1+4e_p^2}{\sqrt{1-e_p^2}}\\ &\left(\cos(i)\sin(\Omega)(\arccos(-\frac{1}{e})+\sqrt{e^2-1})\right.\\ &\left.-(\cos(\Omega)\sin(2\omega)+\cos(i)\sin(\Omega)\cos(2\omega))\frac{(e^2-1)^{\frac{3}{2}}}{3e^2}\right)\end{aligned}$$

The maximum is reached for $i = \pi/4$, $\Omega = \pi/2$ and $\omega = \pi/2$. Thus, we obtain

$$\Delta i_p \lesssim \frac{GM_*}{\sqrt{GM_{\rm HD106906}}}\frac{a_p^{\frac{3}{2}}}{VD^2}\frac{1+4e_p^2}{\sqrt{1-e_p^2}}$$

Longitude of the periastron change

The secular evolution of the total longitude of the periastron $\bar{\omega_p} = \omega_p + \Omega_p$ obtained at the quadrupole level writes:

$$\frac{d\bar{\omega_p}}{dt} = -\frac{3Gm_3a_p^{\frac{3}{2}}\sqrt{\left(1-e_p^2\right)}(R^2-4R_x^2+R_y^2)}{2R^5\sqrt{GM_{12}}}$$

We then integrate as before to compute the change of inclination $\Delta\bar{\omega_{p}}_p$.

$$\begin{aligned}\Delta\bar{\omega_p} =& \frac{1}{4}\frac{GM_*}{\sqrt{GM_{\rm HD106906}}}\frac{a_p^{\frac{3}{2}}}{VD^2}\sqrt{1-e_p^2}\\ &\left(6\cos^2(i)\cos^2(\omega)-5(\cos(2i)-3)\cos^2(\omega)\cos(2\Omega)\right.\\ &\left.+2\cos(2i)(3-5\cos(2\Omega))\sin^2(\omega)-10\cos(i)\sin(2\omega)\sin(2\Omega)\right)\end{aligned}$$

The maximum is reached for $i = \pi/2$, $\Omega = 0$ and $\omega = 0$. Thus, we obtain

$$\Delta\bar{\omega_p} \lesssim 5\frac{GM_*}{\sqrt{GM_{\rm HD106906}}}\frac{a_p^{\frac{3}{2}}}{VD^2}\sqrt{1-e_p^2}$$

Maximal altitude

The maximum altitude $z_{\max}$ reached by the planet on its orbit is given as a function of its orbital elements:

$$z_{\max} = a_p\sin(i_p)\left(\sqrt{1-e_p^2\cos^2(\omega_p)}+e_p|\sin(\omega_p)|\right) \quad . \tag{15}$$

It thus depends on the evolution of a_p, e_p, i_p and ω_p.

Due to the term $\sin(i_p)$, the same approach than above leads to neglecting all evolution but that of the inclination. It is consistent with the fact that in the previous expressions, $\Delta_i p \gg \Delta e_p, \Delta i_p$ when the eccentricity tends to 1. We get:

$$\Delta z_{\max} = a_p\sqrt{1-e_p^2}\Delta i_p \tag{16}$$

$$\lesssim \frac{GM_*}{\sqrt{GM_{\rm HD106906}}}\frac{a_p^{\frac{5}{2}}}{VD^2}(1+4e_p^2) \quad . \tag{17}$$

However, this estimate is not valid anymore when $\Delta_i p$ approaches $\pi/2$, that is when $\sin(i_p)$ approaches 1. At this point, the estimates of Δe_p and $\Delta\bar{\omega}$ must be taken into account. In order to comprise all the different evolution scales, we thus simply estimate the maximal altitude by replacing directly the computed evolution in the definition formula:

$$\Delta z_{\max} \lesssim a_p\sin\left(\tilde{i_p}\right)\left(\sqrt{1-\tilde{e_p}^2\cos^2\left(\tilde{\omega}\right)}+\tilde{e_p}|\sin\left(\tilde{\omega}\right)|\right) \tag{18}$$

where $\tilde{i_p} = \max(\Delta i_p, \frac{\pi}{2})$, $\tilde{e_p} = e_p - \Delta e_p$ and $\tilde{\omega} = \max(\Delta\bar{\omega}_p, \frac{\pi}{2})$.

Additional materials for HD 106906 fly-by simulations

Fig. 13 and 14 represents the distribution of the coordinates of the bodies in the simulations.

Fig. 15 and 16 describe the case where the two perturbers are bound. The coordinates of the bodies are drawn from the observational constraints with the same process that for the non-bound case, but we discarded the configurations where the eccentricity of the relative orbit is greater than 1. The resulting semi-major axis and eccentricity distributions are presented here, along with the effect of the fly-bys on the planet periastron, which is very similar to the non-bound case.

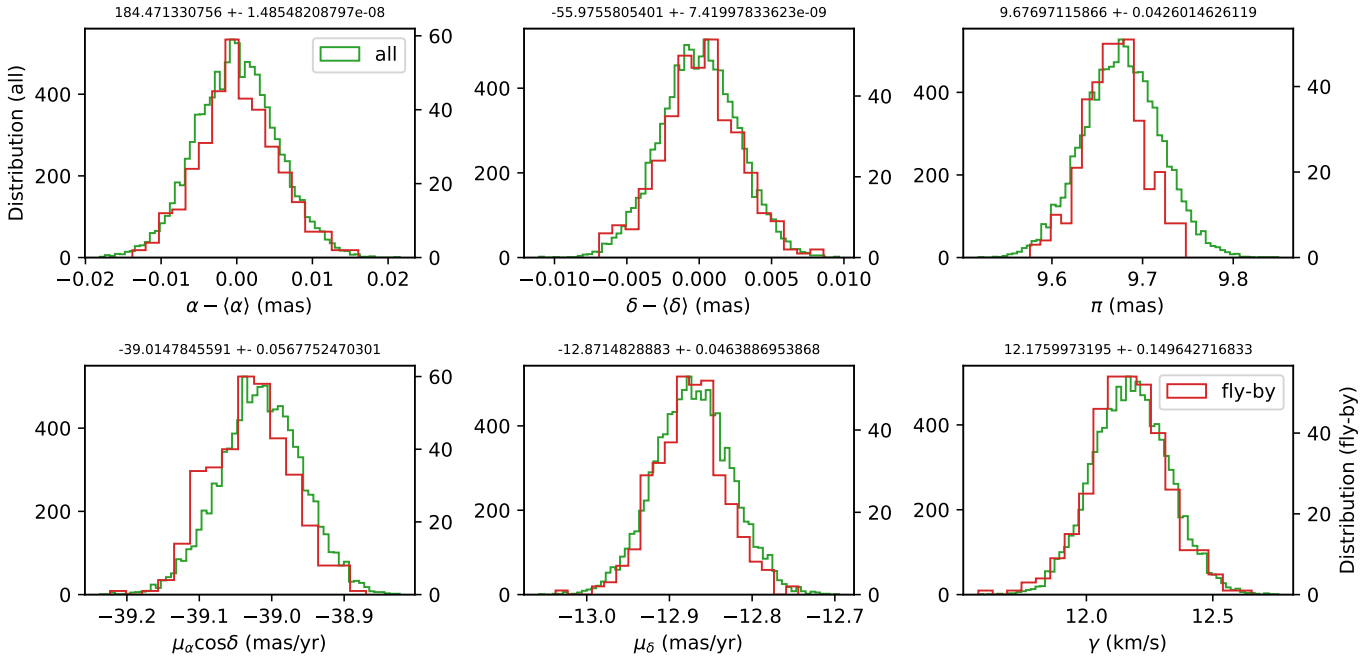

Fig. 13. Initial distribution (today) of HD 106906 coordinates and velocities for the 10,000 simulated cases (green), and for the 359 cases where a fly-by closer than 0.1 pc occurred (red).

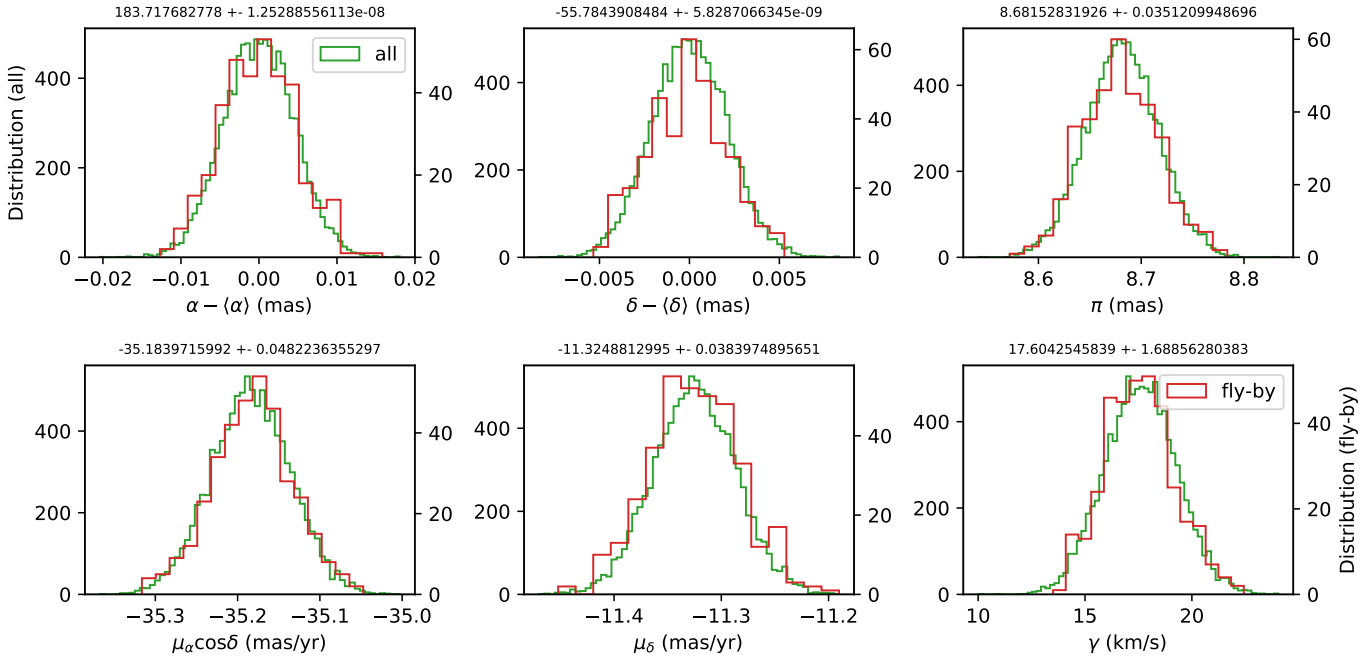

Fig. 14. Initial distribution (today) of HIP 59721 coordinates and velocities for the 10,000 simulated cases (green), and for the 359 cases where a fly-by closer than 0.1 pc occurred (red).

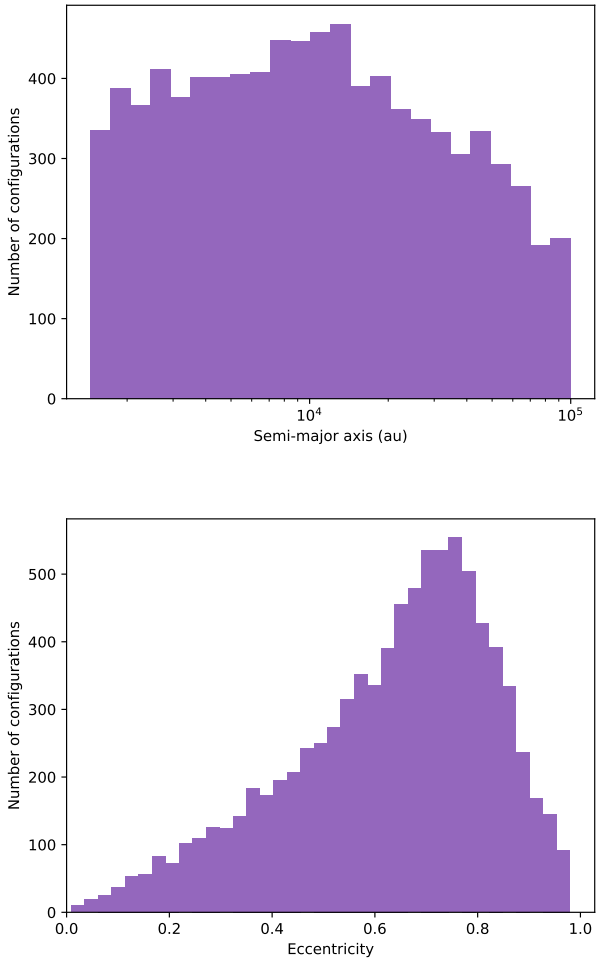

Fig. 15. Semi-major axis and eccentricity distributions for the relative orbit of the two perturbers HIP 59716 and HIP 59721, assuming they are bound.

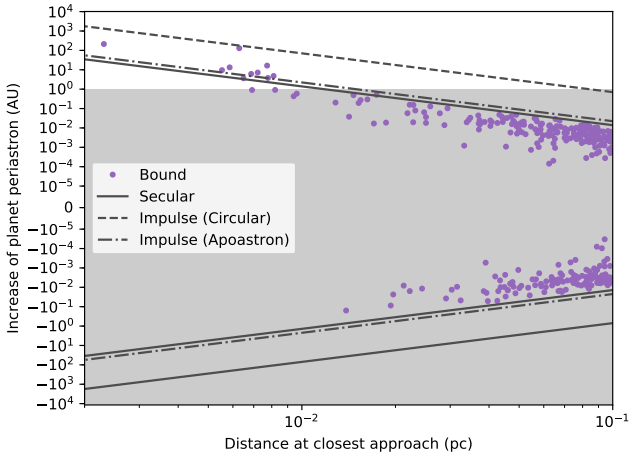

Fig. 16. Periastron increase with respect to the distance at closest approach, from N-body simulations (dots) and theoretical approaches (lines), for the closer fly-bys, for an initial planetary apoastron of 1,000 au, in the case where the two perturbers are bound.

Chapter 2

Orbital fitting of imaged companions

Contents

1 Levenberg-Marquardt algorithm (LM) 115

2 Markov Chain Monte Carlo (MCMC) 117

2.1 Overview 117

2.2 The Metropolis-Hastings algorithm for transition probability 117

2.3 Guiding the walk in multiple dimensions: the Gibbs sampler 119

2.4 Evaluation of the convergence 120

2.5 Beginning the walk 121

2.6 Building a consistent sample 121

3 Application to orbital fitting 122

3.1 Likelihood 122

3.2 Prior distributions 123

3.3 Choice of the MCMC parameters 125

3.4 Analysis 126

3.5 Comparison with alternative approaches for orbital fitting 129

4 Improvements 132

4.1 Modular organization 132

4.2 Convergence 133

4.3 Analysis of the chains 133

4.4 Handling systematic offsets between data sets 136

5 Application to the characterization of companions observed with SPHERE 137

5.1 HR 2562: A brown dwarf carving a debris disk 137

5.2 51 Eri: An eccentric giant planet in a hierarchical system 153

5.3 HD 206893: An intriguing brown dwarf 169

5.4 HD 100453: A stellar companion shaping a protoplanetary disk? 173

5.5 GJ 504: two different ages and a possible obliquity 177
6 Application to the astrometric binaries 181
6.1 TWA 22: good accordance with evolutionary model predictions 182
6.2 GJ 2060: underluminous and eccentric binary in the AB Dor moving group 182
6.3 AB Dor B: toward empirical isochrones for the AB Dor moving group 208
7 Combining absolute and relative astrometry 211

Constraining the orbital parameters of any detected companion (exoplanet, brown-dwarf) is an essential part in the characterization of extrasolar systems. Besides the description of the position and velocity of the bodies with respect to time, retrieving the orbital parameters enables the investigation of the past and future dynamical evolution of a system. High eccentricity, misalignment, mean-motion resonances, these features are the keys to decipher a system's history. Additionally, orbital fitting gives an estimate of the total mass or even, in some cases, the individual masses, which characterize the system and constrain the physical evolution of the bodies.

Theoretically, the relative position and velocity at a given time is enough to entirely retrieve the orbital elements. However, two main problems arise in real life, which complexify the orbital fitting processes.

First, we are not able to access the three-dimensional position and velocity at one epoch. In the case of direct imaging, an observation consists in the relative projected separation and position angle. Conventional direct imaging methods do not provide the instantaneous speed. Several epochs are therefore needed to suppress the degeneracy.

Second, all observations come with uncertainties. One can thus never obtain the orbital elements with an infinite precision, and the uncertainties must be propagated.

The propagation of the uncertainties of projected coordinates from several epochs give birth to a complex analytical problem. The uncertainties are often taken into account through the formalism of probability distribution. If the true value of the parameters of an orbit are $\boldsymbol{\theta}$, a measurement x_i with Gaussian uncertainty σ_i will have a probability of

$$p\left(x_i|\boldsymbol{\theta}\right) = \frac{1}{\sqrt{2\pi\sigma_i^2}} \exp\left(-\frac{\left(x_i - x\left(t_i, \boldsymbol{\theta}\right)\right)^2}{2\sigma_i^2}\right) \tag{2.1}$$

where $x(t_i, \boldsymbol{\theta})$ is the theoretical value, computed from the parameters $\boldsymbol{\theta}$. Moreover, we usually have some geometrical or physical constraints on the parameters, independently from the measured data. This probability $p(\boldsymbol{\theta})$ is called the *prior*.

From the probabilities of each of our measurements, we can introduce the *likelihood* of the parameters $\mathcal{L}(\boldsymbol{\theta})$:

$$\mathcal{L}(\boldsymbol{\theta}) = p\left((x_i)|\boldsymbol{\theta}\right) = \prod_i p(x_i|\boldsymbol{\theta}) \propto e^{-\frac{1}{2}\chi^2} \tag{2.2}$$

where $\chi^2 = \sum_i \frac{(x_i - x(t_i,\boldsymbol{\theta}))^2}{\sigma_i^2}$. The likelihood of $\boldsymbol{\theta}$ will be maximum when χ^2 is minimum. It can be noted that this expression of the χ^2 is valid only if the measurements (x_i) are independent, which we will assume in the rest of the chapter. If this is not the case, the correlations have to be taken into account through a covariance matrix. After the measurements, the Bayesian inference framework gives us the *posterior* probability of the parameters:

$$p\left(\boldsymbol{\theta}|(x_i)\right) = \frac{\mathcal{L}(\boldsymbol{\theta})p(\boldsymbol{\theta})}{p\left((x_i)\right)} \propto \mathcal{L}(\boldsymbol{\theta})p(\boldsymbol{\theta}) \quad . \tag{2.3}$$

Eventually, orbital fitting boils down to the characterization of the posterior probability distribution over the parameter space. Maximization of the likelihood will provide the best fit, maximization of the posterior will provide the most probable parameters, but the shape of the distribution is essential to evaluate the confidence interval. This, however, is not straightforward, especially when the number of parameters is high, and brute-force approach becomes impracticable.

Deriving a trustworthy estimate of the orbital elements despite these difficulties have been a central problem in the exoplanet field, whatever the detection techniques. Numerical approaches progressively superseded the first semi-analytical and geometrical approaches. In particular, Levenberg-Marquardt (LM) algorithms have been first used for orbital fitting, and Markov-Chain Monte Carlo (MCMC) algorithms have then been introduced in the early 2000s. MCMC is the approach I have adopted during my Ph.D, combined with a first LM minimization. In this chapter, I will first present the principles of the LM algorithm, before describing the basics of the MCMC approach. In this thesis, I used and improved an in-house code. I set out the statistical and implementation choices that have been adopted in Secs. 2, 3 and 4. Section 3.5 presents quickly the other codes available and a comparison of their approaches to ours. In sections 5 and 6, I present eight systems observed with SPHERE, for which I derived orbital elements estimates. I describe in particular in Sec. 6 three astrometric binaries that were characterized through their orbital fit, that gave an independent estimate of their dynamical masses. Finally, I introduce in Sec. 7 my work to take into account both absolute and relative astrometry in the orbital fitting procedure, a development that will be needed with the growing importance of the astrometric detection technique, that uses the projected motion of a host star on the skyplane.

1 Levenberg-Marquardt algorithm (LM)

To get a first estimate of the fitting of the parameters of a model, it is common to start with a "simple" minimization procedure, a local minimization of the χ^2 from a first guess. The *Levenberg-Marquardt algorithm*, also called Least-Squared Levenberg-Marquardt (LSLM), is specifically designed for local minimization of non-linear problems.

Let us consider χ^2 as a function of the parameters $\boldsymbol{\theta}$:

$$\chi^2(\boldsymbol{\theta}) = \sum_i \frac{\left(x_i - x(t_i, \boldsymbol{\theta})\right)^2}{\sigma_i^2} \quad . \tag{2.4}$$

Retrieving the best fit is equivalent to finding $\hat{\boldsymbol{\theta}}$ that verifies $\mathrm{d}\chi^2/\mathrm{d}\boldsymbol{\theta} \mid_{\hat{\boldsymbol{\theta}}} = 0$.

From a first guess $\boldsymbol{\theta_0}$, we are searching a step $\boldsymbol{\delta}$ such that $\hat{\boldsymbol{\theta}} = \boldsymbol{\theta_0} + \boldsymbol{\delta}$. Let $\boldsymbol{J_i}$ be the gradient vector of $x(t_i, .)$, evaluated in $\boldsymbol{\theta_0}$. When

$$\frac{\partial^2 x(t_i, \boldsymbol{\theta})}{\partial\theta_\alpha \partial\theta_\beta} \left(x_i - x(t_i, \boldsymbol{\theta})\right) \ll \frac{\partial x(t_i, \boldsymbol{\theta})}{\partial\theta_\alpha} \frac{\partial x(t_i, \boldsymbol{\theta})}{\partial\theta_\beta} \quad , \tag{2.5}$$

that is for linear models or in weakly correlated cases, we have

$$\chi^2(\boldsymbol{\theta_0}+\boldsymbol{\delta}) = \chi^2(\boldsymbol{\theta_0}) + \frac{\mathrm{d}\chi^2}{\mathrm{d}\boldsymbol{\theta}}\Big|_{\boldsymbol{\theta_0}}\boldsymbol{\delta} + \frac{1}{2}\,{}^t\boldsymbol{\delta}\,{}^t\frac{\mathrm{d}^2\chi^2}{\mathrm{d}\boldsymbol{\theta}^2}\Big|_{\boldsymbol{\theta_0}}\boldsymbol{\delta} + o(\delta^3) \tag{2.6}$$

$$= \chi^2(\boldsymbol{\theta_0}) - 2\sum_i \frac{x_i - x(t_i,\boldsymbol{\theta_0})}{\sigma_i^2}\boldsymbol{J_i}\boldsymbol{\delta} + {}^t\boldsymbol{\delta}\sum_{i,j}{}^t\boldsymbol{J_i}\boldsymbol{J_j}\boldsymbol{\delta} + o(\delta^3) \quad . \tag{2.7}$$

where ^{t} stands for the transpose. Moreover,

$$\frac{\mathrm{d}\chi^2}{\mathrm{d}\boldsymbol{\theta}}\Big|_{\hat{\boldsymbol{\theta}}} = \frac{\mathrm{d}\chi^2(\boldsymbol{\theta_0}+\boldsymbol{\delta})}{\mathrm{d}\boldsymbol{\delta}}\Big|_{\hat{\boldsymbol{\theta}}} = 0 \tag{2.8}$$

Thus, at first order, $\boldsymbol{\delta}$ must verify

$$\sum_{i,j}{}^t\boldsymbol{J_i}\boldsymbol{J_j}\boldsymbol{\delta} = \sum_i \frac{x_i - x(t_i,\boldsymbol{\theta_0})}{\sigma_i^2}\,{}^t\boldsymbol{J_i} \quad . \tag{2.9}$$

This is a set of linear equations, which can be solved for $\boldsymbol{\delta}$. To make up for the potential badness of the approximations, Levenberg suggested to replace this equation by a damped version:

$$(\sum_{i,j}{}^t\boldsymbol{J_i}\boldsymbol{J_j} + \lambda\boldsymbol{I})\boldsymbol{\delta} = \sum_i \frac{x_i - x(t_i,\boldsymbol{\theta_0})}{\sigma_i^2}\,{}^t\boldsymbol{J_i} \tag{2.10}$$

where $\boldsymbol{I}$ is the identity matrix and λ the damping factor, which is adjusted at each iteration. If the convergence is quick, then λ is decreased, and it is increased if the convergence is slow.

After the desired convergence is reached (condition on the closeness of successive estimates of $\chi^2(\hat{\boldsymbol{\theta}})$ for example), we obtain a good estimate of $\hat{\boldsymbol{\theta}}$, the best-fit parameters. However, it is crucial to obtain an interval of confidence around the best-fit parameters to evaluate the reliability of the results. From the output of the Levenberg-Marquardt procedure, the interval $\boldsymbol{d\theta}$ is such as $\chi^2(\hat{\boldsymbol{\theta}}+\boldsymbol{d\theta}) - \chi^2(\hat{\boldsymbol{\theta}}) = 1$. That is

$$\frac{1}{2}\boldsymbol{d\theta}\mathcal{H}\boldsymbol{d\theta} = 1 \tag{2.11}$$

where $\mathcal{H}$ is the Hessian matrix of χ^2 with respect to the parameters, evaluated in $\hat{\boldsymbol{\theta}}$. As the Hessian matrix is definite positive ($\hat{\boldsymbol{\theta}}$ is a minimum), then it is diagonalizable with change of basis matrix V (eigenvectors matrix) and diagonal matrix D. The interval of confidence is finally given by

$$\boldsymbol{d\theta} = V\begin{pmatrix}\sqrt{2/D_{11}}\\ \dots \\ \sqrt{2/D_{dd}}\end{pmatrix} \approx \begin{pmatrix}\sqrt{2\mathcal{H}^{-1}_{11}}\\ \dots \\ \sqrt{2\mathcal{H}^{-1}_{dd}}\end{pmatrix} \tag{2.12}$$

where d is the dimension of the parameters space. Nevertheless, this interval is not robust to correlations and does not grasp the potential peculiarities of the final probability distribution (asymmetries, multi-modes...).

2 Markov Chain Monte Carlo (MCMC)

Markov Chain Monte Carlo procedures are a powerful Bayesian tool to characterize the likelihood and fit the parameters of a model and their uncertainties. It is particularly well adapted for high dimension parameters space and monomodal likelihood. The following introduction is based on Gilks et al. (1996), Gelman et al. (2003) and Ford (2005). The particular setup described here has been implemented at IPAG in a code designed by Pr. Beust, described briefly in Chauvin et al. (2012), and that I contributed to expand. An overview of the procedure is presented on Fig. 2.1.

2.1 Overview

A procedure is referred to as *Monte-Carlo* when it relies on repeated random sampling to obtain numerical results. This technique is widely used in all fields of science, and appeared at the beginning of the computer era. It is named after a Monaco district known for the gambling. Monte-Carlo procedures comprise various types of approaches, especially regarding the specificity of the random choices. Some procedures adopt a sampling where each draw is independent from the others. This strategy is often chosen for the computation of integrals.

On the other hand, orbital fitting requires the computation of the relative likelihood of parameters in the neighborhood of its peak. Markov chains are well adapted to this problem. A *Markov chain* is a stochastic model describing a sequence of possible events in which the probability of each event depends only on the state attained in the previous event. Thus, the random choice of a point in the parameters space is not independent of the previous draw, so that the sampling can be thought of as a chain. Given a proper sampling, a Markov chain will eventually converge towards the stationary distribution it probes. A proper sampling is guaranteed by reversibility, irreducibility and aperiodicity. *Reversibility* ensures that a probability of being in a state $\boldsymbol{\theta}$ and going to a state $\boldsymbol{\theta}'$ from $\boldsymbol{\theta}$ is equal to being in a state $\boldsymbol{\theta}'$ and going from $\boldsymbol{\theta}'$ to $\boldsymbol{\theta}$. In other words, if state $\boldsymbol{\theta}'$ is twice more probable than state $\boldsymbol{\theta}$, the probability of going from $\boldsymbol{\theta}$ to $\boldsymbol{\theta}'$ will be twice the probability of going from $\boldsymbol{\theta}'$ to $\boldsymbol{\theta}$. *Irreducibility* ensures it is possible for the chain to reach every state with non-zero probability from any initial state.

2.2 The Metropolis-Hastings algorithm for transition probability

Such Markov chains can be built using the *Metropolis-Hastings* algorithm. In this formalism, the probability of a transition from a state $\boldsymbol{\theta}$ (corresponding to a vector of parameters) to an other $\boldsymbol{\theta}'$ is the probability $q(\boldsymbol{\theta}'|\boldsymbol{\theta})$ to consider $\boldsymbol{\theta}'$ from $\boldsymbol{\theta}$ times the probability $\alpha(\boldsymbol{\theta}'|\boldsymbol{\theta})$ of accepting this trial. The Metropolis-Hastings algorithm acceptance probability is

$$\alpha(\boldsymbol{\theta}'|\boldsymbol{\theta}) = \min\left(\frac{q(\boldsymbol{\theta}|\boldsymbol{\theta}')p(\boldsymbol{\theta}'|(x_i))}{q(\boldsymbol{\theta}'|\boldsymbol{\theta})p(\boldsymbol{\theta}|(x_i))}, 1\right) \tag{2.13}$$

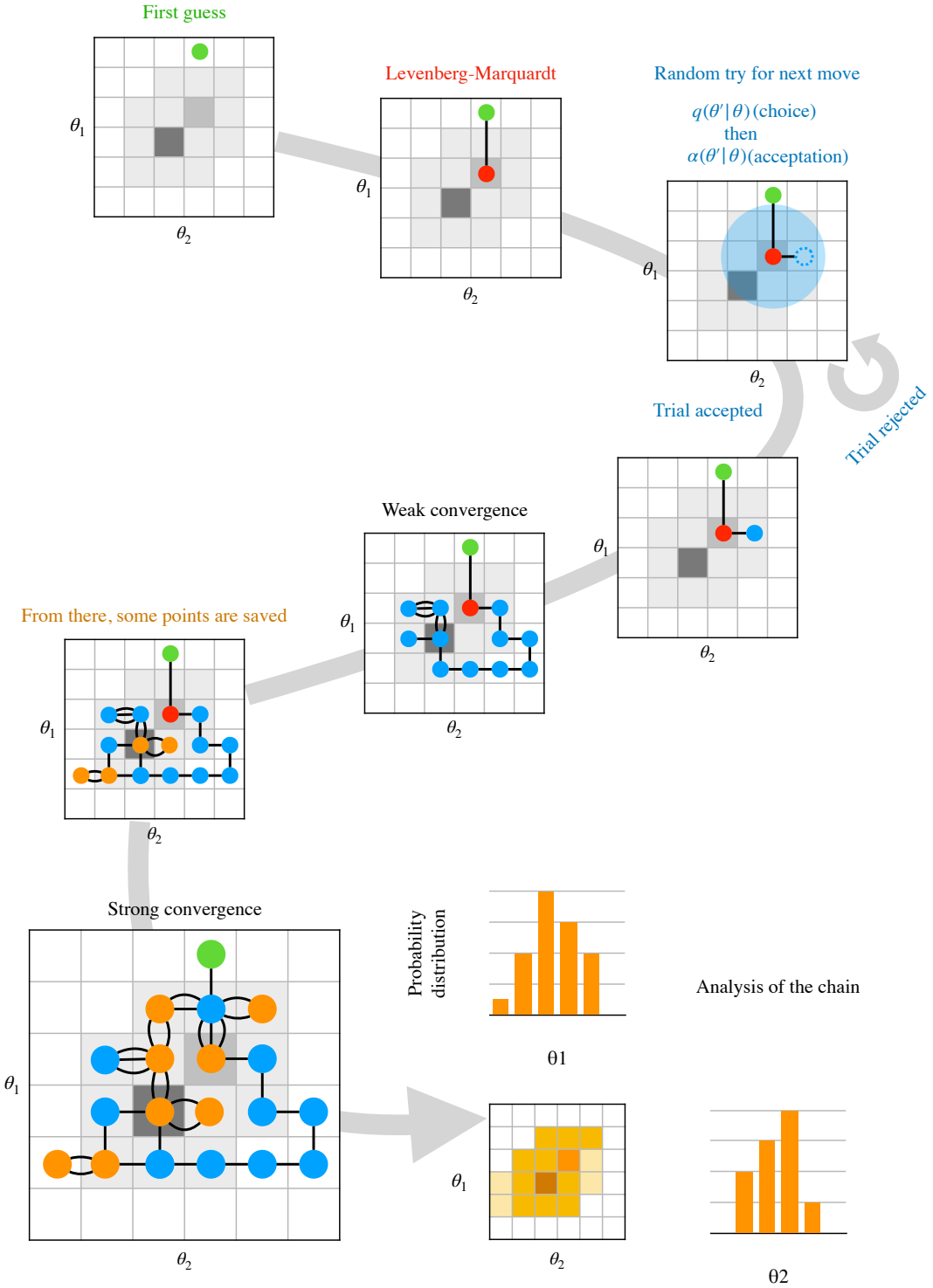

Figure 2.1 – Schematic of the procedure to retrieve the probability distribution of the parameters θ_1 and θ_2. The maps represent the 2D histogram of the χ^2. The Gibbs sampler prevents diagonal moves. The discretization is for better readability and is not a feature of the code.

where $p(\boldsymbol{\theta}|(x_i))$ is the probability of state $\boldsymbol{\theta}$ given the set of data (x_i). In that case, whatever the choice of $q(\boldsymbol{\theta}'|\boldsymbol{\theta})$, the Markov chain is reversible.

In our case, we pre-select each transition $\boldsymbol{\theta} \to \boldsymbol{\theta}'$ with a normal distribution centered on the state $\boldsymbol{\theta}$, with a fixed deviation independent from $\boldsymbol{\theta}$. It follows that $q(\boldsymbol{\theta}'|\boldsymbol{\theta}) = q(\boldsymbol{\theta}|\boldsymbol{\theta}')$. Thus, the acceptance probability boils down to 1 when $p(\boldsymbol{\theta}'|(x_i)) > p(\boldsymbol{\theta}|(x_i))$, and $p(\boldsymbol{\theta}'|(x_i))/p(\boldsymbol{\theta}|(x_i))$ when $p(\boldsymbol{\theta}'|(x_i)) < p(\boldsymbol{\theta}|(x_i))$.

This method has the advantage of requiring only the probability ratios. Thus, the normalization that appears in the likelihood, in the form of a tedious integral, is not needed, with counterpart that we will retrieve only a relative probability distribution.

2.3 Guiding the walk in multiple dimensions: the Gibbs sampler

The choice of $q(\boldsymbol{\theta}'|\boldsymbol{\theta})$ to select a tentative transition is a delicate issue. A common choice is a Gaussian distribution centered around $\boldsymbol{\theta}$, but there remains the important choices of the dispersion, that is the scales and correlations between each parameters.

If the trial states are chosen with a too large dispersion then a large fraction of the trial states will be rejected, causing the chain to remain at each state for several trials and to converge very slowly. If the trial states are chosen with a too small dispersion, then the small step size will cause the chain to behave like a random walk. Monitoring the fraction of trial states that are accepted is one way to verify that the scale chosen for $q(\boldsymbol{\theta}'|\boldsymbol{\theta})$ is not too inefficient. Optimal values for the acceptance rate have been estimated for Gaussian posterior distributions at about 0.44 when $\boldsymbol{\theta}$ has one dimension, 0.23 otherwise.

Handling multi-dimensionality requires deeper consideration because of the possible correlations between the parameters. A simple method to tackle the issue is called *Gibbs sampling*. In this sampling, a step corresponds to the successive evolution of each parameter. When updating the parameter j, a tentative parameter is proposed by the candidate transition probability function $q(\theta'_j|\theta_j)$, then the move is accepted with probability $\alpha(\boldsymbol{\theta}'|\boldsymbol{\theta})$, where $\boldsymbol{\theta}$ and $\boldsymbol{\theta}'$ are the current parameters, that is the new ones from ranks 1 to $j-1$, and the old ones from ranks $j+1$ to d, where d is the dimension of the parameters space. To remove any possible bias regarding the order of the parameters, at each step the parameters ranks are randomly permuted before the evolution.

However, roaming the parameters space along the direction of each parameters is not necessarily the most efficient way, because of the possible correlations between parameters. Thus, after a significant evolution of the walk, we compute the covariance matrix and derive orthonormal eigenvectors. Then, we travel the parameters space along the directions of the eigenvectors.

Choosing the scale of the transition function is easy within the Gibbs sampler, because each parameters (or combination of parameters) evolves separately. In our algorithm, before the true launch of the Markov chains, tentative steps are made in order to tune the value of the scale β. From an initial guess, β is updated until the acceptance rate on each dimension is 0.44 with a 10% precision. The update of β is scaled on the ratio between the current and expected acceptance rates, and the

frequency of update is decreasing following the progress of the convergence. The detailed procedure is described in Ford (2006).

2.4 Evaluation of the convergence

Deciding when the walk should stop is the most challenging part of the procedure, as we have to determine when the chains are representative of the true probability distribution (or, equivalently, have converged). A common approach is to use Gelman-Rubin convergence diagnosis (Gelman et al. 1992; Ford 2006). Alternative criteria exist, using for example the autocorrelation time (see `emcee`, Sec. 3.5.1). The convergence diagnosis depends strongly on the overall set-up (numbers of chains, sampler...). In the Gelman-Rubin framework, several Markov chains are started. The parallel computation of independent chains allows both a better sampling of the parameter space and the evaluation of the convergence by comparing the state of the different chains. The Gelman-Rubin statistics is based on the computation of the variance of the parameters in a given chain and in all the chains.

A first criterion that is computed is $\hat{R}$, the factor by which the scale of the estimate of the distribution could be reduced by continuing to calculate longer Markov chains. For a given parameter, It corresponds roughly to the ratio between an unbiased estimator of the dispersion and the average dispersion over all chains. For a parameter θ_j, if we consider N_c chains of lengths L_c, it writes

$$\hat{R}(\theta_j) = \sqrt{\frac{\hat{\text{var}}(\theta_j)}{W(\theta_j)}} = \sqrt{1 + \frac{1}{L_c}(\frac{B(\theta_j)}{W(\theta_j)} - 1)} \tag{2.14}$$

where $\hat{\text{var}}(\theta_j)$ is an unbiased estimator of the variance, $W(\theta_j)$ the average of the variances over the chains, and $B(\theta_j)$ is L_c times the variance of the means. As the Markov chains approach convergence, $\hat{R}(\theta_j)$ approaches 1 from above. In our algorithm, we launch ten chains and set two thresholds: when all the $\hat{R}$ are below 1.1 (weak) and when the $\hat{R}$ are below 1.01 (strong).

On the other hand, a second criterion is $\hat{T}$, the estimate of the effective number of independent draws. It is roughly the number of draws $N_c \times L_c$ weighted by the ratio between an unbiased estimator of the variance and the variance of the averages over all chains. It writes

$$\hat{T}(\theta_j) = L_c N_c \min\left(\frac{\hat{\text{var}}(\theta_j)}{B(\theta_j)}, 1\right) \quad . \tag{2.15}$$

A high $\hat{T}$ ensures that our distribution is not biased by auto-correlation. In our algorithm, the weak threshold is set to 100 and the strong to $1,000$.

Thus, along the walk of the Markov chains, we repeatedly compute the $\hat{R}$ and $\hat{T}$ to evaluate the convergence (see Fig. 2.2). To avoid chance good values, when the criteria first pass the threshold, we increase the Markov chains of 1, 2, 3, 4 and 5% successively and evaluate the criteria each time. If they pass again the test, then the convergence is likely (at least we could not disprove it).

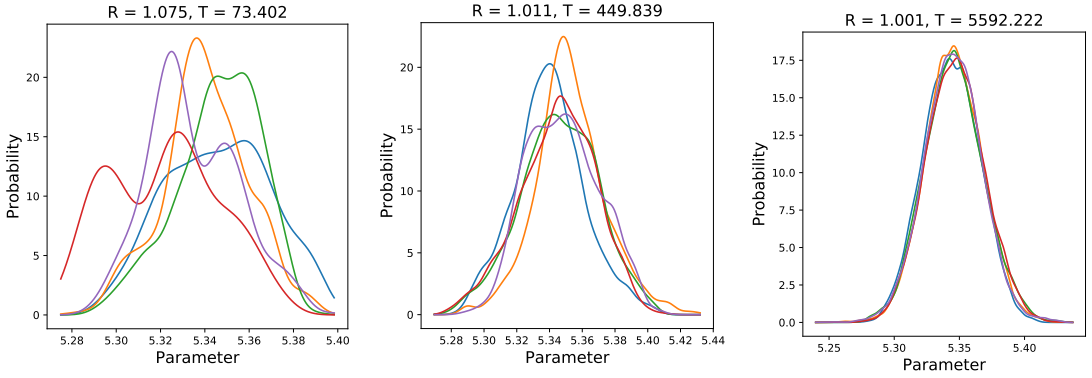

Figure 2.2 – Example of the probability distributions function of 5 chains that respectively have not converged, have weakly converged and strongly converged, according to the Gelman-Rubin statistics.

2.5 Beginning the walk

The initial points in the Markov chains are theoretically irrelevant to the final estimated probability distributions, but are in fact important regarding two aspects.

First, though the MCMC procedure is more global than the Levenberg-Marquardt algorithm and can potentially retrieve a multimodal distribution, it will in practice not be the case if the peaks are separated by a zone with very small probability. Thus, the beginning value should be comprised within a reasonably probable zone around the more probable part of the parameters space.

Moreover, the convergence may be extremely slowed by a chain struggling to reach the probable zone. This first part of the chain is often discarded by default in the end (a process called *burning*), for storage issue, as it brings only bias to the estimated probability distribution. In our code, the parts of the chains before the weak convergence threshold has been reached are discarded.

From this point, two approaches are possible: sampling the beginning points randomly through the parameters space, or beginning the walk already in the identified probable zone. The first approach decreases the risk of incomplete sampling, the second optimizes the convergence time. In our algorithm, we choose the second version, as there are rarely several distinct local maxima in the likelihood function in orbital fitting problems. Indeed, the problem is not strongly degerate if the constraints are good (precise astrometry, long baseline), and the walks explore all the parameters space if the problem is underconstrained. To locate the probable part of the parameters space, the parameters are roughly estimated manually, with tentative trials. Then, when a reasonable χ^2 is obtained, a Levenberg-Marquardt procedure is launched to locate the exact position of the best fit. All Markov chains are then started from this position (see Fig. 2.3).

2.6 Building a consistent sample

A more practical problem is that the Markov chains can grow excessively long before convergence is reached. Storing the entire chain might be computationally costly, and is not needed to retrieve the desired probability distribution. Indeed, the nature

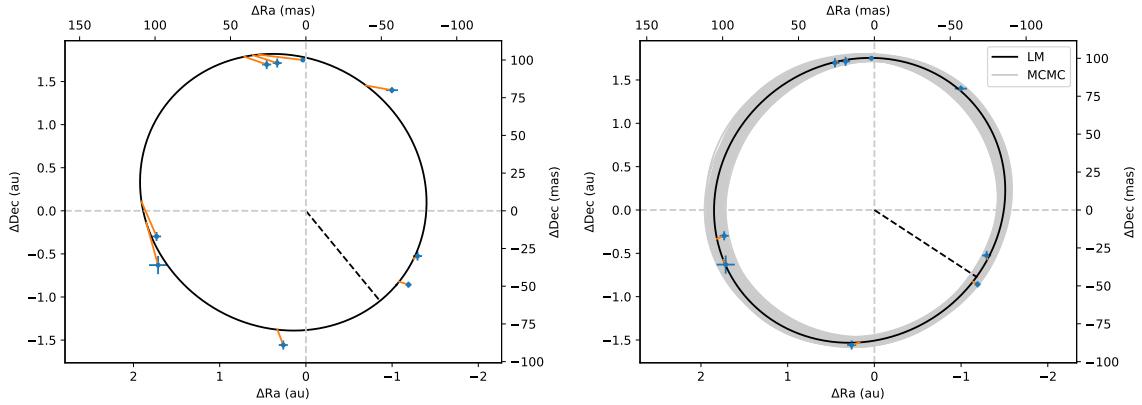

Figure 2.3 – Example of first guess (left), Levenberg-Marquart and MCMC procedures (right) for orbital fitting.

of the Markov chain creates a strong auto-correlation between successive values of a parameter, so that the complete chain is strongly redundant. The position at a given time is slowly forgotten as the chain pursue its random walk, but it may take hundreds of steps before the autocorrelation becomes negligible. Moreover, the Markov chain only needs the latest parameters to run.

Along the walks, we will store a given number $N_{\rm mod}$ of random positions of the walks. This number should be large enough to correctly sampled the probability distribution throughout all the dimensions of the parameters space. First, nothing is stored before the weak convergence threshold is reached. Then, the points are stored with a given probability, computed to roughly optimized the sampling so that enough points are sampled before the strong convergence is reached. If nevertheless $N_{\rm mod}$ points are already stored before the end of the walk, then the sampling continue and a new point replaces a randomly selected previous point.

If the sampling has the advantage of preventing a useless massive storage, it has the inconvenient of meddling the sequence of the Markov chains, which prevents some converging diagnosis to be performed afterwards. However, we can be careful not to blend together the Markov chains to allow for comparisons between their distributions (see Sec. 4.2).

3 Application to orbital fitting

3.1 Likelihood

Characterizing the likelihood over the parameters space is a tedious process when the dimension is high, unless a Monte Carlo approach is adopted. Orbital fitting with direct imaging involve 6 parameters in the simplest case (only astrometry), 9 if radial velocity measurements are included, 11 if we fit absolute astrometry, and even more if we account for additional systematic offsets between data-sets. Moreover, there are rarely very distinct solutions to orbital fitting problems. MCMC is thus a natural approach to tackle the issue.

The model that we will be fitting here is a pure Keplerian motion, and the

parameters are the orbital elements. The simplest are the period P, the eccentricity e, the longitude of the ascending node Ω, the inclination i, the argument of periastron ω and the time of periastron passage t_p (for precise definition of these quantities, refer to the introduction). Fitting these 6 elements requires to know the total mass of the system (to retrieve the semi-major axis a) and its distance (to convert arcseconds in astronomical units). To retrieve the total mass, a 7 parameters description can be chosen, by fitting independently both a and P. This dynamical mass can then be used as an input in the evolutionary models (see Sec. 6).

$$\boldsymbol{\theta} = (P, e, \Omega, i, \omega, t_p) \tag{2.16}$$

From the six/seven orbital elements $\boldsymbol{\theta}$, we can compute the prediction of the model for each epoch t_i in terms of projected positions $x(t_i, \boldsymbol{\theta})$ and $y(t_i, \boldsymbol{\theta})$. The only difficulty is to solve the Kepler equation $2\pi(t_i - t_p)/P = u - e\sin(u)$ to retrieve the eccentric anomaly u at the time t_i as a function of t_p, P and e. The procedure to solve the equation is described in the Appendix. First, the predicted positions are computed in the orbital plane (X, Y):

$$X = a(\cos(u) - e) \tag{2.17}$$
$$Y = a\sqrt{1 - e^2}\sin(u) \tag{2.18}$$

In the skyplane, the coordinates of the unit vectors of the orbital plane are given by:

$$\boldsymbol{u_X} = \begin{pmatrix} \cos^2(\frac{i}{2})\cos(\omega + \Omega) + \sin^2(\frac{i}{2})\cos(\omega - \Omega) \\ \cos^2(\frac{i}{2})\sin(\omega + \Omega) - \sin^2(\frac{i}{2})\sin(\omega - \Omega) \end{pmatrix} \tag{2.19}$$
$$\boldsymbol{u_Y} = \begin{pmatrix} -\cos^2(\frac{i}{2})\sin(\omega + \Omega) - \sin^2(\frac{i}{2})\sin(\omega - \Omega) \\ \cos^2(\frac{i}{2})\cos(\omega + \Omega) - \sin^2(\frac{i}{2})\cos(\omega - \Omega) \end{pmatrix} \tag{2.20}$$

Finally, the predicted positions on the skyplane are given by

$$\begin{pmatrix} x(t_i, \boldsymbol{\theta}) \\ y(t_i, \boldsymbol{\theta}) \end{pmatrix} = X\boldsymbol{u_X} + Y\boldsymbol{u_Y} \tag{2.21}$$

An example of representation of an orbit in the two planes is drawn on Fig. 2.4.

The χ^2 is then naturally

$$\chi^2 = \sum_i \frac{(x_i - x(t_i, \boldsymbol{\theta}))^2}{\sigma_{x,i}^2} + \sum_i \frac{(y_i - y(t_i, \boldsymbol{\theta}))^2}{\sigma_{y,i}^2} \tag{2.22}$$

3.2 Prior distributions

Before any observations, we have an a priori knowledge on the orbital elements probability distribution.

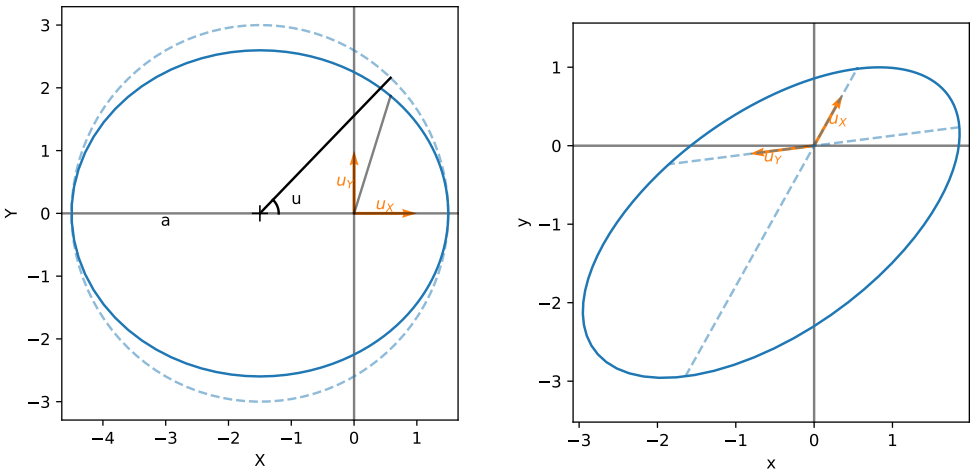

(a) Orbital plane (b) Skyplane

Figure 2.4 – Orbit in the orbital plane and projected on the skyplane. The orbital elements are: $a = 3$, $e = 0.5$, $i = 60°$, $\Omega = 30°$, and $\omega = 50°$.

First, there is no preferred orbital plane, so that the direction of the angular momentum vector $\boldsymbol{C}$ is uniformly distributed. This direction is given by the angles i and Ω, with the formula

$$\boldsymbol{C} = C \begin{pmatrix} \sin(i)\sin(\Omega) \\ \sin(i)\cos(\Omega) \\ \cos(i) \end{pmatrix} \tag{2.23}$$

i and Ω are equivalent to the angles in the spherical coordinates description, and the dimensionless surface element at constant radius is $dS = \sin(i)\,\mathrm{d}i\,\mathrm{d}\Omega$ in this framework. The probability of these angles in the case of a uniform distribution of direction of $\boldsymbol{C}$ is thus proportional to $\sin(i)$.

Once the orbital plane is defined, the direction of the eccentric vector (or equivalently of the periastron) is also uniformly distributed, so that the probability of ω is constant.

The probability of the mean anomaly $M = 2\pi(t - t_p)/P$ is also constant, as there is no preferred time of periastron passage in the Universe.

The probability of the eccentricity e is supposed constant. Few information is known on the distribution of eccentricities in planetary systems, especially for planets on wide orbit that are not currently well monitored by radial velocity. On the other hand, the distribution of eccentricity in binary stars is more or less consistent with a flat prior (see Introduction).

Finally, the probability of P is set to $1/P$ to ensure scale invariance ($1/a$ if a is also a parameter). This law is sometimes referred to as Opik's law (Öpik 1924). Scale invariance is a purely physical consequence of the equation of motion, which states that there are no preferred scale for an orbit. Of course, additional considerations (size and composition of protoplanetary disks, ...) qualifies this assumption for planetary systems. But here again, the distribution of periods and semi-major axes

is not satisfyingly constrained by the observations. For binary systems however, Opik's law is a valid approximation (see Introduction).

The choice of prior is always partially arbitrary, as it depends on the information we choose to take into account for our problem (geometry, addition of theoretical considerations on energy and momentum, observed distributions...). Other possibilities have been adopted in the literature (Blunt et al. 2017; O'Neil et al. 2018).

Theoretically, some of these prior probabilities are ill-defined, for their integration over the parameters space is improper, which is not acceptable for a probability distribution. It is in particular the case for the period, as the integration spans until infinity. However, most of the times, the likelihood function is sufficiently constraining to ensure the good definition of the posterior probability. If it is not the case, an upper bound is manually defined.

3.3 Choice of the MCMC parameters

The six parameters and their prior distributions introduced above are the natural description of the orbit and are relevant to study its dynamical evolution, but they are not optimal regarding their definition properties and their correlations.

The properties of the angles (definition modulo 2π) are difficult to handle in a random walk. To solve this issue, we use instead their cos and sin, properly defined between -1 and 1. For the inclination, defined from 0 to 180°, the sine is enough if we consider $\sin(i/2)$.

Moreover, for any orbital solution, the couples (Ω, ω) and $(\Omega + \pi, \omega + \pi)$ yield the same astrometric data, as both parameters appear only as $\omega + \Omega$ and $\omega - \Omega$ in Eqs. 2.19 and 2.20. This can be understood geometrically: orbits with (Ω, ω) and $(\Omega + \pi, \omega + \pi)$ are symmetric with respect to the skyplane, so that their projection is identical. Thus, the algorithm fits $\omega + \Omega$ and $\omega - \Omega$, which are not affected by the degeneracy. To conclude on the choice of (Ω, ω) requires to determine if the planet moves away from us or toward us. This information can be obtained with one measure of the relative radial velocity.

On the other hand, the argument of periastron is ill-defined when e is null. Thus, some parameters have a factor e to prevent unnecessary wandering in the ω space at low eccentricity. Also, the longitude of node is ill-defined when the inclination is null. Similarly, a factor $\sin(i/2)$ will be added when necessary.

Finally, it has been found preferable in some cases to sample $\sqrt{1-e^2}$ instead of e, to avoid the divergences associated with eccentricities greater than 1.

All in all, tests to optimize the convergences have been performed with the previous constraints, and the following sets of parameters have been chosen:

$$\boldsymbol{\theta} = \left(\frac{1}{P}\cos(\omega + \Omega + \nu), \frac{1}{P}\sin(\omega + \Omega + \nu), \frac{e\cos(\omega + \Omega)}{\sqrt{1-e^2}}, \frac{e\sin(\omega + \Omega)}{\sqrt{1-e^2}}, \right.$$
$$\left. \sin\left(\frac{i}{2}\right)\cos(\omega - \Omega)(1-e^2)^{\frac{1}{4}}, \sin\left(\frac{i}{2}\right)\sin(\omega - \Omega)(1-e^2)^{\frac{1}{4}} \right) \quad . \tag{2.24}$$

where ν is the true anomaly.

The prior distributions become then more complicated. In fact, the individual priors are not necessary in order to run an MCMC, only the ratio of the total probabilities of two events are needed, to compute the acceptance probability. To retrieve this total probability ratio, we compute the Jacobian J of the new parameters expressed as functions of the orbital elements. We get

$$p_{\text{prior}}\left((P, e, \Omega, i, \omega, t_p)\right) \propto \frac{\sin(i)}{P} \tag{2.25}$$

$$p_{\text{prior}}(\boldsymbol{\theta}) \propto \frac{P}{\sin(i)}|J| \propto \frac{e\left(1+e\cos(\theta)\right)^2}{\left(1-e^2\right)^3 P^2} \tag{2.26}$$

3.4 Analysis

When the Markov chains have converged (see Sec. 2.4), we get the consistent sample that have been built along the walks (see Sec. 2.6). It consists here in a set of 1,000,000 different vectors of parameters $\boldsymbol{\theta}$, that have been converted into orbital elements. From there, multiple approaches can be used to visualized and interpret the result of the orbital fitting.

The following approaches were coded by Prof. Beust in the GreG language, that is part of the GILDAS working group software developed by IPAG and IRAM in Grenoble. As part of this PhD, I have redeveloped and enhanced them in Python to provide a better flexibility and portability.

3.4.1 Corner plot

Naturally, the first approach to visualize the output of the MCMC procedure is to compute independent probability distribution of each of the orbital elements. The general properties of each distribution are then easily accessible: shape (one peak or multimodal), mean, median, interval of confidence, lower and upper boundaries... To get a more complete view of the overall probability distribution of the parameters, the correlations can be visualized with two-dimension histograms. We indicated the best fit in each plot, and the shortest 68 % interval of confidence around the peak (see Sec. 4.3) in the individual probability distribution.

Correlations between the different dimensions of the Markov chains walks are not necessarily prejudicial, but will slow down the convergence of the chains. Complex correlation patterns can also prevent part of the parameters space to be visited. However, depending on the measurements and orbital configurations, the correlations between the orbital elements may not be easily overcame (semi-major axis correlated to eccentricity for insufficient orbital coverage, eccentricity to inclination...).

An example of a corner plot is represented on Fig. 2.5. It corresponds to a well-sampled orbit, so that the distributions all exhibit a clear peak of maximum probability. The longitude of node and argument of periastron both exhibit two distinct peaks separated by 180°, because of the degeneracy introduced in the previous subsection.

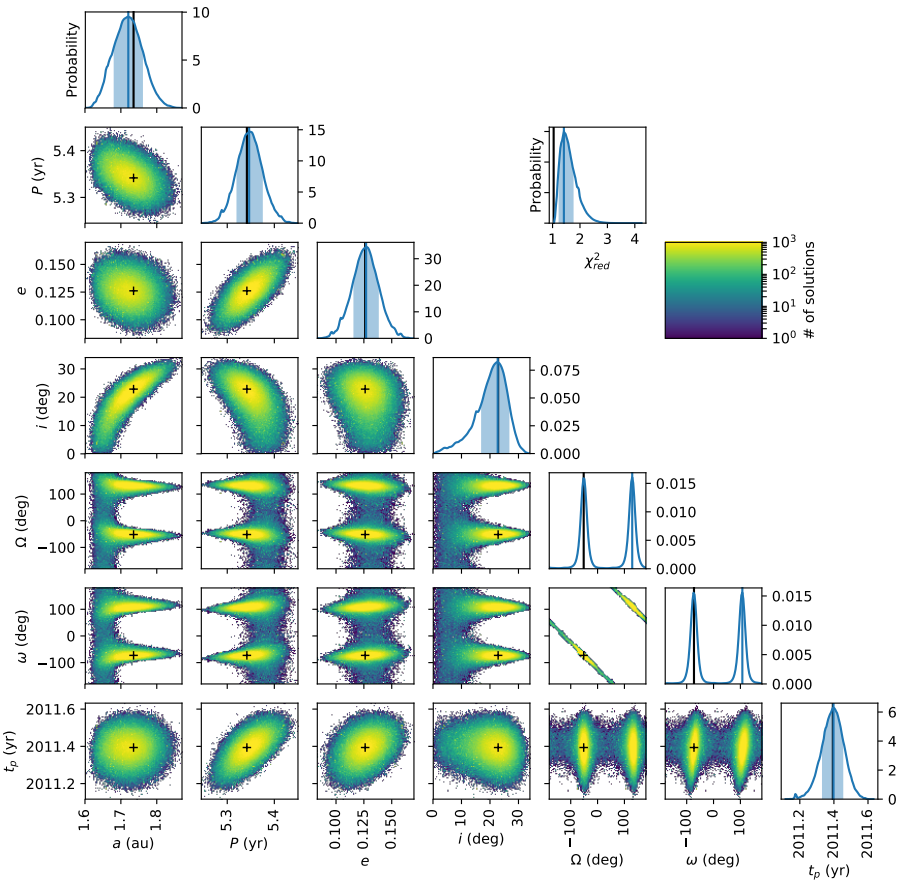

Figure 2.5 – Example of a corner plot presenting the results of a MCMC orbital fitting procedure with 7 orbital parameters. The black lines and crosses correspond to the results of the LM procedure (best fit). The blue shade corresponds to the 68 % interval around the peak.

Evaluating the absolute goodness of a fit is not straightforward. The χ^2 is used to compare two solutions within the same model, and is used in particular to guide the walks of the Markov chains. However, the χ^2 is an indicator that increases with the number of measurements and decreases with the number of parameters. Thus, a common criterion to evaluate the goodness of an orbital fit is the so-called reduced χ^2:

$$\chi^2_{\rm red} = \frac{1}{N-d}\chi^2 \quad . \tag{2.27}$$

If the model is linear with respect to the parameters, $\chi^2_{\rm red}$ is expected to be 1. A value inferior to 1 suggests an overestimation of the errorbars, and superior to 1 indicates a relatively bad fit (which remains acceptable below 2 or 3). In our case however, the Keplerian model is not linear nor in most of the orbital elements, neither on the parameters chosen for the MCMC. We still decide to adopt this criterion for

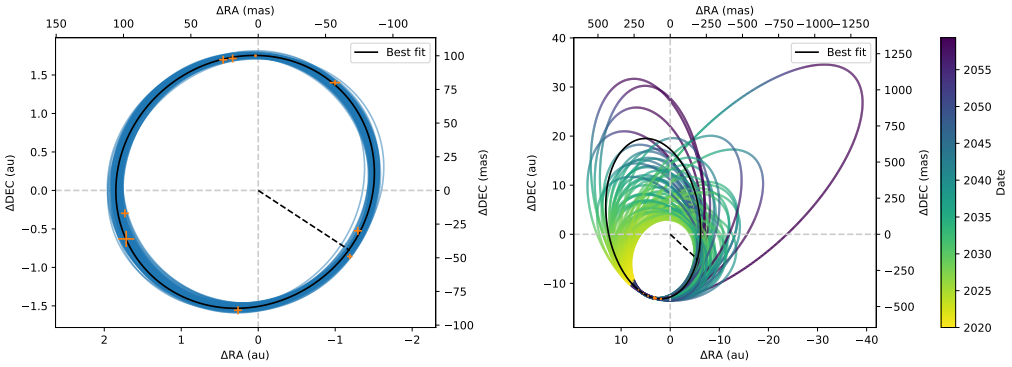

Figure 2.6 – Example of two representations on the sky plane of 100 orbits (colored) from an MCMC orbital fitting procedure. The black orbit corresponds to the results of the LM procedure (best fit).

it allows comparing the different solutions, and it still gives an order of magnitude of the offset between the observations and the predictions of the fit relative to the uncertainties.

3.4.2 Representation on the sky plane and temporal evolution

Eventually, the best way to evaluate the goodness of a fit is to draw a representative sample of solutions directly over the observations on the sky plane. It is essential to see the relative consistence of all the observations, evaluate possible problems with the measurements (underestimated errorbars, systematic offsets...), have an overview of the possible orbits and plan the future observations.

An example of representation on the sky plane is drawn on Fig. 2.6. To give an idea of the diversity of the solutions, a hundred solutions, selected randomly among the final distribution of the MCMC, are plotted along the best fit. The temporal evolution can be suggested by a color scale.

However, one has to remember that the goodness of the fit cannot be obtained simply by looking at the matching between the observations and the solutions of the fit on the sky plane. Indeed, the temporal aspect is hidden on the figure, so that a fitted solution that matches perfectly a set of astrometric measurements on the sky plane might not be in phase with the observations epochs.

In order to evaluate the consistency of the observations with the fitted solutions, the temporal evolution of different observational quantities are often represented. An example of such representation is drawn on Fig. 2.7.

The evolution of the position angle (PA) measures the orbital coverage, and get a rough estimate of the period. On the other hand, the absolute orientation of the field is usually inferred from the observations of different reference astronomic fields (clusters), and this orientation is not derived in a homogeneous way for all the instruments. Thus, the position angle is particularly submitted to systematic offsets between different instruments, so that it is important to look for these systematics by eye (at first, see Sec. 4.4) on the temporal evolution figure.

The evolution of the separation evaluates the information we have on the cur-

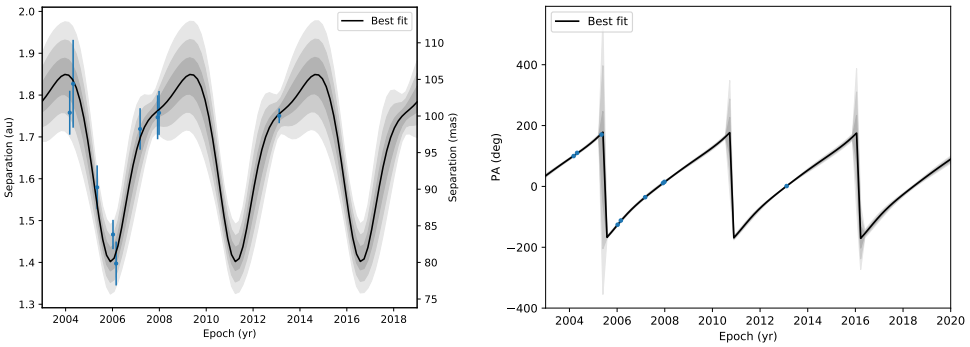

Figure 2.7 – Example of the temporal evolution of the separation and position angle from the results of a MCMC orbital fitting procedure. At each time, the standard deviation σ is computed and the 1-σ, 2-σ and 3-σ intervals are represented in different shades of grey. The observations are represented in blue.

vature of the orbit, and determines if the orbital coverage is sufficient to get strong constraints on the orbital elements. An example of a bad orbital coverage is drawn on Fig. 2.17.

Finally, when astrometry and radial velocity are combined, the evolution of the radial velocity allows determining the part of the RV in the orbital fitting, depending on the dispersion of solutions compared with the radial velocity uncertainties. It can also help to evaluate the activity-related noise in the measurements.

3.5 Comparison with alternative approaches for orbital fitting

The approach that I just presented is a particular implementation designed for the orbital fitting of directly imaged orbits, derived from Ford (2005) and Ford (2006) and optimized with additional mathematical and numerical techniques (orthonormal basis of the parameter space, parallelization of the different Markov chains). It has proven to be a versatile tool, able to fit efficiently the orbits, whether the problem is well constrained or not (see the different applications in Secs. 5 and 6). I will present here three alternative approaches that are often encountered in the literature.

3.5.1 `emcee`

`emcee` is a Python package proposing a general MCMC implementation which is very different from our approach (Foreman-Mackey et al. 2013). It is based on so-called ensemble MCMC: the chains are not independent from one another, so that the choice function $q(\theta'|\theta)$ is a global function including all the chains. In the algorithm, the new position of a chain is chosen along the direction of one of the other chains (picked randomly).

The convergence is measured with the integrated autocorrelation time, which is an estimate of the number of steps needed in the chain in order to get independent samples. The ensemble algorithm used in `emcee` decreases efficiently this number.

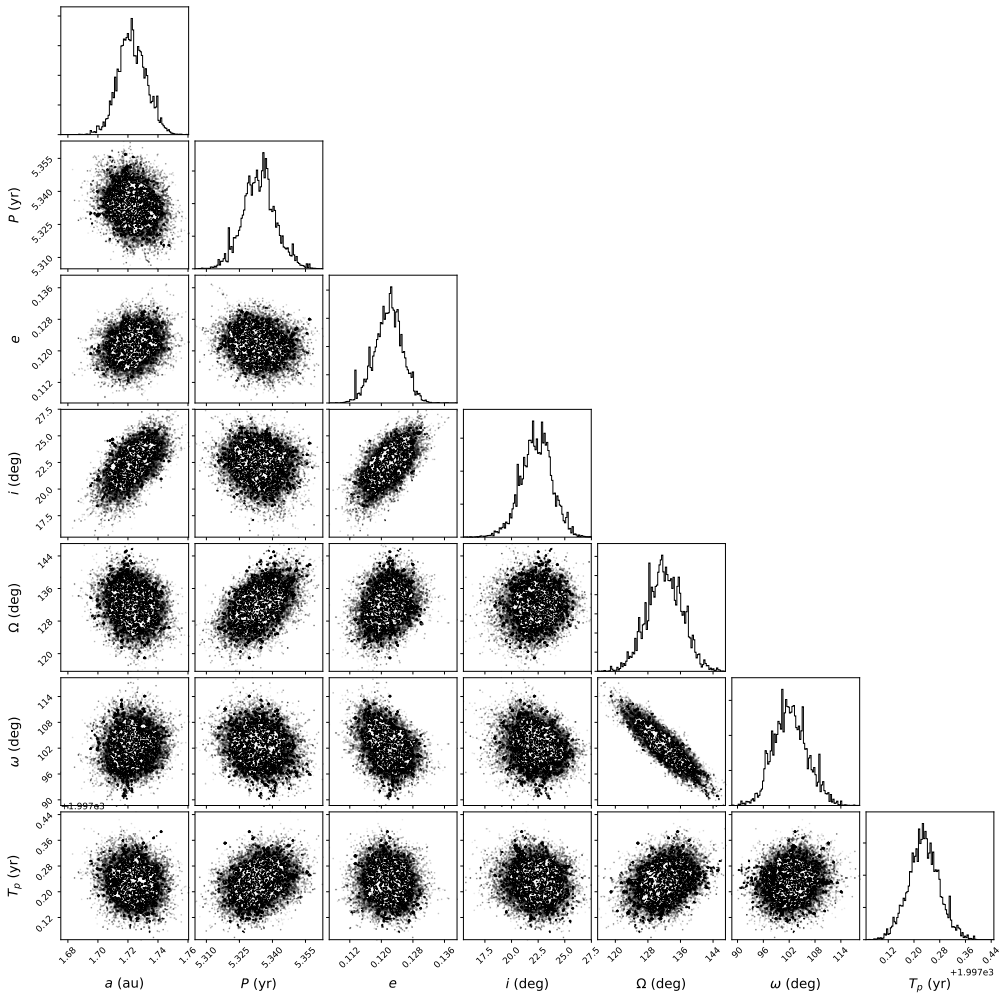

Figure 2.8 – Corner plot presenting the results of the `emcee` orbital fitting procedure of TWA 22 A-B relative orbit. The plots are centered around the main peak. The degeneracy in Ω and ω is not dealt with. This figure can be compared to Fig. 15 in Rodet et al. (2018) (below).

The algorithm is optimized for a large number of chains (typically hundreds). Several adjustments of the setups may be necessary to reach a fair acceptance rate.

`emcee` uses the large number of chains to be faster, but the disadvantage is that some of these chains can be blocked into local minima and slow down the overall convergence. As an example, I performed the orbital fitting of TWA 22 binary (see Sec. 6) by `emcee`, with 100 chains, a first burning phase of $10,000$ steps and then the compilation of $1,000$ steps. According to the autocorrelation time, this number of iterations should be enough. I computed the corner plot with the Python Corner module (Fig. 2.8). The results are similar to the results of our MCMC procedure depicted in Rodet et al. (2018) (Fig. 15), with some lost chains blocked into a local χ^2 minima (Fig. 2.9).

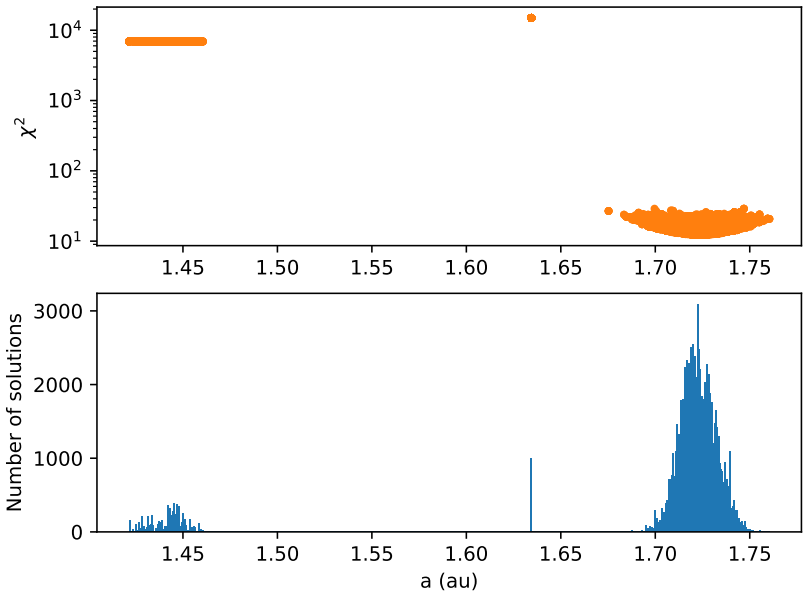

Figure 2.9 – Histogram of the semi-major axes of TWA 22 A-B relative orbit at the end of an emcee run, and the corresponding χ^2. Some chains are trapped in a local χ^2 minima far from the general minimum.

3.5.2 `OFTI`

`OFTI`, for Orbits For The Impatient, is a Monte-Carlo algorithm designed to efficiently compute posterior distributions of orbital elements for data covering short fractions of long-period orbits (Blunt et al. 2017). The sampling follows a classical random Monte Carlo sampling with priors (no Markov chain), but selects a reference epoch to reduce the dimension of the explored parameters space. Indeed, 4 orbital elements are first fixed (e, i, ω and t_p) and the two additional ones (a and Ω) are chosen to fit the reference epoch. This step is called scale-and-rotate. Then, the likelihood is computed and a classical probability rejection is applied.

The priors that are chosen in `OFTI` are identical to ours, except for the eccentricity, where a slope of -2.18 was adopted, from the observed distribution of exoplanets detected by the radial velocity method (Nielsen et al. 2008). The acceptation probability $\alpha(\theta'|\theta)$ is slightly different to ours: the comparison between the χ^2 of the new step and the one of the old step $\exp(-\chi'^2/\chi^2)$ is replaced by a normalization by the minimum χ^2 found $\exp\left(-(\chi'^2 - \chi^2_{\min})\right)$.

This approach is designed explicitly for highly incomplete orbital coverage, and is not suited to the problem otherwise. Indeed, the algorithm particularizes one epoch, which is assumed to be representative of the arc of trajectory. When the problem is underconstrained, the `OFTI` procedure is more efficient compared to the MCMC approach. Adopting a Monte-Carlo approach without Markov Chain avoids an inefficient sampling by the chains of the parameter space, especially relative to the most underconstrained parameters, which are often the semi-major axis (queue of solutions toward the highly eccentric and wide orbits) and the longitude of nodes

(correlated with the argument of periastron). An example of poor constraints on these parameters due to insufficient orbital covering can be seen on Fig. 2.15.

`OFTI` has been compared with our MCMC procedure in the study of Maire et al. (2019) (see Sec. 3). The observational constraints were loose (around 5%), and the results were very similar.

3.5.3 LSMC

The family of LSMC methods, for Least-Squared Monte-Carlo, consists in minimizing the χ^2 (such as the Levenberg-Marquardt algorithm) multiple times, varying the set of measurements and/or the initial guess of parameters. Random realizations of the measurements are drawn assuming Gaussian distributions defined by the observational errors. Initial guesses are drawn randomly through the parameters space, assuming some prior probabilities.

Such an approach was used for example in Maire et al. (2015), with the four-planet system HR 8799, and in Maire et al. (2018), for the study of HR 2562 (described in Sec. 5). It is more compliant than MCMC, so that it can be used for exploratory fits, where the effects of additional constraints may be studied (orbital resonances, coplanarity...). The Monte-Carlo approach without Markov chains probes the local minima of the probability distribution.

In practice, our MCMC procedure has been compared to an LSMC implementation in three studies: Maire et al. (2018), Maire et al. (2019) and Bonnefoy et al. (2018) (all described in Section 5). In the first two cases, the shapes of the probability distribution were very similar. On the other hand, in the last case, the two probability distributions did not exactly match: the parameters space were not similarly explored despite the same priors, resulting in different peaks for some orbital elements. However, the orbital coverage was very scarce, so that the constraints on these elements were not usable in any case. An other implementation of MCMC was compared to the LSMC approach in Ginski et al. (2013), resulting in similar confidence intervals for the orbital elements.

4 Improvements

The previous description of the algorithm corresponds to a version already implemented before my thesis work. Here I detail several aspects that I added to the procedure for easier utilization, completeness (convergence tests), better post-processing or for taking into account new features in the data (systematic offsets).

4.1 Modular organization

Different versions of the code were implemented at the beginning of my thesis, depending on the fitted parameters and the nature of the observations (with or without a fixed total mass, purely astrometric or radial velocity measurements...). Most of the $\sim$ 2000 lines of code are similar in all the versions, only the initialization routines and the computation of the positions and positions derivatives (for the LM part) are different. I thus separated the core part of the code from the more

specialized parts, to get a more flexible architecture. This organization makes it more adapted to diffusion and future developments, in particular through `git`-types platforms.

Moreover, I grouped the various analyses tools that I coded (Sec. 3.4) in a modular package dedicated to post-processing. It is designed to be highly flexible, and can take as inputs the data from the different orbital fitting procedures (with or without mass, radial velocity...).

All these practical considerations are made necessary by the strong need for orbital fitting, due to the growing quantity of observational constraints on the imaged companions. Within my PhD, I performed orbital fitting on eight different systems (see Secs. 5 and 6). For each of these systems, the procedure were launched multiple times, from 3 to more than 30 times, with new or corrected observational data, different observational sets, systematic offsets, different distances... It is thus necessary to have the most automated and readable procedure, to minimize the time cost.

4.2 Convergence

Despite the careful use of Gelman-Rubin statistics to ensure the convergence of the Markov chains, the convergence cannot be established with certainty. Indeed, the full complexity of the multi-parameters probability distributions cannot be entirely described by the two quantities $\hat{R}$ and $\hat{T}$ (Eqs 2.14 and 2.15). To be convinced of the robustness of the results, a last check can be performed by comparing visually the outcomes of the different chains.

I thus slightly modified the original algorithm in order to not lose tracks of the chains during the sampling. This is done within the steps separating the weak from the strong convergence (see Sec. 2.6). At first, the steps are stored orderly, each chain following the others. Then, when the desired number of steps is reached, instead of overwriting randomly in the storing array, the index of a new stored step must be, modulo the number of chains, the index of its chain of origin. Thus, the different distributions produced by the chains can be separately analyzed and compared.

Finally, I added a module to automatically plot the distributions of the chains for each parameters. An example of such output is displayed on Fig. 2.10. The comparison may be used to evaluate the relevance of a peak or feature in the overall probability distribution. In the case of Fig. 2.10, most of the distributions seem robust, but the argument of periastron and the second peak of the periastron passage are not.

4.3 Analysis of the chains

In the mono-dimensional distribution of the corner plot, I chose to replace the histograms by probability distribution functions. Indeed, the discontinuities between bins inherent to the histogram representation is not mathematically relevant to the description of the problem. Moreover, the choice of the origins and centers of the bins is arbitrary, and there is no mathematical guidance for binning methods (equal

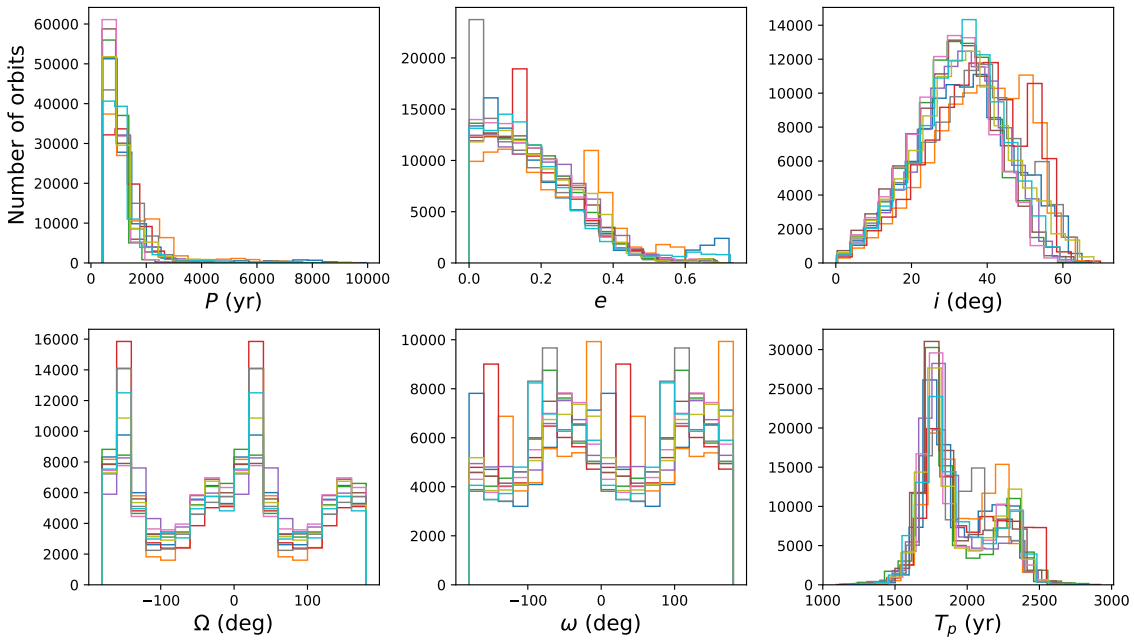

Figure 2.10 – Comparison between the outcomes of 10 different Markov chains, in the case of six fitted parameters. It corresponds to the corner plot of Fig. 2.15. Most of the distributions seem robust, but the argument of periastron ω and the second peak of the periastron passage T_p are not.

spacing, number of points...). An example of the importance of proper representation is displayed on Fig. 2.11.

To compute a probability distribution function f from a sample population (p_i) of size n, I perform a convolution with a Gaussian Kernel K of deviation h:

$$f(p,h) = \frac{1}{nh}\sum_{i=1}^{N} K\left(\frac{p-p_i}{h}\right) \quad . \tag{2.28}$$

The only remaining choice is that of h, called the bandwidth or smoothing parameter. If the underlying density being estimated is Gaussian, the optimal choice for h (that is, the bandwidth that minimizes the mean integrated squared error), is called Siverman's rule of thumb and writes:

$$h = \left(\frac{4\sigma^5}{3n}\right)^{\frac{1}{5}} \tag{2.29}$$

where σ is the standard deviation of the samples. This is thus a natural choice for the bandwidth, as we have no information on the shape of the sampled density distribution.

A particular care has to be given to the angular parameters distribution function, because of their cyclic nature, and to the eccentricity distribution, because of the often reached 0 lower bound. The treatments of these cases are provided by the python package `PyQt-Fit`.

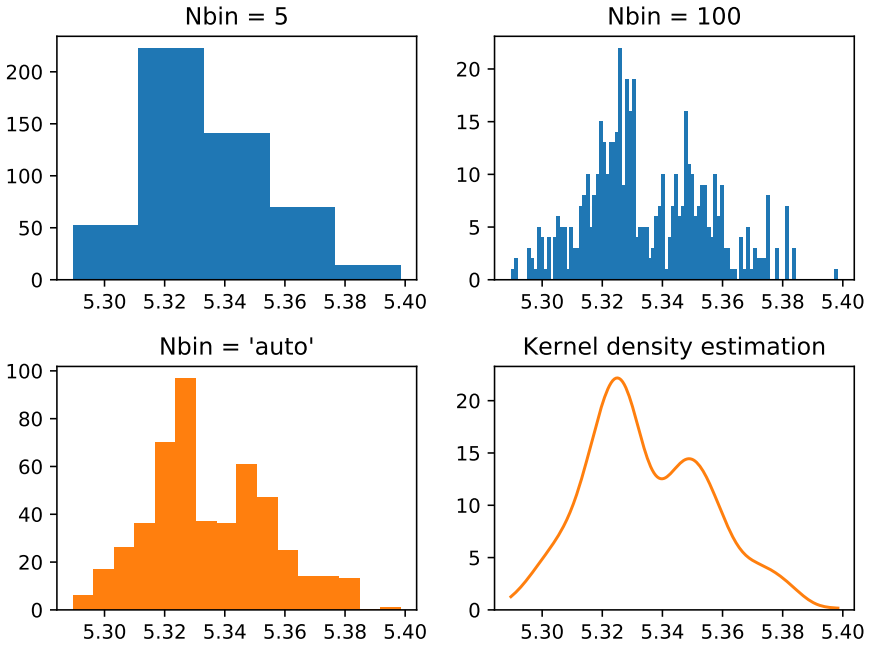

Figure 2.11 – Example of the importance of choosing an appropriate representation for the analysis of a probability distribution.

The computation of the probability distribution function from a population of 10^6 orbital elements can be computationally costly. To have a first overview of the results, the histogram representation is used, with mathematically driven approach to compute the numbers of bins k. I use the 'auto' options of the numpy package, which uses the maximum of the Sturges estimate $s_s = \lceil \log_2 n \rceil + 1$, that is optimal for Gaussian data, and the Freedman Diaconis estimate $s_{fd} = 2\mathrm{IQR}(x)/n^{1/3}$, where IQR stands for the interquartile range, which takes into account the variability of the distribution.

The same approach could be used for the bi-dimensional distributions of the corner plot, but there are often strongly non-Gaussian so that the computation of the probability distribution function is challenging and computationally costly.

For the temporal evolutions, I inspired from Montet et al. (2015) and represented the interval of confidence of the separation and position angle directly along the evolution. Moreover, inspiring from De Rosa et al. (2015), I added a module in the skyplane representation to color-code the orbital evolution.

Finally, I added a module to estimate different intervals of confidence from each mono-dimensional probability distribution, and represent it on the corner plot. The four choices are represented on Fig. 2.12. The classical one is to use the mean and standard deviation. This has the advantage to be easy to compute and to convey an easy mathematical understanding. However, the overall probability of the interval computed from these quantities may be very weak, for example in case of bimodality. To face this issue, we choose to compute the 68%, 95% and 99% confidence intervals, that corresponds respectively to the 1σ, 2σ and 3σ ranges around the mean in case of Gaussian distribution. But even then, plenty of choices remain for the interval.

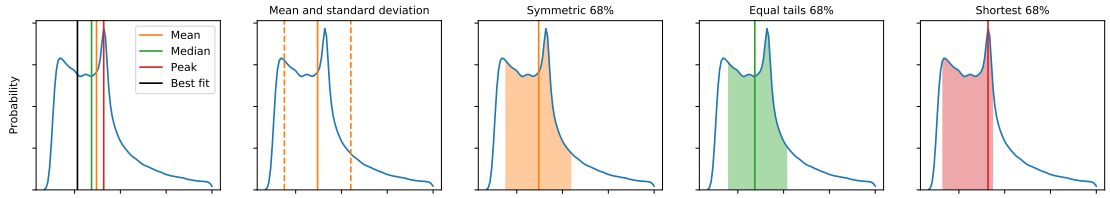

Figure 2.12 – Different intervals of confidence from the same probability distribution.

Three are often considered: symmetric, equal tails and shortest (see Fig. 2.12). The *symmetric* interval of confidence corresponds to equal ranges around the mean. The *equal tails* takes the median and ensures that each tail outside the interval has a 16% probability. Finally, the *shortest* corresponds to the shortest possible interval comprising 68% of the probability around the maximal peak. In that case, the boundaries of the intervals have the same probability. All three frameworks are rigorously acceptable, and are equivalent if the probability distribution is Gaussian. I chose to use the shortest interval approach. This interval is not relevant in case of multi-modal distributions.

4.4 Handling systematic offsets between data sets

Two quantities are necessary to retrieve a consistent set of astrometry from the observations: the pixel scale and the true North (see Introduction Sec. 3. If the pixel scale's calibration is reliable, the precise derivation of true North is subject to systematic changes between epochs, but mostly between instruments. The typical variation for a given setup in SPHERE is of order 0.15 °, which is similar than the typical PSF-induced error. Its calibration is done frequently, with carefully chosen calibration targets (clusters, binaries) (Maire et al. 2016). The stability of the True North for a given instrument may be compromised after technical interventions, or in case of imperfect synchronization with the telescope, but the frequent calibration with the same calibration procedure limit the possible offsets. However, the control of the relative offset is not ensured when different instruments are considered, because of the different calibration strategies. When the same target is observed at the same epoch with different instruments, the offset may appear clearly as in the study of 51 Eri, Sec. 5.2, with SPHERE and GPI, or in the study of β Pictoris, with NACO, SPHERE and GPI (Chauvin et al. 2012; Wang et al. 2016).

Estimating the systematic offsets between the different datasets is often crucial, especially when the orbital coverage is small. A rough guess can be integrated to the observation uncertainty, but the nature of the errors will then be lost. The most proper way to take them into account is to add them as additional parameters to the orbital fit.

I included this possibility in the code, for an arbitrary number of subsets. For n different instruments, $n-1$ systematic offsets must be considered, and one instrument must be declared the reference. The choice of the reference instrument scarcely matters, as it will only affect the longitude of the node by a small error (the order of magnitude of the PA offsets rarely exceeds 1°. I assumed a flat prior and takes

directly the angular offsets as parameters for the MCMC procedure.

The advantage of this approach are multiple. First, it takes into account systematic bias without overestimating the observation random noise. Second, it gives estimates of the probability distribution of the reference position angle difference between two instruments.

I have applied the algorithm to two systems: the binary orbit of system GJ 2060 (Sec 6) and the companion orbit in system 51 Eri (Sec. 5.2). In the first case, the offset has been found negligible (0.1°) between the two main instruments (AstraLux and SPHERE), thanks to the robustness of the derived orbit. In the second case, given the poor orbital coverage, the fit of the offset did not give a precise constraint ($0.6 \pm 0.6°$). As the orbital monitoring of the long period companions will continue with all the available instruments, the need to take all data into account will grow accordingly, so that handling the systematic offsets might be an important part of the orbital fitting procedure in the coming years.

5 Application to the characterization of companions observed with SPHERE

I have applied the orbital fitting technique described above to several systems during this PhD, all observed with SPHERE. Indeed, multiple direct imaging instruments have been used to follow the orbit of detected planets and brown dwarfs since the first lights of instrument NaCo in 2002, providing more than a decade of orbital coverage.

5.1 HR 2562: A brown dwarf carving a debris disk

HR 2562 A is a nearby F5V star around which a low-mass brown dwarf, HR 2562 b, has been imaged by Konopacky et al. (2016) with the GPI instrument. The companion is located at a projected distance of 0.6" (20 au) from the star. It has then been observed multiple times by SPHERE. Moreover, an extended outer debris disk have been identified by Moór et al. (2014) in the infrared with Herschel/PACS, but its structure is strongly unconstrained. The debris disk is not detected by GPI or SPHERE in the near-infrared.

The system is precious, as it is one of the rare cases where an imaged substellar companion has been resolved in a system with a known debris disk (see Introduction). The only other similar brown dwarf companion is HD 206893 (presented below). The position of the companion, within the disk, makes it a valuable laboratory to analyze disk-companions interactions. Furthermore, the mass ratio of the pair is very low (0.02 ± 0.01), far from the usual mass ratio of F-type star companions (around 0.3, higher for short period binaries, Raghavan et al. 2010). This is one of the typical case where a planetary-like formation (gravitational instability or core accretion) may have created a brown dwarf.

Five astrometric measurements of the relative position of the companion have been obtained over the $\sim$ 2 years monitoring, that corresponds to about 1% of the orbital period. No curvature is evidenced by the astrometry, and only 1 to 3° of

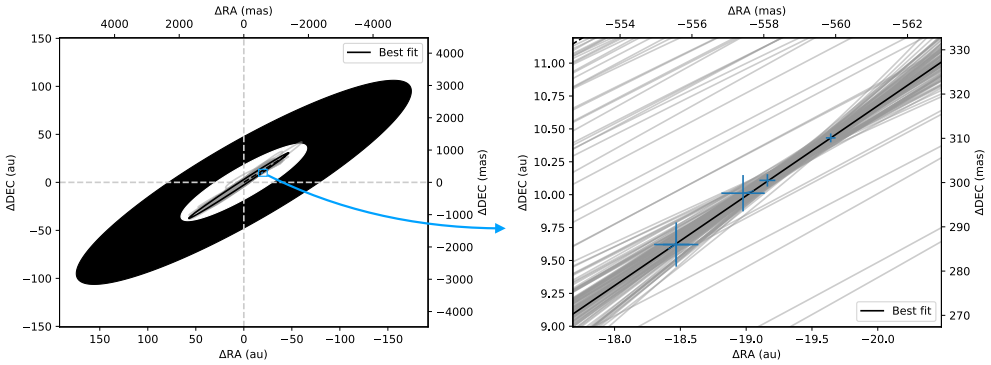

Figure 2.13 – Representation on the sky plane of the results the MCMC orbital fitting procedure of HR 2562 A-b relative orbit. The black orbit corresponds to the results of the LM procedure (best fit). A hundred random solutions are plotted in grey. The astrometric observations are represented in blue, and the disk range in black.

angular evolution have been detected. Thus, the orbit is poorly constrained, and the result of the orbital fit is not very informative for most orbital elements, except for the inclination, which is likely edge-on. It suggests that the companion orbit and the disk have a small relative inclination (see Fig. 2.13).

In Maire, Rodet et al. 2018, the orbital fit is performed with a LSMC algorithm (see Sec. 3.5.3). The MCMC procedure was also applied although the results are not detailed in the paper. The result was similar to the output of the LSMC procedure, as can be seen by comparing Fig. 2.14 and Fig. 3 in the paper below. This is one of the only paper which compared our MCMC implementation with another code, in particular a LSMC code.

We also studied the interactions between the companion and the disk. For that, I ran N-body simulations including 10,000 test particles for 100 Myr with `Swift RMVS`, testing various orbital configurations allowed by the orbital fitting. Then, I computed the density distribution and associated it with a luminosity, assuming a radial temperature profile for the dust grains and black body emission. Finally, I convoluted the result with Herschel/PACS PSF and compared the images with the observation. Unfortunately, the poor constraints on both the orbit and the inner radius of the disk limited the range of the analysis, and the poor resolution of the disk image was not able to definitely rule out the presence of eccentricity-induced structures, so that an eccentric orbit could not be discarded. Concluding on the eccentricity of the brown dwarf's orbit is essential to constrain its dynamical history, and in particular its formation process. This will be achieved by extending the orbital coverage and observing the debris disk with a better spatial resolution (ESO P104 program submitted).

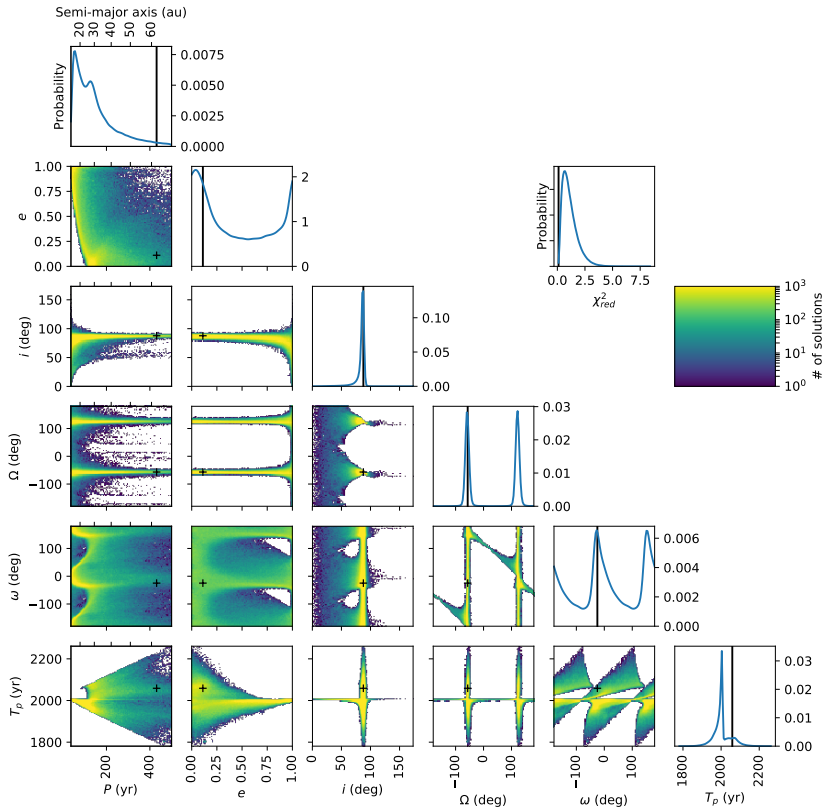

Figure 2.14 – Corner plot presenting the results of the MCMC orbital fitting procedure of HR 2562 A-b relative orbit. The black lines and crosses correspond to the results of the LM procedure (best fit).

A&A 615, A177 (2018)
https://doi.org/10.1051/0004-6361/201732476
© ESO 2018

Astronomy & Astrophysics

VLT/SPHERE astrometric confirmation and orbital analysis of the brown dwarf companion HR 2562 B⋆

A.-L. Maire[1], L. Rodet[2], C. Lazzoni[3,4], A. Boccaletti[5], W. Brandner[1], R. Galicher[5], F. Cantalloube[1], D. Mesa[6,3], H. Klahr[1], H. Beust[2], G. Chauvin[2,7], S. Desidera[3], M. Janson[8,1], M. Keppler[1], J. Olofsson[9,10,1], J.-C. Augereau[2], S. Daemgen[11], T. Henning[1], P. Thébault[5], M. Bonnefoy[2], M. Feldt[1], R. Gratton[3], A.-M. Lagrange[2], M. Langlois[12,13], M. R. Meyer[14,11], A. Vigan[13], V. D'Orazi[3], J. Hagelberg[2], H. Le Coroller[13], R. Ligi[15,13], D. Rouan[5], M. Samland[1], T. Schmidt[5], S. Udry[16], A. Zurlo[17,18,13,3], L. Abe[19], M. Carle[13], A. Delboulbé[2], P. Feautrier[2], Y. Magnard[2], D. Maurel[2], T. Moulin[2], A. Pavlov[1], D. Perret[5], C. Petit[20], J. R. Ramos[1], F. Rigal[21], A. Roux[2], and L. Weber[16]

(Affiliations can be found after the references)

Received 15 December 2017 / Accepted 9 April 2018

ABSTRACT

Context. A low-mass brown dwarf has recently been imaged around HR 2562 (HD 50571), a star hosting a debris disk resolved in the far infrared. Interestingly, the companion location is compatible with an orbit coplanar with the disk and interior to the debris belt. This feature makes the system a valuable laboratory to analyze the formation of substellar companions in a circumstellar disk and potential disk-companion dynamical interactions.
Aims. We aim to further characterize the orbital motion of HR 2562 B and its interactions with the host star debris disk.
Methods. We performed a monitoring of the system over ∼10 months in 2016 and 2017 with the VLT/SPHERE exoplanet imager.
Results. We confirm that the companion is comoving with the star and detect for the first time an orbital motion at high significance, with a current orbital motion projected in the plane of the sky of 25 mas (∼0.85 au) per year. No orbital curvature is seen in the measurements. An orbital fit of the SPHERE and literature astrometry of the companion without priors on the orbital plane clearly indicates that its orbit is (quasi-)coplanar with the disk. To further constrain the other orbital parameters, we used empirical laws for a companion chaotic zone validated by N-body simulations to test the orbital solutions that are compatible with the estimated disk cavity size. Non-zero eccentricities (>0.15) are allowed for orbital periods shorter than 100 yr, while only moderate eccentricities up to ∼0.3 for orbital periods longer than 200 yr are compatible with the disk observations. A comparison of synthetic *Herschel* images to the real data does not allow us to constrain the upper eccentricity of the companion.

Key words. brown dwarfs – methods: data analysis – stars: individual: HR 2562 – planets and satellites: dynamical evolution and stability – techniques: high angular resolution – techniques: image processing

1. Introduction

HR 2562 (HD 50571, HIP 32775) is a nearby F5V star of mass 1.3 $M_\odot$ (Gray et al. 2006; Casagrande et al. 2011) with high proper motion ($d = 33.64 \pm 0.45$ pc, $\mu_\alpha = 4.872 \pm 0.040$ mas yr^{-1}, $\mu_\delta = 108.568 \pm 0.040$ mas yr^{-1}, Gaia Collaboration 2016) known to host an extended debris disk of outer radius 187 ± 20 au with a fractional luminosity of the infrared excess $L_{\rm disk}/L_\star = (1.0 \pm 0.3) \times 10^{-4}$ and a large inner hole of radius ∼18–70 au (Moór et al. 2006, 2011, 2015), and a late-L brown dwarf companion (Konopacky et al. 2016b).

Modelings of the stellar spectral energy distribution (SED) show evidence for a single cold (∼40–70 K) outer component (Moór et al. 2011, 2015; Pawellek et al. 2014). Pure SED fittings give a cold disk average radius of 58–71 au (Moór et al. 2011, 2015), whereas *Herschel*/PACS image fittings point towards a larger average radius, 104–138 au (Pawellek et al. 2014; Moór et al. 2015). Kral et al. (2017) estimated this parameter to be 181 au from an SED fit combined with the blackbody radius correction proposed by Pawellek & Krivov (2015) assuming an equal mixture of ices and astrosilicates. The inclination and the position angle of the disk were estimated to be 78.0 ± 6.3° and 120.1 ± 3.2° by Moór et al. (2015) from the fit of a geometrical disk model to *Herschel*/PACS images. Pawellek et al. (2014) estimated an index for the size distribution of the dust grains of 4.01 ± 0.49, which is consistent with predictions from collisional cascade models (e.g., Dohnanyi 1969; Thébault & Wu 2008; Krivov et al. 2013).

The age estimate of the system is quite uncertain with a range of 300–900 Myr (Konopacky et al. 2016b), translating into a mass range for the brown dwarf companion of 15–45 $M_{\rm J}$. Thanks to the large stellar proper motion and the high astrometric accuracy of the GPI instrument, Konopacky et al. (2016b) were able to confirm that the companion is physically bound to HR 2562 using observations taken one month apart. Although the limited orbital coverage prevent them from performing an orbital analysis of the companion, they noted that its location is compatible with an orbital plane coplanar with the debris disk with a projected separation (∼20 au) interior to the debris belt. Together with the HD 206893 system (Milli et al. 2017), HR 2562 therefore represents a valuable laboratory for studying

⋆ Based on observations collected at the European Organisation for Astronomical Research in the Southern Hemisphere under ESO programme 198.C-0209.

Table 1. Observing log.

UT date	ϵ ($''$)	τ_0 (ms)	AM start/end	Mode	Bands	DIT (s) × Nfr	ΔPA (°)	SR
2016/12/12	1.6–2.2	2	1.23–1.25	IRDIFS	YJ+H	16(64) × 256(64)	28.1	0.30–0.53
2017/02/07	0.4–0.9	4–8	1.24–1.26	IRDIFS	YJ+H	16(64) × 320(80)	34.9	0.72–0.92
2017/09/29	0.5–1.0	2–4	1.39–1.26	IRDIFS_EXT	YJH+$K1K2$	48(64) × 100(75)	27.6	0.69–0.87

Notes. The columns provide the observing date, the seeing measured by the differential image motion monitor (DIMM) at 0.5 μm, the associated coherence time, the airmass (AM) at the beginning and the end of the sequence, the observing mode, the spectral bands, the detector integration time (DIT) multiplied by the number of frames in the sequence (Nfr), the field of view rotation, and the Strehl ratio measured by the adaptive optics system at 1.6 μm. For the DIT × Nfr column, the numbers in parentheses are for the IFS data.

the formation of substellar companions in a circumstellar disk in a higher-mass regime with respect to other known debris disk systems hosting planetary mass companions (e.g., HR 8799, β Pic, HD 95086, 51 Eri; Marois et al. 2008, 2010; Lagrange et al. 2010; Rameau et al. 2013; Macintosh et al. 2015). Recently, Mesa et al. (2018) reassessed the stellar properties using the isochrones of Bressan et al. (2012) and a Bayesian determination approach (see details in Desidera et al. 2015) and found a mass value similar to previous estimates (1.368 ± 0.018 $M_\odot$) but a slightly younger age range of 200–750 Myr.

We present in this paper high-contrast images of HR 2562 obtained with the instrument VLT/SPHERE (Beuzit et al. 2008) as part of the SpHere INfrared survey for Exoplanets (SHINE, Chauvin et al. 2017). Our goals are to further characterize the orbital motion and parameters of HR 2562 B. A spectrophotometric analysis of the companion is presented in Mesa et al. (2018). We describe the observations and the data reduction (Sect. 2). Subsequently, we use the new astrometry of HR 2562 B to confirm its companionship and analyze its orbital motion jointly with the GPI astrometry (Sect. 3). We subsequently fit the SPHERE and GPI astrometry to derive first constraints on the companion's orbit (Sect. 4). We analyze its potential dynamical interactions with the host-star debris disk (Sect. 5). Finally, we discuss potential formation scenarios for the companion, the possibility to estimate its dynamical mass, and further insights into the system that will be provided by further astrometric monitoring of the brown dwarf companion and ALMA observations of the disk.

2. Observations and data analysis

We observed HR 2562 on 2016 December 12, 2017 February 7, and 2017 September 29 with the SPHERE near-infrared (NIR) camera IRDIS (Dohlen et al. 2008) and integral field spectrometer IFS (Claudi et al. 2008) simultaneously (Table 1). For the first two epochs, the IRDIS data were acquired in the H-band broad-band filter (λ_H = 1.6255 μm) with the aim to image the debris disk and IFS in YJ mode (0.95–1.35 μm). As the disk was not detected with this setup, for the latest epoch, we used the IRDIFS_EXT mode, that is, IRDIS with the $K12$ narrow-band filter pair (λ_{K1} = 2.110 μm and λ_{K2} = 2.251 μm, Vigan et al. 2010) and IFS covering the YJH bands (0.95–1.65 μm). The star was imaged with an apodized pupil Lyot coronagraph (Martinez et al. 2009; Carbillet et al. 2011) of inner working angle 95 mas (December 2016 and February 2017 data) or 120 mas (September 2017 data). The observing conditions were poor for the first observation, but the companion could still be detected and its astrometry extracted from the IRDIS data. Observing conditions were good to average for the second and third epochs. For calibrating the flux and the centering of the images, we

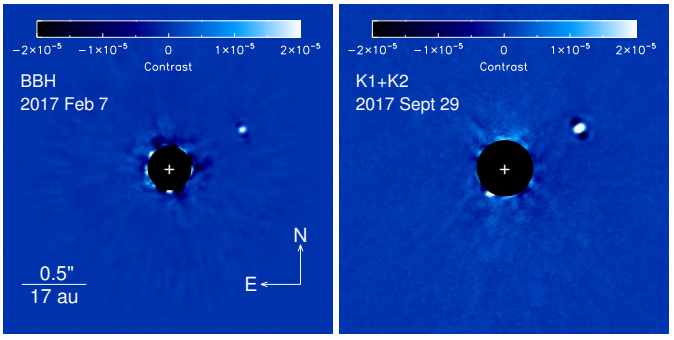

Fig. 1. SPHERE/IRDIS TLOCI images of HR 2562 obtained in the broad H-band filter (λ_H = 1.6255 μm, *left*) and with the combination of the narrow-band $K12$ filter pair images (λ_{K1} = 2.110 μm, λ_{K2} = 2.251 μm, *right*). The central regions of the images were numerically masked out to hide bright stellar residuals. The white crosses indicate the location of the star.

acquired at the beginning and end of the sequences unsaturated non-coronagraphic images of the star (hereafter point-spread function or PSF) and coronagraphic images with four artificial crosswise replica of the star (Langlois et al. 2013). For the third sequence, the stellar replica were used for the whole sequence to minimize the centering errors in the astrometric error budget. Other calibration data (sky backgrounds, darks, detector flats) were obtained after the observations or during the daytime.

The data were reduced with the SPHERE Data Center[1] pipeline (Delorme et al. 2017), which uses the Data Reduction and Handling software (v0.15.0; Pavlov et al. 2008) and additional routines for the IFS data reduction (Mesa et al. 2015). The pipeline corrects for the cosmetics and instrument distortion, performs the wavelength calibration, and extracts the IFS image cubes, registers the frames, and normalizes their flux. Then, we sorted the frames using visual inspection and the statistics of their flux and selected about 60% to 90% of the best frames according to the data set. For the second IRDIS data set, we subsequently binned it temporally by a factor of two to avoid long computing times during the data post-processing while keeping the azimuthal smearing of the companion negligible. After these steps, for the IRDIS science cubes, we were left with 159, 129, and 92 frames, respectively. Finally, the data were analyzed with a consortium image processing pipeline (Galicher et al. 2018). We show in Fig. 1 median-collapsed contrast IRDIS images obtained with Template Locally Optimized Combination of Images algorithm (TLOCI; Marois et al. 2014). For the IFS data, only the two last data sets could be used for extracting

[1] http://sphere.osug.fr/spip.php?rubrique16&lang=en

Table 2. SPHERE astrometry relative to the star of HR 2562 B.

Epoch	Filter	ρ (mas)	PA (deg)	ΔRA (mas)	ΔDec (mas)	Pixel scale (mas/pix)	North correction angle (°)
				IRDIS			
2016.95	H	637.8 ± 6.4	297.81 ± 0.54	−564.1 ± 4.9	297.6 ± 4.1	12.251 ± 0.009	−1.808 ± 0.043
2017.10	H	644.0 ± 2.3	297.82 ± 0.19	−569.6 ± 1.8	300.5 ± 1.4	12.251 ± 0.009	−1.712 ± 0.058
2017.75	$K1$	661.2 ± 1.3	297.97 ± 0.16	−583.9 ± 1.1	310.1 ± 0.8	12.267 ± 0.009	−1.735 ± 0.043
2017.75	$K2$	658.9 ± 1.6	298.08 ± 0.17	−581.4 ± 1.2	310.2 ± 1.0	12.263 ± 0.009	−1.735±0.043
				IFS			
2017.10	YJ	643.8 ± 3.2	297.51 ± 0.28	−571.0 ± 2.7	297.4 ± 1.8	7.46 ± 0.02	−102.19 ± 0.11
2017.75	YJH	657.5 ± 2.6	297.65 ± 0.21	−582.4 ± 2.1	305.1 ± 1.5	7.46 ± 0.02	−102.22 ± 0.11

Notes. The astrometric error bars were derived assuming an error budget including the measurement and systematic errors. The uncertainties in the estimation of the location of the star were derived to be 2.7 and 0.94 mas for the December 2016 and February 2017 IRDIS data sets, respectively. For the February 2017 IFS data set, this uncertainty is estimated to be 0.11 mas. The September 2017 data sets were acquired simultaneously with the satellite spots in the field of view.

the companion astrometry. For the data analysis, we kept 63 and 50 frames, respectively.

The known brown dwarf companion is detected at all epochs. Its astrometry was measured using TLOCI applied to each spectral channel of the science cubes separately. To attenuate the stellar residuals in an image, TLOCI subtracts from the image a model image of the stellar residuals built using the frames obtained in the same observing sequence. To account for the local properties of the stellar residuals, this model image or reference image is computed for each frame in a science cube in annuli with a width of 1.5 times the full width at half maximum (FWHM), and divided into sectors. To avoid large photometric and astrometric biases on putative point sources, the reference images were built using the best linear combination of the 80 most correlated frames for which the self-subtraction of mock point sources, modeled using the observed PSF, was at maximum 15% (December 2016 data set) and 30% (February and September 2017 data sets). To accurately estimate the astrometry and photometry of HR 2562 B while accounting for the TLOCI biases, we created a science cube with only a mock companion modeled from the observed PSF inserted at the rough location (within a pixel accuracy) of the measured companion accounting for the field-of-view rotation (Galicher & Marois 2011). We then processed the data with TLOCI assuming the algorithm coefficients computed for the analysis without the mock companion. After, the subpixel position and flux of the model companion image were optimized to minimize the image residuals within a disk of radius 1.5 FWHM centered on the measured companion. The astrometry reported in Table 2 was calibrated following the methods described in Maire et al. (2016). We compared the IRDIS positions of stars in fields in 47 Tuc and NGC 3603 to HST positions (A. Bellini, priv. comm.; Khorrami et al. 2016) to determine the pixel scale and the correction angle to align the images with the North direction. Since the IFS observations are performed simultaneously with the IRDIS observations, we calibrated the IFS data of HR 2562 using the IRDIS calibration and an additional angle offset accounting for the relative orientation between the two instrument fields of view. We compared the TLOCI astrometry to the results from the ANgular DiffeRential OptiMal Exoplanet Detection Algorithm (ANDROMEDA; Mugnier et al. 2009; Cantalloube et al. 2015) and a principal component analysis algorithm (Mesa et al. 2015). All values are compatible given the error bars and we decided to use the IRDIS astrometry extracted with TLOCI in the H and $K1$ bands for the astrometric and orbital analyses.

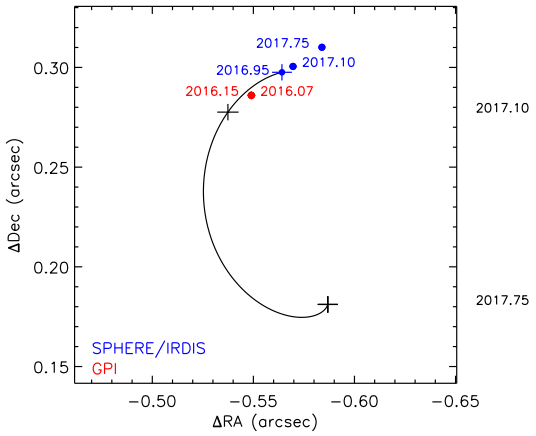

Fig. 2. SPHERE relative astrometry of HR 2562 B (blue points). The black curve shows its motion if it is a stationary background object. The black crosses represent the locations at epochs 2017.10 and 2017.75 (see labels on the right side outside the plot) under the stationary background hypothesis accounting for the uncertainties in the stellar proper motion and distance. The GPI astrometry (red points) is shown for comparison. For most of the data points, the uncertainties are smaller than the size of the symbols.

3. Astrometric confirmation and orbital motion

We show in Fig. 2 the common proper motion test of the companion. Already considering only the December 2016 and February 2017 epochs, the companion does not follow the stationary background track at 5.7σ in right ascension and 5.2σ in declination. The addition of the September 2017 epoch reveals a significant orbital motion for the companion (see below) that is not consistent with the motion expected for a stationary background object.

Subsequently, we combined the SPHERE/IRDIS astrometry with the GPI data reported in Konopacky et al. (2016b) to analyze the companion's orbital motion. The total time baseline of the measurements represents ∼1.7 yr. With respect to the last GPI epoch (late February 2016), the separation of the companion in early February 2017 increased by ∼25 mas at ∼7–8σ significance with a current orbital motion projected in the plane of the sky of ∼25 mas (∼0.85 au) per year, whereas its position angle does not show any significant variations (see Sect. 4). The strong increase in separation is too large to be

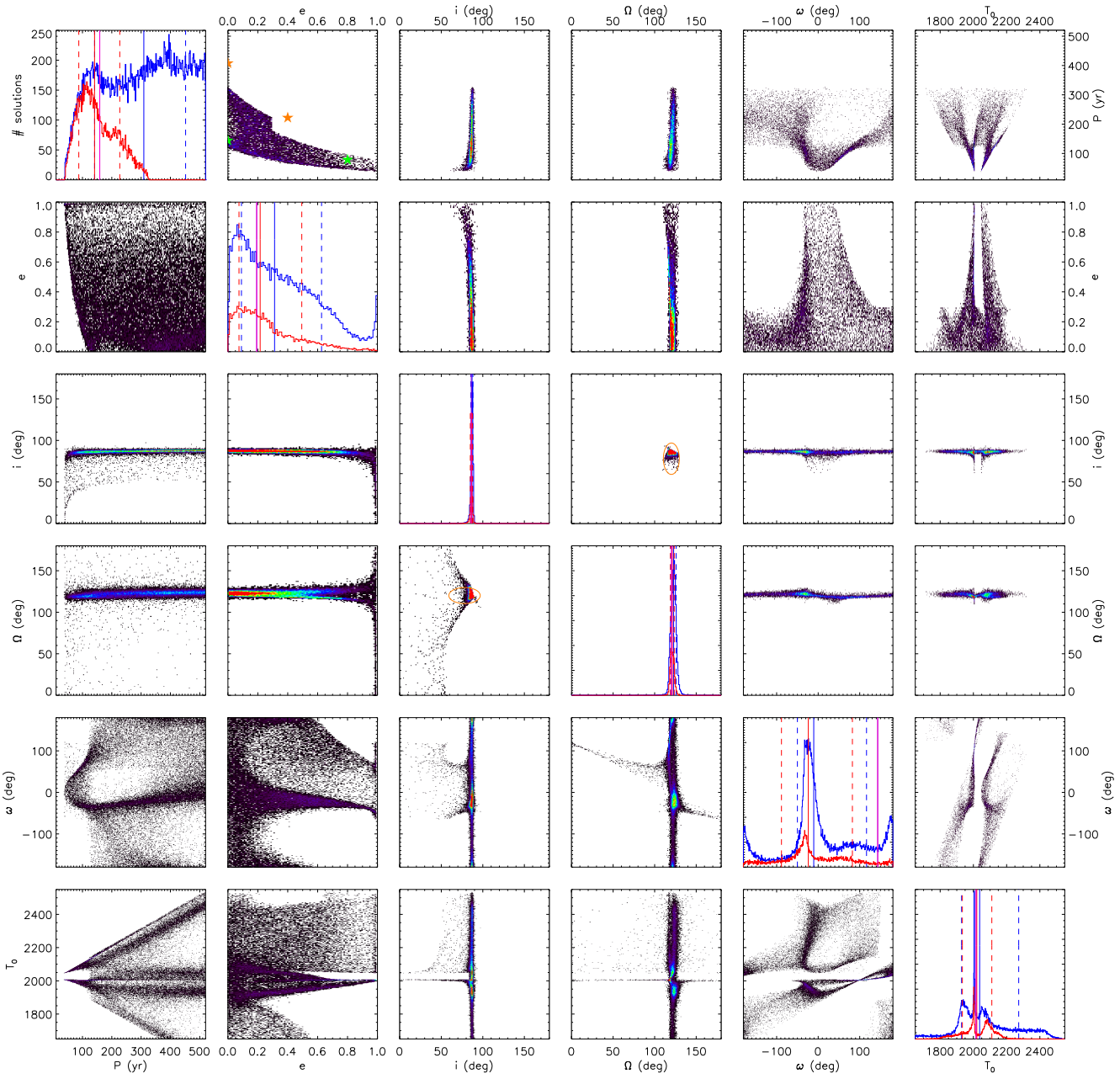

Fig. 3. LSMC distributions of the six Campbell orbital elements for all the fitted solutions with $\chi^2_{\rm red} < 2$ among 2 000 000 random trials. The diagrams displayed on the diagonal from *top left to lower right* represent the 1D histograms for the individual elements (blue: all solutions, red: solutions compatible with the estimated disk geometry at 3σ and disk cavity size). The *off-diagonal diagrams* show the correlations between pairs of orbital elements, with diagrams below and to the left of the diagonal showing all the fitted solutions, and the diagrams above and to the right of the diagonal only showing solutions which are compatible with the estimated disk geometry and cavity size (see Sect. 5). The linear color scale in the correlation plots account for the relative local density of orbital solutions. In the histograms, the purple and magenta solid lines indicate the best χ^2 fitted solutions for all solutions and the disk-compatible solutions, respectively. The solid and dashed lines of a given color show the 50% percentile values and the intervals at 68% (blue: all solutions, red: disk-compatible solutions). The orange ellipses in the i-Ω plots show the disk inclination and position angle estimated by Moór et al. (2015) at 3σ. The stars in the eccentricity-period diagram for the restricted solutions (*top row, second panel* from the left) indicate the configurations tested in the N-body simulations described in Sect. 5 (green: allowed, orange: excluded).

accounted for by small systematic errors between the SPHERE and GPI astrometry. The separation measured in the SPHERE September 2017 data confirms the observed trend (increase of ~15 mas with respect to February 2017). The large separation increase also rules out a face-on circular orbit. For the position angles, we could not exclude small systematic errors between SPHERE and GPI when considering the 2016 and early 2017 data points. Nevertheless, the SPHERE September 2017 data point confirms that the observed evolution for the position angle is genuine.

4. Orbital fitting

We used a least-square Monte Carlo (LSMC) procedure to fit the SPHERE and GPI astrometry (Esposito et al. 2013; Maire et al. 2015). We assumed for the system the *Gaia* distance and a

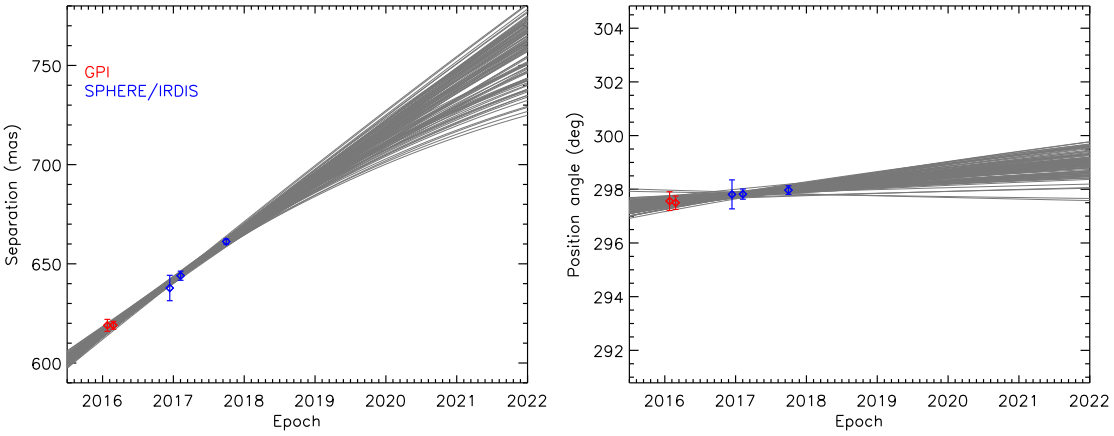

Fig. 4. Temporal evolution of the separation and position angle of HR 2562 B measured by GPI and SPHERE. Predicted separations and position angles for 100 randomly selected orbital solutions in the upper-right part of Fig. 3 are also shown.

total mass of 1.3 $M_\odot$. We drew 2 000 000 random realizations of the astrometric measurements assuming Gaussian distributions around the nominal values, and then fitted the six Campbell elements simultaneously using a debugged version of the downhill simplex `AMOEBA` algorithm[2] (Eastman et al. 2013): orbital period P, inclination i, longitude of node Ω, argument of periastron passage ω, and time at periastron passage T_0. Initial guesses for the orbital elements were drawn assuming uniform distributions. Given the limited orbital coverage of the data, we considered two cases: (1) no priors on the orbital elements except for the period ($P = 10$–2000 yr), and (2) orbits with the same period prior and coplanar with the debris disk measured with *Herschel* ($i \sim 78.0 \pm 6.3°$, $\Omega \sim 120.1 \pm 3.2°$; Moór et al. 2015). We found that without any prior, the orbital solutions clearly favor a coplanar configuration with the disk. To test the presence of biases in the fitted eccentricity and time at periastron passage because of the small covered orbital arc, we used the correction proposed by Konopacky et al. (2016a) but did not find large differences between the derived distributions and we decided to keep the non-corrected distributions for the analysis.

The lower-left part of Fig. 3 shows the histogram distributions and the correlation diagrams of the orbital parameters for the case without using the disk measured inclination and position angle constraints for all the derived solutions with $\chi^2_{\rm red} < 2$. The 68% intervals for the parameters are: $e \sim 0.09$–0.63, $i \sim 86$–$88°$, $\Omega \sim 119$–$126°$. The period is unconstrained. The distribution for the argument of periastron exhibits two peaks around $-25°$ and at $\sim 175°$. The distribution for the time at periastron passage shows a very narrow peak in ~2000 with two broader side peaks in ~1940 and ~2050.

We compared these results with those from a Markov-chain Monte Carlo (MCMC) tool (Chauvin et al. 2012) assuming uniform priors in $\log P$, e, $\cos i$, $\Omega + \omega$, $\omega - \Omega$, and T_0. We found similar ranges for the inclination, the longitude of node, and the argument of periastron. However, the MCMC period and time at periastron distributions are better defined and the corresponding eccentricity distribution shows a very strong peak close to $e = 1$. A high-eccentricity peak is also seen in the LSMC distribution but significantly weaker. Additional checks showed that the better constraints on the period and time at periastron as well as the strong high-eccentricity peak obtained in the MCMC analysis are related to the period prior. The high-eccentricity peak feature can be explained by the almost radial motion without curvature and the absence of significant change in position angle of the companion over the time baseline. We also note that this almost radial motion of the companion results in the well-constrained orbit plane derived in the orbital fits.

We also used the imorbel online tool[3] to apply the small arc analysis of Pearce et al. (2015). We derived 68% intervals of $0.16^{+0.02}_{-0.02}$ for the dimensionless parameter B and $6.99^{+3.33}_{-3.42}$ deg for the angle ϕ between the projected separation and velocity vectors of the companion. Using these values and Figs. 5 and 6 in Pearce et al. (2015), we can set constraints on the minimum semi-major axis, minimum eccentricity, and maximum inclination for the companion. The minimum semi-major axis is 13^{+1}_{-2} au at 3σ. (Quasi-)circular and/or edge-on orbits cannot be excluded. These constraints are compatible with the LSMC results, but the latter are more stringent for the inclination.

Moór et al. (2015) derived from a geometrical model fitted to *Herschel*/PACS data an average dust radius of 112.1 ± 8.4 au, an inner hole radius of $\sim 38 \pm 20$ au, and an average outer dust radius of $\sim 187 \pm 20$ au. Because of inconsistencies between the fitted values of the average dust radius between the *Herschel*/PACS images and the SED (64 ± 6 au, Moór et al. 2015), Konopacky et al. (2016b) performed a simultaneous fit of the SED and *Herschel* image and derived an inner hole radius of ~75 au. From this constraint and assuming a circular orbit for the companion, Konopacky et al. (2016b) derived an upper mass limit for the companion of ~0.24 $M_\odot$, which is much larger than the upper limit from evolutionary models (when using an inner hole radius of 38 au, the value is ~20 $M_{\rm J}$). Konopacky et al. (2016b) propose that this apparent discrepancy for the companion mass could be solved if the companion has an eccentric orbit. This hypothesis is compatible with the results of our orbital analysis, although new observations are required to obtain robust constraints.

Figure 4 represents the predicted separations and position angles for 100 randomly selected fitted orbits compatible with the disk geometry and cavity size constraints (see Sect. 5). Monitoring the system in subsequent years will be critical for improving the orbital constraints, especially if orbital curvature can be measured. We note that, because of the small baseline of the measurements, the separations of the most extreme orbital predictions diverge quickly with time after the last SPHERE epoch and that the maximum difference in separations is already ~15 mas in early 2019. A significant deviation from linearity could therefore be measured, that would favor short-period orbits with non-zero eccentricities over long-period and circular orbits. If this is the case, the robust rejection of circular orbits will

[2] The own built-in routine provided by the Interactive Data Language (IDL) programming language truncates the stepping scales to floating point precision, regardless of the input data type.

[3] `http://drgmk.com/imorbel/`

however require a longer follow-up. If no or small deviation from linearity is measured, this would reject a few short-period orbits and bring only little improvement on the derived orbital elements. We also emphasize that our orbital constraints are preliminary and that robust constraints will be possible once at least one-third of the complete companion orbit can be monitored.

Finally, we used the methods in Pearce et al. (2014) to test the scenario of an unseen inner low-mass companion which could bias the orbital eccentricity of HR 2562 B toward large values due to the orbital motion that the unseen companion induces on the host star. For this, we used the period and eccentricity distributions derived from the orbital fit for the non-restricted case. Figure 5 shows the mass of a putative inner companion as a function of the eccentricity of HR 2562 B. Such a companion would lie at an angular separation of 0.1″. We estimated the TLOCI contrast limit in the SPHERE/IRDIS February 2017 data set at this separation including the coronagraph transmission (Boccaletti et al. 2018) and the small sample statistics correction (Mawet et al. 2014) and derived a value of $\sim 1.6 \times 10^{-3}$. This corresponds to a mass of $\sim 0.1\ M_{\odot}$ for a system age of 450 Myr according to the evolutionary and atmospheric models of Baraffe et al. (2003, 2015). Thus, we can conclude that if HR 2562 B has an eccentricity larger than ∼0.6, this eccentricity is genuine and does not result from an unseen low-mass inner companion. For smaller eccentricities, we cannot exclude an unseen inner companion as potential origin. As discussed in Mesa et al. (2018), there is no clear evidence for binarity of the host star, although additional observations are required to definitely rule out this hypothesis.

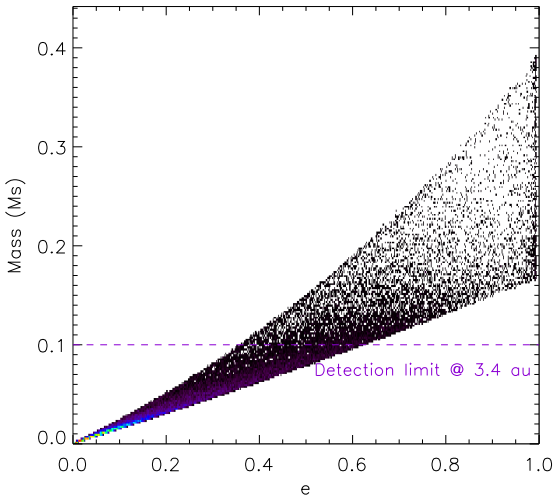

Fig. 5. Mass (in solar masses) of an unseen inner companion that could bias the orbital eccentricity measured for HR 2562 B for the unrestricted case (lower-left part of Fig. 3) compared to the SPHERE/IRDIS detection limit at the separation predicted for this putative companion (purple line, see text).

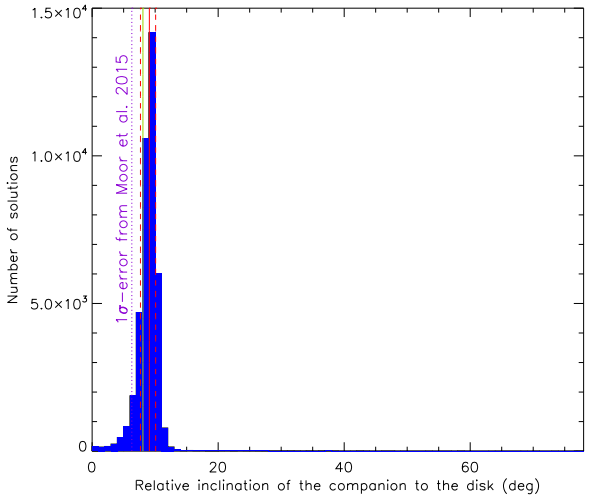

Fig. 6. Relative inclination of HR 2562 B with respect to the debris disk from the unrestricted orbital fit given the constraints in Moór et al. (2015). The red solid and dashed lines show the 50% percentile value and the interval at 68%, the green solid line shows the best-fit solution, and the purple dotted line indicates the 1σ uncertainty on the inclination estimate in Moór et al. (2015).

5. Disk-companion dynamical analysis

5.1. Empirical and numerical dynamical analysis

The positions we observed for HR 2562 B represent a very small part of its orbit, and the orbital fit is thus not able to give strong constraints. Konopacky et al. (2016b) showed that the companion mass is consistent with a stirring of the dust up to the outer edge of the disk given the constraints on the system age. By simulating dynamical interactions between the companion and the debris disk, we can further constrain the companion's orbit by removing solutions that do not match the observational constraints on the disk (e.g., measured cavity size, resolved image).

A word of caution about the accuracy on the disk parameters estimated by Moór et al. (2015) is needed here as the disk is only marginally resolved in the *Herschel* data because of a large instrument PSF. The *Herschel* constraints must therefore be treated with caution, especially for the size of the cavity. The fact that the disk is not detected in the SPHERE images, despite being highly inclined, indicates a low surface brightness in the NIR, which in turn suggests a spatially extended disk.

The distribution of the relative inclination of the companion orbit to the debris disk indicates that they are coplanar at the ∼1.5-σ level (Fig. 6). Therefore, we restricted our problem to orbits coplanar with the disk. We checked that a small misalignment of 20° between the companion orbit and the disk plane has little influence on the carving of the disk by the companion (Appendix A).

N-body simulations being time consuming, we first used empirical laws to obtain rough estimates of the parameter space of the orbital solutions compatible with the estimated disk cavity radius. The only relevant orbital parameters are the semi-major axis a (or, equivalently, the period P) and the eccentricity e. Given these two parameters, we used the formulae in Wisdom (1980) and Mustill & Wyatt (2012) to compute the size of the gap opened by a companion following the approach of Lazzoni et al. (2018). Unfortunately, the constraints on the disk gap radius are rather blurry, from 38 ± 20 au to about 75 au. If we suppose that the disk gap radius is 75 au, we can still exclude a posteriori a large part of the orbital fit results, as represented in the eccentricity-period panels in Fig. 3.

To test the validity of the empirical results, we then used the symplectic N-body code SWIFT_RMVS3 (Levison & Duncan 1994) to simulate the disk dynamics. The code does not simulate collisions between particles. For the initial parameters of the particles, we assumed 10 000 particles with a uniform distribution for their distance to the star between 1 and 200 au, hence their surface density is inversely proportional to their distance. Their eccentricity and their relative inclination to the disk i_r were drawn assuming uniform priors in eccentricity between 0 and

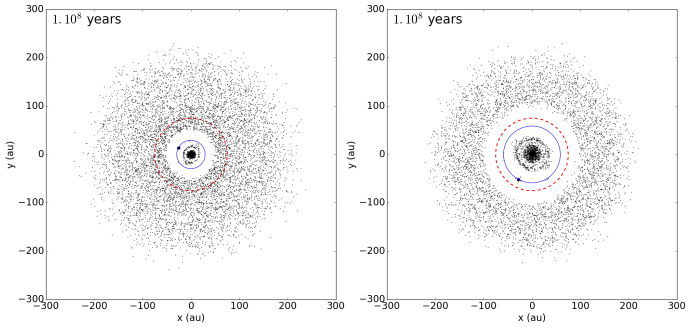

Fig. 7. N-body simulated images of the HR 2562 system after 100 Myr of evolution assuming a coplanar circular orbit for the companion with semi-major axes 30 au (*left*) and 60 au (*right*). The blue solid line shows the companion orbit and the red dashed line the maximum gap radius allowed by the observations.

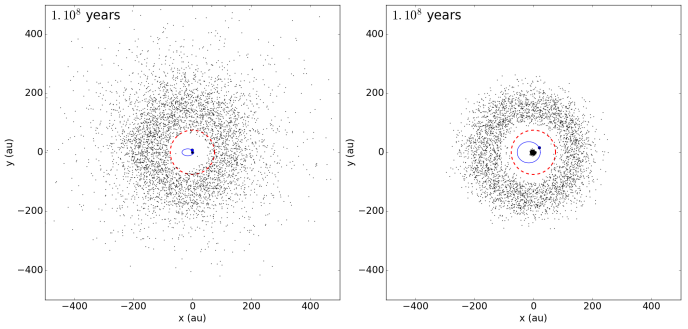

Fig. 8. As in Fig. 7 but for eccentric orbits of the companion. *Left*: $a = 20$ au, $e = 0.8$. *Right*: $a = 40$ au, $e = 0.4$. The diagrams have different horizontal and vertical image cuts with respect to Fig. 7.

0.05 and in $\sin(i_r)$ between 0° and 2°, respectively. We finally set the mass of the companion to 30 M_J. We checked with additional simulations that the mass assumed for the companion has little effect on the disk properties within the constraints from evolutionary models. The revolution of a companion within a debris disk is expected to first cause a gap in the dust distribution, that will be completely formed after 10 000 companion revolutions (see e.g., Holman & Wiegert 1999), and then the propagation of a spiral structure towards the outer edge of the disk, that will become more and more tightly wound because of the disk's secular precession and will eventually disappear (Wyatt 2005). The age of the system is not well constrained either; Konopacky et al. (2016b) found estimates from 180 Myr to 1.6 Gyr in the literature (Asiain et al. 1999; Rhee et al. 2007; Casagrande et al. 2011; Moór et al. 2011, 2015; Pace 2013), but concluded on an age range of 300–900 Myr. Mesa et al. (2018) determined a younger age upper limit of 750 Myr. Simulating a debris disk interacting with a companion for several hundred million years requires significant computing time; we therefore calculated the typical timescale τ of the dissipation of the wave from Wyatt (2005). We then set the duration of our simulations to 100 Myr accordingly. This duration is supposed to correspond to a steady state. In fact, simulations revealed that the disk undergoes practically no change from an age of 10 Myr.

We first performed simulations setting the companion eccentricity to zero. According to the orbital fit, such orbits are likely to have a semi-major axis between 20 and 60 au, with a stronger probability between 20 and 30 au. On the other hand, the empirical gap-opening formula from Wisdom (1980) predicts that if the cavity radius is 75 au, the companion semi-major axis has to be below 50 au. In Fig. 7, we represent the simulation outcome for a circular orbit of 30 au and 60 au. As predicted, the former configuration is compatible with the observations, while the latter configuration is not: the gap would be too extended. For semi-major axes smaller than 50 au, we note that the disk would not be cleared out to the largest allowed inner cavity, which could suggest the presence of an additional companion beyond the orbit of HR 2562 B responsible for sculpting the disk. From the AMES-COND detection limits in Mesa et al. (2018), we can exclude giant planet companions with projected separations beyond 40 au more massive than 5 M_J (200 Myr), 8 M_J (450 Myr), and 10 M_J (750 Myr). For projected separations beyond 60 au, the detection limits are >3 M_J (200 Myr), >5 M_J (450 Myr), and >6 M_J (750 Myr).

We then considered eccentric orbits. Figure 8 shows the simulation results for two configurations: $a = 20$ au and $e = 0.8$, and $a = 40$ au and $e = 0.4$. Because of the cavity's eccentricity, whether the outcome of a simulation matches the observations or not is not as obvious as in the circular case. As a consequence, the border between the parameter spaces of the orbital solutions compatible with the disk cavity constraints and those excluded is not well defined but is blurry. This has to be kept in mind when using the empirical gap formula for eccentric orbits from Lazzoni et al. (2018) to exclude orbital solutions (see top row of Fig. 3, second panel from the left).

5.2. Comparison to Herschel data

Finally, we compared the N-body images of the two simulated configurations compatible with the estimated disk cavity to the *Herschel*/PACS image at 70 μm from Moór et al. (2015). We assumed that the population of simulated bodies is, at first order, a good tracer of the dust grains probed by *Herschel*. After adequately orienting the disk plane in the simulated images, we assumed a radial temperature profile for the dust grains (see Eq. (3) in Backman & Paresce 1993) and that the dust grains emit like black bodies. The temperatures predicted for the dust grains are ~370 K at 1 au, 120 K at 10 au, and 40 K at 100 au. For the surface density particles, we recall that it is set at the beginning of the N-body simulations and is inversely proportional to the distance to the star. Subsequently, we used the derived temperatures to weight the contributions to the flux density of the individual particles using Planck's law. To create an image, we summed pixel by pixel all the individual contributions from particles in a column subtended by a pixel and each resulting image was convolved with the *Herschel* PSF.

When comparing the synthetic *Herschel* images to the measured data, we noted a large flux ratio between the inner and outer parts of the disk in the simulated images, the likes of which is not measured in the data. This feature in the simulated images appears because the inner disks, even small or with low density, are the main contributors to the disk emission. It is expected that an inner disk should be depleted in an old debris disk, such as HR 2562, because of the "inside-out" evolution of the dust grains (e.g., Kenyon & Bromley 2008). Briefly, large planetesimals will progressively disappear through collisions and the production of smaller and smaller dust grains. This evolution is must faster in the innermost regions because of the shorter dynamical timescales. This results in a large population of small grains close to the star that will be expelled from the inner disk by the stellar radiation pressure. Interestingly, Pawellek et al. (2014) found for HR 2562 a larger minimum grain size than the blowout-limit grain size, which is consistent with this scenario. In fact, no warm disk component was identified by

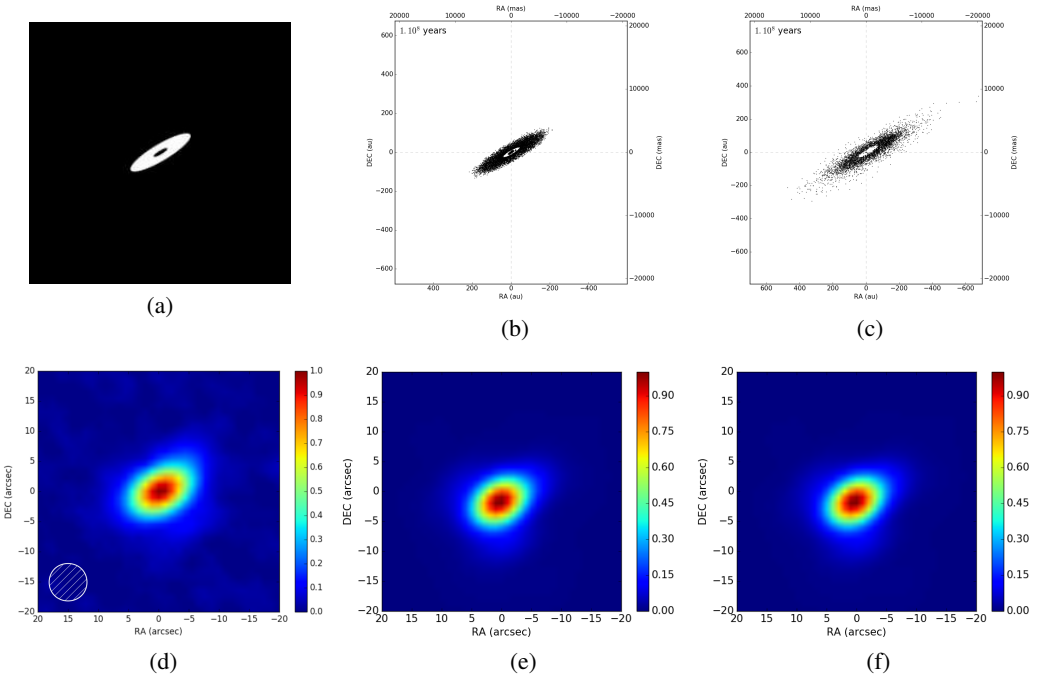

Fig. 9. *Panel a*: geometrical fit to the *Herschel*/PACS image at 70 μm adapted from Moór et al. (2015) shown in panel d. *Panels b* and *c*: simulated images consistent with the estimated disk cavity for a circular configuration ($a = 30$ au, $e = 0$) and for an eccentric configuration ($a = 40$ au, $e = 0.4$), respectively. *Panel d*: *Herschel* image. *Panels e* and *f*: synthetic *Herschel* images corresponding to panels b and c (see text).

Moór et al. (2015) from the analysis of the target SED. The fact that inner disks persist in our N-body simulations stems from the non-inclusion of collisions between bodies. Since the *Herschel* image and the SED of HR 2562 do not show evidence for an inner disk, we removed the contribution from the simulated inner disks to obtain the synthetic *Herschel* images shown in Fig. 9. We find that a circular orbit and a very eccentric orbit for the companion produce similar synthetic disk images and therefore cannot be distinguished.

5.3. Effects on derived orbital parameters

We used the constraints on the companion chaotic zone and the 3-σ estimates on the disk inclination and position angle to further refine the orbital solutions derived in the lower-left part of Fig. 3 (Sect. 4). The strong high-eccentricity peak is strongly attenuated in the resulting distribution because of the removal of non-coplanar orbits. These additional constraints allow to sharpen the histogram distributions as shown in the upper-right part of the figure, especially for the period and the time at periastron passage. The 68% intervals are (Table 3): $P \sim 87$–227 yr, $e \sim 0.07$–0.49, $i \sim 85$–88°, $\Omega \sim 119$–124°, $T_0 = 1934$–2111, and $a \sim 22$–41 au (distribution not shown for the latter parameter). The distribution of arguments of periastron shows now only a marginal peak around −30°. The distribution of time at periastron exhibits two peaks, one sharp peak in ∼2000 and a broader peak in ∼2080.

5.4. Shaping of the disk cavity by HR 2562 B

We finally represent in Fig. 10 the distribution of the outer extent of the clearing zone associated with the orbits compatible with the disk observations assuming the relations in Lazzoni et al. (2018). We note that the disk cavity estimate of 38 au from Moór et al. (2015) is located at the low end of the distribution. We thus conclude that the current orbit of the companion is likely responsible for the shaping of the gap. If the companion separation continues to increase in the coming years without any sign of deceleration, this would mean that the actual disk cavity edge is located further than 38 au. Depending on the outcome of further astrometric monitoring of the companion, the analysis of Moór et al. (2015) may or may not be rejected because of the large uncertainty they estimated for the inner edge of the debris belt (±20 au).

Table 3. Preliminary orbital parameters of HR 2562 B from the combined astrometric and dynamical analysis.

Parameter	Unit	Median	Lower	Upper	$\chi^2_{\rm min}$
P	yr	141	87	227	159
a	au	30	22	41	32
e		0.22	0.07	0.49	0.19
i	°	87	85	88	86
Ω	°	121	119	124	120
ω	°	−24	−88	82	143
T_0		2020	1934	2111	2016

Notes. The parameters are the period, semi-major axis, eccentricity, inclination, longitude of node, argument of periastron, and time at periastron.

6. Discussion

6.1. Formation scenarios for the companion

The fact that the brown dwarf orbit is (quasi-)coplanar with the debris disk might suggest a formation process in the disk for the companion, similar to a planet-like scenario. With a mass ratio to the star of 0.02, the companion seems too massive to have formed through core accretion (Mizuno 1980; Pollack et al. 1996; Mordasini et al. 2012). Its mass and semi-major axis are compatible with predictions from disk gravitational instabilities (Boss 1997; Forgan & Rice 2013) and from collapse and

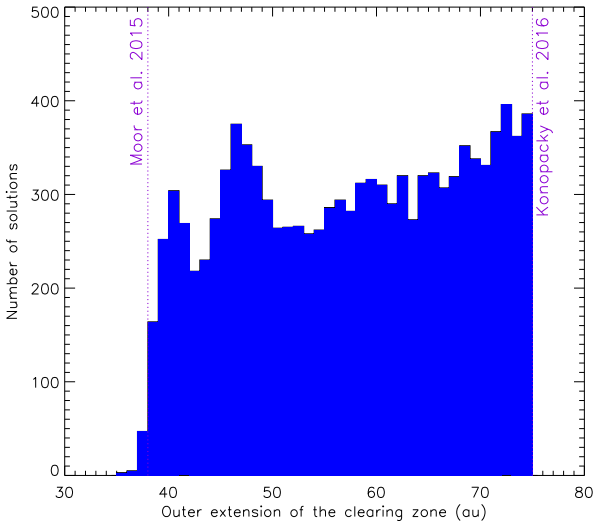

Fig. 10. Distribution of the outer extent of the clearing zone of HR 2562 B for the orbital solutions compatible with the disk geometry and cavity constraints according to the relations in Lazzoni et al. (2018). The vertical lines show the disk cavity estimates of Moór et al. (2015) and Konopacky et al. (2016b).

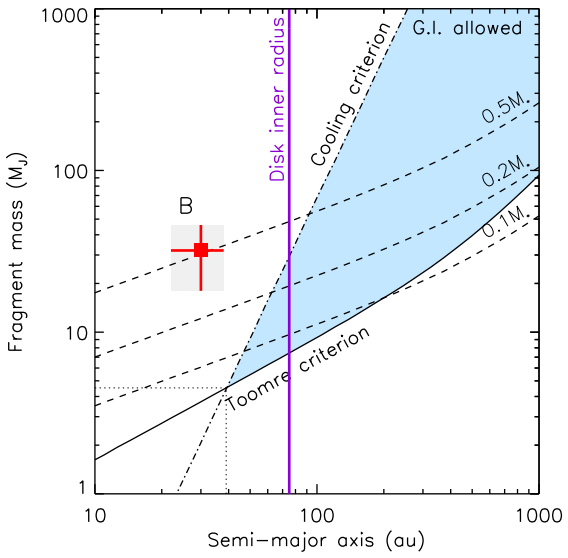

Fig. 11. Masses of fragments that could be produced in-situ via disk gravitational instabilities for HR 2562 as a function of the semi-major axis to the star (blue area). Fragments with masses above the curve labeled "Cooling criterion" cannot cool efficiently enough, while those below the curve labeled "Toomre criterion" do not satisfy the Toomre criterion. The location of HR 2562 B is indicated with the red square with error bars. The primordial disk masses required to support fragments of a given mass are shown with black dashed curves for several masses expressed as fractions of the stellar mass. The purple vertical solid line indicates the inner radius of the debris disk from Konopacky et al. (2016b).

fragmentation of a dense molecular cloud (Bate 2009). In particular, a large companion eccentricity could be a natural outcome from a formation process by collapse with fragmentation of a dense molecular cloud, whereas it could be more difficult to explain it in a disk gravitational instability scenario (but see discussion below). In the following, we further discuss a disk gravitational instability scenario as a potential formation process of HR 2562 B.

We applied a disk gravitational instability model (Klahr et al., in prep.), which predicts the masses of fragments that could form in situ following this mechanism as a function of the semi-major axis to the star. The underlying fragmentation criteria are presented in Mordasini et al. (2010) and Janson et al. (2011) and have been confirmed in local high-resolution 3D simulations (Baehr et al. 2017). Briefly, fragments can form if they satisfy the Toomre criterion for self-gravitating clumps (Toomre 1964) and if they are able to cool faster than the local Keplerian timescale. The model inputs include the stellar luminosity at the zero age main sequence point and the stellar metallicity. We estimated the former parameter from the isochrones of Bressan et al. (2012) and assumed for the latter parameter the value of 0.10 ± 0.06 dex derived in Mesa et al. (2018). The results are shown in Fig. 11. We see that fragments less massive than 4 M_J cannot be formed at any distance to the star. HR 2562 B appears too close and too massive to have formed in situ via disk gravitational instabilities. If we assume its nominal mass and that this mass originates from the formation process alone, it would require a very massive primordial disk with mass ~40% of the stellar mass. Such a massive primordial disk appears unlikely, because the corresponding Toomre parameter would be <0.2. These results combined together suggest that the companion could have formed at a larger distance to the star from a less massive fragment and subsequently migrated inward to its current location while still accreting mass from the surrounding disk material.

If the companion has a large eccentricity, this property might be difficult to explain in a disk gravitational instability scenario because disk interactions tend to damp the eccentricities of orbiting companions. This might imply subsequent dynamical interactions with another body to stir the eccentricity of HR 2562 B. Nevertheless, we note that for very massive substellar companions (>4–5 M_J) with low inclinations to the disk plane (<10°), numerical simulations have shown that interactions with a protoplanetary disk can stir their eccentricity (Papaloizou et al. 2001; Kley & Dirksen 2006; Bitsch et al. 2013).

6.2. Dynamical constraints on the companion mass

Dynamical mass measurements of young low-mass companions offer a powerful and independent way to constrain their predicted cooling models. These models are currently highly uncertain at young ages and low masses because of the lack of observations of suitable benchmark objects. However, they are commonly used to estimate the mass of directly imaged substellar companions.

We used the equations in Lazzoni et al. (2018) to represent the width of the chaotic zone created by a substellar companion in units of its semi-major axis as a function of its mass ratio to HR 2562 for several orbital eccentricities in Fig. 12. The chaotic zone width is defined as $(\Delta a/a)_{\rm chaos} = (a_{\rm cav} - a)/a$, where $a_{\rm cav}$ is the cavity radius. For a given chaotic zone width and companion eccentricity, this plot gives an estimate of the companion mass. Unfortunately, these two parameters have large uncertainties so the constraints on the companion mass are quite loose and can be in the stellar regime. If we assume that the companion is a brown dwarf given the estimates on its spectral properties and that the cavity is carved exclusively by the current orbit of the companion[4], we see that the latter cannot be on a circular

[4] Other phenomena not accounted for in the formulae of Lazzoni et al. (2018; migration of the companion, instabilities in the primordial disk, additional bodies in the system) could enlarge the cavity.

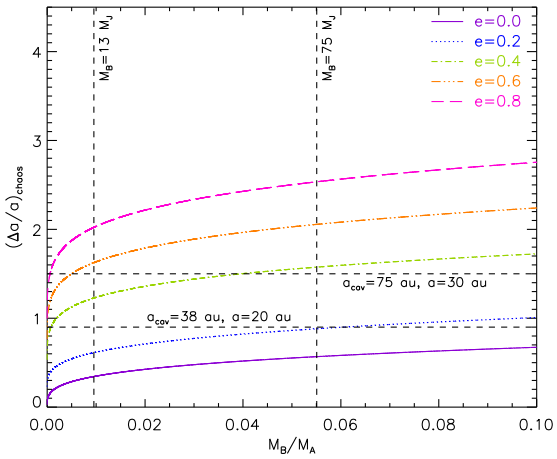

Fig. 12. Width of the chaotic zone $(\Delta a/a)_{\rm chaos} = (a_{\rm cav} - a)/a$ as a function of the mass ratio to the star of a substellar companion carving the disk cavity of HR 2562 for several eccentricities according to the relations in Lazzoni et al. (2018). The vertical dashed lines delimit the brown dwarf mass regime and the horizontal dashed lines show examples of chaotic zone width for two (disk cavity radius, companion semi-major axis) couples.

orbit if the chaotic zone width is larger than ∼0.6. Under the same hypotheses, the chaotic zone width has to be smaller than ∼2.5 if the companion has an eccentricity of 0.8. For non-zero eccentricities, an even more stringent upper limit on the companion mass can be set if the eccentricity is larger and/or the chaotic zone width is smaller. For a disk cavity radius of 38 au and a companion semi-major axis of 20 au, we see that the companion needs to have a lower eccentricity of ∼0.2, whereas its upper eccentricity is ∼0.3. For a disk cavity radius of 75 au and a companion semi-major axis of 30 au, the eccentricity constraints are ∼0.4–0.5. We acknowledge that these results are strongly dependent on the assumed criterion for the cavity shaping. For comparison, we show similar diagrams to Fig. 12 in Appendix B based on the equations of Petrovich (2015) and Regály et al. (2018).

As already discussed in Sect. 4, further astrometric monitoring of the companion will be essential to measure inflexions in its orbital motion that will help to discriminate between an eccentric short-period orbit and a circular long-period orbit. On the other hand, disk observations at higher resolutions will be valuable to refine the estimates of its cavity shape and size (see Sect. 6.3). Such combined constraints will provide powerful insights into the architecture of the system and the dynamical mass of the companion.

6.3. Constraints on the disk properties from ALMA data

(Sub-)millimeter observations of the HR 2562 disk at high angular resolutions with ALMA will be valuable to further refine the estimates on the extent and shape of its cavity. Regály et al. (2018) discuss the potential of ALMA data for analyzing dynamical interactions between substellar companions and debris disks. In particular, they provide a method to estimate the orbital eccentricity and mass of a giant planet carving the disk cavity. This involves measurements of the cavity size and offset with respect to the star by ellipse fitting to a given intensity contour level, which itself depends on the image resolution (the optimal contour level is larger for poorer resolutions). The robustness of the empirical relations was checked against the planetesimals' initial eccentricity and inclination by simulating hot and cold disks and against the stellar mass and age for ranges of 0.6–1 Gyr and 0.5–2 $M_\odot$, respectively. They found relations for the cavity size and for the cavity center offset with respect to the star which only depend on the planet/star mass ratio and the planet eccentricity for eccentric orbits, allowing to break the degeneracies between these two unknowns. They also show that the cavity eccentricity cannot be used as a direct proxy for the planet eccentricity because they are not identical and their relation is not a monotonic function. A disk cavity can be eccentric while a perturbing planet orbit is circular. The eccentricity of the disk cavity is only equal to that of the giant planet perturber for a narrow range of intermediate planet eccentricities (0.3–0.6 for a 5-$M_{\rm J}$ giant planet). Another observable disk feature that could be suggestive of a large planetary eccentricity outlined by Regály et al. (2018) would be the detection of an azimuthal brightness asymmetry or "glow" with a large contrast (up to ∼50% for a 5-$M_{\rm J}$ planet) located beyond the disk cavity wall and near the position angle of the planet apastron.

Using the relations for the cavity size and offset with respect to the star in Regály et al. (2018), we estimated that if these quantities could be measured with accuracies of ∼10%[5], the eccentricity and mass ratio to the star of the planet could be assessed with accuracies of ∼20% and ∼40%, respectively. The stellar mass being constrained with an accuracy of <2% (Mesa et al. 2018), the dynamical mass estimate of HR 2562 B would be slightly more accurate than the ∼45%–50% uncertainties of the evolutionary model predictions (Konopacky et al. 2016b; Mesa et al. 2018) but independent from assumptions on the formation mechanism and the system age.

Such disk cavity measurements require high-resolution images. With a diameter of 0.5″ for the ALMA instrument beam, the HR 2562 disk cavity would be resolved with ∼4.5 resolution elements for the smallest diameter estimate of 38 × 2 au from Moór et al. (2015), and ∼9 resolution elements for the largest diameter estimate of 75 × 2 au from Konopacky et al. (2016b). These resolutions are in the range of the resolutions for which the methods proposed by Regály et al. (2018) could be applied. Higher resolutions could be achieved but at the cost of longer integration times to compensate for the instrument sensitivity loss.

7. Summary

We present VLT/SPHERE observations of the young system of HR 2562 to redetect and further characterize the orbit of its brown dwarf companion. The SPHERE data show a strong increase of the companion separation of ∼40 mas (∼1.3 au) over 1.7 yr with respect to the GPI measurements, ruling out a face-on circular orbit. The joint fit of the SPHERE and GPI astrometry clearly indicates for the companion an orbit (quasi-) coplanar with the known debris disk without any prior on the orbital plane. Furthermore, the eccentricity distribution suggests a non-zero eccentricity, which could reconcile the mass estimates from the evolutionary models and from dynamical considerations assuming that the object is responsible for the truncation of the debris belt. Assuming a debris belt inner edge at 75 au, a dynamical analysis based on analytical and numerical approaches allows to reject eccentricities larger than ∼0.3 for periods longer than 200 yr and eccentricities smaller than 0.15

[5] Limitations to the accuracy of these measurements include the shape of the instrument beam (an elliptical beam can introduce artifacts in the images like brightness asymmetries), instrument pointing accuracy, and the scatter induced by the planet orbital phase.

for periods shorter than 100 yr. If the companion has formed through disk gravitational instabilities, our analysis suggests that its current location and mass can be accounted for by formation at a larger distance to the star from a less massive disk fragment followed by inward migration with mass accretion. Further astrometric monitoring of the companion in order to detect curvature in its orbital motion will allow to better constrain its period and eccentricity. In addition, far-IR or millimeter images at higher resolutions are needed to determine more precisely the disk geometry and its cavity extent. With such information combined with a lower limit on the orbital eccentricity of the companion, the dynamical mass of HR 2562 B could be strongly constrained, making it a valuable benchmark object close to the L/T transition for evolutionary and atmospheric models of substellar companions.

Acknowledgements. The authors thank the ESO Paranal Staff for support in conducting the observations and Philippe Delorme and Eric Lagadec (SPHERE Data Center) for their help with the data reduction. We also thank Attila Moór for kindly providing the *Herschel* data, Grant Kennedy, Virginie Faramaz, and Nicole Pawellek for useful discussions about the system, and Grant Kennedy for his public imorbel web interface. We finally thank the referee, Alexander Mustill, for a constructive report that helped to improve the manuscript. We acknowledge financial support from the Programme National de Planétologie (PNP) and the Programme National de Physique Stellaire (PNPS) of CNRS-INSU. This work has also been supported by a grant from the French LabEx OSUG@2020 (Investissements d'avenir – ANR10 LABX56). The project is supported by CNRS, by the Agence Nationale de la Recherche (ANR-14-CE33-0018). J. O. acknowledges financial support from ICM Núcleo Milenio de Formación Planetaria, NPF. This work has made use of the SPHERE Data Centre, jointly operated by OSUG/IPAG (Grenoble), PYTHEAS/LAM/CeSAM (Marseille), OCA/Lagrange (Nice), and Observatoire de Paris/LESIA (Paris). This research made use of the SIMBAD database and the VizieR Catalogue access tool, both operated at the CDS, Strasbourg, France. The original description of the VizieR service was published in Ochsenbein et al. (2000, A&AS 143, 23). This research has made use of NASA's Astrophysics Data System Bibliographic Services. SPHERE is an instrument designed and built by a consortium consisting of IPAG (Grenoble, France), MPIA (Heidelberg, Germany), LAM (Marseille, France), LESIA (Paris, France), Laboratoire Lagrange (Nice, France), INAF – Osservatorio di Padova (Italy), Observatoire astronomique de l'Université de Genève (Switzerland), ETH Zurich (Switzerland), NOVA (Netherlands), ONERA (France), and ASTRON (Netherlands), in collaboration with ESO. SPHERE was funded by ESO, with additional contributions from the CNRS (France), MPIA (Germany), INAF (Italy), FINES (Switzerland), and NOVA (Netherlands). SPHERE also received funding from the European Commission Sixth and Seventh Framework Programs as part of the Optical Infrared Coordination Network for Astronomy (OPTICON) under grant number RII3-Ct-2004-001566 for FP6 (2004–2008), grant number 226604 for FP7 (2009–2012), and grant number 312430 for FP7 (2013–2016).

References

Asiain, R., Figueras, F., Torra, J., & Chen, B. 1999, A&A, 341, 427
Backman, D. E., & Paresce, F. 1993, in Protostars and Planets III, eds. E. H. Levy, & J. I. Lunine, 1253
Baehr, H., Klahr, H., & Kratter, K. M. 2017, ApJ, 848, 40
Baraffe, I., Chabrier, G., Barman, T. S., Allard, F., & Hauschildt, P. H. 2003, A&A, 402, 701
Baraffe, I., Homeier, D., Allard, F., & Chabrier, G. 2015, A&A, 577, A42
Bate, M. R. 2009, MNRAS, 392, 590
Beuzit, J.-L., Feldt, M., Dohlen, K., et al. 2008, in SPIE Conf. Ser., eds. I. S. McLean, & M. M. Casali, 7014, 701418
Bitsch, B., Crida, A., Libert, A.-S., & Lega, E. 2013, A&A, 555, A124
Boccaletti, A., Sezestre, E., Lagrange, A.-M., et al. 2018, A&A, 614, A52
Boss, A. P. 1997, Science, 276, 1836
Bressan, A., Marigo, P., Girardi, L., et al. 2012, MNRAS, 427, 127
Cantalloube, F., Mouillet, D., Mugnier, L. M., et al. 2015, A&A, 582, A89
Carbillet, M., Bendjoya, P., Abe, L., et al. 2011, Exp. Astron., 30, 39
Casagrande, L., Schönrich, R., Asplund, M., et al. 2011, A&A, 530, A138
Chauvin, G., Lagrange, A.-M., Beust, H., et al. 2012, A&A, 542, A41
Chauvin, G., Desidera, S., Lagrange, A.-M., et al. 2017, in SF2A-2017: Proc. of the Annual meeting of the French Society of Astronomy and Astrophysics, eds. C. Reylé, P. Di Matteo, F. Herpin, et al., 331
Claudi, R. U., Turatto, M., Gratton, R. G., et al. 2008, SPIE Conf. Ser., 7014, 70143E
Delorme, P., Meunier, N., Albert, D., et al. 2017, in SF2A-2017: Proceedings of the Annual meeting of the French Society of Astronomy and Astrophysics, eds. C. Reylé, P. Di Matteo, F. Herpin, et al., 347
Desidera, S., Covino, E., Messina, S., et al. 2015, A&A, 573, A126
Dohlen, K., Langlois, M., Saisse, M., et al. 2008, SPIE Conf. Ser., 7014, 70143L
Dohnanyi, J. S. 1969, J. Geophys. Res., 74, 2531
Eastman, J., Gaudi, B. S., & Agol, E. 2013, PASP, 125, 83
Esposito, S., Mesa, D., Skemer, A., et al. 2013, A&A, 549, A52
Forgan, D., & Rice, K. 2013, MNRAS, 432, 3168
Gaia Collaboration (Brown, A. G. A., et al.) 2016, A&A, 595, A2
Galicher, R., & Marois, C. 2011, Proc. AO4ELT2, P25
Galicher, R., Boccaletti, A., Mesa, D., et al. 2018, A&A, 615, A92
Gray, R. O., Corbally, C. J., Garrison, R. F., et al. 2006, AJ, 132, 161
Holman, M. J., & Wiegert, P. A. 1999, AJ, 117, 621
Janson, M., Bonavita, M., Klahr, H., et al. 2011, ApJ, 736, 89
Kenyon, S. J., & Bromley, B. C. 2008, ApJS, 179, 451
Khorrami, Z., Lanz, T., Vakili, F., et al. 2016, A&A, 588, L7
Kley, W., & Dirksen, G. 2006, A&A, 447, 369
Konopacky, Q. M., Marois, C., Macintosh, B. A., et al. 2016a, AJ, 152, 28
Konopacky, Q. M., Rameau, J., Duchêne, G., et al. 2016b, ApJ, 829, L4
Kral, Q., Matrà, L., Wyatt, M. C., & Kennedy, G. M. 2017, MNRAS, 469, 521
Krivov, A. V., Eiroa, C., Löhne, T., et al. 2013, ApJ, 772, 32
Lagrange, A.-M., Bonnefoy, M., Chauvin, G., et al. 2010, Science, 329, 57
Langlois, M., Vigan, A., Moutou, C., et al. 2013, in Proc. of the Third AO4ELT Conf., eds. S. Esposito, & L. Fini, 63
Lazzoni, C., Desidera, S., Marzari, F., et al. 2018, A&A, 611, A43
Levison, H. F., & Duncan, M. J. 1994, Icarus, 108, 18
Macintosh, B., Graham, J. R., Barman, T., et al. 2015, Science, 350, 64
Maire, A.-L., Skemer, A. J., Hinz, P. M., et al. 2015, A&A, 576, A133
Maire, A.-L., Langlois, M., Dohlen, K., et al. 2016, SPIE Conf. Ser., 9908, 990834
Marois, C., Macintosh, B., Barman, T., et al. 2008, Science, 322, 1348
Marois, C., Zuckerman, B., Konopacky, Q., Macintosh, B., & Barman, T. 2010, Nature, 468, 1080
Marois, C., Correia, C., Galicher, R., et al. 2014, SPIE Conf. Ser., 9148, 91480U
Martinez, P., Dorrer, C., Aller Carpentier, E., et al. 2009, A&A, 495, 363
Mawet, D., Milli, J., Wahhaj, Z., et al. 2014, ApJ, 792, 97
Mesa, D., Gratton, R., Zurlo, A., et al. 2015, A&A, 576, A121
Mesa, D., Baudino, J.-L., Charnay, B., et al. 2018, A&A, 612, A92
Milli, J., Hibon, P., Christiaens, V., et al. 2017, A&A, 597, L2
Mizuno, H. 1980, Prog. Theor. Phys., 64, 544
Moór, A., Ábrahám, P., Derekas, A., et al. 2006, ApJ, 644, 525
Moór, A., Pascucci, I., Kóspál, Á., et al. 2011, ApJS, 193, 4
Moór, A., Kóspál, Á., Ábrahám, P., et al. 2015, MNRAS, 447, 577
Mordasini, C., Klahr, H., Alibert, Y., Benz, W., & Dittkrist, K.-M. 2010, ArXiv e-prints [arXiv:1012.5281]
Mordasini, C., Alibert, Y., Benz, W., Klahr, H., & Henning, T. 2012, A&A, 541, A97
Mugnier, L. M., Cornia, A., Sauvage, J.-F., et al. 2009, J. Opt. Soc. Am. A, 26, 1326
Mustill, A. J., & Wyatt, M. C. 2012, MNRAS, 419, 3074
Pace, G. 2013, A&A, 551, L8
Papaloizou, J. C. B., Nelson, R. P., & Masset, F. 2001, A&A, 366, 263
Pavlov, A., Möller-Nilsson, O., Feldt, M., et al. 2008, SPIE Conf. Ser., 7019, 701939
Pawellek, N., & Krivov, A. V. 2015, MNRAS, 454, 3207
Pawellek, N., Krivov, A. V., Marshall, J. P., et al. 2014, ApJ, 792, 65
Pearce, T. D., Wyatt, M. C., & Kennedy, G. M. 2014, MNRAS, 437, 2686
Pearce, T. D., Wyatt, M. C., & Kennedy, G. M. 2015, MNRAS, 448, 3679
Petrovich, C. 2015, ApJ, 808, 120
Pollack, J. B., Hubickyj, O., Bodenheimer, P., et al. 1996, Icarus, 124, 62
Rameau, J., Chauvin, G., Lagrange, A.-M., et al. 2013, ApJ, 779, L26
Regály, Z., Dencs, Z., Moór, A., & Kovács, T. 2018, MNRAS, 473, 3547
Rhee, J. H., Song, I., Zuckerman, B., & McElwain, M. 2007, ApJ, 660, 1556
Thébault, P., & Wu, Y. 2008, A&A, 481, 713
Toomre, A. 1964, ApJ, 139, 1217
Vigan, A., Moutou, C., Langlois, M., et al. 2010, MNRAS, 407, 71
Wisdom, J. 1980, AJ, 85, 1122
Wyatt, M. C. 2005, A&A, 440, 937

[1] Max-Planck-Institut für Astronomie, Königstuhl 17, 69117 Heidelberg, Germany
e-mail: maire@mpia.de
[2] Univ. Grenoble Alpes, CNRS, IPAG, 38000 Grenoble, France
[3] INAF – Osservatorio Astronomico di Padova, Vicolo dell'Osservatorio 5, 35122 Padova, Italy
[4] Dipartimento di Fisica e Astronomia "G. Galilei", Università di Padova, Via Marzolo, 8, 35121 Padova, Italy
[5] LESIA, Observatoire de Paris, PSL Research University, CNRS, Université Paris Diderot, Sorbonne Paris Cité, UPMC Paris 6, Sorbonne Université, 5 place J. Janssen, 92195 Meudon, France
[6] INCT, Universidad de Atacama, calle Copayapu 485, Copiapó, Atacama, Chile
[7] Unidad Mixta Internacional Franco-Chilena de Astronomía CNRS/INSU UMI 3386 and Departamento de Astronomía, Universidad de Chile, Casilla 36-D, Santiago, Chile
[8] Department of Astronomy, Stockholm University, AlbaNova University Center, 106 91 Stockholm, Sweden
[9] Instituto de Física y Astronomía, Facultad de Ciencias, Universidad de Valparaíso, Av. Gran Bretaña 1111, Playa Ancha, Valparaíso, Chile
[10] Núcleo Milenio Formación Planetaria - NPF, Universidad de Valparaíso, Av. Gran Bretaña 1111, Valparaíso, Chile
[11] ETH Zurich, Institute for Particle Physics and Astrophysics, Wolfgang-Pauli-Strasse 27, 8093 Zurich, Switzerland
[12] CRAL, UMR 5574, CNRS/ENS-Lyon/Université Lyon 1, 9 avenue Charles André, 69561 Saint-Genis-Laval, France
[13] Aix-Marseille Univ., CNRS, LAM, Laboratoire d'Astrophysique de Marseille, Marseille, France
[14] Department of Astronomy, University of Michigan, 1085 S. University Ave, Ann Arbor, MI 48109-1107, USA
[15] INAF – Osservatorio Astronomico di Brera, via Bianchi 46, 23807 Merate (LC), Italy
[16] Geneva Observatory, University of Geneva, Chemin des Maillettes 51, 1290 Versoix, Switzerland
[17] Núcleo de Astronomía, Facultad de Ingeniería, Universidad Diego Portales, Avenida Ejército 441, Santiago, Chile
[18] Millennium Nucleus "Protoplanetary Disk", Departamento de Astronomía, Universidad de Chile, Casilla 36-D, Santiago, Chile
[19] Université Côte d'Azur, OCA, CNRS, Lagrange, France
[20] DOTA, ONERA, Université Paris Saclay, 91123 Palaiseau, France
[21] Anton Pannekoek Institute for Astronomy, Science Park 904, 1098 XH Amsterdam, The Netherlands

Appendix A: Dynamical simulation results for a slightly non-coplanar companion

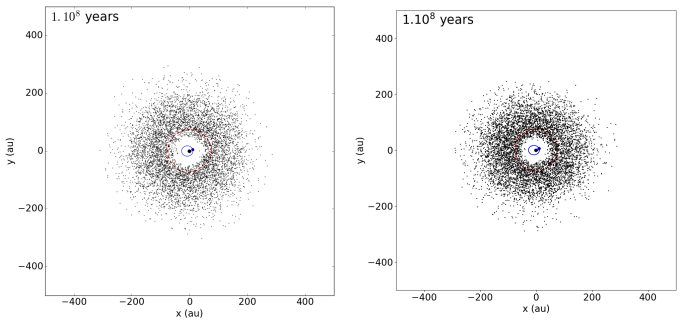

Fig. A.1. Simulated images of the disk for an eccentric (e = 0.4) companion orbit of semi-major axis 20 au coplanar with the disk (*left*) and with a relative inclination of 20° (*right*).

Figure A.1 shows the simulated images of the disk for a companion orbit with a semi-major axis of 20 au and an eccentricity of 0.4 for a coplanar configuration and a relative inclination of 20° with the disk. The simulated relative inclination has no significant effects on the cavity size. The only difference is that in the non-coplanar case, the companion stirs the inclination of the disk particles, which gives the disk a non-negligible thickness (which cannot be seen on the face-on image).

Appendix B: Width of the chaotic zone predicted by other relations

We show in Fig. B.1 the width of the chaotic zone created by a substellar companion in the disk of HR 2562 for several eccentricities according to the empirical relations of Petrovich (2015) and Regály et al. (2018).

We first used the equation in Petrovich (2015), which is an empirical dynamical stability criterion for two-planet systems against collisions with the star and/or ejections from the system. The formula was validated using numerical simulations for planet/star mass ratios 10^{-4}–10^{-2} and mutual inclinations $\lesssim$40°. In order to apply this relation to the HR 2562 companion-disk system, we assumed that the outer planet has a negligible mass (the most extreme mass ratio between the planets is 1/100 in Petrovich 2015). The 1.15 constant term in the formula includes a margin of 0.5 to account for disk regions which are potentially unstable. In order not to overestimate the cavity size and to make the comparison to the criteria in Lazzoni et al. (2018) and Regály et al. (2018) coherent, we therefore decreased the constant term in the formula of Petrovich (2015) by 0.5. We finally assumed a null eccentricity for the debris belt, which is exterior to the companion. Contrary to the formula in Lazzoni et al. (2018) and Regály et al. (2018), the formula of Petrovich (2015) depends on the cavity radius and companion semi-major axis. We chose $a_{\rm cav}$ = 75 au and a = 30 au. We represent the resulting curves in the left panel of Fig. B.1. The eccentricity is not well constrained with respect to the predictions of Lazzoni et al. (2018) (Fig. 12) and can lie in the range ~0.2–0.7.

Subsequently, we considered the relations in the recent work of Regály et al. (2018), which predict the size of the cavity of a debris disk shaped by a giant planet perturber interior to the debris belt. They were determined using N-body simulations assuming a giant planet with mass ratios to the star 1.25×10^{-3}–10^{-2} with eccentricities 0–0.9. Quasi-circular orbits cannot be excluded for a disk cavity size of 38 au and a companion semi-major axis of 20 au, whereas eccentricities as large as ~0.3 are allowed for the smallest mass range compatible with a brown dwarf. For a disk cavity size of 75 au and a companion semi-major axis of 30 au, the eccentricity is also poorly constrained with respect to the predictions of Lazzoni et al. (2018) and can range from ~0.2 up to more than 0.8.

The more stringent constraints on the companion eccentricity obtained using the relations in Lazzoni et al. (2018) stem from the flatter global slopes of the relations with respect to those in Petrovich (2015) and Regály et al. (2018). The relations in Lazzoni et al. (2018) predict wider chaotic zones at mass ratios below ~0.02 and eccentricities larger than 0.2 with respect to the equations of Petrovich (2015) and Regály et al. (2018) while predict narrower chaotic zones for mass ratios larger than ~0.04 and eccentricities smaller than 0.6.

We finally note that the relations in Petrovich (2015) and Regály et al. (2018) usually predict similar values for the chaotic zone widths, except for a circular orbit and large companion/star mass ratios ($\gtrsim$0.03) and for highly-eccentric orbits ($\gtrsim$0.6).

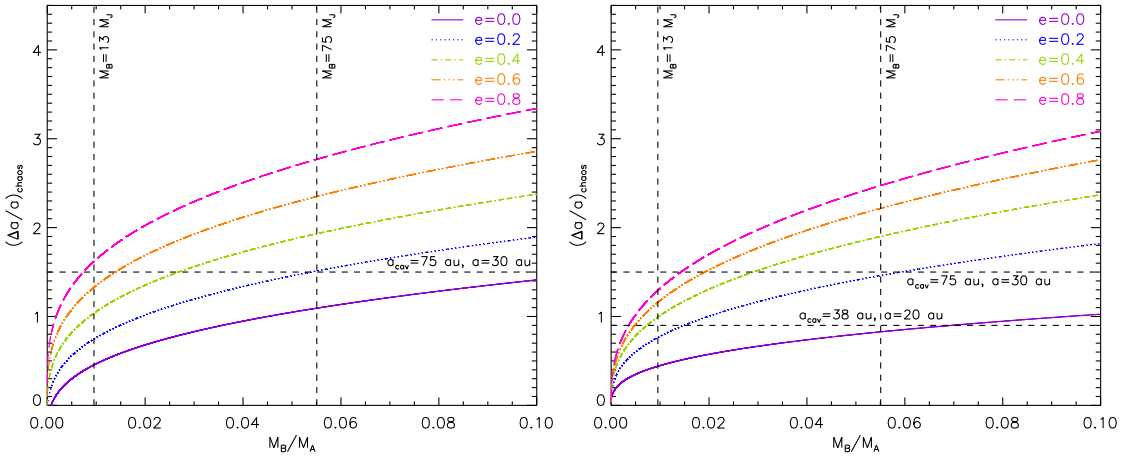

Fig. B.1. Same as Fig. 12 but for the relations in Petrovich (2015; *left*) and Regály et al. (2018; *right*).

5.2 51 Eri: An eccentric giant planet in a hierarchical system

51 Eri A is a nearby F-type star that belongs to the young β-Pictoris moving group. In 2015, the GPI instrument imaged a companion, 51 Eri b, with mass 2-10 M_J, at around 0.45" (13 au) (Macintosh et al. 2015; De Rosa et al. 2015). An inner and an outer debris disks have also been inferred from infrared excess, with very ill-constrained radii (Patel et al. 2014; Riviere-Marichalar et al. 2014). Moreover, 51 Eri forms a hierarchical system with the binary GJ 3305, 2,000 au away, whose orbit (GJ 3305 B around GJ 3305 A) has been precisely monitored (Montet et al. 2015).

Completing the preliminary orbital monitoring by GPI, 6 SPHERE points are presented in Maire, Rodet et al. 2019, for a total orbital coverage of 4 years, or 20°. A 1° offset has been evidenced between SPHERE and GPI data points. The orbit is eccentric ($e \sim 0.5$) and inclined (130°), compatible with coplanarity with the stellar rotation (null obliquity). Three algorithms have been used and compared for the orbital fitting: LSMC (Sec. 3.5.3), MCMC (my contribution) and OFTI (Sec. 3.5.2). Despite the weak constraints, they give very similar results (see Figs. 4, D.1. and E.1. of the paper).

51 Eri b belong to the select club of directly imaged planets. It has the closest separation after β-Pic b, so that a robust orbital fitting will be possible within the next decades. The non-negligible eccentricity of the planet is intriguing, because the formation scenario still struggle to form eccentric planets (see Introduction). The debris disk has a warm and cold components encircling the companion, but they have not been resolved. Resolving the features of the disk might give better constraints on the dynamical history of the planet and could hint for additional companions, that could have triggered the observed eccentricity.

Astronomy & Astrophysics manuscript no. ms
March 20, 2019
©ESO 2019

arXiv:1903.07620v1 [astro-ph.EP] 18 Mar 2019

Hint of curvature in the orbital motion of the exoplanet 51 Eridani b using 3 years of VLT/SPHERE monitoring⋆

A.-L. Maire[1,2,⋆⋆], L. Rodet[3], F. Cantalloube[1], R. Galicher[4], W. Brandner[1], S. Messina[5], C. Lazzoni[6,7], D. Mesa[6,8], D. Melnick[9], J. Carson[9,1], M. Samland[1,⋆⋆⋆], B. A. Biller[10,1], A. Boccaletti[4], Z. Wahhaj[11,12], H. Beust[3], M. Bonnefoy[3], G. Chauvin[3,13], S. Desidera[6], M. Langlois[14,12], T. Henning[1], M. Janson[15,1], J. Olofsson[16,17,1], D. Rouan[4], F. Ménard[3], A.-M. Lagrange[3], R. Gratton[6], A. Vigan[12], M. R. Meyer[18,19], A. Cheetham[20], J.-L. Beuzit[12,3], K. Dohlen[12], H. Avenhaus[1,19], M. Bonavita[10,6], R. Claudi[6], M. Cudel[3], S. Daemgen[19], V. D'Orazi[6], C. Fontanive[10], J. Hagelberg[3,19], H. Le Coroller[12], C. Perrot[4,16,17], E. Rickman[20], T. Schmidt[4,21], E. Sissa[6], S. Udry[20], A. Zurlo[22,23,12,6], L. Abe[24], A. Origné[12], F. Rigal[25], G. Rousset[4], A. Roux[3], and L. Weber[20]

(Affiliations can be found after the references)

Received 8 January 2019 / Accepted 15 March 2019

ABSTRACT

Context. The 51 Eridani system harbors a complex architecture with its primary star forming a hierarchical system with the binary GJ 3305AB at a projected separation of 2000 au, a giant planet orbiting the primary star at 13 au, and a low-mass debris disk around the primary star with possibly a cold component and a warm component inferred from the spectral energy distribution.
Aims. We aim to better constrain the orbital parameters of the known giant planet.
Methods. We monitored the system over three years from 2015 to 2018 with the VLT/SPHERE exoplanet imaging instrument.
Results. We measure an orbital motion for the planet of ∼130 mas with a slightly decreasing separation (∼10 mas) and find a hint of curvature. This potential curvature is further supported at 3σ significance when including literature GPI astrometry corrected for calibration systematics. Fits of the SPHERE and GPI data using three complementary approaches provide broadly similar results. The data suggest an orbital period of 32^{+17}_{-9} yr (i.e. 12^{+4}_{-2} au in semi-major axis), an inclination of 133^{+14}_{-7} deg, an eccentricity of $0.45^{+0.10}_{-0.15}$, and an argument of periastron passage of 87^{+34}_{-30} deg [mod 180°]. The time at periastron passage and the longitude of node exhibit bimodal distributions because we do not detect yet if the planet is accelerating or decelerating along its orbit. Given the inclinations of the planet's orbit and of the stellar rotation axis (134–144°), we infer alignment or misalignment within 18° for the star-planet spin-orbit. Further astrometric monitoring in the next 3–4 years is required to confirm at a higher significance the curvature in the planet's motion, determine if the planet is accelerating or decelerating on its orbit, and further constrain its orbital parameters and the star-planet spin-orbit.

Key words. planetary systems – methods: data analysis – stars: individual: 51 Eridani – planet and satellites: dynamical evolution and stability – techniques: high angular resolution – techniques: image processing

1. Introduction

51 Eridani b is the first giant planet discovered in the GPI exoplanet imaging survey (Macintosh et al. 2015). The methane-rich planet is a bound companion to the young star 51 Eridani, which is a member of the 24-Myr β Pictoris moving group (Zuckerman et al. 2001; Torres et al. 2008; Bell et al. 2015). The star is located at 29.78±0.15 pc[1] (Gaia Collaboration et al. 2018) and forms a hierarchical system with the M-dwarf binary GJ 3305AB with separation ∼10 au located at a projected separation of 2000 au (Feigelson et al. 2006; Montet et al. 2015). Simon & Schaefer (2011) measured a stellar radius of 1.63±0.03 $R_\odot$ with the CHARA interferometer and inferred a stellar mass of 1.75±0.05 $M_\odot$. The primary star also harbors a debris disk inferred from the spectral energy distribution (Riviere-Marichalar et al. 2014; Patel et al. 2014). Riviere-Marichalar et al. (2014) estimated a low infrared (IR) fractional luminosity $L_{\rm IR}/L_\odot = 2.3\times10^{-6}$ from *Herschel* photometry. Since their analysis is based on fitting a 3-parameter model of a modified blackbody to three data points with excess IR emission at wavelengths ≥70 µm, the resulting value for the inner edge of the cold dust belt is largely uncertain with 82^{+677}_{-75} au. They also estimated an upper limit for the dust mass of 1.6×10^{-3} $M_\oplus$ and did not report gas detection ([OI], [CII]). Patel et al. (2014) observed the target with WISE as part of a survey for warm debris disks and inferred a warm disk with temperature 180 K (upper limit 344 K) and radius 5.5 au (lower limit 1.5 au) assuming the disk radiates as a blackbody. 51 Eridani could therefore harbor a two-belt debris disk architecture, a feature observed in other young systems with giant planets like HR 8799 (Marois et al. 2008; Marois et al. 2010; Su et al. 2009) and HD 95086 (Rameau et al. 2013b; Moór et al. 2013).

⋆ Based on observations collected at the European Organisation for Astronomical Research in the Southern Hemisphere under ESO programmes 095.C-0298, 096.C-0241, 198.C-0209, and 1100.C-0481.
⋆⋆ F.R.S.-FNRS Postdoctoral Researcher.
⋆⋆⋆ International Max Planck Research School for Astronomy and Cosmic Physics, Heidelberg, Germany
[1] This value is derived taking the inverse of the parallax measured by *Gaia*. It is in good agreement with the value derived with an optimized approach (29.76±0.12 pc, Bailer-Jones et al. 2018). Our uncertainty of 0.15 pc includes in addition to the statistical error of 0.12 pc an uncertainty term of 0.1 mas to account for potential parallax systematics (https://www.cosmos.esa.int/web/gaia/dr2).

Table 1. Observing log of SPHERE observations of 51 Eridani.

UT date	ϵ ($''$)	τ_0 (ms)	AM start/end	Mode	Bands	DIT (s) × Nfr	FoV rot. (°)	SR
2015/09/25	0.5–1.0	4–9	1.10–1.09	IRDIFS_EXT	YJH+$K12$	16×256	41.5	0.68–0.88
2015/09/26	0.7–1.3	6–12	1.10–1.09	IRDIFS	YJ+BBH	4(64)×918(64)	42.6	0.66-0.90
2016/01/16	1.6–2.3	1	1.09–1.10	IRDIFS	YJ+$H23$	16(64)×256(64)	41.8	0.63–0.86
2016/12/12	1.6–2.8	2	1.09–1.16	IRDIFS	YJ+$H23$	64×54	25.2	0.55–0.62
2016/12/13	0.6–1.0	4–8	1.10–1.09	IRDIFS	YJ+$H23$	64×72	44.4	0.78–0.92
2017/09/28	0.4–0.7	5–12	1.10–1.09	IRDIFS_EXT	YJH+$K12$	24(32)×192(144)	44.1	0.85–0.91
2018/09/18	0.7–1.2	2–5	1.21–1.08	IRDIFS_EXT	YJH+$K12$	24(32)×200(160)	38.5	0.64–0.87

Notes. The columns provide the observing date, the seeing and coherence time measured by the differential image motion monitor (DIMM) at 0.5 µm, the airmass at the beginning and the end of the sequence, the observing mode, the spectral bands, the DIT (detector integration time) multiplied by the number of frames in the sequence, the field of view rotation, and the Strehl ratio measured by the adaptive optics system at 1.6 µm. For the DIT×Nfr column, the numbers in parentheses are for the IFS data.

The planet 51 Eridani b has a projected separation of ~13 au from the primary star. Macintosh et al. (2015) could not confirm the companionship with a proper motion test because of the very short time baseline of their GPI measurements (~1.5 months, between December 2014 and January 2015). Instead, the planetary nature hypothesis is based on the spectrum showing methane absorption. De Rosa et al. (2015) presented a new GPI astrometric epoch obtained in September 2015, confirming that the planet is gravitationnally bound, and detected orbital motion. They also carried out a preliminary assessment of its orbital elements using Bayesian rejection sampling and Markov-chain Monte Carlo methods. Their analysis suggests most probable values with 1σ error bars for the semi-major axis of 14^{+7}_{-3} au, for the period of 41^{+35}_{-12} yr, and for the inclination of 138^{+15}_{-13} deg. The other parameters are marginally constrained. The authors also noted that the orbital inclination of the planet is different from the inclination of the orbital plane of the binary GJ 3305AB ($i = 92.1 \pm 0.2°$, Montet et al. 2015), implying that they cannot be coplanar.

We present in this paper astrometric follow-up observations of 51 Eridani b obtained with the instrument VLT/SPHERE (Beuzit et al. 2019) as part of the SpHere INfrared survey for Exoplanets (SHINE, Chauvin et al. 2017). We describe the observations and the data reduction (Sect. 2). Then, we use the new astrometric data of the planet to analyze its orbital motion (Sect. 3). We subsequently fit the SPHERE astrometry in combination with GPI data to derive its orbital parameters (Sect. 4).

2. Observations and data analysis

We observed 51 Eridani eight times from September 2015 to September 2018 with the IRDIFS mode of SPHERE. In this mode, the near-IR camera IRDIS (Dohlen et al. 2008; Vigan et al. 2010) and integral field spectrograph IFS (Claudi et al. 2008) are operated in parallel, either in the YJ bands for IFS and the $H23$ filter pair for IRDIS (standard IRDIFS mode) or in the YJH bands for IFS and the $K12$ filter pair for IRDIS (IRDIFS_EXT mode). Four datasets were published in an analysis of the planet's spectral energy distribution in Samland et al. (2017). Table 1 lists the published observations used for astrometry and the new observations. We only considered the IRDIS data in this work because the planet astrometry could be extracted from a higher number of datasets due to signal-to-noise limitations. Due to the planet's challenging contrast, it could be detected and its astrometry measured in six datasets only (Table 2).

For all sequences, an apodized pupil Lyot coronagraph (Carbillet et al. 2011; Martinez et al. 2009) was used. For calibrating the flux and the centering of the images, we acquired unsaturated non-coronagraphic images of the star (hereafter reference point-spread function or reference PSF) and coronagraphic images with four artificial crosswise replicas of the star (Langlois et al. 2013) at the beginning and end of the sequences. For all datasets obtained starting from December 2016, the science images were recorded with the stellar replicas simultaneously, to minimize the frame centering uncertainties in the astrometric error budget. Nighttime sky background frames were taken and additional daytime calibration performed following the standard procedure at ESO.

The data were reduced with the SPHERE Data Center pipeline (Delorme et al. 2017), which uses the Data Reduction and Handling software (v0.15.0, Pavlov et al. 2008) and custom routines. It corrects for the cosmetics and instrument distortion, registers the frames, and normalizes their flux. Then, we sorted the frames using visual inspection to reject poor-quality frames (adaptive optics open loops, low-wind effect) and an automatic criterion to reject frames with low flux in the coronagraphic spot (semi-transparent mask). After this step, we were left with 77–97% of the frames depending on the sequence. Finally, the data were analyzed with a consortium image processing pipeline (Galicher et al. 2018). Figure 1 shows the IRDIS images obtained for the best epochs with a two-step process[2]: simultaneous spectral differential imaging (SDI, Racine et al. 1999) and angular differential imaging with the Template Locally Optimized Combination of Images algorithm (TLOCI, Marois et al. 2014).

For all epochs, the planet astrometry and photometry was measured in the SDI+TLOCI images using the fit of a model of planet image built from the reference PSF and processed with TLOCI (Galicher et al. 2018). The position and flux of the model of planet image was optimized to minimize the image residuals within a circular region of radius 1.5 FWHM centered on the measured planet location. The values reported in Table 2 were calibrated following the methods in Maire et al. (2016). We also compared them with the astrometry extracted using SDI in combination with the ANgular DiffeRential Optimal Method Exoplanet Detection Algorithm (ANDROMEDA, Mugnier et al. 2009; Cantalloube et al. 2015) and found most values to agree within the TLOCI measurement uncertainties (Appendix A). We use the SDI+TLOCI astrometry for the astrometric and orbital

[2] The 2015 September 26 dataset was obtained with the broad H-band filter, so it was processed with angular differential imaging only.

Table 2. SPHERE astrometry relative to the star of 51 Eridani b.

Epoch	Filter	ρ (mas)	PA (°)	ΔRA (mas)	ΔDec (mas)	Pixel scale (mas/pix)	North correction angle (°)
2015.74	$K1$	453.4±4.6	167.15±0.56	100.8±2.9	−442.0±3.6	12.267±0.009	−1.813±0.046
2015.74	H	453.9±16.3	166.1±2.0	108.7±8.8	−440.7±13.7	12.251±0.009	−1.813±0.046
2016.04	$H2$	456.7±6.9	165.50±0.84	114.3±4.5	−442.2±5.2	12.255±0.009	−1.82±0.06
2016.95	$H2$	453.6±5.7	160.30±0.72	152.9±3.4	−427.1±4.6	12.255±0.009	−1.808±0.043
2017.74	$K1$	449.0±2.9	155.67±0.38	185.0±2.0	−409.2±2.1	12.267±0.009	−1.735±0.043
2018.72	$K1$	443.3±4.2	150.23±0.55	220.2±2.8	−384.8±3.1	12.267±0.009	−1.796±0.068

Notes. The astrometric error bars were derived assuming an error budget including the measurement uncertainties (image post-processing) and the systematic uncertainties (calibration). The uncertainties in the estimation of the star location for the sequences obtained without the stellar replicas in the science images were estimated using calibration data taken before and after the science images (see text). The values are 0.32, 7.87, and 2.02 mas for the 2015 September 25, 2015 September 26, and January 2016 datasets, respectively.

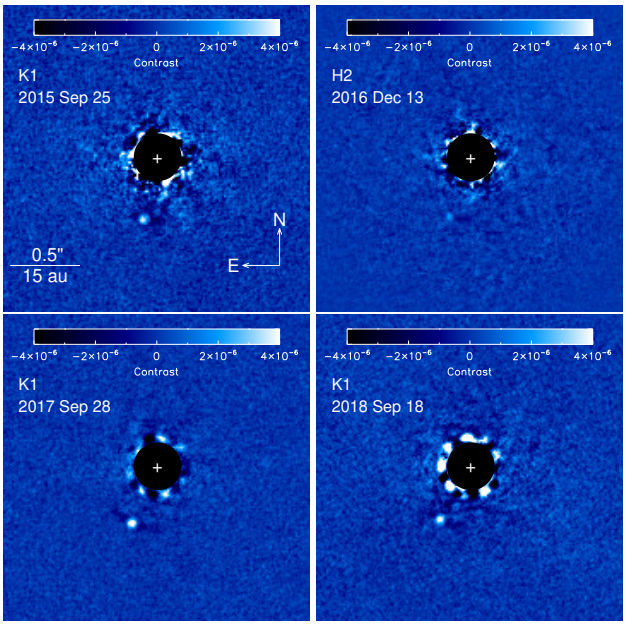

Fig. 1. SPHERE/IRDIS SDI+TLOCI contrast images of 51 Eridani at four epochs obtained with a narrow-band filter in $H2$ ($\lambda_{H2} = 1.593$ µm, December 2016) and in $K1$ ($\lambda_{K1} = 2.110$ µm, all other epochs). The central regions of the images were numerically masked out to hide bright stellar residuals. The white crosses indicate the location of the star.

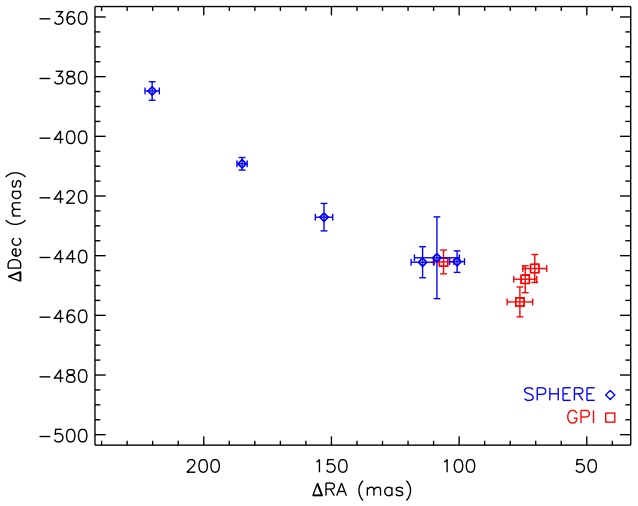

Fig. 2. Compilation of the astrometric measurements of 51 Eridani b. The GPI data are taken from De Rosa et al. (2015) without recalibration on the SPHERE data.

analyses in the next sections, because TLOCI was tested and validated on a larger number of SPHERE datasets to retrieve the astrometry and photometry of detected companions (Galicher et al. 2018).

3. Orbital motion

The astrometry of the planet is given in Table 2. The data are represented in Fig. 2 with the GPI measurements reported by De Rosa et al. (2015), who also revised the astrometry published in Macintosh et al. (2015). The SPHERE data over three years confirm the orbital motion of the planet at a high significance: ~119 mas at ~30σ in right ascension and ~57 mas at ~12σ in declination. While there is a hint for a decrease in separation by ~10 mas, the position angle clearly decreases at a rate of 5.7±0.2°/yr. The trend in position angle is similar to the trend seen in the GPI data (De Rosa et al. 2015). The position angle variation is not compatible with the expectations for a face-on circular orbit (~10°/yr, assuming a semi-major axis for the planet of 13 au and a stellar mass of 1.75 $M_\odot$), suggesting an inclined and/or eccentric orbit. The data also show signs of curvature, hinting at orbital inflexion (see below).

The GPI data obtained in December 2014 and January 2015 show a discrepant increasing trend in separation (in particular, the separations measured in two consecutive nights in January 2015 are not included within the measurement uncertainties of each other hence disagree at the 1-σ level: 454.0 ± 6.4 mas on January 30 and 461.8 ± 7.1 mas on January 31). Macintosh et al. (2015) noted that the conditions for this last observation was average. We also note a small systematic offset in position angle between the SPHERE and GPI data using two measurements obtained close in time in September 2015 (the GPI point has PA = 166.5 ± 0.6°, which is smaller by 1.1 σ from the PA of the SPHERE point which was obtained more than three weeks later, we should also expect due to the orbital motion of the planet over this elapsed time a further displacement of ~-0.38 ± 0.02° in PA). This offset is likely due to systematic uncertainties related to differences in the astrometric calibration of the instruments (see Appendix B). It is well accounted for by an offset in

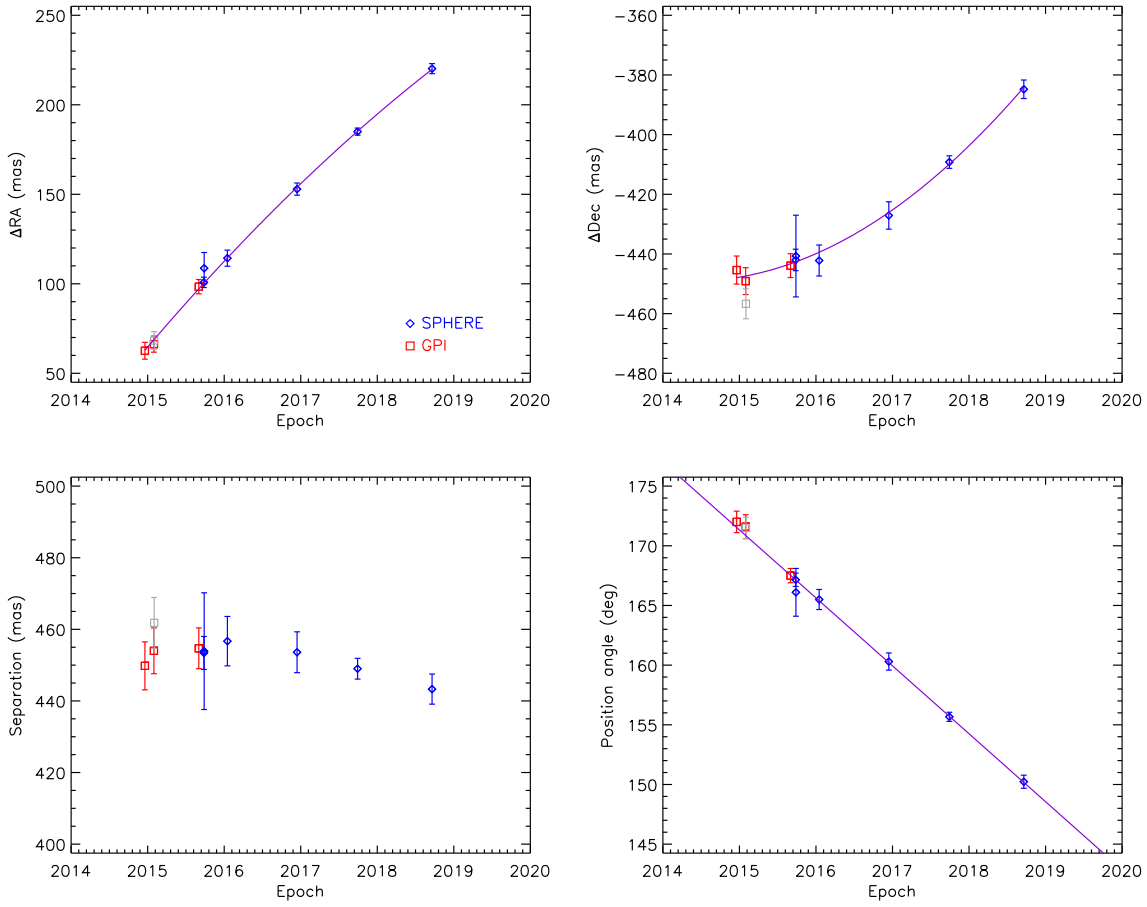

Fig. 3. Temporal evolution of the relative right ascension (*top left*), relative declination (*top right*), separation (*bottom left*) and declination (*bottom right*) of 51 Eridani b. With respect to Fig. 2, the GPI astrometry is recalibrated by adding a position angle offset of 1.0° (see text). In the top panels, second-order polynomial fits on the SPHERE and GPI data points are also indicated to highlight the curvature in the planet motion (purple curves). In the bottom-right panel is shown a linear fit to the SPHERE data (purple line). The data point in light gray was not considered for the acceleration analysis and the orbital fits (see text).

the measured position angles of 1.0±0.2°. The inclusion of the recalibration uncertainty in the GPI measurement uncertainties has negligible effects.

We show the recalibrated GPI data and the SPHERE measurements in Fig. 3, which represents the temporal evolution of the relative right ascension, relative declination, separation, and position angle. The curvature of the SPHERE data which was hinted in Fig. 2 is better seen. We also show second-order polynomial fits to all the SPHERE and GPI data except for the GPI data point taken on 2015 January 31 due to its discrepant separation with respect to the other GPI data points[3]. Second-order polynomial fits provide significantly better unreduced chi-square goodness-of-fit parameters (1.4 for ΔRA vs time and 1.0 for ΔDec vs time) with respect to linear fits (7.4 and 12.2, respectively). We followed the approach of Konopacky et al. (2016a) to test if acceleration is detected (the measured acceleration plus its uncertainty at 3σ shall stay negative). From the second-order polynomial fits abovementioned, we estimated the cartesian components of the acceleration and converted them into radial and tangential components. The radial acceleration component is -4.03 ± 1.34 mas.yr^{-2}, which implies that acceleration is detected at the 3.0σ level. New measurements should help to confirm the acceleration estimate, and measure it with a better accuracy.

[3] The separation measured for this epoch is 461.8 mas whereas the other data points have separations smaller than 455 mas (upper limit of 460.4 mas at 1σ). Even when increasing the error bars on this data point to include the other GPI measurements, the LSMC orbital fit is still affected and shows a stronger paucity in low-eccentricity orbits with respect to a fit where this data point is excluded.

4. Orbital analysis

4.1. Determination of the orbital parameters

We assumed for the system the distance estimated from the *Gaia* parallax and a total mass of 1.75 $M_\odot$ (Simon & Schaefer 2011). We also make the assumption that the GJ 3305AB binary does not dynamically disturb the planet's orbit. Montet et al. (2015) showed that given the wide separation of the binary and the young age of the system, it appears unlikely that Lidov-Kozai oscillations (Kozai 1962; Lidov 1962) could have had the time to disturb the planet's semi-major axis (typical timescale of 200 Myr for a perturber on a circular orbit). Nevertheless, moderate changes in the planet's inclination and eccentricity cannot be excluded (Fabrycky & Tremaine 2007). Quicker dynamical effects (secular precession due to, e.g., an unseen inner companion) could suppress Lidov-Kozai oscillations. On the other hand, assuming the criterion in Holman & Wiegert (1999), we could

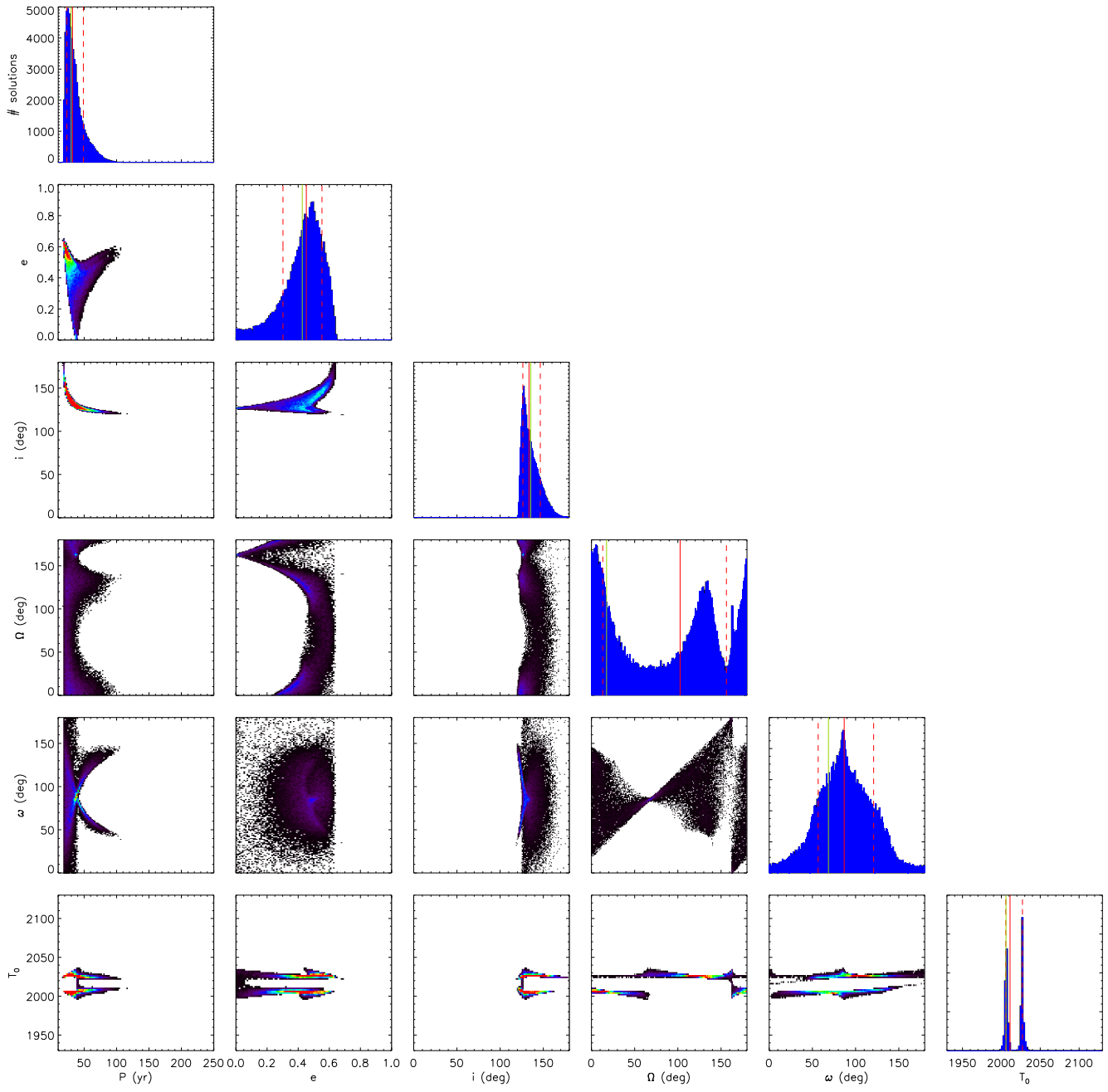

Fig. 4. LSMC distributions of the six Campbell orbital elements for all the fitted solutions with $\chi^2_{\rm red} < 2$ among 1 000 000 random trials. The diagrams displayed on the diagonal from top left to lower right represent the 1D histogram distributions for the individual elements. The off-diagonal diagrams show the correlations between pairs of orbital elements. The linear color scale in the correlation plots accounts for the relative local density of orbital solutions. In the histograms, the green solid line indicates the best χ^2 fitted solution, the red solid line the 50% percentile value, and the red dashed lines the interval at 68%.

also expect that the planet's current orbit remains unchanged despite the wide binary.

We first used a least-square Monte Carlo (LSMC) procedure to fit the SPHERE and GPI astrometry (Esposito et al. 2013; Maire et al. 2015, Appendix C). We also performed complementary analyses using a Markov-chain Monte Carlo (MCMC) procedure (Chauvin et al. 2012, Appendix D) and the Bayesian rejection sampling approach OFTI (Blunt et al. 2017, Appendix E).

We checked with the LSMC and OFTI methods the effects on the parameter distributions of the inclusion of the GPI astrometric points. Adding the GPI data strengthens short-period and eccentric orbits. We also used these two approaches to test the effect of a different initial eccentricity distribution on the resulting eccentricity distribution, given that the analyses favor eccentric orbits over circular orbits. We used a distribution that gives more weight to low-eccentricity orbits, similar to the fit to the eccentricity distribution of radial-velocity planets in Nielsen et al. (2008). The resulting eccentricity distributions have similar shapes using both types of initial distributions. Finally, we checked that the uncertainty on the stellar mass (<3%) has negligible effects on the parameter distributions.

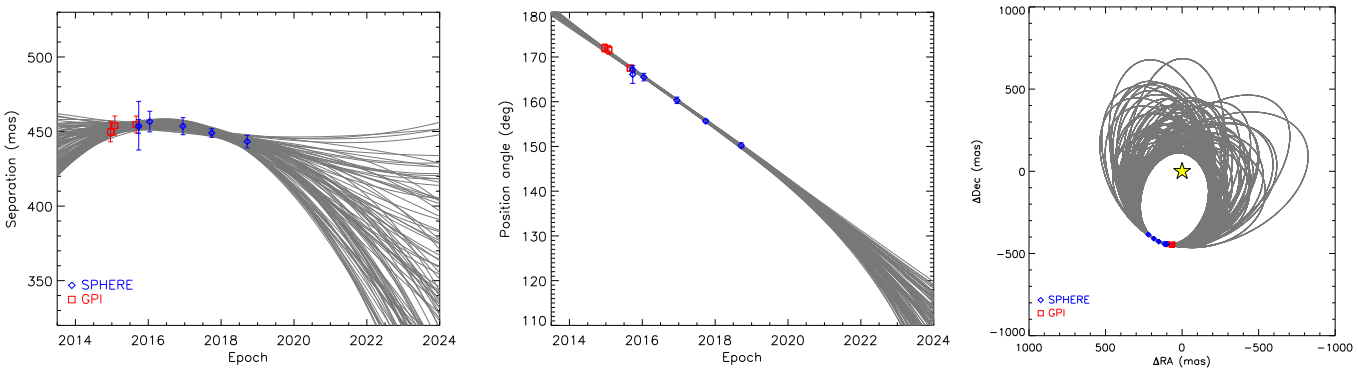

Fig. 5. Predictions for the separation (*left*) and position angle (*middle*) of 51 Eridani b for 100 randomly selected orbital solutions in Fig. 4. The *right* panel displays the orbits in the plane of the sky.

Further constraints could also be obtained with detection limits from archival high-contrast imaging data by rejecting orbits predicting too large separations for the planet in the past. Unfortunately, the current detection limits are not deep enough to provide useful constraints (Heinze et al. 2010; Biller et al. 2013; Rameau et al. 2013a; Hagan et al. 2018; Stone et al. 2018).

4.2. Parameter intervals and correlations

The LSMC distributions and intervals of the orbital parameters are shown in Fig. 4 and Table 3. The shapes of the distributions and the parameter intervals are broadly similar to those obtained with the MCMC and OFTI approaches. The three T_0 distributions show two peaks around ~2005 and ~2025. The three Ω distributions display two broad peaks around ~10° and ~130°. Nevertheless, we note some differences in the detailed shape of the distributions. The LSMC eccentricity distribution does not show a high-eccentricity tail (correlated with a long-period tail) as seen in the MCMC and OFTI distributions. We checked that this is due to the correction for the LSMC fitted orbits of the bias on the time at periastron passage for eccentric orbits (Konopacky et al. 2016a). The LSMC distribution for i has a more pronounced peak toward values smaller than ~135° with respect to the MCMC and OFTI distributions. This is caused by a larger number of low-eccentricity orbits with Ω around ~160° in the LSMC fitted orbits. The LSMC distribution for Ω exhibits a deeper dip between the two broad peaks mentioned above with respect to the MCMC and OFTI distributions. This feature is related to a paucity of orbits with Ω around ~65° and low to moderate eccentricities (up to ~0.4) in the LSMC fitted orbits. The MCMC distribution for ω looks sharper than the LSMC and OFTI distributions.

When comparing our results obtained with the OFTI approach with those of De Rosa et al. (2015), who employed a similar method, we note that most of the parameters are better defined in our analysis[4]. We derive a 68% interval for the inclination of 126–147°, which is slightly better constrained with respect to the range of 125–153° in De Rosa et al. (2015). Thus, we confirm after De Rosa et al. (2015) that the planet's orbital plane cannot be coplanar with the orbital plane of the wide-separated binary GJ 3305AB ($i = 92.1 \pm 0.2°$, Montet et al. 2015). Our eccentricity interval is 0.33–0.57 at 68%, which suggests eccentric orbits. This feature is related to our more extended dataset with respect to De Rosa et al. (2015) (Appendix E). Nevertheless, orbits with low to moderate eccentricities are not formally excluded. Low-eccentricity orbits are characterized by parameters around $\Omega \sim 160°$, $i \sim 130°$, and $P \sim 35$–40 yr. New data covering a larger fraction of the planet's orbit are needed to check the hint for large eccentricities.

Figure 5 shows a random sample of fitted orbits from the LSMC analysis. In particular, low-eccentricity orbits predict steeper decreases of the separation and position angle in the next coming years. If new data taken in the next couple of years show a weak decrease of the separation and still follow the linear trend in position angle seen with the current data, this will rule out low-eccentricity orbits.

Table 3. Preliminary orbital parameters of 51 Eridani b.

Parameter	Unit	Median	Lower	Upper	$\chi^2_{\rm min}$
P	yr	32	23	49	30
a	au	12	10	16	12
e		0.45	0.30	0.55	0.43
i	°	133	126	147	135
Ω	°	103	13	156	17
ω	°	87	57	121	69
T_0		2011	2006	2027	2006

Notes. The parameters are the period, semi-major axis, eccentricity, inclination, longitude of node (mod 180°), argument of periastron passage (mod 180°), and time at periastron passage. The median value is the 50% percentile value, the lower and upper values are the lower and upper bounds of the 68% interval, and the $\chi^2_{\rm min}$ value is the best-fit value.

4.3. An unseen inner companion that could bias the planet's eccentricity?

Finally, we used the methods in Pearce et al. (2014) to test the scenario of an unseen inner low-mass companion which could bias the eccentricity of 51 Eridani b toward large values due to

[4] The 68% interval for the longitude of node in De Rosa et al. (2015) was derived by wrapping the values to the range 30–120°, whereas we consider the full [0;180°] range. For the time of periastron passage, the distribution in De Rosa et al. (2015) shows a stronger peak around epoch ~2005, whereas in our study the peak around epoch ~2025 is slightly more pronounced. They also wrapped their distribution to the range 1995–1995+P, whereas our distributions extend to previous epochs. Nevertheless, we checked that applying a similar wrapping has a negligible effect on the derived T_0 ranges in our analysis. Further monitoring is required to solve for the ambiguity in this parameter.

the orbital motion that the unseen companion induces on the host star around the center of mass of the system. We considered the case where this putative inner companion lies on a circular orbit. For this, we used the period and eccentricity distributions in Fig. 4. Figure 6 shows the minimum mass of a putative inner companion as a function of the planet's eccentricity. Such a companion would lie at an angular separation of ~0.21″[5] (~6 au). By comparing these masses to the SPHERE/IRDIS mass limit of ~3 M_J measured at this separation (Samland et al. 2017) according to the atmospheric and evolutionary models of Baraffe et al. (2015, 2003), we can conclude that if 51 Eridani b has a non-zero eccentricity, this eccentricity is genuine and does not result from an unseen low-mass inner companion.

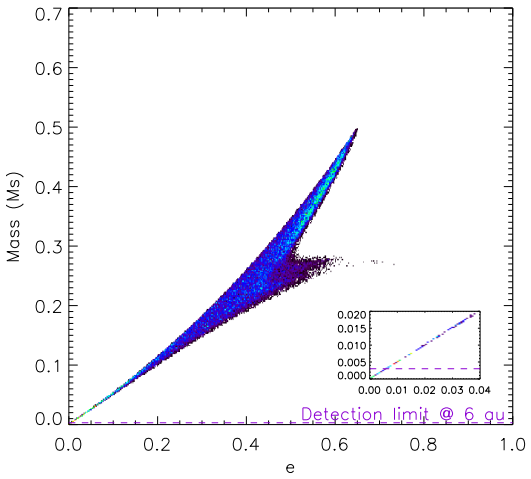

Fig. 6. Minimum mass (in solar masses) of an unseen inner companion on a circular orbit that could bias the eccentricity measured for 51 Eridani b compared to the SPHERE/IRDIS detection limit at 6 au (see text). The inset provides a zoom at low eccentricities and masses to better show the detection limit.

5. Conclusions

We presented VLT/SPHERE observations over three years of the young giant exoplanet 51 Eridani b to further characterize its orbital motion and parameters. The planet moved by ~130 mas over this elapsed time with hints for orbital curvature and a decreasing trend in its separation to the star. We compared the results of three orbital fitting approaches based on LSMC, MCMC, and Bayesian rejection sampling, and found similar distribution shapes for all parameters. With respect to the study of De Rosa et al. (2015), our orbital analysis based on a similar Bayesian rejection sampling approach provides narrower ranges for the orbital parameters. The time at periastron passage and the longitude of node exhibit bimodal distributions, the ambiguity being related to the non-detection of changes in the orbital speed of the planet. We derived an inclination range of 126–147°, which is slightly narrower than the 125–153° range derived by De Rosa et al. (2015). We note that the planet's orbital inclination is compatible with an orbit lying in the stellar equatorial plane (the stellar rotation axis has an inclination of 134–144°, see Appendix F) or offsetted by less than 18°. Given that the star is expected to host a debris disk, this might suggest a coplanar planet-disk configuration and dynamical interactions. Further astrometric monitoring will help to refine the planet's orbital inclination and the analysis of the system spin-orbit.

Our orbital analysis suggests an eccentric orbit for the planet with a 68% interval of 0.30–0.55. If the planet's eccentricity is indeed genuine, this may hint at dynamical interactions between the planet and another body in the system to produce such a large eccentricity. This putative additional body could be an unseen inner or outer planet, although we note that the current imaging detection limits are quite deep (>4 M_J beyond 5 au and >2 M_J beyond 9 au assuming hot-start models, Samland et al. 2017). Another possibility would be gravitational perturbations from GJ 3305AB like Kozai-Lidov oscillations, but this scenario may face timescale issues because of the large separation of the binary and the system youth. Fabrycky & Tremaine (2007) predict that a close-in giant planet experiencing Kozai-Lidov oscillations from a distant binary companion to its host star will typically have an orbit misaligned with the stellar equatorial plan. Our analysis favors alignment or misalignment within 18° for the spin-orbit of the 51 Eridani star-planet system. Interactions of the planet with the circumstellar disk could also be a possible mechanism. Although this kind of interactions is usually thought to damp a planet's eccentricity, simulations have shown that for massive giant planets (>4–5 M_J) lying near the disk midplane (<10°) interactions with a protoplanetary disk increase their eccentricity (Papaloizou et al. 2001; Kley & Dirksen 2006; Bitsch et al. 2013). The current mass estimate of 51 Eridani b is ~2–4 M_J assuming hot-start models but it could be as large as 12 M_J assuming warm-start models (Samland et al. 2017).

Further astrometric monitoring in the next 3–4 years will be critical to confirm at a higher significance the curvature in the planet's motion, determine if the planet is accelerating or decelerating on its orbit, and further constrain its orbital parameters. It will also be critical for preparing future observations. If the planet's angular separation strongly decreases, this might prevent its follow-up near its periastron passage with SPHERE, GPI, and JWST to better constrain its orbital and atmospheric properties and leave such observations feasible with ELT instruments only.

In addition to further orbital follow-up, resolved images of the host star debris disk will be valuable to determine if the planet orbits in the disk plane by providing the disk orientation and, if the data confirm the two disk belts inferred from the stellar spectral energy distribution, if it dynamically shapes these belts by providing their radial extent. Such information would also help to better characterize its orbital period and eccentricity.

Acknowledgements. We thank an anonymous referee for a constructive report that helped to improve the manuscript. The authors thank the ESO Paranal Staff for support in conducting the observations and Philippe Delorme, Eric Lagadec, and Nadège Meunier (SPHERE Data Center) for their help with the data reduction. We also thank Remko Stuik for discussions about the analysis of the MASCARA data and Sarah Blunt, Henry Ngo, Jason Wang, Isabel Angelo, Devin Cody, Robert De Rosa, and Logan Pearce for making the orbitize code publicly available. We acknowledge financial support from the Programme National de Planétologie (PNP) and the Programme National de Physique Stellaire (PNPS) of CNRS-INSU. This work has also been supported by a grant from the French Labex OSUG@2020 (Investissements d'avenir – ANR10 LABX56). The project is supported by CNRS, by the Agence Nationale de la Recherche (ANR-14-CE33-0018). D.M. was supported by the South Carolina Space Grant Consortium. J.C. was supported by the Fulbright Colombia program as well as the South Carolina Space Grant Consortium. This work has made use of the SPHERE Data Centre, jointly operated by OSUG/IPAG (Grenoble), PYTHEAS/LAM/CeSAM (Marseille), OCA/Lagrange (Nice) and Observatoire de Paris/LESIA (Paris). This research made use of the SIMBAD database and the VizieR Catalogue access tool, both operated at the CDS, Strasbourg, France. The original description of the VizieR service was published in Ochsenbein et al. (2000, A&AS 143, 23). This research has made use of NASA's Astrophysics Data System Bibliographic Services. SPHERE is an instrument designed and built by a consortium consisting of IPAG (Grenoble, France), MPIA

[5] This companion could in theory lie at a larger separation but its mass would be larger, hence its detection would be even easier.

(Heidelberg, Germany), LAM (Marseille, France), LESIA (Paris, France), Laboratoire Lagrange (Nice, France), INAF – Osservatorio di Padova (Italy), Observatoire astronomique de l'Université de Genève (Switzerland), ETH Zurich (Switzerland), NOVA (Netherlands), ONERA (France), and ASTRON (Netherlands), in collaboration with ESO. SPHERE was funded by ESO, with additional contributions from the CNRS (France), MPIA (Germany), INAF (Italy), FINES (Switzerland), and NOVA (Netherlands). SPHERE also received funding from the European Commission Sixth and Seventh Framework Programs as part of the Optical Infrared Coordination Network for Astronomy (OPTICON) under grant number RII3-Ct-2004-001566 for FP6 (2004–2008), grant number 226604 for FP7 (2009–2012), and grant number 312430 for FP7 (2013–2016).

References

Bailer-Jones, C. A. L., Rybizki, J., Fouesneau, M., Mantelet, G., & Andrae, R. 2018, AJ, 156, 58
Baraffe, I., Chabrier, G., Barman, T. S., Allard, F., & Hauschildt, P. H. 2003, A&A, 402, 701
Baraffe, I., Homeier, D., Allard, F., & Chabrier, G. 2015, A&A, 577, A42
Bell, C. P. M., Mamajek, E. E., & Naylor, T. 2015, MNRAS, 454, 593
Beuzit, J. L., Vigan, A., Mouillet, D., et al. 2019, A&A, submitted, arXiv:1902.04080
Biller, B. A., Liu, M. C., Wahhaj, Z., et al. 2013, ApJ, 777, 160
Bitsch, B., Crida, A., Libert, A.-S., & Lega, E. 2013, A&A, 555, A124
Blunt, S., Ngo, H., Wang, J., et al. 2019, sblunt/orbitize: Expand default orbit plots
Blunt, S., Nielsen, E. L., De Rosa, R. J., et al. 2017, AJ, 153, 229
Cantalloube, F., Mouillet, D., Mugnier, L. M., et al. 2015, A&A, 582, A89
Carbillet, M., Bendjoya, P., Abe, L., et al. 2011, Exp. Astron., 30, 39
Chauvin, G., Desidera, S., Lagrange, A.-M., et al. 2017, in SF2A-2017, ed. C. Reylé, P. Di Matteo, F. Herpin, E. Lagadec, A. Lançon, Z. Meliani, & F. Royer, 331–335
Chauvin, G., Gratton, R., Bonnefoy, M., et al. 2018, A&A, 617, A76
Chauvin, G., Lagrange, A.-M., Beust, H., et al. 2012, A&A, 542, A41
Claudi, R. U., Turatto, M., Gratton, R. G., et al. 2008, in SPIE Conf. Ser., Vol. 7014, 70143E
De Rosa, R. J., Nielsen, E. L., Blunt, S. C., et al. 2015, ApJL, 814, L3
Delorme, P., Meunier, N., Albert, D., et al. 2017, in SF2A-2017, ed. C. Reylé, P. Di Matteo, F. Herpin, E. Lagadec, A. Lançon, Z. Meliani, & F. Royer, 347–361
Dohlen, K., Langlois, M., Saisse, M., et al. 2008, in SPIE Conf. Ser., Vol. 7014, 70143L
Eastman, J., Gaudi, B. S., & Agol, E. 2013, PASP, 125, 83
Esposito, S., Mesa, D., Skemer, A., et al. 2013, A&A, 549, A52
Fabrycky, D. & Tremaine, S. 2007, ApJ, 669, 1298
Feigelson, E. D., Lawson, W. A., Stark, M., Townsley, L., & Garmire, G. P. 2006, AJ, 131, 1730
Ford, E. B. 2006, The Astrophysical Journal, 642, 505
Gaia Collaboration, Brown, A. G. A., Vallenari, A., et al. 2018, A&A, 616, A1
Galicher, R., Boccaletti, A., Mesa, D., et al. 2018, A&A, 615, A92
Hagan, J. B., Choquet, É., Soummer, R., & Vigan, A. 2018, AJ, 155, 179
Heinze, A. N., Hinz, P. M., Sivanandam, S., et al. 2010, ApJ, 714, 1551
Holman, M. J. & Wiegert, P. A. 1999, AJ, 117, 621
Kley, W. & Dirksen, G. 2006, A&A, 447, 369
Koen, C. & Eyer, L. 2002, MNRAS, 331, 45
Konopacky, Q. M., Marois, C., Macintosh, B. A., et al. 2016a, AJ, 152, 28
Konopacky, Q. M., Rameau, J., Duchêne, G., et al. 2016b, ApJL, 829, L4
Konopacky, Q. M., Thomas, S. J., Macintosh, B. A., et al. 2014, in Society of Photo-Optical Instrumentation Engineers (SPIE) Conference Series, Vol. 9147, Ground-based and Airborne Instrumentation for Astronomy V, 914784
Kozai, Y. 1962, AJ, 67, 591
Lagrange, A. M., Boccaletti, A., Langlois, M., et al. 2019, A&A, 621, L8
Langlois, M., Vigan, A., Moutou, C., et al. 2013, in Proceedings of the Third AO4ELT Conference, ed. S. Esposito & L. Fini, 63
Lidov, M. L. 1962, Planetary and Space Science, 9, 719
Luck, R. E. 2017, AJ, 153, 21
Macintosh, B., Graham, J. R., Barman, T., et al. 2015, Science, 350, 64
Maire, A.-L., Langlois, M., Dohlen, K., et al. 2016, in SPIE Conf. Ser., Vol. 9908, 990834
Maire, A. L., Rodet, L., Lazzoni, C., et al. 2018, A&A, 615, A177
Maire, A.-L., Skemer, A. J., Hinz, P. M., et al. 2015, A&A, 576, A133
Marois, C., Correia, C., Galicher, R., et al. 2014, in SPIE Conf. Ser., Vol. 9148, 91480U
Marois, C., Macintosh, B., Barman, T., et al. 2008, Science, 322, 1348
Marois, C., Zuckerman, B., Konopacky, Q., Macintosh, B., & Barman, T. 2010, Nature, 468, 1080
Martinez, P., Dorrer, C., Aller Carpentier, E., et al. 2009, A&A, 495, 363
Montet, B. T., Bowler, B. P., Shkolnik, E. L., et al. 2015, ApJL, 813, L11
Moór, A., Ábrahám, P., Kóspál, Á., et al. 2013, ApJ, 775, L51
Mugnier, L. M., Cornia, A., Sauvage, J.-F., et al. 2009, Journal of the Optical Society of America A, 26, 1326
Nielsen, E. L., Close, L. M., Biller, B. A., Masciadri, E., & Lenzen, R. 2008, ApJ, 674, 466
Papaloizou, J. C. B., Nelson, R. P., & Masset, F. 2001, A&A, 366, 263
Patel, R. I., Metchev, S. A., & Heinze, A. 2014, ApJS, 212, 10
Pavlov, A., Möller-Nilsson, O., Feldt, M., et al. 2008, in SPIE Conf. Ser., Vol. 7019, 701939
Pearce, T. D., Wyatt, M. C., & Kennedy, G. M. 2014, MNRAS, 437, 2686
Perrin, M. D., Ingraham, P., Follette, K. B., et al. 2016, in Society of Photo-Optical Instrumentation Engineers (SPIE) Conference Series, Vol. 9908, Ground-based and Airborne Instrumentation for Astronomy VI, 990837
Perrin, M. D., Maire, J., Ingraham, P., et al. 2014, in SPIE Conf. Ser., Vol. 9147, 3
Perryman, M. A. C., Lindegren, L., Kovalevsky, J., et al. 1997, A&A, 500, 501
Racine, R., Walker, G. A. H., Nadeau, D., Doyon, R., & Marois, C. 1999, PASP, 111, 587
Rajan, A., Rameau, J., De Rosa, R. J., et al. 2017, AJ, 154, 10
Rameau, J., Chauvin, G., Lagrange, A.-M., et al. 2013a, A&A, 553, A60
Rameau, J., Chauvin, G., Lagrange, A.-M., et al. 2013b, ApJ, 779, L26
Rameau, J., Nielsen, E. L., De Rosa, R. J., et al. 2016, ApJ, 822, L29
Reiners, A. & Schmitt, J. H. M. M. 2003, A&A, 412, 813
Riviere-Marichalar, P., Barrado, D., Montesinos, B., et al. 2014, A&A, 565, A68
Roberts, D. H., Lehar, J., & Dreher, J. W. 1987, AJ, 93, 968
Royer, F., Zorec, J., & Gómez, A. E. 2007, A&A, 463, 671
Samland, M., Mollière, P., Bonnefoy, M., et al. 2017, A&A, 603, A57
Scargle, J. D. 1982, ApJ, 263, 835
Simon, M. & Schaefer, G. H. 2011, ApJ, 743, 158
Stone, J. M., Skemer, A. J., Hinz, P. M., et al. 2018, AJ, 156, 286
Su, K. Y. L., Rieke, G. H., Stapelfeldt, K. R., et al. 2009, ApJ, 705, 314
Talens, G. J. J., Spronck, J. F. P., Lesage, A. L., et al. 2017, A&A, 601, A11
Torres, C. A. O., Quast, G. R., Melo, C. H. F., & Sterzik, M. F. 2008, Young Nearby Loose Associations, ed. B. Reipurth, 757
van Leeuwen, F., Evans, D. W., Grenon, M., et al. 1997, A&A, 323, L61
Vigan, A., Moutou, C., Langlois, M., et al. 2010, MNRAS, 407, 71
Wang, J. J., Graham, J. R., Dawson, R., et al. 2018, AJ, 156, 192
Wang, J. J., Graham, J. R., Pueyo, L., et al. 2016, AJ, 152, 97
Zuckerman, B., Song, I., Bessell, M. S., & Webb, R. A. 2001, ApJL, 562, L87
Zurlo, A., Vigan, A., Galicher, R., et al. 2016, A&A, 587, A57

[1] Max-Planck-Institut für Astronomie, Königstuhl 17, D-69117 Heidelberg, Germany
[2] STAR Institute, Université de Liège, Allée du Six Août 19c, B-4000 Liège, Belgium
e-mail: almaire@uliege.be
[3] Univ. Grenoble Alpes, CNRS, IPAG, F-38000 Grenoble, France
[4] LESIA, Observatoire de Paris, Université PSL, CNRS, Sorbonne Université, Univ. Paris Diderot, Sorbonne Paris Cité, 5 place Jules Janssen, F-92195 Meudon, France
[5] INAF Catania Astrophysical Observatory, via S. Sofia 78, 95123 Catania, Italy
[6] INAF–Osservatorio Astronomico di Padova, Vicolo dell'Osservatorio 5, I-35122 Padova, Italy
[7] Dipartimento di Fisica e Astronomia "G. Galilei", Università di Padova, Via Marzolo, 8, 35121 Padova, Italy
[8] INCT, Universidad de Atacama, calle Copayapu 485, Copiapó, Atacama, Chile
[9] Department of Physics & Astronomy, College of Charleston, 66 George Street, Charleston, SC 29424, USA
[10] Institute for Astronomy, The University of Edinburgh, Royal Observatory, Blackford Hill View, Edinburgh, EH9 3HJ, UK
[11] European Southern Observatory, Alonso de Cordova 3107, Casilla 19001 Vitacura, Santiago 19, Chile
[12] Aix Marseille Université, CNRS, CNES, LAM, Marseille, France
[13] Unidad Mixta Internacional Franco-Chilena de Astronomía CNRS/INSU UMI 3386 and Departamento de Astronomía, Universidad de Chile, Casilla 36-D, Santiago, Chile
[14] CRAL, UMR 5574, CNRS/ENS-L/Université Lyon 1, 9 av. Ch. André, F-69561 Saint-Genis-Laval, France
[15] Department of Astronomy, Stockholm University, AlbaNova University Center, 106 91 Stockholm, Sweden
[16] Instituto de Física y Astronomía, Facultad de Ciencias, Universidad de Valparaíso, Av. Gran Bretaña 1111, Playa Ancha, Valparaíso, Chile
[17] Núcleo Milenio Formación Planetaria - NPF, Universidad de Valparaíso, Av. Gran Bretaña 1111, Playa Ancha, Valparaíso, Chile
[18] Department of Astronomy, University of Michigan, 1085 S. University Ave, Ann Arbor, MI 48109-1107, USA
[19] Institute for Particle Physics and Astrophysics, ETH Zurich, Wolfgang-Pauli-Strasse 27, 8093 Zurich, Switzerland
[20] Geneva Observatory, University of Geneva, Chemin des Maillettes 51, 1290 Versoix, Switzerland
[21] Hamburger Sternwarte, Gojenbergsweg 112, 21029 Hamburg, Germany
[22] Núcleo de Astronomía, Facultad de Ingeniería y Ciencias, Universidad Diego Portales, Av. Ejercito 441, Santiago, Chile
[23] Escuela de Ingenieria Industrial, Facultad de Ingenierá y Ciencias, Universidad Diego Portales, Av. Ejercito 441, Santiago, Chile
[24] Université Côte d'Azur, OCA, CNRS, Lagrange, France
[25] NOVA Optical Infrared Instrumentation Group, Oude Hoogeveensedijk 4, 7991 PD Dwingeloo, The Netherlands

Appendix A: Comparison of astrometric measurements from different algorithms

Table A.1. SPHERE astrometry relative to the star of 51 Eridani b obtained with SDI+TLOCI and SDI+ANDROMEDA.

Epoch	Spectral band	ρ (mas)	PA (°)
SDI+TLOCI			
2015.74	$K1$	453.4±4.4	167.15±0.55
2015.74	H	453.9±15.9	166.1±2.0
2016.04	$H2$	456.7±6.6	165.50±0.83
2016.95	$H2$	453.6±5.7	160.30±0.72
2017.74	$K1$	449.0±2.9	155.67±0.37
2018.72	$K1$	443.3±4.2	150.23±0.54
SDI+ANDROMEDA			
2015.74	$K1$	448.6±1.4	167.45±0.06
2015.74	H	467.4±2.9	167.09±0.07
2016.04[a]	$H2$	–	–
2016.95	$H2$	456.1±1.6	160.06±0.06
2017.74	$K1$	447.9±1.3	155.80±0.04
2018.72	$K1$	439.0±1.2	150.09±0.03

Notes. The uncertainties are from the measurement procedure only and are given at 1σ.
[a] It was not possible to extract the planet's astrometry.

Appendix B: Comparison of the SPHERE and GPI astrometry without GPI/SPHERE recalibration

Figure B.1 shows further comparisons of all the SPHERE astrometry and the GPI astrometry reported in De Rosa et al. (2015) without applying any recalibration of the latter on the SPHERE data. While we do not see any clear GPI/SPHERE offset in the separations (Fig. 3), we note that the position angle of the GPI point taken on 2015 September 1 is smaller by 0.65° (1.1 times the measurement uncertainty) than the PA of a SPHERE point taken three weeks later, on 2015 September 25. However, we expect due to the planet's orbital motion an additional decrease in PA of ∼0.38±0.02° between the GPI and SPHERE epochs, so that the actual offset between these two measurements is possibly ∼1° (1.7 times the measurement uncertainty).

We did not consider for the comparison the SPHERE point taken on 2015 September 26 because the PA measured at this epoch has significantly larger uncertainties and deviates from a linear fit matching well all the other SPHERE data points (purple line in the bottom panel of Fig. B.1). Contrary to the other SPHERE datasets, this dataset was not obtained with the dual-band imaging mode of IRDIS that allows for simultaneous imaging in two spectral bands in and out a methane absorption band. Therefore, SDI could not be used in the image post-processing to attenuate fast quasi-static stellar speckles which are not attenuated with angular differential imaging, resulting in a poorer detection of the planet. We did not also consider other GPI and SPHERE data points because they were taken far in time. We note that the GPI PA measurements exhibit a steeper slope with respect to the SPHERE data although the measured uncertainties are large (−6.7±1.3°) and include the slope value derived from the SPHERE data (−5.7±0.2°).

In order to further analyze potential PA systematics between the SPHERE and GPI data, we reduced all the GPI H-band data of 51 Eridani available in the Gemini archive (eight datasets taken from December 2014 to November 2017) using the GPI data reduction pipeline v1.4.0 (Perrin et al. 2014, 2016), which applies an automatic correction for the North offset of −1.00±0.03° measured by Konopacky et al. (2014). Then, we post-processed them using SDI+ANDROMEDA. The SDI step was necessary to enhance the S/N of the planet. For this, we selected spectral channels where the planet is not expected to show large fluxes due to strong methane absorptions (Macintosh et al. 2015; Samland et al. 2017; Rajan et al. 2017). We could recover the planet in five of the datasets. The GPI PA measurements shown in Fig. B.2 display a decreasing slope (−5.9±0.3°) in agreement with the slope measured with the SPHERE data but are offsetted by 0.65±0.17° toward smaller values. We also note that our GPI measurements in common with De Rosa et al. (2015) are offsetted by ∼0.35±0.05° toward larger values.

From these analyses, we applied a recalibration in PA of 1.0±0.2° to the GPI measurements in De Rosa et al. (2015) before fitting the SPHERE and GPI data. Due to the location of 51 Eridani b, the offset in PA produces an offset mainly in relative RA as seen in the top-left panel of Figure B.1.

The large GPI/SPHERE PA offset that we found in our analysis is likely related to differences in the astrometric calibration of the instruments. It is currently unclear if this PA offset should be considered systematically when combining SPHERE and GPI astrometry in orbital fits because it is not seen for other targets observed with both instruments and with published observations close in time (HD 95086, HR 2562, β Pictoris, HR 8799, Rameau et al. 2016; Konopacky et al. 2016b; Wang et al. 2016, 2018; Chauvin et al. 2018; Maire et al. 2018; Lagrange et al. 2019; Zurlo et al. 2016). Further analysis is needed to conclude on this point but is considered to be beyond the scope of this paper.

Appendix C: LSMC orbital fitting

We drew 1 000 000 random realizations of the astrometric measurements assuming Gaussian distributions around the nominal values. Then, we fit the six Campbell elements simultaneously using the downhill simplex `AMOEBA` procedure provided in the EXOFAST library (Eastman et al. 2013): orbital period P, eccentricity e, inclination i, longitude of node Ω, argument of periastron passage ω, and time at periastron passage T_0. Initial guesses of the parameters were drawn assuming uniform distributions in $\log P$, e, $\cos i$, Ω, ω, and T_0. We considered no restricted ranges except for the period (P=10–1000 yr). We also included the correction for the bias on the eccentricity and time at periastron passage due to the small orbital arc covered by the data following the method in Konopacky et al. (2016a) (∼34% of fitted orbits are rejected when applying this method, because of long periods, large eccentricities and/or times at periastron passage close to the epochs of the data).

For the corner plot and the 68% intervals of the parameters shown in Sect. 4, we retained for the analysis all the derived solutions with $\chi^2_{\rm red} < 2$. The longitude of node and the argument of periastron passage are restrained in the [0;180°] range to account for the ambiguity on the longitude of node inherent to the fitting of imaging data alone.

We note two broad peak features around ∼10° and 130° in the distribution of the longitude of node, which are associated with eccentricities of ∼0.2–0.5 and show correlations with the time at periastron passage. The peak around ∼10° seems to produce more orbits with T_0 around ∼2005, whereas the peak around ∼130° seems to produce more orbits with T_0 around ∼2025.

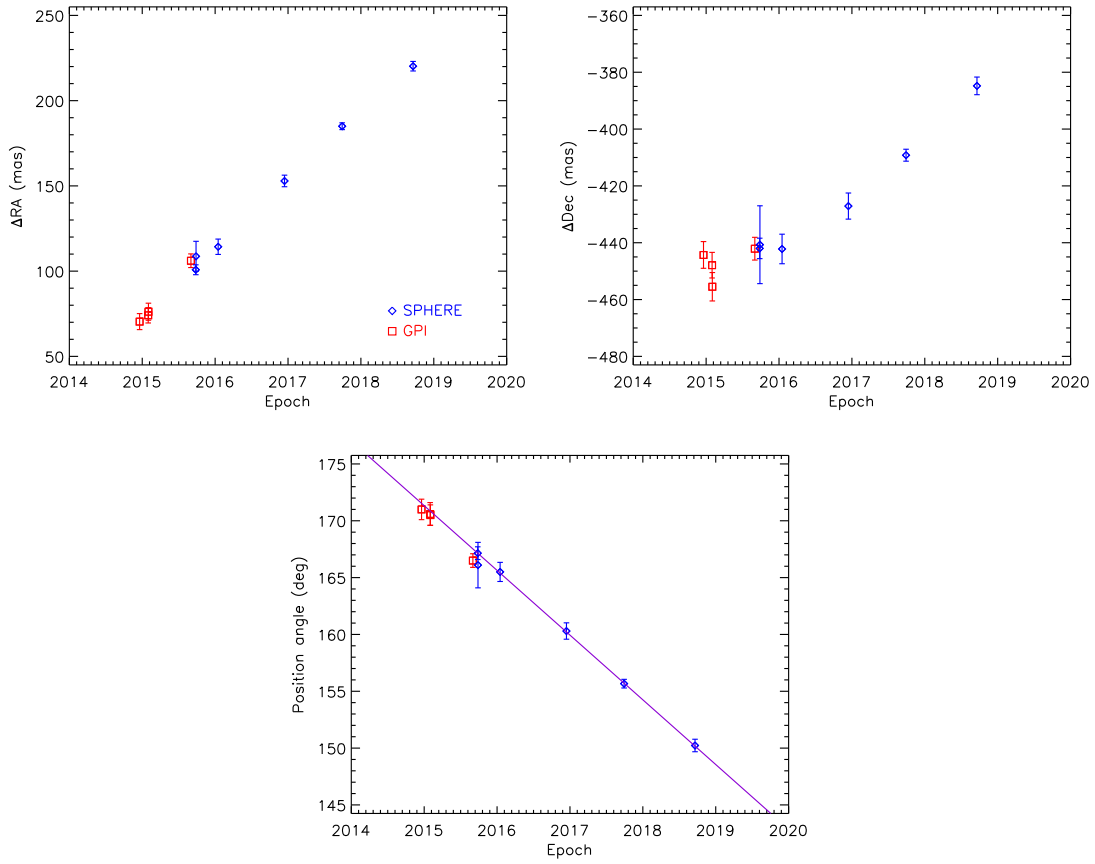

Fig. B.1. Temporal evolution of the relative right ascension (*top left*), relative declination (*top right*), and position angle (*bottom*) of 51 Eridani b. The GPI astrometry is taken from De Rosa et al. (2015) without applying a recalibration of the PA measurements (see Sect. 3). In the bottom-right panel is shown a linear fit to the SPHERE data (purple line).

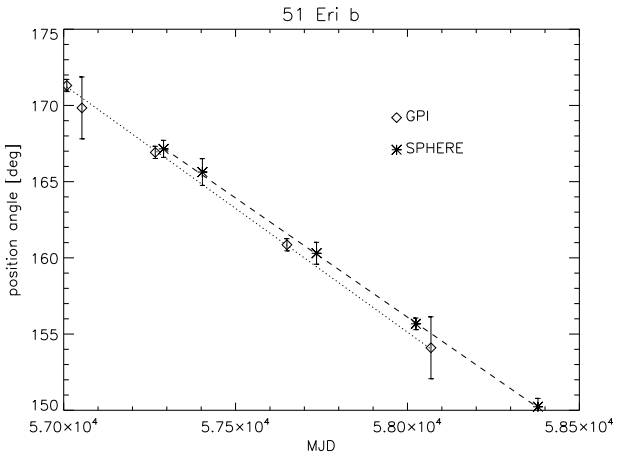

Fig. B.2. Temporal evolution of the position angle of 51 Eridani b measured in the SPHERE data (stars) and our analysis of the GPI archival data (diamonds). Linear fits are shown for each data series separately (SPHERE: dashed line, GPI: dotted line).

Appendix D: MCMC orbital fitting

We provide in this appendix the parameter distribution obtained using an MCMC approach (see details in Chauvin et al. 2012). We assumed uniform priors in log P, e, cos i, $\Omega+\omega$, $\omega-\Omega$, and T_0. Ten chains of orbital solutions were conducted in parallel, and we used the Gelman–Rubin statistics as convergence criterion (see the details in Ford 2006). We picked a random sample of 500 000 orbits from those chains following the convergence.

Table D.1. Orbital parameters of 51 Eridani b derived from the MCMC analysis.

Parameter	Unit	Median	Lower	Upper	$\chi^2_{\rm min}$
P	yr	30	23	46	53
a	au	12	10	15	17
e		0.49	0.36	0.58	0.39
i	°	135	126	146	124
Ω	°	76	14	139	5
ω	°	85	54	111	121
T_0		2007	2005	2027	2009

Appendix E: OFTI orbital fitting

We provide in this appendix the parameter distribution obtained using a custom IDL implementation of the Orbits For The Impatient (OFTI) approach described in Blunt et al. (2017). Briefly, we drew random orbits from uniform distributions in e, cos i, ω, and T_0 and adjusted their semi-major axis and longitude of node by scaling and rotating the orbits to match one of the measured astrometric points. As explained in Blunt et al. (2017), the scale-and-rotate method to adjust the semi-major axis and longitude

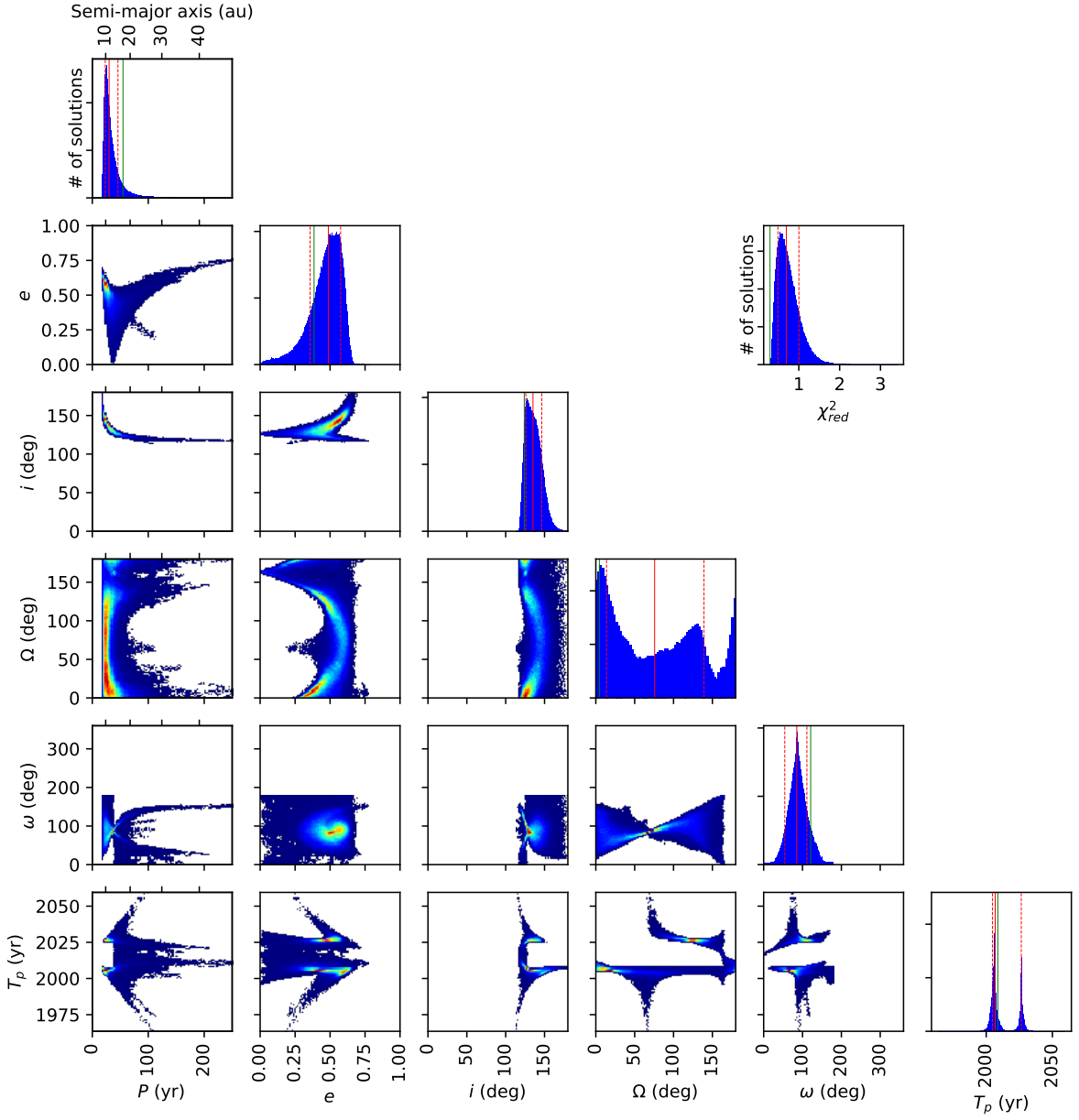

Fig. D.1. MCMC distributions of the six Campbell orbital elements. The diagrams displayed on the diagonal from top left to lower right represent the 1D histogram distributions for the individual elements. The off-diagonal diagrams show the correlations between pairs of orbital elements. The linear color scale in the correlation plots accounts for the relative local density of orbital solutions. The diagram in the top-right part shows the histogram distribution of the reduced χ^2.

of node imposes uniform priors in $\log P$ and Ω. Then, the χ^2 probability of each orbit was computed assuming uncorrelated Gaussian errors before performing the rejection sampling test. To speed up the procedure to obtain a meaningful number of orbits (29 870), we applied the procedure at each iteration over 8 000 trial orbits simultaneously and we also restrained the prior ranges using the statistics of the first 100 accepted orbits.

We cross-checked our code with the OFTI procedure available as part of the Python orbitize package (Blunt et al. 2019). We also performed as a check a fit using only GPI data points (2014 December 18, 2015 January 30, and 2015 September 1) from De Rosa et al. (2015) and assuming the same priors for the parameters and found parameter distributions and intervals very similar to those that they obtained.

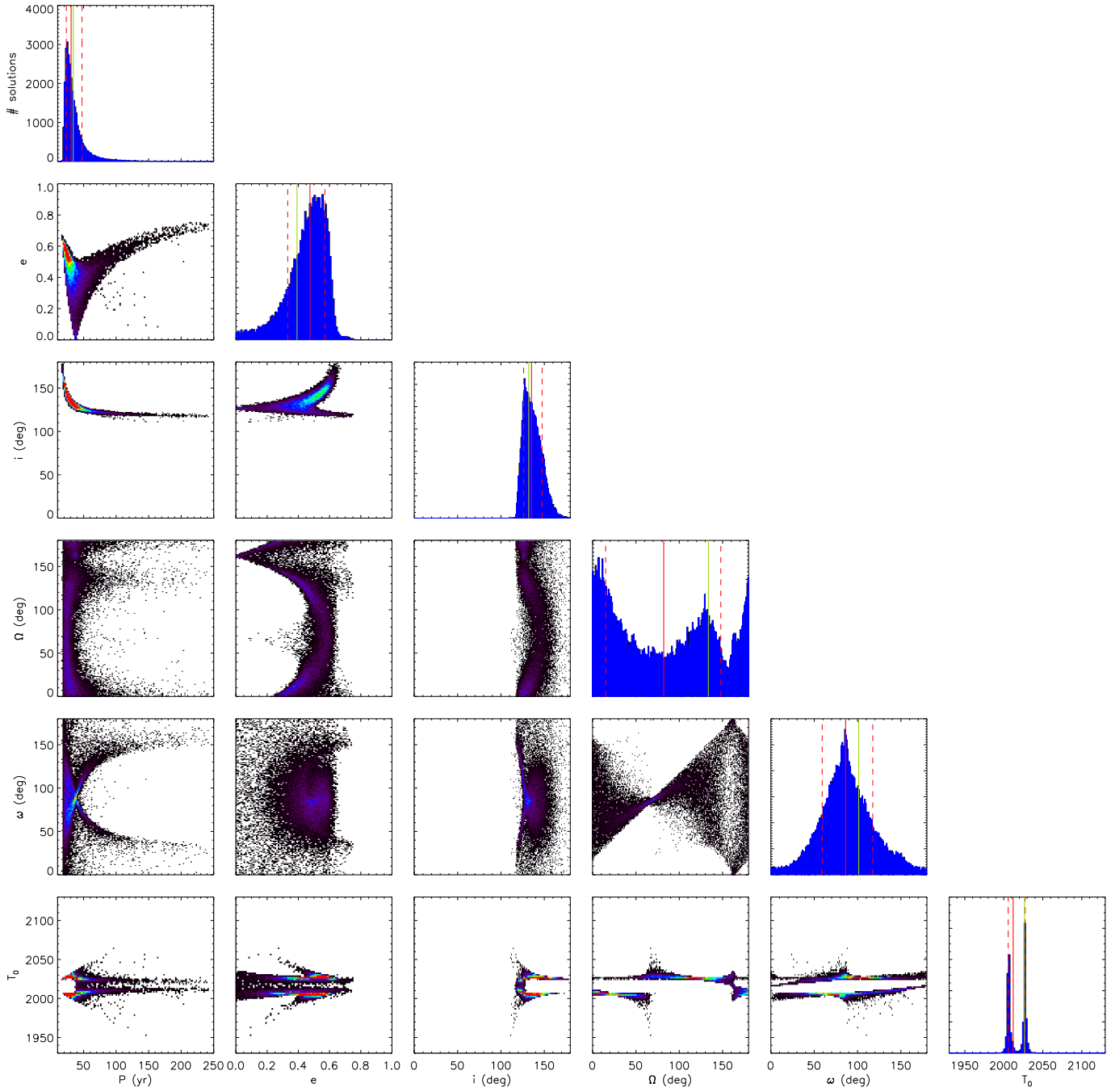

Fig. E.1. Same as Fig. 4 but obtained using the OFTI approach (see text).

Appendix F: Stellar rotation axis

Koen & Eyer (2002) estimated a rotation period of 0.65 d for 51 Eridani from *Hipparcos* photometric data without giving an uncertainty. This rotation period was used by Feigelson et al. (2006) with a stellar projected rotational velocity of $v \sin i_\star = 71.8 \pm 3.6$ km s^{-1} (Reiners & Schmitt 2003) and a stellar radius of 1.5 $R_\odot$ to estimate an inclination of 45° for the star's rotation axis.

In order to better constrain the stellar rotation axis and estimate in particular an uncertainty on this parameter, we reanalyzed the *Hipparcos* photometric data (Perryman et al. 1997; van Leeuwen et al. 1997). Figure F.1 shows the results. Both the Lomb-Scargle periodogram (Scargle 1982) and the CLEAN periodogram (Roberts et al. 1987) show a peak at $P_\star = 0.65 \pm 0.03$ d. We also analyzed as a cross-check analysis archival data from MASCARA (Talens et al. 2017) and found a rotation period in good agreement with the value derived from the Hipparcos data ($P_\star = 0.66$ d, Fig. F.2). We considered only the Hipparcos results in the remainder of the analysis.

Using a V magnitude $V = 5.20$ mag, a distance $d = 29.78 \pm 0.15$ pc, a bolometric correction $BC_V = 0$ mag, and an average effective temperature from the literature $T_\star = 7250$ K, we infer a stellar radius $R_\star = 1.53 \pm 0.04$ $R_\odot$. Combining the rotation period, the stellar radius, and an average projected rotational velocity $v \sin i_\star = 83 \pm 3$ km s^{-1} (estimated from an average of the measurements in Royer et al. 2007;

Table E.1. Orbital parameters of 51 Eridani b derived from the OFTI analysis.

Parameter	Unit	Median	Lower	Upper	$\chi^2_{\rm min}$
P	yr	31	23	47	34
a	au	12	10	16	13
e		0.47	0.33	0.57	0.39
i	°	135	126	147	132
Ω	°	82	15	148	134
ω	°	86	59	118	101
T_0		2012	2006	2027	2026

Luck 2017, 84 km s^{-1} and 81.2 km s^{-1}, respectively), we infer an inclination of the stellar rotation axis with respect to the line of sight $39° < i_\star < 51°$ or $129° < i_\star < 141°$. Given the derived orbital inclination of the planet (126–147°), this suggests alignment for the spin-orbit of the star-planet system. Using the stellar radius measurement of 1.63 ± 0.03 $R_\odot$ in Simon & Schaefer (2011) gives $36° < i_\star < 46°$ or $134° < i_\star < 144°$, which also suggests spin-orbit alignment.

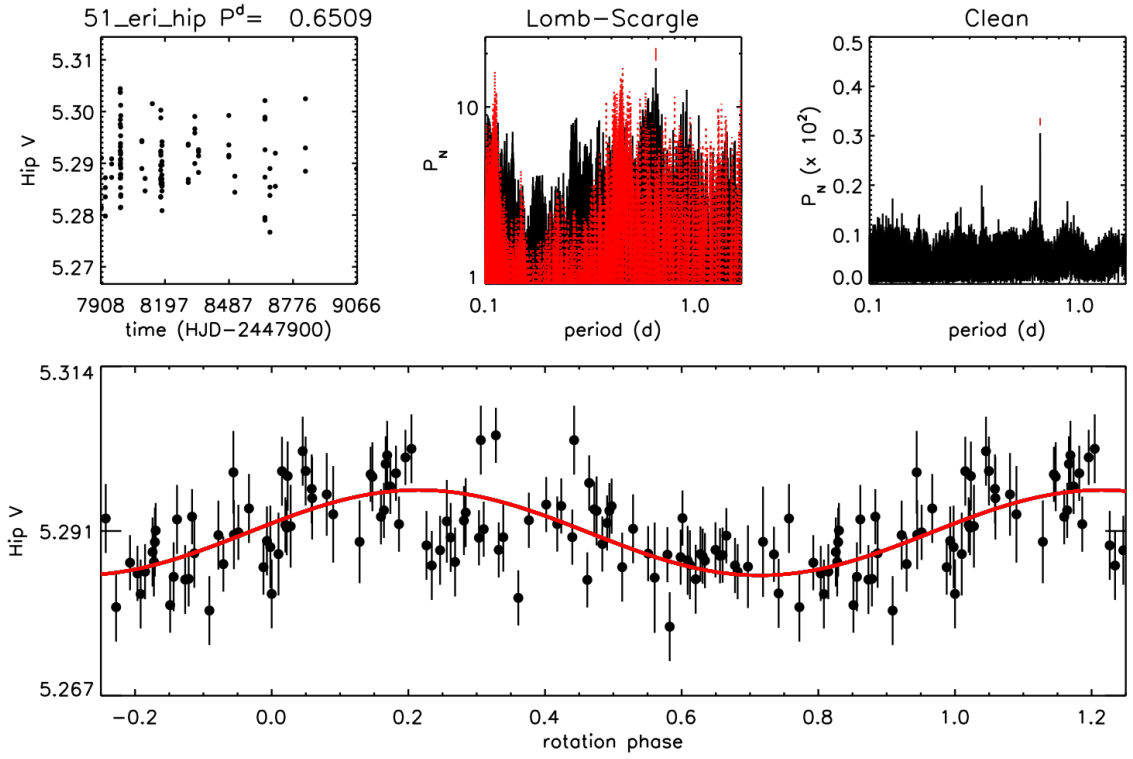

Fig. F.1. Photometric analysis of 51 Eridani based on Hipparcos data. *Top row from left to right*: V-band magnitudes versus Heliocentric Julian Day, Lomb-Scargle periodogram, and CLEAN periodogram. For the Lomb-Scargle periodogram, we show the spectral window function (in red) and the peak corresponding to the rotation period (red vertical mark). *Bottom panel*: Light curve phased with the rotation period. The solid red curve represents the sinusoidal fit.

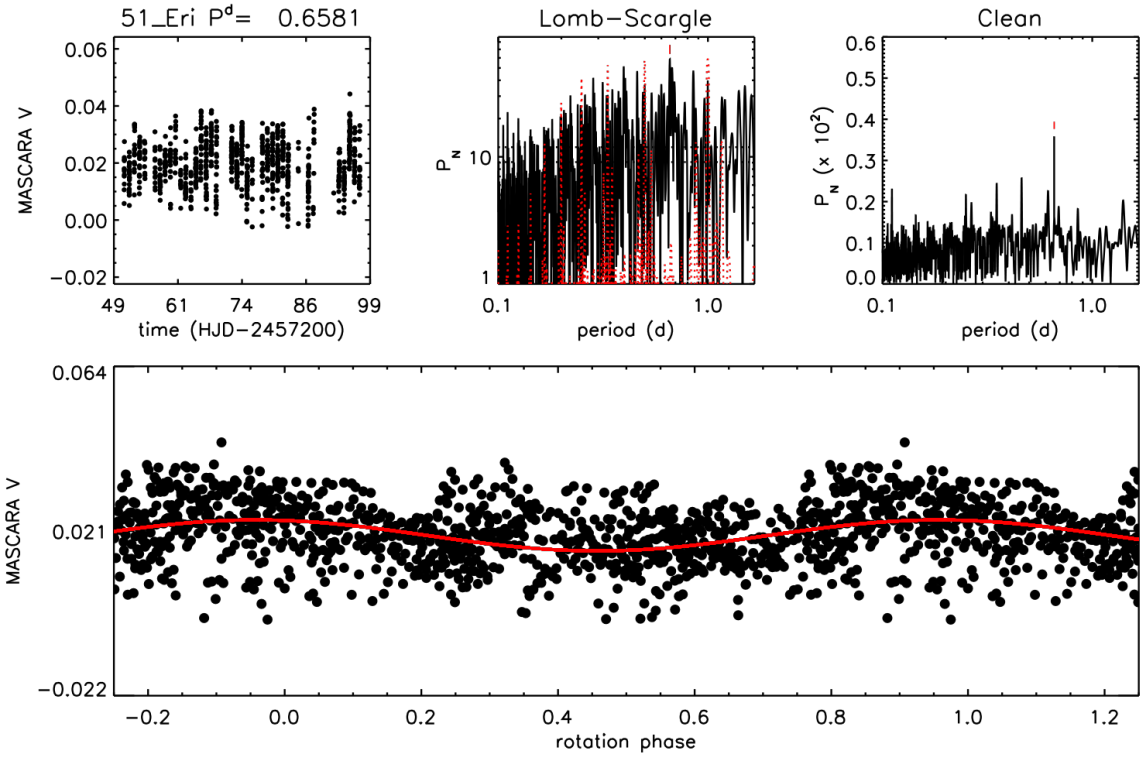

Fig. F.2. Same as for Fig. F.1 but for the MASCARA data.

5.3 HD 206893: An intriguing brown dwarf

HD 206893 (or HIP 107412) A is a F-type star around which a companion at $\sim$ 11 au, HD 206893 B, has been imaged in 2016 by Milli et al. (2017) with SPHERE. Due to the uncertainty on the system age (50-700 Myr) and its unusually red spectrum, the mass of the companion is not well constrained (15-30 M_J) but its brown dwarf nature is established (Delorme et al. 2017). The system also hosts an outer debris disk with an inner radius around 50 au, evidenced by its spectral energy distribution with Spitzer and marginally resolved with Herschel.

A first LSMC approach was performed on the 1-yr baseline astrometric data, but no clear constraints could be derived (Delorme et al. 2017). Adding a constraint of coplanarity with the debris disk selects solutions with a low non-zero eccentricity ($e \sim 0.2$) and a semi-major axis around 10 au.

As part of the Delorme et al. (2017) study, I performed N-body simulations with Swift RMVS to try to improve the constraints on the orbital elements by studying possible interactions with the debris disk. It turns out that all orbits found by the preliminary fit are compatible with an inner radius of 50 au. However, none of them could be responsible for such a large gap. If the system is young (10-20 Myr) and the orbit eccentric, the simulations show that a spiral density wave affects strongly the disk shape. This spiral dissipates for older ages. In any case, the morphology of the disk is strongly unconstrained, so that spiral structures could remain unnoticed.

Finally, a new study by Grandjean et al. (2019) presents more astrometric points, along with radial velocity measurements and constraints from Hipparcos and Gaia. I contributed to the development of the procedure to perform an orbital fitting combining these three types of data, using the `emcee` package (see Sec. 3.5.1). Hipparcos and Gaia's data allow the computation of the difference of stellar orbital velocity projected on the skyplane between two epochs $\sim$ 20 yr apart. In practice, this is done by computing the proper motion difference, taken into account as two additional terms (proper motion difference on the declination and on the right ascension) to the χ^2. This new type of analysis has been made possible with the Gaia DR2.

The star is active and its radial velocity estimate is noisy (100 m/s dispersion), so that the constraints remain loose despite a longer time baseline. Hipparcos and Gaia information provides an estimate of the proper motion variation over 24 years of orbital motion. Radial velocity and proper motions constrain the mass ratio, and the ill-constrained mass of the companion. However, the retrieved mass ($110 - 350$ M_J) is inconsistent with its spectra and magnitude. An unresolved companion might thus be responsible of the radial drift, and would prevent a reliable orbital fitting of HD 206893 B relative motion.

HD 206893 B is unique in many respects. First, it is the brown-dwarf companion with the closest projected separation ever imaged, and it belongs to one of the few such systems comprising a debris disk. The short separation and the low mass ratio ($q = 0.01 - 0.02$) points toward a planetary-like formation (gravitational instability or core accretion). In that respect, the system is very similar to HR 2562, presented above. Moreover, HD 206893 B has the reddest near-infrared color among all known substellar objects, either orbiting a star or isolated. This hints for an extremely dusty atmosphere, and makes the object an essential benchmark for

atmospheric and evolutionary models. Finally, the presence of both a debris disk and a possible additional companion suggested by the radial velocity drift indicate rich dynamical interactions that will be investigated as we gather more observational information (orbital monitoring, constraints on the structures of the disk, detection of the putative additional companion).

A&A 608, A79 (2017)
DOI: 10.1051/0004-6361/201731145
© ESO 2017

Astronomy & Astrophysics

In-depth study of moderately young but extremely red, very dusty substellar companion HD 206893B⋆

P. Delorme[1,⋆⋆], T. Schmidt[2], M. Bonnefoy[1], S. Desidera[3], C. Ginski[4,26], B. Charnay[2], C. Lazzoni[3], V. Christiaens[5,23], S. Messina[6], V. D'Orazi[3], J. Milli[7], J. E. Schlieder[8,9], R. Gratton[3], L. Rodet[1], A.-M. Lagrange[1], O. Absil[5,⋆⋆⋆], A. Vigan[10], R. Galicher[2], J. Hagelberg[1], M. Bonavita[11], B. Lavie[22,12], A. Zurlo[10,13], J. Olofsson[8,14], A. Boccaletti[2], F. Cantalloube[8], D. Mouillet[1], G. Chauvin[1], F.-J. Hambsch[15], M. Langlois[25,10], S. Udry[22], T. Henning[8], J.-L. Beuzit[1], C. Mordasini[12], P. Lucas[16], F. Marocco[16], B. Biller[24], J. Carson[8,17], A. Cheetham[22], E. Covino[18], V. De Caprio[18], A. Delboulbe[1], M. Feldt[8], J. Girard[7], N. Hubin[19], A.-L. Maire[8], A. Pavlov[8], C. Petit[20], D. Rouan[2], R. Roelfsema[21], and F. Wildi[22]

(Affiliations can be found after the references)

Received 10 May 2017 / Accepted 22 July 2017

ABSTRACT

Context. The substellar companion HD 206893b has recently been discovered by direct imaging of its disc-bearing host star with the Spectro-Polarimetric High-contrast Exoplanet REsearch (SPHERE) instrument.
Aims. We investigate the atypical properties of the companion, which has the reddest near-infrared colours among all known substellar objects, either orbiting a star or isolated, and we provide a comprehensive characterisation of the host star-disc-companion system.
Methods. We conducted a follow-up of the companion with adaptive optics imaging and spectro-imaging with SPHERE, and a multi-instrument follow-up of its host star. We obtain a $R = 30$ spectrum from 0.95 to 1.64 μm of the companion and additional photometry at 2.11 and 2.25 μm. We carried out extensive atmosphere model fitting for the companions and the host star in order to derive their age, mass, and metallicity.
Results. We found no additional companion in the system in spite of exquisite observing conditions resulting in sensitivity to 6 $M_{\rm Jup}$ (2 $M_{\rm Jup}$) at 0.5″ for an age of 300 Myr (50 Myr). We detect orbital motion over more than one year and characterise the possible Keplerian orbits. We constrain the age of the system to a minimum of 50 Myr and a maximum of 700 Myr, and determine that the host-star metallicity is nearly solar. The comparison of the companion spectrum and photometry to model atmospheres indicates that the companion is an extremely dusty late L dwarf, with an intermediate gravity (log $g \sim 4.5$–5.0) which is compatible with the independent age estimate of the system.
Conclusions. Though our best fit corresponds to a brown dwarf of 15–30 $M_{\rm Jup}$ aged 100–300 Myr, our analysis is also compatible with a range of masses and ages going from a 50 Myr 12 $M_{\rm Jup}$ planetary-mass object to a 50 $M_{\rm Jup}$ Hyades-age brown dwarf. Even though this companion is extremely red, we note that it is more probable that it has an intermediate gravity rather than the very low gravity that is often associated with very red L dwarfs. We also find that the detected companion cannot shape the observed outer debris disc, hinting that one or several additional planetary mass objects in the system might be necessary to explain the position of the disc inner edge.

Key words. brown dwarfs – planets and satellites: atmospheres – techniques: high angular resolution – planet-disk interactions

1. Introduction

The discovery of young extrasolar giant planets found with high-contrast imaging techniques (Chauvin et al. 2004; Marois et al. 2008; Lagrange et al. 2010; Rameau et al. 2013; Delorme et al. 2013; Bailey et al. 2014; Macintosh et al. 2015; Gauza et al. 2015) offers the opportunity to directly probe the properties of their photosphere. The improved contrast and spectroscopic capabilities of the new generation of adaptive optics (AO) instruments such as Spectro-Polarimetric High-contrast Exoplanet REsearch (SPHERE; Beuzit et al. 2008) and GPI (Macintosh et al. 2012) have made it possible to study the molecular composition and physical processes taking place in the atmospheres of extrasolar giant planets (Zurlo et al. 2016; Bonnefoy et al. 2016; Vigan et al. 2016; De Rosa et al. 2016; Chilcote et al. 2017).

These previous studies have shown that while young exoplanets have a spectral signature quite distinct from field brown dwarfs of equivalent effective temperature, they have many atmospheric properties in common with isolated brown dwarfs recently identified in young moving groups (Liu et al. 2013; Gagné et al. 2015a; Aller et al. 2016; Faherty et al. 2016). They notably share a very red spectral energy distribution (SED) in the near-infrared (NIR) that can be attributed to the presence of very thick dust clouds in their photosphere. This trend was qualitatively expected by atmosphere models because the lower surface gravity of these planetary mass objects inhibits dust settling and naturally increases the dust content within the photosphere. However, all atmosphere models fail to quantitatively match the very red NIR colours of young planetary mass objects via a self-consistent physical model, and have to resort to parametrising the sedimentation efficiency of the dust to match these observations, as done for instance in the *Dusty* models where there is no dust settling (Allard et al. 2001) or the parametrised cloud

⋆ Based on observations made with ESO Telescopes at the Paranal Observatory under Programs ID 097.C-0865(D) (SPHERE GTO, SHINE Program) and Program ID: 082.A-9007(A) (FEROS) 098.C-0739(A), 192.C-0224(C) (HARPS). This work has made use of the SPHERE Data Centre.
⋆⋆ Corresponding author: P. Delorme,
e-mail: Philippe.Delorme@univ-grenoble-alpes.fr
⋆⋆⋆ F.R.S.-FNRS Research Associate.

Astronomy & Astrophysics manuscript no. 206893_draft
December 4, 2018
©ESO 2018

HD206893B mass determination by coupling radial velocity, direct imaging and astrometry

A. Grandjean[1], A.-M. Lagrange[1], H. Beust[2], L.Rodet[1], P.Rubini[3], N.Meunier[1], J. Milli[4], C. Babusiaux[1], S. Aigrain[5], N. Zicher[5], M. Bonnefoy[1], D.-L. Baudino[6], B. A. Biller[7], M. Bonavita[7], A Boccaletti[8], A. Cheetham[9], J. H. V. girard[10], J. Hagelberg[9], M. Janson[11], J. Lannier[1], C. Lazzoni[12], R. ligi[13], A.-L. Maire[12], D. Mesa[14], C. Perrot[8], D. Rouan[8], and A. Zurlo[15,16,17]

[1] Univ. Grenoble Alpes, CNRS, IPAG, F-38000 Grenoble, France
e-mail: Antoine.Grandjean1@univ-grenoble-alpes.fr
[2] Univ. Grenoble Alpes, CNAP, IPAG, F-38000 Grenoble, France
[3] INRIA, Freelance Software Developer, WinSoft International
[4] ESO Office Santiago,ESO
[5] Department of Astrophysics, University of Oxford
[6] Department of Physics, University of Oxford
[7] The Royal Observatory, Edinburgh, Institute for Astrophysics
[8] LESIA, Observatoire de Paris, PSL Research University, CNRS, Sorbonne Universités, UPMC Univ. Paris 06, Univ. Paris Diderot
[9] Observatoire de Genève, University of Geneva, 51 Chemin des Maillettes, 1290, Versoix, Switzerland
[10] Space Telescope Science Institute, Baltimore, United States
[11] Department of Astronomy, Stockholm University, AlbaNova University Center, 106 91 Stockholm, Sweden
[12] INAF - Osservatorio Astronomico di Padova
[13] INAF–Osservatorio Astronomico di Brera, Via E. Bianchi 46, I-23807, Merate, Italy
[14] Astronomical Observatory of Padova/Asiago
[15] Aix Marseille Univ, CNRS, CNES, LAM, Marseille, France
[16] Núcleo de Astronomía, Facultad de Ingeniería y Ciencias, Universidad Diego Portales, Av. Ejercito 441, Santiago, Chile
[17] Escuela de Ingeniería Industrial, Facultad de Ingeniería y Ciencias, Universidad Diego Portales, Av. Ejercito 441, Santiago, Chile

Received date / Accepted date

ABSTRACT

Context. High contrast direct imaging allows determining light companions (planets, brown dwarfs) orbital parameters and to estimate model and age dependent masses from their observed magnitudes or spectra. Combining astrometric positions with radial velocity allows constraining directly the dynamical mass of companions in addition to better constrain their orbit. A brown dwarf was discovered with SPHERE in 2016 around HD206893. Given the important uncertainity on the systeme age, its mass could not be well constrained.
Aims. We aim to constrain HD206893B's orbit and dynamical mass.
Methods. We combined radial velocity data obtained with HARPS spectra and astrometric data obtained with the high contrast imaging VLT/SPHERE and VLT/NaCo instruments, with a time baseline less than 3 years. We then combine those data with astrometry data obtained by HIPPARCOS and Gaia with a time baseline of 24 years. We use an MCMC approach to estimate the orbital parameters and dynamical mass of the brown dwarf from those data.
Results. We infer a dynamical mass of : 131^{+67}_{-59} M_J, an orbital period of 23.84^{+1}_{-1} yr and an orbital inclination of 152^{+4}_{-4} degrees for HD206893 in case of a single planetary system. This mass is not compatible with the observed near IR spectrum of the object. The presence of an inner body could explain the drift in the RV.

Key words. Techniques: radial velocities – Techniques: high angular resolution – astrometry –Stars: brown dwarfs – Stars: binaries : close

1. Introduction

Mass estimation of planets and Brown dwarfs (BD) from high contrast direct imaging depends on evolutionary models. These models still need to be calibrated, especially at young ages. Such calibrations can be done using systems for which the companion mass is independently measured. Combining radial velocity (RV) and astrometric data, information given by high contrast direct imaging and HIPPARCOS/Gaia, permits to measure or constrain the companion's dynamical mass.

HD206893 is a F5V nearby star, located at 40.81 pc (Gaïa DR2). It hosts the reddest known brown dwarf (Delorme et al. 2017). Its age is estimated between 0.2 and 2 Gyr (Zuckerman & Song 2004), so is not well constrained.

A BD was discovered around HD206893 by direct imaging using VLT/SPHERE in 2017 by Milli et al. (2017) with

5.4 HD 100453: A stellar companion shaping a protoplanetary disk?

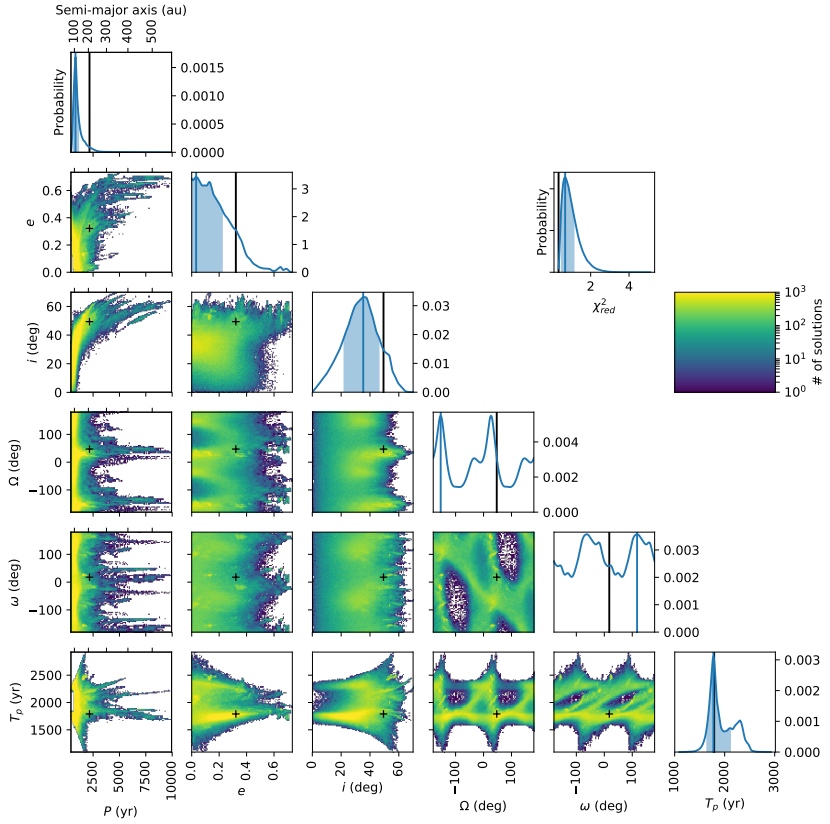

Figure 2.15 – Corner plot presenting the results of the MCMC orbital fitting procedure of HD 100453 A-B relative orbit. The black lines and crosses correspond to the results of the LM procedure (best fit).

HD 100453 A is a young (10 Myr) A9V star whose protoplanetary disk was revealed to host a global two-armed spiral structure, extending over 40 au (Wagner et al. 2015). The star has a M-type companion at a projected separation of 1" (108 au), HD 100453 B, whose relative motion has been monitored for 14 yr (5°) with NaCo, SPHERE and MagAO/Clio-2. It is unsure whether this companions is responsible for the observed disk patterns.

A first orbital fitting has been performed in Wagner et al. (2018) with a grid-search approach. The fit suggests low eccentricity and a semi-major axis close to the projected separation. The inclination of the orbit is low (20-40°), and compatible with a coplanarity with the disk. The study concludes incorrectly on a low relative inclination between the orbital plane and the disk plane. However, equal inclinations from the skyplane does not imply a null relative inclination. To conclude on the coplanarity, the difference of the longitudes of nodes must be considered. Wagner et al. (2018) performed hydrodynamic and radiative transfer simulations in the

coplanar case and shows that the structures in the disk are likely triggered by the companion.

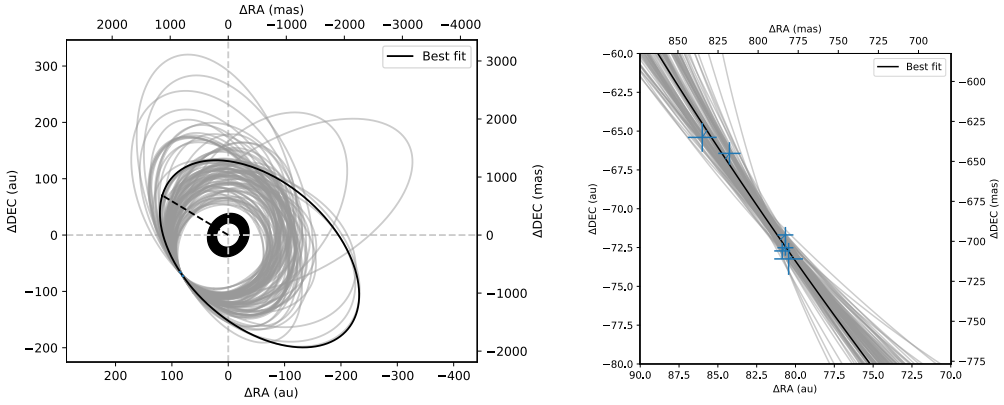

Figure 2.16 – Representation on the sky plane of the results the MCMC orbital fitting procedure of HD 100453 A-B relative orbit. The black orbit corresponds to the results of the LM procedure (best fit). A hundred random solutions are plotted in grey. The disk range is represented in black, and the observations in blue.

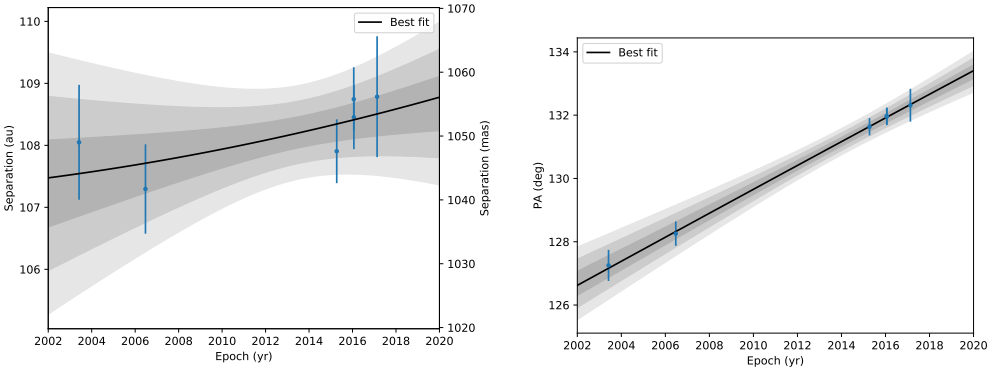

Figure 2.17 – Temporal evolution of the separation and position angle from the results of the MCMC orbital fitting procedure of HD100453 A-B relative orbit. At each time, the standard deviation σ is computed and the 1-σ, 2-σ and 3-σ intervals are represented in different shades of grey. The observations are represented in blue.

A second study was then performed in van der Plas et al. (2019) to study the interaction between the companion and the disk. In this study, I performed an MCMC orbital fitting with the same astrometry, and derive similar constraints. However, using the longitude of nodes, I computed the relative inclination and excluded orbits coplanar with the disk, to the difference of Wagner et al. (2018). This is consistent with the analysis of the ALMA data, exhibiting ^{12}CO overlapping with the projected separation of the companion.

HD 100453 is a complex system and a good laboratory to test spiral formation theory. Understanding the structures within protoplanetary disks are essential to understand disk evolution and planet formation. HD 100453's well-resolved disk

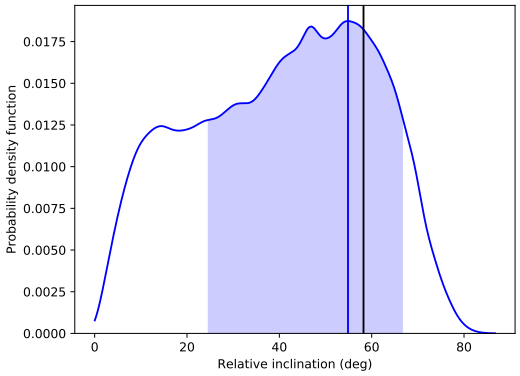

Figure 2.18 – Probability distribution from the results of the MCMC orbital fitting procedure of HD 100453 A-B relative orbit of the relative inclination between the orbit and the disk plane. The black line corresponds to the output of the LM procedure (best fit).

features and the detection and monitoring of a companion near the extent of the disk makes it unique within the known systems with protoplanetary disks. The non-coplanarity of the companion orbit does not solve the mechanisms of spiral formation. Further numerical simulations should be performed to elucidate the interaction of a gaseous disk with such a companion. An alternative hypothesis is the presence of an additional companion inner to the disk.

Astronomy & Astrophysics manuscript no. aa-vdplas-accepted
February 5, 2019
©ESO 2019

ALMA study of the HD 100453 AB system and the tidal interaction of the companion with the disk

G. van der Plas[1], F. Ménard[1], J.-F. Gonzalez[2], S. Perez[3,4], L. Rodet[1], C. Pinte[1,5], L. Cieza[6], S. Casassus[3,4], and M. Benisty[1,4]

[1] Univ. Grenoble Alpes, CNRS, IPAG (UMR 5274), F-38000 Grenoble, France
[2] Univ Lyon, Univ Lyon1, Ens de Lyon, CNRS, Centre de Recherche Astrophysique de Lyon UMR5574, F-69230, Saint-Genis-Laval, France
[3] Millenium Nucleus Protoplanetary Disks in ALMA Early Science, Universidad de Chile, Casilla 36-D, Santiago, Chile
[4] Departamento de Astronomia, Universidad de Chile, Casilla 36-D, Santiago, Chile
[5] Monash Centre for Astrophysics (MoCA) and School of Physics and Astronomy, Monash University, Clayton Vic 3800, Australia
[6] Nucleo de Astronomia, Facultad de Ingenieria, Universidad Diego Portales, Av Ejercito 441, Santiago, Chile

Received ...; accepted ...

arXiv:1902.00720v1 [astro-ph.SR] 2 Feb 2019

ABSTRACT

Context. The complex system HD 100453 AB with a ring-like circumprimary disk and two spiral arms, one of which is pointing to the secondary, is a good laboratory to test spiral formation theories.
Aims. To resolve the dust and gas distribution in the disk around HD 100453 A and to quantify the interaction of HD 100453 B with the circumprimary disk.
Methods. Using ALMA band 6 dust continuum and CO isotopologue observations we study the HD 100453 AB system with a spatial resolution of $0\farcs09 \times 0\farcs17$ at 234 GHz. We use SPH simulations and orbital fitting to investigate the tidal influence of the companion on the disk.
Results. We resolve the continuum emission around HD 100453 A into a disk between $0\farcs22$ and $0\farcs40$ with an inclination of 29.5° and a position angle of 151.0°, an unresolved inner disk, and excess mm emission cospatial with the northern spiral arm which was previously detected using scattered light observations. We also detect CO emission from 7 au (well within the disk cavity) out to $1\farcs10$, i.e., overlapping with HD 100453 B at least in projection. The outer CO disk PA and inclination differ by up to 10° from the values found for the inner CO disk and the dust continuum emission, which we interpret as due to gravitational interaction with HD 100453 B. Both the spatial extent of the CO disk and the detection of mm emission at the same location as the northern spiral arm are in disagreement with the previously proposed near co-planar orbit of HD 100453 B.
Conclusions. We conclude that HD 100453 B has an orbit that is significantly misaligned with the circumprimary disk. Because it is unclear whether such an orbit can explain the observed system geometry we highlight an alternative scenario that explains all detected disk features where another, (yet) undetected, low mass close companion within the disk cavity, shepherds a misaligned inner disk whose slowly precessing shadows excite the spiral arms.

Key words. protoplanetary disks – Herbig Ae/Be stars

1. Introduction

Protoplanetary (PP) disks are a natural byproduct of star formation. These disks dissipate with a typical timescale of 2 to 3 million years (see e.g. the review by Williams & Cieza 2011, and references therein) and planet formation during the evolution and dissipation of the disk appears to be the rule rather than the exception (e.g, Dressing & Charbonneau 2015). The mechanisms that allow the gas and small dust grains in the disk to coalesce into planetary systems are not clear yet and high angular resolution studies of PP disks are necessary to solve this part of the planet formation puzzle.

Our current best tools to study PP disks at high spatial resolution are (sub-)mm interferometers such as ALMA and extreme AO high-contrast imagers such as the Gemini Planet Imager (Gemini/GPI Macintosh et al. 2014) and the Spectro-Polarimetric High-contrast Exoplanet REsearch (VLT/SPHERE Beuzit et al. 2008). Each of them now routinely yields spatial resolutions below $0\farcs1$ but each traces different regions of the disks. The scattered light traces the small ≈ micron sized dust grains high up in the disk surface, while the longer wavelength observations can trace both the larger, typically mm sized, dust grains in the disk mid plane, as well as the intermediate disk layers through many different molecular gas lines.

As we observe PP disks at increasingly high spatial resolution it becomes clear that substructures in these disks are common, and that understanding these substructures is essential to understand disk evolution and planet formation. The most common structures found so far are [1] opacity cavities ranging between a few to over 100 au that sometimes contain a small misaligned inner disk (such as, e.g., HD 142527, see Marino et al. 2015), where this disk also casts a shadow on the outer disk (Casassus et al. 2012), [2] (multiple) rings and / or cavities (e.g. Andrews et al. 2016; Avenhaus et al. 2018), [3] large spiral arms (such as i.e. HD 142527, see Christiaens et al. 2014) , or HD 100453, see Wagner et al. (2015), and [4] azimuthal dust concentrations with various contrast often interpreted as dust trapping in vortices (such as i.e. IRS 48 and HD 34282, see van der Marel et al. 2013; van der Plas et al. 2017). All of these

5.5 GJ 504: two different ages and a possible obliquity

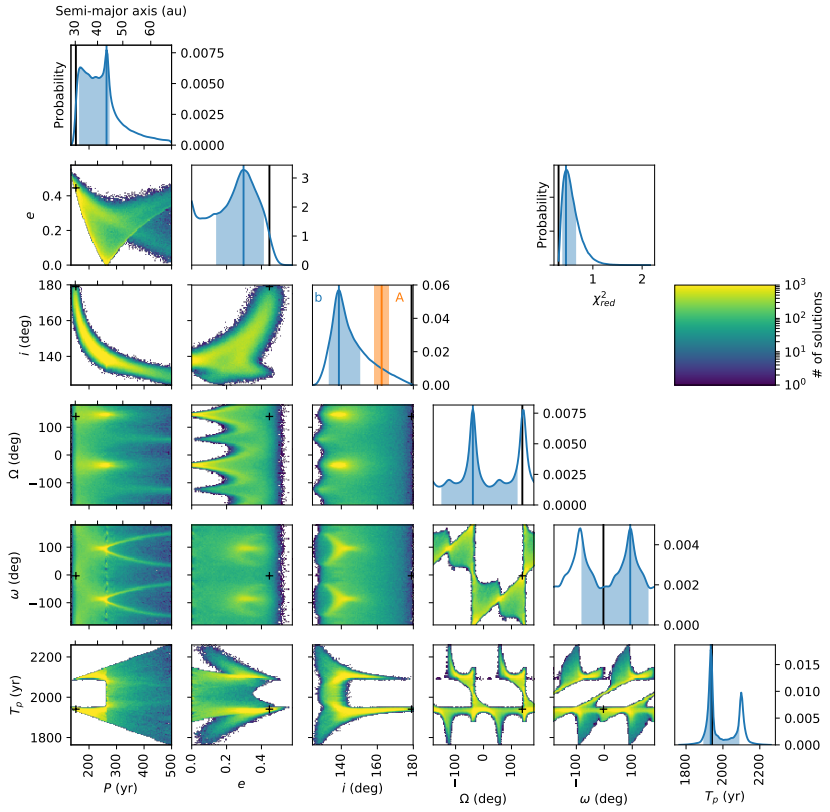

Figure 2.19 – Corner plot presenting the results of the MCMC orbital fitting procedure of GJ 504 A-b relative orbit. The black lines and crosses correspond to the results of the LM procedure (best fit). The inclination of the stellar rotation axis is indicated in orange.

GJ 504 A is a nearby G-type star around which a companion, GJ 504 b, has been imaged in 2011 by Kuzuhara et al. (2013) with the Subaru/HiCIAO adaptative-optics instrument. Follow-up campaigns at Subaru from 2011 to 2012 and with VLT/SPHERE from 2015 to 2018 have confirmed that GJ 504 b is one of the coolest and faintest companion ever imaged ($T_{\rm eff} = 550 \pm 50$ K) (Kuzuhara et al. 2013; Janson et al. 2013; Bonnefoy et al. 2018). Isochronal analyses led to two possible ages for the system (Bonnefoy et al. 2018), corresponding to a companion mass of $1,3^{+0.6}_{-0.3}$ M_J for the young estimate (21 ± 2 Myr) or 23^{+10}_{-9} M_J for the old estimate (4.0 ± 1.8 Gyr).

To determine the age of the system and the nature of the companion, Bonnefoy et al. (2018) performed an in-depth study of the system with interferometric observations, radial velocity measurements and high contrast imaging data. If the study did not succeed to solve the age controversy, we could still perform a first orbital fitting using the 6 years of relative astrometry gathered by Subaru/HiCIAO and

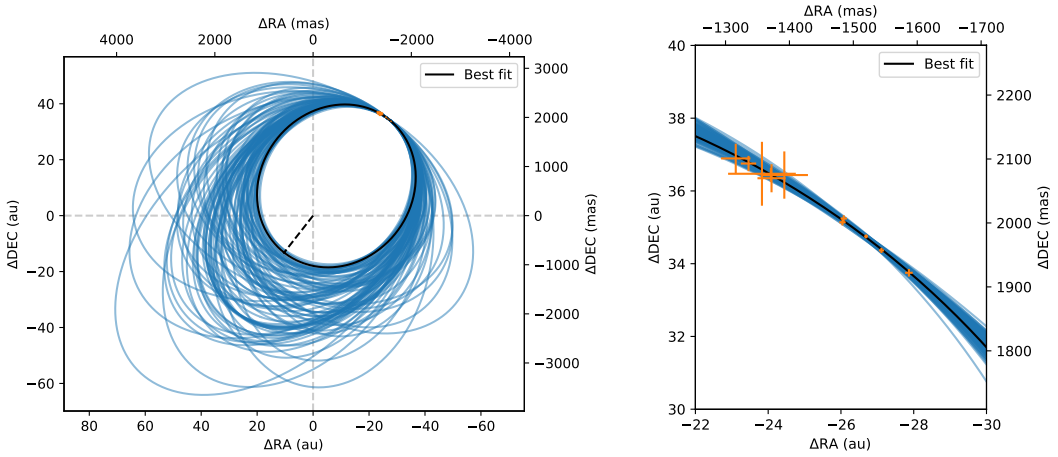

Figure 2.20 – Representation on the sky plane of the results the MCMC orbital fitting procedure of GJ 504 A-b relative orbit.

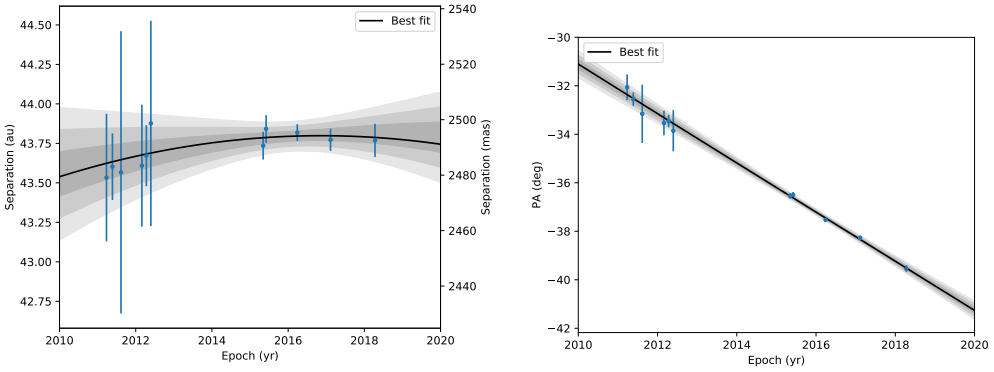

Figure 2.21 – Temporal evolution of the separation and position angle from the results of the MCMC orbital fitting procedure of GJ 504 A-b relative orbit

SPHERE (10° total position angle displacement). The results are displayed on Figs. 2.19, 2.20 and 2.21.

Due to the short orbital coverage, the constraints are quite loose. A first peak of solutions appears at short period (< 300 yr, $a < 45$ au) corresponding to the companion being currently at apoastron on an eccentric retrograde face-on orbit ($e \sim 0.4$). A second peak, more precise, corresponds to a period close to 300 yr ($a \sim 45$ au) and a circular and moderately inclined ($i \sim 140°$) orbit. Finally, a queue of solutions range from periods 300 to more than 500 yr, corresponding to moderately eccentric and inclined orbit. The reduced χ^2 distribution (less than 1) indicates a good fit and overestimated errorbars (which can be hinted from Fig. 2.20).

Moreover, using the interferometric and radial velocity measurement of the stellar radius and rotation period, we could retrieve the line-of-sight inclination of GJ 504 A rotation axis ($162.4^{+3.8}_{-4.3}$ °). The difference Δi between the star inclination and the orbital inclination of GJ 504 b gives a lower bound on the companion obliquity, i.e. the relative orientation of the stellar spin axis and orbital angular momentum

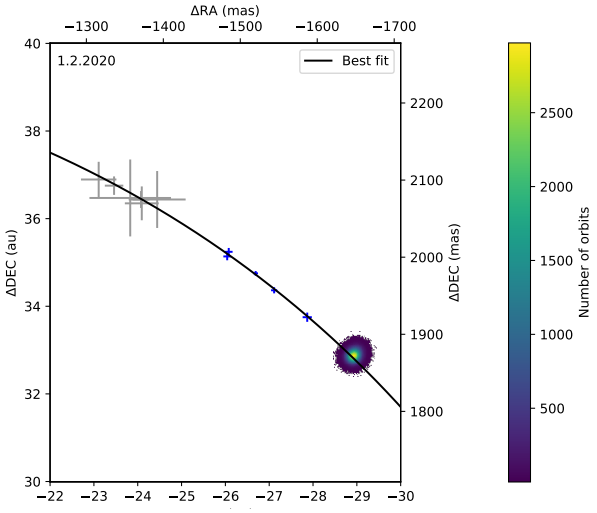

Figure 2.22 – Prediction for the relative position of GJ 504 b in February 2020, for the P104 submitted proposal. This point would improve the constraints on the orbit curvature.

vector (Bowler et al. 2017). Most of our solutions presently lead to Δi values above 10 degrees (see Fig. 2.19). However, we cannot yet firmly exclude a null obliquity, mostly due to the first peak of short-period orbits.

In order to get better constraints on the orbital elements, especially the inclination, and discriminate between the two solution peaks, the orbital monitoring must continue. I am leading a SPHERE proposal to get one extra data point in 2020 (see Fig. 2.22). The proposal suggests 1h30 of observations, and includes 25 co-authors. It will be completed by using the difference between Hipparcos and GAIA proper motions (20 years baseline) as an additional observational constraints, when the precise proper motion of GJ 504 A will be released by GAIA in the early DR3 (bright sources, 2020) (Calissendorff & Janson 2018; Grandjean et al. 2019).

A&A 618, A63 (2018)
https://doi.org/10.1051/0004-6361/201832942
© ESO 2018

Astronomy & Astrophysics

The GJ 504 system revisited

Combining interferometric, radial velocity, and high contrast imaging data*

M. Bonnefoy[1], K. Perraut[1], A.-M. Lagrange[1], P. Delorme[1], A. Vigan[2], M. Line[3], L. Rodet[1], C. Ginski[4], D. Mourard[5], G.-D. Marleau[6], M. Samland[7], P. Tremblin[8], R. Ligi[9], F. Cantalloube[7], P. Mollière[4], B. Charnay[10], M. Kuzuhara[11,12], M. Janson[13], C. Morley[14], D. Homeier[15], V. D'Orazi[16], H .Klahr[7], C. Mordasini[6], B. Lavie[17,6], J.-L. Baudino[9,18], H. Beust[1], S. Peretti[17], A. Musso Bartucci[7], D. Mesa[16,19], B. Bézard[10], A. Boccaletti[10], R. Galicher[10], J. Hagelberg[17,20], S. Desidera[16], B. Biller[7,21], A.-L. Maire[7], F. Allard[15], S. Borgniet[10], J. Lannier[1], N. Meunier[1], M. Desort[1], E. Alecian[1], G. Chauvin[1,22], M. Langlois[15], T. Henning[7], L. Mugnier[23], D. Mouillet[1], R. Gratton[16], T. Brandt[24], M. Mc Elwain[25], J.-L. Beuzit[1], M. Tamura[11,12,26], Y. Hori[11,12], W. Brandner[7], E. Buenzli[7], A Cheetham[17], M. Cudel[1], M. Feldt[7], M. Kasper[1,27], M. Keppler[7], T. Kopytova[1,3], M. Meyer[28,29], C. Perrot[10], D. Rouan[10], G Salter[2], T. Schmidt[10], E. Sissa[16], A. Zurlo[2,30,31], F. Wildi[17], P. Blanchard[2], V. De Caprio[16], A. Delboulbé[1], D. Maurel[1], T. Moulin[1], A. Pavlov[7], P. Rabou[1], J. Ramos[7], R. Roelfsema[32], G. Rousset[10], E. Stadler[1], F. Rigal[32], and L. Weber[17]

(Affiliations can be found after the references)

Received 2 March 2018 / Accepted 28 June 2018

ABSTRACT

Context. The G-type star GJ504A is known to host a 3–35 $M_{\rm Jup}$ companion whose temperature, mass, and projected separation all contribute to making it a test case for planet formation theories and atmospheric models of giant planets and light brown dwarfs.
Aims. We aim at revisiting the system age, architecture, and companion physical and chemical properties using new complementary interferometric, radial-velocity, and high-contrast imaging data.
Methods. We used the CHARA interferometer to measure GJ504A's angular diameter and obtained an estimation of its radius in combination with the HIPPARCOS parallax. The radius was compared to evolutionary tracks to infer a new independent age range for the system. We collected dual imaging data with IRDIS on VLT/SPHERE to sample the near-infrared (1.02–2.25 μm) spectral energy distribution (SED) of the companion. The SED was compared to five independent grids of atmospheric models (`petitCODE`, `Exo-REM`, `BT-SETTL`, Morley et al., and `ATMO`) to infer the atmospheric parameters of GJ 504b and evaluate model-to-model systematic errors. In addition, we used a specific model grid exploring the effect of different C/O ratios. Contrast limits from 2011 to 2017 were combined with radial velocity data of the host star through the `MESS2` tool to define upper limits on the mass of additional companions in the system from 0.01 to 100 au. We used an MCMC fitting tool to constrain the companion's orbital parameters based on the measured astrometry, and dedicated formation models to investigate its origin.
Results. We report a radius of $1.35 \pm 0.04\ R_{\odot}$ for GJ504A. The radius yields isochronal ages of 21 ± 2 Myr or 4.0 ± 1.8 Gyr for the system and line-of-sight stellar rotation axis inclination of $162.4^{+3.8}_{-4.3}$ degrees or $18.6^{+4.3}_{-3.8}$ degrees. We re-detect the companion in the Y2, Y3, J3, H2, and K1 dual-band images. The complete 1–4 μm SED shape of GJ504b is best reproduced by T8-T9.5 objects with intermediate ages ($\leq$1.5Gyr), and/or unusual dusty atmospheres and/or super-solar metallicities. All atmospheric models yield $T_{\rm eff} = 550 \pm 50$ K for GJ504b and point toward a low surface gravity (3.5–4.0 dex). The accuracy on the metallicity value is limited by model-to-model systematics; it is not degenerate with the C/O ratio. We derive $\log L/L_{\odot} = -6.15 \pm 0.15$ dex for the companion from the empirical analysis and spectral synthesis. The luminosity and $T_{\rm eff}$ yield masses of $M = 1.3^{+0.6}_{-0.3}\ M_{\rm Jup}$ and $M = 23^{+10}_{-9}\ M_{\rm Jup}$ for the young and old age ranges, respectively. The semi-major axis (sma) is above 27.8 au and the eccentricity is lower than 0.55. The posterior on GJ 504b's orbital inclination suggests a misalignment with the rotation axis of GJ 504A. We exclude additional objects (90% prob.) more massive than 2.5 and 30 $M_{\rm Jup}$ with semi-major axes in the range 0.01–80 au for the young and old isochronal ages, respectively.
Conclusions. The mass and semi-major axis of GJ 504b are marginally compatible with a formation by disk-instability if the system is 4 Gyr old. The companion is in the envelope of the population of planets synthesized with our core-accretion model. Additional deep imaging and spectroscopic data with SPHERE and JWST should help to confirm the possible spin-orbit misalignment and refine the estimates on the companion temperature, luminosity, and atmospheric composition.

Key words. techniques: high angular resolution – stars: fundamental parameters – techniques: radial velocities – techniques: interferometric – planets and satellites: atmospheres – planets and satellites: formation

* Based on observations collected at the European Organisation for Astronomical Research in the Southern Hemisphere under ESO programs 093.C-0500, 095.C-0298, 096.C-0241, and 198.C-0209, and on interferometric observations obtained with the VEGA instrument on the CHARA Array.

In summary, the orbital characterization of these five systems observed with SPHERE led to five articles (two 2$^{\rm nd}$ author, 4$^{\rm th}$ author, one 5$^{\rm th}$ author, one 7$^{\rm th}$ author, and one 14$^{\rm th}$ author) and one PI ESO proposal. These systems are important pieces for the understanding of the formation of disk structures and the evolution of planetary-mass and brown dwarf companions.

6 Application to the astrometric binaries

An interesting application of orbital fitting is the computation of the dynamical mass(es) of binary stars. Studying stellar dynamics is the only way to determine the stellar masses independently from the evolutionary models. It is thus essential to the calibration of these models, especially in the mass and age range where they are less reliable (young low-mass stars, see Introduction). The objectives are twofold: understanding the underlying physics in the evolution of stellar and substellar objects, and improve the precision of mass predictions. Understanding the stellar evolution is essential to the characterization of stellar to planetary mass objects. We use the model-based age of host stars to estimate the mass of their imaged companions.

There are two types of binary stars for which the dynamical mass can be computed: astrometric binaries and SB2 eclipsing binaries. Indeed, the only possibility to derive the total mass of the system is to compute independently the semi-major axis and the period, and to use then the 3rd Kepler law. For astrometric binaries, the angular semi-major axis and the period are readily measurable, so that the total mass can be retrieved assuming we know the distance of the system. However, the semi-major axis is not retrievable with only radial velocity measurements, only the period and amplitude of the signal are measurable. The amplitude K of one component radial velocity is:

$$K = \frac{2\pi}{P} a \sin(i) \frac{m_1}{m_1 + m_2} \quad . \tag{2.30}$$

By measuring the two components radial velocities (SB2), the mass ratio and the term $a \sin(i)$ can be derived. Thus, the inclination is needed to compute the masses. When the binary is transiting, the inclination (90°) is strongly constrained. In that case, the individual masses are also retrieved. To get the individual masses from astrometric binaries, either their absolute orbits on the skyplane must be fitted, or the radial velocity amplitude of one component must be observed. The former is currently rarely achieved, but will be generalized with the final Gaia release (see Sec. 7).

In the following subsections, I present a thorough orbital fit of three rare pairs of M-type binary stars. Their robust belonging to young moving groups make them ideal calibrators of the evolutionary models. Moreover, they are tight enough to allow a complete orbital coverage in a reasonable time ($P < 10$ yr).

6.1 TWA 22: good accordance with evolutionary model predictions

TWA 22 AB is a pair of M-type stars belonging to the 25 Myr old β Pic moving group. Its relative orbit is strongly constrained by a decade (2 orbital periods) of monitoring with the adaptive-optics imager NaCo at VLT, completed by a later observation with SPHERE (Bonnefoy et al. 2009; Rodet et al. 2018). Moreover, its parallax has been thoroughly studied in Teixeira et al. (2009).

An MCMC orbital fit has been performed in Rodet et al. (2018) (below) with all the available astrometric measurements. The angular separation was determined with a 3 mas precision (3 %) and the period with a 0.04 yr precision (<1 %). However, through the cubic power of the semi-major axis in the second Kepler law, the precision on the mass is around 10 %.

Finally, the fit predicts for TWA 22 a total dynamical mass of 0.18 $M_{\odot}$. This is perfectly consistent with the estimate age of its moving group, given its luminosity (see Fig. 8 in the paper below), according to the two evolutionary models we used.

6.2 GJ 2060: underluminous and eccentric binary in the AB Dor moving group

GJ 2060 AB is a pair of M-type stars belonging to the AB Doradus moving group, whose age constraint is loose (50-150 Myr). Its relative orbit can be strongly constrained through 15 yr (2 orbital periods) of astrometric monitoring with 5 different instruments, and radial velocity monitoring with 2 different instruments (Rodet et al. 2018). This article gives the first estimate of the orbital elements of GJ 2060 AB.

The astrometric data are well consistent with each other and allows for a precise determination of all orbital elements: angular separation with a 2 mas precision (<1 %) and period with a 0.03 yr precision (< 1 %). However, the relatively imprecise Hipparcos parallax of the pair (3% error) does not enable a mass precision better precision than 10%. Moreover, we show that the radial velocities of the two components are blended and strongly biased by stellar activity.

According to six different evolutionary models, GJ 2060 AB is strongly underluminous for its mass, whatever its age. The potential reason for the discrepancy is discussed in details in the paper. A legitimate hypothesis would be that the strong magnetic activity of the stars (evidenced by the jitter in the radial velocity measurements) induces a non-negligible spot coverage, which decreases the observed luminosity (Somers & Pinsonneault 2015).

In order to improve the precision of the study, Gaia DR3 parallaxes (that takes into account the binarity of sources) are needed. In the mean time, further monitoring of the sources is not critical, given the already excellent orbital coverage. Data at the periastron of the very eccentric orbit, in 2021, might however improve significantly the fit, assuming we are able to resolve the two stars.

A&A 618, A23 (2018)
https://doi.org/10.1051/0004-6361/201832924
© ESO 2018

Astronomy & Astrophysics

Dynamical masses of M-dwarf binaries in young moving groups

I. The case of TWA 22 and GJ 2060

L. Rodet[1], M. Bonnefoy[1], S. Durkan[2,3], H. Beust[1], A.-M. Lagrange[1], J. E. Schlieder[4,5], M. Janson[3], A. Grandjean[1], G. Chauvin[1,6], S. Messina[7], A.-L. Maire[5], W. Brandner[5], J. Girard[8,1], P. Delorme[1], B. Biller[9], C. Bergfors[5,10], S. Lacour[11], M. Feldt[5], T. Henning[5], A. Boccaletti[11], J.-B. Le Bouquin[1], J.-P. Berger[1], J.-L. Monin[1], S. Udry[12], S. Peretti[12], D. Segransan[12], F. Allard[13], D. Homeier[14], A. Vigan[15], M. Langlois[13,15], J. Hagelberg[1], F. Menard[1], A. Bazzon[18], J.-L. Beuzit[1], A. Delboulbé[1], S. Desidera[7], R. Gratton[7], J. Lannier[1], R. Ligi[15], D. Maurel[1], D. Mesa[7], M. Meyer[18], A. Pavlov[5], J. Ramos[5], R. Rigal[17], R. Roelfsema[16], G. Salter[15], M. Samland[5], T. Schmidt[11], E. Stadler[1], and L. Weber[12]

(Affiliations can be found after the references)

Received 28 February 2018 / Accepted 13 June 2018

ABSTRACT

Context. Evolutionary models are widely used to infer the mass of stars, brown dwarfs, and giant planets. Their predictions are thought to be less reliable at young ages (<200 Myr) and in the low-mass regime (<1 $M_\odot$). GJ 2060 AB and TWA 22 AB are two rare astrometric M-dwarf binaries, respectively members of the AB Doradus (AB Dor) and Beta Pictoris (β Pic) moving groups. As their dynamical mass can be measured to within a few years, they can be used to calibrate the evolutionary tracks and set new constraints on the age of young moving groups.
Aims. We provide the first dynamical mass measurement of GJ 2060 and a refined measurement of the total mass of TWA 22. We also characterize the atmospheric properties of the individual components of GJ 2060 that can be used as inputs to the evolutionary models.
Methods. We used NaCo and SPHERE observations at VLT and archival Keck/NIRC2 data to complement the astrometric monitoring of the binaries. We combined the astrometry with new HARPS radial velocities (RVs) and FEROS RVs of GJ 2060. We used a Markov chain Monte-Carlo (MCMC) module to estimate posteriors on the orbital parameters and dynamical masses of GJ 2060 AB and TWA 22 AB from the astrometry and RVs. Complementary data obtained with the integral field spectrograph VLT/SINFONI were gathered to extract the individual near-infrared (1.1–2.5 μm) medium-resolution ($R \sim 1500-2000$) spectra of GJ 2060 A and B. We compared the spectra to those of known objects and to grids of BT-SETTL model spectra to infer the spectral type, bolometric luminosities, and temperatures of those objects.
Results. We find a total mass of $0.18 \pm 0.02\,M_\odot$ for TWA 22, which is in good agreement with model predictions at the age of the β Pic moving group. We obtain a total mass of $1.09 \pm 0.10\,M_\odot$ for GJ 2060. We estimate a spectral type of $M1 \pm 0.5$, $L/L_\odot = -1.20 \pm 0.05$ dex, and $T_{\rm eff} = 3700 \pm 100$ K for GJ 2060 A. The B component is a $M3 \pm 0.5$ dwarf with $L/L_\odot = -1.63 \pm 0.05$ dex and $T_{\rm eff} = 3400 \pm 100$ K. The dynamical mass of GJ 2060 AB is inconsistent with the most recent models predictions (BCAH15, PARSEC) for an AB Dor age in the range 50–150 Myr. It is 10%–20% (1–2σ, depending on the assumed age) above the model's predictions, corresponding to an underestimation of 0.10–0.20 $M_\odot$. Coevality suggests a young age for the system (~50 Myr) according to most evolutionary models.
Conclusions. TWA 22 validates the predictions of recent evolutionary tracks at ~20 Myr. On the other hand, we evidence a 1–2σ mismatch between the predicted and observed mass of GJ 2060 AB. This slight departure may indicate that one of the stars hosts a tight companion. Alternatively, this would confirm the model's tendency to underestimate the mass of young low-mass stars.

Key words. techniques: high angular resolution – binaries: visual – astrometry – stars: low-mass – stars: pre-main sequence – stars: individual: TWA 22 – stars: individual: GJ 2060

1. Introduction

Our understanding of stellar evolution has made a lot of progress since the introduction of the Hertzsprung-Russell diagram (HRD) a hundred years ago. The beginning of a star life, before it reaches the zero age main sequence, has been in particular deeply investigated through the development of evolutionary models. The latter rely on equations of state describing the stellar interior structure, and can make use of atmospheric models to define boundary conditions and predict emergent spectra. Different families of models exist (D'Antona & Mazzitelli 1997; Siess et al. 2000; Tognelli et al. 2012; Bressan et al. 2012; Feiden 2015; Baraffe et al. 2015), and their physical and chemical ingredients (e.g., nuclear rates, opacity, atmospheric parameters) have been updated in the recent years (e.g., Baraffe et al. 2015). The models can predict the age and mass of stellar and substellar objects from the measured broad band photometry, surface gravity, radius, luminosity, and effective temperature. The mass is the fundamental parameter which allows to comprehend the object nature and formation pathways.

The models predictions remain to be calibrated in various mass and age regimes (e.g., Hillenbrand & White 2004; Mathieu et al. 2007). Uncertainties related to the object formation process (formation mechanism, early accretion history, etc.) exist in the pre-main sequence (PMS) regime (e.g., Baraffe et al. 2002; Baraffe & Chabrier 2010). Further uncertainties may be added for low-mass stars, which have strong convection, rotation and magnetic activity (Mathieu et al. 2007). About 50 low-mass (below 1 $M_\odot$) pre-main sequence stars had their mass determined thus far (e.g., Simon et al. 2000; Gennaro et al. 2012; Stassun et al. 2014; Mizuki et al., in prep.). Most of these systems have been studied through their disk kinematics, and are

Open Access article, published by EDP Sciences, under the terms of the Creative Commons Attribution License (http://creativecommons.org/licenses/by/4.0), which permits unrestricted use, distribution, and reproduction in any medium, provided the original work is properly cited.

thus younger than 10 million years (e.g., Guilloteau et al. 2014; Simon et al. 2017). Moreover, this method only allows to determine the total mass of the system, disk included. The disk mass can be a nonnegligible fraction of the total mass (e.g., Andrews et al. 2013, Fig. 9), so that uncertainties remain on the stellar mass. A dozen of the stars with dynamical mass are SB2 eclipsing binaries, for which the orbital inclination can be strongly constrained and the mass determined from the orbit. However, eclipsing binaries are very tight stellar pairs (orbital periods 1–10 d) so that each star strongly influences the other one (tides, high rotation speed, convection inhibition). Thus, their evolution may not be representative of typical stars (Chabrier et al. 2007; Kraus et al. 2011; Stassun et al. 2014). Consequently, evolution models remain poorly constrained for low-mass stars for most of the pre-main sequence stellar evolution. This can induce systematic offsets and disparate mass predictions (Hillenbrand & White 2004; Mathieu et al. 2007).

Some rare young (age < 200 Myr) and nearby (d < 100 pc) binaries resolved with high-resolution imaging techniques (adaptive optics, speckle interferometry, lucky imaging, sparse aperture masking) have orbital periods that are shorter than a decade. Combined with a precise parallax, astrometric follow-up of the relative orbit of the two components gives the total dynamical mass of the system. Knowledge of the individual masses can then be gained from additional radial velocity measurements. These systems offer a good prospect for calibrating the PMS tracks and the underlying physics of the models. To date and to our knowledge, only nine such systems in the intermediate PMS regime (10–100 Myr) have dynamical mass estimates below 1 $M_{\odot}$, with various model agreements: HD 98800 B (Boden et al. 2005), TWA 22 (Bonnefoy et al. 2009), HD 160934 (Azulay et al. 2014), AB Dor (Azulay et al. 2015; Close et al. 2007), GJ 3305 (Montet et al. 2015), V343 Nor A (Nielsen et al. 2016), NLTT 33370 (Dupuy et al. 2016), GJ 2060 (this work), and GJ 1108 (Mizuki et al., in prep.). Here we provide a refined dynamical mass for TWA 22 and a first determination for GJ 2060.

The calibration is nonetheless often limited by uncertainties on the age and distance of these benchmarking systems. These uncertainties are mitigated for systems belonging to known young nearby associations and moving groups (YMGs). The age of the YMG can be inferred via several approaches (lithium depletion boundary, kinematics, etc.) and parallaxes can be measured for individual members (*Gaia*, Arenou et al. 2017, Hipparcos, Van Leeuwen 2007). Moreover, these systems have the same age (8–150 Myr) as the substellar companions resolved during direct imaging surveys (planets and brown dwarfs; e.g., Chauvin et al. 2004; Lagrange et al. 2010; Marois et al. 2008, 2010; Rameau et al. 2013a,b) whose mass determination also depends on PMS evolutionary models.

TWA 22 and GJ 2060 are two precious astrometric M-dwarf binaries with orbital periods of a few years. They are proposed members of the young β Pic and AB Dor moving groups, respectively. Both systems have well-measured parallaxes. We initiated their follow-up in 2004 with various ground-based facilities in order to measure their dynamical masses and characterize their components. This paper presents an in-depth study of these two systems using published and additional observations, and discusses the agreement between their orbits, their atmospheric properties, the ages of their moving groups, and the PMS evolutionary models. We first review the observations and membership studies previously performed (Sect. 2), and then present new imaging and spectroscopic data (Sect. 3). We analyze the spectroscopic properties of GJ 2060 (Sect. 4). We derive in Sect. 5 the dynamical masses from orbital fits, and use them to probe the evolutionary models (Sect. 6). The agreement between models and data is finally discussed in Sect. 7.

2. Age and membership of TWA 22 and GJ 2060

2.1. TWA 22

TWA 22 (2MASS J10172689-5354265), located at d = 17.5 ± 0.2 pc (Teixeira et al. 2009), was originally proposed as a member of the ~10 Myr old (Bell et al. 2015) TW Hydrae association (TWA) by Song et al. (2003). This classification was based on its strong Li 6708 Å absorption and Hα emission lines and sky position near other TWA members. A subsequent kinematic analysis of all TWA members proposed at the time by Mamajek (2005) revealed that the available kinematics of TWA 22 were largely inconsistent with the bulk of other TWA members and provided a low probability of membership. Possible membership in either TWA or the older β Pictoris moving group (~25 Myr, Bell et al. 2015) was then proposed by Song et al. (2006).

TWA 22 was included in 2003 as a target in an adaptive optics (AO) imaging survey to search for low-mass companions (Chauvin et al. 2010). It was resolved into a ~100 mas, equal luminosity binary, and was considered as a potential benchmark target for dynamical mass measurements and model calibration. For this purpose, Teixeira et al. (2009) measured the parallax, provided revised proper motion and radial velocity measurements, and performed a detailed kinematic analysis of TWA 22, and found further evidence for membership in the β Pic group, but were unable to fully rule out TWA membership. Then, Bonnefoy et al. (2009) presented resolved spectra of the components, measured spectral types (later refined by Bonnefoy et al. 2014a to M5 ± 1 for TWA 22 A and M5.5 ± 1 for TWA 22 A), and performed an astrometric orbit fit to the available observations. This revealed that the total mass of the system was incompatible with model predictions, considering an age range consistent with the age of TWA. The authors noted, however, that the models may simply be underpredicting the system mass at such a young age.

TWA 22 has now been adopted as a bona fide member of the β Pic group on the basis of Bayesian methods for determining membership to kinematic moving groups (BANYAN I, Malo et al. 2013; BANYAN II, Gagné et al. 2014). The TWA 22 kinematics were used to develop the β Pic group kinematic model implemented in the BANYAN Bayesian estimator (with >99% probability of membership). The amount of lithium observed in TWA 22 is consistent with the age of the TWA association, but we know now that it is also compatible with its membership to the β Pic group, as Li may still subsist in the components at the age of β Pic. The age of the β Pic group has been revised multiple times in recent years using isochronal methods that rely on all group members (Malo et al. 2014; Bell et al. 2015), the lithium depletion boundary of the group (Binks & Jeffries 2014; Malo et al. 2014; Messina et al. 2016; Shkolnik et al. 2017), the rotation distribution of known members (Messina et al. 2016), and model comparisons to dynamical masses of binaries in the group (Montet et al. 2015; Nielsen et al. 2016). This wide variety of age determination methods converge toward a group age of ~25 Myr (see Table 1).

In this work we adopt the β Pic group age for TWA 22, provide new astrometric measurements of the binary components, combine these data with previous data to perform an updated orbital fit and measure the system mass, and compare

Table 1. Age estimates of the Beta Pictoris moving group.

Paper	Age (Myr)	Method
Malo et al. (2014)	15–28	Isochronal methods
	26 ± 3	Lithium depletion boundary
Bell et al. (2015)	24 ± 3	Isochronal methods
Binks & Jeffries (2014)	21 ± 4	Lithium depletion boundary
Shkolnik et al. (2017)	22 ± 6	Lithium depletion boundary
Messina et al. (2016)	25 ± 3	Rotation distribution and Lithium depletion boundary
Montet et al. (2015)	37 ± 9	Dynamical mass of binaries
Nielsen et al. (2016)	26 ± 3	Dynamical mass of binaries

Table 2. Age estimates of the AB Doradus moving group.

Paper	Age (Myr)	Method
Zuckerman et al. (2004)	50 ± 10	Isochronal methods
Luhman et al. (2005)	100–125	Isochronal methods
Lopez-Santiago et al. (2006)	30–50	Isochronal methods
Bell et al. (2015)	149^{+51}_{-19}	Isochronal methods
Ortega et al. (2007)	119 ± 20	Stellar dynamics
Messina et al. (2010)	~70	Rotation periods
Barenfeld et al. (2013)	>110	Kine-chemical analysis
Nielsen et al. (2005)	50–100	AB Dor C
Boccaletti et al. (2008)	75 ± 25	AB Dor C
Guirado et al. (2011)	40–50	AB Dor A
Azulay et al. (2015)	40–50	AB Dor B

the derived mass to estimates from the latest stellar evolution models. The binary period is relatively short (~5 yr); TWA 22 was regularly observed from 2004 to 2007 and later in 2013 and 2015, enabling a very good characterization through the orbital fit. The two components are the least massive stars in the β Pic group for which a dynamical mass has been computed. They complete the mass sampling between the giant planet β Pictoris b (Lagrange et al. 2010) and the higher mass binaries GJ 3305 (total mass 1.1 $M_\odot$; Montet et al. 2015) and V343 Nor (total mass 1.4 $M_\odot$; Nielsen et al. 2016). TWA 22 is thus an essential benchmark to test the predictions of the evolutionary models in the young group in the 0.1 $M_\odot$ mass range.

2.2. GJ 2060

GJ 2060 (2MASS J07285137-3014490) is an early M dwarf at $d = 15.69 \pm 0.45$ pc (Van Leeuwen 2007) that was first identified as a small separation binary by the HIPPARCOS satellite (Dommanget & Nys 2000). The star was subsequently identified as a nearby young star in the paper presenting the discovery of the AB Doradus moving group (Zuckerman et al. 2004). This work presented GJ 2060 and ~30 other stars as having both Galactic kinematics consistent with the well studied young system AB Dor and independent indicators of youth (X-ray and H-alpha emission, large $v \sin i$, etc.). Along with AB Dor itself and six other nearby stars within a ~5 pc radius, GJ 2060 is a member of the AB Dor moving group nucleus. The system has since been verified as a bona fide member of the AB Dor moving group using revised group kinematic distributions and Bayesian methods with an estimated membership probability of >99% (Malo et al. 2013; Gagné et al. 2014). GJ 2060 was first resolved into an 0.175" multiple system by Daemgen et al. (2007) using adaptative optics imaging. The system has been observed multiple times since with high-resolution imaging and exhibited rapid orbital motion (see Janson et al. 2014). The age of the AB Dor moving group, and thereby GJ 2060, was first proposed to be ~50 Myr by Zuckerman et al. (2004). Yet, the age of the group remains relatively poorly constrained, and ages ranging from the original ~50 Myr to ~150 Myr have been proposed over the last decade (e.g., Close et al. 2005; Nielsen et al. 2005; Luhman et al. 2005; Lopez-Santiago et al. 2006; Ortega et al. 2007; Torres et al. 2008; Barenfeld et al. 2013; Bell et al. 2015). The system components of the group's namesake quadruple system AB Dor have been studied in detail (Close et al. 2005; Nielsen et al. 2005; Guirado et al. 2011; Azulay et al. 2015) and comparisons to stellar evolution models indicate discrepancies between the measured masses of the components and point toward ages <100 Myr. This is in conflict with group ages estimated from the individual components of AB Dor and from the ensemble of stars using HR diagram placement (Luhman et al. 2005; Bell et al. 2015), rotation periods (Messina et al. 2010), and Li depletion (Barenfeld et al. 2013). These works find that individual members and the ensemble of proposed AB Dor members have properties consistent with the Pleiades open cluster and likely have a comparable age (~120 Myr; Stauffer et al. 1998; Barrado y Navascués et al. 2004; Dahm 2015). Here we use new astrometric and radial velocity measurements of the GJ 2060 system to derive component masses and perform similar comparisons to stellar evolution models. No orbital fit had been performed on this system yet, so that its orbital elements and dynamical mass are first determined in the present article.

3. Observation and data processing

A summary of the new observations of TWA 22 and GJ 2060 is given in Table 3. We describe the datasets and related reduction processes in more detail below.

3.1. TWA 22

3.1.1. NaCo observations

TWA 22 AB was observed in field-tracking mode on February 11, 2013, with the NAOS-CONICA (NaCo) adaptive-optics instrument mounted on the VLT/UT4 (Lenzen et al. 2003; Rousset et al. 2003) as part of a program dedicated to the orbit monitoring of young binaries (PI Bonnefoy; program ID 090.C-0819). The S13 camera was associated with the H-band filter ($\lambda_c = 1.66\,\mu$m, $\Delta\lambda = 0.33\,\mu$m), yielding a square field of view of 13.5 arcsec. The wavefront sensing was achieved in the near-infrared on the pair (seen as a whole). We acquired 32 frames (NEXPO) of the binaries consisting of 0.345 s × 30 (DIT × NDIT) averaged exposures each. Small (±3″) dithers were applied every four frames to allow for an efficient sky and bias subtraction at the data processing step. We observed immediately after TWA 22 AB the M 6 star GSC08612-01565 to calibrate the point-spread function (PSF) of the instrument using the same adaptive-optics setup and the same DIT, NDIT, and NEXPO as for TWA 22 AB. On the following night we observed the crowded field of stars around Θ Ori C to calibrate the platescale and field orientation with the same filter and camera and the visible wavefront sensor. That astrometric field was already used in Bonnefoy et al. (2009) for the previous observations of TWA 22.

Table 3. Observing log.

UT date	Target	Instrument	Mode	DIT × NDIT × N_{EXPO}	θ (deg)	⟨Seeing⟩[a] (")	⟨τ_0⟩ (ms)	Airmass
2013/02/11	TWA 22 AB	NaCo	H-S13	0.345 s × 30 × 32	n.a.	1.0	5.7	1.15
2013/02/11	GSC08612-01565	NaCo	H-S13	0.345 s × 30 × 32	n.a.	1.0	6.0	1.22
2013/02/12	Θ Ori C	NaCo	H-S13	3 s × 3 × 25	n.a.	0.9	6.1	1.06
2015/02/03	TWA 22 AB	SPHERE	IRDIS-K12	4 s × 16 × 15	n.a.	2.5	1.4	1.15
2015/02/03	TWA 22 AB	SPHERE	IFS-YH	32 s × 2 × 17	n.a.	2.5	1.4	1.16
2012/11/21	Θ Ori C	NaCo	H-S13	3 s × 5 × 26	n.a.	0.6	3.7	1.08
2012/11/25	GJ 2060 AB	NaCo	H-S13	0.15 s × 100 × 7	n.a.	1.0	1.7	1.01
2012/11/25	GJ 3305 AB	NaCo	H-S13	0.12 s × 200 × 4	n.a.	0.8	2.1	1.08
2013/11/22	GJ 2060 AB	SINFONI	J	1 s × 4 × 11	n.a.	0.8	1.9	0.93
2013/11/22	GJ 2060 AB	SINFONI	$H+K$	0.83 s × 4 × 11	n.a.	0.8	2.1	0.92
2013/11/22	HIP 036092	SINFONI	J	6 s × 2 × 1	n.a.	0.9	2.2	1.01
2013/11/22	HIP 036092	SINFONI	$H+K$	5 s × 2 × 1	n.a.	0.8	2.4	1.01
2015/02/05	GJ 2060 AB	SPHERE	IRDIS-K12	2 s × 32 × 10	n.a.	2.0	2.6	1.14
2015/02/05	GJ 2060 AB	SPHERE	IFS-YH	32 s × 2 × 11	n.a.	1.8	2.6	1.14
2015/03/16	GJ 2060 AB	AstraLux	z'	0.015 s × 20000 × 1	n.a.	n.a.	n.a.	1.48
2015/03/16	GJ 2060 AB	AstraLux	i'	0.015 s × 20000 × 1	n.a.	n.a.	n.a.	1.54
2015/10/01	GJ 2060 AB	NIRC2	K_{cont}	0.2 s × 50 × 6	0.67	n.a.	n.a.	1.81
2015/11/18	GJ 2060 AB	NIRC2	K_{cont}	0.2 s × 50 × 9	1.71	n.a.	n.a.	1.56
2015/11/29	GJ 2060 AB	SPHERE	IRDIS-H23	4 s × 40 × 4	n.a.	1.12	3.4	1.06
2015/11/29	GJ 2060 AB	SPHERE	IFS-YJ	16 s × 10 × 4	n.a.	1.12	3.4	1.06
2015/12/25	GJ 2060 AB	AstraLux	z'	0.015 s × 10000 × 1	n.a.	n.a.	n.a.	1.01
2015/12/26	GJ 2060 AB	SPHERE	IRDIS-H23	16 s × 14 × 16	2.3	0.8	3.5	1.26
2015/12/26	GJ 2060 AB	SPHERE	IFS-YJ	8 s × 7 × 16	2.3	0.8	3.5	1.26
2015/12/28	GJ 2060 AB	AstraLux	z'	0.015 s × 10000 × 1	n.a.	n.a.	n.a.	1.15
2016/03/27	GJ 2060 AB	SPHERE	IRDIS-H23	2 s × 40 × 16	n.a.	0.5	2.6	1.08
2016/03/27	GJ 2060 AB	SPHERE	IFS-YJ	16 s × 20 × 5	n.a.	0.5	2.6	1.08
2017/02/07	GJ 2060 AB	SPHERE	IRDIS-K12	4 s × 8 × 16	1.87	0.6	15.4	1.11
2017/02/07	GJ 2060 AB	SPHERE	IFS-YH	16 s × 2 × 16	1.65	0.6	15.2	1.11

Notes. The field rotation θ is given when the observations are performed in pupil-tracking mode. [(a)]DIMM for the VLT.

Table 4. Summary of TWA 22 astrometry.

UT Date	Band	ΔRA (mas)	ΔDec (mas)	Instrument	Reference
2004/03/05	NB2.17	99 ± 3	−17 ± 3	NaCo	Bonnefoy et al. (2009)
2004/04/27	NB1.75	98 ± 6	−36 ± 6	NaCo	Bonnefoy et al. (2009)
2005/05/06	H-ND	15 ± 3	−89 ± 3	NaCo	Bonnefoy et al. (2009)
2006/01/08	H	−68 ± 2	−49 ± 2	NaCo	Bonnefoy et al. (2009)
2006/02/26	H	−74 ± 3	−30 ± 3	NaCo	Bonnefoy et al. (2009)
2007/03/06	H	−57 ± 4	80 ± 2	NaCo	Bonnefoy et al. (2009)
2007/12/04	H	19 ± 3	98 ± 3	NaCo	Bonnefoy et al. (2009)
2007/12/26	H	26 ± 3	97 ± 3	NaCo	Bonnefoy et al. (2009)
2013/02/11	H	2 ± 1	100 ± 1	NaCo	This work
2015/02/05	IFS-YH	−43 ± 1	93 ± 1	SPHERE	This work

All the data were reduced with the `eclipse` sofware (Devillard 1997). The `eclipse` routines carried out the basic cosmetic steps: bad pixel flagging and interpolation, flat field calibration, sky subtraction, and cross-correlation and shift of the dithered frames. We extracted the position of the Θ Ori stars and compared them to those reported in McCaughrean & Stauffer (1994) to infer a platescale of 13.19 ± 0.08 mas pixel^{-1} and a true north of −0.90 ± 0.15° for those observations. We used a deconvolution algorithm dedicated to the stellar field blurred by the adaptive-optics corrected point spread functions to deblend the overlaping point spread functions of TWA 22 A and B in the final NaCo image (Veran & Rigaut 1998) and to measure the position and the photometry of each component. The same tool was used in Bonnefoy et al. (2009). The algorithm is based on the minimization in the Fourier domain of a regularized least-squares objective function using the Levenberg–Marquardt method. It is well suited to our data which are Nyquist sampled. We cross-checked our results using the IDL `Starfinder` PSF fitting package (Diolaiti et al. 2000), which implements a custom version of the CLEAN algorithm to build a flux distribution model of the binary but does not perform any spatial deconvolution. We find a contrast $\Delta H = 0.52 \pm 0.05$ mag consistent with

the values derived at previous epochs (Bonnefoy et al. 2009). The binary is found at a PA = 1.15 ± 0.15° and separation ρ = 100 ± 3 mas.

3.1.2. SPHERE observations

The binary was observed on February 3, 2015, as part of the SpHere INfrared survey for Exoplanets (SHINE) survey (Chauvin et al. 2017) with the high-contrast instrument SPHERE at UT3/VLT (Beuzit et al. 2008). The observations were scheduled as part of a subprogram (filler) of SHINE devoted to the astrometric monitoring of tight binaries.

SPHERE was operated in field-tracking mode. No coronagraph was inserted into the light path. The IRDIFS_EXT mode enabled for simultaneous observations with the dual-band imaging sub-instrument IRDIS (Dohlen et al. 2008; Vigan et al. 2010) in the $K1$ (λ_c = 2.110 μm; $\Delta\lambda$ = 0.102 μm) and $K2$ (λ_c = 2.251 μm; $\Delta\lambda$ = 0.109 μm) filters in parallel with the lenslet-based integral field spectrograph (IFS, Claudi et al. 2008; Mesa et al. 2015) in the Y–H band (0.96–1.64 μm). Only the IRDIS data were exploited because the low-resolution ($R \sim 30$) IFS observations are superseeded by the Spectrograph for INtegral Field Observations in the Near Infrared (SINFONI) spectra ($R \sim 1500$–2000) of the binary exploited in Bonnefoy et al. (2009 and 2014a).

We acquired 240 × 4 s IRDIS frames of the binary. The IRDIS dataset was reduced at the SPHERE Data Center[1] (DC) using the SPHERE Data Reduction and Handling (DRH) automated pipeline (Pavlov et al. 2008; Delorme et al. 2017). The DC carried out the basic corrections for bad pixels, dark current, and flat field. It also included correction for the instrument distortion (Maire et al. 2016a).

The wavefront-sensing of the adaptive optics system SAXO (Fusco et al. 2006; Petit et al. 2014) was able to operate on the target in spite of its faintness at optical wavelengths (V = 13.8 mag; Zacharias et al. 2005) and of the adverse observing conditions (Table 3). The tip-tilt mirror occasionally produced a strong, undesired offset of TWA 22 in the field of view, and part of the sequence was affected by low Strehl ratio. We then selected by eye 71 frames with the best angular resolution. We measured the relative position of the binary in the remaining frames using a custom cross-correlation IDL script. The frames were then re-aligned using subpixel shifts with a tanh interpolation kernel. The registered frames were averaged to produce a final frame using the `Specal` pipeline (Galicher et al., in prep.).

TWA 22 A and B are well resolved into the final $K1$ and $K2$ images (see Fig. 1). We did not observe a reference star to calibrate the point-spread-function and so we were not able to use a deconvolution algorithm for that epoch. However, the high Strehls of the SPHERE observations mitigate the cross-contamination of the binary components. We measured their position in the $K1$ image (offering the best angular resolution) fitting a Moffat function within an aperture mask (4 pixel radii) centered on the estimated position of the stars. We varied the aperture size (±1 pixels in radius) and considered alternative fitting functions (Gaussian, Lorentzian) to estimate an error on the astrometry. We used a true north value of 1.72 ± 0.06° and a platescale of 12.267 ± 0.009 mas pixel^{-1} derived from the observations of Θ Orionis C as part of the long-term analysis of the SHINE astrometric calibration (same field as that observed with NaCo; Maire et al. 2016a,b). This leads to a position angle PA = 114.90 ± 0.10° and a separation ρ = 103 ± 1 mas between the two components of TWA 22.

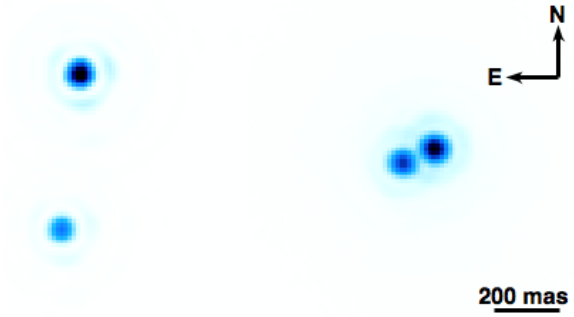

Fig. 1. SPHERE/IRDIS $K1$ (λ = 2.11 nm) observations of GJ 2060 AB (*left*) and TWA 22 AB (*right*). They were taken respectively in February 2017 and February 2015.

3.2. GJ 2060

3.2.1. NaCo data

We observed GJ 2060 with NaCo (Program 090.C-0698; PI Delorme) in the H-band in the course of a direct imaging survey of M dwarfs (Delorme et al. 2012; Lannier et al. 2016). The observations were performed in field tracking mode with the detector cube mode enabling for short integration time (0.15 s). We also observe the astrometric calibrator Θ Ori C with the same setup. The data were all reduced with the `eclipse` tool. We find a platescale of 13.19 ± 0.06 mas pixel^{-1} and a true north value of −0.60 ± 0.33° for those observations. GJ 2060 AB was tight (69 mas) in the images. This required the use of a deconvolution algorithm to deblend the binary components. We reduced for that purpose the data of GJ 3305 observed the same night (Table 3). GJ 3305 is itself a tight pair of M dwarfs and is a member of the Beta Pictoris moving group (Zuckerman et al. 2001). The separation of GJ 3305 in November 2012 (290 mas) and the Strehl ratio were sufficient to mitigate the self-contamination of the binary component. We were then able to extract a subfield centered on GJ 3305 A that could serve as a reference PSF. Nonetheless, in addition we used three isolated bright stars from the θ Orionis field observed on four nights before GJ 2060 at a close airmass to evaluate the dependency of the results related to the PSF choice. The deconvolution algorithm of Veran & Rigaut (1998) yields a PA = 232.2 ± 2.3° and ρ = 69 ± 2 mas for GJ 2060 AB. This measurement is confirmed by the `Starfinder` tool.

3.2.2. NIRC2 archival data

We collected and reduced two sets of archival data obtained in pupil-tracking mode with the Keck/NIRC2 adaptive optics instrument (van Dam et al. 2004) on October 1, 2015 (program N101N2; PI Mann), and November 18, 2015 (program H269N2; PI Gaidos). They were both obtained with the K_{cont} filter (λ_c = 2.2706 μm, $\Delta\lambda$ = 0.0296 μm).

Each of the two sequences contains two sets of frames that correspond to a position of the source on the detector. We averaged each set of three frames to produce two resulting frames. These resulting frames were then used to subtract the sky and bias contributions into the six original frames. We registered the frames on a common origin, applied a rotation to re-align them

[1] http://sphere.osug.fr

Table 5. Contrasts and apparent magnitude of GJ 2060 A and B.

Date	Band	Contrast (mag)	GJ 2060 A (mag)	GJ 2060 B (mag)
2012/11/25	H	0.80 ± 0.20		
2015/10/01	$K_{\rm cont}$	0.95 ± 0.10		
2015/11/18	$K_{\rm cont}$	0.87 ± 0.10		
2013/11/22	$J_{\rm synth}$	0.94 ± 0.06		
2013/11/22	$H_{\rm synth}$	0.98 ± 0.06	6.34 ± 0.06	7.32 ± 0.09
2013/11/22	$Ks_{\rm synth}$	0.90 ± 0.06	6.09 ± 0.06	7.04 ± 0.07
2013/11/22	$K1_{\rm synth}$	0.90 ± 0.06		
2013/11/22	$K2_{\rm synth}$	0.87 ± 0.06		
2015/02/05	$K1$	1.00 ± 0.04	6.12 ± 0.04	7.08 ± 0.07
2015/02/05	$K2$	0.90 ± 0.04	6.07 ± 0.04	6.95 ± 0.06
2015/02/05	$J_{\rm synth}$	0.97 ± 0.01	6.99 ± 0.03	7.96 ± 0.04
2015/11/29	$H2$	0.99 ± 0.05		
2015/11/29	$H3$	0.99 ± 0.05		
2015/12/26	$H2$	1.00 ± 0.01	6.33 ± 0.04	7.33 ± 0.05
2015/12/26	$H3$	0.99 ± 0.02		
2016/03/27	$H2$	1.02 ± 0.02		
2016/03/27	$H3$	1.00 ± 0.01	6.33 ± 0.04	7.33 ± 0.05
2017/02/07	$K1$	0.96 ± 0.06		
2017/02/07	$K2$	0.88 ± 0.05		
2017/02/07	$J_{\rm synth}$	0.97 ± 0.03		

to the north, and averaged them to produce the final frames. The last step enabled us to filter out part of the bad pixels.

We fitted a Moffat function on each star flux distribution to retrieve its relative position. For both epochs, we considered the platescale (9.971 ± 0.005 mas pixel^{-1}) and the absolute orientation on the sky (0.262 ± 0.022°) reported in Service et al. (2016). The estimated contrasts and astrometry are reported in Tables 5 and 6, respectively.

3.2.3. SPHERE observations

The binary was observed as part of the SHINE survey on February 2015 and February 2017 in field and pupil tracking mode, respectively. For both nights, the IRDIFS_EXT mode was used.

The reduction of the IFS data was performed following the procedure described in Mesa et al. (2015) and Zurlo et al. (2014). The calibrated spectral datacubes are made of 39 narrow band images. We rotated the datacubes corresponding to each exposures to align them to the north and averaged them. We extracted from the resulting cube the flux ratio between each component of the binary for both epochs (74 mas circular aperture).

We made use of the IRDIS data for the astrometric monitoring. We followed the procedure described in Sect. 3.1.2 to reduce those data. We used the true north and platescale values reported in Sect. 3.1.2 for the 2015 observations. We adopted a true north on sky of 1.702 ± 0.058° and a platescale of 12.250 ± 0.009 mas pixel^{-1} from the observations of NGC3603 obtained on February 7, 2017, as part of the long-term astrometric calibration of the instrument (Maire et al. 2016b). The binary position in the final images was measured with a Moffat function and is reported in Table 6. Figure 1 displays the 2017 epoch.

3.2.4. AstraLux observations

Three of the AstraLux data points presented here are previously unpublished. They were obtained as a continuation of the AstraLux orbital monitoring campaign for young M-dwarf binaries, with a particular focus on young moving group members (Janson et al. 2014, 2017). The new data were acquired in March and December of 2015 with the lucky imaging camera `AstraLux Sur` (Hippler et al. 2009) at the ESO NTT telescope (programs 094.D-0609(A) and 096.C-0243(B)). They were reduced in an identical way to that used previously in the survey (e.g., Janson et al. 2014). For the March run, the cluster NGC 3603 was used as astrometric calibrator, giving a pixel scale of 15.23 mas pixel^{-1} and a true north angle of 2.9°. In the December run, the Trapezium cluster was used for astrometric calibration, yielding a pixel scale of 15.20 mas pixel^{-1} and a true north angle of 2.4°.

3.2.5. SINFONI integral field spectroscopy

GJ 2060 AB was finally observed on November 22, 2013, with the SINFONI instrument mounted on the VLT/UT4 as part of our dedicated program for the orbital characterization of dynamical calibrators (PI Bonnefoy; program ID 090.C-0819). SINFONI couples a modified version of the adaptive optics module MACAO (Bonnet et al. 2003) to the integral field spectrograph SPIFFI (Eisenhauer et al. 2003) operating in the near-infrared (1.10–2.45 μm). SPIFFI slices the field of view into 32 horizontal slitlets that sample the horizontal spatial direction and rearranges them to form a pseudo long slit. That pseudo-slit is dispersed by the grating on the 2048 × 2048 SPIFFI detector. GJ 2060 A was bright enough at R band to allow for an efficient adaptive optics correction. We used the pre-optics providing 12.5 mas × 25 mas rectangular spaxels on sky and a square field of view of 0.8" side. The target was observed during two consecutive sequences with the J and $H + K$ gratings, covering the 1.10−1.40 and 1.45−2.45 μm wavelength range at $R \sim 2000$ and 1500 resolving powers, respectively. We obtained 11 frames with the binary in the field of view. Between each frame, the binary was dithered to increase the final field of view and filter out residual nonlinear and hot pixels. We also obtained an exposure on the sky at the end of each sequence to efficiently subtract the sky emission lines, detector bias, and residual detector defects. The observatory obtained observations of HIP 036092 immediately after GJ 2060. HIP 036092 is a B8V star that was used to evaluate and remove the telluric absorption lines.

We used the version 3.0.0 of the ESO data handling pipeline (Abuter et al. 2006) through the workflow engine `Reflex` (Freudling et al. 2013), which allowed for an end-to-end automatized reduction. `Reflex` performed the usual cosmetic steps on the bi-dimensional raw frames (flat field removal, bad-pixel flagging, and interpolation). These steps rely on calibration frames taken on the days following our observations. The distortion and wavelength scale were calibrated on the entire detector. The positions of the slitlets on the detector were measured and used to build the datacubes containing the spatial (X, Y) and spectral dimensions (Z). In the final step, the cubes corresponding to individual exposures were merged into a master cube.

GJ 2060 is well resolved into the J and $H + K$ master cubes but the sources contaminate each other. We applied the `CLEAN3D` tool described in Bonnefoy et al. (2017) to deblend the sources at each wavelength. The PSF at each wavelength is built from the duplication of the profile of GJ 2060 A following a PA = 0°. The tool produced two datacubes where one of the two components of the system is removed. We extracted the J and $H + K$ band spectra of each component integrating the flux within circular apertures of radius 147 and 110 mas at each wavelength in the datacubes, respectively. We extracted the telluric standard star spectrum using the same aperture sizes and corrected its continuum with a 12120 K blackbody (Theodossiou & Danezis 1991).

Table 6. Summary of GJ 2060 astrometry.

UT Date	Band	Position angle (deg)	Separation (mas)	ΔRA (mas)	ΔDec (mas)	Instrument	Reference
2002/12/28	Kp	180.3 ± 0.2	425 ± 4	−2 ± 2	−425 ± 4	Keck_ NIRC2	Janson et al. (2014)
2005/11/30	H	143.7 ± 1.5	175 ± 11	104 ± 11	−141 ± 12	Gemini_ NIRI	Daemgen et al. (2007)
2008/11/12	z'	169.7 ± 0.3	479 ± 5	86 ± 4	−471 ± 6	Astralux	Bergfors et al. (2010)
2010/01/31	z'	176.2 ± 0.3	458 ± 5	30 ± 3	−457 ± 6	Astralux	Janson et al. (2012)
2010/10/25	z'	181.1 ± 0.3	423 ± 4	−8 ± 3	−423 ± 4	Astralux	Janson et al. (2014)
2012/01/06	z'	191.6 ± 0.3	294 ± 3	−59 ± 3	−288 ± 4	Astralux	Janson et al. (2014)
2012/11/25	H	232.3 ± 3.0	69 ± 5	−55 ± 4	−42 ± 4	NaCo	Janson et al. (2014)
2015/02/05	IRD_ EXT	161.7 ± 0.2	393 ± 1	123 ± 2	−373 ± 2	SPHERE	This work
2015/03/16	z'	162.3 ± 0.5	399 ± 4	121 ± 5	−380 ± 5	Astralux	This work
2015/10/01	Kc	166.3 ± 0.2	439 ± 4	105 ± 3	−426 ± 5	Keck_ NIRC2	This work
2015/11/18	Kc	167.1 ± 0.2	447 ± 4	101 ± 3	−436 ± 5	Keck_ NIRC2	This work
2015/11/29	IRD_ EXT	66.8 ± 0.1	449 ± 1	103 ± 1	−437 ± 1	SPHERE	This work
2015/12/25	z'	167.5 ± 0.2	453 ± 2	98 ± 2	−442 ± 3	Astralux	This work
2015/12/26	IRD_ EXT	167.0 ± 0.1	453 ± 1	102 ± 1	−441 ± 1	SPHERE	This work
2015/12/28	z'	167.5 ± 0.2	454 ± 2	98 ± 2	−443 ± 3	Astralux	This work
2016/03/27	IRD_ EXT	168.6 ± 0.1	463 ± 1	92 ± 1	−454 ± 1	SPHERE	This work
2017/02/07	IRD_ EXT	173.1 ± 0.2	478 ± 1	57 ± 2	−474 ± 2	SPHERE	This work

The hydrogen and helium lines were interpolated using a third-order Legendre polynomial. The GJ 2060 A and B spectra could then be divided by the telluric standard star spectrum to correct for atmospheric absorptions.

We computed the 2MASS J-, H-, and K-band contrasts, and the $K1$ and $K2$ SPHERE contrasts from the GJ 2060 A and B spectra prior to the telluric line correction (Table 5). The H, $K1$, and $K2$ synthetic contrasts match those derived from the SPHERE and NaCo data within the error bars. We therefore used the synthetic 2MASS H- and K-band contrasts and the 2MASS magnitude of the system (Cutri et al. 2003) to retrieve the individual magnitudes of GJ 2060 A and B. The J-band contrasts were extracted from the SPHERE IFS data. They agree with the value derived with SINFONI. We used the contrast value of the 2015 SPHERE data to derive the J-band magnitude of the system components.

The 2MASS J magnitudes could then be used to flux-calibrate the J-band spectra using the 2MASS filter response curves and tabulated zero points[2]. We used the $K1$ magnitude measured with VLT/SPHERE and a spectrum of Vega (Mountain et al. 1985; Hayes 1985) to flux-calibrate the $H + K$ spectra.

3.2.6. HARPS data

High S/N spectra have been acquired with HARPS (Mayor et al. 2003): one night in April 2014 (JDB = 2456774.493808) and five nights in October 2016 (between JDB = 2457666.881702 and 2457671.850830). Each spectrum contains 72 spectral orders, covering the spectral window [3800 Å, 6900 Å]. The spectral resolution is approximately 100 000. The S/N of the spectra is ≈100 at 550 nm. The number of spectra per night is two (consecutive), except for the first night, when only one was taken. The data provided by HARPS's Data Reduction Software (DRS) 3.5 were first processed with SAFIR, a home-built tool that uses the Fourier interspectrum method described in Chelli (2000) and Galland et al. (2005) to measure radial velocities of stars with high $v \sin i$. SAFIR also estimates other observables such as the cross-correlation functions, as defined in Queloz et al. (2001), and the bisector velocity spans (BVS), R0HK indexes, etc. For a detailed description of SAFIR, see Galland et al. (2005).

Table 7. Summary of HARPS radial velocity measurements of the SB1 GJ 2060.

Obs. JD-2454000	Radial velocity ($km\,s^{-1}$)
2774.49	28.99 ± 0.01
3666.88	28.34 ± 0.02
3666.89	28.27 ± 0.02
3668.86	27.86 ± 0.02
3668.88	27.89 ± 0.02
3669.88	27.91 ± 0.01
3669.89	27.93 ± 0.01
3670.89	27.91 ± 0.02
3670.90	27.79 ± 0.02
3671.84	28.18 ± 0.02
3671.85	28.15 ± 0.02

The values obtained in October 2016 show a very strong dispersion, probably due to the high magnetic activity of the star. The orbit of the binary is ∼8 yr long, so that we do not expect the radial velocities to vary more than ∼0.01 $km\,s^{-1}$ within a few consecutive days, very different from the 0.40 $km\,s^{-1}$ variation we observed. Moreover, we note a strong correlation between the star bisector and the radial velocity measurements. We will therefore add this noise to the instrument uncertainty.

3.2.7. FEROS data

Ten radial velocity measurements have been obtained using the Fiberfed Extended Range Optical Spectrograph (FEROS; Kaufer et al. 1999) mounted at the ESO-MPG 2.2 m telescope

[2] https://www.ipac.caltech.edu/2mass/releases/allsky/doc/sec6_4a.html

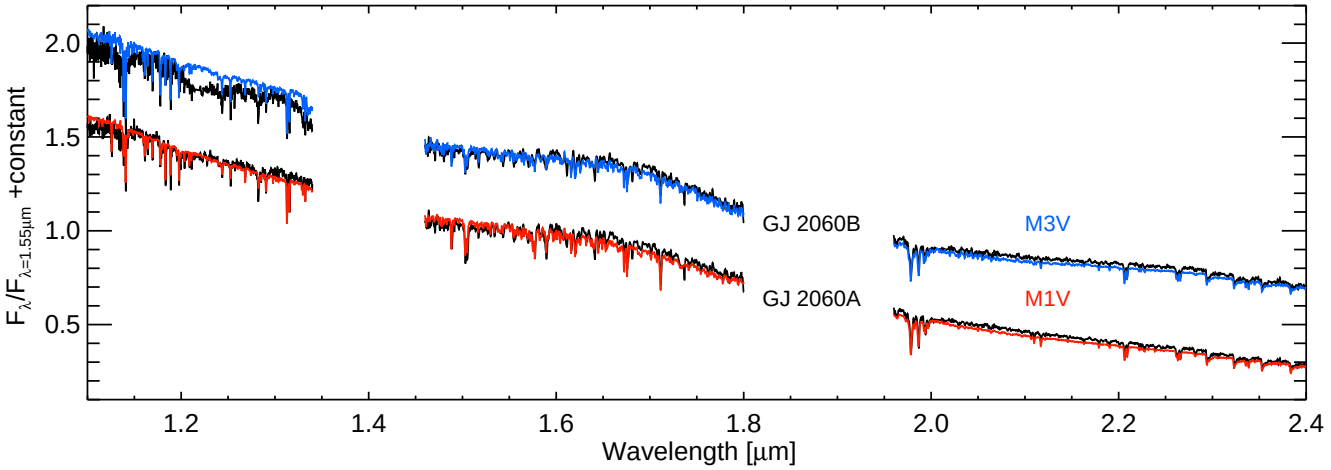

Fig. 2. SINFONI spectra (1.1–2.45 μm) of GJ 2060 A and B renormalized at 1.55 μm.

at La Silla Observatory. FEROS is an echelle spectrograph covering the wavelength range 3500–9200 Å across 39 orders with R ≈ 48000. The measurements are reported in Durkan et al. (2018) as part of a radial velocity monitoring survey of young, low-mass binaries. The data reduction process is described therein. They cover a 12 yr span from 2005 to 2017.

The jitter evidenced in the HARPS data (Sect. 3.2.6) must be taken into account in the FEROS set. Thus, we combined quadratically this estimated activity-related noise (0.40 km s^{-1}) to each FEROS uncertainty.

4. Spectrophotometric analysis

We compared the SINFONI spectra of GJ2060 A and B to the medium-resolution ($R \sim 2000$) spectra of K and M dwarfs from the IRTF library (Cushing et al. 2005; Rayner et al. 2009). The 1.1–2.5 μm spectral slopes of GJ 2060 A is best reproduced by the Gl 229 A spectrum (M1V; Fig. 2). The detailed absorptions and slopes of the J-band and K-band spectra are also reproduced by that template (Fig. A.1). The lack of water band absorption from 1.3 to 1.4 μm in the spectrum of GJ 2060 A confirms that the object has a spectral type earlier than M2. The M0.5 and M1.5 dwarfs Gl 846 and Gl 205 fit equally well the K and H band spectra, respectively, of GJ 2060 A (Figs. A.1 and A.2). Therefore, we estimate that GJ 2060 A is a M1 ± 0.5 dwarf.

The spectral slope of GJ 2060 B is reproduced by the spectrum of the M3 dwarf Gl 388. The comparison at J band evidences departures from 1.1 to 1.2 μm and 1.24 to 1.33 μm between our object spectrum and the templates (Fig. A.1). These departures are also evidenced in the SINFONI spectra of GJ 3305 A and B obtained as part of our observation program (Durkan et al. 2018). It likely arises from the SINFONI instrument. The multiple atomic lines (K I, Na I, Fe I, Al I) and the water band absorption from 1.3 to 1.35 μm indicate that the object has a spectral type later than M2. The H-band spectrum is best represented by the one of the M3.5 dwarf Gl 273 while the K-band is perfectly reproduced by the spectrum of the M3 template (Figs. A.1 and A.2). We conclude that GJ 2060 B is a M3 ± 0.5 dwarf.

These spectral types confirm the estimates made in Bergfors et al. (2010) from the optical colors. We used them together with the bolometric corrections of Pecaut & Mamajek (2013) and the J-band magnitude (Table 5) of each component to infer a $\log(L/L_\odot) = -1.20 \pm 0.05$ dex and $\log(L/L_\odot) = -1.63 \pm 0.05$ dex for GJ 2060 A and B, respectively.

We performed a χ^2 comparison of GJ 2060 A and B spectra to a grid of BT-SETTL atmosphere models (Baraffe et al. 2015) and show the best fitting solutions in Fig. 3. The grid covers $1500 \leq T_{\rm eff}({\rm K}) \leq 5500$ (in steps of 100 K), $2.5 \leq \log\, g({\rm dex}) \leq 5.5$ (in steps of 0.5 dex), and considers solar abundances. We find $T_{\rm eff} = 3700 \pm 100$ K and $\log\, g > 4.0$ dex for GJ 2060 A. Similarly, we find $T_{\rm eff} = 3400 \pm 100$ K and $\log\, g \geq 3.5$ dex for GJ 2060 B. The $T_{\rm eff}$ are in good agreement with the estimates ($T_{\rm eff} = 3615 - 3775$ K for A and $T_{\rm eff} = 3300 - 3475$ K for B) derived from Table 5 of Pecaut & Mamajek (2013) for the estimated spectral type of the binary components. As these results rely on atmosphere models, they do not depend on the system age. Both the $T_{\rm eff}$ and bolometric luminosities are used as input of evolutionary models for the calibration of their mass predictions in Sect. 6.

5. Orbital fit and dynamical mass

The orbits of the two systems have been observed on several occasions covering a time span longer than their periods, so that we are now able to derive precise estimates of their orbital elements. In both cases, we fit the relative orbit of the B component with respect to the A component, assuming a Keplerian orbit projected on the plane of the sky. In this formalism, the astrometric position of the companion can be written as

$$x = \Delta{\rm Dec} = r\,(\cos(\omega + \theta)\cos\Omega - \sin(\omega + \theta)\cos i \sin\Omega)\,, \quad (1)$$

$$y = \Delta{\rm RA} = r\,(\cos(\omega + \theta)\sin\Omega + \sin(\omega + \theta)\cos i \cos\Omega)\,, \quad (2)$$

where Ω is the longitude of the ascending node (measured counterclockwise from north); ω is the argument of periastron; i is the inclination; θ is the true anomaly; and $r = a(1 - e^2)/(1 + e\cos\theta)$ is the radius, where a stands for the semi-major axis and e for the eccentricity.

The orbital fit we performed uses the observed astrometries depicted in Tables 4 and 6 to derive probability distributions for elements a, P (period), e, i, Ω, ω, and time for periastron passage $t_{\rm p}$. Elements a and P are probed separately so that we can deduce the probability distribution of the total mass as a by-product, as a function of the distance of the star d.

We used two complementary fitting methods, as described in Chauvin et al. (2012): a least-squares Levenberg–Marquardt

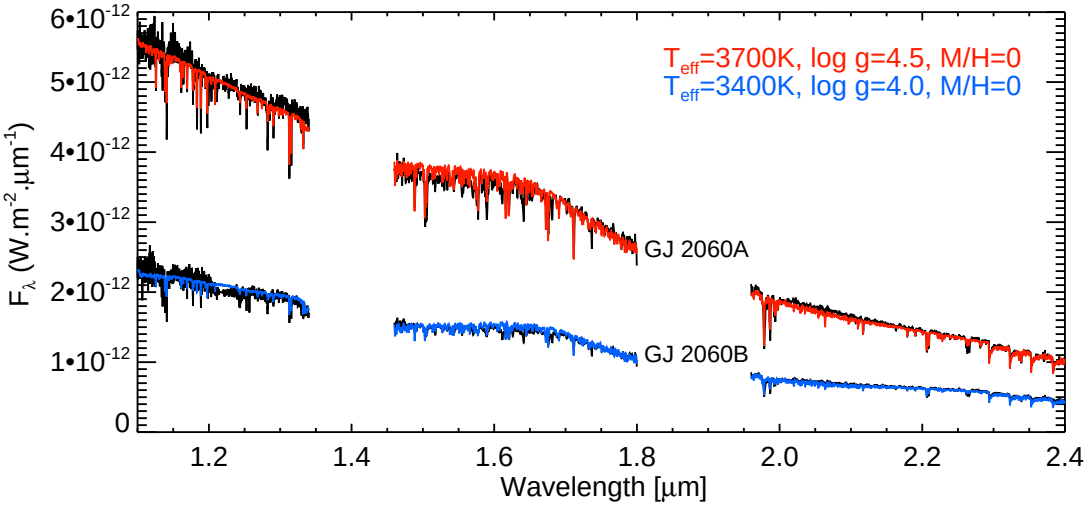

Fig. 3. Spectra (apparent flux) of GJ 2060 A and B compared to the best fitting BT-SETTL synthetic spectra.

(LSLM) algorithm to search for the model with the minimal reduced χ^2, and a more robust statistical approach using the Markov chain Monte Carlo (MCMC) Bayesian analysis technique (Ford 2005, 2006) to probe the distribution of the orbital elements. Ten chains of orbital solutions were conducted in parallel, and we used the Gelman–Rubin statistics as convergence criterion (see the details in Ford 2006). We picked a random sample of 500 000 orbits from those chains following the convergence. This sample is assumed to be representative of the probability (posterior) distribution of the orbital elements for the given priors. We chose the priors to be uniform in $x = (\ln a, \ln P, e, \cos i, \Omega + \omega, \omega - \Omega, t_p)$ following Ford (2006). For any orbital solution, the couples (ω, Ω) and $(\omega + \pi, \Omega + \pi)$ yield the same astrometric data; this is why the algorithm fits $\Omega + \omega$ and $\omega - \Omega$, which are not affected by this degeneracy. The system distance has to be given to the algorithm. No input on the mass is needed as it can be derived directly from a and P by Kepler's third law. The resulting MCMC distributions are well peaked when the data adequately sample the orbits, as is the case in this study. The complete set of posterior distributions and correlations are given in the Appendix B.

5.1. TWA 22

Bonnefoy et al. (2009) already performed an orbital fit of TWA 22 based on astrometric data from 2004 to 2007. At that time the data covered about three-quarters of a period. The authors used a pure Levenberg–Marquardt algorithm, which finds local minima and estimates the uncertainties from the resulting covariance matrix. We intend here to improve the orbital fit by using the new astrometric data (two periods are now covered) and the refined algorithm described above, which allow a fine sampling of the phase parameters and a robust determination of the probability distributions.

The astrometric measurements gathered with NaCo on the system are particularly homogeneous and sample the orbit well. Therefore, we excluded the SPHERE point from the fit at first in order to avoid the possible bias associated with the change of instrument. We then checked the agreement between the results and the SPHERE point afterward.

The MCMC algorithm gives an estimate of the orbital elements (see Table 8), with a precision of 0.02 on the eccentricity, 0.05 au on the semi-major axis, 0.04 yr for the period, or 6° on the inclination (see Appendix B). The portrayed orbit has a low eccentricity (~0.1) and inclination (~22°), as can be seen from its on-sky representation in Fig. 4. This figure shows the best fit obtained with the LSLM algorithm together with a hundred orbits picked up randomly within the 500 000 total sample used to derive the posteriors. The orbital elements derived by Bonnefoy et al. (2009) are all retrieved within 1σ.

Table 8. Orbital elements from the MCMC fit of TWA 22 relative orbit, compared to the last orbit determination by Bonnefoy et al. (2009).

Parameter	This work	Bonnefoy et al. (2009)
a (au)	$1.72 \pm 0.05 \left(\frac{d}{17.5\text{pc}}\right)$	1.77 ± 0.04
P (yr)	5.35 ± 0.04	5.15 ± 0.09
e	0.13 ± 0.02	0.10 ± 0.04
i (°)	22 ± 6	27 ± 5
Ω (°)	129 or −51 ±18	135 ± 1
ω (°)	106 or −74 ±17	100 ± 10
t_p (yr, AD)	2006.04 ± 0.07	2006.04 ± 0.01

Notes. The uncertainties on the fitted parameters correspond to the 68% interval of confidence of the distribution probabilities (see Appendix B). The astrometric data only allow determination of the couple (Ω, ω) modulo π.

The total system mass was computed from the semi-major axis and period corresponding to each orbit explored by the MCMC chains. For any distance d, we find a resulting total mass of $m_{\text{tot}} = a^3/T^2 = 0.179 \pm 0.018\, M_\odot \left(\frac{d}{17.5\text{pc}}\right)^3$. Using the parallax distance and propagating its uncertainty, we finally obtain a dynamical mass of $m_{\text{tot}} = 0.18 \pm 0.02\, M_\odot$ for the pair.

We checked the consistency between the fitted orbit and the SPHERE point that we did not consider: the astrometry falls within the 68% confidence interval of the orbital fit, between 0.4 and 0.9σ from the probability peak (2–3° in position angle, 2–3 mas in radius). Running the algorithm with this extra data point gives very similar orbital elements (all well inside the 68% confidence interval). It yields the same dynamical mass, but with smaller error bars ($0.18 \pm 0.01\, M_\odot$).

A dynamical mass of $m_{\text{tot}} = 0.21 \pm 0.02\, M_\odot$ was obtained in Bonnefoy et al. (2009) with less than 4 yr coverage via a LSLM algorithm. This value is close to the one we obtain, but our peak

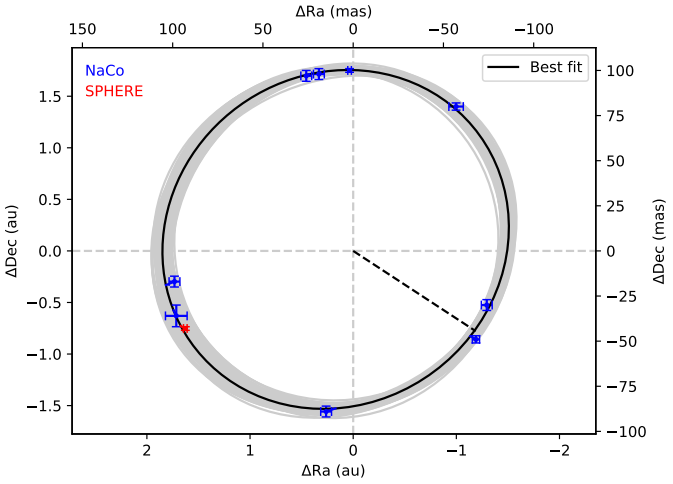

Fig. 4. Plots of a hundred orbits obtained with the MCMC algorithm for system TWA 22. Astrometric measurements are color-coded by instrument, and the position on the fit is also shown. Only NaCo data are used in the orbital fit. The orbit in black, obtained with the LSLM algorithm, corresponds to the lower χ^2.

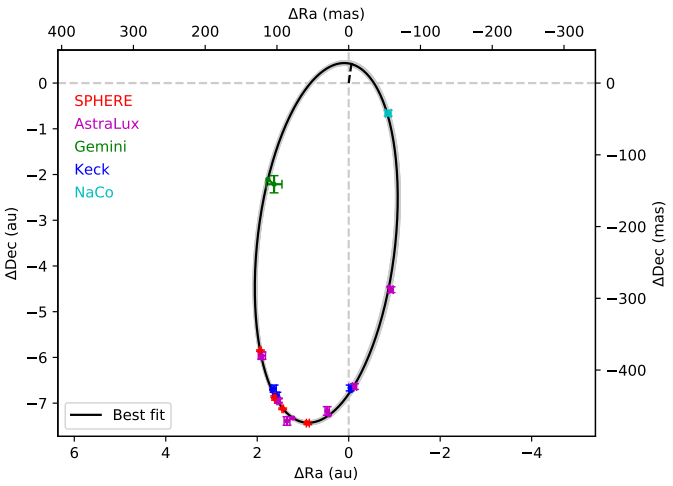

Fig. 5. Plots of a hundred orbits obtained with the MCMC algorithm for system GJ 2060. Astrometric measurements are color-coded according to the instrument, and their position on the fit is also shown. The orbit in black, obtained with the LSLM algorithm, corresponds to the lower χ^2.

value is outside the 1σ confidence interval. However, the error bars on the orbital elements in Bonnefoy et al. (2009) may be slightly underestimated as they are roughly estimated from the covariance matrix. The present determination should therefore be more robust.

5.2. GJ 2060

Radial velocity measurements (RVs) from HARPS and FEROS (Durkan et al. 2018) help to refine the orbital fit. The binary is not resolved by the spectrometers (SB1). We only considered the FEROS data to get homogeneous measurements. This is legitimate, as taking into account HARPS data would not bring significant constraints. Indeed, HARPS data come down to two epochs (April 2014 and October 2016) that are close to FEROS epochs (see Fig. 6), and we have to fit an additional RV offset if we want to include data from another instrument.

The code we use is a slightly modified version of the code used for TWA 22, similar to the code used in Bonnefoy et al. (2014b) for β Pic b. In addition to the orbital elements, it evaluates the probability distributions of the offset velocity v_0 and amplitude K of the radial velocity, with a prior uniform in $(v_0, \ln K)$ assumed for these extra variables (Ford 2006). In the formalism described previously, assuming a Keplerian orbit, the radial velocity is

$$v_{\rm rad} = K \frac{\cos\omega(\cos\theta + e) - \sin\omega\sin\theta}{\sqrt{1-e^2}} + v_0. \quad (3)$$

If the binary is a pure SB1, the amplitude derives from the fractional secondary mass $m_{\rm B}/m_{\rm tot}$ as

$$K = \frac{2\pi}{P}\frac{m_{\rm B}}{m_{\rm tot}} a \sin i. \quad (4)$$

The introduction of the radial velocity breaks the degeneracy of the couple (Ω, ω) and unique values can thus be derived for these two variables.

The astrometric data are more numerous than in the case of TWA 22, but less homogeneous. Therefore, small systematic errors may bias the orbital fit (Table 6). These errors are discussed in Sect. 6.1. These 15 yr of data cover approximately twice the relative orbit, but the passages near periastron are not very well constrained and suggest a very quick displacement in that zone, hinting at a high eccentricity. The results of the MCMC algorithm are displayed in Table 9. The distribution of orbital elements are very peaked, especially that on the eccentricity (see Appendix B). We obtain a precision of 0.01 on the eccentricity, 0.04 au on the semi-major axis, 0.04 yr on the period, and 3° on the inclination. Noticeably, the eccentric distribution peaks at $e = 0.89$, but does not extend up to $e = 1$: the components are bound. These orbital elements, and in particular the eccentricity, are very robust, and we obtain the same constraint when we fit only the astrometry. A hundred orbits, selected randomly within the 500 000 orbits used to derive the posteriors, are plotted in Fig. 5. Figure 6 displays the radial velocity data. The portrayed orbit confirms the very high <1 eccentricity.

Table 9. Orbital elements from the MCMC fit of GJ 2060 AB relative orbit.

Parameter	This work
a (au)	$4.03 \pm 0.03 \left(\frac{d}{15.69\text{pc}}\right)$
P (yr)	7.77 ± 0.03
e	0.89 ± 0.01
i (°)	36 ± 3
Ω (°)	8 ± 4
ω (°)	-20 ± 5
$t_{\rm p}$ (yr, AD)	2005.27 ± 0.03
v_0 (km s^{-1})	28.8 ± 0.2
K (km s^{-1})	2.3 ± 0.9

Notes. The uncertainties on the fitted parameters correspond to the 68% interval of confidence of the distribution probabilities (see Appendix B).

For any distance d, we infer a dynamical mass of $m_{\rm tot} = 1.09 \pm 0.03\, M_\odot \left(\frac{d}{15.69\text{pc}}\right)^3$ for the pair. The fractional mass could be computed for each orbit thanks to the fit of the radial velocity amplitude (Eq. (3)). Considering our system as a pure SB1 (Eq. (4)), we obtain a fractional mass of $m_{\rm B}/m_{\rm tot} = 0.26 \pm 0.10 \left(\frac{15.69\,\text{pc}}{d}\right)$. However, this naive approach is questionable

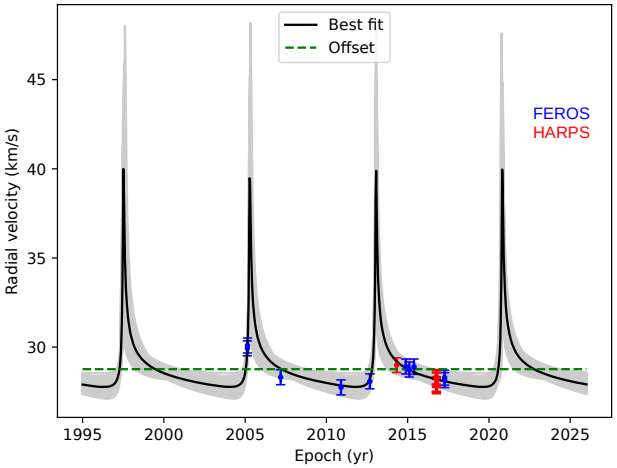

Fig. 6. Plots of a hundred radial velocity evolution obtained with the MCMC algorithm for system GJ 2060. Radial velocity measurements are color-coded according to the instrument, and their position on the fit is also shown. Only FEROS data are used in the orbital fit. The orbit in black, obtained with the LSLM algorithm, corresponds to the lower χ^2.

giving the flux ratio of the two components at FEROS wavelengths (~0.25). Thus, we used the method proposed by Montet et al. (2015) and considered our RVs to be the flux-weighted sum of the two individual RVs. The amplitude K fitted by the orbital fit could then be written as

$$K = (1 - F)K_A - FK_B, \quad (5)$$

$$= \frac{2\pi}{P} a \sin i \left((1 - F)\frac{m_B}{m_{tot}} - F\frac{m_A}{m_{tot}} \right), \quad (6)$$

where $F = L_B^V/(L_A^V + L_B^V) = 0.2$, L_A^V and L_B^V are the components luminosities in the visible spectrum, and K_A and K_B are respectively the amplitudes from A and B. From this relation, for any distance d, we obtain a fractional mass of $m_B/m_{tot} = 0.46 \pm 0.10 \left(\frac{15.69\text{pc}}{d}\right)$. Using the parallax distance and propagating its uncertainty, we finally obtain $m_{tot} = 1.09 \pm 0.10\, M_\odot$ and $\frac{m_B}{m_{tot}} = 0.46 \pm 0.10$.

The uncertainty on the total mass mainly comes from the uncertainty on the distance d, as $\Delta m_{tot}/m_{tot} = 3\Delta d/d$. The parameters d and Δd derive from the parallax released within the new reduction of Hipparcos data (Van Leeuwen 2007). The binarity of the system was taken into account in Hipparcos reduction through two additional variables in the proper motion fit. Moreover, the high eccentricity of the orbit prevents a good sampling of the radial velocity, in particular close to the periastron passage. This leads to high error bars in the inclination and velocity amplitude K. These errors propagate on the fractional secondary mass (see Eq. (4)). A higher accuracy on the orbital elements determination would certainly be achieved if the periastron passage were sampled in the available astrometric and spectroscopic data. This is unfortunately not the case yet.

On the other hand, the uncertainty on the fractional mass mainly comes from the very low constraints provided by the RVs. During most of the orbital revolution, the RV variation has a similar magnitude to that of the noise evidenced by the HARPS measurements. Only the sampling of the periastron passage could provide meaningful points that can refine the fractional mass. The next passage corresponds to October 2020. We can also see that the difference is very significant between the naive (SB1) and corrected (flux-weighted) approach: the fractional mass nearly doubles. Averaging the flux-weighted RVs is a first-order method, and is probably not precise enough to disentangle the two lines in our case where the luminosity of the secondary is nonnegligible compared to the primary. A more refined method (e.g., Czekala et al. 2017) would be necessary to trace back the individual RVs from our measurements and compute a robust fractional mass. Thus, we use only the total mass in the next sections.

6. Comparison to the models

Both our systems now have a dynamical mass and an estimated age given by their membership to moving groups, as well as a robust estimate of their bolometric luminosities L and effective temperatures T_{eff}. Thus, we are able to probe the accuracy of the PMS evolutionary models at these mass ranges.

There are several evolutionary models for PMS stars that rely on different physics (e.g., atmospheric models, convection efficiency). Two of them are suitable for 0.1 $M_\odot$ objects, the DM97 model (D'Antona & Mazzitelli 1997) and the BHAC15 model (Baraffe et al. 2015). Four more models are suitable for higher mass PMS stars: the SDF00 model (Siess et al. 2000), the PISA model (Tognelli et al. 2011, 2012), the PARSEC model (Bressan et al. 2012) with the Chen et al. (2014) corrections for low-mass stars, and the Darmouth model (Dotter et al. 2008) with the Feiden (2016) integrations of the magnetic field. Testing the predictions of different models enables us to compare the relevance of their approach, and thus to achieve a better understanding of the underlying physics.

6.1. TWA 22

According to the previous sections, TWA 22 has a total dynamical mass of $0.18 \pm 0.02\, M_\odot$ and an age of ~25 Myr. We first considered the isochrones and iso-masses predicted by evolutionary models in a (T_{eff}, L) plane. We used the bolometric luminosities and effective temperatures derived by Bonnefoy et al. (2014a). Figure 9 compares our observed T_{eff} and L to the BHAC15 tracks. The two components, A and B, are not located on the same isochrone, the primary at 10 Myr and the secondary at 20 Myr, but their positions are consistent with coevality between 10 and 25 Myr within 1σ. On the other hand, the predicted masses are respectively around 0.06 and 0.07 $M_\odot$ for A and B, at the lower end of the stellar regime, which gives a total mass of 0.13 $M_\odot$. Nevertheless, when we impose coevality at the moving group age and allow for a shift of T_{eff} within the 1σ interval, we retrieve the total dynamical mass, with masses of about 0.08 and 0.1 $M_\odot$ for A and B. The corresponding diagram is shown in the Appendix C for the DM97 model. Underprediction of the total mass and noncoevality are again retrieved, but once again the discrepancy disappears when we impose coevality at the moving group's age and allow for a shift of T_{eff}.

Unlike the bolometric luminosity and dynamical mass, the effective temperature predicted by the models is not robust as it depends strongly on the atmosphere model. For each component, we thus used the measured luminosity to compute the predicted mass for a range of ages with the BHAC15 and DM97 models. The corresponding plot is displayed in Fig. 8; the data have been linearly interpolated where necessary to provide predictions at the required ages. The prediction at the moving group age is consistent with the dynamical mass.

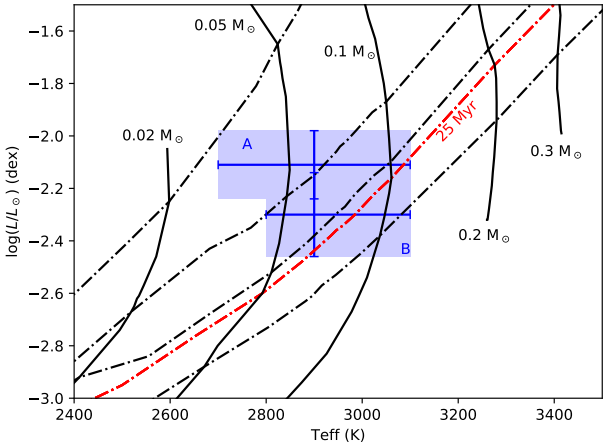

Fig. 7. Isochrones and iso-mass curves predicted by BHAC15. Shown are the 1, 10, 20, 25, and 50 Myr isochrones (dash-dotted lines from left to right), and the iso-mass curves (solid lines). The 25 Myr isochrone corresponds to the age of the β Pic-MG, and is drawn in red. The blue shaded areas correspond to the observed values and their error bars for each component of system TWA 22, A and B.

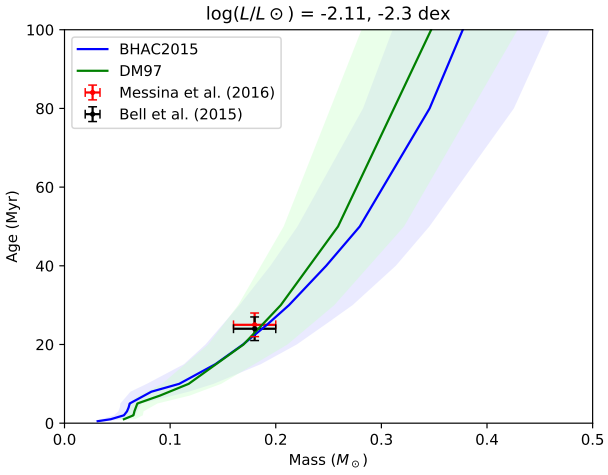

Fig. 8. Comparison of TWA 22 direct mass measurements for two different β Pic-MG age estimations with the predicted masses of the BHAC15 and DM97 tracks derived from the bolometric luminosity. Errors on the photometry are propagated on predictions (shaded area). The error on the distance is taken into account here.

6.2. GJ 2060

According to the previous sections, GJ 2060 has a total dynamical mass of $m_{\rm tot} = 1.09 \pm 0.10\,M_{\odot}$, and its age estimate can go from 30 to 200 Myr.

We first considered the isochrones and iso-masses predicted by evolutionary models in a ($T_{\rm eff}$, L) plane. Figure 9 compares our observed $T_{\rm eff}$ and L to the BHAC15 tracks. The two components, A and B, are located on the same isochrone, at approximately 40 Myr, which is consistent with the younger estimations of the AB Dor-MG age. On the other hand, the predicted masses are respectively at approximately 0.55 and 0.3 $M_{\odot}$ for A and B, which gives a total mass of 0.85 $M_{\odot}$, far (2σ) from the 1.09 $M_{\odot}$ obtained by the orbital fit. We tried to impose a total mass of 0.85 $M_{\odot}$ in the orbital fit in order to evaluate how this would change the distribution of χ^2. In this case, it leads to orbits with $\chi^2_{\rm red} > 8.5$ for a distance of 15.69 pc, and $\chi^2_{\rm red} > 2.5$ for the 1σ distance 15.24 pc, compared to 0.5 when the mass is set free.

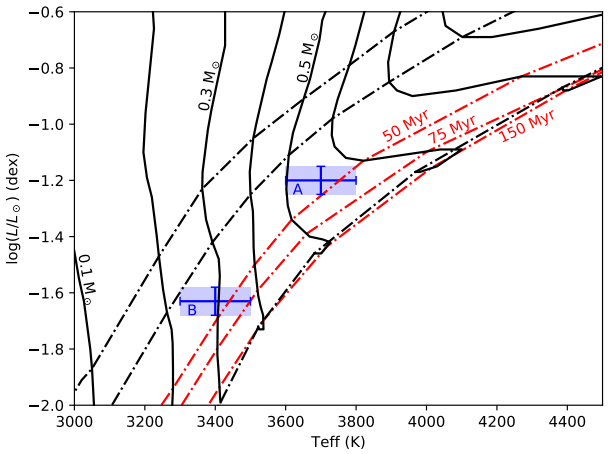

Fig. 9. Isochrones and iso-mass curves predicted by BHAC15. Shown are the 10, 20, 50, 75, 150, and 600 Myr isochrones (dash-dotted lines from left to right), while one iso-mass is drawn as a solid line every 0.1 $M_{\odot}$ from 0.1 (left) to 1 $M_{\odot}$ (right). The 50, 75, and 150 Myr isochrones correspond to possible ages for AB Dor-MG, and are drawn in red. The blue shaded areas correspond to the observed values and their error bars for each component of system GJ 2060, A and B.

Therefore, the predicted mass does not account for the astrometry of the system.

The corresponding diagrams are shown in the Appendix C for all the other models. Underprediction of the total mass are retrieved in each case. Coevality is sometimes only marginally achieved (PARSEC), and a very young age can be predicted (20 Myr, DM97).

As in the TWA 22 case, we then used each component measured luminosity to compute the predicted mass for a range of ages with the six models (BHAC15, DM97, PARSEC, PISA, Darmouth and SDF00) and we infer a plot linking the mass and age for the observed luminosity. These plots are displayed in Fig. 10. We retrieve the ∼20% underestimation of the total mass (2σ deviation) if a young age is assumed. Conversely, an old age (>150 $M_{\odot}$) gives a mass marginally compatible (1σ) with the orbital fit.

From the plots, we computed the predicted mass for each model and different ages of the AB Dor moving group. The results are displayed in Table 10. In order to avoid summing correlated errors, we drew the mass-age relation for several distances, and determined the system mass in each case. We computed the spread and deduced the uncertainty due to the distance $\sigma_{\rm d}$. For the most probable distance, we then derived the age uncertainty due to the luminosities $\sigma_{\rm L}$. The final ages uncertainties are then the quadratic sum of the independent errors $\sigma_{\rm L}$ and $\sigma_{\rm d}$. Only the >100 Myr case fits marginally within the 68 % interval of confidence of the MCMC probability distribution of the dynamical mass. This age is inconsistent with the positions of the two stars on the temperature-luminosity diagram for all models, except for PARSEC.

7. Discussion

The discrepancy in the dynamical mass of GJ 2060 AB ranges from 1 to 2σ, depending on the system's age. Such a disparity is not statistically impossible as it represents respectively the edge of the 68% and 95% confidence interval. As an example, a 1–2σ overestimation of the parallax could resolve the issue while being a legitimate statistical realization. We present below some alternative hypotheses.

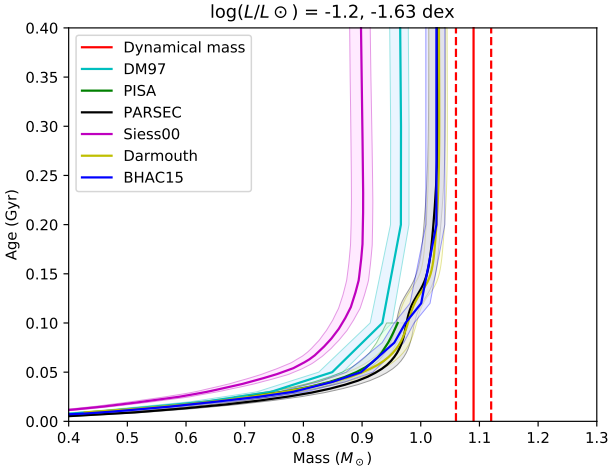

Fig. 10. Mass–age relations according to the six different evolutionary models, for GJ 2060 observed luminosities. A distance of 15.69 pc is assumed. The dynamical mass and its uncertainty are shown in red.

Table 10. Predicted mass (in solar mass units) for system GJ 2060 depending on the evolutionary model, from its luminosity and for several assumed ages.

Model	50 Myr	75 Myr	100 Myr	150 Myr	200 Myr
BHAC15	$0.90^{+0.03}_{-0.04}$	$0.95^{+0.03}_{-0.04}$	$0.97^{+0.03}_{-0.03}$	$1.01^{+0.03}_{-0.03}$	$1.03^{+0.02}_{-0.04}$
PISA	$0.89^{+0.03}_{-0.04}$	$0.94^{+0.03}_{-0.04}$	$0.96^{+0.03}_{-0.03}$	x	x
PARSEC	$0.92^{+0.05}_{-0.03}$	$0.97^{+0.02}_{-0.04}$	$0.98^{+0.02}_{-0.04}$	$1.01^{+0.03}_{-0.03}$	$1.02^{+0.03}_{-0.02}$
SDF00	$0.76^{+0.05}_{-0.04}$	$0.83^{+0.03}_{-0.03}$	$0.87^{+0.03}_{-0.04}$	$0.90^{+0.03}_{-0.04}$	$0.90^{+0.03}_{-0.03}$
DM97	$0.85^{+0.03}_{-0.04}$	$0.89^{+0.03}_{-0.03}$	$0.93^{+0.05}_{-0.03}$	$0.95^{+0.03}_{-0.03}$	$0.97^{+0.01}_{-0.04}$
Darmouth	$0.90^{+0.05}_{-0.04}$	$0.96^{+0.03}_{-0.04}$	$0.98^{+0.03}_{-0.04}$	$1.02^{+0.03}_{-0.04}$	$1.03^{+0.03}_{-0.03}$

Notes. The error on the distance is taken into account here. The dynamical mass is $1.09 \pm 0.10\,M_{\odot}$.

Table 11. Mean predicted mass (in solar mass units) for GJ 2060 A and B, from their luminosities.

Component	50 Myr	75 Myr	100 Myr	150 Myr	200 Myr
GJ 2060 A	0.55	0.55	0.55	0.57	0.57
GJ 2060 B	0.32	0.37	0.40	0.41	0.42

7.1. Data derivation and interpretation

The SINFONI spectra of GJ 2060 A and B are well fitted by the BT-SETTL model (Fig. 3). Consistent estimates of the bolometric luminosities can be inferred from the multi-epoch observations of the pair (Table 5). Thus, we can focus on vetting the dynamical mass estimate.

GJ 2060 astrometry has been measured with many different instruments, so that systematic errors can lead to important biases if they are not accounted for in the error bars. However, we performed the MCMC fit to each instrument astrometry, with and without the radial velocity measurements, and found values very close to those given in Sect. 5 for orbital elements and for total mass peak values that can definitely not account for the 0.1 or $0.2\,M_{\odot}$ difference. We find a total mass of $m_{\rm tot} = 1.10 \pm 0.14\,M_{\odot}$ when we only consider the largest homogeneous sample of astrometric epochs (AstraLux), and $m_{\rm tot} = 1.05 \pm 0.12\,M_{\odot}$ when we consider the three main sets of astrometric epochs (AstraLux, SPHERE, Keck). We estimate $1.08 \pm 0.12\,M_{\odot}$ when we consider all the astrometry and exclude the radial velocity measurements. In all these cases, as the orbit is less constrained, the mass can agree within 1σ with the model predictions for the old age ranges of the AB Dor moving group.

The absolute orientation of the field is usually inferred from the observations of different reference astrometric fields (clusters). This orientation could not be derived in a homogeneous way for all our astrometric epochs and instruments. Therefore, it may introduce a bias on the orbital parameter determination of GJ 2060 AB. A systematic on the pixel scale of the instruments is less likely to change our results given the short separation of GJ 2060 AB. Therefore, we added parameters to the MCMC algorithm in order to estimate and account for systematic angular offsets in the astrometry. Our astrometry consists of five different samples, but only three of them (AstraLux, SPHERE, and Keck) contain more than two data points. We performed an orbital fit with only these samples along with the RVs, with AstraLux data (which are more numerous) taken as reference. Two offset parameters, α_1 and α_2, thus had to be added to the original MCMC algorithm: the AstraLux data are fitted as they are with a model corresponding to Eqs. (1) and (2), while the SPHERE data are first rotated through the angle α_1 and the Keck data through the angle α_2. We modified the algorithm to allow any number N of samples (which are N different instruments) as astrometry input. One sample has to be designated as the reference, and the algorithm fits $N - 1$ angular offsets assuming a flat prior (e.g., Montet et al. 2015). The results are then displayed with posterior distributions and correlations to the other parameters. We found a distribution centered around $-0.18°$ for the offset between AstraLux and SPHERE data, with standard deviation of $0.2°$. For the offset between AstraLux and Keck, the distribution is centered around $0.10°$, with standard deviation of $0.3°$. Near apoastron, an angular offset of $0.3°$ corresponds to a 2–3 mas offset on the right ascension. However, the total and fractional mass remain unaffected. We are then confident that our dynamical mass estimate is not strongly affected by these angular offsets.

7.2. Model imprecision at the moving group ages

Pre-main sequence models have a well-known tendency to significantly underestimate the mass of low-mass stars (Hillenbrand & White 2004; Mathieu et al. 2007). Mathieu et al. (2007) studied the 23 PMS stars for which a dynamical mass had been derived, and compared these masses to the predictions of the evolutionary models given the bolometric luminosity and effective temperature of the stars. They highlighted a mean underestimation of 20–30% for low-mass stars ($<1\,M_{\odot}$), similar to the underestimation of GJ 2060 mass. Since then, new evolutionary models have been designed. Moreover, dozens of new dynamical masses have been obtained for PMS stars in the mean time (most of them for stars younger than 10 Myr). These studies often confirm the previously reported mass discrepancy (e.g., Simon et al. 2017; Mizuki et al., in prep.).

Among these systems, some are comparable to our objects. In the AB Dor moving group, the systems AB Dor Bab (Azulay et al. 2015; Janson 2018, in prep.) and C (Close et al. 2005, 2007; Luhman & Potter 2006; Boccaletti et al. 2008; Azulay et al. 2017) have been deeply analyzed in relation to the discussion about the age of the moving group. The dynamical masses and luminosities of AB Dor Ba and Bb are not consistent with the PMS isochrones (Janson 2018, in prep., Paper II). At the given luminosities and for a moving group age of 150 Myr,

the predicted masses are ∼25% below the dynamical masses, which are similar to that of GJ 2060 B. The study of AB Dor C is consistent with any age between 20 and 120 Myr, and the mass derived from the models is slightly underestimated (10%) but still consistent with the dynamical mass, which is similar to that of the TWA 22 components (Azulay et al. 2017).

On the other hand, NTT 33370 AB is a 80 Myr low-mass binary very similar to TWA 22 in terms of mass (Schlieder et al. 2014; Dupuy et al. 2016). Both individual masses are strongly underpredicted by the BHAC15 model (2σ, 46^{+16}_{+19}%), which contrasts with the perfect agreement we found for TWA 22.

This issue does not disappear for older ages of the PMS regime. System 2M1036 is a triple M-dwarf stellar system in the Ursa Major moving group, whose age is estimated at 400–500 Myr (Brandt & Huang 2015; Jones et al. 2015). Calissendorff et al. (2017) evidenced a 1σ underestimation on each component mass. Conversely, in the same moving group, the dynamical masses of the *K* binary system NO UMa are in good agreement with the model predictions (Schlieder et al. 2016).

Evolutionary models have not yet entirely mastered the physics of PMS stars, as can be seen from the frequent mass underestimation. It is particularly surprising that two very similar systems can encounter very different prediction agreements. Confronted with the mass overestimation of system GJ 1108 A, Mizuki et al. (in prep.) compared the dynamical masses of a dozen PMS stars with the predictions of the BHAC15 model, and report a ≤10% offset toward underestimation, and ∼20% scatter. Their results also confirm that the tendency to underpredict the mass is neither associated with a mass range nor with an age.

Magnetic activity is also often brought up as a cause of discrepancy in low-mass stars, as it greatly affects convection and induces large spot coverage fractions that may lead to displacements on the HR diagram (e.g., Feiden 2015; Somers & Pinsonneault 2015). The high jitter in HARPS RV measurements (∼400 m s^{-1}) indicates that GJ 2060 has strong magnetic activity. Somers & Pinsonneault (2015) studied the influence of spots on PMS stars and showed that it could lead to nonnegligible radius inflation, which would then lower the effective temperatures and luminosities of the stars. The gap between the normal and spotted case depends a little on the star's age and strongly on the star's mass. Following Fig. 1.B in Somers & Pinsonneault (2015), we assumed a ΔL of −10% and $\Delta T_{\rm eff}$ of −5% for the primary, and a ΔL of −20% and $\Delta T_{\rm eff}$ of −8% for the secondary. We then plot the new position of GJ 2060 A and B on the BHAC15 isochrones in Fig. C.2f. The positions are shifted of 0.04 dex and 0.1 dex toward the brighter luminosities, and 200 K and 300 K toward the hotter temperatures. The diagram is now consistent with coevality at 150 Myr, and the total mass that is derived matches the dynamical estimate. These corrections are computed with a spot surface coverage of 50%. The intense activity of the stars could thus account for the disagreement with the models. A shift in temperature could also resolve the slight mismatch of TWA 22 that appears in the HR diagram. However, a higher luminosity would lead to an excessive mass. This hints at a reduced activity-induced effect for TWA 22 components. In order to test this hypothesis, it would be worth comparing the activity indicators of different PMS binaries with their predicted mass discrepancy. Such a study was done recently for eclipsing binaries by Stassun et al. (2014), who showed that activity was not the only cause of the disparity. Finally, in our case where the two components are regularly (at each periastron passage) very close to each other (<1 au), tidal interactions may also affect the evolution of the stars, although the effects are expected to be weaker than in the eclipsing binary cases, which are constantly undergoing strong interactions. An in-depth study would be needed, however, to determine the effect of tidal forces on the interiors of eccentric binaries.

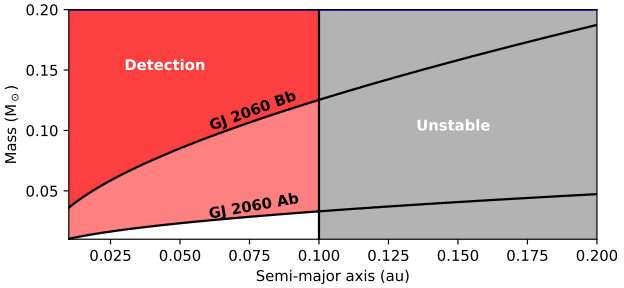

(a) Mass, coplanar case

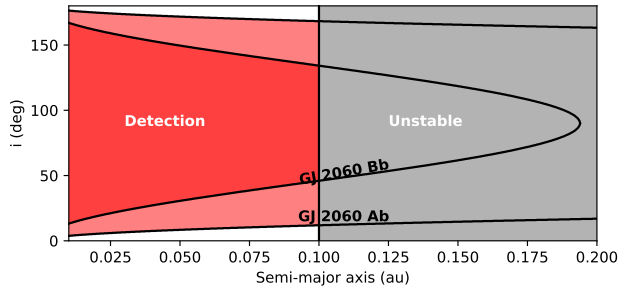

(b) Inclination, m_{inner} = 0.1 $M_\odot$

Fig. 11. Radial velocity detection limits around GJ 2060 A and B as a function of the inner orbit radius (coplanar case) in terms of the inner companion's *panel a*: mass and *panel b*: inclination. For *panel a* the orbits are coplanar (i = 36°) and for *panel b* the inner mass is set to 0.1 $M_\odot$.

Table 12. GJ 2060 missing mass (in solar mass units) depending on models and age.

Model	50 Myr	75 Myr	100 Myr	150 Myr	200 Myr
BHAC15	$0.18^{+0.09}_{-0.08}$	$0.13^{+0.09}_{-0.08}$	$0.11^{+0.09}_{-0.09}$	$0.07^{+0.09}_{-0.09}$	$0.05^{+0.11}_{-0.08}$
PISA	$0.19^{+0.09}_{-0.08}$	$0.14^{+0.09}_{-0.08}$	$0.12^{+0.09}_{-0.09}$	x	x
PARSEC	$0.16^{+0.09}_{-0.10}$	$0.11^{+0.10}_{-0.08}$	$0.10^{+0.10}_{-0.08}$	$0.07^{+0.09}_{-0.08}$	$0.06^{+0.10}_{-0.09}$
SDF00	$0.32^{+0.09}_{-0.09}$	$0.25^{+0.09}_{-0.09}$	$0.21^{+0.09}_{-0.09}$	$0.18^{+0.09}_{-0.09}$	$0.18^{+0.09}_{-0.08}$
DM97	$0.23^{+0.09}_{-0.08}$	$0.19^{+0.09}_{-0.08}$	$0.15^{+0.09}_{-0.09}$	$0.13^{+0.09}_{-0.08}$	$0.11^{+0.11}_{-0.08}$
Darmouth	$0.18^{+0.09}_{-0.09}$	$0.12^{+0.09}_{-0.08}$	$0.10^{+0.09}_{-0.08}$	$0.06^{+0.09}_{-0.08}$	$0.05^{+0.10}_{-0.08}$
Mean	0.21	0.16	0.13	0.10	0.09

Notes. Error propagation values were obtained from the MCMC posterior dispersion, the luminosity uncertainty at given distances, and the errors on the distance assuming independency.

On the other hand, Simon et al. (2017) suggested that all underestimations come from hidden components within the systems. If it is unlikely that this explanation accounts for all the observed discrepancies, in particular within tight binaries, it is nevertheless a suggestion worth studying for GJ 2060, especially given its unusually high eccentricity (e ∼ 0.9).

7.3. Missing mass: existence of GJ 2060 Ab or Bb

Hidden mass close to the primary could explain the strong disagreement between models and data for GJ 2060. An additional

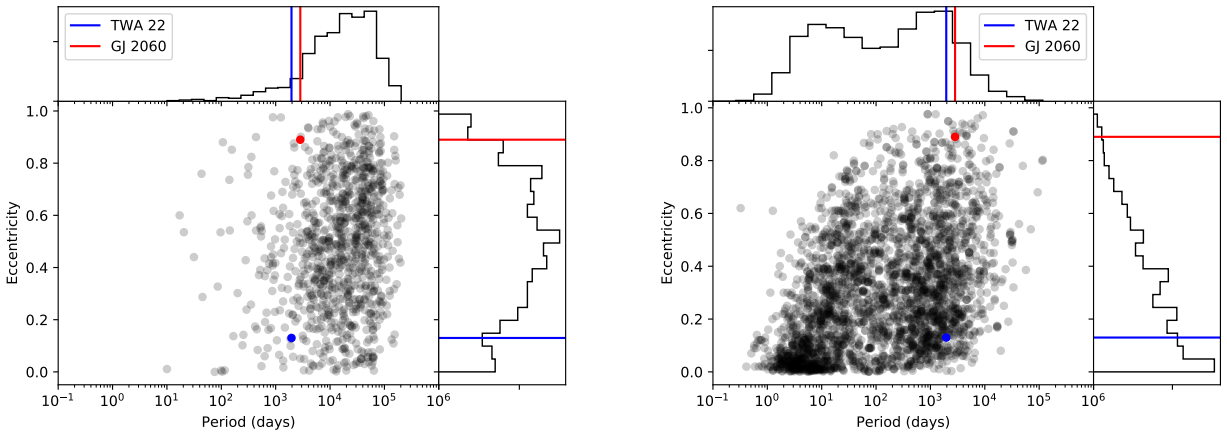

(a) ORB6 (b) SB9

Fig. 12. Period–eccentricity diagrams from two catalogs of binary stars: *panel a*: visual binaries from ORB6 and *panel b*: spectroscopic binaries from SB9.

companion of 0.1–0.2 $M_\odot$ (depending on the system's age) could account for the mass underestimation (see Table 12) and could have been missed in the SPHERE datasets if close enough to one of the two components.

Quick dynamical simulations with a symplectic integrator (SWIFT_ HJS Beust 2003, see Appendix D) show that an additional companion should orbit closer than 0.1 au (6 mas) to either of the companions to remain bound for the system's lifetime.

The PSFs of GJ 2060 A and B are not elongated, even in the SPHERE images ($FWHM \sim 30$ mas). In these images, we injected models of putative companions with different fluxes and separations and checked whether they would induce a PSF lengthening that could be seen by eye. The models of the putative companion were built using a flux-normalized PSF. The PSF is the other component of the system (e.g., B if the binarity of A is investigated, and vice versa). Using the BHAC15 models, we estimate that we would have just missed a 0.25 $M_\odot$ companion at a projected separation 0.45 au. Thus, a 0.2 solar mass object at 0.1 au would have gone unnoticed by the imagers.

As for the spectrograph, the available RV data are too sparse to resolve in frequency an additional orbit, and the flux ratio in the optical prevents the detection of any spectral signature. However, the closer the object, the stronger the radial velocity perturbation amplitude. A simple comparison between the perturbation amplitude on GJ 2060 A and B radial velocities and our measurements standard deviation σ is summarized in Fig. 11 for the circular case, for semi-major axis versus mass and semi-major axis versus inclination. We used the predicted mass of GJ 2060 A and B from Table 11 at an age of 100 Myr for that purpose. We chose 3σ dispersion of the RVs as a detection threshold, and represented the corresponding frontier on the plots. The limit of the dynamical stability has been set to 0.1 au; the accurate stability limit depends on the third companion's mass and inclination, but in all cases it is $\lesssim$0.1 au. In the coplanar case, a mass higher than 0.1 $M_\odot$ could have been unnoticed around the secondary. This is not the case for a putative companion around the primary because the light we observe comes mostly from the primary, so that most signals would be easily spotted. However, a 0.1 or even 0.2 $M_\odot$ at 0.1 au could be compatible with our deviation in both situations, primary or secondary, for small enough inclinations, respectively 10° and 5° around the primary, and 45° and 25° around the secondary.

If there is indeed a hidden companion, its luminosity would add to the luminosity of the nearest component, so that the latter measured flux would be biased. According to the BHAC15, a 50–75 Myr 0.2 $M_\odot$ companion has $\log(L/L_\odot) = -1.9, -2$ dex, and a 0.1 $M_\odot$ companion has $\log(L/L_\odot) \sim -2.3$ dex. The component hosting a hidden companion would appear overluminous for its temperature (slightly for the primary, significantly for the secondary), shifting its position on Fig. 9 toward the younger isochrones and straining coevality. In the PARSEC isochrones (see Appendix C) a significant luminosity shift (corresponding to a 0.2 $M_\odot$ companion) of the primary could achieve coevality. Conversely, the same companion around the secondary would induce a luminosity shift that would break coevality in all models.

Finally, the high eccentricity (0.90 ± 0.01) of the visual orbit is noticeable, and we wondered if it could indicate strong dynamical interactions. From the ORB6 catalog[3], we computed the periods and eccentricities of visual binary stars with reliable orbital elements (according to the grades given in the catalog). From the SB9 catalog (Pourbaix et al. 2004) we computed the periods and eccentricities of spectroscopic binary stars. Our two binaries fall near the limit of each catalog's period coverage, so that while it gives an interesting overview, more binaries would be needed to draw robust statistical conclusions. *Gaia*'s next data releases will significantly contribute to overcoming this lack. The resulting diagrams are shown in Fig. 12. While not so common, the eccentricity of GJ 2060 does not seem so rare at this range of periods and ages (before circularization). Moreover, no mechanism is known to enhance the eccentricity of an outer companion at such a period ratio (greater than 200, which excludes any meaningful mean-motion resonance). Only close encounters could dynamically raise the eccentricity, but the configuration would then not be stable. All in all, the high eccentricity is likely uncorrelated to the potential existence of a third companion.

8. Conclusion

We considered two systems of young astrometric M-dwarf binaries, TWA 22 and GJ 2060, and used existing astrometric and spectroscopic data along with new Keck, SPHERE, NaCo, HARPS, and FEROS data to derive the total mass of these systems. We consolidated the total dynamical mass estimate of TWA 22: 0.18 ± 0.02 $M_\odot$. We derived the first estimate of the total mass of GJ 2060: 1.08 ± 0.10 $M_\odot$. The orbits of the two

[3] http://www.usno.navy.mil/USNO/astrometry/optical-IR-prod/wds/orb6

systems are well constrained thanks to our additional data, and the errors are carefully estimated through the MCMC approach. The orbit of GJ 2060 has an unusually high eccentricity, around 0.9. The cross-contamination of GJ 2060 primary and secondary spectra into the FEROS and HARPS data prevents us from deriving accurate dynamical masses of the individual components.

The study of the photometry and spectroscopy of the two systems, along with their membership to moving groups and accurate distances, allow us to test the PMS evolutionary models predictions. The dynamical mass of TWA22 AB is correctly predicted by the models at the age of the β Pictoris moving group. The placement of GJ 2060 A and B on evolutionary tracks confirms the system coevality at an age compatible with the AB Doradus moving group (∼50 Myr). However, all models underpredict the total mass of GJ 2060 AB, by 10–20% (0.1–0.2 $M_{\odot}$, 1–2σ). A new precise parallax (likely to come in the *Gaia* DR3 release) would strongly decrease the uncertainty on the dynamical mass and could improve the statistical relevance of the discrepancy.

GJ 2060 AB's underpredicted mass is consistent with a trend found for other systems in the same mass range. It could be explained by luminosity and temperature drop caused by high starspot coverage. In that case, we would retrieve coevality at 150 Myr. We also discussed the potential existence of a third companion close to one component of GJ 2060 that could account for this disagreement. Dynamical modeling shows that such a companion would have to be very close to one of the stars, less than 0.1 au (6 mas), in order to remain stable for millions of years. Such a close companion could have gone unnoticed, although the RVs are putting some constraints on its mass and inclination. Astrometric and spectroscopic data at periastron and the use of RV disentanglement techniques might help clarify the origin of the discrepancy, and in particular if only one of GJ 2060 AB's components has an underpredicted mass.

A dozen new PMS stellar mass measurements have become available in the last decade. A complete reassessment of the dynamical mass determinations of subsolar mass stars and a homogeneous comparison of these measurements to the latest PMS models would help arrive at a conclusion regarding the model's reliability. On the other hand, the upcoming data releases of the *Gaia* mission should yield a statistical sample of dynamical mass determination of low-mass stars (Pourbaix 2011). Additional studies are needed in any case to infer the luminosity and temperatures of these many systems and to allow a detailed comparison of the masses to evolutionary models predictions.

Acknowledgements. We thank Carine Babusiaux, Benjamin Montet, and Thierry Forveille for fruitful discussions, as well as the anonymous referee for reviewing our work and for insightful and constructive comments which improved the manuscript. The project is supported by CNRS, by the Agence Nationale de la Recherche (ANR-14-CE33-0018, GIPSE), the OSUG@2020 Labex, and the Programme National de Planétologie (PNP, INSU) and Programme National de Physique Stellaire (PNPS, INSU). Most of the computations presented in this paper were performed using the Froggy platform of the CIMENT infrastructure (https://ciment.ujf-grenoble.fr), which is supported by the Rhône-Alpes region (GRANT CPER07_13 CIRA), the OSUG@2020 Labex (reference ANR10 LABX56), and the Equip@Meso project (reference ANR-10-EQPX-29-01) of the programme Investissements d'Avenir, supervised by the Agence Nationale pour la Recherche. This research has made use of the SIMBAD database operated at the CDS (Strasbourg, France). Research on moving groups by Thomas Henning is supported by the DFG-SFB 881 "The Milky Way System." SPHERE is an instrument designed and built by a consortium consisting of IPAG (Grenoble, France), MPIA (Heidelberg, Germany), LAM (Marseille, France), LESIA (Paris, France), Laboratoire Lagrange (Nice, France), INAF–Osservatorio di Padova (Italy), Observatoire de Genève (Switzerland), ETH Zurich (Switzerland), NOVA (Netherlands), ONERA (France), and ASTRON (Netherlands) in collaboration with ESO. SPHERE was funded by ESO, with additional contributions from CNRS (France), MPIA (Germany), INAF (Italy), FINES (Switzerland), and NOVA (Netherlands). SPHERE also received funding from the European Commission Sixth and Seventh Framework Programmes as part of the Optical Infrared Coordination Network for Astronomy (OPTICON) under grant number RII3-Ct-2004-001566 for FP6 (2004–2008), grant number 226604 for FP7 (2009–2012), and grant number 312430 for FP7 (2013–2016). We also acknowledge financial support from the Programme National de Planétologie (PNP) and the Programme National de Physique Stellaire (PNPS) of CNRS-INSU in France. This work has also been supported by a grant from the French Labex OSUG@2020 (Investissements d'avenir – ANR10 LABX56). The project is supported by CNRS, by the Agence Nationale de la Recherche (ANR-14-CE33-0018). It has also been carried out within the frame of the National Centre for Competence in Research PlanetS supported by the Swiss National Science Foundation (SNSF). MRM, HMS, and SD are pleased to acknowledge the financial support of the SNSF. Finally, this work has made use of the the SPHERE Data Centre, jointly operated by OSUG/IPAG (Grenoble), PYTHEAS/LAM/CESAM (Marseille), OCA/Lagrange (Nice), and Observatoire de Paris/LESIA (Paris). We thank P. Delorme and E. Lagadec (SPHERE Data Centre) for their efficient help during the data reduction process.

References

Abuter, R., Schreiber, J., Eisenhauer, F., et al. 2006, New Astron. Rev., 50, 398
Andrews, S. M., Rosenfeld, K. A., Kraus, A. L., & Wilner, D. J. 2013, ApJ, 771, 129
Arenou, F., Luri, X., Babusiaux, C., et al. 2017, A&A, 599, A50
Azulay, R., Guirado, J., Marcaide, J., Marti-Vidal, I., & Arroyo-Torres, B. 2014, A&A, 561, A38
Azulay, R., Guirado, J. C., Marcaide, J. M., et al. 2015, A&A, 578, A16
Azulay, R., Guirado, J., Marcaide, J., et al. 2017, A&A, 607, A10
Baraffe, I., & Chabrier, G. 2010, A&A, 521, A44
Baraffe, I., Chabrier, G., Allard, F., & Hauschildt, P. 2002, A&A, 382, 563
Baraffe, I., Homeier, D., Allard, F., & Chabrier, G. 2015, A&A, 577, A42
Barenfeld, S. A., Bubar, E. J., Mamajek, E. E., & Young, P. A. 2013, ApJ, 766, 6
Barrado y Navascués, D., Stauffer, J. R., & Jayawardhana, R. 2004, ApJ, 614, 386
Bell, C. P. M., Mamajek, E. E., & Naylor, T. 2015, MNRAS, 454, 593
Bergfors, C., Brandner, W., Janson, M., et al. 2010, A&A, 520, A54
Beust, H. 2003, A&A, 400, 1129
Beuzit, J.-L., Feldt, M., & Dohlen, K. 2008, in Proc. SPIE., 7014, 701418
Binks, A. S., & Jeffries, R. D. 2014, MNRAS, 438, L11
Boccaletti, A., Chauvin, G., Baudoz, P., & Beuzit, J.-L. 2008, A&A, 482, 939
Boden, A. F., Sargent, A. I., Akeson, R. L., et al. 2005, ApJ, 635, 442
Bonnefoy, M., Chauvin, G., Dumas, C., et al. 2009, A&A, 506, 799
Bonnefoy, M., Chauvin, G., Lagrange, A.-M., et al. 2014a, A&A, 562, A127
Bonnefoy, M., Marleau, G.-D., Galicher, R., et al. 2014b, A&A, 567, L9
Bonnefoy, M., Chauvin, G., Dougados, C., et al. 2017, A&A, 597, A91
Bonnet, H., Ströbele, S., Biancat-Marchet, F., et al. 2003, in Proc. SPIE, 4839, 329
Brandt, T. D., & Huang, C. X. 2015, ApJ, 807, 58
Bressan, A., Marigo, P., Girardi, L., et al. 2012, MNRAS, 427, 127
Calissendorff, P., Janson, M., Köhler, R., et al. 2017, A&A, 604, A82
Chabrier, G., Gallardo, J., & Baraffe, I. 2007, A&A, 472, L17
Chauvin, G., Lagrange, A.-M., Dumas, C., et al. 2004, A&A, 425, L29
Chauvin, G., Lagrange, A.-M., Bonavita, M., et al. 2010, A&A, 509, A52
Chauvin, G., Lagrange, A.-M., Beust, H., et al. 2012, A&A, 542, A41
Chauvin, G., Desidera, S., Lagrange, A., et al. 2017, in SF2A-2017: Proceedings of the Annual meeting of the French Society of Astronomy and Astrophysics, eds. C. Reylé, P. Di Matteo, F. Herpin, et al., 331
Chelli, A. 2000, A&A, 358, L59
Chen, Y., Girardi, L., Bressan, A., et al. 2014, MNRAS, 444, 2525
Claudi, R. U., Turatto, M., Gratton, R. G., et al. 2008, in Proc. SPIE, 7014, 70143E
Close, L. M., Lenzen, R., Guirado, J. C., et al. 2005, Nature, 433, 286
Close, L. M., Thatte, N., Nielsen, E. L., et al. 2007, ApJ, 665, 736
Cushing, M. C., Rayner, J. T., & Vacca, W. D. 2005, ApJ, 623, 1115
Cutri, R. M., Skrutskie, M. F., van Dyk, S., et al. 2003, VizieR Online Data Catalog: II/246
Czekala, I., Mandel, K. S., Andrews, S. M., et al. 2017, ApJ, 840, 49
Daemgen, S., Siegler, N., Reid, I. N., & Close, L. M. 2007, ApJ, 654, 558
Dahm, S. E. 2015, ApJ, 813, 108
D'Antona, F., & Mazzitelli, I. 1997, Mem. Soc. Astron. Ital., 68, 807
Delorme, P., Lagrange, A. M., Chauvin, G., et al. 2012, A&A, 539, A72
Delorme, P., Meunier, N., Albert, D., et al. 2017, in SF2A-2017: Proceedings of the Annual meeting of the French Society of Astronomy and Astrophysics, eds. C. Reylé, P. Di Matteo, F. Herpin, et al., 347
Devillard, N. 1997, The Messenger, 87, 19

Diolaiti, E., Bendinelli, O., Bonaccini, D., et al. 2000, in Proc. SPIE, 4007, 879
Dohlen, K., Langlois, M., Saisse, M., et al. 2008, in Proc. SPIE, 7014, 70143L
Dommanget, J., & Nys, O. 2000, A&A, 363, 991
Dotter, A., Chaboyer, B., Jevremović, D., et al. 2008, A&AS, 178, 89
Dupuy, T. J., Forbrich, J., Rizzuto, A., et al. 2016, ApJ, 827, 23
Durkan, S., Janson, M., Ciceri, S., et al. 2018, A&A, ArXiv e-prints [arXiv: 1806.05133]
Eisenhauer, F., Abuter, R., Bickert, K., et al. 2003, in Proc. SPIE, 4841, 1548
Feiden, G. A. 2015, Proc. IAU, 10, 79
Feiden, G. A. 2016, A&A, 593, A99
Ford, E. B. 2005, ApJ, 129, 1706
Ford, E. B. 2006, ApJ, 642, 505
Freudling, W., Romaniello, M., Bramich, D. M., et al. 2013, A&A, 559, A96
Fusco, T., Rousset, G., Sauvage, J.-F., et al. 2006, Opt. Express, 14, 7515
Gagné, J., Lafrenière, D., Doyon, R., Malo, L., & Artigau, É. 2014, ApJ, 783, 121
Galland, F., Lagrange, A.-M., Udry, S., et al. 2005, A&A, 443, 337
Gennaro, M. Prada Moroni, P. G., & Tognelli, E. 2012, MNRAS, 420, 986
Guilloteau, S., Simon, M., Piétu, V., et al. 2014, A&A, 567, A117
Guirado, J., Marcaide, J., Martí-Vidal, I., et al. 2011, A&A, 533, A106
Hayes, D. S. 1985, in IAU Symp., 111, 225
Hillenbrand, L. A., & White, R. J. 2004, ApJ, 604, 741
Hippler, S., Bergfors, C., Brandner, W., et al. 2009, The Messenger, 137, 14
Janson, M., Hormuth, F., Bergfors, C., et al. 2012, ApJ, 754, 44
Janson, M., Bergfors, C., Brandner, W., et al. 2014, ApJS, 214, 17
Janson, M., Durkan, S., Hippler, S., et al. 2017, A&A, 599, A70
Jones, J., White, R., Boyajian, T., et al. 2015, ApJ, 813, 58
Kaufer, A., Stahl, O., Tubbesing, S., et al. 1999, The Messenger, 95, 8
Kraus, A. L., Tucker, R. A., Thompson, M. I., Craine, E. R., & Hillenbrand, L. A. 2011, ApJ, 728, 48
Lagrange, A.-M., Bonnefoy, M., Chauvin, G., et al. 2010, Science, 329, 57
Lannier, J., Delorme, P., Lagrange, A., et al. 2016, A&A, 596, A83
Lenzen, R., Hartung, M., Brandner, W., et al. 2003, in Proc. SPIE, 4841, 944
Lopez-Santiago, J., Montes, D., Crespo-Chacon, I., & Fernandez-Figueroa, M. J. 2006, ApJ, 643, 1160
Luhman, K. L., & Potter, D. 2006, ApJ, 638, 887
Luhman, K. L., Stauffer, J. R., & Mamajek, E. E. 2005, ApJ, 628, L69
Maire, A.-L., Bonnefoy, M., Ginski, C., et al. 2016a, A&A, 587, A56
Maire, A.-L., Langlois, M., Dohlen, K., et al. 2016b, in Proc. SPIE, 9908, 990834
Malo, L., Doyon, R., Lafrenière, D., et al. 2013, ApJ, 762, 88
Malo, L., Doyon, R., Feiden, G. A., et al. 2014, ApJ, 792, 37
Mamajek, E. E. 2005, ApJ, 634, 1385
Marois, C., Macintosh, B., Barman, T., et al. 2008, Science, 322, 1348
Marois, C., Zuckerman, B., Konopacky, Q. M., Macintosh, B., & Barman, T. 2010, Nature, 468, 1080
Mathieu, R. D., Baraffe, I., Simon, M., Stassun, K. G., & White, R. 2007, Protostars Planets V, 411
Mayor, M., Pepe, F., Queloz, D., et al. 2003, The Messenger, 114, 20
McCaughrean, M. J., & Stauffer, J. R. 1994, AJ, 108, 1382
Mesa, D., Gratton, R., Zurlo, A., et al. 2015, A&A, 576, A121
Messina, S., Desidera, S., Turatto, M., Lanzafame, A. C., & Guinan, E. F. 2010, A&A, 520, A15
Messina, S., Lanzafame, A. C., Feiden, G. A., et al. 2016, A&A, 596, A29
Montet, B. T., Bowler, B. P., Shkolnik, E. L., et al. 2015, ApJ, 813, L11
Mountain, C. M., Selby, M. J., Leggett, S. K., Blackwell, D. E., & Petford, A. D. 1985, A&A, 151, 399
Nielsen, E. L., Close, L. M., Guirado, J. C., et al. 2005, Astron. Nachr., 326, 1033
Nielsen, E. L., De Rosa, R. J., Wang, J., et al. 2016, ApJ, 152, 175
Ortega, V. G., Jilinski, E., de la Reza, R., & Bazzanella, B. 2007, MNRAS, 377, 441
Pavlov, A., Möller-Nilsson, O., Feldt, M., et al. 2008, in Proc. SPIE, 7019, 701939
Pecaut, M. J., & Mamajek, E. E. 2013, ApJS, 208, 9
Petit, C., Sauvage, J.-F., Fusco, T., et al. 2014, in Proc. SPIE, 9148, 91480O
Pourbaix, D. 2011, AIPC, 1346, 122
Pourbaix, D., Tokovinin, A. A., Batten, A. H., et al. 2004, A&A, 424, 727
Queloz, D., Henry, G., Sivan, J., et al. 2001, A&A, 379, 279
Rameau, J., Chauvin, G., Lagrange, A.-M., et al. 2013a, ApJ, 772, L15
Rameau, J., Chauvin, G., Lagrange, A.-M., et al. 2013b, ApJ, 779, L26
Rayner, J. T., Cushing, M. C., & Vacca, W. D. 2009, ApJS, 185, 289
Rousset, G., Lacombe, F., Puget, P., et al. 2003, in Proc. SPIE, 4839, 140
Schlieder, J. E., Bonnefoy, M., Herbst, T., et al. 2014, ApJ, 783, 27
Schlieder, J. E., Skemer, A. J., Maire, A.-L., et al. 2016, ApJ, 818, 1
Service, M., Lu, J. R., Campbell, R., et al 2016, PASP, 128, 095004
Shkolnik, E. L., Allers, K. N., Kraus, A. L., Liu, M. C., & Flagg, L. 2017, AJ, 154, 69
Siess, L., Dufour, E., & Forestini, M. 2000, A&A, 358, 593
Simon, M., Dutrey, A., & Guilloteau, S. 2000, ApJ, 545, 1034
Simon, M., Guilloteau, S., Di Folco, E., et al. 2017, ApJ, 844, 158
Somers, G., & Pinsonneault, M. H. 2015, ApJ, 807, 174
Song, I., Zuckerman, B., & Bessell, M. 2003, ApJ, 599, 342
Song, I., Schneider, G., Zuckerman, B., et al. 2006, ApJ, 652, 724
Stassun, K. G., Feiden, G. A., & Torres, G. 2014, New Astron. Rev., 60, 1
Stauffer, J. R., Schultz, G., & Kirkpatrick, J. D. 1998, ApJ, 499, L199
Teixeira, R., Ducourant, C., Chauvin, G., et al. 2009, A&A, 503, 281
Theodossiou, E., & Danezis, E. 1991, Ap&SS, 183, 91
Tognelli, E., Moroni, P. G. P., & Degl'Innocenti, S. 2011, A&A, 533, A109
Tognelli, E., Degl'Innocenti, S., & Moroni, P. G. P. 2012, A&A, 548, A41
Torres, C. A. O., Quast, G. R., Melo, C. H. F., & Sterzik, M. F., 2008, in Young Nearby Loose Associations, 757
van Dam, M. A., Le Mignant, D., & Macintosh, B. A. 2004, Appl. Opt., 43, 5458
Van Leeuwen, F. 2007, A&A, 474, 653
Veran, J.-P., & Rigaut, F. J., 1998, in Proc. SPIE, 3353, 426
Vigan, A., Moutou, C., Langlois, M., et al. 2010, MNRAS, 407, 71
Zacharias, N., Monet, D. G., Levine, S. E., et al. 2005, VizieR Online Data Catalog: I/297
Zuckerman, B., Song, I., Bessell, M. S., & Webb, R. A. 2001, ApJ, 562, L87
Zuckerman, B., Song, I., & Bessell, M. S. 2004, ApJ, 613, L65
Zurlo, A., Vigan, A., Mesa, D., et al. 2014, A&A, 572, A85

[1] Univ. Grenoble-Alpes, CNRS, IPAG, 38000 Grenoble, France
e-mail: laetitia.rodet@univ-grenoble-alpes.fr
[2] Astrophysics Research Centre, Queens University Belfast, Belfast, UK
[3] Department of Astronomy, Stockholm University, Stockholm, Sweden
[4] Exoplanet and Stellar Astrophysics Laboratory, Code 667, NASA Goddard Space Flight Center, Greenbelt, MD 20771, USA
[5] Max Planck Institute for Astronomy, Königstuhl 17, 69117 Heidelberg, Germany
[6] Unidad Mixta Internacional Franco-Chilena de Astronomía, CNRS/INSU UMI 2286 and Departemento de Astronomía, Universidad de Chile, Casilla 36-D, Santiago, Chile
[7] INAF – Osservatorio Astronomico di Padova, Vicolo della Osservatorio 5, 35122 Padova, Italy
[8] European Southern Observatory (ESO), Alonso de Córdova 3107, Vitacura, 19001 Casilla, Santiago, Chile
[9] Institute for Astronomy, University of Edinburgh, Blackford Hill, Edinburgh EH9 3HJ, UK
[10] University College London, London, UK
[11] LESIA, Observatoire de Paris, PSL Research University, CNRS, Sorbonne Universités, UPMC, Univ. Paris 06, Univ. Paris Diderot, Sorbonne Paris Cité, 5 Place Jules Janssen, 92195 Meudon, France
[12] Geneva Observatory, University of Geneva, Chemin des Maillettes 51, 1290 Versoix, Switzerland
[13] CRAL, UMR 5574, CNRS, Université de Lyon, École Normale Supérieure de Lyon, 46 Allée d'Italie, 69364 Lyon Cedex 07, France
[14] Zentrum für Astronomie der Universität Heidelberg, Landesternwarte, Königstuhl 12, 69117 Heidelberg, Germany
[15] Aix-Marseille Université, CNRS, LAM (Laboratoire d'Astrophysique de Marseille) UMR 7326, 13388 Marseille, France
[16] NOVA Optical Infrared Instrumentation Group, Oude Hoogeveensedijk 4, 7991 PD Dwingeloo, The Netherlands
[17] Anton Pannekoek Institute for Astronomy, Science Park 904, 1098 XH Amsterdam, The Netherlands
[18] Institute for Particle Physics and Astrophysics, ETH Zurich, Wolfgang-Pauli-Strasse 27, 8093 Zurich, Switzerland

Appendix A: Spectrophotometry

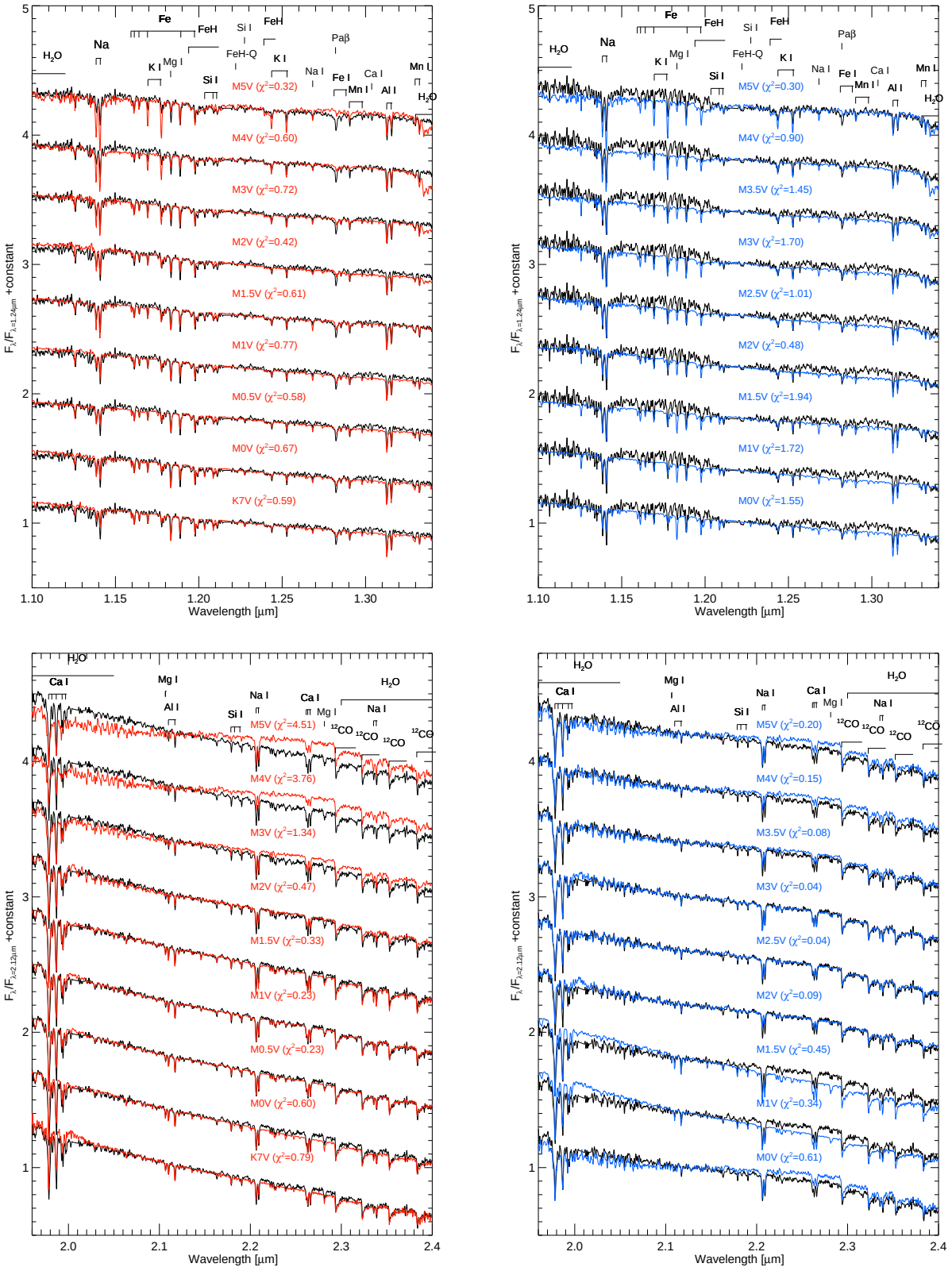

Fig. A.1. Comparison of the *J*- and *K*-band spectra of GJ 2060 A (red) and GJ 2060 B (blue) to M-dwarf spectra.

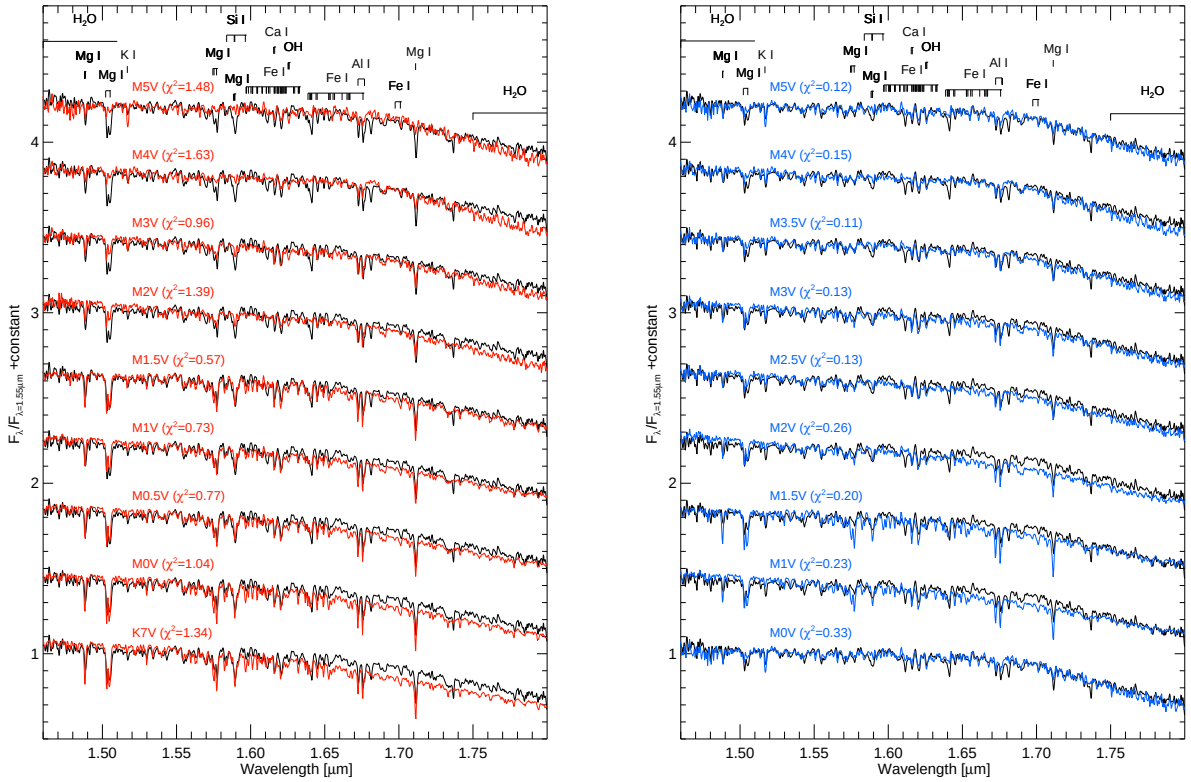

Fig. A.2. Comparison of the *H*-band spectra of GJ 2060 A (red) and GJ 2060 B (blue) to M-dwarf spectra.

Appendix B: Orbital fit

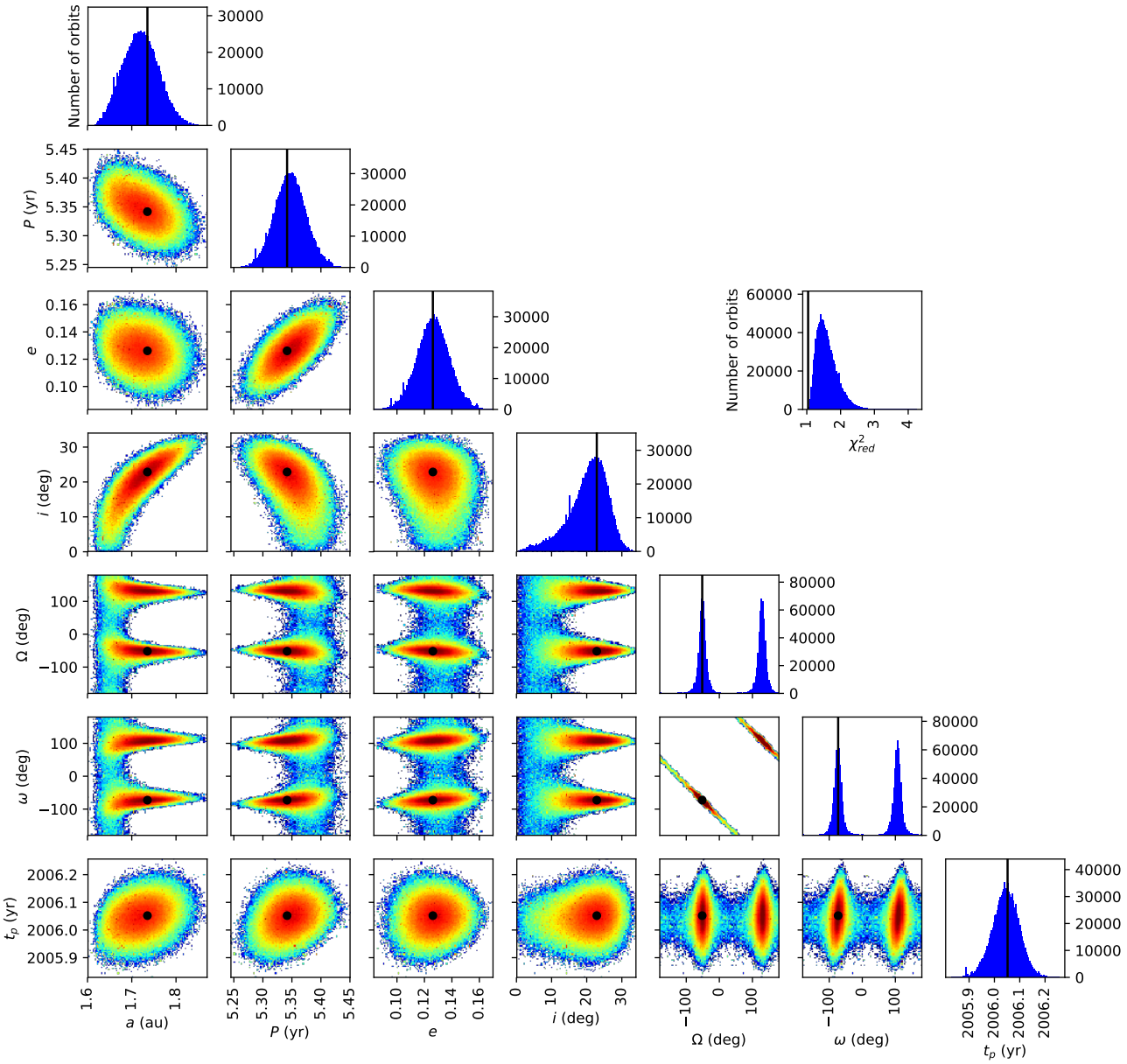

Fig. B.1. Distribution and correlations of each of the orbital elements fitted by the MCMC algorithm for system TWA 22. The black lines and points depict the best fitting orbit (lower χ^2) obtained with the LSLM algorithm. The color scale is logarithmic; blue corresponds to 1 orbit and red to 1000.

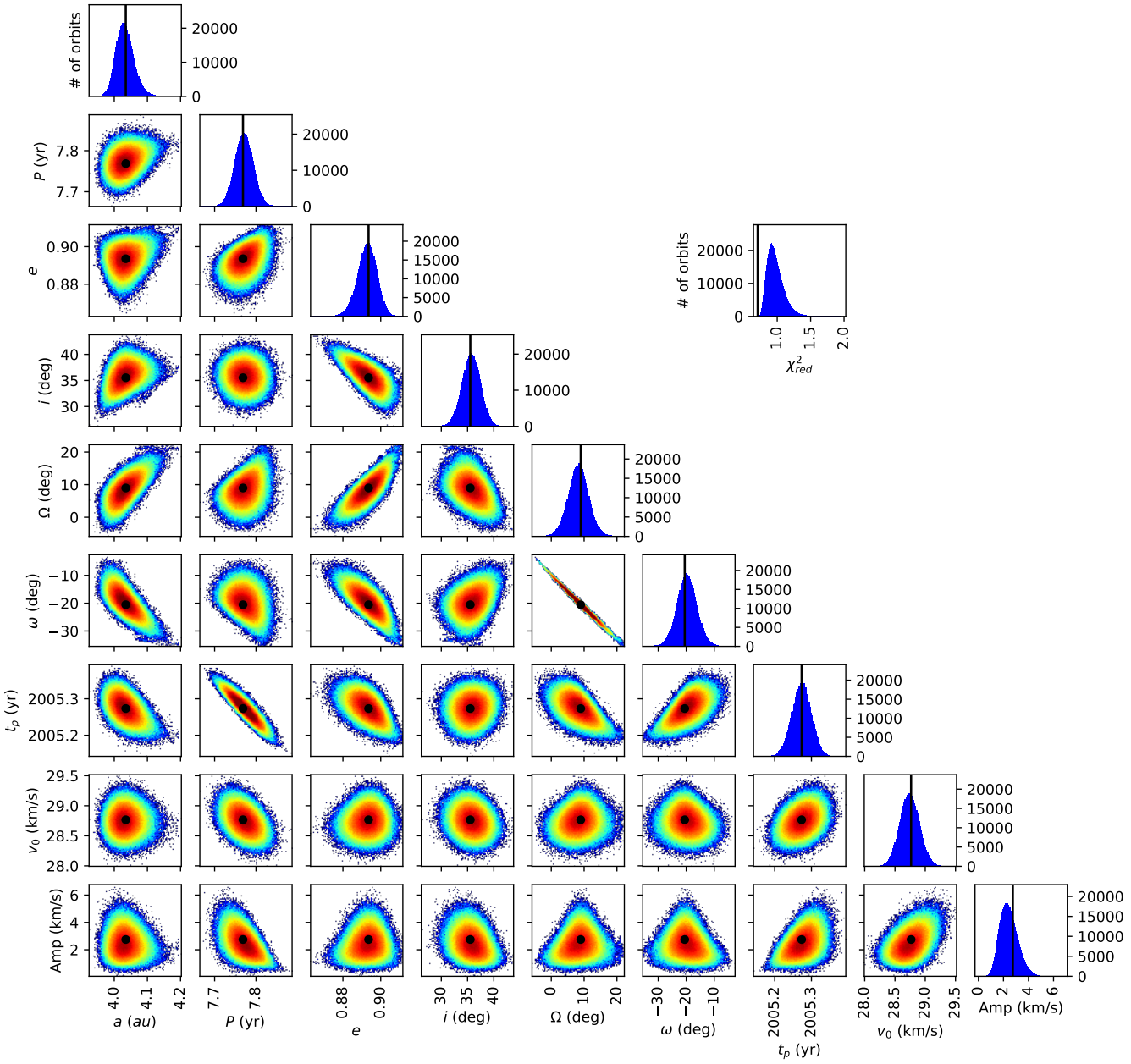

Fig. B.2. Distribution and correlations of each of the orbital elements fitted by the MCMC algorithm for system GJ 2060. The black lines and points depict the best fitting orbit (lower χ^2) obtained with the LSLM algorithm. The color scale is logarithmic; blue corresponds to 1 orbit and red to 1000.

Appendix C: Model comparison

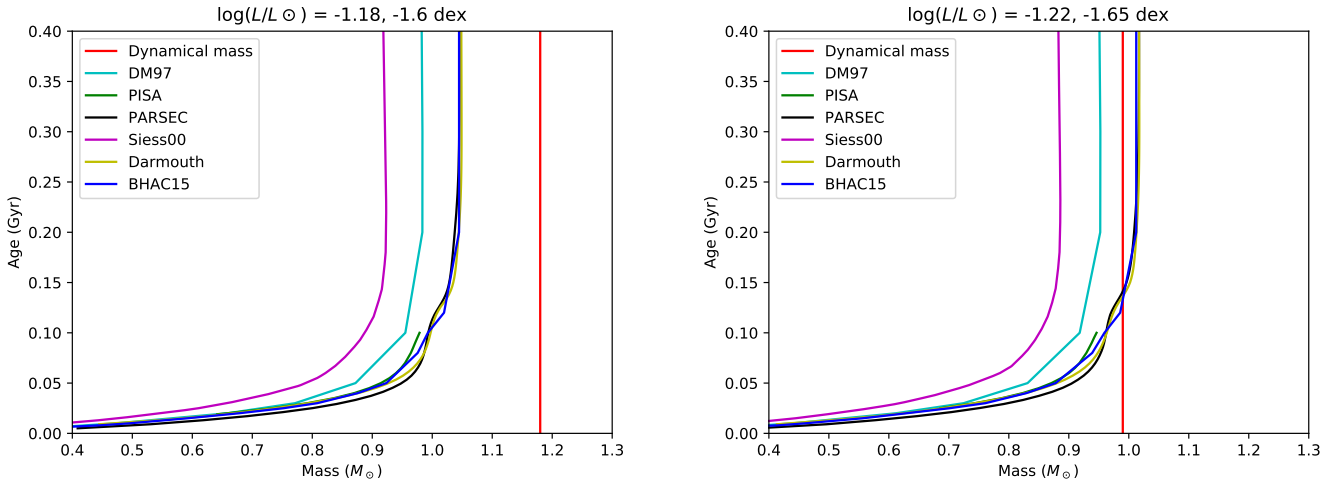

(a) d = 16.14 pc (b) d = 15.24 pc

Fig. C.1. Mass–age relations according to the six different evolutionary models for the GJ 2060 observed luminosities. The dynamical mass is depicted in red. *Panel a*: highest boundary of the distance (16.14 pc), *panel b*: lowest boundary (15.24 pc).

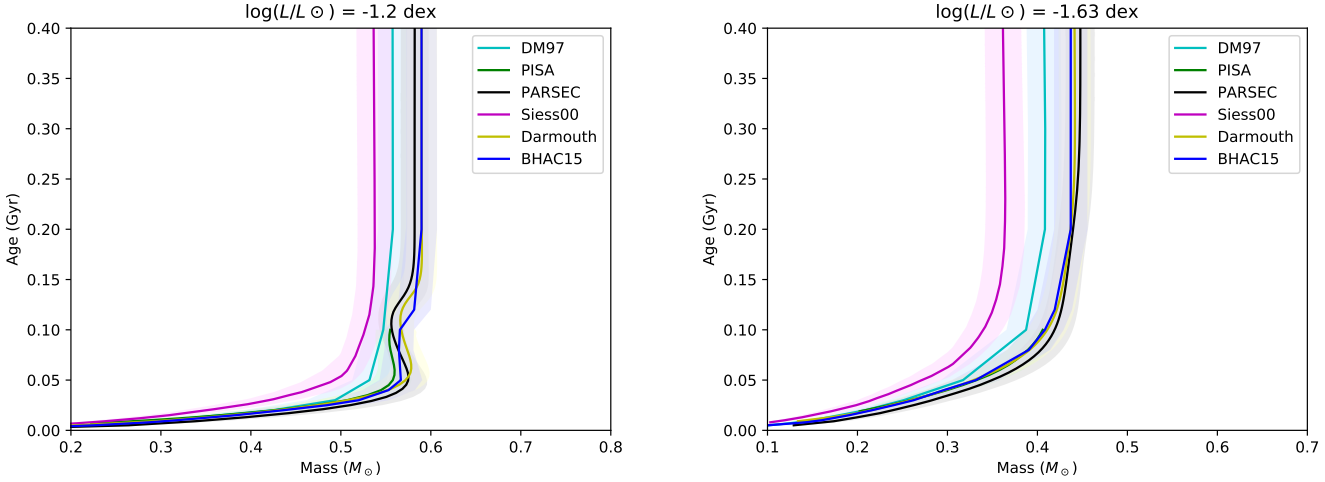

(a) GJ 2060 A (b) GJ 2060 B

Fig. C.2. Mass–age relations according to the six different evolutionary models for the GJ 2060 observed luminosities. *Panel a*: primary, *panel b*: secondary. The error on the distance is taken into account.

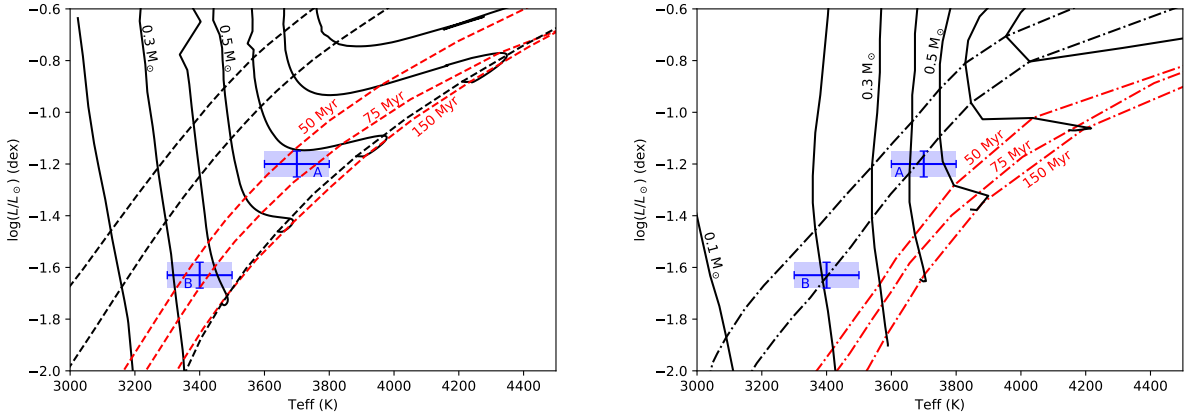

(a) Darmouth (b) DM97

(c) PARSEC (d) PISA

(e) SDF00 (f) BHAC15+spots, $f_{\rm spot}$ = 0.5

Fig. C.3. Isochrones and iso-mass curves predicted by different evolutionary models. Shown are the 10, 20, 50, 75, 150, and 600 Myr isochrones (dash-dotted lines, from *top to bottom panels*; except for the Pisa and DM97 models, that stop respectively at 100 and 500 Myr), while one iso-mass is drawn every 0.1 $M_\odot$ from 0.1 (*left panels*) to 1 $M_\odot$ (*right panels*). The 50, 75, and 150 Myr isochrones correspond to possible ages for AB Dor-MG, and are drawn in red. The blue shaded regions correspond to the observed values and the error bars for each component of system GJ 2060, A and B.

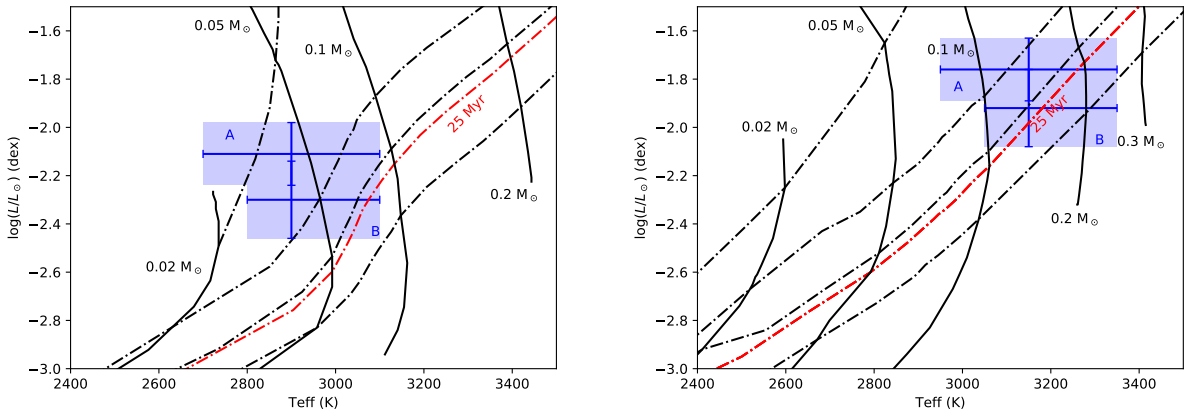

(a) DM97 (b) BHAC15+spots, f_{spot} = 0.5

Fig. C.4. Isochrones and iso-mass curves predicted by different evolutionary models. Shown are the 1, 10, 20, 25 and 50 Myr isochrones (dash-dotted lines, from *top to bottom panels*), and the iso-mass curves (solid lines). The 25 Myr isochrone correspond to the age of the β Pic-MG, and is drawn in red. The blue shaded areas correspond to the observed values and their error bars for each component of system TWA 22, A and B.

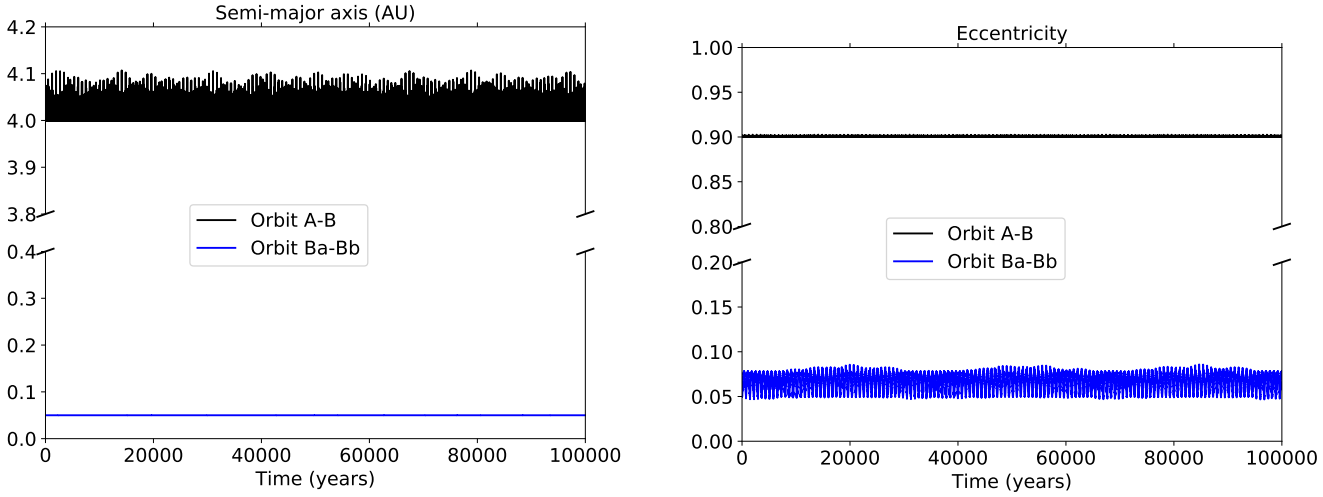

(a) (b)

Fig. D.1. 100 000 yr evolution of the semi-major axis and eccentricity of the two orbits represented in Fig. D.2.

Appendix D: Dynamical analysis

Dynamical simulations were performed with SWIFT_HJS, a symplectic N-body code designed for multiple systems (Beust 2003), to test the stability of a three-body evolution. No stability criterion can be easily derived for three close bodies with similar masses, especially in the case of highly eccentric perturbers such as these. Some configurations were tested around both components assuming null eccentricity for the internal orbit (most stable case) and a coplanar situation. An example of stable configuration around the primary is depicted in Fig. D.2. The corresponding semi-major axis and eccentricity evolution for 100 000 yr, more than 10 000 times the longer period, is depicted in Fig. D.1. The parameters of the simulations are described below. Within the constraints that we imposed (circular coplanar orbit), our dynamical simulations show that the high eccentricity of the A–B relative orbit would force the putative component to be closer than 0.1 au from the primary. The same criterion holds for an orbit around the secondary.

A 100 000-yr dynamical simulation was performed with the configuration of Fig. D.2, with SWIFT_HJS. A time step of 0.001 yr was chosen. The inner orbit has initially a semi-major axis of 0.05 au and eccentricity 0.05, while the outer orbit is set with semi-major axis 4 au and eccentricity 0.9. The masses are respectively 0.55, 0.21, and 0.32 $M_\odot$ for the primary, the putative companion, and the secondary. The orbits are taken as coplanar, with an initial mean anomaly difference of 45°. The evolutions of the semi-major axis and eccentricity show a strong stability of the orbits.

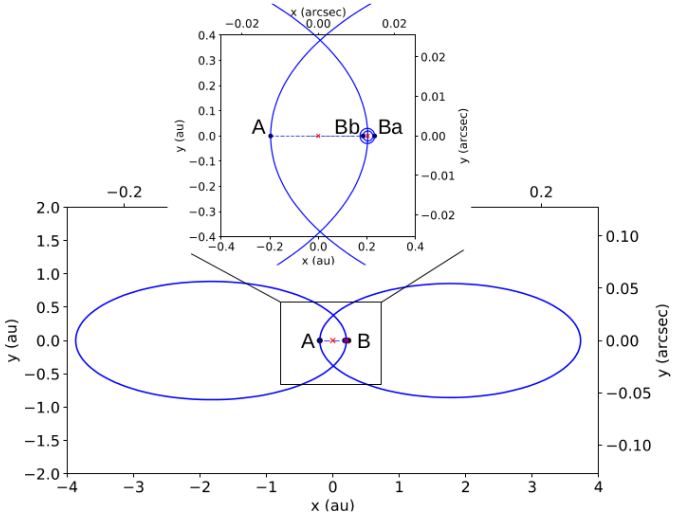

Fig. D.2. Face-on example of a hypothetical stable three-body configuration consistent with the data. Only components A and Ba have been detected to date.

6.3 AB Dor B: toward empirical isochrones for the AB Dor moving group

The stellar system AB Dor is a quadruple system in the AB Dor moving group, consisting in two pairs of binaries, AB Dor A and AB Dor B, separated by $\sim 9''$ (135 au). AB Dor B is a pair of M-type stars whose orbit can be constrained through 5 yr (5 orbital periods) of astrometric monitoring by many different instruments, including absolute position measurements in the radio band (Azulay et al. 2015; Janson et al. 2018). With the previous knowledge brought by the studies of other systems in the AB Dor moving group (GJ 2060, AB Dor A), estimating the dynamical mass of AB Dor B could lead to a better understanding of the local mass-luminosity isochrones.

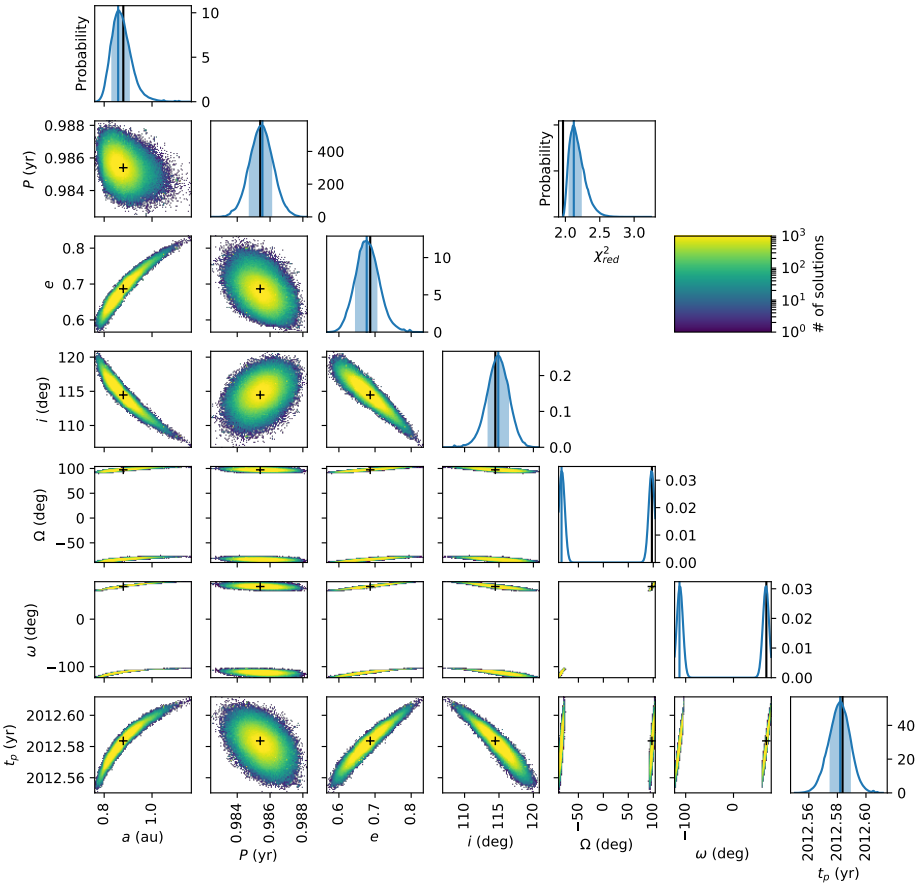

Figure 2.23 – Corner plot presenting the results of the MCMC orbital fitting procedure of AB Dor B A-B relative orbit. The black lines and crosses correspond to the results of the LM procedure (best fit).

In Janson et al. (2018), I performed an MCMC orbital fitting of the relative orbit (see Figs.2.23, 2.24 and 2.25). The data are not all consistent with each other (in particular the archival NaCo data, blue on the figures), and the periastron is poorly sampled, so that the precision on the angular semi-major axis is not optimal (3 mas,

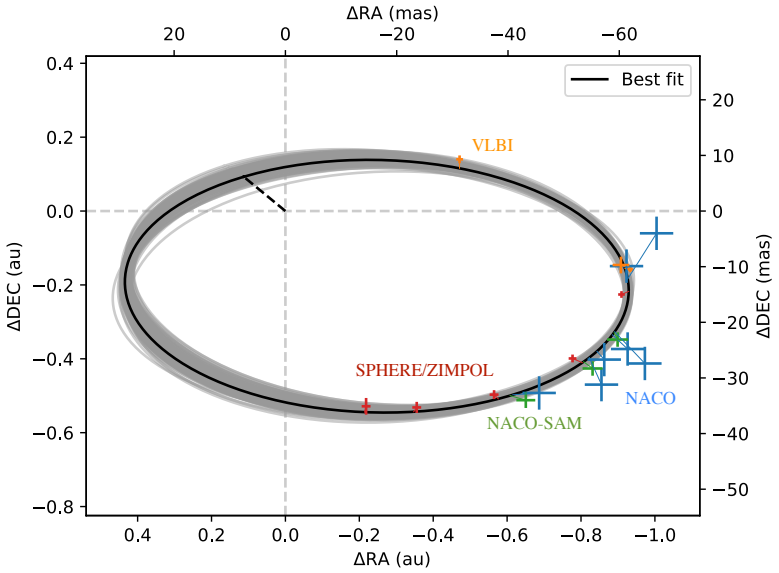

Figure 2.24 – Representation on the sky plane of the results the MCMC orbital fitting procedure of AB Dor B A-B relative orbit.

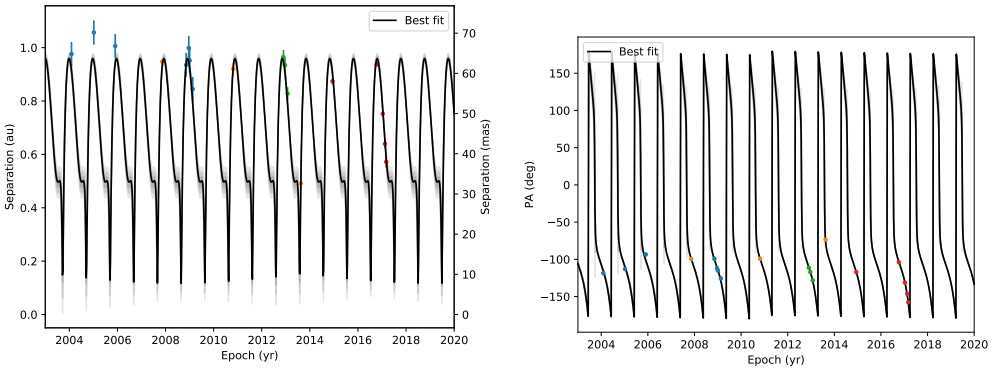

Figure 2.25 – Temporal evolution of the separation and position angle from the results of the MCMC orbital fitting procedure of AB Dor B A-B relative orbit

6 %). This induces a 18 % uncertainty on the total mass. We get however a very good precision on the period (<1 d) and reveal a high eccentricity (0.67).

Like GJ 2060, the stars appear underluminous with respect to their masses, according to the evolutionary models. A better sampling of the orbit and new measurements similar astrometric binaries will confirm or reject the bias trend in the AB Dor moving group.

In a previous study, Azulay et al. (2015) performed a Levenberg-Marquardt orbital fit taking into account the absolute position of the two stars. This allowed them to retrieve the individual masses of each component with a 20 % precision. In the next subsection, I present the integration of absolute astrometric measurement in our MCMC procedure, and show that I could not reproduce the results of Azulay et al. (2015), which exhibit some inconsistencies, so that only the relative orbital fit were included in our study.

A&A 620, A33 (2018)
https://doi.org/10.1051/0004-6361/201833375
© ESO 2018

Astronomy & Astrophysics

Dynamical masses of *M*-dwarf binaries in young moving groups

II. Toward empirical mass-luminosity isochrones⋆

Markus Janson[1], Stephen Durkan[1,2], Mickaël Bonnefoy[3], Laetitia Rodet[3], Rainer Köhler[4,5], Sylvestre Lacour[6], Wolfgang Brandner[7], Thomas Henning[7], and Julien Girard[8]

[1] Department of Astronomy, Stockholm University, Stockholm, Sweden
e-mail: markus.janson@astro.su.se
[2] Astrophysics Research Center, Queens University Belfast, Belfast, UK
[3] Univ. Grenoble Alpes, IPAG, Grenoble, France
[4] Institut für Astro- und Teilchenphysik, Universität Innsbruck, Innsbruck, Austria
[5] Department of Astrophysics, University of Vienna, Vienna, Austria
[6] LESIA, Observatoire de Paris, Meudon, France
[7] Max Planck Institute for Astronomy, Heidelberg, Germany
[8] Space Telescope Science Institute, Baltimore, MA, USA

Received 6 May 2018 / Accepted 19 September 2018

ABSTRACT

Low-mass stars exhibit substantial pre-main sequence evolution during the first ∼100 Myr of their lives. Thus, young M-type stars are prime targets for isochronal dating, especially in young moving groups (YMGs), which contain large amounts of stars in this mass and age range. If the mass and luminosity of a star can both be directly determined, this allows for a particularly robust isochronal analysis. This motivates in-depth studies of low-mass binaries with spatially resolvable orbits, where dynamical masses can be derived. Here we present the results of an observing campaign dedicated to orbital monitoring of AB Dor Ba/Bb, which is a close *M*-dwarf pair within the quadruple AB Dor system. We have acquired eight astrometric epochs with the SPHERE/ZIMPOL and NACO instruments, which we combine with literature data to improve the robustness and precision for the orbital characterization of the pair. We find a system mass $0.66^{+0.12}_{-0.12}\,M_{\odot}$ and bolometric luminosities in $\log L/L_{\odot}$ of -2.02 ± 0.02 and -2.11 ± 0.02 for AB Dor Ba and Bb, respectively. These measurements are combined with other YMG pairs in the literature to start building a framework of empirical isochrones in mass–luminosity space. This can be used to calibrate theoretical isochrones and to provide a model-free basis for assessing relative stellar ages. We note a tentative emerging trend where the youngest moving group members are largely consistent with theoretical expectations, while stars in older associations such as the AB Dor moving group appear to be systematically underluminous relative to isochronal expectations.

Key words. binaries: visual – stars: low-mass – stars: pre-main sequence

1. Introduction

Stellar systems that are both young and nearby are of importance for a range of present-day scientific topics, not least for the purpose of direct imaging of exoplanets (e.g. Marois et al. 2008; Macintosh et al. 2015; Chauvin et al. 2017) and disks (e.g. Schneider et al. 2009; Thalmann et al. 2013; Boccaletti et al. 2015). This has led to an increased interest in young moving groups (YMGs), which are associations of stars that are unbound but clustered in phase space, and thus are expected to have originated from a mutual birth cluster (e.g. Torres et al. 2008). One such group that is particularly close, and thus particularly useful for many purposes, is the AB Dor moving group (ABMG; e.g. Zuckerman et al. 2004). While ABMG is clearly older than 5–20 Myr, which is the approximate age of the youngest YMGs such as the TW Hya or β Pic associations (e.g. Bell et al. 2015), its specific age has remained uncertain, with different studies suggesting age ranges from a lower limit of 30 Myr (Close et al. 2005) all the way to an upper limit of 200 Myr (Bell et al. 2015).

The defining member of the ABMG, AB Dor itself, is a complex and intriguing system. The primary AB Dor A is a K-type star, which has long been known to share a common proper motion with the M-type secondary AB Dor B (Rossiter 1955) at a separation of ∼10″. However, more recently it has been discovered that A and B can each be resolved into tight stellar pairs. AB Dor C is a ∼90 $M_{\rm jup}$ star near the hydrogen burning limit in a 11.75-year orbit around AB Dor A (Guirado et al. 1997; Close et al. 2005; Azulay et al. 2017b). AB Dor B is in fact a nearly equal-mass stellar pair (Janson et al. 2007) designated as AB Dor Ba and Bb. The Ba/Bb pair has been the subject of particular attention in several studies, due to its particular properties. Both stars are M5–M6 type stars, which means that unlike earlier-type stars, they still reside in the pre-main sequence (PMS) phase at the age of the ABMG. Furthermore, orbital monitoring of the system (e.g. Wolter et al. 2013; Azulay et al. 2015; hereafter W14 and A15, respectively) has shown that the orbital period is only ∼1 year, which benefits the determination of precise stellar masses and ages. Azulay et al. (2015) estimate masses of $0.28 \pm 0.05\,M_{\odot}$ and $0.25 \pm 0.05\,M_{\odot}$ for the Ba and Bb components, respectively. This implies a total mass 23% lower than the $0.69\,M_{\odot}$ derived by W14, although

⋆ Based on observations collected at the European Southern Observatory, Chile (Programmes 090.C-0819, 60.A-9386, 098.C-0262, and 099.C-0265).

7 Combining absolute and relative astrometry

Once the two bodies of an orbit are resolved, the retrieval of the relative astrometry is rather straightforward. Occasional calibrations with some objects of the field give the pixel scale and true North, which are used to obtain a consistent set of data (separations and position angles of the relative position vectors). The computation of the absolute astrometry of the two elements is more challenging. The calibration must be precise enough to locate within milliarcseconds the positions of each body on the skyplane, and controlled so that the positions can be compared over successive epochs, separated by several years. The main providers of such measurements are the spatial telescopes Hipparcos (Van Leeuwen 2007) and Gaia (Brown et al. 2018). At the present days, few orbits have absolute astrometric data. However, the field will developed dramatically at the final release of Gaia in the mid-2020s, when the intermediate data of the mission will be available and hundreds of new planets will be indirectly revealed.

The absolute astrometry of only one of the two bodies is enough to characterize the orbit and the individual masses. Fitting an orbit to the positions is complicated by the proper motion of the center of mass relative to the Sun, and by the motion of Earth around the Sun. This 1-yr-period motion, so-called parallactic, creates loops in the apparent motion of each body on the skyplane. The closer the object, the stronger the perturbation, with order of magnitude of around $1/d$ arcseconds, with d the distance in parcsec. This number is called the parallax π. The parallactic motion is thus far from negligible for targets closer than 1,000 pc. The example of the trajectory of HD 106906, where the influence of the planet is negligible over the short baseline, is drawn on Fig. 2.26.

Disentangling the parallactic motion from the wobble induced by a companion is the challenge taken up by Gaia. As an example, the effect of a 1 M_J companion at 5 au on a Solar-type star have a maximum amplitude of 0.05 mas. For long-period orbits, the comparison between Hipparcos and Gaia proper motions due to orbital motions can already improve some relative orbital fit and could theoretically give a mass ratio (Calissendorff & Janson 2018; Grandjean et al. 2019).

The number of parameters increases dramatically when fitting absolute data, from 7 (when T and a are fitted independently) to 13 or even 15 when a linear proper motion does not reproduce the trajectory well. The additional parameters are:

- The parallax π, that corresponds to the radius of the parallactic loops;
- The position of the center of mass at the reference epoch, usually given in the equatorial coordinates (α_0, δ_0), where α is the right ascension and δ is the declination;
- The 2-dimension proper motion p_α and p_δ;
- The mass ratio $\mu = m_B/m_{\rm tot}$;
- (optional) The 2-dimension proper acceleration q_α and q_δ.

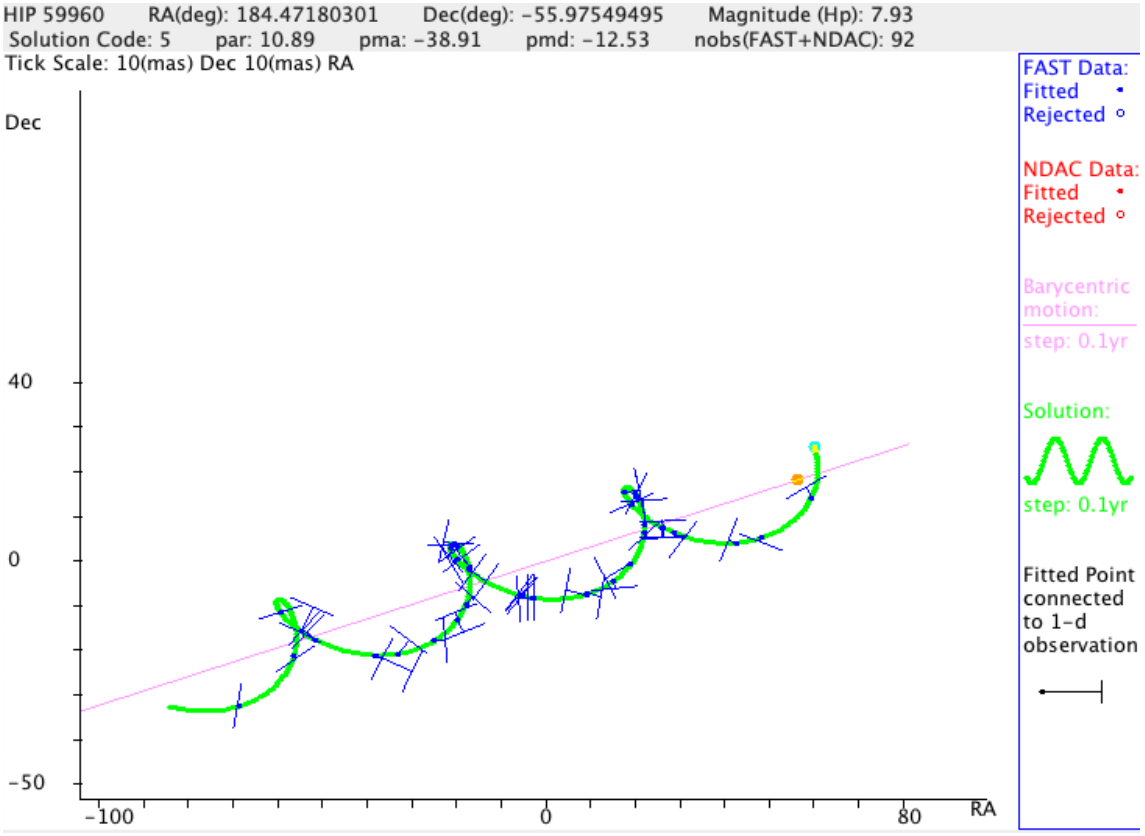

Figure 2.26 – HD 106906 apparent motion on the skyplane (around 3 years), fitted from the intermediate data from Hipparcos. The orbital motion induced by the planet is negligible over 3 years, so that the trajectory only corresponds to a linear proper motion with a parallactic component. The fit gives the parallax of the system and its proper motion with a precision of around 1 mas and 0.5 mas/yr respectively.

The relative astrometry is often given in the *projected* equatorial coordinates, which are $(\alpha^*, \delta) = (\alpha \cos(\delta), \delta)$. As the relative angles are measured from the true North, along the declination line, the previously introduced x corresponds to δ and y to α^*. Then, the evolution of the absolute position of two component A and B writes:

$$\alpha_A(t) = \alpha_G(t) - \mu\ y(t, P, a, e, i, \Omega, \omega, t_p)/\cos(\delta_0) \tag{2.31}$$
$$\delta_A(t) = \delta_G(t) - \mu\ x(t, P, a, e, i, \Omega, \omega, t_p) \tag{2.32}$$
$$\alpha_B(t) = \alpha_G(t) + (1-\mu)\ y(t, P, a, e, i, \Omega, \omega, t_p)/\cos(\delta_0) \tag{2.33}$$
$$\delta_B(t) = \delta_G(t) + (1-\mu)\ x(t, P, a, e, i, \Omega, \omega, t_p) \tag{2.34}$$

where α_G and δ_G are the position of the center of mass, that is

$$\alpha_G(t) = \alpha_0 + p_\alpha(t-t_0)\left(+q_\alpha(t-t_0)^2\right) + \pi P_\alpha(t) \tag{2.35}$$
$$\delta_G(t) = \delta_0 + p_\delta(t-t_0)\left(+q_\delta(t-t_0)^2\right) + \pi P_\delta(t) \tag{2.36}$$

To fit the parallactic motion $P_{\alpha,\delta}(t)$, we have to compute independently the motion of the Earth with respect to the center of mass of the Solar System. I computed a data file from the NASA Horizon website with the daily coordinates $(X_\oplus, Y_\oplus)$ of the Earth with respect to the Solar System's center of mass for the last decades. This evolution is then interpolated so that we can precisely retrieve the coordinates for each observational epoch. From these coordinates, the parallactic factors are (simple change of reference frame):

$$P_\alpha(t) = \frac{X_\oplus \sin(\alpha) - Y_\oplus \cos(\alpha)}{\cos(\delta)} \tag{2.37}$$

$$P_\delta(t) = X_\oplus \cos(\alpha)\sin(\delta) + Y_\oplus \sin(\alpha)\sin(\delta) - Z_\oplus \cos(\delta) \tag{2.38}$$

The parallactic motion, as well as the orbital motion on the right ascension, thus depends on the coordinates α and δ of the target, which we are trying to obtain. However, the studied variations of α and δ are small, typically of order 1", that is $3.10^{-4\circ}$, so that fixing them to α_0 and δ_0 produces negligible error.

As part of the study of the astrometric binary AB Dor B (Sec. 6, Janson et al. 2018), I began to implement a new version of the orbital fitting routine, to use both absolute and relative astrometry. On top of the relative positions of AB Dor Bb with respect to AB Dor Ba, the absolute positions of both stars have been measured at multiple times with the VLTI (Azulay et al. 2015). A previous orbital fitting with a Levenberg-Marquardt algorithm, performed by Azulay et al. (2015), gave a solution and rough uncertainties using all data (except for the new relative astrometry presented in our article). For this system, the proper accelerations have to be considered, because of the influence of the nearby component AB Dor A.

The first step was to use the best fit parameters of Azulay et al. (2015), to test the formula, retrieve their figures and used this as a first guess for the orbital fitting. However, I could not reproduce their results. Fig. 2.27 presents the tentative reproduction of Azulay et al.'s best fit: the trajectories of the two bodies and their center of mass on the skyplane and the orbits (trajectory without proper motion and parallactic motion) from this work and from the work of Azulay's et al.. In my figure, the solution does not fit satisfyingly the observations, in particular the 1993 point, while it fits all the points in the representation of Azulay et al.. This point originally comes from the work of Guirado et al. (2006), which computed 5 absolute positions for the Ba components. However, the Bb components was not resolved in the observations, and Azulay et al. states that most observations are not consistent with their new measurements, probably because of a confusion of the two nearly-equal-mass components. They say however that two points are consistent, in 1992 and 1993. We can reproduce the agreement with the former, but not with the latter. This discrepancy is visible on the trajectories including the proper motions and parallactic motions. Moreover, contrary to what is indicated in their paper, the relative sizes of the two absolute orbits suggest that the Ba component is lighter than the Bb component. There is thus at least one clear discrepancy on Azulay et al.'s paper.

A possible mistake on my side could lie in Eqs (2.31) to (2.38), on the coordinates used for the Solar System barycenter, or in their numerical implementation. As a

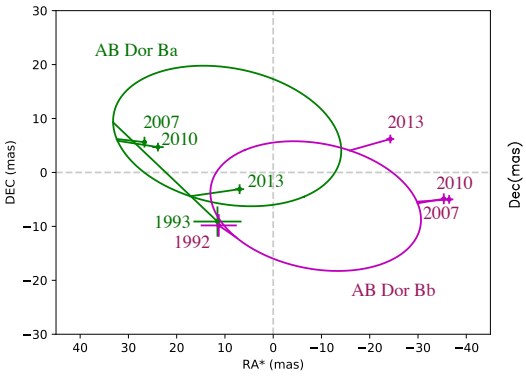

(a) Absolute orbits (this work)

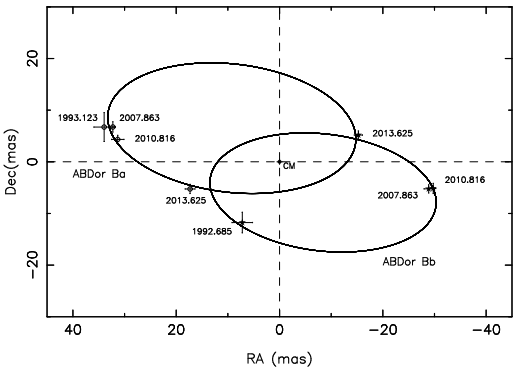

(b) Absolute orbits (Azulay et al. 2015)

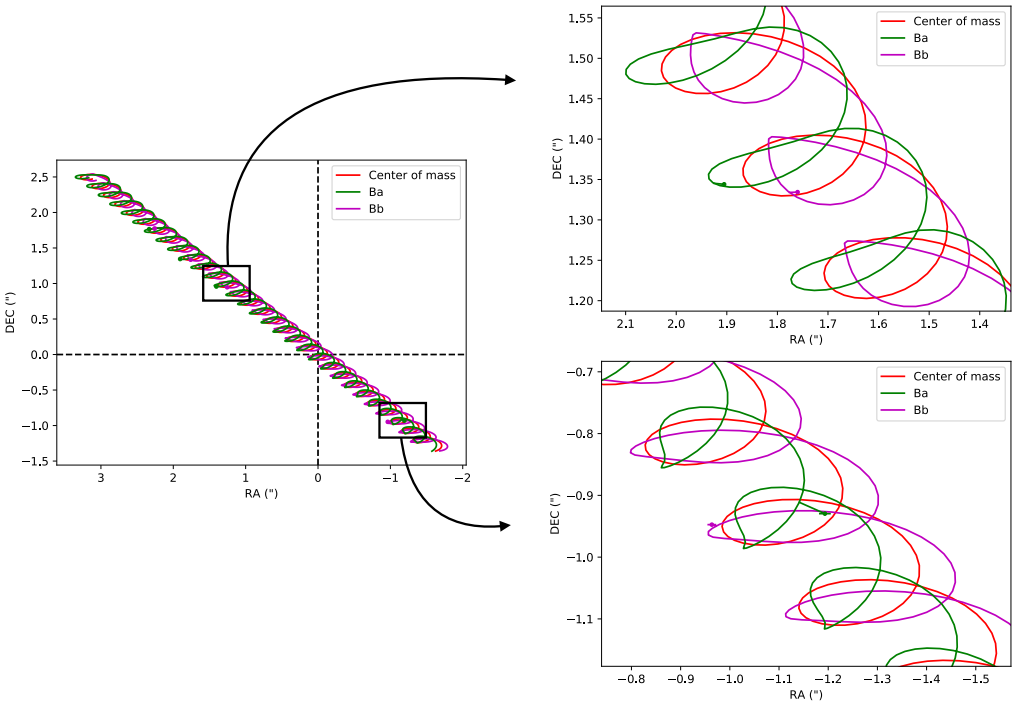

(c) Absolute trajectories

Figure 2.27 – Test of the best fit solution of Azulay et al. (2015) for the AB Dor B system. The plots above represent the data corrected from the proper and parallactic motions.

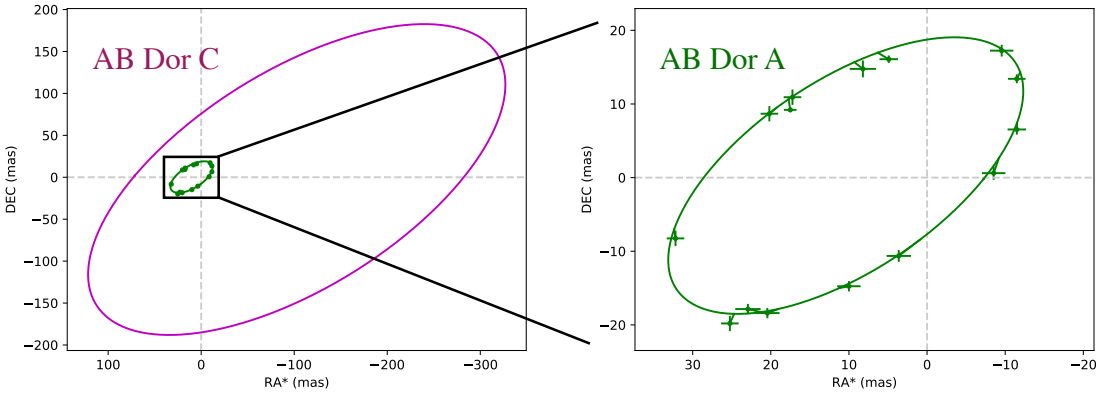

(a) Absolute orbits

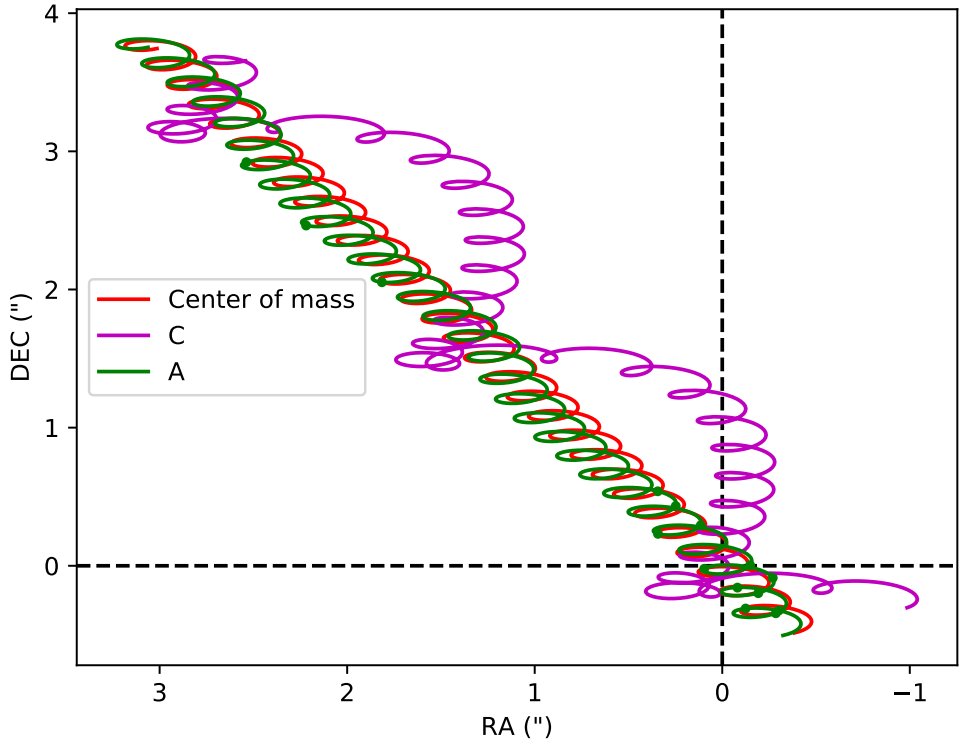

(b) Absolute trajectories

Figure 2.28 – Test of the best fit solution of Azulay et al. (2017) for the AB Dor AC system. The plots above represent the data corrected from the proper and parallactic motions. The solution fits perfectly the data.

deep search did not reveal any error, I tried to reproduce the figures of another study by the same team, Azulay et al. (2017), presenting the AB Dor AC astrometric binary. Multiple absolute measurements were available for the A component. The figures I derived from Azulay et al. (2017)'s best fit and observations are represented in Fig. 2.28. The solution fits perfectly the data, suggesting no mistakes in my implementation.

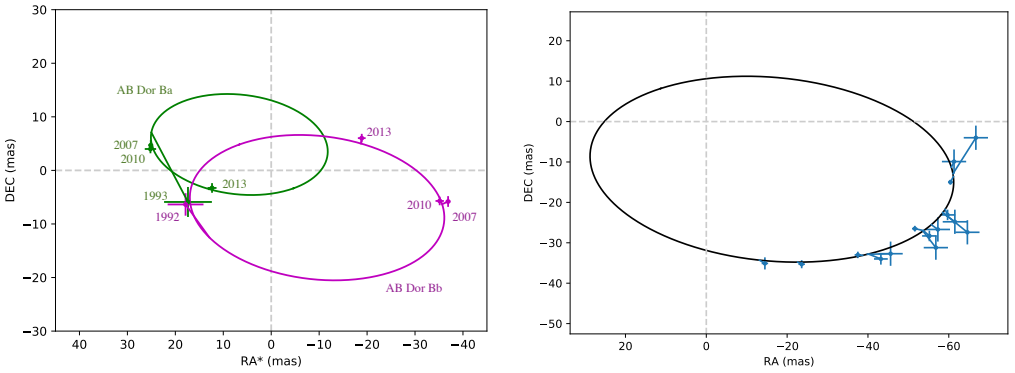

Figure 2.29 – Absolute and relative orbits of system AB Dor B, according to the best fit of the MCMC orbital fitting procedure using both relative and astrometric data. The 1993 epoch is still not well reproduced.

I have implemented the absolute part of the astrometric into the computation of the χ^2 in the Levenberg-Marquardt algorithm and the MCMC algorithm. Uniform priors were adopted by default, but the precision of the constraints is sufficiently high so that the dependence on any possible prior for the new variables would be negligible. Applying the Levenberg-Marquardt algorithm to the ABDor B system, I noticed that the result depends strongly on the initial guess, suggesting numerous local minima and poor reliability. Contrary to Azulay et al. (2015), I found that the observational constraints were not enough to properly constrain all the parameters. Indeed, if 5 epochs of the center of mass should be enough to constrain the 7 parameters π, α_0, δ, p_α, $p_/delta$, q_α and q_δ, the poor precision/agreement of the first two epochs hinder the fit. The absolute MCMC does not converge when the parallax is a free parameter, and the preliminary LM cannot produce any errorbars. I could only reach a convergence by fixing the value to the best fit of Azulay et al..

The results of the MCMC appeared nevertheless robust, with Gaussian probability distributions and weak or linear correlations (see Fig. 2.30). No possible solutions were found to take into account the 1993 point within 1-sigma. The best fit in the Markov chains is represented on Fig. 2.29. Finally, the solutions for Azulay et al. (2015)'s LM approach, the complete MCMC approach or the MCMC approach fitting only the relative data (Janson et al. 2018, see Sec. 6,) are given on Table 2.1.

The three approaches are consistent at 1-sigma. The MCMC approaches often give more precise results on the relative orbital elements because additional relative measurements were used compared to the Azulay et al. (2015)'s study. The period and parallax are relatively well constrained ($< 1\%$), so that the angular semi-major axis and its uncertainty are the key parameters to compute the mass. However,

Parameter	LM (Azulay et al. 2015)	MCMC (this work)	MCMC (Janson et al. 2018)
π (mas)	66.4 ± 0.5		
α_0 (h m s)	5 28 44.4840 ± 0.0003	5 28 44.4845 ± 0.0006	
δ_0 (° ' ")	-65 26 46.057 ± 0.002	-65 26 46.057 ± 0.002	
p_α (s/yr)	0.0105 ± 0.0002	0.0106 ± 0.00006	
p_δ ("/yr)	0.1287 ± 0.0005	0.1290 ± 0.0002	
q_α (s/yr^2)	$(8 \pm 1).10^{-6}$	$-(6 \pm 5).10^{-6}$	
q_δ ("/yr^2)	$-(10 \pm 5).10^{-4}$	$-(12 \pm 2).10^{-4}$	
μ	0.52 ± 0.05	0.40 ± 0.06	
P (yr)	0.986 ± 0.008	0.9869 ± 0.0008	0.9856 ± 0.0009
a (mas)	52 ± 2	53 ± 2	57 ± 4
e	0.6 ± 0.1	0.59 ± 0.04	0.67 ± 0.04
i (°)	121 ± 5	118 ± 2	115 ± 2
Ω (°)	270 ± 15	93 ± 3	97 ± 3
ω (°)	54 ± 20	61 ± 4	68 ± 4
t_p (yr)	2003.68 ± 0.05	2003.68 ± 0.02	2009.63 ± 0.01
$m_{\rm tot}$ ($M_\odot$)	0.49 ± 0.06	0.51 ± 0.06	0.66 ± 0.12

Table 2.1 – Astrometric parameters of the system AB Dor B according to different approaches. The derivation of the total mass for the MCMC analyses uses the parallax of Azulay et al. (2015) and its uncertainty.

parts of the orbit are not well monitored, especially with the relative astrometry, so that the relative MCMC gives a poor precision on the total mass (20%).

All in all, I developed the ingredients for combining absolute and relative astrometry in orbital fitting procedures. The addition of 5 to 7 parameters makes the procedure heavier, and strong constraints are needed to ensure convergence. For the AB Dor B cases, additional absolute astrometric data is essential to constrain all the parameters including the parallax. The relative fit can be improved by measurements of the relative positions near periastron (bodies ~ 10 mas apart). The small relative separation may be resolved with SPHERE/ZIMPOL. Moreover, statistical methods outside MCMC, such as nested sampling, could be used to characterize the loosely constrained systems.

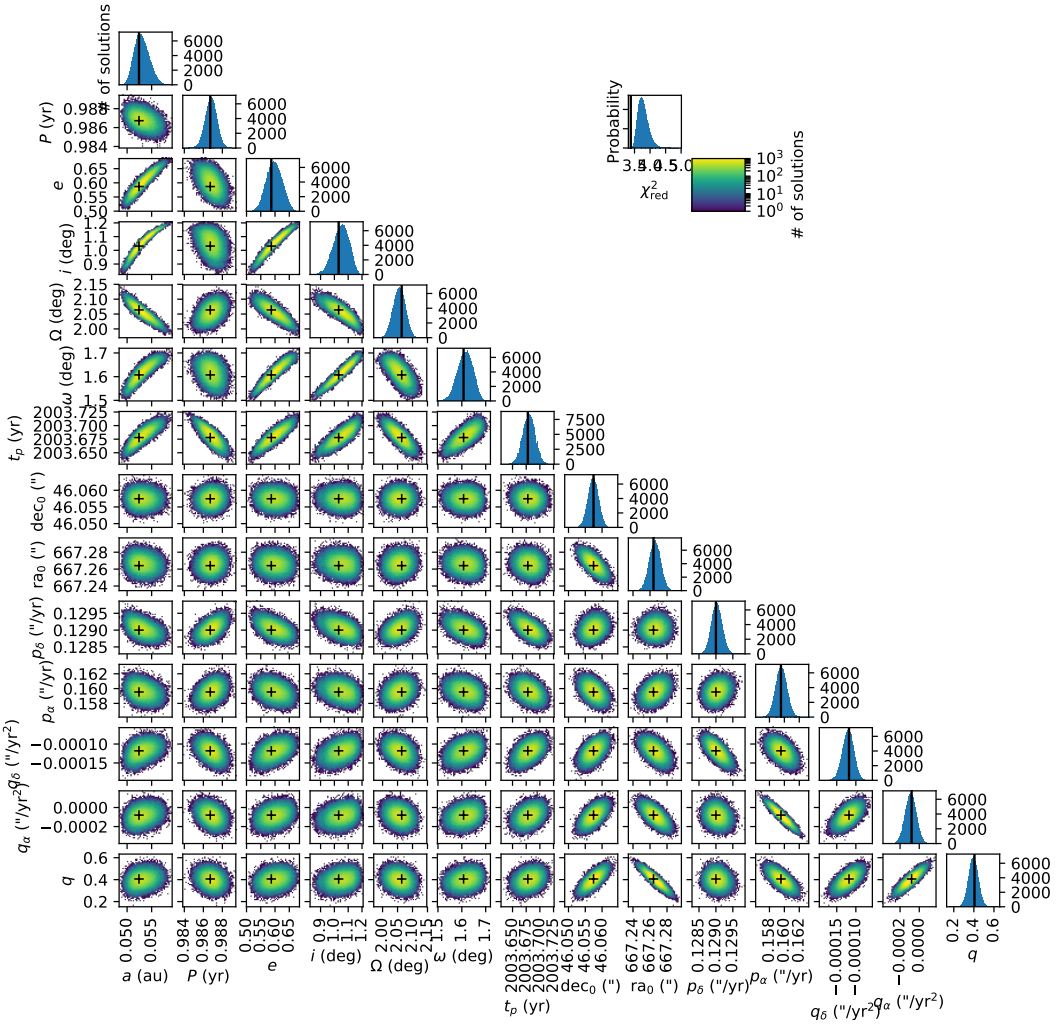

Figure 2.30 – Corner plot presenting the results of the MCMC orbital fitting procedure of AB Dor B using both relative and astrometric data. The black lines and crosses correspond to the best fit.

Conclusion and Perspectives

This manuscript presents the three years work of my Ph.D dedicated to the dynamical study of extrasolar systems imaged by SPHERE. It consisted of characterizing the multiple components of the observed systems (planets, stellar companions, disks), and in the design of dynamical scenarios to investigate their formation and evolution. The thesis is composed of two main parts: N-body simulations and orbital fitting. It takes place in a context of spectacular development of the direct imaging performance, that provides unprecedented constraints on the architecture of extrasolar systems.

In the first chapter, I tackle the dynamical analyses from the perspective of N-body simulations. After a review of the principal approaches, classical or symplectic, and the associated codes, I presented our in-house code `Swift HJS`. It is a powerful integrator that goes beyond conventional Solar-System-type architecture. `Swift HJS` is however restricted to stable hierarchies in lightly perturbed orbits and does not resist to the occasionally high perturbations referred to as close encounters. To overcome these limitations, I developed a new code, `ODEA`, that handles both hierarchy changes and close encounters by generalizing the approaches of algorithms designed for Solar-System-type architectures. `ODEA` is currently at the end of its developing phase and will be available online with dedicated post-processing tools in Python. A first version including hierarchical changes is already in working order.

I had the occasion to extensively use the codes for the dynamical study of the intriguing system HD 106906, a tight binary star surrounded by an asymmetric debris disk and which comprises a wide planetary-mass companion observed with SPHERE. In a first paper, I designed a scenario that accounts for the large separation of the planet without appealing to star-like formation mechanisms. This scenario is based on the complex entanglement of different classical ingredients, such as migration, mean-motion resonances, and stellar fly-by. In a second paper, I studied the two stellar fly-bys that were evidenced in the Gaia data by an American team, following the conclusions of my first paper.

HD 106906 has still a lot to reveal in the near future. Its slight orbital motion might be detectable by direct imaging (a few mas per year) or radial velocity measurements (a few km/s), depending on its current trajectory. The stellar fly-bys can be further characterized by reaching a better precision on their radial velocities and parallaxes (which might be provided by the next data release of Gaia). Finally, the structures within the debris disk can be better constrained by higher contrast observations, for example with the long-awaited JWST. If our theory is confirmed, HD 106906 would be the only proven example of an extrasolar system in which a planet has been ejected, as well as the only planetary system that has undergone

a stellar fly-by. If, on the other hand, the fly-by turns out to be non-significant, it will support the idea that HD 106906 b formed in-situ, and therefore that planets on wide orbits can form like stars, from the collapse of their own molecular clouds.

In the second chapter, I presented the orbital fitting procedure that I used for the study of systems observed with SPHERE. I described my team's implementation of an MCMC framework dedicated to the problem, compared it to the alternative approaches in the literature, and presented the post-processing tools I developed. This code was used in the study of 8 different systems comprising planets, brown dwarfs and debris disks. My contribution was not only to retrieve estimates for the orbital elements, but also to determine the coplanarity with a disk (HR 2562, HD 100453) or the stellar rotation plane (GJ 504), compare the outcome of different orbital fitting approaches (HR 2562, 51 Eri, HD 206893, GJ 504, AB Dor B), investigate the dynamical interactions with the environment (HR 2562, GJ 504), and retrieve the total dynamical mass of tight binaries (TWA 22, GJ 2060, AB Dor B). I led a dedicated paper that presented two astrometric binaries, TWA 22 and GJ 2060, as ideal calibrators for the evolutionary models. The cases of GJ 2060 and AB Dor B illustrate the uncertainties of the evolutionary models for pre-main sequence low-mass stars.

Most of these studies will be naturally pursued as their monitoring baseline will increase, refining the constraints on the orbital elements. This is particularly true for the system GJ 504, for which I submitted a observing time proposal, where better estimates of the orbital elements will confirm the obliquity of the companion, the latter being critical to understand the dynamical history of the system (engulfment scenario of another close-in companion). Moreover, as part of the SPHERE consortium and in collaboration with the AstraLux M-dwarf multiplicity survey, I will contribute to the study of astrometric binaries by conducting the orbital fitting analyses.

In parallel, I began to work on tools to take into account both relative and absolute astrometry. The subsequently high number of parameters makes the procedure computationally heavy so that alternatives to the MCMC approach could be possibly considered, such as nested sampling or neural networks. Alternatively, other types of MCMC could be considered (ensemble, differential evolution).

In this context of increasing planet detection, the need for efficient and versatile dynamical tools able to model the diversity of system architectures is critical. In the coming years, N-body algorithms are bound to be an active branch of the exoplanet field. After the final development of `ODEA`, new features could be added for a more complete simulation of the systems, such as tidal interactions, migration, or modeling of a simulated debris disk emission in scattered light. In parallel, analytic considerations are effective to predict periodic pattern and stability, in particular within resonant configuration (mean-motion, secular, Kozai). They often allow avoiding hours of numerical simulations, while obtaining informative and robust results. Many mechanisms remain to be investigated within the N-body problem, notably by including the new more complex ingredients essential to the evolution of extrasolar system: tidal forces, interactions with the gas reservoir, entanglement between migration and resonances...

On top of the different projects into which I plan to stay involved, I would like

to continue to characterize and study benchmark systems, following the evolution of our understanding of planet evolution and formation. SPHERE's adaptive optics will be soon upgraded to achieve a better contrast and sensitivity, and a new characterization mode will be provided by the coupling with high spectral resolution spectrographs. This should allow the detection of planets closer to their stars for which complementary constraints could be set by GAIA measurements (a decade of monitoring). The coupling of the absolute and relative astrometry should become an intense field of research especially in the context of a possible extension of the GAIA mission beyond the nominal mission. On the E-ELT, the direct imaging instruments HARMONI ($\sim$ 2025), MICADO ($\sim$ 2026) and METIS ($\sim$ 2026) will be the perfect tools to resolve and characterize companions down to $\sim$ 20 mas from the star (1 au at 50 pc). Both the ELT and the JWST (2021) may detect colder planets in more mature and dynamically relaxed systems, and they will enable us to resolve new structures in debris disks. Finally, the ending K2 mission, the recent launch of telescope TESS whose main scientific results should be released throughout 2019 and 2020, and the future launch of PLATO (2026) will refine the statistics of the population of short periods planets. All these new missions will require dedicated dynamical analyses to confirm the stability of the detected systems, get insights on undetected planets, and for a detailed characterization of the most interesting systems. The distribution of key characteristics (eccentricity, mean-motion resonance, relative inclinations) will encourage the design of complex dynamical scenarios. The coming periods will thus bring plenty of new insights on the architecture of extrasolar systems, and, consequently, will shed a new light on our own Solar System.

Bibliography

Asensio-Torres, R., Janson, M., Bonavita, M., et al. 2018, arXiv preprint arXiv:1807.08687

Azulay, R., Guirado, J., Marcaide, J., et al. 2015, Astronomy & Astrophysics, 578, A16

Azulay, R., Guirado, J., Marcaide, J., et al. 2017, Astronomy & Astrophysics, 607, A10

Bailey, V., Meshkat, T., Reiter, M., et al. 2014, Astrophysical Journal, Letters, 780, L4

Baraffe, I., Chabrier, G., Allard, F., & Hauschildt, P. 2002, Astronomy & Astrophysics, 382, 563

Baraffe, I., Chabrier, G., & Barman, T. 2010, Reports on Progress in Physics, 73, 016901

Baraffe, I., Chabrier, G., Barman, T. S., Allard, F., & Hauschildt, P. H. 2003, Astronomy & Astrophysics, 402, 701

Baraffe, I., Homeier, D., Allard, F., & Chabrier, G. 2015, Astronomy & Astrophysics, 577, A42

Baron, F., Artigau, É., Rameau, J., et al. 2018, The Astronomical Journal, 156, 137

Baruteau, C., Bai, X., Mordasini, C., & Mollière, P. 2016, Space Science Reviews, 205, 77

Baruteau, C., Crida, A., Paardekooper, S.-J., et al. 2014, Protostars and Planets VI, 667

Beust, H. 2003, Astronomy & Astrophysics, 400, 1129

Beust, H., Bonnefoy, M., Maire, A.-L., et al. 2016, Astronomy & Astrophysics, 587, A89

Beust, H. & Morbidelli, A. 1996, Icarus, 120, 358

Beuzit, J.-L., Feldt, M., Dohlen, K., et al. 2008, in Society of Photo-Optical Instrumentation Engineers (SPIE) Conference Series, Vol. 7014, Ground-based and Airborne Instrumentation for Astronomy II, 701418

Blunt, S., Nielsen, E. L., De Rosa, R. J., et al. 2017, The Astronomical Journal, 153, 229

Bonavita, M., Desidera, S., Thalmann, C., et al. 2016, Astronomy & Astrophysics, 593, A38

Bonfils, X., Astudillo-Defru, N., Díaz, R., et al. 2018, Astronomy & Astrophysics, 613, A25

Bonnefoy, M., Chauvin, G., Dumas, C., et al. 2009, Astronomy & Astrophysics, 506, 799

Bonnefoy, M., Milli, J., Ménard, F., et al. 2017, Astronomy & Astrophysics, 597, L7

Bonnefoy, M., Perraut, K., Lagrange, A.-M., et al. 2018, Astronomy and Astrophysics, 618, 63

Boss, A. P. 1997, Science, 276, 1836

Bowler, B. P., Kraus, A. L., Bryan, M. L., et al. 2017, The Astronomical Journal, 154, 165

Brogan, C., Pérez, L., Hunter, T., et al. 2015, The Astrophysical Journal Letters, 808, L3

Brouwer, D. 1937, The Astronomical Journal, 46, 149

Brown, A., Vallenari, A., Prusti, T., et al. 2018, arXiv preprint arXiv:1804.09365

Bulirsch, R. & Stoer, J. 1966, Numerische Mathematik, 8, 1

Cai, M. X., Kouwenhoven, M. B. N., Portegies Zwart, S. F., & Spurzem, R. 2017, Monthly Notices of the Royal Astronomical Society, 470, 4337

Calissendorff, P. & Janson, M. 2018, Astronomy & Astrophysics, 615, A149

Chabrier, G., Baraffe, I., Allard, F., & Hauschildt, P. 2000, Astrophysical Journal, 542, 464

Chabrier, G., Johansen, A., Janson, M., & Rafikov, R. 2014, in Protostars and Planets VI, ed. H. Beuther, R. S. Klessen, C. P. Dullemond, & T. Henning, 619

Chambers, J. E. 1999, Monthly Notices of the Royal Astronomical Society, 304, 793

Chambers, J. E., Quintana, E. V., et al. 2002, AJ, 123, 2884

Chauvin, G. 2016, PhD thesis

Chauvin, G., Desidera, S., Lagrange, A. M., et al. 2017, in SF2A-2017: Proceedings of the Annual meeting of the French Society of Astronomy and Astrophysics, Di

Chauvin, G., Desidera, S., Lagrange, A.-M., et al. 2017, Astronomy & Astrophysics, 605, L9

Chauvin, G., Lagrange, A.-M., Beust, H., et al. 2012, Astronomy & Astrophysics, 542, A41

Cheetham, A., Bonnefoy, M., Desidera, S., et al. 2018, Astronomy & Astrophysics, 615, A160

Chen, C. H., Jura, M., Gordon, K. D., & Blaylock, M. 2005, Astrophysical Journal, 623, 493

Chen, C. H., Mamajek, E. E., Bitner, M. A., et al. 2011, Astrophysical Journal, 738, 122

Crida, A. & Morbidelli, A. 2007, Monthly Notices of the Royal Astronomical Society, 377, 1324

Cumming, A., Helled, R., & Venturini, J. 2018, Monthly Notices of the Royal Astronomical Society, 477, 4817

Daemgen, S., Todorov, K., Quanz, S. P., et al. 2017, Astronomy & Astrophysics, 608, A71

Danby, J. & Burkardt, T. 1983, Celestial Mechanics, 31, 95

De Rosa, R. J. & Kalas, P. 2019, The Astronomical Journal, 157, 125

De Rosa, R. J., Nielsen, E. L., Blunt, S. C., et al. 2015, The Astrophysical Journal Letters, 814, L3

De Zeeuw, P., Hoogerwerf, R. v., de Bruijne, J. H., Brown, A., & Blaauw, A. 1999, Astrophysical Journal, 117, 354

Delfosse, X., Beuzit, J. L., Marchal, L., et al. 2004, in Astronomical Society of the Pacific Conference Series, Vol. 318, Spectroscopically and Spatially Resolving the Components of the Close Binary Stars, ed. R. W. Hilditch, H. Hensberge, & K. Pavlovski, 166–174

Delorme, P., Schmidt, T., Bonnefoy, M., et al. 2017, Astronomy & Astrophysics, 608, A79

Dieterich, S. B., Henry, T. J., Golimowski, D. A., Krist, J. E., & Tanner, A. M. 2012, Astronomical Journal, 144, 64

Doyle, L. R., Carter, J. A., Fabrycky, D. C., et al. 2011, Science, 333, 1602

Duchêne, G. & Kraus, A. 2013, Annual Review of Astronomy and Astrophysics, 51, 269

Duncan, M. J., Levison, H. F., & Lee, M. H. 1998, The Astronomical Journal, 116, 2067

Duriez, L. 2002, Laboratoire d'astronomie de l'université de Lilles, 1

Everhart, E. 1985, in International Astronomical Union Colloquium, Vol. 83, Cambridge University Press, 185–202

Feiden, G. A., Jones, J., & Chaboyer, B. 2015, in Cambridge Workshop on Cool Stars, Stellar Systems, and the Sun, Vol. 18, 18th Cambridge Workshop on Cool Stars, Stellar Systems, and the Sun, ed. G. T. van Belle & H. C. Harris, 171–176

Fernández, D., Figueras, F., & Torra, J. 2008, Astronomy & Astrophysics, 480, 735

Fischer, D. A. & Valenti, J. 2005, Astrophysical Journal, 622, 1102

Ford, E. B. 2005, The Astronomical Journal, 129, 1706

Ford, E. B. 2006, The Astrophysical Journal, 642, 505

Foreman-Mackey, D., Hogg, D. W., Lang, D., & Goodman, J. 2013, Publications of the Astronomical Society of the Pacific, 125, 306

Fulton, B. J., Petigura, E. A., Howard, A. W., et al. 2017, Astronomical journal, 154, 109

Gagné, J., Allers, K. N., Theissen, C. A., et al. 2018, The Astrophysical Journal Letters, 854, L27

Gagné, J. & Faherty, J. K. 2018, The Astrophysical Journal, 862, 138

Gagné, J., Lafrenière, D., Doyon, R., Malo, L., & Artigau, É. 2014, The Astrophysical Journal, 798, 73

Galicher, R., Marois, C., Macintosh, B., et al. 2016, Astronomy & Astrophysics, 594, A63

Garufi, A., Benisty, M., Pinilla, P., et al. 2018, arXiv preprint arXiv:1810.04564

Gelman, A., Carlin, J. B., Stern, H. S., et al. 2003, Bayesian data analysis (Chapman and Hall/CRC)

Gelman, A., Rubin, D. B., et al. 1992, Statistical science, 7, 457

Gilks, W. R., Richardson, S., & Spiegelhalter, D. J. 1996, Markov chain Monte Carlo in practice, 1, 19

Gillon, M., Jehin, E., Lederer, S. M., et al. 2016, Nature, 533, 221

Ginski, C., Neuhäuser, R., Mugrauer, M., Schmidt, T., & Adam, C. 2013, Monthly Notices of the Royal Astronomical Society, 434, 671

Give'on, A., Kern, B., Shaklan, S., Moody, D. C., & Pueyo, L. 2007, in Astronomical Adaptive Optics Systems and Applications III, Vol. 6691, International Society for Optics and Photonics, 66910A

Grandjean, A., Lagrange, A.-M., Beust, H., Rodet, L., et al. 2019, submitted to A& A

Guirado, J. C., Martí-Vidal, I., Marcaide, J., et al. 2006, Astronomy & Astrophysics, 446, 733

Haffert, S. Y., Bohn, A. J., de Boer, J., et al. 2019, arXiv e-prints, arXiv:1906.01486

Haisch, Karl E., J., Lada, E. A., & Lada, C. J. 2001, Astrophysical Journal, 553, L153

Hamers, A. S., Antonini, F., Lithwick, Y., Perets, H. B., & Portegies Zwart, S. F. 2017, Monthly Notices of the Royal Astronomical Society, 464, 688

Heggie, D. C. & Rasio, F. A. 1996, Monthly Notices of the Royal Astronomical Society, 282, 1064

Hernandez, D. M. 2019, submitted to MNRAS

Hillenbrand, L. A. & White, R. J. 2004, Astrophysical Journal, 604, 741

Holman, M. J. & Wiegert, P. A. 1999, Astronomical Journal, 117, 621

Hughes, A. M., Duchêne, G., & Matthews, B. C. 2018, Annual Review of Astronomy and Astrophysics, 56, 541

Janson, M., Brandt, T. D., Kuzuhara, M., et al. 2013, The Astrophysical Journal Letters, 778, L4

Janson, M., Durkan, S., Bonnefoy, M., et al. 2018, Astronomy and Astrophysics, 620, A33

Jílková, L. & Zwart, S. P. 2015, Monthly Notices of the Royal Astronomical Society, 451, 804

Johnson, J. A., Aller, K. M., Howard, A. W., & Crepp, J. R. 2010, Publications of the Astronomical Society of the Pacific, 122, 905

Kalas, P. G., Rajan, A., Wang, J. J., et al. 2015, Astrophysical Journal, 814, 32

Kennedy, G. M. & Wyatt, M. C. 2010, Monthly Notices of the Royal Astronomical Society, 405, 1253

Kenyon, S. J. & Bromley, B. C. 2004, The Astronomical Journal, 127, 513

Keppler, M., Benisty, M., Müller, A., et al. 2018, Astronomy & Astrophysics, 617, A44

Kokubo, E., Yoshinaga, K., & Makino, J. 1998, Monthly Notices of the Royal Astronomical Society, 297, 1067

Konopacky, Q. M., Rameau, J., Duchêne, G., et al. 2016, The Astrophysical Journal Letters, 829, L4

Kouwenhoven, M. B. N. 2006, PhD thesis

Kozai, Y. 1962, Astronomical Journal, 67, 591

Kral, Q., Matrà, L., Wyatt, M. C., & Kennedy, G. M. 2017, Monthly Notices of the Royal Astronomical Society, 469, 521

Kumar, S. S. 1962, Astronomical Journal, 67, 579

Kuzuhara, M., Tamura, M., Kudo, T., et al. 2013, The Astrophysical Journal, 774, 11

Lagrange, A.-M., Langlois, M., Gratton, R., et al. 2016, Astronomy & Astrophysics, 586, L8

Lagrange, A.-M., Mathias, P., Absil, O., et al. 2019, Astronomy & Astrophysics, in press

Lagrange, A.-M., Meunier, N., Chauvin, G., et al. 2013, Astronomy & Astrophysics, 559, A83

Lai, D. 2012, Monthly Notices of the Royal Astronomical Society, 423, 486

Lazzoni, C., Desidera, S., Marzari, F., et al. 2018, Astronomy & Astrophysics, 611, A43

Levison, H. F. & Duncan, M. J. 1994, icarus, 108, 18

Li, D., Mustill, A. J., & Davies, M. B. 2019, arXiv preprint arXiv:1902.09804

Lin, D. & Papaloizou, J. 1986, Astrophysical Journal, 309, 846

Macintosh, B., Graham, J., Barman, T., et al. 2015, Science, 350, 64

Maire, A.-L., Langlois, M., Dohlen, K., et al. 2016, in Ground-based and Airborne Instrumentation for Astronomy VI, Vol. 9908, International Society for Optics and Photonics, 990834

Maire, A.-L., Rodet, L., Cantalloube, F., et al. 2019, Accepted in A& A

Maire, A.-L., Rodet, L., Lazzoni, C., et al. 2018, Astronomy & Astrophysics, 615, A177

Maire, A.-L., Skemer, A., Hinz, P. M., et al. 2015, Astronomy & Astrophysics, 576, A133

Malmberg, D., Davies, M. B., & Heggie, D. C. 2011, Monthly Notices of the Royal Astronomical Society, 411, 859

Marois, C., Lafrenière, D., Doyon, R., Macintosh, B., & Nadeau, D. 2006, Astrophysical Journal, 641, 556

Marshall, J. P., Moro-Martín, A., Eiroa, C., et al. 2014, Astronomy & Astrophysics, 565, A15

Martin, D. V. 2018, Handbook of Exoplanets, 1

Mathieu, R. D., Baraffe, I., Simon, M., Stassun, K. G., & White, R. 2007, Protostars and Planets V, 411

Mayor, M., Marmier, M., Lovis, C., et al. 2011, arXiv:1109.2497

Meshkat, T., Mawet, D., Bryan, M. L., et al. 2017, Astronomical Journal, 154, 245

Milli, J., Hibon, P., Christiaens, V., et al. 2017, Astronomy & Astrophysics, 597, L2

Montet, B. T., Bowler, B. P., Shkolnik, E. L., et al. 2015, The Astrophysical Journal Letters, 813, L11

Moór, A., Kóspál, Á., Ábrahám, P., et al. 2014, Monthly Notices of the Royal Astronomical Society, 447, 577

Morbidelli, A. 2002, Modern celestial mechanics : aspects of solar system dynamics

Morbidelli, A. 2013, Planets, Stars and Stellar Systems: Volume 3: Solar and Stellar Planetary Systems, 63

Morbidelli, A. 2018, Dynamical Evolution of Planetary Systems, 145

Morbidelli, A. & Moons, M. 1993, Icarus, 102, 316

Morbidelli, A. & Raymond, S. N. 2016, Journal of Geophysical Research (Planets), 121, 1962

Morbidelli, A., Tsiganis, K., Crida, A., Levison, H. F., & Gomes, R. 2007, Astronomical Journal, 134, 1790

Mordasini, C. 2013, Astronomy & Astrophysics, 558, A113

Mordasini, C., Alibert, Y., Benz, W., & Naef, D. 2009, Astronomy & Astrophysics, 501, 1161

Motte, F., Nony, T., Louvet, F., et al. 2018, Nature Astronomy, 2, 478

Mulders, G. D. 2018, Handbook of Exoplanets, 1

Mustill, A. J. & Wyatt, M. C. 2012, Monthly Notices of the Royal Astronomical Society, 419, 3074

Nayakshin, S. 2017, Publications of the Astronomical Society of Australia, 34

Nesvold, E. R., Naoz, S., & Fitzgerald, M. P. 2017, Astrophysical Journall, 837, L6

Nesvorný, D. 2018, Annual Review of Astronomy and Astrophysics, 56, 137

Nielsen, E. L., Close, L. M., Biller, B. A., Masciadri, E., & Lenzen, R. 2008, The Astrophysical Journal, 674, 466

Nielsen, E. L., De Rosa, R. J., Macintosh, B., et al. 2019, arXiv e-prints, arXiv:1904.05358

O'Neil, K. K., Martinez, G., Hees, A., et al. 2018, arXiv preprint arXiv:1809.05490

Öpik, E. 1924, Publications of the Tartu Astrofizica Observatory, 25, 1

Patel, R. I., Metchev, S. A., & Heinze, A. 2014, The Astrophysical Journal Supplement Series, 212, 10

Petrovich, C. 2015, Astrophysical Journal, 808, 120

Pfalzner, S., Bhandare, A., & Vincke, K. 2018, Astronomy & Astrophysics, 610, A33

Pfalzner, S., Davies, M. B., Gounelle, M., et al. 2015, Physica Scripta, 90, 068001

Pollack, J. B., Hubickyj, O., Bodenheimer, P., et al. 1996, Icarus, 124, 62

Porras, A., Christopher, M., Allen, L., et al. 2003, The Astronomical Journal, 126, 1916

Press, W. H., Flannery, B. P., Teukolsky, S. A., Vetterling, W. T., et al. 1989, Numerical recipes

Raghavan, D., McAlister, H. A., Henry, T. J., et al. 2010, The Astrophysical Journal Supplement Series, 190, 1

Rameau, J., Chauvin, G., Lagrange, A. M., et al. 2013, Astronomy & Astrophysics, 553, A60

Reche, R., Beust, H., & Augereau, J.-C. 2009, Astronomy & Astrophysics, 493, 661

Regály, Z., Dencs, Z., Moór, A., & Kovács, T. 2018, Monthly Notices of the Royal Astronomical Society, 473, 3547

Rein, H., Hernandez, D. M., Tamayo, D., et al. 2019, Monthly Notices of the Royal Astronomical Society

Rein, H. & Liu, S.-F. 2012, Astronomy & Astrophysics, 537, A128

Rein, H. & Spiegel, D. S. 2014, Monthly Notices of the Royal Astronomical Society, 446, 1424

Rein, H. & Tamayo, D. 2017, Monthly Notices of the Royal Astronomical Society, 473, 3351

Riviere-Marichalar, P., Barrado, D., Montesinos, B., et al. 2014, Astronomy & Astrophysics, 565, A68

Rodet, L., Beust, H., Bonnefoy, M., et al. 2017, Astronomy & Astrophysics, 602, A12

Rodet, L., Beust, H., Bonnefoy, M., et al. 2019, Submitted to Astronomy & Astrophysics

Rodet, L., Bonnefoy, M., Durkan, S., et al. 2018, Astronomy & Astrophysics, 618, A23

Rodriguez, J. E., Loomis, R., Cabrit, S., et al. 2018, The Astrophysical Journal, 859, 150

Russell, H. N. 1914, Popular Astronomy, 22, 331

Saha, P. & Tremaine, S. 1994, arXiv preprint astro-ph/9403057

Sahlmann, J., Ségransan, D., Queloz, D., et al. 2011, Astronomy & Astrophysics, 525, A95

Santos, N. C., Israelian, G., & Mayor, M. 2004, Astronomy & Astrophysics, 415, 1153

Siess, L., Dufour, E., & Forestini, M. 2000, Astronomy & Astrophysics, 358, 593

Snellgrove, M. D., Papaloizou, J. C. B., & Nelson, R. P. 2001, Astronomy & Astrophysics, 374, 1092

Somers, G. & Pinsonneault, M. H. 2015, Astrophysical Journal, 807, 174

Spiegel, D. S. & Burrows, A. 2012, Astrophysical Journal, 745, 174

Sumi, T., Kamiya, K., Bennett, D., et al. 2011, Nature, 473, 349

Teixeira, R., Ducourant, C., Chauvin, G., et al. 2009, Astronomy & Astrophysics, 503, 281

Teyssandier, J., Lai, D., & Vick, M. 2019, Monthly Notices of the Royal Astronomical Society, 926

Uyama, T., Hashimoto, J., Kuzuhara, M., et al. 2017, Astronomical Journal, 153, 106

van der Marel, N., Williams, J. P., Ansdell, M., et al. 2018, The Astrophysical Journal, 854, 177

van der Plas, G., Ménard, F., Gonzalez, J. F., et al. 2019, Accepted in A& A, arXiv:1902.00720

Van Leeuwen, F. 2007, Astronomy & Astrophysics, 474, 653

Vigan, A., Bonavita, M., Biller, B., et al. 2017, Astronomy & Astrophysics, 603, A3

Wagner, K., Apai, D., Kasper, M., & Robberto, M. 2015, Astrophysical Journal, Letters, 813, L2

Wagner, K., Dong, R., Sheehan, P., et al. 2018, The Astrophysical Journal, 854, 130

Walsh, K. J., Morbidelli, A., Raymond, S. N., O'Brien, D. P., & Mandell, A. M. 2011, Nature, 475, 206

Wang, J. J., Graham, J. R., Pueyo, L., et al. 2016, The Astronomical Journal, 152, 97

Winn, J. N. & Fabrycky, D. C. 2015, Annual Review of Astronomy and Astrophysics, 53, 409

Wisdom, J. 1980, Astronomical Journal, 85, 1122

Wisdom, J. 2016, Monthly Notices of the Royal Astronomical Society, 464, 2350

Wisdom, J. & Holman, M. 1991, AJ, 102, 1528

Wu, Y.-L., Close, L. M., Bailey, V. P., et al. 2016, The Astrophysical Journal, 823, 24

Wyatt, M. C. 2005, Astronomy & Astrophysics, 440, 937

Wyatt, M. C. 2018, Debris Disks: Probing Planet Formation, 146

Wyatt, M. C., Dermott, S. F., Telesco, C. M., et al. 1999, Astrophysical Journal, 527, 918

Xu, W. & Lai, D. 2017, Monthly Notices of the Royal Astronomical Society, 468, 3223

Yoshida, H. 1990, Physics letters A, 150, 262

Zhu, W., Petrovich, C., Wu, Y., Dong, S., & Xie, J. 2018, Astrophysical Journal, 860, 101

Zuckerman, B. & Song, I. 2004, Annu. Rev. Astron. Astrophys., 42, 685

Appendix

1 Definition of the orbital elements

Let there be two massive bodies of masses m_1 and m_2, interacting only through gravitational interactions. We place ourselves in a Galilean referential whose origin is at the center of mass of the two bodies (m_1+m_2). The positions of the two bodies in that referential are $\boldsymbol{R_1}$ and $\boldsymbol{R_2}$, and their relative position is $\boldsymbol{r} \equiv \boldsymbol{R_2} - \boldsymbol{R_1}$. The equations of motion writes then

$$m_1 \ddot{\boldsymbol{R_1}} = \frac{G m_1 m_2}{r^3} \boldsymbol{r} \tag{1}$$

$$m_2 \ddot{\boldsymbol{R_2}} = -\frac{G m_1 m_2}{r^3} \boldsymbol{r} \tag{2}$$

where G is the gravitational constant. These equations are equivalent to

$$m_1 \ddot{\boldsymbol{R_1}} + m_2 \ddot{\boldsymbol{R_2}} = 0 \tag{3}$$

$$\ddot{\boldsymbol{r}} = -\frac{G(m_1+m_2)}{r^3} \boldsymbol{r} \quad . \tag{4}$$

Our choice of referential implies no movement for the center of mass (Eq. 3), so that the problem is reduced to a single body problem, equivalent to the motion of one particle in an external potential (Eq. 4). We note $\mu \equiv G(m_1+m_2)$ for easier readability. From this equation, three quantities can be derived that will remain constant during the motion.

The first one is the energy E (per unit mass), obtained by integrating the scalar product between Eq. 1 and the position $\boldsymbol{r}$:

$$E = \frac{1}{2}|\dot{\boldsymbol{r}}|^2 - \frac{\mu}{r} \quad . \tag{5}$$

The second one is the angular momentum $\boldsymbol{C}$ (per unit mass), obtained by integrating the vector product between Eq. 1 and $\boldsymbol{r}$:

$$\boldsymbol{C} = \boldsymbol{r} \wedge \dot{\boldsymbol{r}} \quad . \tag{6}$$

The motion of the bodies are located in $\boldsymbol{C}$'s orthogonal plane. Taking the norm of $\boldsymbol{C}$, we retrieve Kepler's second law: $r^2\dot{\theta} = C$ is constant, where θ is the angle of the relative vector $\boldsymbol{r}$ in the plane of motion. Moreover, the *inclination* i of the

orbit is defined as the angle between $\boldsymbol{C}$ and the z axis: $\cos(i) = \boldsymbol{C}.\boldsymbol{e_z}/C$. It ranges from 0°(prograde) to 180°(retrograde). The *longitude of the ascending node* Ω is defined as the angle between the x axis and the lines of node, that is the line of intersection of the x-y plane and the plane of motion: $\cos(\Omega) = -\boldsymbol{C}.\boldsymbol{e_y}/(C\sin(i))$ and $\sin(\Omega) = \boldsymbol{C}.\boldsymbol{e_x}/(C\sin(i))$.

Finally, the third conserved quantity is the eccentricity vector (or Laplace integral), obtained by integrating the vector product between Eq. 1 and $\boldsymbol{C}$:

$$\boldsymbol{e} = \frac{\dot{\boldsymbol{r}} \wedge \boldsymbol{C}}{\mu} - \frac{\boldsymbol{r}}{r} \tag{7}$$

$\boldsymbol{e}$ is in the plane of motion (perpendicular to $\boldsymbol{C}$), and we will choose it as the reference from which the polar angle θ is measured: $\cos(\theta) = \boldsymbol{r}.\boldsymbol{e}/(re)$. It is referred to as the *true anomaly*. The angle it forms with the line of node is called the argument of the periastron ω, and is defined as $\cos(\omega) = -(\boldsymbol{C} \wedge \boldsymbol{e}).\boldsymbol{e_z}/(Ce\sin(i))$ and $\sin(\omega) = \boldsymbol{e}.\boldsymbol{e_z}/(e\sin(i))$.

From Eq. 7, taking the scalar product with $\boldsymbol{r}/r$, we obtain the equation of motion in the plane of the orbit:

$$r = \frac{C^2}{1 + e\cos(\theta)} \tag{8}$$

The relative position vector thus follows a conic section, the nature of which depends on the value of the *eccentricity* e: ellipse below 1, parabola if 1, or hyperbola above. The smaller approach between the two bodies (periastron) corresponds to $\theta = 0$, so that the eccentricity vector points toward the periastron.

The eccentricity e depends directly from the energy and angular momentum. Indeed, when we compute the vector product of $\boldsymbol{e}$ and $\boldsymbol{C}$, we obtain

$$e = \sqrt{1 + \frac{2EC^2}{\mu^2}} \quad . \tag{9}$$

The parabolic case corresponds thus to $E = 0$, the elliptic to $E < 0$, and the hyperbolic to $E > 0$. In the case of an elliptic orbit, we define the *semi-major axis* such as

$$E = \pm\frac{\mu}{2a} \tag{10}$$

With the previous relations, we can show that this is equivalent to $a = 0.5(r(\theta = 0) + r(\theta = \pi))$, which is indeed the geometrical definition of the semi-major axis of an ellipse.

Thus, we described here two ways of characterizing the trajectory of the two body motion including each five free parameters: whether E, $\boldsymbol{C}$ and the orientation of $\boldsymbol{e}$ in the plane of motion, or a, e, i, Ω and ω. To describe the evolution of the bodies on this orbit, we now need the relation between the true anomaly and the time.

Using Eq. 1 and Eq. 5, we retrieve the differential equation of r with respect to time. This equation is not directly solvable, but it is with respect to τ, which is defined as $\mathrm{d}t = r\mathrm{d}\tau$. It gives:

$$\frac{\mathrm{d}^2 r}{\mathrm{d}\tau^2} - 2Er = \mu \tag{11}$$

For elliptic orbits, we solve this equation with the initial condition at the periastron passage time $r(t_p) = a(1-e)$ and $\mathrm{d}r/\mathrm{d}\tau = 0$:

$$r = a(1 - e\cos(u)) \tag{12}$$
$$M = u - e\sin(u) \tag{13}$$

where $u = \sqrt{-2E}\tau$ is the *eccentric anomaly*, $M = \sqrt{\mu/a^3}(t - t_p)$ the *mean anomaly*, and Eq. 13 is known as the Kepler equation. The eccentric anomaly has a geometrical interpretation that is represented on Fig. 7 in the Introduction. Similar relations can be retrieved for the hyperbolic case (with hyperbolic functions and opposite signs).

2 Solving the Kepler equation

The Kepler equation is the key relation that links the temporal evolution to the geometrical evolution in the Keplerian framework. Its solution is known as series, but most of the times, iterative approaches are used. The simplest one is the fixed-point method, the Newton's method converges more efficiently, but multiple analyses have been done to improve the efficiency of the classical methods for the peculiar case of the Kepler equation. A robust one is from Danby & Burkardt (1983), that gives a very precise estimate of the root of function $f(u) = u - e\sin(u) - M$. We adopt the suggested quintic convergence: an initial guess is chosen ($u = M$ is the simplest, but many more complicated possibilities are described) and the next estimate is given by

$$u_{n+1} = u_n + \delta n3 \tag{14}$$
$$\delta_{n1} = -\frac{f}{f'} \tag{15}$$
$$\delta_{n2} = -\frac{f}{f' + \frac{1}{2}\delta_{n1} f''} \tag{16}$$
$$\delta_{n3} = -\frac{f}{f' + \frac{1}{2}\delta_{n2} f'' + \frac{1}{6}\delta_{n2}^2 f'''} \tag{17}$$

where the arguments u_n are omitted from f and its derivatives to ease the notation. For low eccentricities, only one iteration is necessary to obtain an estimate within computer round-off error. For medium eccentricity (typically 0.2 to 0.8), two iterations are performed. And for high eccentricity, three iterations are required (see Fig. 31).

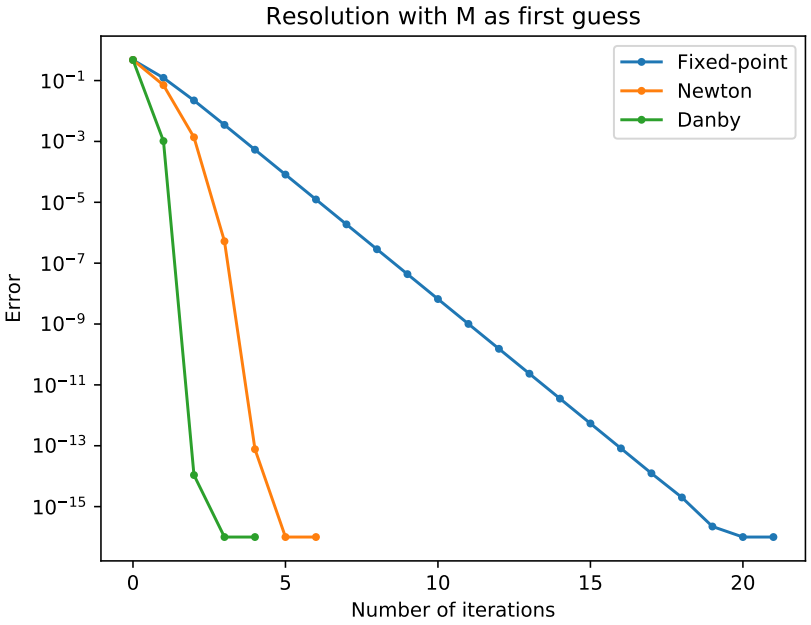

Figure 31 – Three methods to solve Kepler equation, with initial guess $u = M$, and for medium eccentricity $e = 0.5$. A more complex initial guess can reduce the number of steps by 1 or 2.

3 Perturbation by an inner companion

As an example of perturbed 2-body problem, let us compute the effect of an inner companion on the orbit of an outer body in the coplanar case. This test case is the basis of most of the analyses of system HD 106906 (Chapter 1 Sec. 3), and was used to draw the Hamiltonian maps in the Introduction (Fig. 9). The notations are described on Fig. 32.

The system is conservative, and the total Hamiltonian is, in the referential of the center of mass:

$$H = \frac{1}{2m'_1}\boldsymbol{p_1}^2 + \frac{1}{2m'_2}\boldsymbol{p_2}^2 - \frac{Gm'_1M_1}{r_1} - \frac{Gm'_2M_2}{r_2} + U \tag{18}$$

$$= -\frac{Gm'1M_1}{2a_1} - \frac{Gm'2M_2}{2a_2} + U \tag{19}$$

with

$$U = \frac{Gm'_2M_2}{r_2} - \frac{Gm_1m_3}{r_{13}} - \frac{Gm_2m_3}{r_{23}} \tag{20}$$

$$= Gm'2M_2\left(\frac{1}{r_2} - \frac{1-q}{|\boldsymbol{r_2} + q\boldsymbol{r_1}|} - \frac{q}{|\boldsymbol{r_2} - (1-q)\boldsymbol{r_1}|}\right) \tag{21}$$

where $\boldsymbol{p_1} = m'_1\dot{\boldsymbol{r_1}}$ and $\boldsymbol{p_2} = m'_1\dot{\boldsymbol{r_2}}$ following the notations of Fig. 32, and where we introduced the mass ratio $q = m_2/(m_1 + m_2)$.

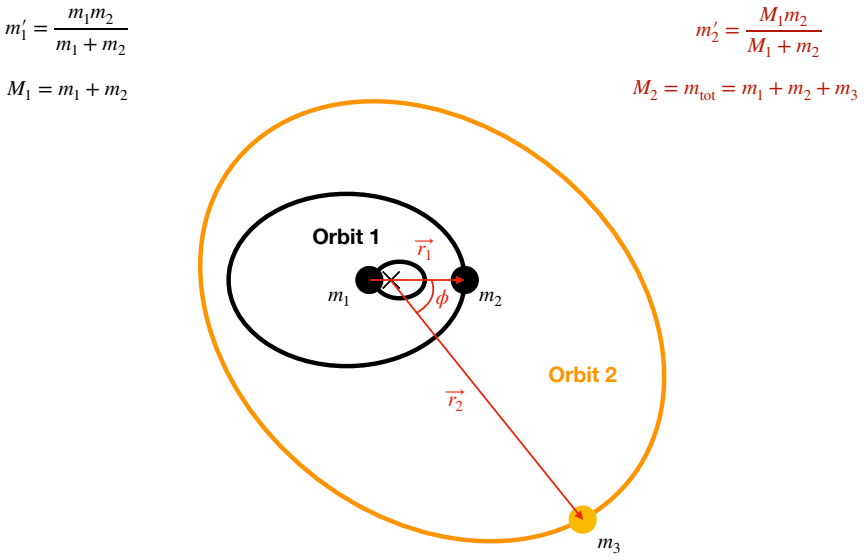

Figure 32 – Schematic of an outer body (orange) perturbed by an inner companion.

We suppose that $r_1 \ll r_2$, that is that the potential U is small with respect to the total Hamiltonian, so that the two trajectories are nearly Keplerian and the orbital elements provide a meaningful description. At the first orders in r_1/r_2, the potential is

$$U = \frac{G m_2' M_2 q(1-q)\left(1 - 3\cos(\phi)\right) r_1^2}{2 r_2^3} \tag{22}$$

$$+ \frac{G m_2' M_2 q(1-q)(1-2q)\cos(\phi)\left(3 - 5\cos^2(\phi)\right) r_1^3}{2 r_2^4} + O\left(\frac{r_1^4}{r_2^4}\right) \tag{23}$$

To use the Lagrange equations, we must express H as a function of the orbital elements. For that, we will use the following relations, derived from Sec. 4.1:

$$r_1 = \frac{a_1(1-e_1^2)}{1 + e_1\cos(\theta_1)} \tag{24}$$

$$r_2 = \frac{a_2(1-e_2^2)}{1 + e_2\cos(\theta_2)} \tag{25}$$

$$\cos(\phi) = \cos(\theta_2 - \theta_1 + \omega_2 - \omega_1) \tag{26}$$

Theoretically, we can now use the Lagrange equations. However, in practice, we are not interested in the fluctuations of the orbital elements at the time scale of one orbital period, but in the secular (long-scale) fluctuations. The secular potential is obtained by averaging over time the rapidly oscillating terms θ_1 and θ_2, and replacing the orbital elements by their mean. We suppose that the orbital periods

are not commensurable (no MMR), so that the two motions are independent and two separate integrations are performed. Recalling that the differential element $dt = d\theta r^2/\sqrt{GMa(1-e^2)}$, we obtain the average perturbation

$$\begin{aligned}\bar{U} = & -\frac{Gm_2' M_2 q(1-q)(1+\frac{3}{2}\bar{e_1}^2)\bar{a_1}^2}{4(1-\bar{e_2}^2)^{\frac{3}{2}}\bar{a_2}^3} \\ & + \frac{15Gm_2' M_2 q(1-q)(1-2q)\bar{e_1}\bar{e_2}(1+\frac{3}{4}\bar{e_1}^2)\bar{a_1}^3}{16(1-\bar{e_2}^2)^{\frac{5}{2}}\bar{a_2}^4}\cos(\bar{\omega_2}-\bar{\omega_1}) + O\left(\frac{\bar{a_1}^4}{\bar{a_2}^4}\right)\end{aligned} \tag{27}$$

where the bars designate averaged quantities This secular potential can now be used in the Lagrange equations to study the long term variation of the orbital elements. Let us suppose that the outer body does not affect the orbit of the inner body. The perturbation of orbit 2 is given by

$$\frac{\mathrm{d}\bar{a_2}}{\mathrm{d}t} = 0 \tag{28}$$

$$\frac{\mathrm{d}\bar{e_2}}{\mathrm{d}t} = -\frac{2\pi}{\bar{P_2}}\frac{15q(1-q)(1-2q)\bar{e_1}(1+\frac{3}{4}\bar{e_1}^2)\bar{a_1}^3}{16(1-\bar{e_2}^2)^2\bar{a_2}^3}\sin(\bar{\omega_2}-\bar{\omega_1}) + O\left(\frac{\bar{a_1}^4}{\bar{a_2}^4}\right) \tag{29}$$

$$\begin{aligned}\frac{\mathrm{d}\bar{\omega_2}}{\mathrm{d}t} = & \frac{2\pi}{\bar{P_2}}\frac{3q(1-q)(1+\frac{3}{2}\bar{e_1}^2)\bar{a_1}^2}{4(1-\bar{e_2}^2)^2\bar{a_2}^2} \\ & - \frac{2\pi}{\bar{P_2}}\frac{15q(1-q)(1-2q)\bar{e_1}(1+\frac{3}{4}\bar{e_1}^2)(1+4\bar{e_2}^2)\bar{a_1}^3}{16\bar{e_2}(1-\bar{e_2}^2)^3\bar{a_2}^3}\cos(\bar{\omega_2}-\bar{\omega_1}) + O\left(\frac{\bar{a_1}^4}{\bar{a_2}^4}\right)\end{aligned} \tag{30}$$

Solving the coupled differential equations for $\bar{e_2}$ and $\bar{\omega_2}$ is not straightforward, but the resolution can be performed for small e_2. The derivation is described in Wyatt (2005), and in the Appendix C of my first paper in Sec. 3 in a more complicated case with an additional outer body. In the low eccentricity approximation, the secular precession period is

$$P_w = \frac{2(1-\bar{e_2}^2)}{3q(1-q)(1+\frac{3}{2}\bar{e_1}^2)}\frac{\bar{a_2}^2}{\bar{a_1}^2}\bar{P_2} \tag{31}$$

and the amplitude of the eccentric oscillations is

$$\Delta e_{\max} = \frac{5\bar{e_1}(1+\frac{3}{4}\bar{e_1}^2)(1-2q)}{4(1+\frac{3}{2}\bar{e_1}^2)}\frac{\bar{a_1}}{\bar{a_2}} \tag{32}$$

where P_2 is the orbital period of orbit 2. As an example, the precession period induced by a 1-au eccentric ($e_1 = 0.4$) super giant on a body at 3 au is around 500 orbital periods, while a $q = 0.1$ binary star will induce a precession period of 50 orbital periods in the same situation. However, the amplitude of the oscillation is not proportional to the mass ratio, so that both situation will produce roughly the same eccentricity amplitude (around 0.1). As the secular Hamiltonian has only two degrees of freedom, $\bar{\omega_2} - \bar{\omega_1}$ and $\bar{e_2}$, the previous study can be represented by a contour map (see Fig. 9 in the Introduction)